

MATER. TEHNOL.	LETNIK VOLUME	50	ŠTEV. NO.	6	STR. P.	835–1040	LJUBLJANA SLOVENIJA	NOV.–DEC. 2016
-------------------	------------------	----	--------------	---	------------	----------	------------------------	----------------

## VSEBINA – CONTENTS

## IZVIRNI ZNANSTVENI ČLANKI – ORIGINAL SCIENTIFIC ARTICLES

<b>The microstructure of metastable austenite in X5CrNi18-10 steel after its strain-induced martensitic transformation</b> Mikrostruktura metastabilnega avstenita po pretvorbi v napetostno inducirani martenzit v jeklu X5CrNi18-10 A. Kurc-Lisiecka, W. Ozgowicz, E. Kalinowska-Ozgowicz, W. Maziarz . . . . .	837
<b>The structure and morphology of the surface of duplex layers after saturation of the base layer with carbon</b> Struktura in morfologija površine dupleks plasti po nasičenju osnovne plasti z ogljikom W. Skoneczny . . . . .	845
<b>Modeling of shot-peening effects on the surface properties of a (TiB + TiC)/Ti-6Al-4V composite employing artificial neural networks</b> Modeliranje vpliva hladnega površinskega kovanja na lastnosti površine (TiB + TiC)/Ti-6Al-4V kompozita s pomočjo umetnih nevronske mreže E. Maleki, A. Zabihollah . . . . .	851
<b>Analysis of twin-roll casting AA8079 alloy 6.35-<math>\mu</math>m foil rolling process</b> Analiza procesa valjanja 6,35 $\mu$ m folije iz zlitine AA8079 ulite med dvema valjema A. Can, H. Arıkan, K. Çınar . . . . .	861
<b>Antimicrobial modification of polypropylene with silver nanoparticles immobilized on zinc stearate</b> Protimikrobno spreminjanje polipropilena z nanodelci srebra, imobiliziranih na cinkovem stearatu G. Jandikova, P. Holcapkova, M. Hrabalíkova, M. Machovsky, V. Sedlarik . . . . .	869
<b>A new wideband negative-refractive-index metamaterial</b> Novi širokopasovni metamaterial z negativnim lomnim količnikom S. S. Islam, M. R. Iqbal Faruque, M. J. Hossain, M. T. Islam . . . . .	873
<b>Evaluation of the degree of degradation using the impact-echo method in civil engineering</b> Ocena stopnje degradacije v gradbeništvu z uporabo metode odmeva zvočnih valov D. Štefková, K. Timčáková, L. Topolář, P. Cikrle . . . . .	879
<b>Non-traditional whiteware based on calcium aluminate cement</b> Netradicionalni porcelan na osnovi kalcij aluminatnega cementa R. Sokolar . . . . .	885
<b>Behaviour of new ODS alloys under single and multiple deformation</b> Obnašanje novih ODS zlitin pri enojni in večkratni deformaciji B. Mašek, O. Khalaj, Z. Nový, T. Kubina, H. Jirkova, J. Svoboda, C. Štádl . . . . .	891
<b>Electromagnetic-shielding effectiveness and fracture behavior of laminated (Ni-NiAl<sub>3</sub>) composites</b> Učinkovitost elektromagnetne zaščite in obnašanje pri lomu laminiranega kompozita (Ni-NiAl <sub>3</sub> ) T. Yener, S. C. Yener, S. Zeytin . . . . .	899
<b>Effect of thermomechanical treatment on the intergranular corrosion of Al-Mg-Si-Type alloy bars</b> Vpliv termomehanske predelave na interkristalno korozijo palic iz zlitin Al-Mg-Si P. Sláma, J. Nacházal . . . . .	903
<b>Valorization of brick wastes in the fabrication of concrete blocks</b> Ocena odpadkov iz opeke pri proizvodnji betonskih zidakov Y. Ghernouti, B. Rabehi, T. Bouziani, R. Chaid . . . . .	911
<b>Porous magnesium alloys prepared by powder metallurgy</b> Porozne magnezijeve zlitine, izdelane s pomočjo metalurgije prahov P. Salvetr, P. Novák, D. Vojtěch . . . . .	917
<b>Influence of nano-sized cobalt oxide additions on the structural and electrical properties of nickel-manganite-based NTC thermistors</b> Vpliv dodatka nanodelcev kobaltovega oksida na zgradbo in električne lastnosti NTC termistorjev na osnovi nikeljevega manganita G. Hardal, B. Y. Price . . . . .	923
<b>Durability of alumina silicate concrete based on slag/fly-ash blends against acid and chloride environments</b> Zdržljivost betona na osnovi glinice in silikatov iz mešanice žlindra/leteči pepel na kislino in kloridno okolje R. Gopalakrishnan, K. Chinnaraju . . . . .	929

<b>The size effect of heat-transfer surfaces on boiling</b> Vpliv velikosti površin, ki prenašajo toploto na vrenje P. Kracik, M. Balas, M. Lisy, J. Pospíšil .....	939
<b>Effect of gas atmosphere on the non-metallic inclusions in laser-welded trip steel with Al and Si additions</b> Vpliv plinske atmosfere na nekovinske vključke v lasersko varjenem trip jeklu z dodatkom Al in Si A. Grajcar, M. Róžański, M. Kamińska, B. Grzegorzczak .....	945
<b>Machining parameters influencing in electro chemical machining on AA6061 MMC</b> Parametri strojne obdelave, ki vplivajo na elektrokemijsko strojno obdelavo AA6061 MMC C. J. Thankaraj Mariapushpam, D. Ravindran, M. D. Anand .....	951
<b>Modeling the deep drawing of an AISI 304 stainless-steel rectangular cup using the finite-element method and an experimental validation</b> Modeliranje globokega vleka pravokotne čaše iz AISI 304 nerjavnega jekla z metodo končnih elementov in z eksperimentalnim preverjanjem B. Sener, H. Kurtaran .....	961
<b>Surface and anticorrosion properties of hydrophobic and hydrophilic TiO<sub>2</sub> coatings on a stainless-steel substrate</b> Površinske in protikorozijske lastnosti hidrofobnih in hidrofilnih TiO <sub>2</sub> prevlek na jekleni podlagi M. Conradi, A. Kocijan .....	967
<b>Electroslag remelting: A process overview</b> Elektropretaljevanje pod žlindro – pregled procesa B. Arh, B. Podgornik, J. Burja .....	971
<b>Continuous vertical casting of a NiTi alloy</b> Vertikalno kontinuirno litje NiTi zlitine A. Stambolić, I. Anžel, G. Lojen, A. Kocijan, M. Jenko, R. Rudolf .....	981
<b>Hot tensile testing of SAF 2205 duplex stainless steel</b> Vroči natezni preskusi dupleks nerjavnega jekla SAF 2205 F. Tehovnik, B. Žužek, J. Burja .....	989
<b>STROKOVNI ČLANKI – PROFESSIONAL ARTICLES</b>	
<b>A high-efficiency automatic de-bubbling system for liquid silicone rubber</b> Visokozmogljiv sistem za odpravljanje mehurčkov v tekoči silikonski gumi C.-C. Kuo, C.-M. Huang .....	995
<b>Impact toughness of WMD after MAG welding with micro-jet cooling</b> Udarna žilavost WMD po MAG varjenju z mikro-jet hlajenjem T. Wegrzyn, J. Piwnik, A. Borek, A. Kurc-Lisiecka .....	1001
<b>Forming-limit diagrams and strain-rate-dependent mechanical properties of AA6019-T4 and AA6061-T4 aluminium sheet materials</b> Mejni diagrami preoblikovanja in odvisnost mehanskih lastnosti od hitrosti preoblikovanja aluminijevih pločevin iz AA6019-T4 in AA6061-T4 O. Çavuşoğlu, A. G. Leacock, H. Gürün .....	1005
<b>Effect of alternative heat-treatment parameters on the aging behavior of short-fiber-reinforced 2124 Al composites</b> Vpliv alternativnih parametrov toplotne obdelave na staranje 2124 Al kompozita, ojačanega s kratkimi vlakni Y. Altunpak, S. Aslan, M. Oğuz Güler, H. Akbulut .....	1011



# THE MICROSTRUCTURE OF METASTABLE AUSTENITE IN X5CrNi18-10 STEEL AFTER ITS STRAIN-INDUCED MARTENSITIC TRANSFORMATION

## MIKROSTRUKTURA METASTABILNEGA AVSTENITA PO PRETVORBI V NAPETOSTNO INDUCIRANI MARTENZIT V JEKLU X5CrNi18-10

Agnieszka Kurc-Lisiecka<sup>1</sup>, Wojciech Ozgowicz<sup>2</sup>, Elżbieta Kalinowska-Ozgowicz<sup>3</sup>,  
Wojciech Maziarz<sup>4</sup>

<sup>1</sup>Rail Transport Department, University of Dabrowa Gornicza, Ciepłaka Str. 1C, 41-300 Dabrowa Gornicza, Poland

<sup>2</sup>Institute of Engineering Materials and Biomaterials, Silesian University of Technology, Gliwice, Poland

<sup>3</sup>Fundamentals of Technology Faculty, Lublin University of Technology, Nadbystrzycka Str. 38, 20-618 Lublin, Poland

<sup>4</sup>Institute of Metallurgy and Materials Science of the Polish Academy of Sciences, Reymonta Str. 25, 30-059 Krakow, Poland  
akurc@wp.pl

*Prejem rokopisa – received: 2015-05-19; sprejem za objavo – accepted for publication: 2015-11-05*

doi:10.17222/mit.2015.102

The performed investigations concerned the influence of the degree and temperature of deformation on the microstructure of metastable austenite in the stainless steel X5CrNi18-10 after its strain-induced martensitic transformation. Samples of steel strip were cold rolled within a degree of deformation from 20 % to 70 % and stretched at a low temperature of -196 °C. The microstructure was observed by means of scanning electron microscopy (SEM) and transmission electron microscopy (TEM, HREM). It was found that after cold rolling with a small degree of deformation (20 %) in the tested steel, generally a single-phase microstructure of the matrix  $\gamma$  is found with a high density of dislocations and numerous deformation bands morphologically characteristic of stainless steel with a low stacking-fault energy. After rolling with a 50 % thickness reduction, however, the microstructure displayed deformation twins as well as refined morphologic formations of the phase  $\alpha'$ , mostly localized in the vicinity of the grain boundaries of the metastable matrix  $\gamma$ , and also trace amounts of carbide precipitates. In samples stretched at a temperature of -196 °C the microstructure of the matrix displayed a considerable density of dislocations with lath areas of the martensite  $\alpha'$  and precipitations of the carbides  $M_{23}C_6$ . Moreover, the tested steel revealed a crystallographic dependence of the planes and directions on the identified phases  $\gamma$  and  $\alpha'$ , corresponding to dependences of the Kurdjumov-Sachs type, independent of the method and temperature of the plastic deformation. Tests carried out in the TEM proved that the typical sites of nucleation induced by the plastic deformation of martensite are the shear bands, particularly their intersection. The preferred mechanism of transformation, observed in the conditions of cold rolling is, however, a direct transformation of the type  $\gamma$  (fcc)  $\rightarrow$   $\alpha'$  (bcc).

Keywords: austenitic stainless steels, cold rolling, microstructure, phase transformation, strain-induced martensite

Izvedene so bile preiskave vpliva temperature in stopnje deformacije na mikrostrukturo metastabilnega avstenita po njegovi pretvorbi v napetostno inducirani martenzit v jeklu X5CrNi18-10. Vzorci v obliki trakov so bili hladno valjani s stopnjo deformacije od 20 % do 70 % in natezani pri nizki temperaturi – 196 °C. Mikrostruktura je bila opazovana s pomočjo vrstične elektronske mikroskopije (SEM) in s presevno elektronsko mikroskopijo (TEM, HREM). Ugotovljeno je, da je po hladnem valjanju z majhno stopnjo deformacije (20 %) v preizkušnem jeklu dobljena enofazna mikrostruktura z osnovo  $\gamma$ , z visoko gostoto dislokacij in številnimi deformacijskimi pasovi, ki so morfološka značilnost nerjavnega jekla z nizko energijo napake zloga. Po valjanju s 50 % zmanjšanjem debeline, se v mikrostrukturi kažejo deformacijski dvojčki, kot tudi drobni nastanki faze  $\alpha'$ , večinoma v bližini mej zrn metastabilne osnove  $\gamma$  in tudi sledi izločkov karbidov. V vzorcih natezno obremenjenih pri temperaturi –196 °C je mikrostruktura osnove pokazala precejšnjo gostoto dislokacij z lastatimi področji martenzita  $\alpha'$  in izločki karbidov  $M_{23}C_6$ . Poleg tega je preiskovano jeklo pokazalo kristalografsko odvisnost usmerjenosti ravnin in ploskev v identificiranih fazah  $\gamma$  in  $\alpha'$ , ustrezno odvisnosti vrste Kurdjumov-Sachs, neodvisno od metode in temperature plastične deformacije. Preiskave izvedene na TEM so potrdile, da so značilna mesta nukleacije martenzita, inducirane s plastično deformacijo, strižni pasovi, posebno še njihova križanja. Prednostni mehanizem premene, opažene pri hladnem valjanju, je neposredna premena vrste  $\gamma$  (fcc)  $\rightarrow$   $\alpha'$  (bcc).

Ključne besede: avstenitna nerjavna jekla, hladno valjanje, mikrostruktura, fazna premena, napetostno inducirani martenzit

## 1 INTRODUCTION

Austenitic stainless steels are widely used in many engineering applications, such as in the chemical, machinery, food, automotive, nuclear and shipbuilding industries, due to their excellent corrosion resistance, weldability, and mechanical properties. However, some of these austenitic steels with a lower content of Ni can undergo a transformation to martensite during cold

working.<sup>1</sup> A different martensite morphology can be formed due to these processes, mainly strain-induced or stress-induced martensite.<sup>2</sup> In austenitic stainless steels two types of martensite can form spontaneously, i.e., body-centered cubic (bcc) martensite  $\alpha'$  and hexagonal close-packed (hcp) martensite  $\epsilon$ . The amount of  $\epsilon$  and/or  $\alpha'$  martensite depends on the chemical composition, stacking-fault energy, phase stability and processing parameters, such as stress state, temperature, strain rate.

During the deformation process different transformation sequences take place, such as:  $\gamma \rightarrow \varepsilon \rightarrow \alpha'$  or  $\gamma \rightarrow \alpha'$ . In the transformation mode  $\gamma \rightarrow \varepsilon \rightarrow \alpha'$ ,  $\varepsilon$  martensite acts as the precursor phase of  $\alpha'$ . The formation of  $\alpha'$  is closely related to the shear bands, which are planar defects associated with the overlapping of stacking faults on  $\{111\}\gamma$ . Depending on the nature of the overlapping, twins,  $\varepsilon$  martensite or stacking-fault bundles may be formed. Twins are formed when stacking faults overlap on successive  $\{111\}$  planes, whereas  $\varepsilon$  martensite is generated if the overlapping of the stacking faults occurs on alternate  $\{111\}$  planes. Stacking-fault bundles arise from the irregular overlapping of stacking faults.<sup>1-6</sup>

The presence of deformation-induced martensite may be a harmful phenomenon and may cause a delayed cracking of deep-drawn austenitic stainless-steel components. On the other hand, the formation of martensite resulting from the plastic deformation of metastable austenite is of great interest for the production of high-strength and ductile austenitic stainless steels.<sup>2,3</sup>

The aim of the present study was to analyze the morphological details of strain-induced martensite in cold-rolled Cr-Ni steel.

## 2 MATERIAL AND EXPERIMENTAL PROCEDURE

The investigations concerned austenitic stainless steel of the type X5CrNi18-10 in compliance with PN-EN 10088:1-2007<sup>7</sup> with the chemical composition quoted in **Table 1**. The input material in the form of steel strip, 2 mm thick, 40 mm in width and 700 mm long was supersaturated in water after its austenitizing for 1 h at a temperature of 1100 °C and cold rolled with a 20 %, 50 % and 70 % thickness reduction. After rolling with a draft of 70 %, samples of the tested steel were subjected to a tensile test at a low temperature of -196 °C with a strain rate  $\dot{\varepsilon}$  of about  $10^{-5} \text{ s}^{-1}$ .

**Table 1:** Chemical composition of the investigated steel

**Tabela 1:** Kemijska sestava preiskovanih jekel

Elements content, in mass fractions (w/%)									
C	Mn	Si	P	S	Cr	Ni	Ti	Al	Fe
0.024	1.32	0.43	0.028	0.005	18.53	7.8	0.010	0.01	bal.

The hardness measurements of the investigated cold-rolled steel were carried out with a microhardness tester FM 700 produced by Future-Tech (Japan), according to the standard PN-EN ISO 6507-1:2007.<sup>8</sup> The hardness was also determined in the case of the sample after 70 % degree and stretched at a low temperature of -196 °C with a strain rate  $\dot{\varepsilon}$  of about  $10^{-5} \text{ s}^{-1}$ . The measurements were made using the Vickers method on metallographic samples with a load of 50 N for a time of 30 s.

The microstructural investigations were performed with scanning (SEM) and transmission electron micro-

scopy, as well as high-resolution electron microscopy (HREM). Applying SEM, a metallographic polished section after cold rolling with a draft of 20 % and stretching at the temperature of liquid nitrogen was detected. These observations were made by means of SEM of the SUPRA type from Zeiss (Germany) with a magnification of 15.000 $\times$ .

The section that was mechanically polished was etched in the reagent Mi17Fe.<sup>9</sup> TEM observations were carried out using thin foils on the samples of strip after cold rolling with a draft of 50 %, and on samples stretched at a temperature of -196 °C. The preparation of the foils comprised a cutting out of disks, 3 mm in diameter, from a strip with a thickness of 1.0 and 0.6 mm, grinding with abrasive paper until the samples reached a thickness of 0.1 mm. The Tenupol-5 double jet electropolisher was used for thin foil preparation from the samples in an electrolyte containing nitric acid and methanol (1:3). The microstructure was observed by means of TEM of the type Technai G<sup>2</sup> F20 applying an accelerating voltage of 200 kV equipped with high-angle annular dark-field (HAADF) and energy-dispersive (EDS) detector. The phases were identified based on electron diffraction. The procedure was aided by the

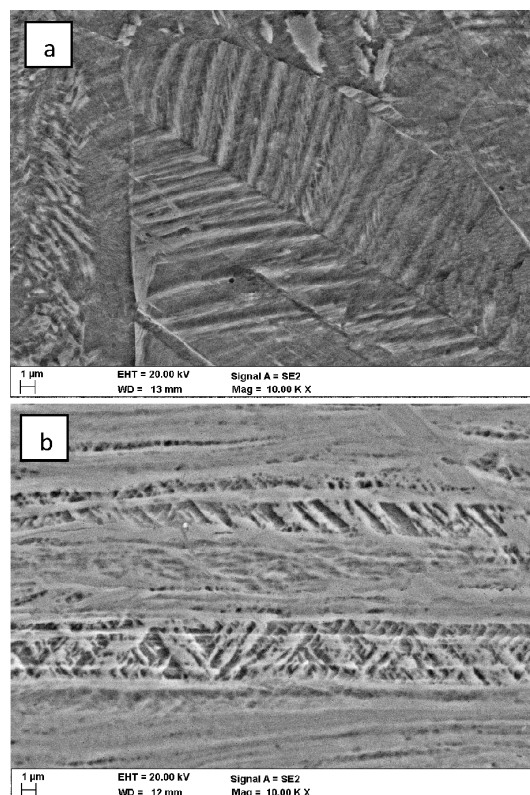


**Figure 1:** Microstructure of investigated steel X5CrNi18-10: a) after 20 % of deformation, b) after cold-rolling with 70 % and tensile test at -196 °C, etching- Mi17Fe

**Slika 1:** Mikrostruktura preiskovanega jekla X5CrNi18-10: a) po 20 % deformaciji, b) po hladnem valjanju s 70 % in nateznim preizkusom pri -196 °C, jedkano z Mi17Fe

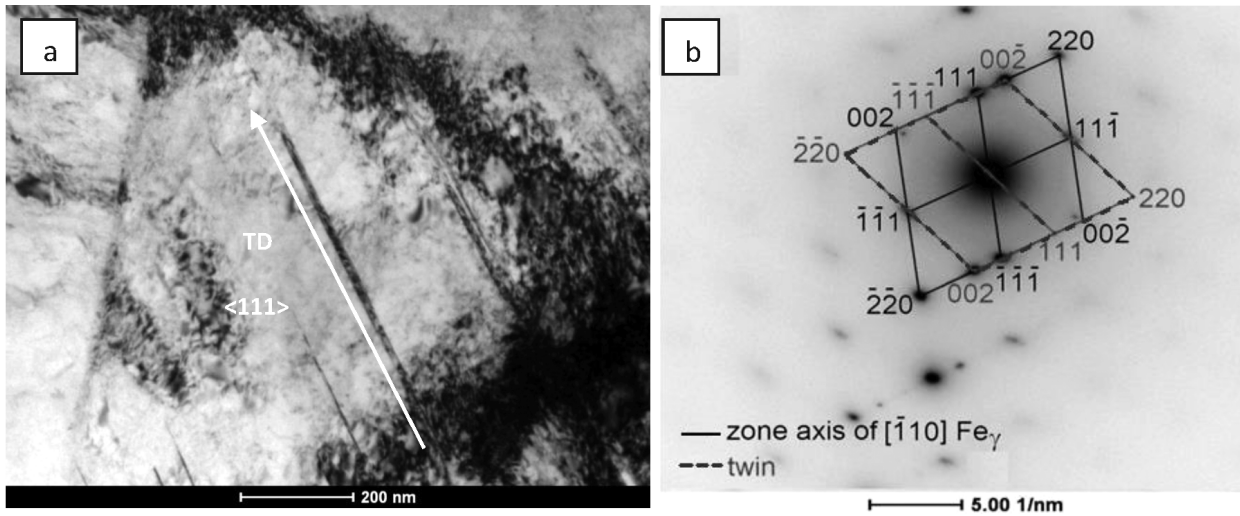


**Figure 2:** TEM micrograph of X5CrNi18-10 steel after 50 % of deformation: a) a band of austenite containing microtwins, b) diffraction pattern  
**Slika 2:** TEM-posnetek jekla X5CrNi18-10 po 5 % deformaciji: a) pas avstenita, ki vsebuje mikrovojčke, b) uklonska slika

computer software Gatan and a crystallographic database.

### 3 RESULTS AND DISCUSSION

In the supersaturated state the investigated steel displays a single-phase austenite structure with a diameter of the average grains in the matrix  $\gamma$  amounting to about 75  $\mu\text{m}$  and a hardness of about 125 HV0.5, containing many annealed twins and single clusters of non-metallic inclusions. After cold rolling in the range 20–30 % metallographically distinctly elongated grains of the matrix  $\gamma$  with a hardness of 323 HV5 (**Table 2**) could be detected with numerous effects of work hardening in the form of fine parallel and intersected lines and slip bands, as well as shear bands, which are probably sites of martensite  $\alpha'$  nucleation.

**Table 2:** Results of the hardness measurement of the investigated cold-rolled and stretched steel

**Tabela 2:** Meritve trdote preiskovanih hladno valjanih in natezanih jekel

No.	Material condition	Hardness, HV			Hardness, HV 5
		Number of measurement			
		1	2	3	
1	supersaturated	144.7	148.5	145.8	146.3
2	cold rolled $z_h=20\%$	321.5	322.7	325.9	323.4
3	cold rolled $z_h=50\%$	411.5	410.8	408.7	410.3
4	cold rolled $z_h=70\%$	418.5	417.4	418.6	418.1
5	cold rolled with $z_h=70\%$ and stretched at $-196^\circ\text{C}$	460.1	461.3	459.2	460.2

The results of the observation of the microstructure of the investigated steel after cold-rolling with a degree of deformation of 20 % and 70 % and after stretching at a temperature of  $-196^\circ\text{C}$  carried out on a scanning electron microscope (SEM) are presented in the micrographs

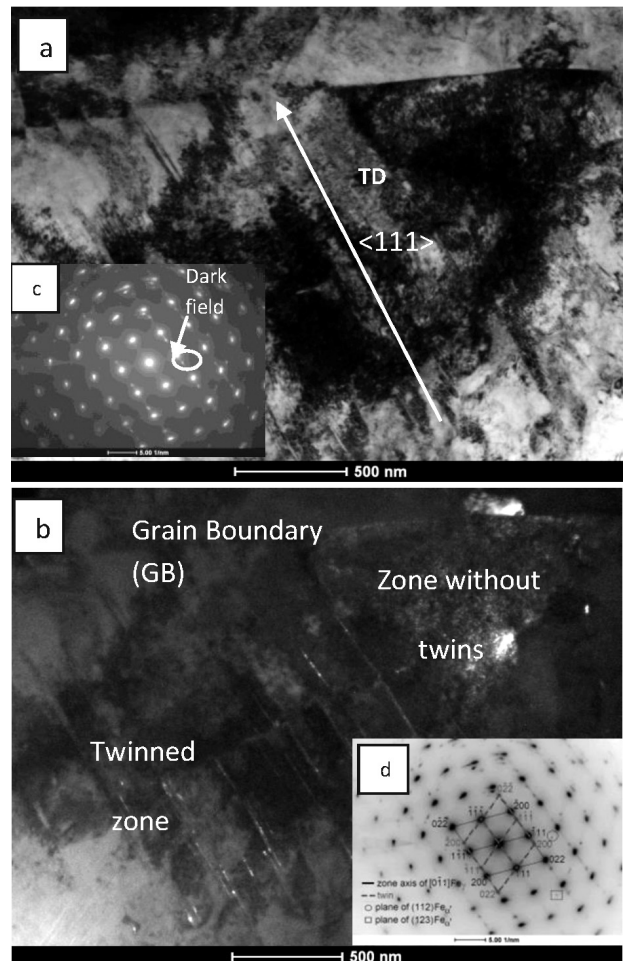


**Figure 3:** TEM micrograph structure of X5CrNi18-10 steel after 50 % of deformation: a) microstructure of the matrix  $\gamma$  containing microtwins and martensite  $\alpha'$ , b) dark field taken of reflection (200)  $\gamma$ , c), d) diffraction pattern

**Slika 3:** TEM-posnetek strukture jekla X5CrNi18-10 po 50 % deformaciji: a) mikrostruktura osnovne  $\gamma$ , ki vsebuje mikrovojčke in martenzit  $\alpha'$ , b) temno polje pri odsevu (200)  $\gamma$ , c), d) uklonska slika



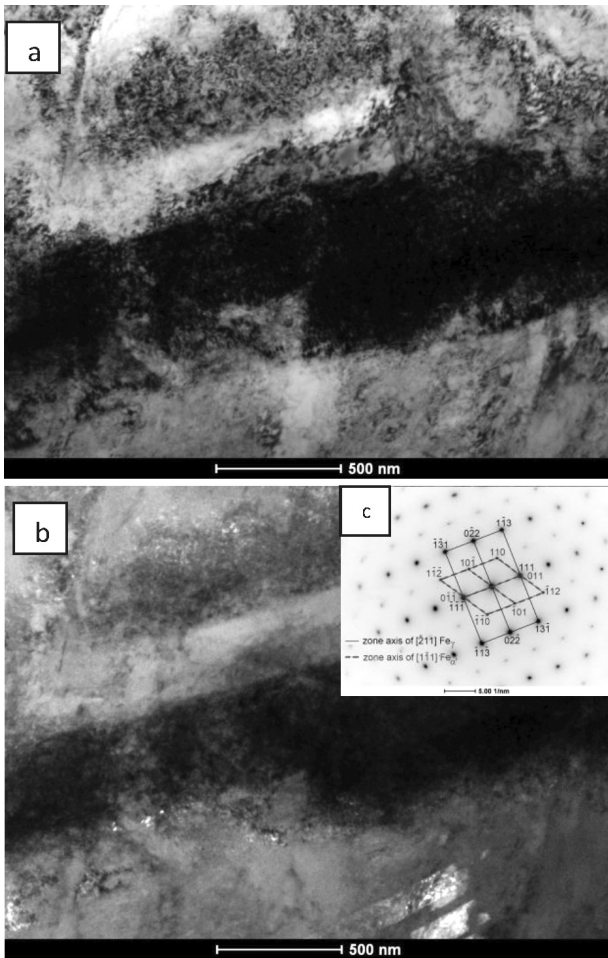


**Figure 4:** TEM micrograph structure of X5CrNi18-10 steel after 50 % of deformation: a) subgrain of austenite containing a high density of dislocations and  $\alpha'$ , bright field, b) dark field taken of the reflection  $(110)\alpha'$ , c) diffraction pattern

**Slika 4:** TEM-posnetek strukture jekla X5CrNi18-10 po 50 % deformaciji: a) podzrna avstenitna vsebujejo veliko gostoto dislokacij in  $\alpha'$ , svetlo polje, b) temno polje pri odsevu  $(110)\alpha'$ , c) uklonska slika

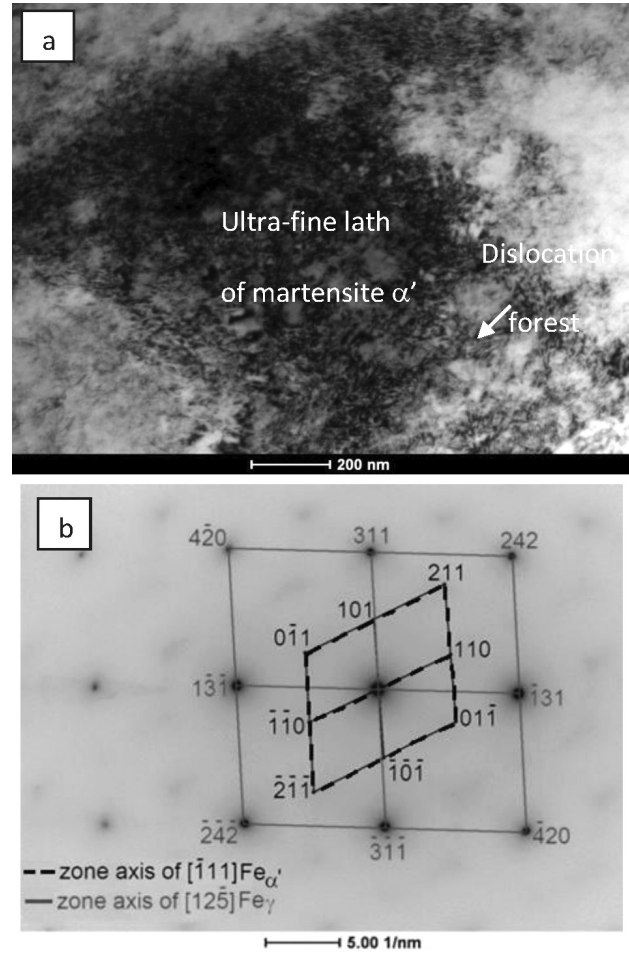


**Figure 5:** TEM micrograph structure of X5CrNi18-10 steel after 50 % of deformation: a) cell microstructure of austenite containing a variable dislocation density and ultra-fine lath of martensite  $\alpha'$ , b) diffraction pattern

**Slika 5:** TEM-posnetek strukture jekla X5CrNi18-10 po 50 % deformaciji: a) celična mikrostruktura avstenitna vsebuje različno gostoto dislokacij in ultra drobni latasti martenzit  $\alpha'$ , b) uklonska slika

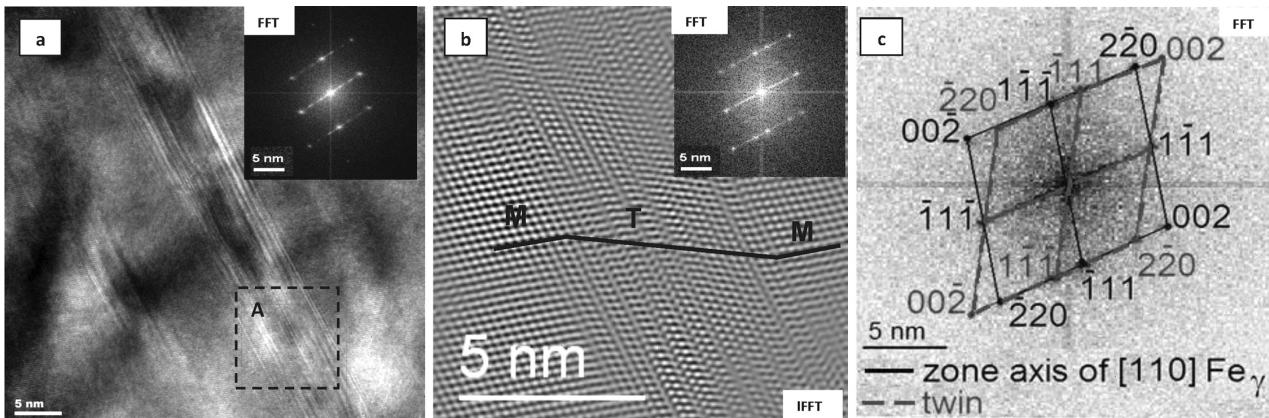


**Figure 6:** High-resolution (HREM) micrograph: a) dislocation structure of the matrix  $\gamma$  of steel B after cold rolling ( $z_h=50\%$ ) and Fourier transform (FFT), b) detail A of **Figure 6a** – modulated structure (IFFT) with microtwins bands and Fourier transform (FFT), c) solution of Fourier transform in **Figures 6a** and **6b**

**Slika 6:** Visokoločljivi posnetek (HREM): a) struktura dislokacij v osnovi  $\gamma$  jekla B po hladnem valjanju ( $z_h=50\%$ ) in Fourierjeva pretvorba (FFT), b) detajl A na **Sliki 6a** modulirana struktura (IFFT) s pasovi mikro dvojčkov in Fourierjeva pretvorba (FFT), c) rešitev Fourierjeve pretvorbe na **Slikah 6a** in **6b**

in **Figure 1**. In the structure of the steel, complex effects of deformation inside the grains  $\gamma$  and at the boundaries are revealed (**Figure 1a**). Plastic deformation leads to a distinct elongation of the grains in the direction of rolling and to the formation of numerous slide bands and shear bands, in which probably the martensite  $\alpha'$  is localized (**Figure 1b**). The hardness of the examined steel increases with an increasing degree of deformation. With the increase of the cold rolling degree from 50 % to 70 % the hardness of the investigated steel increases from 410 to 418 HV<sub>5</sub>, respectively (**Table 2**). As suggested in<sup>10,11</sup> the twins, the dislocation density, the nucleation of martensite  $\alpha'$  and the increase of the volume fraction of martensite  $\alpha'$  phase during the transformation are the major factors influencing the hardness of the investigated steel.

Heterogeneities in the plastic deformation in the form of shear bands were found mainly in the case of larger, cold plastic working and tensile tests at reduced tempe-

ratures up to  $-196\text{ }^{\circ}\text{C}$ . Thin foils in the TEM revealed in steel X5CrNi18-10, cold rolled with a degree of deformation of 50 %, a cellular structure of dislocations of an austenitic matrix with a considerable density of dislocations with local twins (**Figure 2**). Also, single reflexes of the type  $(112)\alpha'$  and  $(123)\alpha'$  were observed, resulting from the martensitic phase  $\alpha'$  (**Figure 3d**). Based on electron diffraction and the dark-field method, the localisation of the deformation twins could be identified and the direction of twinning (TD)  $\langle 111 \rangle_o$  was determined (**Figures 2b** and **3d**). In the microstructure of the investigated steel, highly elongated subgrain  $\gamma$  and shearing bands dominate, and also an ultra-fine lath of martensite  $\alpha'$  with a characteristic dislocation forest (**Figures 4** and **5**). After cold rolling, observed in high-resolution microscopy (HREM), the structure of the investigated steel reveals significant morphological details – on the nanometer scale – microbands of mechanical twinning as well as in the range of periodicity of the structure and its modulated character (**Figure 6**). The disclosed structural periodicity is reflected in the

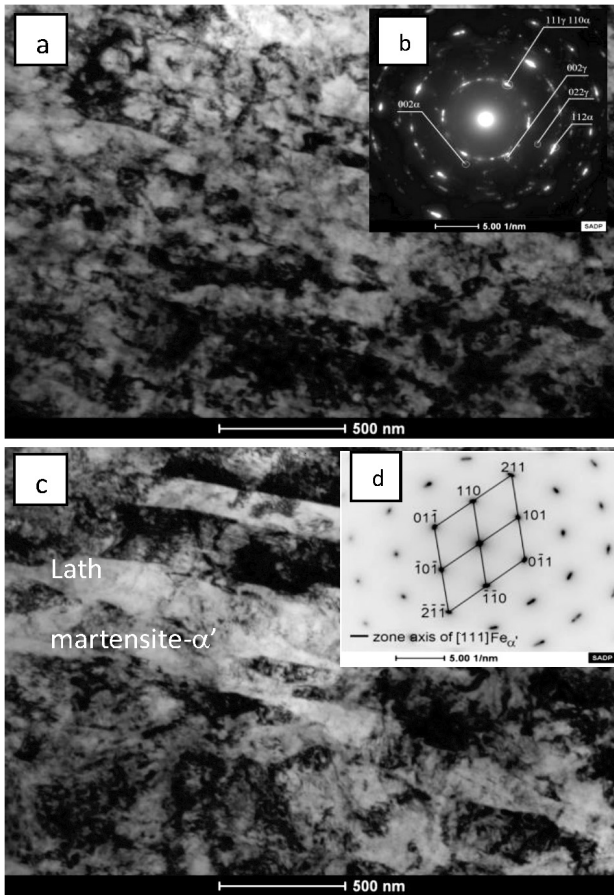


**Figure 7:** TEM micrograph structure of X5CrNi18-10 steel after cold-rolling with 70 % and tensile test at temperature of  $-196\text{ }^{\circ}\text{C}$  with a strain rate of  $10^{-5}\text{ s}^{-1}$ : a) microstructure of elongated subgrain  $\gamma$  with shear bands and heavily deformed lath of martensite  $\alpha'$ , b) diffraction pattern from (a), c) detail in **Figure a**, d) diffraction pattern from (c)

**Slika 7:** TEM-posnetek strukture jekla X5CrNi18-10 po hladnem valjanju, 70 % in nateznem preizkusu pri  $-196\text{ }^{\circ}\text{C}$ , s hitrostjo obremenjevanja  $10^{-5}\text{ s}^{-1}$ : a) mikrostruktura razpotegnjenih podzrn  $\gamma$ , s strižnimi pasovi in močno deformiranimi latami martenzita- $\alpha'$ , b) uklonska slika iz a, c) detajl iz slike a, d) uklonska slika iz c

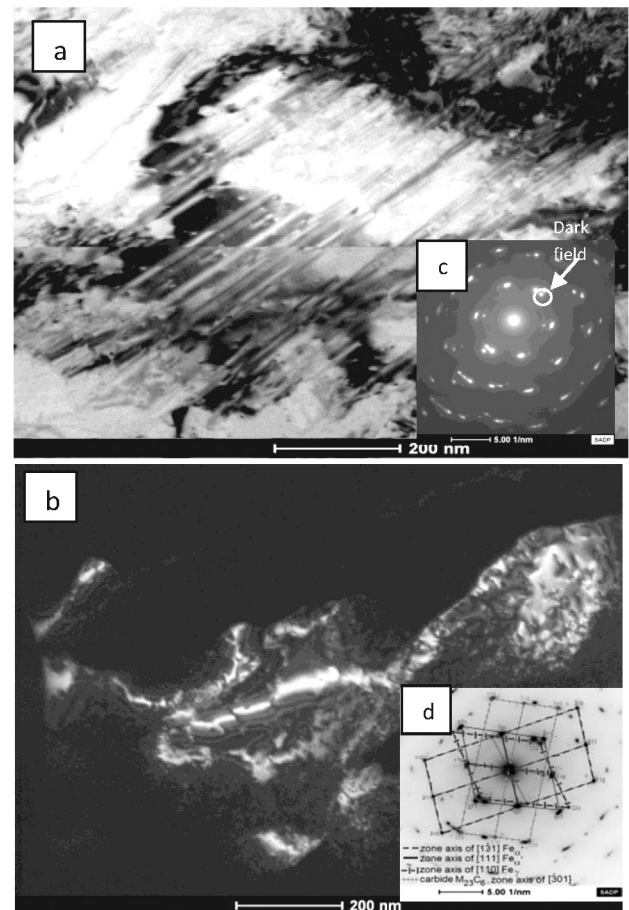


**Figure 8:** TEM micrograph structure of the X5CrNi18-10 steel: a) mechanical twins after 70 % of deformation and tensile test at temperature of  $-196\text{ }^{\circ}\text{C}$  with  $\epsilon=10^{-5}\text{ s}^{-1}$ , b) dark field in  $(002)\gamma$ , c), d) diffraction pattern

**Slika 8:** TEM-posnetek strukture jekla X5CrNi18-10: a) mehanski dvojčki po 70 % deformaciji in nateznem preizkusu pri  $-196\text{ }^{\circ}\text{C}$ , z  $\epsilon=10^{-5}\text{ s}^{-1}$ , b) temno polje pri  $(002)\gamma$ , c), d) uklonska slika



distribution of the atomic cores in the inverse Fourier transform (IFFT) (**Figure 6c**). High-resolution analysis of the sequence of microtwin bands (**Figure 6a**) and the corresponding Fourier transforms (FFT), comprising the entire area of HREM (**Figure 6b**) and the marked area of the microstructure (**Figure 6c**) justify the statement that the visible and most intense reflections result mainly from the matrix  $\gamma$  oriented as a zone axis of orientation  $[011]$  (**Figure 6b**). The additional weak reflections between the reflections of the planes  $(002)\gamma$  and  $(1\bar{1}\bar{1})\gamma$  can be attributed to the deformation twins (**Figure 6b**). However, the presence of two weak reflections between the beam passing  $(000)$  and the planes  $(\bar{1}\bar{1}\bar{1})\gamma$  and  $(1\bar{1}\bar{1})\gamma$ , dividing these distances into three equal parts with a length of  $1/3 (\bar{1}\bar{1}\bar{1})\gamma$ , require an explanation. The presence of these reflections is not justified, however, in the case of twin orientations.<sup>12</sup> In the transform (FFT) concerning the area of the band of microtwins (**Figure 6c**) there is a twin orientation with strong defocusing reflections in the planes  $(1\bar{1}\bar{1})\gamma$ . The inverse Fourier transform resulting from a transform (FFT) (**Figure 6c**) after filtering out the noise reveals that in the matrix  $\gamma$  (M-matrix) a microtwin (T-twin) is located with a width of about 5 nm, inside which the modulation effects are visible. Modulations are caused by periodic sequences of stacking faults occurring on the following planes  $(1\bar{1}\bar{1})\gamma$  (**Figure 6d**).

The investigated cold-rolled steel with the degree of deformation of 70 % and then subjected to a tensile test at strain rate ( $\dot{\epsilon}$ ) of about  $10^{-5} \text{ s}^{-1}$  at cryogenic temperatures  $-196 \text{ }^\circ\text{C}$  displayed – similar to the cold-rolling – a subgrain structure elongated in the rolling direction with a high density of dislocations (**Figure 7**) and a considerably higher density of microtwinning (**Figure 8**). The hardness in these areas reaches about 460 HV5 (**Table 2**). The subgrain boundaries and the microtwins constitute potential locations for the phase  $\alpha'$ , in the form of elongated lamellar areas with a width of approximately  $0.1 \mu\text{m}$  (**Figure 7b**). It can be assumed that the nucleation of the phase  $\alpha'$  occurs preferentially in microtwins areas, mainly at their borders. It is significantly associated with the accumulation of the stress in a dislocation field, as suggested in<sup>11</sup>. Electron-diffraction analysis of the investigated steel not only provides evidence for the presence in its structure of martensitic phase  $\alpha'$  (**Figures 3d, 4b, 5b, 7a, 7b and 8d**) and  $\text{M}_{23}\text{C}_6$  type carbides (**Figure 8d**), but also the occurrence of a crystallographic relationship between the matrix  $\gamma$  and phase  $\alpha'$  type K-S, namely:  $(111)\gamma \parallel (011)\alpha'$  and  $\langle 011 \rangle_\gamma \parallel \langle 111 \rangle_{\alpha'}$  (**Figure 4b**), also quoted with respect to similar grades of Cr-Ni steel.<sup>11,13</sup>

#### 4 CONCLUDING REMARKS

The structural investigations of the steel X5CrNi18-10 conducted in a TEM and the analysis of

the obtained results allows us to draw the following conclusions:

The plastic deformation of the investigated steel X5CrNi18-10 induces the direct transformation of metastable austenite to the deformation martensite  $\alpha'$  of the (bcc) lattice during both the cold-rolling process, as well as the tensile test at temperatures lowered to  $-196 \text{ }^\circ\text{C}$ .

The microstructure of the investigated steel after cold rolling with a degree of deformation in the range from 50 % to 70 % observed in the TEM, displays a high dislocation density in the matrix  $\gamma$  and the presence of mechanical twins, as well as shearing bands in the area where the lamellar formations of the martensite  $\alpha'$  phase nucleate.

The cold rolling and stretching at low temperature of the austenitic stainless-steel sheets resulted in the occurrence of the strain-induced  $\gamma \rightarrow \alpha'$  phase transformation. During plastic deformation the volume fraction of martensite  $\alpha'$  phase increases, which causes the hardening of the investigated steel. The hardness of the cold-rolled steel within the draft from 20–70 % is from the range 323–418 HV5, whereas in the case of samples after 70 % degree of cold rolling and stretching at  $-196 \text{ }^\circ\text{C}$  it is about 460 HV5.

High-resolution electron microscopy (HREM) of the microstructure revealed essential morphological details of the resulting microbands of twins on the nanometer scale. The application of Fourier's reverse transform (IFFT) indicated a periodicity of the analyzed structure and its modulated character in the range of appearing sequentially, the local disorder of the crystalline lattice.

The transformations  $\gamma \rightarrow \alpha'$  of the investigated steel induced by plastic deformation indicate a typical crystallographic relationship between austenite and martensite  $\alpha'$  given by Kurdjumov-Sachs, in the form:  $(111)_\gamma \parallel (011)_{\alpha'}$  and  $\langle 011 \rangle_\gamma \parallel \langle 111 \rangle_{\alpha'}$ .

#### Acknowledgements

The authors gratefully acknowledge financial support from the research project: Innovative sanitary sewage system DEMONSTRATOR + NCBR under the contract No. UOD-DEM-1-591/001.

#### 5 REFERENCES

- <sup>1</sup> K. H. Lo, C. H. Shek, J. K. L. Lai, Morphologies and characteristics of deformation induced martensite during tensile deformation of 304 LN stainless steel, *Materials Science and Engineering*, 65R (2009) 4–6, 39–104, doi:10.1016/j.msea.2007.09.005
- <sup>2</sup> A. Das, S. Sivaprasad, M. Ghosh, P. C. Chakraborti, S. Tarafder, Morphologies and characteristics of deformation induced martensite during tensile deformation of 304 LN stainless steel, *Materials Science and Engineering*, 486A (2008), 283–286, doi:10.1016/j.msea.2007.09.005
- <sup>3</sup> J. Huang, X. Ye, Z. Xu, Effect of Cold Rolling on Microstructure and Mechanical Properties of AISI 301LN Metastable Austenitic Stain-

- less Steels, *Journal of Iron and Steel Research International*, 19 (2012) 10, 59–63, doi:10.1016/S1006-706X(12)60153-8
- <sup>4</sup> C. J. Gunter, R. P. Reed, *Transaction of American Society for Metals*, 55 (1962) 3, 399–419
- <sup>5</sup> S. Rajasekhara, L. P. Karjalainen, A. Kyröläinen, P. J. Ferreira, *Microstructure evolution in nano/submicron grained AISI 301LN stainless steel*, *Materials Science and Engineering*, 527A (2010), 1986–1996, doi:10.1016/j.msea.2009.11.037
- <sup>6</sup> T. Angel, *Journal of the Iron and Steel Institute*, 177 (1954), 165–174
- <sup>7</sup> European Standard, *Stainless Steels - Part 1: List of stainless steels*, Polish version PN-EN 10088:1-2007
- <sup>8</sup> European Standard, *Metals. Hardness measurements made by Vickers's method*, Polish version PN-EN ISO 6507-1:2007
- <sup>9</sup> ASTM E407, *Standard Practice for Microetching Metals and Alloys*
- <sup>10</sup> W. S. Lee, C. F. Lin, *The morphologies and characteristics of impact-induced martensite in 304L stainless steel*, *Scripta Materialia*, 43 (2000) 8, 777–782, doi:10.1016/S1359-6462(00)00487-5
- <sup>11</sup> J. A. Venables, *The martensite transformation in stainless steel*, *Philosophical Magazine*, 73 (1962) 7, 35–44, doi:10.1080/14786436208201856
- <sup>12</sup> W. Maziarz, *Structure changes of Co–Ni–Al ferromagnetic shape memory alloys after vacuum annealing and hot rolling*, *Journal of Alloys and Compounds*, 448 (2008) 1–2, 223–226, doi:10.1016/j.jallcom.2006.12.044
- <sup>13</sup> M. Blicharski, S. Gorczyca, *Structural inhomogeneity of deformed austenitic stainless steel*, *Metal Science*, 12 (1978) 7, 303–312, doi:10.1179/msc.1978.12.7.303





# THE STRUCTURE AND MORPHOLOGY OF THE SURFACE OF DUPLEX LAYERS AFTER SATURATION OF THE BASE LAYER WITH CARBON

## STRUKTURA IN MORFOLOGIJA POVRŠINE DUPELKS PLASTI PO NASIČENJU OSNOVNE PLASTI Z OGLJIKOM

Władysław Skoneczny

University of Silesia, Ul. Żytnia 10, 41-200 Sosnowiec, Poland  
Wladyslaw.Skoneczny@us.edu.pl

*Prejem rokopisa – received: 2015-05-29; sprejem za objavo – accepted for publication: 2015-12-15*

doi:10.17222/mit.2015.108

The paper presents a new method of obtaining aluminium-oxide-based, duplex-type layers. In the first stage, the base layer is produced via the hard anodising of aluminium alloys in order to obtain the optimal structural and morphological properties. Following anodising, the samples with an  $Al_2O_3$  layer are rinsed in distilled water in order to remove the electrolyte. Graphite was introduced into the structure of aluminium oxide during a thermal treatment in a solid medium consisting of graphite dust. Afterwards, the properties of the obtained layers were determined using a scanning electron microscope, a transmission electron microscope and an atomic force microscope (AFM), as well as X-ray diffraction. The structure of the duplex-type layers contains carbon and other precipitates, which are typical for an alloy with additions of Fe, Mn, Cr and other elements. Carbon precipitates have a relatively weak connection with the matrix, as an envelope with numerous discontinuities forms around each carbon precipitate. Carbon precipitates are considerably larger than alloy precipitates, have micrometre dimensions, occur in groups and are composed of small grouped nanometric particles that form larger agglomerates. This means that there are nanometric particles inside the micrometric ones.

Keywords: aluminium alloys, nano-layers, SEM, AFM, EDS

Članek predstavlja novo metodo za izdelavo dupleksne plasti aluminijevega oksida. V prvi stopnji se izdelava osnovna plast s trdim anodiziranjem aluminijevih zlitin, da se dobi optimalno strukturo in morfološke lastnosti. Po anodizaciji so vzorci z  $Al_2O_3$  plastjo potopljeni v destilirano vodo, da se izpere elektrolit. V strukturo aluminijevega oksida se uvede grafit med toplotno obdelavo v trdem mediju, ki je vseboval grafitni prah. Potem so bile določene lastnosti dobljenih plasti, s pomočjo vrstičnega elektronskega mikroskopa, presevnega mikroskopa in mikroskopa na atomsko silo (AFM), kot tudi z rentgensko difrakcijo. Struktura dupleksnih plasti je vsebovala izločke ogljika in druge izločke, ki so značilni za zlitine, z dodatkom Fe, Mn, Cr in drugih elementov. Izločki ogljika imajo relativno šibko povezavo z osnovo, saj nastaja okrog vsakega izločka ogljika ovojnica s številnimi diskontinuitetami. Izločki ogljika so mnogo večji kot izločki zlitin, imajo mikrometrске dimenzije, se pojavljajo v skupinah in so sestavljeni iz malih gruč nanometričnih delcev, ki tvorijo večje skupke. To pomeni, da so znotraj mikrometrskih delcev prisotni nanometrski delci.

Ključne besede: aluminijeve zlitine, nanoplasti, SEM, AFM, EDS

## 1 INTRODUCTION

Aluminium alloys and the composite layers formed on them are widely used in engineering (components of heat engines and power machines, in aircraft and space industries) owing to their very good thermal conductivity, low density and high strength.

Oxide layers obtained via hard anodising may, to a large degree, change their properties, depending on the process conditions. Thanks to their characteristic porous structure,  $Al_2O_3$  layers can be used in a number of technology fields. Oxide coatings have been used in surface engineering as protective-decorative or electro-isolating layers for many years. In recent years,  $Al_2O_3$  layers have been used for the sliding couples in heat engines:<sup>1-6</sup>

- cylinder bearing surfaces in lubricant-free compressors,
- combustion-engine pistons,
- cylinder bearing surfaces in lubricant-free pneumatic servo-motors,

- shock-absorber components.

One of the most recent applications of oxide layers are the moulds used for producing nano-elements with a diameter of 4–200 nm.<sup>7</sup>

Machine components produced from aluminium or its alloys with a specially prepared surface layer are used more and more frequently. The main arguments for broadening the scope of applications for aluminium-oxide-based, duplex-type layers in surface engineering are as follows:

- easy access to devices and very inexpensive operation,
- the possibility of conducting a surface treatment on all Al groups and its alloys,
- high efficiency of the duplex-type treatment,
- the possibility of obtaining electro-isolating and protective-decorative coatings, as well as hard, abrasion-resistant layers,
- satisfactory quality of the surface after processing,

- the possibility of forming surface layers with a gradient, composite and, first of all, an amorphous structure.

The wear of materials used in machine building takes place mostly on the surface and determines the operational durability of a given appliance. The past few years have been a period of intensive development in state-of-the-art, duplex, hybrid technologies. It seems that only a combination of different surface-engineering technologies, which is the foundation of the duplex technology can lead to surfaces with versatile qualities that are to meet the requirements of modern technology. As the name indicates, the duplex technology involves a sequential application of two defined surface-engineering technologies to produce a surface composed of combined properties, unattainable by any other individual form of surface engineering.

This paper presents a wide range of possibilities to shape the properties of aluminium-oxide-based surface layers using the duplex method.

For technological reasons, hard anodising is applied for lubricant-free sliding couples. The most widespread method so far has been anodising in sulphuric or oxalic acids at lowered temperatures, from 263 K to 278 K, depending on the type of electrolyte. Therefore, research has been conducted for years on anodizing at elevated temperatures. The purpose of the research has been to apply such an electrolyte that would make it possible to obtain hard oxide layers at room temperature. Elimination of the electrolyte cooling stage would considerably reduce the cost of producing oxide coatings. It would be possible if hard anodising could be conducted at temperatures of 293–313 K and higher. At the same time, coatings with better properties could be obtained owing to the  $\text{Al}_2\text{O}_3$  oxide phase transition at a temperature of 293 K. An increase in temperature accompanying the oxidation process is conducive to etching aluminium oxide fibres. As a consequence, an oxide cell of a more regular (ideal) structure is formed.<sup>1,8,9</sup> Increasing the electrolyte temperature would also have a considerable effect on the porosity of the oxide coating.<sup>1-4</sup> The porosity of the obtained oxide layers is of major importance to their utilisation for a sliding interaction with plastic materials.

Adding organic substances with surface-active properties to the electrolyte has a large influence on the mechanism of the formation of oxide coatings on aluminium. The mechanism of the influence of organic substances depends on the properties of the addition and on the composition and properties of the electrolyte. A supposition can be made that under proper conditions, surface-active substances fully or partly cover the surface of the anode (on active places), as a result of which the oxidation of aluminium is considerably hindered. On the other hand, the adsorption of organic substances at the anode – the electrolyte interface causes the secondary dissolution of the layer by the electrolyte to stop. The role of this mechanism is performed precisely by the

addition of the above-mentioned organic (dicarboxylic) acids. The method developed in the Division of Upper Layer Technologies, University of Silesia, does not require cooling and the process heat is used to control the properties of the obtained oxide coatings. Controlling anodising parameters allows, within some limits, programming the selected functional properties of future upper layers.<sup>3-12</sup>

The above-mentioned method consists of oxidising aluminium and its alloys in three-component electrolytes. Dicarboxylic acid is added to the mixture of sulphuric and oxalic acids. These acids have an aliphatic chain of various lengths in their structure and are arranged in a row:

- 1) malonic acid -  $\text{CH}_2(\text{COOH})_2$
- 2) succinic acid -  $(\text{CH}_2)_2(\text{COOH})_2$
- 3) glutaric acid -  $(\text{CH}_2)_3(\text{COOH})_2$
- 4) adipic acid -  $(\text{CH}_2)_4(\text{COOH})_2$
- 5) pimelic acid -  $(\text{CH}_2)_5(\text{COOH})_2$
- 6) suberic acid -  $(\text{CH}_2)_6(\text{COOH})_2$
- 7) azelaic acid -  $(\text{CH}_2)_7(\text{COOH})_2$
- 8) sebacic acid -  $(\text{CH}_2)_8(\text{COOH})_2$
- 9) phthalic acid -  $\text{C}_6\text{H}_4(\text{COOH})_2$ .

## 2 EXPERIMENTAL PART

The hard anodising method developed in the Division of Upper Layer Technologies, University of Silesia, is the basis for the production of surface layers from aluminium oxide by means of duplex methods. It enables the control of process parameters, which allows, within some limits, programming the selected functional properties of the obtained upper layers. According to the method proposed, anodising is conducted in a three-component water electrolyte that consists, of among others, sulphuric and oxalic acids as well as an addition of succinic acid. Research was carried out on the aluminium alloy  $\text{AlMg}_2$ . The electrolyte temperature during anodising falls within the range 293–313 K, whereas the anodic density of current was between 2  $\text{A}/\text{dm}^2$  and 4  $\text{A}/\text{dm}^2$ . Such a range of temperatures means that the anodising process can be initiated at an ambient temperature. Tests of the structure and morphology of the surface of  $\text{Al}_2\text{O}_3$  layers were conducted using a Philips XL30 scanning microscope (SEM).

An atomic force microscope (AFM) of the VEECO company, MULTOMODE model, operating in the standard contact mode, was used for the examination of the micro-unevennesses of the obtained oxide layers via the electrochemical method in three-component electrolytes after graphite saturation.

A DRON-2 diffractometer was used for an X-ray phase analysis of the obtained  $\text{Al}_2\text{O}_3$  and duplex layers.

$\text{Al}_2\text{O}_3$  layers have a columnar (fibrous) structure, which is shown in **Figure 1**.

The technology of obtaining duplex layers based on aluminium oxide consists of a two-stage production

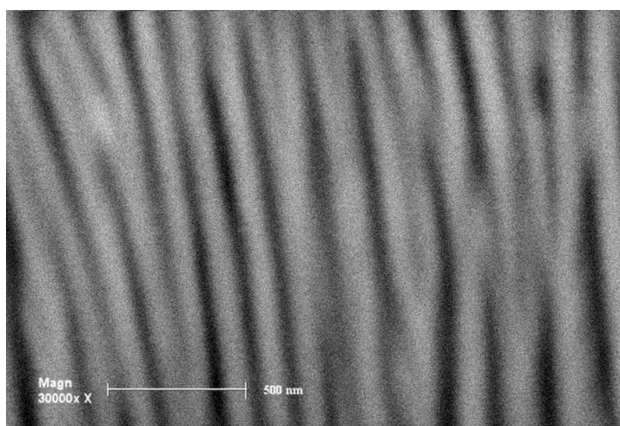


**Figure 1:** Cross-sectional SEM image a columnar-fibrous structure of an oxide layer

**Slika 1:** SEM-posnetek preseka stebrasto-vlaknaste zgradbe oksidne plasti

process. In the first stage, the base layer is produced via hard anodising in order to obtain the optimal structural and morphological properties (gradient structure and high porosity). Prior to the oxidation process, the samples are etched for 40 min in a 5 % solution of KOH and next, in order to reverse the etching reaction, tinned for 10 min in a 10 % HNO<sub>3</sub> solution. The etching and tinning processes are followed by rinsing in distilled water. In the first phase, the surfaces are subjected to anodic oxidation in an electrolyte composed of an aqueous solution of sulphuric, succinic and oxalic acid. Following anodising, the samples with an Al<sub>2</sub>O<sub>3</sub> layer are rinsed in distilled water in order to rinse out the electrolyte. Graphite was introduced into the structure of the aluminium oxide during the thermal treatment in a solid medium consisting of graphite dust. Samples sprinkled with graphite dust are tightly closed in boxes and heated in an electric oven at the following temperatures: (343, 363, 383 and 403) K for (24, 36 and 48) h for each temperature. When the process ends, the samples were cleaned with compressed air.

### 3 RESULTS AND DISCUSSION

A fibrous structure causes micro- and nanoporosity of the Al<sub>2</sub>O<sub>3</sub> layer. An example of the morphology of the surface of the Al<sub>2</sub>O<sub>3</sub> layers, obtained via hard anodising, is shown in **Figure 2**.

The measurement results of the diameter of fibres and the number of fibres and nanopores are juxtaposed in **Table 1**.

Tests of the structure of the duplex-type layers after graphite infiltration were conducted using a transmission electron microscope. The results of the tests of the structure of duplex-type layers after carbonisation of the Al<sub>2</sub>O<sub>3</sub> layers via saturation are presented in **Figures 3** and **4**. An analysis of the chemical composition was also made using a Philips XL30 scanning electron microscope with an EDS attachment. The results of the tests of

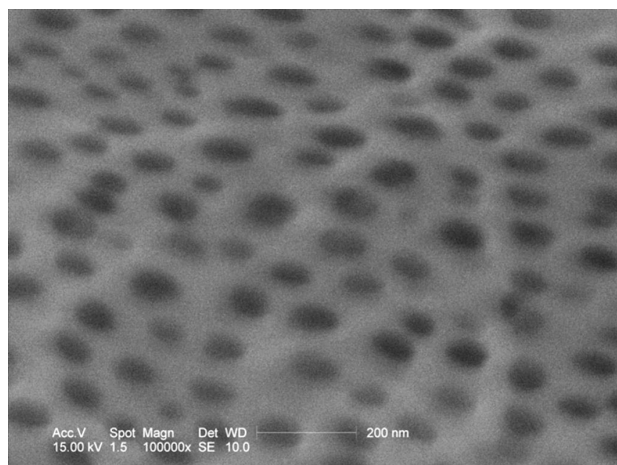


**Figure 2:** SEM image of nanopores in the Al<sub>2</sub>O<sub>3</sub> layer

**Slika 2:** SEM-posnetek nanopor v plasti Al<sub>2</sub>O<sub>3</sub>

**Table 1:** The dimensions, the number of fibres and the number of pores

**Tabela 1:** Dimenzije, število vlaken in število por

Production parameters	Fibre diameter (nm)	Number of fibres per mm <sup>2</sup>	Number of pores per mm <sup>2</sup>
j= 2 A/dm <sup>2</sup> t = 293 K	100	100 × 10 <sup>6</sup>	200 × 10 <sup>6</sup>
j= 2 A/dm <sup>2</sup> t = 303 K	120	64 × 10 <sup>6</sup>	128 × 10 <sup>6</sup>
j= 2 A/dm <sup>2</sup> t = 313 K	200	25 × 10 <sup>6</sup>	50 × 10 <sup>6</sup>
j= 3 A/dm <sup>2</sup> t = 293 K	110	81 × 10 <sup>6</sup>	162 × 10 <sup>6</sup>
j= 3 A/dm <sup>2</sup> t = 302 K	140	49 × 10 <sup>6</sup>	98 × 10 <sup>6</sup>
j= 3 A/dm <sup>2</sup> t = 303 K	160	36 × 10 <sup>6</sup>	72 × 10 <sup>6</sup>

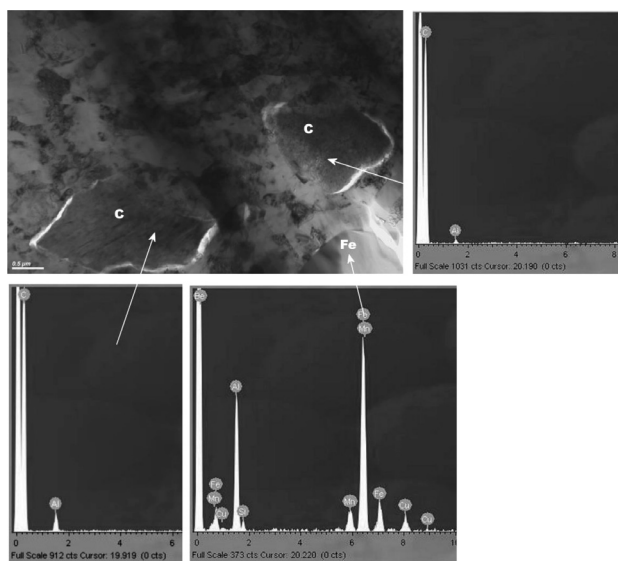


**Figure 3:** Top view of the surface of a duplex-type layer after saturation with graphite, with spectra (transmission microscope)

**Slika 3:** Slika površine dupleksne vrste plasti po nasičenju z grafitom, s spektri (presevni mikroskop)



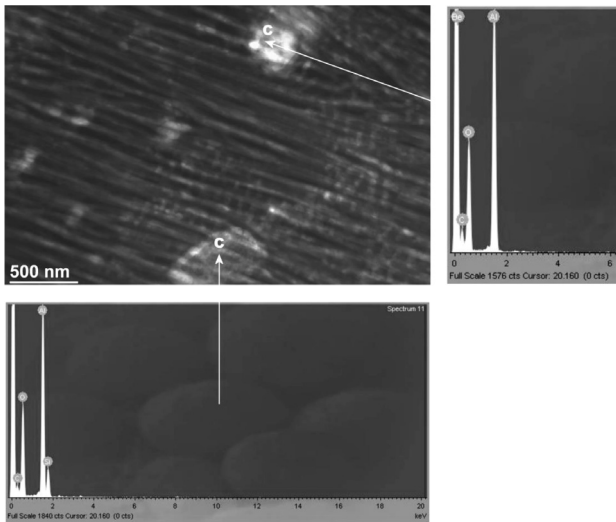


**Figure 4:** Cross-sectional of a duplex-type layer after saturation with graphite, with spectra (transmission microscope)  
**Slika 4:** Presek dupleksne plasti po nasičenju z grafitom, s spektri (presevni mikroskop)

the change in the chemical composition of these layers obtained during carbonisation at the temperatures of 383 K are presented in **Figure 5**.

The structure of the duplex-type layers contains carbon and other precipitates, which are typical for the

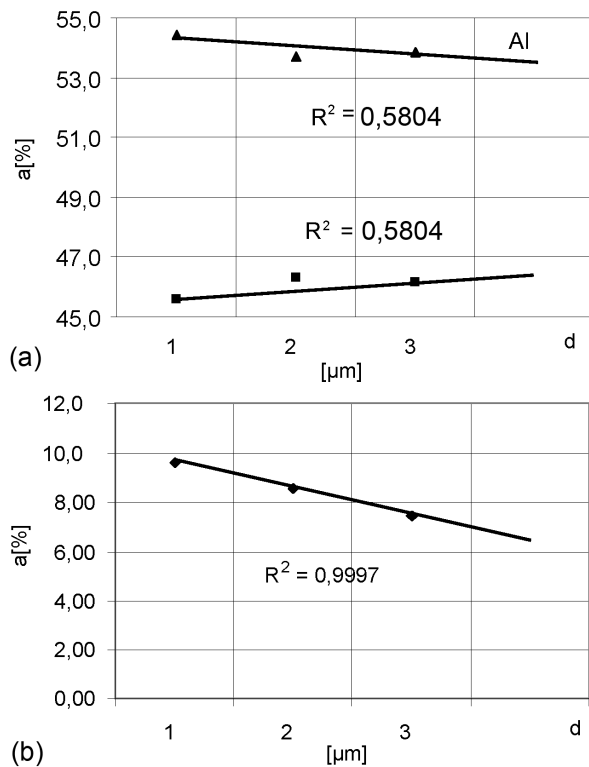


**Figure 5:** Changes in the chemical composition of duplex-type layers obtained after saturation at the temperature of 383 K: a) change in the oxygen and aluminium content, b) change in the graphite content  
**Slika 5:** Spreminjanje kemijske sestave dupleksne plasti, dobljene po nasičenju na temperaturi 383 K: a) spreminjanje vsebnosti kisika in aluminija, b) spreminjanje vsebnosti grafita

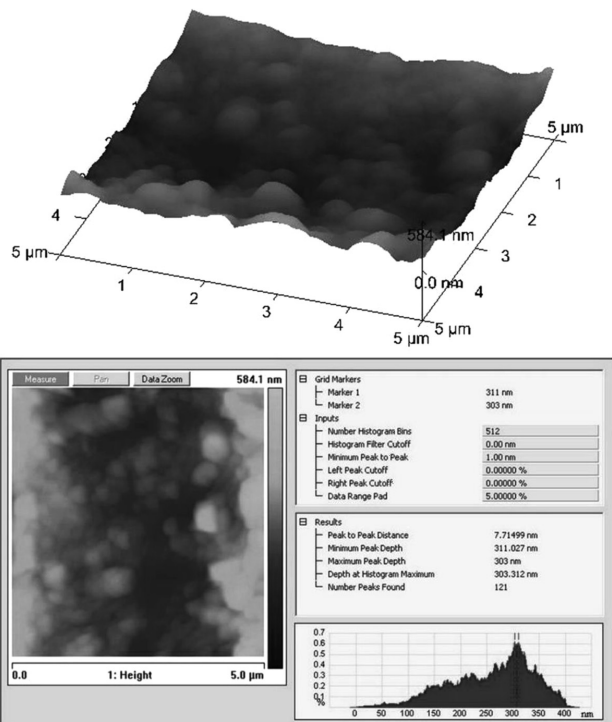


**Figure 6:** a) AFM images of the surface (3D) of duplex-type layers and b) micro-unevennesses of the surface, and a histogram; anodising process parameters:  $j = 3 \text{ A/dm}^2$ ,  $T = 303 \text{ K}$ ,  $t = 1 \text{ h}$ ; carburisation parameters:  $T = 343 \text{ K}$ ,  $t = 24 \text{ h}$

**Slika 6:** a) AFM-posnetek površine (3D) dupleksnih plasti in b) mikro-neravnine na površini in histogram s parametri procesa anodizacije:  $j = 3 \text{ A/dm}^2$ ,  $T = 303 \text{ K}$ ,  $t = 1 \text{ h}$ ; parametri naogljčenja:  $T = 343 \text{ K}$ ,  $t = 24 \text{ h}$

alloy, with additions of Fe, Mn, Cr and other elements. Carbon precipitates have a relatively weak connection with the matrix, as an envelope with numerous discontinuities forms around each carbon precipitate. Carbon precipitates are considerably larger than alloy precipitates, have micrometric dimensions, occur in groups and are composed of small grouped nanometric particles that form larger agglomerates. This means that there are nanometric particles inside micrometric ones. Therefore, the structure of carbon particles is complex.

The results of the tests of duplex-type layers obtained via the electrochemical method in three-component electrolytes after graphite saturation are presented in **Figure 6**. The following is shown: a) a topographic three-dimensional image, b) the geometric microstructure and a histogram.

X-ray diffractograms of the  $\text{Al}_2\text{O}_3$  layer obtained on a crystalline alloy of  $\text{AlMg}_2$  aluminium and aluminium oxide, as well as a duplex layer are presented in **Figure 7**. An X-ray phase analysis has shown that the obtained  $\text{Al}_2\text{O}_3$  layers are amorphous and also contain two peaks characteristic for the crystalline form of Kappa  $\text{Al}_2\text{O}_3$ , a phase of an indeterminate structure type, entered into the crystallographic data catalogue under the number 04-0878. A very strong typical peak from the graphite phase called chaolite (22-1069) is also present.

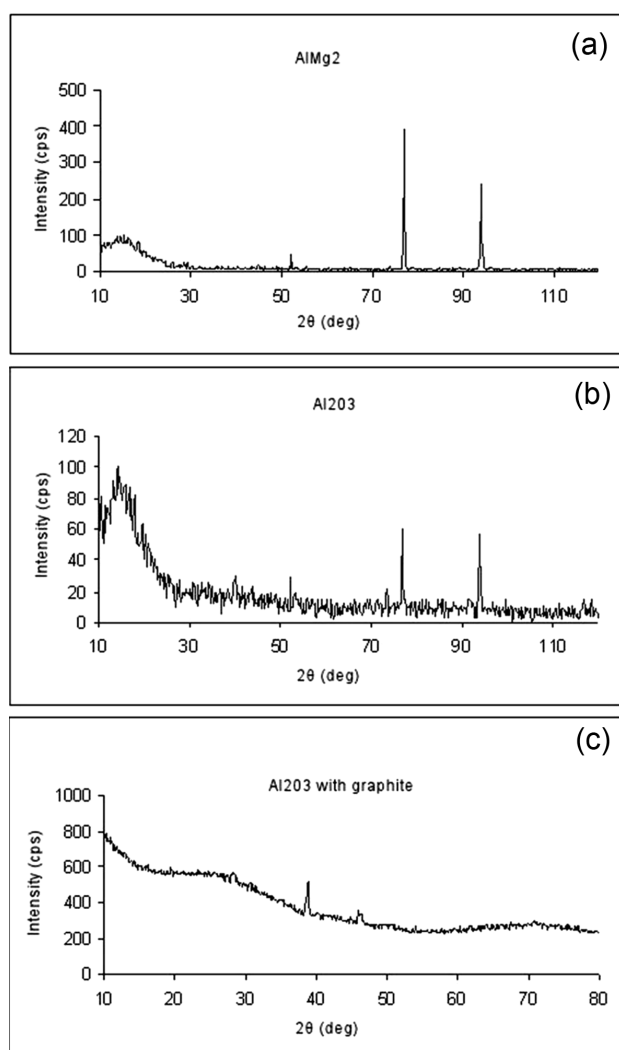


**Figure 7:** XRD spectra of the: a) substrate, b) aluminium oxide and c) a duplex layer

**Slika 7:** Rentgenogram: a) podlaga, b) aluminijev oksid in c) dupleksna plast

The porosity of the  $\text{Al}_2\text{O}_3$  layers has a significant influence on their properties, including their wear resistance, the capacity for the sorption of lubricants, the possibility of a sliding film forming from a plastic (containing graphite) and first of all the susceptibility to further modification, which is used for obtaining layers via the duplex method. It is the micro- and nanoporosity of the  $\text{Al}_2\text{O}_3$  layer that was used during the second stage of the dual technology to form duplex-type surface layers. The second technology used to produce duplex-type layers consisted of infiltration with graphite. Owing to this, it will become possible to fill the above-described structure of the  $\text{Al}_2\text{O}_3$  layer that is obtained via hard anodising with graphite.

#### 4 CONCLUSIONS

The technology of obtaining aluminium-oxide-based duplex layers consists involves a two-stage production

process. In the first stage, the base layer is produced via hard anodising in order to obtain optimal structural and morphological properties (gradient structure and high porosity). Following anodising, the samples with an  $\text{Al}_2\text{O}_3$  layer are rinsed in distilled water in order to rinse out the electrolyte. Graphite was introduced into the structure of aluminium oxide during the thermal treatment in a solid medium consisting of graphite dust.

The structure of the duplex-type layers contains carbon precipitates and other precipitates, which are typical for the aluminium alloy, with additions of Fe, Mn, Cr and other elements. Carbon precipitates have a relatively weak connection with the matrix, as an envelope with numerous discontinuities forms around each carbon precipitate.

Surface layers obtained via the duplex method can have better wear resistance, a lower friction coefficient used to cover cylinders of lubricant-free compressors, pneumatic servo-motors or shock absorber components due to the increase of mechanical properties and the increased graphite content in the structure of the layers (which causes a decrease in the motion resistance of the kinematic nodes). The obtained aluminium-oxide-based, duplex-type surface layers fully confirm the usefulness of the new surface-treatment technologies in increasing the operational durability of the sliding couples of piston machines.

#### 5 REFERENCES

- W. Skoneczny, Model of structure of  $\text{Al}_2\text{O}_3$  layer obtained via hard anodizing method, *Surface Engineering*, 17 (2001), 389–392, doi:10.1179/sureng.026708401101518060
- W. Skoneczny, J. Jurasik, A. Burian, Investigations of the surfaces morphology of  $\text{Al}_2\text{O}_3$  layers by atomic force microscopy, *Materials Science Poland*, 3 (2004), 265–278
- T. Kmita, W. Skoneczny, Gradient layers on aluminum alloys created electrolytically, *Chemical and Process Engineering*, 26 (2005), 735–744
- T. Kmita, J. Szade, W. Skoneczny, Gradient oxide layers with an increased carbon content on an AW-5251 alloy, *Chemical and Process Engineering*, 29 (2008), 375–387
- W. Skoneczny, M. Bara, Aluminum oxide composite layers obtained by the electrochemical method in the presence of graphite, *Material Science Poland*, 25 (2007) 4, 1053–1062
- M. Bara, W. Skoneczny, M. Hajduga, Ceramic-graphite surface layers obtained by the duplex method on an aluminum alloy substrate, *Chemical and Process Engineering*, 30 (2009), 431–442
- S. Jeong, H. Hwang, S. Hwang, K. Lee, Carbon nanotubes based on anodic aluminum oxide nano-template, *Carbon*, 42 (2004), 2073–2080, doi:10.1016/carbon.2004.04.015
- K. Wada, T. Shimohina, M. Yamada, N. Baba, Microstructure of porous anodic oxide films on aluminum, *Journal of Materials Science*, 21 (1986), 3810–3816, doi:10.1007/J.MSBF00553432
- J. Mikulskas, S. Joudkazis, S. Jagminas, S. Meskins, J. G. Dumas, J. Vaitkus, R. Tomasiunas, Aluminum oxide film for 2D photonic structure; room temperature formation, *Optical Materials*, 17 (2001), 343–346, doi:10.1016/Opt.MatS0925-3467(01)00100-8
- J. De Leat, H. Terryn, J. Vereecken, Development of an optical model for steady state porous anodic films on aluminium formed in phosphoric acid, *Thin Solid Films*, 320 (1997), 241–252, doi:10.1016/S0040-6090(97)00741-4

- <sup>11</sup> M. J. Bartolome, V. Lopez, E. Escudero, G. Caruana, J. A. Gonzales, Changes in the specific surface area of porous aluminium oxide films during sealing, *Surface & Coatings Technology*, 200 (2006), 4530–4537, doi:10.1016/j.surfcoat.2005.03.019
- <sup>12</sup> V. Lopez, E. Otero, A. Bautista, J. Gonzales, Sealing of anodic films obtained in oxalic acid baths, *Surface and Coatings Technology*, 124 (2000), 76–84, doi:10.1016/S0257-8972(99)00626-X

## MODELING OF SHOT-PEENING EFFECTS ON THE SURFACE PROPERTIES OF A (TiB + TiC)/Ti-6Al-4V COMPOSITE EMPLOYING ARTIFICIAL NEURAL NETWORKS

### MODELIRANJE VPLIVA HLADNEGA POVRŠINSKEGA KOVANJA NA LASTNOSTI POVRŠINE (TiB + TiC)/Ti-6Al-4V KOMPOZITA S POMOČJO UMETNIH NEVRONSKIH MREŽ

Erfan Maleki, Abolghassem Zabihollah

Sharif University of Technology, International Campus, Department of Mechanical Engineering, Kish Island, 7941776655, Iran  
maleki\_erfan@kish.sharif.edu, maleky.erfan@gmail.com

*Prejem rokopisa – received: 2015-06-29; sprejem za objavo – accepted for publication: 2015-11-13*

doi:10.17222/mit.2015.140

Titanium matrix composites (TMCs) have wide application prospects in the field of aerospace, automobile and other industries because of their good properties, such as high specific strength, good ductility, and excellent fatigue properties. However, in order to improve their fatigue strength and life, crack initiation and growth at the surface layers must be suppressed using surface treatments. Shot peening (SP) is an effective surface mechanical treatment method widely used in industry which can improve the mechanical properties of a surface. However, artificial neural networks (ANNs) have been used as an efficient approach to predict and optimize the science and engineering problems. In the present study the effects of SP on TMC were modeled by means of ANN and the capability of the ANN in predicting the output parameters is investigated. A back-propagation (BP) error algorithm is developed for the network training. Data of experimental tests on the (TiB + TiC)/Ti-6Al-4V composite are employed in order to train the network. The volume fractions of the reinforcements (TiB + TiC) were 5 % and 8 %. ANN testing is accomplished using different experimental data that were not used during the network training. The distance from the surface (depth) and SP intensity are regarded as input parameters and residual stress and hardness of the Ti-6Al-4V before and after the SP and adding reinforcements are gathered as the output parameters of the network. A comparison was made between experimental and predicted data. The predicted results were in good agreement with experimental ones, which indicates that developed neural network can be used for modeling the SP process on TMCs.

Keywords: titanium matrix composites, surface treatment, shot peening, artificial neural networks, residual stress, hardness

Kompoziti na osnovi titana (TMCs) imajo široko možnost uporabe na področju letalstva, avtomobilske in druge industrije zaradi njihovih dobrih lastnosti, kot so: velika specifična trdnost, dobra duktilnost in odlična odpornost na utrujanje. Vseeno pa je za povečanje odpornosti na utrujanje in življenjsko dobo, potrebna površinska obdelava, da se zavre nastanek razpok in njihova rast na površini. Hladno površinsko kovanje (SP) je učinkovita mehanska metoda, ki se v industriji pogosto uporablja za izboljšanje mehanskih lastnosti površine. Umetne nevronske mreže (ANNs) se uporabljajo kot učinkovit približek za napovedovanje in optimiranje znanstvenih osnov in inženiringa tega problema. V študiji so bili modelirani vplivi SP na TMC s pomočjo ANN in preiskovana je bila zmožnost napovedovanja izhodnih parametrov z ANN. Za usposabljanje mreže je bil razvit algoritem vzvratnega širjenja napak (BP). Podatki iz eksperimentalnih preizkusov na (TiB + TiC)/Ti-6Al-4V kompozitu so uporabljeni za usposabljanje mreže. Volumska deleža delcev (TiB + TiC) za ojačanje sta bila 5 % in 8 %. ANN preizkušanje je bilo izvedeno z uporabo različnih eksperimentalnih podatkov, ki niso bili uporabljeni pri usposabljanju mreže. Razdalja od površine (globina) in intenziteta SP sta uporabljeni kot vhodna parametra, preostala, napetost in trdota Ti-6Al-4V, pred in po SP, in dodatku delcev za ojačanje, sta izbrana kot izhodna parametra mreže. Izvedena je bila primerjava med eksperimentalnimi in predvidenimi podatki. Predvideni rezultati so se dobro ujemali z eksperimentalnimi, kar kaže na to, da se razvito nevronska mreža lahko uporabi pri modeliranju SP postopka na TMC.

Ključne besede: kompoziti na osnovi titana, obdelava površine, hladno kovanje površine, umetna nevronska mreža, zaostale napetosti, trdota

## 1 INTRODUCTION

Titanium matrix composites (TMCs) have attracted considerable interest due to their attractive properties over titanium alloys, such as high elastic modulus, high strength, superior creep and fatigue resistances at ambient and elevated temperatures.<sup>1-4</sup> The fabrication of TMCs using in-situ technology is simple and does not result in the pollution of an interface.<sup>5,6</sup> TMCs can be reinforced with continuous fibers, whiskers or particles.<sup>7</sup> As is well known, the mechanical properties of the composites depend on matrix, reinforcement and reinforce-

ment/matrix interface, which bonds the formers together.<sup>8</sup> Compared with continuous fibers, TMCs reinforced with whiskers or particles exhibit more isotropic behaviors. The fabrication of these materials is more convenient and cost effective; therefore, they have drawn extensive attention recently.<sup>9</sup> Titanium monoboride (TiB) whiskers and titanium carbide (TiC) particles offer high modulus, relative chemical stability, and high thermal stability, while maintaining similar density and thermal expansion coefficient to those of the titanium matrix, as well as clean interfaces without any unfavorable reaction between the precipitates and the titanium matrix.<sup>10-12</sup> The

reinforcements were obtained according to the high-temperature reactions as follows in Equations (1) and (2):<sup>13,14</sup>



TMCs co-reinforced with TiB whiskers and TiC particles have been fabricated and investigated for their mechanical properties<sup>15-17</sup> and have been extensively demonstrated to possess superior mechanical properties over the single TiB or TiC reinforced discontinuously reinforced titanium matrix composites (DRTMCs).<sup>18-21</sup>

As an effective and important surface-treatment method, shot peening (SP) can introduce high residual compressive stress (RCS) and microstructure variation at near surface layers, which can enhance their fatigue properties compared to non-peened materials. The process of SP involves the bombardment of spherical balls of a hard material against the surface of components, which induces the strong elastic-plastic deformation at the surface and sub-surface regions. In the deformation layers, high RCS and microstructure refinements are introduced after SP. The residual stresses and hardness are very important properties of materials after the SP treatment.

In the field of science and engineering, artificial neural networks (ANNs) are some of the most important research areas. ANN is a modeling tool to solve linear and nonlinear multivariate regression problems.<sup>22</sup> Recently, ANN models were widely utilized to interpret and correlate the variable relationships in complex nonlinear data sets. The present study proposes a new approach based on ANNs to investigate the effects of SP process on mechanical and metallurgical properties (TiB + TiC)/Ti-6Al-4V composite. Residual stress and hardness were modeled by ANN. 20 data of experimental tests results from the total of 30, are used to train the networks, while in the networks testing 10 different experimental data which were not used during training are used. Since the experimental results did not include the training sets the performance of the ANN is evaluated in a fine way.

## 2 EXPERIMENTAL PART

The experimental data are obtained from Xie et al.<sup>23</sup> The materials of (TiB + TiC)/Ti-6Al-4V (TiB:TiC = 1:1 (vol.%)) were fabricated via in-situ technology. Two types of theoretical total volume fraction of reinforcements (TiB + TiC) were 5 % and 8 %. The SP treatment was performed using an air-blast machine. The related information of used SP process is demonstrated in **Table 1**. The Almen specimens are A type and the diameter of peening nozzle was 15 mm and the distance between nozzle and sample was 100 mm. In order to obtain the depth distribution of the residual stress and hardness, the thin top surface layers were removed one by one via the method of chemical etch with a solution of water, nitric acid, and hydrofluoric acid in the ratio 31:12:7. All the

measurements were carried out at room temperature. The method of residual stress and hardness measurements are X ray stress analysis and digital microhardness test respectively.<sup>23</sup>

**Table 1:** Parameters of the SP process treatments<sup>23</sup>

**Tabela 1:** Parametri uporabljenega procesa SP<sup>23</sup>

SP intensity (mm A)	Shot material	Shot diameter (mm)	Shot hardness (HV)	Jet pressure (MPa)	SP time (min)	Coverage (%)
0.15	Cast steel	0.6	610	0.2	0.50	100
0.30	Cast steel	0.6	610	0.3	0.50	100

The results indicate that the increased reinforcements and SP intensities enhance the surface roughness after SP. Both the compressive residual stresses and hardness increase with the increase of the SP intensity, which is mainly due to the plastic deformation and high dislocation density in the near surface layer. Moreover, the reinforcement particles can act as the block sources during dislocation movements. After an appropriate SP treatment, the increased CRS and hardness are beneficial to industrial applications. A table shows the obtained values of the experimental results on (TiB + TiC)/Ti-6Al-4V for 30 different samples. The SP intensity for non-peened specimens has been shown by zero in **Table 2**.

## 3 ARTIFICIAL NEURAL NETWORKS

Artificial intelligence (AI) systems such as artificial neural networks (ANNs) have found many applications in science and engineering problems in the past decade. The concept of an ANN has emerged with the idea that it

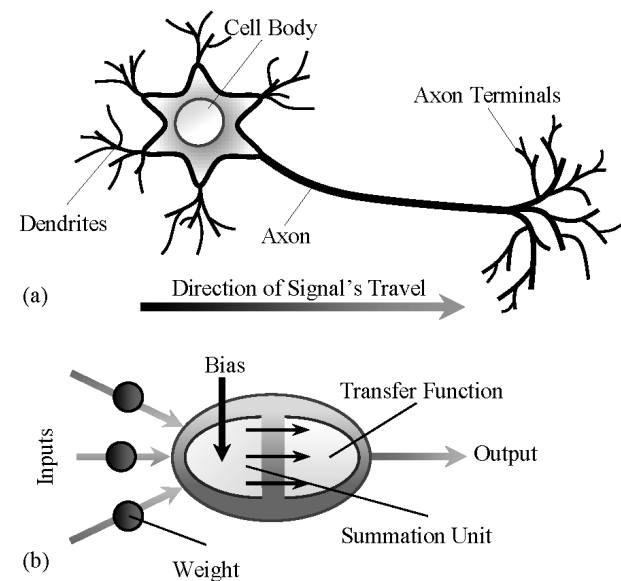


**Figure 1:** Schematic of neuron: a) a biological neuron, b) an artificial neuron

**Slika 1:** Shematski prikaz nevrona: a) biološki nevron, b) umetni nevron



**Table 2:** Values of the SP process effects on residual stress and hardness of (TiB + TiC)/Ti-6Al-4V Composite specimens<sup>23</sup>**Tabela 2:** Vrednosti SP postopka, ki vplivajo na zaostale napetosti in trdoto (TiB + TiC) / Ti-6Al-4V kompozitnih vzorcev<sup>23</sup>

Sample No.	Depth	SP intensity (mm A)	Residual Stress (MPa)			Hardness (HV)		
			matrix	5 % (TiB+TiC)	8 % (TiB+TiC)	matrix	5 % (TiB+TiC)	8 % (TiB+TiC)
1	0	0.00	10.42	18.04	17.93	334.72	380.37	417.57
2	0	0.30	-522.83	-524.25	-575.51	524.87	560.38	637.31
3	0	0.15	-375.97	-434.55	-481.94	484.31	512.07	584.43
4	15	0.00	25.11	5.022	6.84	328.67	393.61	436.62
5	15	0.30	-613.76	-648.62	-657.79	436.11	512.19	628.86
6	15	0.15	-417.53	-499.54	-539.63	418.45	492.85	523.28
7	25	0.00	-9.57	-20.26	-12.97	325.48	381.28	420.16
8	25	0.30	-608.67	-650.57	-672.54	414.97	468.23	557.85
9	25	0.15	-408.92	-465.67	-574.80	387.62	451.56	507.09
10	50	0.00	14.35	-29.48	-9.19	315.39	403.32	411.77
11	50	0.30	-581.27	-608.46	-626.77	378.62	455.55	530.79
12	50	0.15	-397.63	-419.90	-545.84	372.53	431.43	475.18
13	75	0.00	14.48	14.02	-12.72	338.28	381.40	423.67
14	75	0.30	-564.84	-570.02	-586.49	385.38	438.64	538.40
15	75	0.15	-354.00	-386.95	-516.88	358.29	420.55	446.63
16	100	0.00	-12.84	-17.01	-14.41	340.03	396.67	414.43
17	100	0.30	-557.53	-524.25	-515.10	368.47	433.57	509.66
18	100	0.15	-324.71	-337.52	-264.28	349.94	411.35	459.31
19	150	0.00	-5.26	-11.81	-8.67	330.01	375.66	409.48
20	150	0.30	-422.37	-335.69	-299.08	350.72	388.76	438.64
21	150	0.15	-302.74	-249.65	-120.90	340.80	386.23	435.87
22	200	0.00	16.96	-13.89	-4.75	319.14	386.77	429.04
23	200	0.30	-323.74	-220.36	-101.37	354.10	402.29	434.42
24	200	0.15	-236.84	-194.73	-61.16	344.29	382.99	424.21
25	250	0.00	28.21	14.93	17.41	337.86	375.06	424.09
26	250	0.30	-46.11	-20.82	-28.14	343.11	380.31	428.50
27	250	0.15	-31.80	-18.99	-15.97	336.83	378.90	410.87
28	300	0.00	-13.62	-23.50	21.33	344.74	369.26	414.91
29	300	0.30	-35.15	-18.99	-33.63	324.51	381.15	430.88
30	300	0.15	-18.99	-11.67	-16.23	326.86	376.50	419.41

simulates the operating principles of a human brain. The first studies were made with mathematical modeling of biological neurons that make up the brain cells.<sup>24</sup> Basically, the brain functions with a very dense network of neurons. The brain contains a lot of neurons connected to each other by many interconnections. A neuron consists mainly of the following parts: dendrite, cell body and axon.<sup>25</sup> Dendrite gets the signals from various other neurons to the neuron and carries them to the cell body for processing, after that an axon carries the signal from the cell body to various other neurons. Similarly, the neural units in the artificial neural network are developed as a very approximate model of the natural biological neurons.<sup>26</sup> **Figure 1** shows a natural biological neuron (**Figure 1a**) and an artificial neuron (**Figure 1b**) that is a computational and mathematical model of the biological neuron. A single neuron computes the sum of its inputs, which are multiplying with a variant called the weight, adds a bias term, and drives the result through a generally nonlinear transfer function to produce a single output termed the activation level of the neuron.

An ANN model is created by interconnection of many of the neurons in a known configuration. The primary elements characterizing the neural network are the distributed representation of information, local operations and non-linear processing. Structurally, every ANN is made up of three sections: input, hidden and output layers.<sup>27</sup> The structure of an ANN model is determined by the number of its layers and the number of nodes in each layer and the nature of the transfer function.<sup>28,29</sup> Selecting the optimum architecture of the network is one of the challenging steps in ANN modeling. The term "architecture" refers to the number of layers in the network and the number of neurons in each layer. However, there is no straightforward method to estimate the optimal number of hidden layers and neurons in each layer.<sup>30,31</sup> Thus trial-and-error methods have been used by many researchers to determine such case-dependent parameters for studies involving ANN-based models.<sup>32</sup> **Figure 2** represents the architecture of the neural network. In this network, each input consists of  $r$  parameters and each output comprises  $s$  parameters,

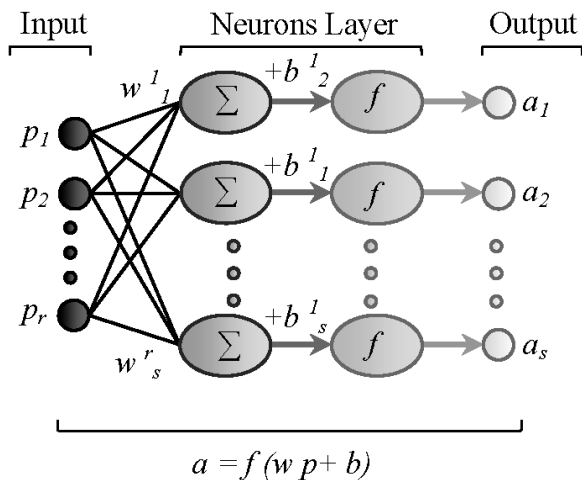


Figure 2: Architecture of neural network<sup>33</sup>  
 Slika 2: Zgradba nevronske mreže<sup>33</sup>

while  $p$ ,  $w$ ,  $b$ ,  $f$  and  $a$  represent the inputs, weight matrixes, bias vectors, transfer function in neurons, and outputs, respectively.<sup>33</sup>

Mathematically, a layer  $n$  may be described by Equations (3) and (4):<sup>34</sup>

$$u_s^n = \sum_{i=1}^r w_s^n p_i \quad (3)$$

$$a_s = f(u_s^n) = f(u_s^n + b_s^n) \quad (4)$$

where  $p_1, p_2, \dots, p_r$  are the input signals,  $w^{k_1}, w^{k_2}, \dots, w^n$ , are the synaptic weights of neuron  $n$ ,  $u^n$  is the linear combiner output due to input signals,  $b^n$  is the bias,  $f$  is the transfer function and  $a_1, a_2, \dots, a_s$  are the output signals of the neuron. The tangent sigmoid (Tansig)  $\phi(x)$ , logarithmic sigmoid (Logsig)  $\psi(x)$  and linear  $\chi(x)$  transfer function are described as follows in Equations (5), (6) and (7):<sup>35</sup>

$$\phi(x) = \frac{2}{1 + e^{-2x}} - 1 \quad (5)$$

$$\psi(x) = \frac{2}{1 + e^{-x}} \quad (6)$$

$$\chi(x) = \text{linear}(x) \quad (7)$$

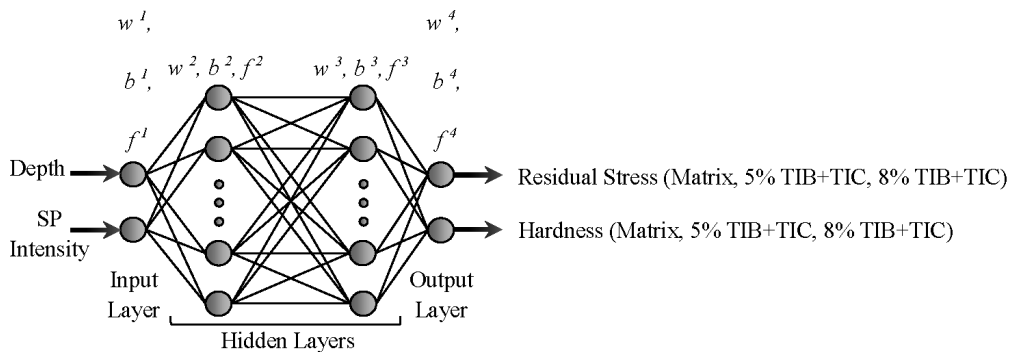


Figure 3: A Conceptual structure of network with four layers  
 Slika 3: Konceptualna zgradba mreže s štirimi nivoji

### 3.1 Training of ANN

The training of the ANN is performed by adjusting the connection weights. It is performed by iteratively adjusting the weights ( $w$ ) of the connections and biases ( $b$ ) in the network in order to minimize a predefined cost function.<sup>36</sup> The ANNs are trained with a training set of input and known output data. An ANN is better trained as more input data are used. The performance of an ANN is generally based on the parameters' architecture and the setting. As was mentioned, one of the most difficult tasks in studying ANNs is finding an appropriate architecture. This task is performed via trial and error and the number of middle layers and neuron presented in each layer is being identified. Appropriate designation of the initial amounts of weights and biases is very effective on the performance of network and the time of calculation. But there is not a reasonable law and process to identify a suitable architecture. The only step which is very time consuming is the trial and error. One can get an idea by looking at a problem and decide to start with simple networks; going on to complex ones until the solution is within acceptable limits of uncertainty. Furthermore, the point that must be considered in training of the network is the rate of input and output data scattering. In this study all values of each input and output data parameters are divided to maximum absolute value of them and normalized also the used data are dimensionless. The normalized data are in range of  $[-1, +1]$ . In the present study, a feed forward ANN based on back propagation (BP) error algorithm, which is the most popular one in training of ANNs is used. BP is a descent algorithm, which attempts to minimize the error during iterations. The weights of the network are adjusted by the algorithm such that the error is decreased along a descent direction. In the back-propagation learning, the actual outputs are compared with the target values to derive the error signals, which are propagated backward layer by layer for the updating of the synaptic weights in all the lower layers.

### 3.2 Implementation of ANN

In this paper the effects of the SP process on surface properties including of (TiB + TiC) / Ti-6Al-4V composite were modeled by means of an ANN. In implementation of the ANN distance from the surface (depth) and SP intensity are regarded as inputs and the residual stress and hardness are gathered as outputs of the networks. Different networks with different architecture and network parameters were trained for the prediction of residual stress and hardness. **Figure 3**, for an example, represents the schematic architecture of ANN for modeling of the mentioned output parameters: a four-layer feed forward with BP algorithm with full interconnection. This neural network model has a powerful input-output mapping capability. With the use of enough hidden neurons, it can effectively approximate any continuous nonlinear function. In the considered network, two inputs are logged into the input layer to determine the two outputs. In the ANN methodology, the sample data is often subdivided into training and testing sets. The distinctions among these subsets are crucial.<sup>37</sup> Ripley defines the following: Training set: a set of examples used for learning that is to fit the parameters of the classifier. Testing set: a set of examples used only to assess the performance of a fully-specified classifier.

### 3.3 Performance evaluation of ANN

The performance of the ANN models in predicting the shot-peening effects on residual stress and hardness of (TiB + TiC)/Ti-6Al-4V composite were statistically evaluated using four prediction score metrics calculated from the test dataset: Pearson coefficient of correlation (PCC), root mean square error (RMSE), mean relative error (MRE) and mean absolute error (MAE). These parameters were determined using the following Equations (8), (9), (10) and (11):

$$PCC = \frac{\sum_{i=1}^n (f_{EXP,i} - F_{EXP}) - (f_{ANN,i} - F_{ANN})}{\sqrt{\sum_{i=1}^n (f_{EXP,i} - F_{EXP})^2 - (f_{ANN,i} - F_{ANN})^2}} \quad (8)$$

$$RMSE = \sqrt{\frac{\sum_{i=1}^n (f_{EXP,i} - f_{ANN,i})^2}{n}} \quad (9)$$

$$MRE = \frac{1}{n} \sum_{i=1}^n \left| \frac{f_{EXP,i} - f_{ANN,i}}{f_{EXP,i}} \right| \times 100 \quad (10)$$

$$MRE = \frac{1}{n} \sum_{i=1}^n |f_{EXP,i} - f_{ANN,i}| \quad (11)$$

where  $n$  is the number of used sample for modeling,  $f_{EXP}$  is the experimental value and  $f_{ANN}$  is the networks predicted value. Also, the values of  $F_{EXP}$  and  $F_{ANN}$  are calculating as follows in Equations (12) and (13):

$$F_{EXP} = \frac{1}{n} \sum_{i=1}^n f_{EXP,i} \quad (12)$$

$$F_{ANN} = \frac{1}{n} \sum_{i=1}^n f_{ANN,i} \quad (13)$$

### 3.4 Generating model function

After the neural network is trained successfully with four layers, the values of the four parameters of the network ( $p$ ,  $b$ ,  $w$  and  $f$ ) can be obtained. The function that correlates the inputs to the corresponding output can be calculated by applying the aforementioned parameters. Finally, the model function can determined in Equations (14) and (15):

$$a^1 = f^1(w^1p + b^1) \quad (14a)$$

$$a^2 = f^2(w^2p^1 + b^2) \quad (14b)$$

$$a^3 = f^3(w^3p^2 + b^3) \quad (14c)$$

$$a^4 = f^4(w^4p^3 + b^4) \quad (14d)$$

$$G(g(1), g(2)) = a^4 = f^4(w^4f^3(w^3f^2(w^2f^1(w^1p + b^1) + b^2) + b^3) + b^4) \quad (15)$$

where  $a^1$ ,  $a^2$  and  $a^3$  are the outputs of the first, second and third layer, respectively;  $a^4$  is the fourth layer output, which is equal to the function  $G(g(1), g(2))$ . The function  $G$  gets the values of the input parameters. The function of  $g(1)$  and  $g(2)$  represent the residual stress and hardness, respectively. The methodology used for neural network application in this study is as follows:

1. Start;
2. Normalize the data (inputs & outputs);
3. Feed the data to artificial neural network;
4. Find network optimum parameters;
5. Execute network training;
6. Obtain Pearson correlation coefficient;
7. If PCC = 0.99 go to 8, if not go back to 4 with revising the parameters of network;
8. Continue processing until obtaining desired convergence between experimental and predicted values;
9. Obtain weights & biases values;
10. Create the model function;
11. Conduct analysis based on model function;
12. Verify the results using experimental values;
13. Calculate the error for each answer;
14. End.

## 4 RESULTS AND DISCUSSION

In order to train the ANNs in this study, the obtained experimental test results on shot peened (TiB + TiC)/Ti-6Al-4V composite specimens are employed. Different networks were trained to achieve the optimum structure (OS) in order to generate a model function (MF). After the OS is selected and the MF is generated, operation of the network is tested with the use of them (OS & MF). Twenty sample data (data of samples 1-20)

were used from the total of 30, as data sets for network training. **Table 3** shows the normalized sample data used for networks training. In the network testing, 10 different sample data (data of samples 21–30) which were not used during training are employed. Therefore, the whole experimental results did not comprise in the training. For investigative purposes, out of 30 samples data, 67 % data had taken for training and 33 % data for testing. Several networks have been trained with different architecture to find the OS of ANNs, to predict the regarded outputs, with the best performance and the highest PCC, the least RMSE, MRE and MAE. Related information of some the different trained networks for modelling of matrix hardness are shown in **Table 4**. The ordinal numbers shown in the "Layer Structure" were used to indicate the

total number of neurons in the input, hidden and output layers, respectively. Results of the networks were investigated and the ANN modelling number 11 with 2×8×16×2 structure is selected for modelling and simulation.

**Figures 4** and **5** show the obtained values of the ANN response in comparison with experimental values for each 20 training samples (samples 1–20) for residual stress and hardness, respectively, using the selected network.

After the network was trained, the selected network is tested. **Figures 6** and **7** have been demonstrated the predicted and experimental values of residual stress and hardness for 10 different testing samples (samples 21–30) respectively.

**Table 3:** Normalized sample data used for networks training

**Tabela 3:** Normalizirani podatki vzorca, uporabljenega pri usposabljanju mreže

Sample No.	Depth	SP intensity	Residual stress			Hardness		
			matrix	5 % (TIB+TIC)	8 % (TIB+TIC)	matrix	5 % (TIB+TIC)	8 % (TIB+TIC)
1	0.0000	0.0	0.0170	0.0277	0.0267	0.6377	0.6788	0.6552
2	0.0000	1.0	-0.8518	-0.8058	-0.8557	1.0000	1.0000	1.0000
3	0.0000	0.5	-0.6126	-0.6680	-0.7166	0.9227	0.9138	0.9170
4	0.0500	0.0	0.0409	0.0077	0.0102	0.6262	0.7024	0.6851
5	0.0500	1.0	-1.0000	-0.9970	-0.9781	0.8309	0.9140	0.9867
6	0.0500	0.5	-0.6803	-0.7678	-0.8024	0.7972	0.8795	0.8211
7	0.0833	0.0	-0.0156	-0.0311	-0.0193	0.6201	0.6804	0.6593
8	0.0833	1.0	-0.9917	-1.0000	-1.0000	0.7906	0.8356	0.8753
9	0.0833	0.5	-0.6663	-0.7158	-0.8547	0.7385	0.8058	0.7957
10	0.1667	0.0	0.0234	-0.0453	-0.0137	0.6009	0.7197	0.6461
11	0.1667	1.0	-0.9471	-0.9353	-0.9319	0.7214	0.8129	0.8329
12	0.1667	0.5	-0.6479	-0.6454	-0.8116	0.7098	0.7699	0.7456
13	0.2500	0.0	0.0236	0.0216	-0.0189	0.6445	0.6806	0.6648
14	0.2500	1.0	-0.9203	-0.8762	-0.8721	0.7342	0.7828	0.8448
15	0.2500	0.5	-0.5768	-0.5948	-0.7685	0.6826	0.7505	0.7008
16	0.3333	0.0	-0.0209	-0.0261	-0.0214	0.6478	0.7079	0.6503
17	0.3333	1.0	-0.9084	-0.8058	-0.7659	0.702	0.7737	0.7997
18	0.3333	0.5	-0.5291	-0.5188	-0.3930	0.6667	0.7341	0.7207
19	0.5000	0.0	-0.0086	-0.0182	-0.0129	0.6287	0.6704	0.6425
20	0.5000	1.0	-0.6882	-0.5160	-0.4447	0.6682	0.6937	0.6883

**Table 4:** Relevant information of 12 different networks for modeling of matrix hardness

**Tabela 4:** Pomembne informacije o 12 različnih mrežah pri modeliranju trdote osnove

ANN Modeling no.	Rate of training	Layers structure	Hidden transfer function	Output transfer function	PCC	RMSE	MRE (%)	MAE
1	0.090	2×2×4×2	Logsig	Linear	0.97035	0.7677	0.1552	0.6680
2	0.095	2×2×6×2	Tansig	Linear	0.97421	0.7018	0.1399	0.5742
3	0.110	2×2×8×2	Logsig	Tansig	0.98460	0.6671	0.1007	0.5018
4	0.100	2×4×4×2	Tansig	Linear	0.98662	0.4163	0.0938	0.4261
5	0.115	2×4×6×2	Logsig	Linear	0.99003	0.2397	0.0875	0.3459
6	0.120	2×4×10×2	Logsig	Linear	0.99150	0.2078	0.0617	0.2822
7	0.115	2×6×10×2	Tansig	Tansig	0.99877	0.3400	0.0587	0.2401
8	0.130	2×6×12×2	Tansig	Linear	0.99901	0.2229	0.0461	0.1886
9	0.145	2×6×16×2	Logsig	Tansig	0.99936	0.1997	0.0384	0.1597
10	0.160	2×8×10×2	Logsig	Logsig	0.99911	0.1609	0.0331	0.1529
11	0.165	2×8×16×2	Logsig	Logsig	0.99979	0.0985	0.0194	0.0853
12	0.165	2×8×20×2	Tansig	Linear	0.99963	0.1265	0.0247	0.1173

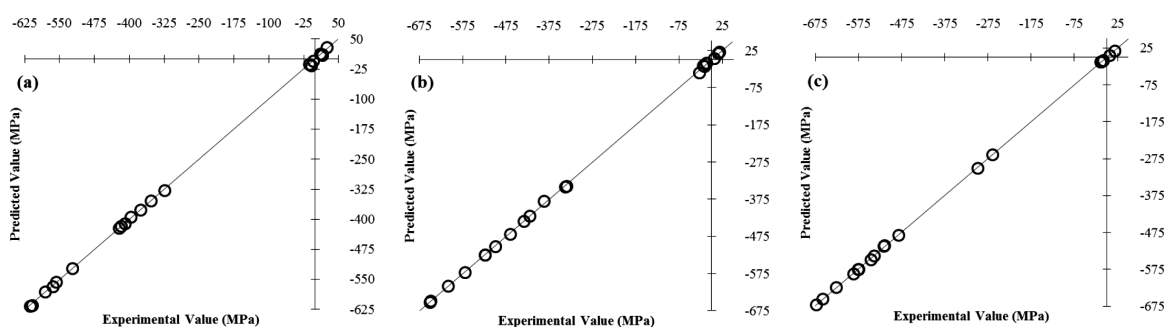


**Figure 4:** Comparison of predicted values (ANN response) with experimental values for each 20 training samples (samples 1–20) for residual stress: a) matrix, b) 5 % TiB+TiC and c) 8 % TiB+TiC

**Figure 4:** Primerjava napovedanih vrednosti (odgovor ANN) z eksperimentalnimi vrednostmi za vsakega od 20 vzorcev usposabljanja (vzorci 1-20) za zaostale napetosti: a) osnova, b) 5 % TiB+TiC in c) 8 % TiB+TiC

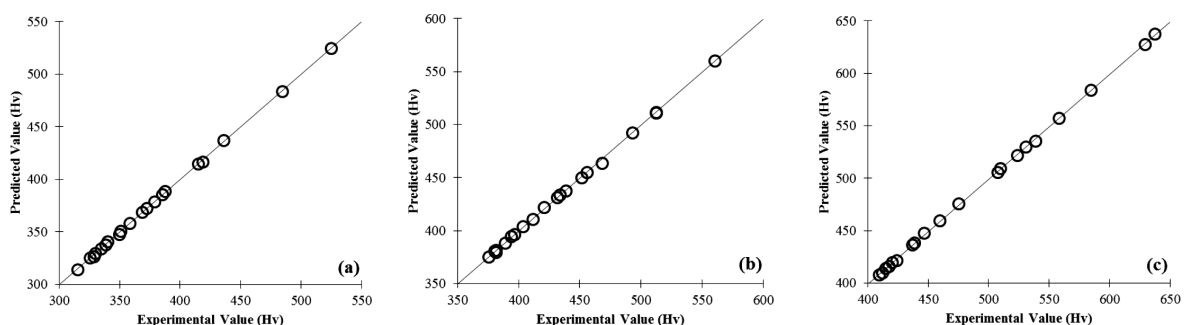


**Figure 5:** Comparison of predicted values (ANN response) with experimental values for each 20 training samples (samples 1–20) for hardness: a) matrix, b) 5 % TiB+TiC and c) 8 % TiB+TiC

**Slika 5:** Primerjava napovedanih vrednosti (odgovor ANN) z eksperimentalnimi vrednostmi za vsakega od 20 vzorcev usposabljanja (vzorci 1-20) za trdoto: a) osnova, b) 5 % TiB+TiC in c) 8 % TiB+TiC

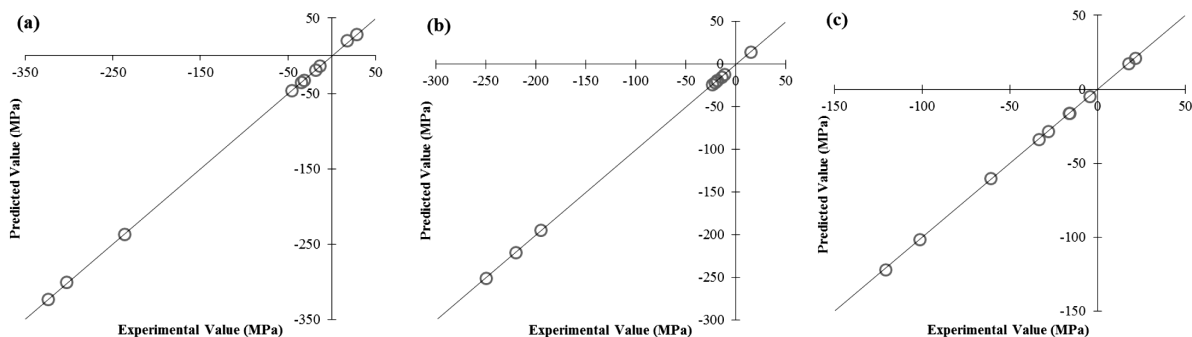


**Figure 6:** Comparison of predicted values (ANN response) with experimental values for each 20 testing samples (samples 21–30) for residual stress: a) matrix, b) 5 % TiB+TiC and c) 8 % TiB+TiC

**Slika 6:** Primerjava napovedanih vrednosti (odgovor ANN) z eksperimentalnimi vrednostmi za vsakega od 20 preizkušenih vzorcev (vzorci 21-30) za zaostale napetosti: a) osnova, b) 5 % TiB+TiC in c) 8 % TiB+TiC

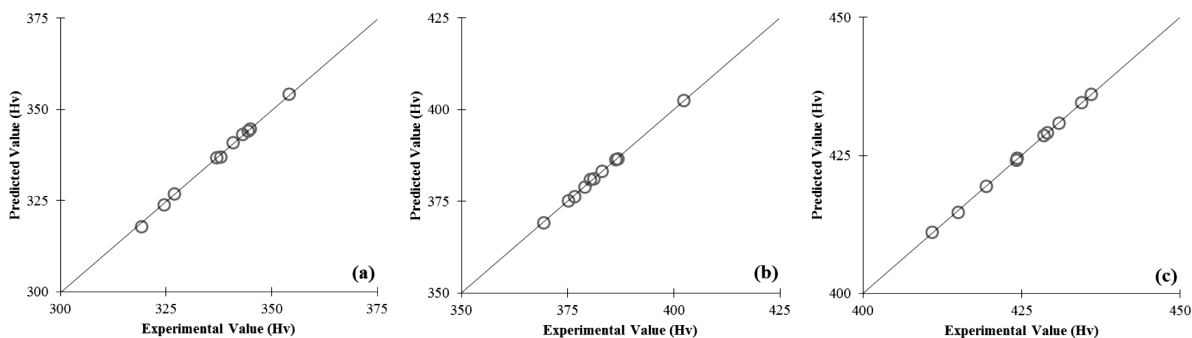


**Figure 7:** Comparison of predicted values (ANN response) with experimental values for each 20 testing samples (samples 21–30) for hardness: a) matrix, b) 5 % TiB+TiC and c) 8 % TiB+TiC

**Slika 7:** Primerjava napovedanih vrednosti (odgovor ANN) z eksperimentalnimi vrednostmi za vsakega od 20 preizkušenih vzorcev (vzorci 21-30) za trdoto: a) osnova, b) 5 % TiB+TiC in c) 8 % TiB+TiC



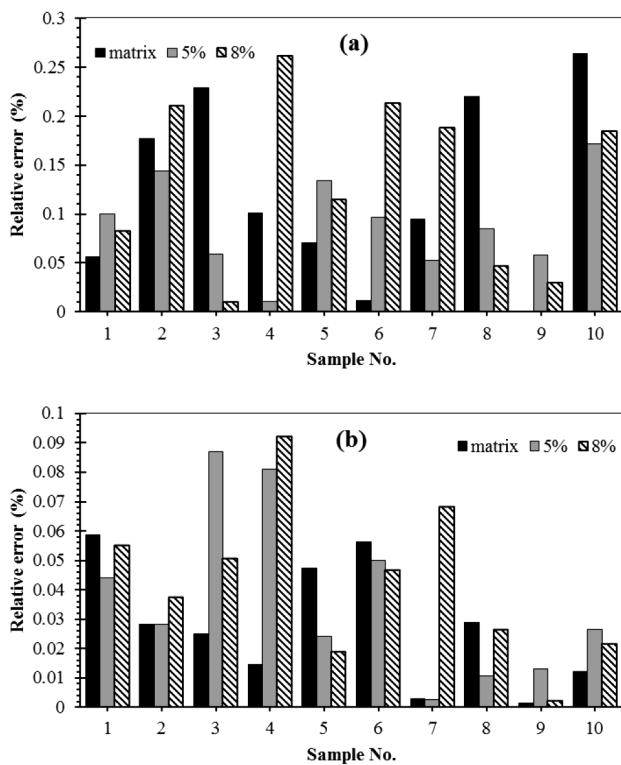


**Figure 8:** Values of obtained relative error for testing samples (samples 21–30) for considered output parameters: a) residual stress, b) hardness

**Slika 8:** Vrednosti dobljene relativne napake preizkušanih vzorcev (vzorci 21-30) pri upoštevanih izhodnih parametrih: a) zaostale napetosti, b) trdota

**Figure 8** illustrates the obtained relative error (RE) values of the residual stress and hardness for the testing samples. In modeling of residual stress, according to the **Figure 8a**, the minimum and maximum (min., max.) determined relative errors for matrix, 5 % reinforcement and 8 % reinforcement are (0.000,0.2633), (0.0103, 0.1714) and (0.0099, 0.2616), respectively. Based on **Figure 8b**, similarly minimum and maximum calculated REs for matrix, 5 % reinforcement and 8 % reinforcement in modeling of hardness are (0.0015, 0.0587), (0.0026, 0.0870) and (0.0023, 0.0919), respectively.

According to the obtained values of the ANN for training and testing samples, data corresponding to the used network are shown in **Table 5**.

**Table 5:** Obtained values of PCC, RMSE, MRE and MAE for trained and tested network

**Tabela 5:** Dobljene vrednosti PCC, RMSE, MRE in MAE pri usposobljeni in pri preizkušeni mreži

Output parameter		Training				Testing			
		PCC	RMSE	MRE (%)	MAE	PCC	RMSE	MRE (%)	MAE
Residual stress	Matrix	0.99914	0.1781	0.1104	0.1099	0.99846	0.2529	0.1223	0.1315
	5 % rein.	0.99875	0.0651	0.0872	0.0471	0.99816	0.0906	0.0910	0.0521
	8 % rein.	0.99766	0.0597	0.1228	0.0382	0.99683	0.0647	0.1342	0.0440
Hardness	Matrix	0.99979	0.0985	0.0194	0.0853	0.99912	0.1154	0.0276	0.0937
	5 % rein.	0.99901	0.1544	0.0313	0.1372	0.99858	0.1783	0.0368	0.1420
	8 % rein.	0.99837	0.1976	0.0346	0.1475	0.99721	0.2071	0.0419	0.1780

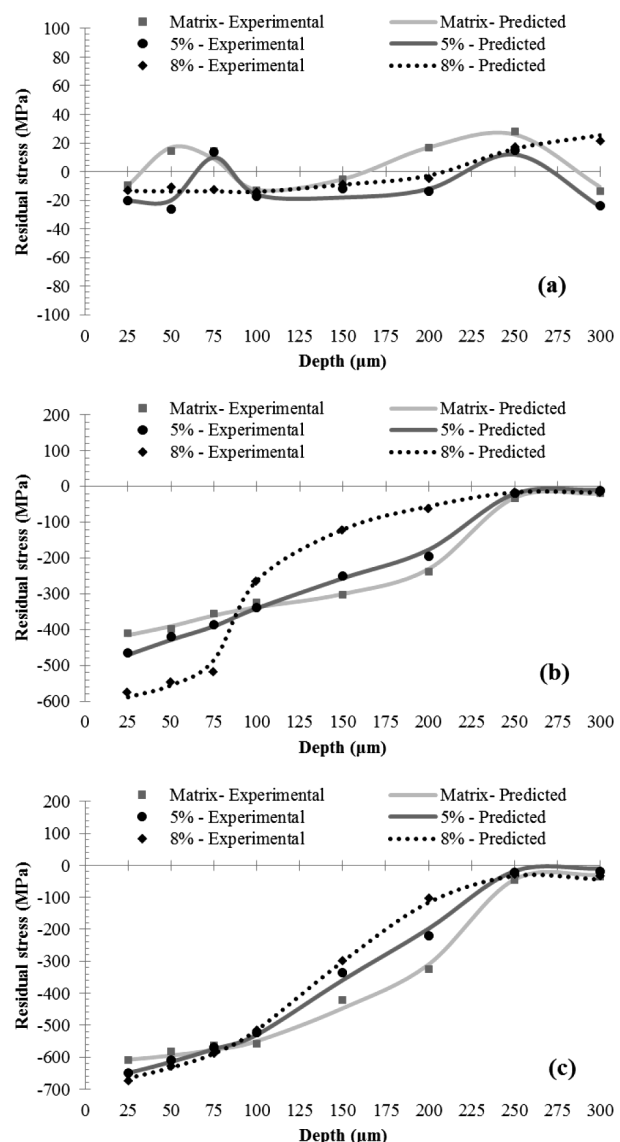


**Figure 9:** Distribution of residual stresses along the depth from the surface obtained by OS and MF of ANN for different SP intensities of: a) 0 mm A, b) 0.15 mm A and c) 0.3 mm A

**Slika 9:** Razporeditev spreminjanja zaostalih napetosti v globino od površine, dobljene pri OS in MF z ANN pri različnih intenzitetah SP: a) 0 mm A, b) 0,15 mm A in c) 0,3 mm A

In network training it is observed that the values of PCC for each considered output parameters are more than 99.7 %. The values of training RMSE, MRE and

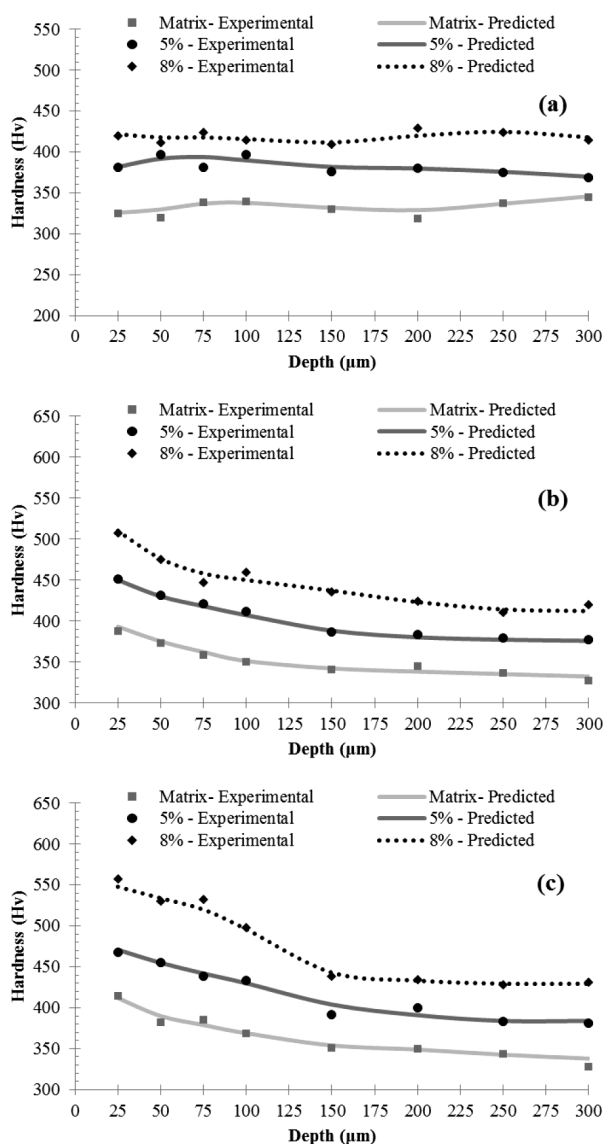


**Figure 10:** Distribution of hardness along the depth from the surface obtained by OS and MF of ANN for different SP intensities of: a) 0 mm A, b) 0.15 mm A and c) 0.3 mm A

**Slika 10:** Razporeditev vrednosti trdote v globino od površine, dobljene z OS in MF z ANM, pri različnih intenzitetah SP: a) 0 mm A, b) 0,15 mm A in c) 0,3 mm A

MAE are very close to 0 and they are in little intervals and their ranges are [0.0597, 0.1976], [0.0194, 0.1228] and [0.0382, 0.14715], respectively. So, it is concluded that networks are trained finely and adjusted carefully. Likewise in network testing the values of PCC are more than 99.6 % and it is observed that values of testing PCC have a negligible reduction in comparison with the training. Moreover, the values of testing RMSE, MRE and MAE are in a tiny span as well and their ranges are [0.0647, 0.2071], [0.0276, 0.1342] and [0.0440, 0.1780], respectively. Based on the achieved values for the statistical errors for both training and testing samples it is concluded that the error values are acceptable and implementation of ANN is accomplished in a good way.

In residual stress modeling for each case of network training and testing, the obtained values for 5 % TiB + TiC., matrix and 8 % TiB + TiC and in modeling of hardness, achieved values for matrix, 5 % TiB + TiC and 8 % TiB + TiC have the smallest errors, respectively. Distributions of the residual stress and hardness from the shot-peened surface to the bulk material (25-300  $\mu\text{m}$ ) for SP intensity of (0.00, 0.15 and 0.30) are shown in **Figures 9 and 10**, which are achieved by OS and MF of the used ANN modeling in this paper.

## 5 CONCLUSION

In present study the application of ANNs was investigated, aiming to create models to predict and optimize the SP process effects with different intensities on the residual stress and hardness of a (TiB + TiC)/Ti-6Al-4V composite. Experimental data show that both the residual stress and the hardness were increased with an improvement of the SP intensities. Residual stress and hardness were modeled using ANN for three cases: matrix, 5 % TiB + TiC and 8 % TiB + TiC. The obtained results indicate that statistical errors for RSME, MRE and MAE are in very small range and so close to 0. Moreover, the values of PCC for all of the regarded output parameters in implemented networks are more than 99 %. According to the achieved results, it can be concluded that when the ANNs are tuned in a good way and adjusted carefully, the modeling results are in reasonable agreement with the experimental results. Therefore, using ANNs, instead of costly and time consuming experiments, decreases the costs and the need for special testing facilities, and the ANNs can be employed to predict and optimize the SP effects on the residual stress and the hardness of TMCs.

## 6 REFERENCES

- <sup>1</sup> S. C. Tjong, Z. Ma, Microstructural and mechanical characteristics of in situ metal matrix composites, *Materials Science and Engineering: R: Reports*, 29 (2000), 49–113, doi:10.1016/S0927-796X(00)00024-3
- <sup>2</sup> S. C. Tjong, Y. W. Mai, Processing-structure-property aspects of particulate-and whisker-reinforced titanium matrix composites, *Composites Science and Technology*, 68 (2008), 583–601, doi:10.1016/j.compscitech.2007.07.016
- <sup>3</sup> L. Huang, L. Geng, H. Peng, In situ (TiBw+ TiCp)/Ti6Al4V composites with a network reinforcement distribution, *Materials Science and Engineering A*, 527 (2010), 6723–6727, doi:10.1016/j.msea.2010.07.025
- <sup>4</sup> A. Mavi, I. Korkut, Machinability of a ti-6al-4v alloy with cryogenically treated cemented carbide tools, *Mater. Tehnol.*, 48 (2014), 577–580
- <sup>5</sup> W. Lu, D. Zhang, X. Zhang, R. Wu, T. Sakata, H. Mori, HREM study of TiB/Ti interfaces in a TiB-TiC in situ composite, *Scripta Materialia*, 44 (2001), 1069–1075, doi:10.1016/S1359-6462(01)00663-7
- <sup>6</sup> H. Man, S. Zhang, F. Cheng, T. Yue, Microstructure and formation mechanism of in situ synthesized TiC/Ti surface MMC on Ti-6Al-4V by laser cladding, *Scripta Materialia*, 44 (2001), 2801–2807

- <sup>7</sup> W. Lu, D. Zhang, X. Zhang, Y. Bian, R. Wu, T. Sakata, H. Mori, Microstructure and tensile properties of in situ synthesized (TiBw+TiCp)/Ti6242 composites, *Journal of Materials Science*, 36 (2001), 3707–3714, doi:10.1023/A:1017917631855
- <sup>8</sup> B. Li, J. Shang, J. Guo, H. Fu, In situ observation of fracture behavior of in situ TiB w/Ti composites, *Materials Science and Engineering A*, 383 (2004), 316–322, doi:10.1016/j.msea.2004.04.071
- <sup>9</sup> T. Saito, T. Furuta, T. Yamaguchi, Development of low cost titanium alloy matrix composite, *Recent Advances in Titanium Metal Matrix Composites*, (1994), 33–44
- <sup>10</sup> Z. Wei, L. Cao, H. Wang, C. Zou, Microstructure and mechanical properties of TiC/Ti-6Al-4V composites processed by in situ casting route, *Materials Science and Technology*, 27 (2011), 1321–1327, doi:10.1179/026708310X12699498462922
- <sup>11</sup> M. Y. Koo, J. S. Park, M. K. Park, K. T. Kim, S. H. Hong, Effect of aspect ratios of in situ formed TiB whiskers on the mechanical properties of TiB w/Ti-6Al-4V composites, *Scripta Materialia*, 66 (2012), 487–490, doi:10.1016/j.scriptamat.2011.12.024
- <sup>12</sup> H. Rastegari, S. Abbasi, Producing Ti-6Al-4V/TiC composite with superior properties by adding boron and thermo-mechanical processing, *Materials Science and Engineering A*, 564 (2013), 473–477, doi:10.1016/j.msea.2012.12.011
- <sup>13</sup> S. Ranganath, M. Vijayakumar, J. Subrahmanyam, Combustion-assisted synthesis of Ti-TiB-TiC composite via the casting route, *Materials Science and Engineering A*, 149 (1992), 253–257, doi:10.1016/0921-5093(92)90386-F
- <sup>14</sup> X. Zhang, W. Lü, D. Zhang, R. Wu, Y. Bian, P. Fang, In situ technique for synthesizing (TiB+TiC)/Ti composites, *Scripta Materialia*, 41 (1999), 39–46, doi:10.1016/S1359-6462(99)00087-1
- <sup>15</sup> M. M. Wang, W. J. Lu, J. N. Qin, D. Zhang, B. Ji, F. Zhu, Superplastic behavior of in situ synthesized (TiB+TiC)/Ti matrix composite, *Scripta Materialia*, 53 (2005), 265–270, doi:10.1016/j.scriptamat.2005.01.049
- <sup>16</sup> J. Lu, J. Qin, W. Lu, Y. Chen, D. Zhang, H. Hou, Effect of hydrogen on superplastic deformation of (TiB+TiC)/Ti-6Al-4V composite, *International Journal of Hydrogen Energy*, 34 (2009), 8308–8314, doi:10.1016/j.ijhydene.2009.07.091
- <sup>17</sup> S. Sun, M. Wang, L. Wang, J. Qin, W. Lu, D. Zhang, The influences of trace TiB and TiC on microstructure refinement and mechanical properties of in situ synthesized Ti matrix composite, *Composites Part B: Engineering*, 43 (2012), 3334–3337, doi:10.1016/j.compositesb.2012.01.075
- <sup>18</sup> M. M. Wang, W. J. Lu, J. Qin, F. Ma, J. Lu, D. Zhang, Effect of volume fraction of reinforcement on room temperature tensile property of in situ (TiB+TiC)/Ti matrix composites, *Materials & Design*, 27 (2006), 494–498, doi:10.1016/j.matdes.2004.11.030
- <sup>19</sup> W. Lu, D. Zhang, X. Zhang, R. Wu, T. Sakata, H. Mori, Microstructure and tensile properties of in situ (TiB+TiC)/Ti6242 (TiB:TiC= 1: 1) composites prepared by common casting technique, *Materials Science and Engineering A*, 311 (2001), 142–150, doi:10.1016/S0921-5093(01)00910-8
- <sup>20</sup> B. R. Bhat, J. Subramanyam, V. B. Prasad, Preparation of Ti-TiB-TiC & Ti-TiB composites by in-situ reaction hot pressing, *Materials Science and Engineering A*, 325 (2002), 126–130, doi:10.1016/S0921-5093(01)01412-5
- <sup>21</sup> D. Ni, L. Geng, J. Zhang, Z. Zheng, Fabrication and tensile properties of in situ TiBw and TiCp hybrid-reinforced titanium matrix composites based on Ti-B 4 C-C, *Materials Science and Engineering A*, 478 (2008), 291–296, doi:10.1016/j.msea.2007.06.004
- <sup>22</sup> M. Khayet, C. Cojocar, M. Essalhi, Artificial neural network modeling and response surface methodology of desalination by reverse osmosis, *Journal of Membrane Science*, 368 (2011), 202–214, doi:10.1016/j.memsci.2010.11.030
- <sup>23</sup> L. Xie, C. Jiang, W. Lu, The influence of shot peening on the surface properties of (TiB+TiC)/Ti-6Al-4V, *Applied Surface Science*, 280 (2013), 981–988, doi:10.1016/j.apsusc.2013.05.135
- <sup>24</sup> M. T. Ozkan, H. B. Ulas, M. Bilgin, Experimental design and artificial neural network model for turning the 50crv4 (sae 6150) alloy using coated carbide/cermet cutting tools, *Mater. Tehnol.*, 48 (2014), 227–236
- <sup>25</sup> A. Mukherjee, S. Schmauder, M. Ru, Artificial neural networks for the prediction of mechanical behavior of metal matrix composites, *Acta metallurgica et materialia*, 43 (1995), 4083–4091, doi:10.1016/0956-7151(95)00076-8
- <sup>26</sup> J. Han, M. Kamber, *Data mining: concepts and techniques*, 2<sup>nd</sup> Ed., Amsterdam, 2006
- <sup>27</sup> D. Afshari, M. Sedighi, M. R. Karimi, Z. Barsoum, Prediction of the nugget size in resistance spot welding with a combination of a finite-element analysis and an artificial neural network, *Mater. Tehnol.*, 48 (2014), 33–38
- <sup>28</sup> U. Özdemir, B. Özbay, S. Veli, S. Zor, Modeling adsorption of sodium dodecyl benzene sulfonate (SDBS) onto polyaniline (PANI) by using multi linear regression and artificial neural networks, *Chemical Engineering Journal*, 178 (2011), 183–190, doi:10.1016/j.cej.2011.10.046
- <sup>29</sup> A. Çelekli, S. S. Birecikligil, F. Geyik, H. Bozkurt, Prediction of removal efficiency of Lanaset Red G on walnut husk using artificial neural network model, *Bioresource technology*, 103 (2012), 64–70, doi:10.1016/j.biortech.2011.09.106
- <sup>30</sup> M. Rezakazemi, S. Razavi, T. Mohammadi, A. G. Nazari, Simulation and determination of optimum conditions of pervaporative dehydration of isopropanol process using synthesized PVA-APTEOS/TEOS nanocomposite membranes by means of expert systems, *Journal of Membrane Science*, 379 (2011), 224–232, doi:10.1016/j.memsci.2011.05.070
- <sup>31</sup> M. Rezakazemi, T. Mohammadi, Gas sorption in H<sub>2</sub>-selective mixed matrix membranes: Experimental and neural network modeling, *International Journal of Hydrogen Energy*, 38 (2013), 14035–14041, doi:10.1016/j.ijhydene.2013.08.062
- <sup>32</sup> L. Wang, B. Yang, R. Wang, X. Du, Extraction of pepsin-soluble collagen from grass carp (*Ctenopharyngodon idella*) skin using an artificial neural network, *Food Chemistry*, 111 (2008), 683–686, doi:10.1016/j.foodchem.2008.04.037
- <sup>33</sup> E. Maleki, K. Sherafatnia, Investigation of single and dual step shot peening effects on mechanical and metallurgical properties of 18CrNiMo7-6 steel using artificial neural network, *International Journal of Materials, Mechanics and Manufacturing*, 4 (2016), 100–105, doi:10.7763/IJMMM.2016.V4.233
- <sup>34</sup> S. Haykin, *Neural Network, A comprehensive foundation*, Neural Networks, 2 (2004)
- <sup>35</sup> T. P. Vogl, J. Mangis, A. Rigler, W. Zink, D. Alkon, Accelerating the convergence of the back-propagation method, *Biological cybernetics*, 59 (1988), 257–263, doi:10.1007/BF00332914
- <sup>36</sup> A. Savran, M. Alci, S. Yildirim, R. Yigit, E. Celik, Application of a neural network for estimating the crack formation and propagation in sol-gel CeO<sub>2</sub> coatings during processing at temperature, *Mater. Tehnol.*, 48 (2014), 453–457
- <sup>37</sup> P. Shabanzadeh, N. Senu, K. Shameli, F. Ismail, M. Mohaghehtabar, Application of artificial neural network (ANN) for the prediction of size of silver nanoparticles prepared by green method, *Digest Journal of Nanomaterials and Biostructures*, 8 (2013), 541–549



## ANALYSIS OF TWIN-ROLL CASTING AA8079 ALLOY 6.35- $\mu\text{m}$ FOIL ROLLING PROCESS

### ANALIZA PROCESA VALJANJA 6,35 $\mu\text{m}$ FOLIJE IZ ZLITINE AA8079 ULITE MED DVEMA VALJEMA

Ahmet Can<sup>1</sup>, Hüseyin Arikan<sup>2</sup>, Kadir Çınar<sup>2</sup>

<sup>1</sup>Necmettin Erbakan University, Faculty of Engineering, Department of Industrial Design, Konya, Turkey

<sup>2</sup>Necmettin Erbakan University, Faculty of Engineering, Department of Mechanical Engineering, Seydişehir, Konya, Turkey  
ahmetcan@konya.edu.tr

*Prejem rokopisa – received: 2015-06-29; sprejem za objavo – accepted for publication: 2015-12-16*

doi:10.17222/mit.2015.134

In this work the rolling process and properties of a 6.35- $\mu\text{m}$  twin-roll casting AA8079 aluminum alloy foil was analyzed. First, the 8-mm-thick sheets were produced with a twin-roll casting technology. This product was annealed and cold rolled to a 6.35- $\mu\text{m}$  foil with suitable processing conditions. The mechanical tests and microhardness measurement was applied to specimens derived from all the foil-rolling process stages. On the other hand, the specimens' surface roughness and the surface structure are visualized with an atomic force microscope and an SEM. The microstructural investigation is realized with an optical microscope and XRD. The von-Mises total effective strain was calculated by determining the incremental work for all of the cold-rolling cycle. The alloy showed very low ductility in the tensile tests because of the second-phase metastable intermetallic particles such as  $\text{Al}_3\text{Fe}$ . The maximum elongation at the breaking value was measured for 256- $\mu\text{m}$ -foil as 4.5 %. On the other hand, the alloy did not show any significant strain hardening after the cold rolling during the plastic-deformation stages.

Keywords: aluminum foil, cold rolling, twin roll casting

V delu je bil analiziran postopek valjanja in latnosti 6,35 folije iz AA8079 aluminijeve zlitine, ulite med dvema valjema. Najprej je bil izdelan 8 mm debel trak po postopku ulivanja med dvema valjema. Trak je bil primerno žarjen in hladno zvaljan v 6,35  $\mu\text{m}$  folijo. Iz vseh stopenj procesa valjanja so bili vzeti vzorci na katerih so bile določene mehanske lastnosti in izmerjena mikro trdota. Poleg tega je bila hrapavost površine in struktura površine vizualizirana z mikroskopom na atomsko silo (AFM) in iz SEM. Preiskava mikrostrukture je bila izvršena s svetlobnim mikroskopom in z rentgensko difrakcijo (XRD). Za določanje stopnjujočega dela, med celotnim ciklom hladnega valjanja, je bila izračunana celotna von-Mises efektivna napetost. Zlitina je pokazala zelo nizko duktilnost pri nateznih preizkusih zaradi vsebnosti delcev sekundarne metastabilne intermetalne faze  $\text{Al}_3\text{Fe}$ . Maksimalni raztezek pri porušitvi je bil pri 256  $\mu\text{m}$  debeli foliji 4.5 %. Po drugi plati pa zlitina ni kazala nobenega občutnega napetostnega utrjevanja med posameznimi fazami plastične deformacije.

Ključne besede: aluminijeve folija, hladno valjanje, ulivanje med dvema valjema

## 1 INTRODUCTION

The production of aluminum alloys with twin roll casting (TRC) technology has been introduced to the industry about 50 years ago. It was claimed that TRC would offer significant reduction in the cost of aluminum sheet and foil production, compared to the conventional production technique, i.e. DC casting and hot rolling. Major evolution in the TRC technology has been attained in the last 5 years. It has been widely accepted due to its low investment cost, operational cost and flexibility provided to the production planning.<sup>1</sup>

The strengthening of metals due to increase in lattice defects during cold deformation makes a thermodynamically unstable structure and promotes subsequent restoration phenomena. The restoration processes can change microstructures as well as mechanical and physical properties of metals and alloys while required mechanical and physical properties may be achieved by adjusting the deformation and annealing variables.<sup>2</sup> Some of the researchers<sup>3-6</sup> studied about cold rolling of

various aluminum alloys. D. Wang et al.<sup>3</sup> studied about severe cold rolling (CR) deformation properties of AA 7050. The strength of the 7050 samples increased with increasing the CR reduction. The yield and ultimate strengths of the CR sample with a reduction of 67 % increased by 16.5 % and 9.2 %, respectively. Wang reported that both the residual dislocations and heterogeneously nucleated fine-phase particles in the matrix increased the strength of the CR samples.

Z. Liang et al.<sup>4</sup> studied the evolution of texture as well as microstructures in an AA 7055 aluminum alloy during cold rolling. Author reported that more micro-bands are formed in the center of the plate with the rolling reduction, while the spacing between two bands decreases.

S. X. Zhou et al.<sup>5</sup> studied about cold Rolling of AA 1050 alloys which are produced by hot finishing rolling and twin roll casting. Authors studied the microstructure mechanical properties such as tensile strength, yield stress elongation area reduction, elastic modulus hardness and impact energy and formability.

J. G. Lenard<sup>6</sup> studied the effect of roll roughness on the rolling parameters during cold rolling of 6061-T6 alloys. The effects of the roughness of the work roll on the roll force roll torque and the forward slip and additionally the frictional mechanisms were identified. Author reported that high roughness appeared to increase the possibility of insufficient lubrication at the interfaces. While both adhesive and ploughing forces were present in all instances, the ploughing forces became dominant at higher rolling speeds. The contribution of ploughing to frictional resistance increased as the roll roughness increased to a certain value and beyond that its behavior depended on the rolling speed. J. G. Lenard and S. Zhang<sup>7</sup> studied a similar work with commercially pure aluminum. Using lighter oil, boundary or mixed lubrication is produced. With higher viscosity oil, negative forward slip is observed, indicating the onset of hydrodynamic lubrication. The coefficients of friction are found to increase with increasing reduction and decreasing rolling speeds.<sup>7</sup>

K. S. S. Sathees et al.<sup>8</sup> studied about with purity aluminum sheets which were subjected to intense plastic straining by constrained Groove pressing method. The tensile behavior evolution with increased straining indicates substantial improvement of yield strength by 5.3 times from 17 MPa to 90 MPa during first pass corroborated to grain refinement observed. Quantitative assessment of degree of deformation homogeneity using micro hardness profiles reveal relatively better strain homogeneity at higher number of passes.

G. Liv<sup>9</sup> studied the development of surface structure forming properties and corrosion resistance during cold rolling of twin-roll cast of AA 3003. It is found that the as-cast surface determines the development of the surface topography during cold rolling. This is due to the large roughness associated with the groove/shingle configuration of the as-cast surface. Author pointed out that, the initial surface topography and the cold rolling are of great importance to the quality of the end product of the cold rolling. Since there are differences in the initial topography induced by the surface of the casting rolls, there will be differences in the development of the surface during the deformation sequence. The rough pattern of the as-cast surface results in large gorges in the first pass. In the second pass shingles are smeared out on top of the gorges. Patches of the shingle are not welded to the bulk sheet.

It must be focused to metallurgical principles of Aluminum alloys for determining the mechanical and formability behavior of Al-Fe alloys. The main concern is propagation of second phase intermetallic particles which is a function of both the cooling rate and the chemical composition of Al-Fe alloys and their effects on mechanical properties. Some of the researchers focused the metallurgical behavior of Al-Fe powders and alloys.<sup>10-13</sup> On the other hand some of the researchers focused the rapid cooling rate and severe deformation effects on the

different Al-Fe alloys.<sup>14-16</sup> M. Aghaie-Khafri and R. Mahmudi<sup>17</sup> have investigated the plastic instability and necking behavior of AA8079 aluminum alloy sheet in temper-annealed and fully annealed conditions.

In this work, the rolling process and properties of 6.35 mm twin roll casting AA8079 aluminum alloy foil was analyzed. Foils production were tested on the level of industrial trials with no rupture by the time rolling process. Firstly the 8 mm thickness sheets were produced by twin roll casting technology. This product was annealed and cold rolled to 6.35  $\mu\text{m}$  foil with suitable process conditions. The mechanical tests and micro hardness measurement is applied to specimens derived from whole foil rolling process stages. On the other hand the specimens' surface roughness and the surface structure is visualized with Atomic Force Microscope and SEM.

## 2 MATERIAL AND EXPERIMENTAL PART

The material used in this experimental investigation was an aluminum-rich eutectic alloy AA8079. As derived from XRF analyses the alloy containing (in mass fractions, w/%) 99 % Al, 0.8 % Fe and 0.12 % Si with minor constituents of 0.02 % Cu, 0.02 % Mn, 0.009 % Zn, and 0.022 % Ti. Notice that this work is not only an experimental work. The whole experimental outputs were derived from a real industrial production process. So, nearly 2000 kg raw material of AA8079 was melted and roll-casted to 8 mm thickness and cold rolled to 4 mm at one step in CR (Cold Rolling Machine). Then the material homogenized at 580 °C for 8 h, furnace cooled, and then cold rolled to the thickness 0.53 mm with four steps. Then the material annealed in a furnace at 450 °C and a holding time of 4 h. Then cold rolled to the initial foil thickness 250  $\mu\text{m}$  with one step. The 250  $\mu\text{m}$  sheet was cold rolled to 100 and then 56  $\mu\text{m}$  with two steps in FR-I rolling machine. The 56  $\mu\text{m}$  foil was cold rolled to 14  $\mu\text{m}$  with two steps in FR-II rolling machine. Then the final thickness foil was derived by cold rolling with twofold (14+14  $\mu\text{m}$  foil on foil) foil in FR-III rolling machine. The diameter of the (CR) cold rolling pin was 400 mm, and the foil rolling (FRI-III) pin was 240 mm. The Rolling speed of CR, FRI, FRII, FRIII were, 12-175-325-560 m/min respectively. After final (6.35  $\mu\text{m}$ ) cold rolling, the annealing in a furnace at 270 °C and a holding time of 11 h is applied.

The experimental samples were derived from all rolling stages. All the experimental numeric outputs such as tensile-yield strength, elongation at break and surface roughness values verified with minimum 3 times repeated tests results. These outputs were averaged and given with derived error band in the graphs. The micro hardness test was realized in NDT MH-140 under 5 g loading forces. The surface roughnesses of the foils were measured with Mitutoyo Surf Test SJ301 roughness measurement device. The 3D surface topography was determined with Park XE-100 Atomic Force Microscope

(AFM). The samples were polished with Struers polishing devices with suitable abrasives. The specimens thinner than 250  $\mu\text{m}$  etched with 0.5 % HF solutions in 30 s and then cleaned with alcohol and dried with air. 8-4-2 mm specimens were etched electrolytically under the 24  $^{\circ}\text{C}$ , 18 V electric current in a 5 % Tetra Fluoroboric acid solution in 120 s. And Nikon stereo light microscope is used for determining the microstructure with X10-500 magnification. The grain dimensions are derived with ASTM E112. The tensile tests were realized with Testometrik DBBMTCL-250 Kgf device. And the pinhole counting is realized with special lighting table with BS-EN 546-4 procedures.

### 3 RESULTS AND DISCUSSION

#### 3.1 Mechanical properties

A tensile test procedure is applied after all foil cold rolling stages and annealing procedures. The ultimate engineering stress before rupture of specimen, Engineering Tensile Stress ( $\sigma_u$ ), Yield Stress ( $\sigma_{0.2}$ ) and Strain at Failure ( $\epsilon_f$ ) values were determined with 100 mm initial length samples ( $A_{100}$ ). Nearly same tendency and graphics were observed in all tensile tests for cold rolled specimens. A specific stress-strain graphics for AA8079 were given in **Figure 1** as representative. Aluminum on the other hand having a FCC crystal structure does not show the definite yield point in comparison to those of the BCC structure materials, but shows a smooth engineering stress-strain curve. The yield strength ( $\sigma_{0.2}$ ) therefore has to be calculated from the load at 0.2 % strain. It can be observed from **Figure 1** that the material does not show any significant strain hardening after yield point. It causes the develop plastic instability and, thereby, very low ductilities. When this situation compared with the previous researchs the same tendency is observed. This undesirable phenomenon and the associated strain localization can be avoided by employing annealing process.<sup>17</sup>

The von-mises total effective strain ( $\epsilon_{vm}$ ) was calculated for determining the incremental work for all

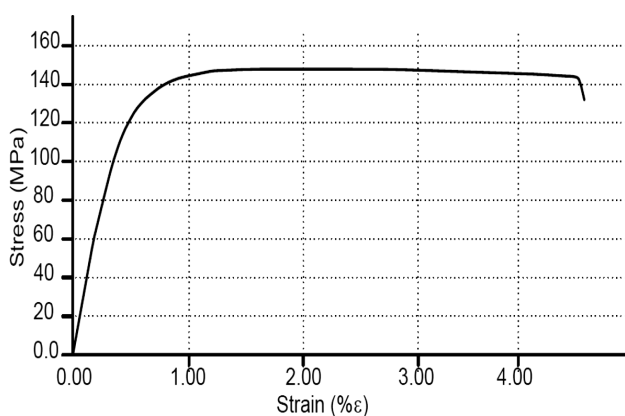


**Figure 1:** The stress-strain graphic for 256  $\mu\text{m}$  specimen  
**Slika 1:** Diagram napetost-raztezek za vzorec debeline 256  $\mu\text{m}$

cold rolling cycle. **Figure 2a** shows the  $\epsilon_{vm}$  versus (Tensile Stress)  $\sigma_u$ , **Figure 2b** shows the  $\epsilon_{vm}$  versus (Yield Stress)  $\sigma_{0.2}$ . As can be seen in **Figures 2a** and **2b** an increase can be observed in after first cold Rolling ( $\epsilon_{vm} = 1.5$ ). It can be explained by strain hardening of cold worked alloy. But nearly no change was observed on tensile and the yield stress between  $\epsilon_{vm} = 1.5$  and 4.2. It can be explained by very low and saturated strain hardening and very long post uniform elongations as depicted in stress-strain curve in **Figure 1**. Notice that the AA8079 material includes 99 % pure aluminum. When the tensile and yield strength graphs are compared with the previous researcher result the same tendency can be observed. K. S. S. Satheesh and T. Raghu<sup>8</sup> reported that the yield strength ( $\sigma_{0.2}$ ) increases significantly after first pass of cold working, whereas the tensile strength ( $\sigma_u$ ) is nearly showed same behavior. Considerable increase in strength observed after first pass is mainly attributed to the significant decrease in

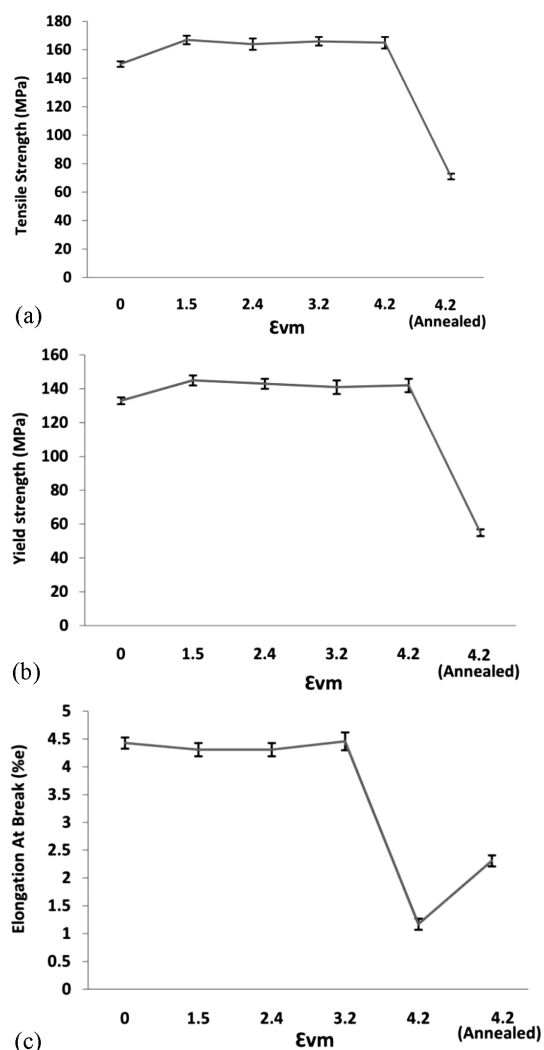


**Figure 2:** The effect of equal strain on mechanical properties: a) tensile strength, b) yield strength, c) elongation at break

**Slika 2:** Vpliv enake napetosti na mehanske lastnosti: a) natezna trdnost, b) meja plastičnosti, c) raztezek ob poružitvi

grain sizes and the increased dislocation density which necessitates higher applied stress for dislocation motion by slip. A horizontal trend in  $\sigma_{0.2}$  &  $\sigma_u$  is observed in subsequent passes which is attributed to the increased recovery/annihilation of dislocations with increasing accumulated strain and formation of micro cracks. Propagation of intermetallic phases in structure has great affect on mechanical properties. Previous researchers indicate that the intermetallic phases reduce the strength and elongation capability of the aluminum alloys. When tensile fracture surfaces of aluminum alloy samples investigated with SEM, it is observed that fracture occurs secondary intermetallic phases and inclusion concentration regions.<sup>18</sup>

P. J. Appsa et al.<sup>15</sup> investigated the effect of coarse second-phase particles on the rate of grain refinement and material properties during severe deformation processing. Authors indicate that the hardness development of the AA8079, with increasing deformation process strain and the hardness of the AA8079 was slightly higher than that of the single-phase alloy, due to the presence of the second-phase particles. During deformation, the work hardening of the AA8079 alloy saturated much more rapidly than the single-phase alloy and reached a plateau at a strain of only  $\epsilon_{vm} \sim 3$  showing little further increase even after a strain of 10. This behavior would be expected to correspond to a continued fast micro structural refinement with increasing strain.

The restoration processes can change microstructures as well as mechanical and physical properties of metals and alloys while required mechanical and physical properties may be achieved by adjusting the deformation and annealing variables.<sup>2</sup> The annealing process was decreased the tensile and the yield strength significantly. Reversely the annealing process was increased the elongation at break values. The maximum elongation at break  $\epsilon_f$  value is observed as 4.4 from 250  $\mu\text{m}$  to 15  $\mu\text{m}$  foils. This value was decreased to 1.2 % for final 6.5  $\mu\text{m}$

foils. Then the last foil annealing treatment increased the elongation value to 2.3 %. It can be concluded that the recovery phenomenon is the major reason of decrease in flow stress. The steep increase in ductility implies that a complete softening due to recrystallization and grain refinement has taken place, and there covered structure, which is expected to be the main cause of the observed premature failure, has been removed.<sup>8,17</sup>

**Figure 3** shows the micro-hardness results of the rolling stages from TRC to last foil annealing. The first cold rolling process after TRC is decreased to micro-hardness from 38 HV to 47 HV. During the deformation process, after the 1st annealing process the hardness of the alloy saturated rapidly and reached a plateau at a 250  $\mu\text{m}$  thickness. This behavior would be expected to correspond to a continued fast micro structural refinement with increasing strain. The annealing at 450 °C and a holding time of four hours decreased the micro-hardness from 47 HV to 29 HV. After annealing the cold rolling was decreased to 29 HV to 42 HV and the micro hardness has no significant change during the cold rolling process until the last annealing process. The micro hardness was decreased to the least value after the last foil annealing process. As compared the micro hardness behavior with previous works; the results are coinciding with each other. Salehi reported the variation of micro-hardness after cold rolling with 20 %, 30 % and 40 % reduction in thickness. As a result, increased cold working increases the micro-hardness of the structure by increased dislocation density and deformed grains.<sup>2,8,15</sup> There is significant increase in hardness after first pass, after 1<sup>st</sup> annealing followed by marginal increase after second pass. During subsequent passes the hardness drops slightly and tends to remain fairly uniform fairly coinciding with earlier findings.<sup>8</sup>

After final cold rolling 14  $\mu\text{m}$  to 6.5  $\mu\text{m}$ , ( $\epsilon_{vm} = 4.2$ ) the annealing in a furnace at 270 °C and a holding time of 11 h is applied. This treatment reduced the tensile and the yield strength of the materials 71 MPa and 55 MPa respectively. The cold rolled and annealed 6.5  $\mu\text{m}$  foils stress-strain graphics were depicted in **Figures 4a** and **4b**. The cold rolled 6.5  $\mu\text{m}$  foil has showed maximum elongation  $\epsilon = 1.2$ . This value was increased to 2.3 % after the last annealing process. These elongations at break values show that this material can be called a brittle material because of low ductility. This undesirable phenomenon and the associated strain localization can be avoided by employing suitable annealing procedures. The annealed specimen's tensile graphics has some differences from cold rolled specimens. The annealed specimens showed a dynamic deformation aging behavior or The Portevin–Le Chatelier effect (PLC) effect. PLC describes a serrated stress-strain curve or jerky flow, which some materials exhibit as they undergo plastic deformation. This behavior is an expected behavior on annealed aluminum alloys only in limited regimes of strain rate. In a uniaxial tension test for instance, this

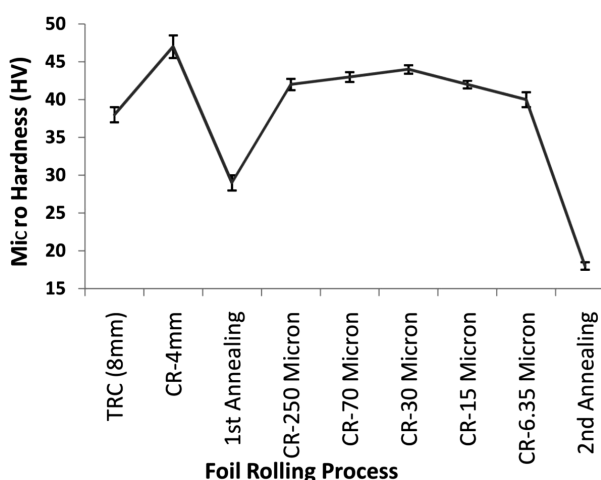


**Figure 3:** The variation of Micro hardness of the foils during cold rolling

**Slika 3:** Spreminjanje mikrotvrdote folij med hladnim valjanjem



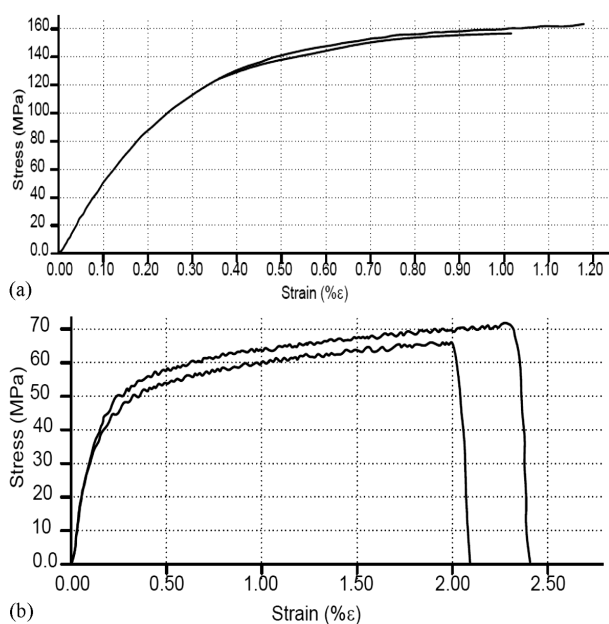


**Figure 4:** The stress-strain graphic for 6.5  $\mu\text{m}$  specimen: a) cold rolled, b) annealed-270  $^{\circ}\text{C}$ , 11 h

**Slika 4:** Diagrami napetost-raztezek pri vzorcu debeline 6,5  $\mu\text{m}$ : a) hladno valjano, b) žarjeno 270  $^{\circ}\text{C}$ , 11 h

irregular flow results in inhomogeneous deformation with various localization bands. These bands can be static, hopping and sometimes propagating along the specimen. It is also observed in presence of this irregular flow that some materials fail by a shear localization mode prior to any diffuse necking in uniaxial tension and even under more complex states of stress.<sup>19</sup>

### 3.2 Microstructure properties

The samples were characterized by XRD with a Bruker D8 advance diffractometer (40 kV, 40 mA), in Bragg-Brentano reflection geometry with Cu- $K\alpha$  radiation ( $\lambda = 0.154 \text{ nm}$ ). The data were obtained between  $10^{\circ}$  and  $90^{\circ}$  in steps of 0.1 with counting time of 3.

When the previous research are investigated various author focused the intermetallic phase formation. On the other hand some of the researchers focused the TRC process which is very important the on the effect on cooling rate. Al-rich portion of the Al-Fe binary phase diagram shows many intermetallic formed by the peritectic reactions.<sup>13</sup> The  $\text{Al}_{13}\text{Fe}_4$ ,  $\text{Al}_5\text{Fe}_2$ ,  $\text{Al}_3\text{Fe}$  ( $\text{Al}_n\text{Fe}_m$ ) etc. are possible intermetallic phases in Aluminum alloys.<sup>1,10</sup> **Figure 5** shows the XRD diffractogram pattern of the 6.35  $\mu\text{m}$  foil of AA8079 alloy. The peak in  $2\theta$   $78^{\circ}$  indicates the  $\alpha$ -Al (311) with miller index. The remaining peaks indicate  $\text{Al}_3\text{Fe}$  intermetallic phases. Alloying of Al with Fe increases the high temperature strength due to a dispersion of second phase particles. Some of the researchers<sup>15</sup> introduces this  $\text{Al}_3\text{Fe}$  intermetallic peak as  $\text{Al}_{13}\text{Fe}_4$ . On the other hand some of the researcher reported that, these two monoclinic structural submicron intermetallics are very close to each other.<sup>12,20</sup>

The rapid cooling and solidification have great effect on formation of the intermetallic phase. However, the development of solidification microstructures along the (Twin Roll Casting) TRC process has some particular characteristics. The TRC makes the solidification with water cooled cylinders and it causes high cooling rate solidification and deforming near the surface.<sup>1</sup> High cooling rates near the surface cause the formation of metastable intermetallic  $\text{Al}_6\text{Fe}$  and  $\text{Al}_m\text{Fe}$  compounds in addition to the stable  $\text{Al}_3\text{Fe}$ . It is often considered that at high cooling rates, due to kinetic restrictions there is not enough time for the atoms to arrange themselves in a stable structure.<sup>1,13</sup> During the cooling stage no nucleation is involved and an epitaxial solidification occurs. Moreover, the onset of solidification at the molten substrate interface is characterized by a solidification velocity that approaches zero, favoring the initial formation of the stable Al- $\text{Al}_3\text{Fe}$  eutectic. This structure probably continues to grow in spite of the sudden increase in the solidification velocity over the surface, i.e., the equilibrium Fe aluminide is not displaced with increasing solidification velocity by a metastable aluminide.<sup>10,14,15</sup>

Previous researchers reported that the Si content is lower than 0.15 % of mass fractions of Si, which is the limiting Si content permitting to avoid  $\text{AlFeSi}$  to be the dominant intermetallic phase.<sup>16</sup> The material used in the experiment (AA8079) has the Si ratio of 0.12 and no  $\text{AlFeSi}$  intermetallic was observed in the structure.

A microstructure samples were derived after all rolling process. The procedure for etching and electro polishing for thick specimens was described in the previous sections. **Figures 6a** and **6b** shows the etched and electro polished optical microscope images respectively. As depicted in **Figures 6a** and **6b** the intermetallic phases needles oriented along the nonhomogeneous grains. Orientation along the casting directions between the grains boundaries were not observed on 8 mm TRC samples. The 8 to 4 mm cold rolled specimen's microstructure was depicted in **Figures 6c** and **6d**. The effect

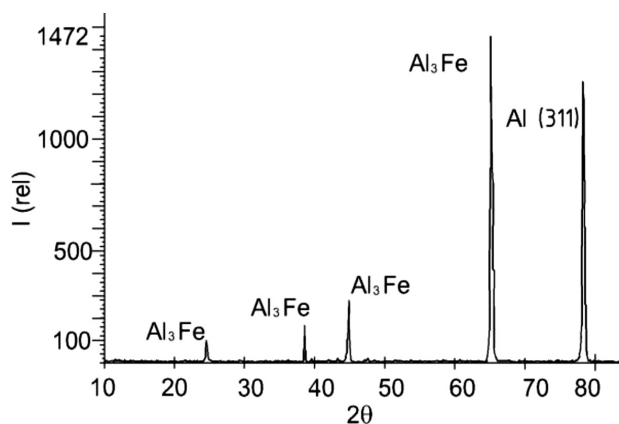


**Figure 5:** X-ray diffractogram of the Twin Roll Casting 6.35  $\mu\text{m}$  AA8079 Foil

**Slika 5:** Rentgenogram 6,35  $\mu\text{m}$  folije iz traku AA8079, ulitega med dvema valjema

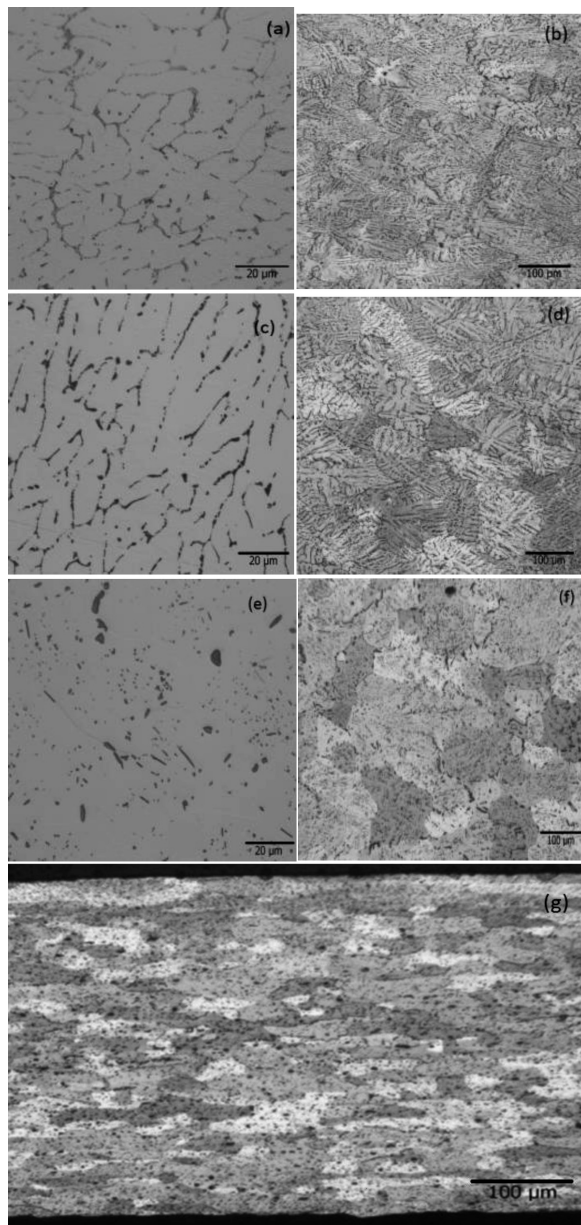


**Figure 6:** Etched and electro polished light microscope images: a), b) twin roll casting, c), d) cold rolled, e), f) 580 °C, 8 h annealed and g) 250  $\mu\text{m}$  foil rolling samples

**Slika 6:** Mikrostruktura po jedkanju in elektropoliranju: a), b) ulito med dvema valjema, c), d) hladno valjano, e), f) žarjeno 8 ur na 580 °C in g) vzorec valjane 250  $\mu\text{m}$  folije

of the 50 % plastic deformation on cold rolling can be observed on these figures. The narrowing affect along the grain boundary can be observed as comparing the **Figures 6a** and **6c**. After 4 mm cold rolling process the annealing (580 °C – 8 h) is applied before the foil rolling process. **Figures 6e** and **6f** show the annealed samples microstructure. The needle shape of the intermetallic particles transforms to bulk shape by the recovery effect. The microstructures of the 250  $\mu\text{m}$  to 6.5  $\mu\text{m}$  foil specimens' light microscope images were determined. The 250  $\mu\text{m}$  foil microstructure is depicted in **Figure 6g** as representative. As depicted in **Figure 6g** the grains are

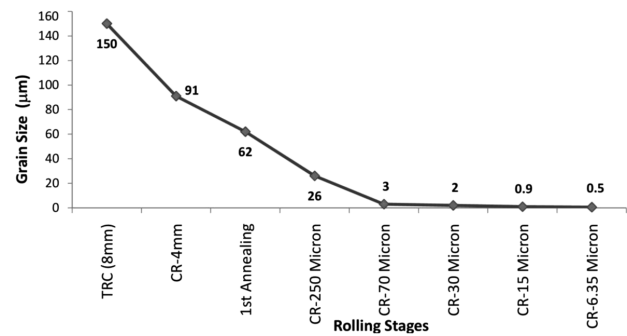


**Figure 7:** The variation of grain size with TRC to foil rolling stages  
**Slika 7:** Spreminjanje velikosti zrn od TRC do končne izvaljane folije

elongated along the rolling direction and the narrowed vertically to rolling direction by comparing the previous stage microstructure as given in **Figures 6a** and **6f**.

The distance between intermetallic particles are decreased with increased plastic deformation ratio. The grain size vertically to rolling direction is measured with image processing and illustrated with grain size vs rolling stages from TRC to 6.5  $\mu\text{m}$  foil in **Figure 7**. As depicted in **Figure 7** the grain size was decreased from 150  $\mu\text{m}$  to 0.5  $\mu\text{m}$ . After  $\epsilon_{\text{vm}} = 2.4$  strain, the submicron grain size were observed in the microstructure.

### 3.3 Surface properties

Not only the metallurgical and mechanical properties of the aluminum sheets and foils are very important, but also the surface properties of the aluminum sheets and foils are very important and it must be characterized to

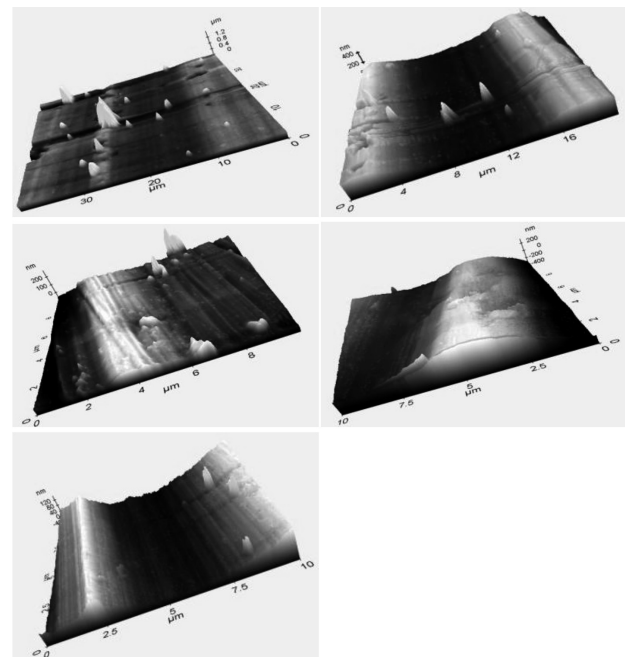


**Figure 8:** The atomic force microscope visualization of the thin foils from 250 to 6.5  $\mu\text{m}$

**Slika 8:** Vizualizacija površine folij od 250  $\mu\text{m}$  do 6,5  $\mu\text{m}$ , z mikroskopom na atomsko silo

desired functions as where they used. The chemical and electrochemical surface properties and the surface structure are very important in lithography sheets and also in food industry. In contrary to hydrophilic lithography sheets the surface must be smooth and shiny in food industry. So in this work the surface properties were determined with atomic force microscope (AFM), surface roughness measurement and optical microscope. And also the pin holes and rolling tracks were determined with the SEM and optically with light source. The AFM scanning images were depicted in **Figure 8** from 250  $\mu\text{m}$  to 6.5  $\mu\text{m}$ . Notice that the vertical scale is used as  $\mu\text{m}$  and nm depending on the roughness of the samples. The valley and the peaks are oriented along the rolling direction. **Figure 9** shows the surface roughness of the rolled samples and the roller pins surface roughness. As depicted in **Figure 9** the surface roughness is decreased with rolling stages. The surface roughness of the rolling pin and the foils are very close in almost all cases especially in thinner foils.

The pin hole counting is realized with a special light source in an dark ambient. The holes are counted for per 1  $\text{dm}^2$  as detailed in ISO-EN 546-4. **Figure 10a** shows a sample pin hole SEM images. The pin hole diameter is measured as 1  $\mu\text{m}$  and meanly 10 pin holes are counted in 1  $\text{dm}^2$  standard area. And also the rolling tracks, porous and the skid effected banked up structure can be observed from **Figures 10a** and **10b**.

#### 4 CONCLUSION

Foils production were tested on the level of industrial trials with no rupture by the time rolling process. It has been shown that selected TRC parameters result in the production of 8 mm sheet of good quality, with especially: fine microstructure with adequate grain refiner addition and annealing conditions.

Although the hard phases (that could lead to porosity problems) in the microstructure the 8 mm to 6.35  $\mu\text{m}$  foil rolling was realized by obtaining the adequate surface properties such as sufficient pin hole, porosity

The von-misses total effective strain was calculated for determining the incremental work for all cold rolling

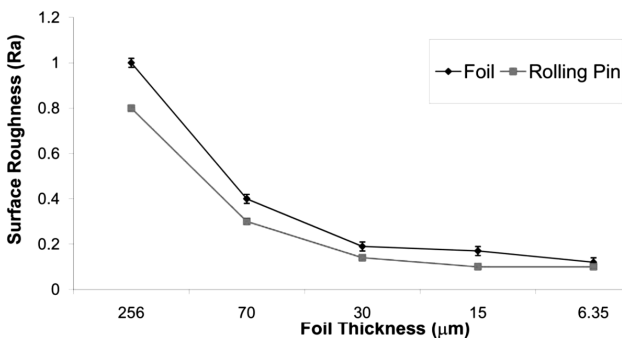


**Figure 9:** The variation of the surface roughness in foil rolling stages  
**Slika 9:** Spreminjanje hrapavosti površine pri valjanju folij

cycle. After first cold rolling ( $\epsilon_{vm} = 1,5$ ) the yield and the tensile stress were increased in a limited range. This increase was explained by strain hardening of cold worked alloy. After continued deformation no change was observed on tensile and the yield stress between  $\epsilon_{vm} = 1.5$  and 4.2. It can be explained by nearly saturated strain hardening behavior after a critical plastic deformation.

On the other hand the maximum elongation at break  $\epsilon_f$  value is observed as 4.4 from 250  $\mu\text{m}$  to 15  $\mu\text{m}$  foils. These elongations at break values show that this material can be called a brittle material because of low ductility.

The first cold rolling 8 mm to 4 mm process after TRC is decreased to micro hardness to the highest value of 47 HV. During the deformation process, after the 1st annealing process the hardness of the alloy saturated rapidly and reached a plateau at a 250  $\mu\text{m}$  thickness. This behavior would be expected to correspond to a continued fast microstructure refinement with increasing strain.

The annealed foil specimens showed a dynamic deformation aging behavior or The Portevin–Le Châtelier effect (PLC) effect in tensile test. PLC describes a serrated stress-strain curve or jerky flow, which some materials exhibit as they undergo plastic deformation.

The XRD analyses shows that the TRC casting AA8079 alloys includes  $\alpha\text{-Al}$  (311) and the  $\text{Al}_3\text{Fe}$  meta-

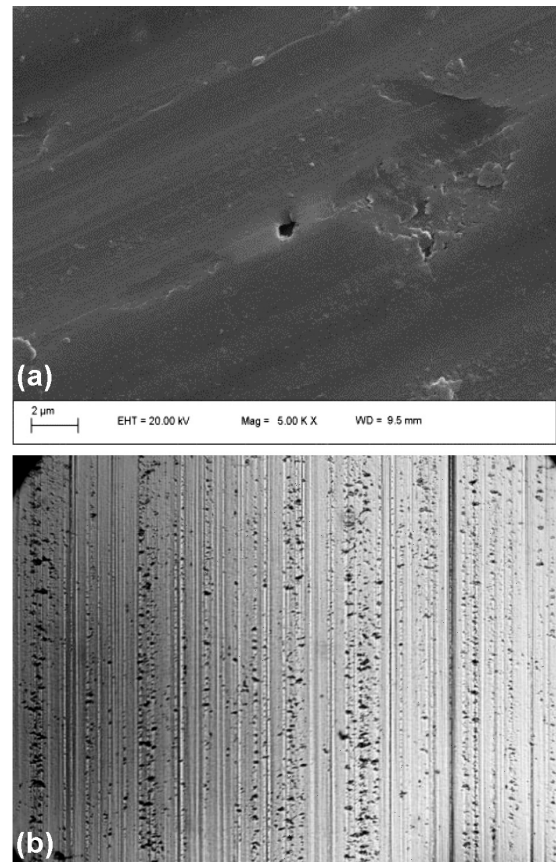


**Figure 10:** The surface structures: a) SEM image of a pin hole 5000  $\times$ , b) rolling trucks and porous of the surface 200  $\times$

**Slika 10:** Struktura površine: a) SEM posnetek luknjice 5000  $\times$ , b) sledi valjanja in porznost površine 200  $\times$



stable inter-metallic phases because of high cooling rates, due to kinetic restrictions there is not enough time for the atoms to arrange themselves in a stable structure.

The AFM scanning images indicates that the valley and the peaks are oriented along the rolling direction. The surface roughness of the rolling pin and the foils are very close in almost all cases especially in thinner foils.

### Acknowledgements

This work was supported by Necmettin Erbakan University Scientific Research Projects (BAP) Coordinatorships and by the Ministry of Industry with project No. 01078.STZ.2011-2.

### 5 REFERENCES

- <sup>1</sup> M. Dündar, The Material Properties management on Aluminum sheet production with twin Roll Casting Technique, 13<sup>th</sup> International Metallurgy and Material Conference, Istanbul, 2006, 1–9
- <sup>2</sup> M. S. Salehi, S. Serajzadeh, Simulation of static softening behavior of an aluminum alloy after cold strip rolling, *Computational Materials Science*, 69 (2013), 53–61, doi:10.1016/j.commatsci.2012.11.028
- <sup>3</sup> D. Wang, Z. Y. Ma, Z. M. Gao, Effects of severe cold rolling on tensile properties and stress corrosion cracking of 7050 aluminum alloy, *Materials Chemistry and Physics*, 117 (2009), 228–233, doi:10.1016/j.matchemphys.2009.05.048
- <sup>4</sup> Z. Liang, C. Junzhou, Y. Shoujie, S. Wenzhou, D. Shenglong, Development of microstructures and texture during cold rolling in AA 7055 aluminum alloy, *Materials Science and Engineering A*, 504 (2009), 55–63, doi:10.1016/j.msea.2008.10.055
- <sup>5</sup> S. X. Zhou, Z. Jue, M. Daheng, F. Paul, Experimental study on material properties of hot rolled and continuously hot aluminum strips in cold rolling, *Journal of Material Processing Technology*, 134 (2003), 363–373, doi:10.1016/S0924-0136(02)01121-4
- <sup>6</sup> J. G. Lenard, The effect of roll roughness on the rolling parameters during cold rolling of an aluminum alloy, *Journal of Materials Processing Technology*, 152 (2004), 144–153, doi:10.1016/j.jmatprotec.2004.03.026
- <sup>7</sup> J. G. Lenard, S. Zhang, A study of friction during the lubricated cold rolling of an aluminum alloy, *Journal of Materials Processing Technology*, 72 (1997), 293–30, doi:10.1016/S0924-0136(97)00183-0
- <sup>8</sup> K. S. S. Satheesh, T. Raghu, Structural and mechanical behavior of severe plastically deformed high purity aluminum sheets processed by constrained groove pressing technique, *Materials and Design*, 57 (2014), 114–120, doi:10.1016/j.matdes.2013.12.053
- <sup>9</sup> G. Liv, Development of surface topography during aluminum cold rolling of twin-roll cast, *Wear*, 192 (1996), 216–227, doi:10.1016/0043-1648(95)06809-0
- <sup>10</sup> B. Felipe, S. M. Elisangela, R. G. Pedro, C. Noe, R. Rudimar, G. Amauri, Laser remelting of Al–1.5 wt% Fe alloy surfaces: Numerical and Experimental analyses, *Optics and Lasers in Engineering*, 49 (2011), 490–497, doi:10.1016/j.optlaseng.2011.01.007
- <sup>11</sup> M. S. Debkumar, C. Suryanarayana, F. H. Froes, Structural Evolution in Mechanically Alloyed Al-Fe Powder, *Metallurgical and Materials Transactions A*, 26 (1995) 8, 1939–1946
- <sup>12</sup> S. S. Nayak, H. J. Chang, D. H. Kim, S. K. Pabi, B. S. Murty, Formation of metastable phases and nanocomposite structures in rapidly solidified Al-Fe alloys, *Materials Science and Engineering A*, 528 (2011), 5967–5973, doi:10.1016/j.msea.2011.04.028
- <sup>13</sup> C. A. Aliravci, M. O. Pekguleruz, Calculation of phase diagrams for the metastable Al-Fe phases forming in direct-chill (DC)-cast aluminum alloy ingots, *Calphad*, 22 (1998), 147–155, doi:10.1016/S0364-5916(98)00020-0
- <sup>14</sup> M. Gremaud, M. Carrard, W. Kurz, The microstructure of rapidly solidified Al-Fe alloys subjected to laser surface treatment, *Acta Metallurgica et Materialia*, 38 (1990) 12, 2587–2599, doi:10.1016/0956-7151(90)90271-H
- <sup>15</sup> P. J. Appsa, J. R. Bowenb, P. B. Prangnell, The effect of coarse second-phase particles on the rate of grain refinement during severe deformation processing, *Acta Materialia*, 51 (2003), 2811–2822, doi:10.1016/S1359-6454(03)00086-7
- <sup>16</sup> C. M. Allen, S. Kumar, L. Carrol, K. A. Q. O'Reilly, H. Cama, Electron beam surface melting of model 1200 Al alloys, *Materials Science and Engineering A*, 304 (2001), 604–607, doi:10.1016/S0921-5093(00)01543-4
- <sup>17</sup> M. Aghaie-Khafri, R. Mahmudi, Flow localization and plastic instability during the tensile deformation of Al alloy sheet, *JOM*, 50 (1998), 50–52, doi:10.1007/s11837-998-0287-5
- <sup>18</sup> T. Tunçay, D. Özyürek, The effects on microstructure and mechanical properties of filtration in Al-Si-Mg alloys, *Journal of the Faculty of Engineering and Architecture of Gazi University*, 29 (2014), 271–279
- <sup>19</sup> A. Benallal, T. Berstad, T. Børvik, O. S. Hopperstad, I. Koutiri, R. Nogueira de Codes, An experimental and numerical investigation of the behavior of AA5083 aluminum alloy in presence of the Portevin–Le Chatelier effect, *International Journal of Plasticity*, 24 (2008), 1916–1945, doi:10.1016/j.ijplas.2008.03.008
- <sup>20</sup> J.-M. Lee, S.-B. Kang, T. Sato, H. Tezuka, A. Kamio, Fabrication of Al/Al<sub>3</sub>Fe composites by plasma synthesis method, *Materials Science and Engineering A*, 343 (2003), 199–209, doi:10.1016/S092-5093(02) 00380-5



# ANTIMICROBIAL MODIFICATION OF POLYPROPYLENE WITH SILVER NANOPARTICLES IMMOBILIZED ON ZINC STEARATE

## PROTIMIKROBNO SPREMINJANJE POLIPROPILENA Z NANODELCI SREBRA, IMOBILIZIRANIH NA CINKOVEM STEARATU

**Gabriela Jandikova, Pavlina Holcapkova, Martina Hrabalíková,  
Michal Machovsky, Vladimír Sedlarík**

Tomas Bata University in Zlín, University Institute, Centre of Polymer Systems, tr. Tomase Bati 5678, 76001 Zlín, Czech Republic  
sedlarik@cps.utb.cz

*Prejem rokopisa – received: 2015-06-30; sprejem za objavo – accepted for publication: 2015-12-01*

doi:10.17222/mit.2015.152

The microwave synthesis of Ag nanoparticles on zinc stearate (ZnSt/Ag) was performed to obtain an antimicrobial additive for a polypropylene matrix. Thermoplastically prepared polymer composites contained (1, 3, 5 and 10) % of mass fractions of ZnSt/Ag. The effect of the presence of additives on the morphology and mechanical properties of composites was studied by scanning electron microscopy and stress-strain analysis. The antimicrobial activity of the composites was studied according to the ISO 22196 standard. The results showed that sufficient antimicrobial activity of the composites against both Gram-positive and Gram-negative bacterial strains was observed in the case of the composites with the highest filling studied.

Keywords: antibacterial, polypropylene composite, zinc stearate, Ag nanoparticles

Izvedena je bila sinteza nanodelcev Ag na cinkovem stearatu (ZnSt/Ag) z mikrovalovi, da bi dobili protimikrobni dodatek polipropilenski osnovi. Termoplastično pripravljene kompozite polimera je vseboval (1, 3, 5 in 10) % masnega deleža ZnSt/Ag. Vpliv prisotnosti dodatkov na morfologijo in mehanske lastnosti kompozitov je bil proučevan z vrstično elektronsko mikroskopijo in analizo napetost-raztezek. Protimikrobna aktivnost kompozita je bila proučevana skladno s standardom ISO 22196. Rezultati so pokazali, da je primerna protimikrobna aktivnost pri sevih, gram pozitivnih in gram negativnih bakterij, dosežena v primeru kompozita z največjim proučevanim dodatkom.

Ključne besede: protibakterijsko, polipropilenski kompozit, cinkov stearat, nanodelci Ag

## 1 INTRODUCTION

Antimicrobial modifications of polymers are used to prevent or inhibit the growth of microorganisms on its surface. Such a modification may find utilization in food packaging, medical applications and especially in hygienic materials or textile production. Nowadays, a commonly used method for the modification of polymers is an addition of an antimicrobial agent/additive directly into the polymer matrix. Currently, silver-based (Ag) additives have received significant attention due to the low toxicity of the active Ag ion to human cells as well as for being a long-lasting biocide with high thermal stability and low volatility.<sup>1,2</sup> Microwave (MW) synthesis is one of the well-known effective methods for the preparation of Ag NPs.<sup>3,4</sup> The immobilization of Ag NPs by MW synthesis on various organic substrates has been studied by P. Bazant et al.<sup>2</sup> The authors successfully immobilized nano-silver, nanostructured ZnO and hybrid nanostructured Ag/ZnO on a wood flour (WF) surface by MW synthesis. Subsequently, the modified WF was compounded into a PVC matrix (5 % of mass fractions loading) and the antimicrobial activity was tested while the most efficient system was the hybrid nanostructured Ag/ZnO. N. Iqbal et al.<sup>1</sup> described the surface modification by the MW synthesis of Ag NPs on the surface of

inorganic substances. The Ag NPs were successfully bonded on hydroxyapatite and caused antimicrobial activity of the prepared system.

The antimicrobial modification of polypropylene with Ag NPs prepared by MW synthesis and immobilized on a zinc stearate surface was studied in this work. The prepared composites were characterized by scanning electron microscopy, stress-strain analysis and antimicrobial testing according to the ISO 22196 standard.

## 2 EXPERIMENTAL PART

### 2.1 Materials

Polypropylene (PP) resin (C706-21 NA HP, density = 0.9 g.cm<sup>-3</sup>, MFR = 21 g.10 min<sup>-1</sup>) used in this work was a product of the Braskem company (Brazil). Zinc stearate (ZnSt) was supplied by Sigma Aldrich (USA). Silver nitrate (AgNO<sub>3</sub>), Hexamethylenetetramine (HMTA) and ethanol were purchased from PENTA, Czech Republic.

### 2.2 Preparation of hybrid ZnSt/Ag particles and PP composites

Hybrid ZnSt/Ag particles were prepared under reflux in the MW open vessel system MWG1K-10 (RADAN,

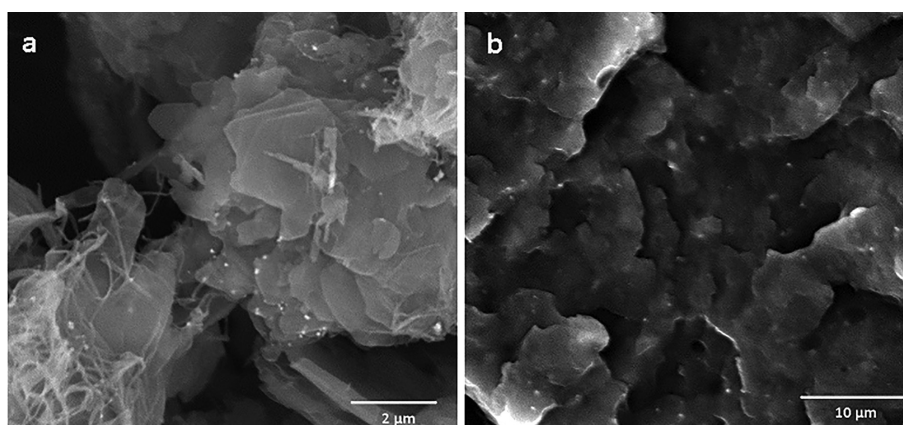


**Figure 1:** Scanning electron micrographs of: a) ZnSt/Ag particles and b) PP 10 % of mass fractions of ZnSt/Ag composite. The Ag nanoparticles can be recognized as white dots.

**Slika 1:** Posnetka z vrstičnim elektronskim mikroskopom: a) ZnSt/Ag delci in b) kompozit PP z 10 % masnega deleža ZnSt/Ag. Nanodelci Ag se kažejo kot bele točke.

Czech Republic; 1.5 kW, 2.45 GHz) operating in continuous mode (zero idle time) with an external cooler. First, 200 mL of  $\text{AgNO}_3$  (0.85 g) solution in water and 450 mL of ZnSt (11.02 g) dispersion in ethanol were transferred into a 1000 mL reaction bottle. The reaction mixture was heated in a MW oven for 2 min. After that, 100 mL of HMTA (7.00 g) solution in water was added and the MW heating continued for 10 min under continuous stirring ( $250 \text{ min}^{-1}$ ). The reaction product was collected by suction microfiltration and left to dry in a laboratory oven ( $50 \text{ }^\circ\text{C}$ ) up to the constant weight. The prepared ZnSt/Ag system contained 2.4 % of mass fractions of Ag (determined by atomic absorption spectroscopy, Agilent DUO 240FS/240Z/UltrAA). The prepared hybrid particles were incorporated into the PP matrix by twin screw micro-compounder DSM Xplore (15 mL chamber volume). The temperature of all three zones was  $200 \text{ }^\circ\text{C}$ , speed  $100 \text{ min}^{-1}$  and time of mixing 10 min. The concentration of the filler was from 1 % to 10 % of mass fractions.

### 2.3 Characterization methods

The structure of the prepared samples was observed by scanning electron microscopy (VEGA IILMU, TESCAN). The specimens were coated with a thin Au/Pd layer. The microscope was operated in vacuum mode at an acceleration voltage of 10 kV.

The mechanical characterization of the samples (dog-bone shaped specimens) was performed with a

M350-5 CT Materials Testing Machine. The cross-head speed was 10 mm/min. Each test consisted of seven replicate measurements. Antimicrobial testing was performed according to the ISO 22196:2007 international standard against *Escherichia coli* and *Staphylococcus aureus*.

### 3 RESULTS AND DISCUSSION

SEM micrographs of the ZnSt/Ag additive and PP 10 % ZnSt/Ag composite are shown in **Figure 1**. Immobilized Ag particles with a size below 100 nm are visible in the case of the pure additive (**Figure 1a**) as well in the composite (**Figure 1b**). The size and shape of the MW prepared Ag NPs correspond to the results published by Bazant et al.<sup>2</sup> where Ag NPs were immobilized on a wood flour. Furthermore, the SEM analysis reveals that immobilized Ag NPs have good cohesion to the ZnSt substrate, even after thermoplastic processing.

The mechanical properties of the composites were noticeably influenced when the loading of the filler was above 5 % of mass fractions. However, the addition of 1 % of mass fractions of ZnSt/Ag improved the tensile strain by approximately 16 % in comparison with neat PP, while the tensile strength remained unchanged. In the case of the composites containing 10 % of mass fractions of ZnSt/Ag the Young's modulus, tensile strength and tensile strain were reduced by approximately 35 %, 20 %, and 81 %, respectively (**Table 1**). The mechanical properties of the composites are most dependent on the

**Table 1:** Summary of stress-strain analysis results of prepared PP/ZnSt/Ag composites

**Tabela 1:** Zbir rezultatov analiz napetost-raztezek pripravljenih kompozitov PP/ZnSt/Ag

	Young's modulus (MPa)	Tensile strength (MPa)	Strain at break (%)
PP	217 ( $\pm 27$ )	22 ( $\pm 1.7$ )	187 ( $\pm 47$ )
PP 1 % ZnSt/Ag	179 ( $\pm 25$ )	22 ( $\pm 0.5$ )	217 ( $\pm 23$ )
PP 3 % ZnSt/Ag	172 ( $\pm 12$ )	22 ( $\pm 1.1$ )	68 ( $\pm 12$ )
PP 5 % ZnSt/Ag	155 ( $\pm 29$ )	21 ( $\pm 1.2$ )	54 ( $\pm 17$ )
PP 10 % ZnSt/Ag	143 ( $\pm 10$ )	18 ( $\pm 0.8$ )	35 ( $\pm 3$ )

**Table 2:** Antimicrobial activity of prepared composites determined according to ISO 22196**Tabela 2:** Protimikrobna aktivnost pripravljenih kompozitov, določena po ISO 22196

Sample	<i>S. aureus</i>		<i>E. coli</i>	
	CFU/cm <sup>2</sup>	R	CFU/cm <sup>2</sup>	R
PP	2,4E+05	–	7,2E+05	–
PP + 5 % ZnSt	1,1E+05	0.4	1,9E+05	0.6
PP + 10 % ZnSt	9,6E+04	0.4	5,0E+04	1.2
PP + 5 % ZnSt/Ag	1,6E+05	0.2	5,5E+04	1.1
PP + 10 % ZnSt/Ag	9,5E+02	2.4	0,0E+00	7.0

ZnSt content without the effect of the Ag NPs presence on it. Changes of the mechanical properties correspond to the results observed in the case of the composites based on PP and unmodified ZnSt.<sup>5</sup>

The antimicrobial activity of the composites is summarized in **Table 2**. There is a slight inhibition of growth of both bacterial strains when the concentration is 5 % of mass fractions of ZnSt (corresponding to 0.08 % of mass fractions of Ag). The samples with the highest filling studied (0.16 % of mass fractions of Ag) exhibit a noteworthy activity against *Escherichia coli* and *Staphylococcus aureus*. Antimicrobial activity is in agreement with studies describing incorporation of Ag NPs into hydrophobic polymer matrices.<sup>2</sup>

#### 4 CONCLUSIONS

The hybrid systems of ZnSt and Ag nanoparticles were prepared by MW synthesis and incorporated into a PP matrix. The prepared composites showed a promising antimicrobial activity at concentration above 5 % of mass fractions. The mechanical properties were noticeably influenced at 10 % of mass fractions of the ZnSt/Ag loading into the PP matrix. However, a noticeable improvement of tensile strength of the composites was observed already at 1 % of mass fractions of ZnSt/Ag, while the tensile strain remained unchanged in comparison with the unmodified PP.

The proposed antimicrobial modification of commonly used additives, such as zinc stearate, represents a promising way of nanoparticle handling and applications.

#### Acknowledgments

This work was supported by the grant of Technology Agency of the Czech Republic (grant No. TE02000006), the Ministry of Education, Youth and Sports of the Czech Republic – Program NPU I (grant No. LO1504) and by Internal Grant Agency of the Tomas Bata University in Zlín (grant No. IGA/CPS/2015/004).

#### 5 REFERENCES

- <sup>1</sup> N. Iqbal, M. R. Abdul Kadir, N. A. N. Nik Malek, N. Humaimi Mahmood, M. Raman Murali, T. Kamarul, Rapid microwave assisted synthesis and characterization of nanosized silver-doped hydroxyapatite with antibacterial properties, *Material Letters*, 89 (2012), 118–122, doi:10.1016/j.matlet.2012.08.057
- <sup>2</sup> P. Bazant, L. Munster, M. Machovsky, J. Sedlak, M. Pastorek, Z. Kozakova, I. Kuritka, Wood flour modified by hierarchical Ag/ZnO as potential filler for wood–plastic composites with enhanced surface antibacterial performance, *Industrial Crops and Products*, 62 (2014), 179–187, doi:10.1016/j.indcrop.2014.08.028
- <sup>3</sup> D. Breitwieser, M. M. Moghaddam, S. Spirk, M. Baghbanzadeh, T. Pivec, H. Fasl, V. Ribitsch, C. O. Kappe, In situ preparation of silver nanocomposites on cellulosic fibers--microwave vs. conventional heating, *Carbohydrate Polymers*, 94 (2013), 677–686, doi:10.1016/j.carbpol.2013.01.077
- <sup>4</sup> X. Zhao, Y. Xia, Q. Li, X. Ma, F. Quan, C. Geng, Z. Han, Biopolymers regulate silver nanoparticle under microwave irradiation for effective antibacterial and antibiofilm activities, *Colloids and Surfaces A: Physicochemical and Engineering Aspects*, 444 (2014), 180–188, doi:10.1016/j.colsurfa.2013.12.008
- <sup>5</sup> C. V. Panin, L. A. Kornienko, T. Nguyen Suan, L. R. Ivanova, M. A. Poltaranin, The effect of adding calcium stearate on wear-resistance of ultra-high molecular weight polyethylene, *Procedia Engineering*, 113 (2015), 490–498, doi:10.1016/j.proeng.2015.07.341





# A NEW WIDEBAND NEGATIVE-REFRACTIVE-INDEX METAMATERIAL

## NOVI ŠIROKOPASOVNI METAMATERIAL Z NEGATIVNIM LOMNIM KOLIČNIKOM

Sikder Sunbeam Islam<sup>1</sup>, Mohammad Rashed Iqbal Faruque<sup>1</sup>, Mohammad Jakir Hossain<sup>1</sup>,  
Mohammad Tariquul Islam<sup>2</sup>

<sup>1</sup>Space Science Centre (ANGKASA)

<sup>2</sup>Universiti Kebangsaan Malaysia, Faculty of Engineering and Built Environment,  
Department of Electrical, Electronic and Systems Engineering, 43600 UKM, Bangi, Selangor, Malaysia  
sikder\_islam@yahoo.co.uk

*Prejem rokopisa – received: 2015-06-30; sprejem za objavo – accepted for publication: 2015-12-15*

doi:10.17222/mit.2015.144

This paper reveals the design and analysis of a new wideband negative-refractive-index (NRI) metamaterial unit cell. The proposed metamaterial unit-cell exhibits resonance in the C-band and displays negative permittivity and permeability there with a wideband NRI property. It also shows a wider negative peak of the refractive index in the major area of the C- and X-band and minor area of the S- and K<sub>u</sub>-band, and a maximum 3-GHz negative bandwidth was achieved compared to the reference metamaterial. In the basic design, a square-shaped copper resonator was constructed with a metal strip on the FR-4 substrate material. The measured result was presented and it shows good conformity with the simulated result. Moreover, an analysis was performed with the same design by replacing the substrate material with the popular Rogers RT 6010 instead of the FR-4 material and then it shows NRI properties in the C-, X- and K<sub>u</sub>-band.

Keywords: metamaterials, negative refractive index, wideband

Članek obravnava zgradbo in analizo osnovne celice novega, širokopasovnega metamateriala z negativnim lomnim količnikom. Predlagana osnovna celica iz metamateriala kaže resonanco v C-pasu in kaže negativno permitivnost ter permeabilnost z lastnostmi NRI širokega pasu. Kaže tudi širši negativni vrh lomnega količnika v večini področja C-pasu in X-pasu in v manjšem področju S-pasu in K<sub>u</sub>-pasu. Največja širina negativnega pasu (3 GHz) je bila dosežena v primerjavi z referenčnim metamaterialom. Osnovna zgradba je bila konstruirana kot bakren rezonator štirikotne oblike, s kovinskim trakom na podlagi iz FR-4 materiala. Predstavljeni so izmerjeni rezultati, ki kažejo dobro ujemanje z rezultati simulacije. Poleg tega je bila izvedena analiza z enako zgradbo in z nadomeščanjem podlage s popularnim Rogers RT 6010 namesto FR-4 materialom in prikazane so NRI lastnosti v C-, X- in K<sub>u</sub>-pasu.

Ključne besede: metamateriali, negativni lomni količnik, širokopasovnost

## 1 INTRODUCTION

Metamaterials are engineered (at the atomic level) materials that have unique and extraordinary properties not found in nature. A metamaterial as a composite material, usually gains these properties due to the arrangement of its constituents (in a unit cell) rather than individual properties. There are some exotic properties that are not possible with naturally available materials, but can be achieved with metamaterials, like negative permittivity ( $\epsilon < 0$ ) or negative permeability ( $\mu < 0$ ), negative refractive index, inverted Snell's law, etc. In 1967 the Russian physicist Victor Veselago<sup>1</sup> predicted that it is possible to develop a material of such reverse characteristics that it will behave opposite to the natural material. It was also stated by him that a material could exhibit a negative refractive index if it gains negative permittivity and permeability. Around 30 years later in 2000 D. R. Smith et al.<sup>2</sup> successfully demonstrated a composite material with such negative properties. Due to these uncommon characteristics it can be used in many important applications, like antenna design, EM absorption reduc-

tion, electromagnetic cloaking operation, filter design, sensor design, etc.<sup>3-7</sup> A metamaterial with both negative permittivity ( $\epsilon$ ) and negative permeability ( $\mu$ ) is called a double-negative (DNG) metamaterial or a negative refractive index (NRI) or negative index material (NIM) or a metamaterial with either permittivity or permeability negative is called a single negative (SNG) metamaterial. However, a metamaterial with the DNG property can only exhibit the negative refractive index property properly. There are many metamaterials found in the literature, but not enough metamaterials with a double negative property are found. However, very few of them were designed to exhibit DNG characteristics in the C-band of the microwave region. H. Benosman et al.<sup>8</sup> presented a double-negative metamaterial, but their metamaterial was applicable for the K<sub>u</sub>-band only. O. Turkmen et al.<sup>9</sup> showed a metamaterial for X-band operation, but their metamaterial was not double negative. A. Dhouibi et al.<sup>10</sup> proposed a metamaterial for C-band applications, but they claimed these properties for an epsilon negative (ENG) metamaterial. S.S. Islam et al.<sup>11</sup> designed an S-band metamaterial, but their

metamaterial was showing ENG properties as well. Moreover, recently in <sup>12</sup>, a DNG material was introduced where a maximum 1.05-GHz bandwidth of the negative refractive index region was claimed.

In this study, a new double-negative metamaterial is revealed that exhibits negative refractive index property in the major region of C- and X-band of microwave spectra with a wider bandwidth. Commercially available finite-difference time-domain (FDTD) based CST-microwave studio software was used to retrieve the S-parameters for the unit cell. For further investigation, the structure was then designed on a Rogers RT 6010 substrate material instead of FR-4 material and an analysis was performed.

## 2 DESIGN AND METHODOLOGY

**Figure 1a** shows the geometry of the proposed square-shaped metamaterial unit cell. The proposed metamaterial unit cell consists of a simple square-shaped copper structure with a vertical copper stripe in the middle of the material, all having a thickness of 0.035 mm. The copper strip in the middle was placed in such a way that it maintains an equal gap for the two opposite sides of the metal strip. The outer length and width of the unit cell were denoted by  $a = b = 10$  mm. The width of the square-shaped structure was expressed by  $w = 1$  mm. The tiny gap at the two ends of the metal strip was symbolized as  $s = 0.5$  mm. The length and width ( $e$ ) of the metal strip were 7 mm and 1 mm. The distance from the central metal strip to the square border was denoted by,  $c = d = 3.5$  mm.

The structure was designed on a 20 mm × 20 mm square-shaped FR-4 substrate material having a dielectric constant of 4.3 and a loss tangent of 0.025. The thickness of the substrate was 1.6 mm. In this study, commercially available finite-difference time-domain

(FDTD) based computer simulation technology (CST) microwave studio software was adopted for the design and calculation of the reflection ( $S_{11}$ ) and transmission ( $S_{21}$ ) coefficients of the unit cell. These parameters were used to compute the effective parameters (permittivity, permeability and refractive index) for the unit cell. **Figure 1** displays the simulation arrangements. For the simulation, the designed unit cell was placed between two waveguide ports of positive, negative of  $z$ -axis, and exited by transverse electromagnetic (TEM) waves. The rest of the axes were defined as perfect electric conductor (PEC) and perfect magnetic conductor (PMC) boundary conditions. The frequency-domain solver was used for the whole simulation. The simulation was executed for the frequency range of 1–15 GHz. For the computation of the effective parameters, the Nicolson-Ross-Weir method was utilized to avoid the inverse cosine-branch-index problem.<sup>13</sup> However, as part of further investigation, the unit cell was rotated by 90° and the  $S$  parameters were estimated for gaining the effective parameters using the same method.

In this study, the open-space measurement technology was adopted. The open-space measurement technology was chosen to observe the realistic effect. For measurement purpose, a prototype of 160 mm × 200 mm was fabricated that contains 8×10 unit cell. The fabricated prototype is seen in **Figure 2a**. The fabricated prototype was placed between two horn antennas. The antennas were acting as the transmitting and receiving end and they were connected to an Agilent E8363D vector network analyzer to calculate the  $S$  parameters. However, the distance between the prototype and the horn antenna was kept at 35 cm to avoid the near-field effect. As a part of calibration process, measurements with and without the prototype were performed as well.

## 3 RESULTS AND DISCUSSION

**Figure 2b** displays the simulated magnitude of the transmission coefficient ( $S_{21}$ ) for the  $z$ -axis wave propagation through the unit cell. It is evident from **Figure 2b** that for the  $z$ -axis wave propagation a clear resonance is seen in the range of the C-band at the frequency of 7.48 GHz of the microwave spectra. **Figure 2c** shows the measured magnitude of the transmission coefficient where it has been compared with the simulated one. It is apparent from **Figure 2c** that the measured result shows almost good conformity with the simulated result. However, a slight distortion is found in the measured magnitude of  $S_{21}$  than the simulated result that might have occurred due to the noise effect in the open-space measurement process and fabrication error.

**Figures 3a** and **3b** show the real magnitude of the effective permittivity and the permeability against the frequency for the  $z$ -axis wave propagation through the unit cell. It is clear from **Figure 3a** that the permittivity curve has two clear resonances at the frequencies of

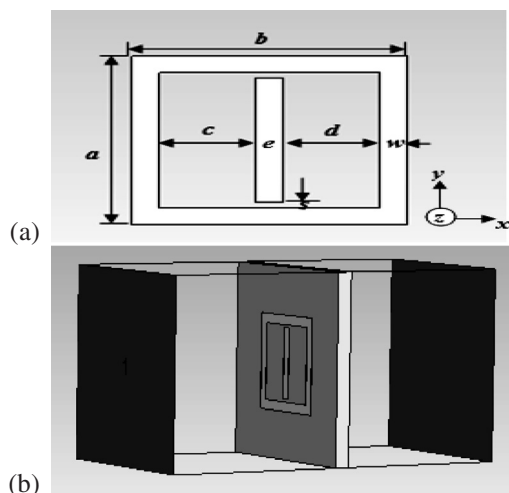


**Figure 1:** a) Design of the unit cell, b) simulation geometry in CST software

**Slika 1:** a) Zgradba osnovne celice, b) simulacija geometrije s CST programsko opremo

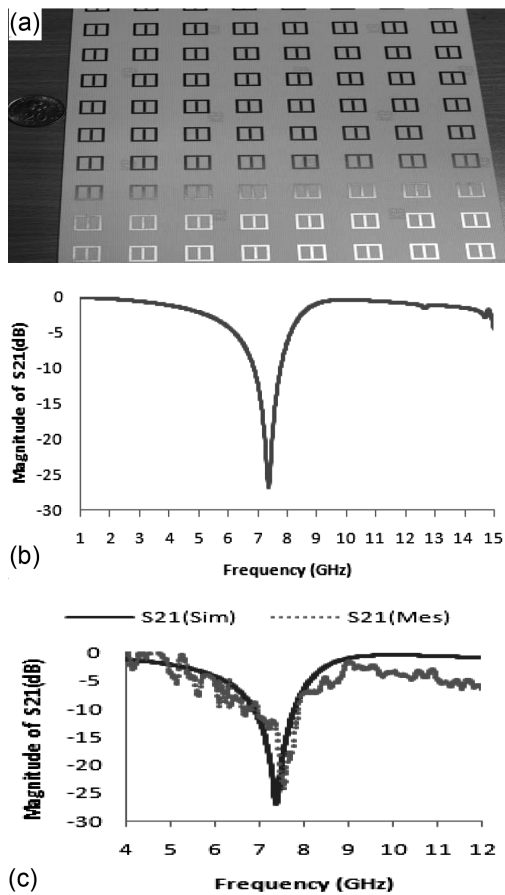


**Figure 2:** a) Prototypes for measurement, b) simulated transmission coefficient ( $S_{21}$ ) for  $z$ -axis wave propagation, c) comparison of measured and simulated result for  $S_{21}$

**Slika 2:** a) Prototipi za merjenje; b) simuliran koeficient prenosa ( $S_{21}$ ) pri napredovanju vala po  $z$ -osi, c) primerjava izmerjenega in simuliranega rezultata za  $S_{21}$

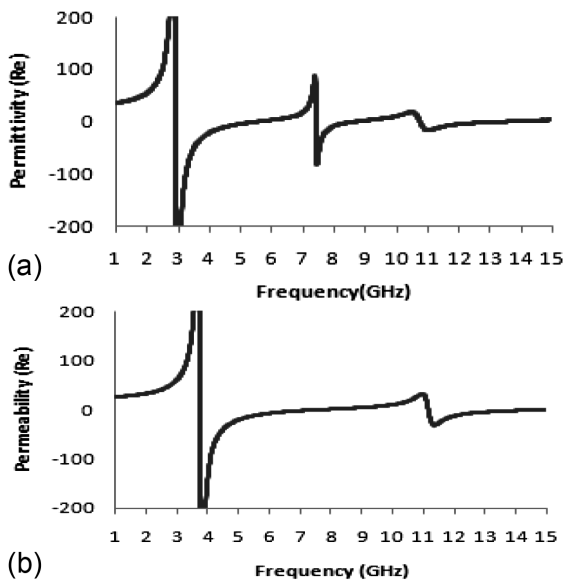


**Figure 3:** a) Real magnitude of permittivity ( $\epsilon$ ) against frequency, b) real magnitude of permeability ( $\mu$ ) versus frequency

**Slika 3:** a) Realna magnituda permitivnosti ( $\epsilon$ ) proti frekvenci, b) realna magnituda permeabilnosti ( $\mu$ ) v odvisnosti od frekvence

2.94 GHz and 7.45 GHz. Moreover, the negative portion of this curve is found from 2.91 GHz to 5.57 GHz, which covers almost 2.66 GHz of bandwidth, more than 1 GHz bandwidth from the frequency of 7.42 GHz to 8.71 GHz, and nearly 3 GHz bandwidth from the frequency of 10.75 GHz to 13.65 GHz. Similarly, the permeability curve of **Figure 3b** displays a negative region from the frequency of 3.74 GHz to 7.51 GHz that covers almost 3.77 GHz bandwidth. Another negative portion is visible there from the frequency of 11.15 GHz to 14.77GHz, which also covers nearly 3.62 GHz bandwidth.

For this design, for the varying magnetic field, a charge builds up in the gaps between the metal strip and the ring. At low frequency the current remains in phase with the applied field, but at higher frequency it starts lagging and produces a negative permeability at that frequency.

**Figure 4** reveals the real magnitude of the refractive index ( $\eta$ ) against frequency for the unit cell. In this paper, it was mentioned earlier that for a material the refractive index curve would be negative if its permittivity and permeability curve appears negative simultaneously. Therefore, from **Figure 4** it is apparent that for the proposed material the refractive index curve exhibits a negative magnitude from the frequency of 3.74 GHz to 5.57GHz; 7.42 GHz to 7.51 GHz and 11.15 GHz to 13.65 GHz. It is notable that two wide bandwidths of 1.83 GHz (3.74 GHz to 5.57GHz) and 3.73 GHz (11.15 GHz to 13.65 GHz) are seen as the negative region in the refractive index curve. These bandwidths have fallen in the few portion of S- and  $K_u$ -band and major portion of C- and X-band of the microwave region.

Moreover, in these negative regions of the refractive index curve, the permittivity and permeability curve are also found to be displaying a negative peak. As a result, the material can be characterized as a double-negative (DNG) metamaterial in these regions of microwave spectra. Another important feature is in the frequency range between 7.42 GHz and 7.51 GHz where the refractive index curve was found to be negative, both the simulated and measured transmittance ( $S_{21}$ ) are also found to be exhibiting sharp resonance clearly at the frequency of 7.48 GHz with a refractive index  $\eta = -4.40$ . Thus, it

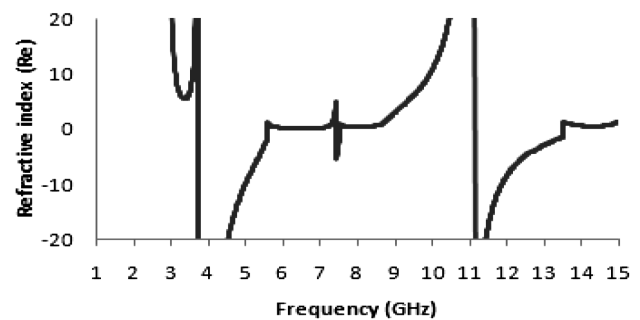


**Figure 4:** Real magnitude of refractive index ( $\eta$ ) versus frequency  
**Slika 4:** Realni obseg lomnega količnika ( $\eta$ ) v odvisnosti od frekvence

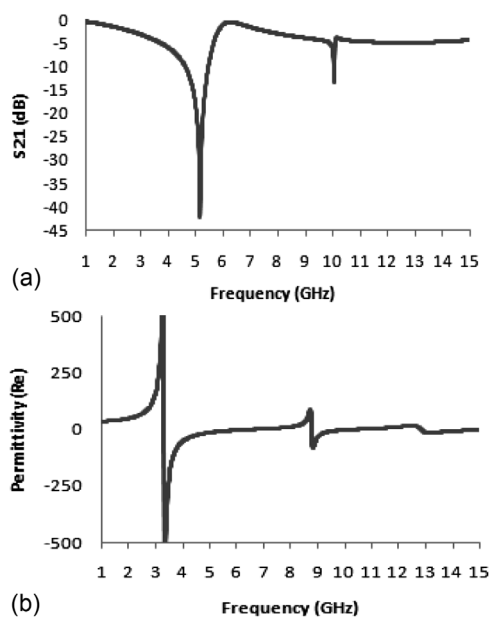


**Figure 5:** a) Transmission coefficient ( $S_{21}$ ) for the unit cell on the Rogers 6010 substrate material, b) real magnitude of permittivity ( $\epsilon$ ) against frequency for the unit cell on the Rogers 6010 substrate

**Slika 5:** a) koeficijent prenosa ( $S_{21}$ ) osnovne celice na podlagi iz materiala Rogers 6010, b) realna magnituda dielektrične konstante ( $\epsilon$ ) v odvisnosti od frekvence osnovne celice na podlagi iz Rogers 6010

reveals that for the  $z$ -axis wave propagation the material is practically applicable for C-band applications in the the microwave spectra.

As a part of a further investigation, the Rogers 6010 substrate material was used instead of the FR-4 substrate material for the unit cell. **Figures 5a** and **5b** depicts the transmission coefficient as well as the real magnitude of permittivity ( $\epsilon$ ) against frequency for the unit cell on the Rogers 6010 substrate material consecutively.

According to **Figure 5a**, the transmission coefficient shows two resonances at the frequencies of 5.14 GHz and 10.06 GHz. These frequencies are in the range of C-band and X-band. The permittivity curve in **Figure 5b** reveals a negative magnitude from the frequency of 3.29 GHz to 6.55 GHz, which covers more than 3 GHz bandwidth in the C-band. Similarly, it also shows negative peak from the frequency of 8.80 GHz to 10.30 GHz in the X-band and 12.84 GHz to 15 GHz in the Ku-band. In **Figures 6a** and **6b** the real magnitude of the permeability and refractive index is depicted. It is apparent from **Figure 6a** that the permeability curve shows a negative peak from the frequency of 4.33 GHz to 8.90 GHz and 13.25 GHz to 15 GHz. Therefore, from the permittivity and permeability curve of **Figures 5b** and **6a** it is evident that the material exhibits a double-negative property from the frequency of 4.33 GHz to 6.55 GHz, 8.80 GHz to 8.89 GHz and 13.25 GHz to 15 GHz.

Usually, the properties of permittivity and permeability are most likely affected by the polarization due to the internal architecture of the material. When electromagnetic waves enter anisotropic materials, which have

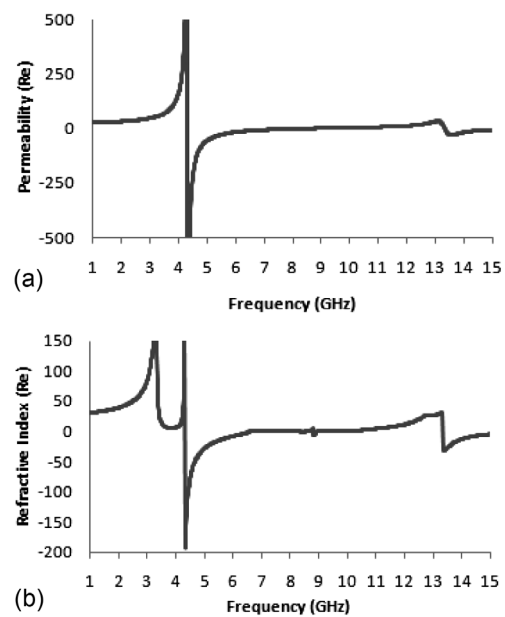


**Figure 6:** a) Real magnitude of permeability ( $\mu$ ) against frequency, b) real magnitude of refractive index ( $\eta$ ) versus frequency for the unit cell on the Rogers 6010 substrate material

**Slika 6:** a) Realen obseg magnituda permeabilnosti ( $\mu$ ) v odvisnosti od frekvence, b) realen obseg lomnega količnika ( $\eta$ ) v odvisnosti od frek-

unequal lattice axes, it is affected by the polarization inside the material. As a result, the value of the permittivity and permeability changes due to changes in the design. In the same way, the refractive index curve is also affected by the polarization.

Similarly, in the refractive index curve in **Figure 6b**, it is clear that the curve shows negative magnitude from the frequency of 4.33 GHz to 6.55 GHz, 8.80 GHz to 8.89 GHz and 13.32 GHz to 15 GHz and these frequency ranges cover 2.22 GHz, 9 MHz, 2.32 GHz bandwidth in the microwave ranges. These regions of negative refractive index curve fall in the range of C, X and  $K_u$ -band of microwave spectra. Moreover, these frequencies obey the permittivity and permeability curves in **Figures 5b** and **6a** as well.

## 4 CONCLUSIONS

In this paper, a new square-shaped negative refractive index metamaterial was demonstrated that exhibits a wider negative peak in the major area of the C- and X-band and the minor area of S- and  $K_u$ -band. A more than 3-GHz wider bandwidth of the negative peak was achieved for the proposed metamaterial than the latest reference metamaterial. The measured result also agrees well with the simulated result. Moreover, the material shows a negative refractive index zone in the C-, X and  $K_u$ -band of the microwave spectra as well as when it is designed on the Rogers 6010 substrate material. However, C- and X-,  $K_u$ -band are widely used for long-distance and satellite communications. So, this metamaterial can be practically applied in these frequency bands,



especially for wider bandwidth application besides the other metamaterials in the microwave range.

## 5 REFERENCES

- <sup>1</sup> V. G. Veselago, The electrodynamics of substances with simultaneously negative values of  $\epsilon$  and  $\mu$ , *Soviet Physics Uspekhi*, 10 (1968), 509–514, doi:10.1070/PU1968v010n04ABEH003699
- <sup>2</sup> D. R. Smith, W. J. Padilla, D. C. Vier, S. C. Nemat-Nasser, S. Schultz, Composite medium with simultaneously negative permeability and permittivity, *Physical Review Letters*, 84 (2000), 4184–418, doi:10.1103/PhysRevLett.84.4184
- <sup>3</sup> S. S. Islam, M. R. I. Faruque, M. T. Islam, An Object-Independent ENZ Metamaterial-Based Wideband Electromagnetic Cloak, *Scientific Reports*, 6 (2016) 33624, 1–10, doi:10.1038/srep33624
- <sup>4</sup> J. Carver, V. Reignault, Engineering of the metamaterial-based cut-band filter, *App. Phys. A*, 117 (2014), 513–516, doi:10.1007/s00339-014-8694-7
- <sup>5</sup> X. Yang, D. Sun, T. Zuo, X. Chen, K. Huang, Analysis and realization of improving the patch antenna gain based on metamaterials, *International Journal of Applied Electromagnetics and Mechanics*, 44 (2014) 1, 17–25, doi:10.3233/JAE-131731
- <sup>6</sup> L.-W. Li, Y.-N. Li, T. S. Yeo, J. R. Mosig, O. J. F. Martin, A broadband and high-gain metamaterial microstrip antenna, *Applied Physics Letters*, 96 (2010) 164101, 1–3, doi:10.1063/1.3396984
- <sup>7</sup> X. Shen, T. J. Cui, J. Zhao, H. F. W. X. Ma, Jiang, H. Li, Polarization-independent wide-angle triple-band metamaterial absorber, *Optical Express*, 19 (2011), 9401–9407, doi:10.1364/OE.19.009401
- <sup>8</sup> H. Benosman, N. B. Hacene, Design and Simulation of Double “S” Shaped Metamaterial, *International Journal of Computer Science Issues*, 9 (2012) 2, 534–537, (Available at: <http://ijcsi.org/papers/IJCSI-Vol-9-Issue-2-No-1.pdf>)
- <sup>9</sup> O. Turkmen, E. Ekmekci, G. Turhan-Sayan, Nested U-ring resonators: a novel multi-band metamaterial design in microwave region, *IET Microwave and Antennas Propagation*, 6 (2012) 10, 1102–1108, doi:10.1049/iet-map.2012.0037
- <sup>10</sup> A. Dhoubi, S. N. Burokur, A. de Lustrac, A. Priou, Study and analysis of an electric Z-shaped meta-atom, *Advanced Electromagnetics*, 1 (2012) 2, 64–70, doi:10.7716/aem.v1i2.82
- <sup>11</sup> S. S. Islam, M. R. I. Faruque, M. T. Islam, Design of a New ENG Metamaterial for S-Band Microwave Applications, *Journal of Electrical and Electronics Engineering*, 7 (2014) 2, 13–16, (Available at: <http://electroinf.uoradea.ro/index.php/jeee.html>)
- <sup>12</sup> M. I. Hossain, M. R. I. Faruque, M. T. Islam, M. H. Ullah, A New Wide-Band Double-Negative Metamaterial for C- and S-Band Applications, *Materials*, 8 (2015) 1, 57–71, doi:10.3390/ma8010057
- <sup>13</sup> S. S. Islam, M. R. I. Faruque, M. T. Islam, A New Direct Retrieval Method of Refractive Index for Metamaterials, *Current Science*, 109 (2015) 2, 337–342, (Available at: <http://www.currentscience.ac.in/php/toc.php?vol=109&issue=02>)



## EVALUATION OF THE DEGREE OF DEGRADATION USING THE IMPACT-ECHO METHOD IN CIVIL ENGINEERING

### OCENA STOPNJE DEGRADACIJE V GRADBENIŠTVU Z UPORABO METODE ODMEVA ZVOČNIH VALOV

**Daniela Štefková, Kristýna Timčáková, Libor Topolář, Petr Cikrle**

Brno University of Technology, Faculty of Civil Engineering, Veveř331/95, 602 00 Brno, Czech Republic  
stefkova.d@fce.vutbr.cz

*Prejem rokopisa – received: 2015-06-30; sprejem za objavo – accepted for publication: 2015-12-15*

doi:10.17222/mit.2015.150

Non-destructive methods such as Impact-echo method are based on the acoustic properties of the material that are dependent on its condition. It allows the studied progress development of micro-defects in the structure of the material and is thus suitable for monitoring the building structure's condition. This acoustic method allows us to identify and locate defects and is thus suitable for monitoring the building structure's condition. The application of this method is widespread; it can be used in mechanical engineering, power engineering and in many industries as well as in the construction industry. Impact-echo uses a short-time mechanical impulse (a hammer blow) that is applied to a surface of the test sample and is detected by means of piezoelectric sensors placed on the surface of the sample. The impulse is reflected by the surface but also by micro-cracks and defects of the specimen that are under investigation. From thus obtained signal the frequency spectrum is determined and is found to be the dominant resonance frequency using fast Fourier transformations. The dominant frequencies give an account of the condition of the structure or determine the location of flaws, at which the waves are rebounded. The signal is digitized by means of a data processing system to be transferred into a computer memory. A piezoelectric MIDI sensor takes the signal response and it is brought to the input of an oscilloscope TiePie engineering Handyscope HS3 two-channel with 16-bit resolution. This paper reports the results of measurements by the Impact-echo method on three applications in civil engineering. The results are obtained in the laboratory during the hardening process in quasi-brittle materials such as alkali-activated slag mortars, the degradation of concrete samples by corrosion caused by the action of chlorides and the degradation of composite materials based on cement by high temperature.

Keywords: predominant frequency, high temperature, impact, mortar, specimens

Neporušna metoda, kot je npr. odmev zvočnih valov, temelji na akustičnih lastnostih materiala, ki so odvisne od stanja materiala. Metoda omogoča študij napredovanja mikronapak v strukturi materiala in je zato primerna za pregled stanja gradbene strukture. Ta akustična metoda omogoča odkrivanje in določanje položaja napake in je zato primerna za pregled stanja zgradbe. Metoda ima široko uporabnost, saj se lahko uporablja v strojništvu, energetiki ter v mnogih drugih industrijah kot tudi v gradbeništvu. Metoda odmeva zvočnih valov uporablja kratke mehanske udarce (udarec s kladivom) po površini preizkušane vzorca, odmeve pa se določi s piezoelektričnim senzorjem, ki je tudi nameščen na površini. Impulz odseva površino in tudi mikrorazpoke in napake v vzorcu, ki se ga preiskuje. Iz tako dobljenega signala, se določi spekter frekvenc in s pomočjo hitre Fourierjeve transformacije se poišče prevladujoča resonančna frekvenca. Prevladujoče frekvence pokažejo stanje zgradbe ali pa določijo lokalne pomanjkljivosti, na katerih valovi poskočijo. Signal se digitalizira s sistemom obdelave podatkov, da se ga lahko prenese v spomin računalnika. Piezoelektrični sensor MIDI prevzame odbit signal, ki se ga usmeri na vhod dvokanalnega osciloskopa TiePie Engineering Handyscope HS3, z ločljivostjo 16 bitov. Članek predstavlja rezultate meritev z metodo odmeva zvočnih valov na treh primerih v gradbeništvu. Rezultati so dobljeni v laboratoriju med procesom utrjevanja v kvazi krhkem materialu, kot je z alkalijami aktivirana žlindra v malтах, degradacijo betonskih vzorcev zaradi korozije, povzročeno s kloridi in visoko temperaturno degradacijo kompozitnega materiala na osnovi betona

Ključne besede: prevladujoča frekvenca, visoka temperatura, udarec, malta, vzorci

## 1 INTRODUCTION

In civil engineering, efficient non-destructive quality control plays an important role in the optimization of resources for manufacturing, maintenance and safety. The impact-echo method is a useful non-destructive technique for flaw detection in concrete. It is based on monitoring the surface motion, resulting from a short-time mechanical impulse. This method overcomes many of the barriers associated with flaw detection in concrete that occur during ultrasonic methods. One of the key features of this method is the transformation of the recorded time-domain waveform of the surface motion into the frequency domain. The impact gives rise to modes of vibration and the frequency of these modes is

related to the geometry of the tested object and the presence of flaws.<sup>1</sup>

A short-time mechanical impulse, generated by tapping a hammer against the surface of a concrete structure (**Figure 1**), produces low-frequency stress waves that propagate into the structure.<sup>2,3</sup> Thus generated waves propagate through the specimen structure and reflect from the defects located in the volume of the specimen or in the surface. Surface displacements caused by the reflected waves are recorded by a transducer located adjacent to the impact.<sup>4</sup> The signal is digitized by an analogue/digital data system and transmitted to a computer memory. This signal describes the transient local vibrations, which are caused by the mechanical wave

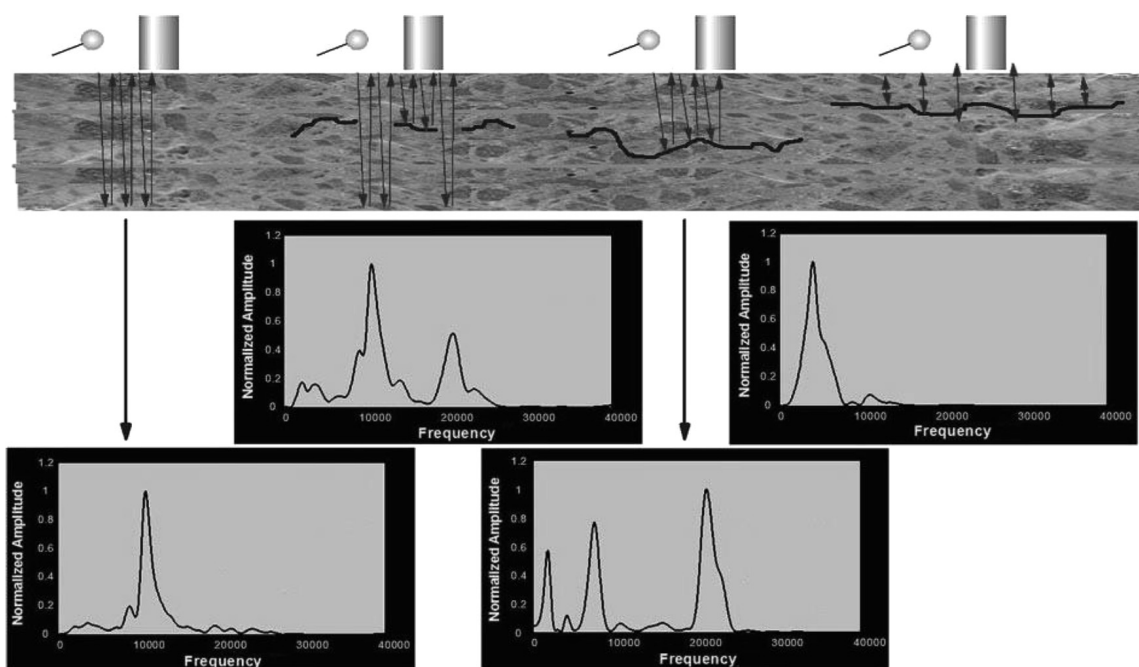


**Figure 1:** Principle of the Impact echo method  
**Slika 1:** Princip metode odmeva zvočnih valov

multiple reflections inside the structure. The dominant frequencies of these vibrations give an account of the condition of the structure that the waves pass through.<sup>5,6</sup>

The signal analysis from the impact-echo method is most frequently performed by using frequency spectra obtained from the fast Fourier transform. Fourier analysis converts time to frequency and vice versa. A fast Fourier transform (FFT) is an algorithm to compute the discrete Fourier transform (DFT) and its inverse. The results of fast Fourier transforms are widely used for many applications in engineering, science, and mathematics. Equation (1) is the expression of the Fourier transform for a continuous function:<sup>7</sup>

$$x(t) = \frac{a_0}{2} + \sum_{n=1}^{\infty} \left[ a_n \cdot \cos\left(\frac{2\pi n t}{T}\right) + b_n \cdot \sin\left(\frac{2\pi n t}{T}\right) \right] \quad (1)$$

$$a_n = \frac{2}{T} \cdot \int_0^T x(t) \cos\left(\frac{2\pi n t}{T}\right) dt$$

$$b_n = \frac{2}{T} \cdot \int_0^T x(t) \sin\left(\frac{2\pi n t}{T}\right) dt$$

$$\frac{2\pi}{T} = \omega$$

where  $a_n$  and  $b_n$  can be calculated from function  $x(t)$  using the following relations.

## 2 EXPERIMENTAL PART

For the impact-echo method a short-time mechanical impulse (a hammer blow) was applied to the surface of the specimen during the test and was detected by means of a piezoelectric sensor (**Figure 2**). The impulse reflects

from the surface but also from micro-cracks and defects present in the specimen that are under investigation. The frequency analysis can be carried out from the response signal by means of a fast Fourier transform and thus dominant resonant frequencies are found. An MIDI piezoelectric sensor was used to pick up the response and the respective impulses were directed into the input of an oscilloscope TiePie engineering Handscope HS3 two-channel with a 16-bit resolution.

### 2.1 Material for the hardening process of alkali-activated slag mortars

The mixture consisted of 450 g of fine-grained granulated blast furnace slag Štramberg 380 (specific surface area  $380 \text{ m}^2 \text{ kg}^{-1}$ ), 180 g of sodium silicate (water glass) with a modulus of 1.6, 1350 g of silica sand (maximum grain size of 2.5 mm) and 95 mL of water. The amount of admixtures was 0.1 % of mass fractions with respect to the slag. CNTs were added in the form of a well-dispersed aqueous dispersion containing 1 % of mass fractions of multi-walled carbon nanotubes



**Figure 2:** Images of measurement with the Impact-Echo method  
**Slika 2:** Posnetka merjenja z metodo odmeva zvočnih valov



(Graphistrengths CW 2-45). Since CNTs are commonly not water-soluble, the dispersion also contained carboxymethyl cellulose (68 g/L) as a dispersing agent.<sup>8</sup> The slurry was poured into steel moulds 40 mm × 40 mm × 160 mm to set. The samples were demoulded after 24 h and one set was tested (marked 0d) and the second set was immersed in water for another 28 d before testing (marked 28 d).

## 2.2 Material for the degradation of concrete samples by corrosion caused by the action of chlorides

The mixture for the production of concrete samples was composed of cement CEM II/B – S 32.5 and 1350 kg of sand with a fraction of aggregate 0–4 mm and 225 L of water. The high water ratio resulted in easier penetration of the degradation agents into the concrete structure. These samples of dimensions 50 mm × 50 mm × 330 mm were reinforced with one standard reinforcing bar of diameter 10 mm and a length of 400 mm passing through the centre of the beam.

The samples were demoulded after 24 h and placed in the water for 27 d, then the dried samples with natural humidity were exposed to accelerated degradation by chlorides. The samples were immersed into a 5 % water solution of NaCl for 16 h and then subsequently placed into a drying oven with an air temperature of 40 °C for 8 h.

## 2.3 Specimens intended to be subjected in the heating process

Mortars of dimensions 40 mm × 40 mm × 160 mm were produced using a type CEM I 42.5 R Portland cement (Českomoravský Cement-Heidelberg Cement Group) and a water-to-cement ratio ( $w/c = 0.46$ ) and quartz sand from Filtrační písky, s.r.o. for the preparation of the test mortar mixture in a ratio of 1 to 3, in compliance with the ČSN 721200 standard. The specimens were left in the moulds for 24 h, then cured in water for 27 d and finally air-cured for 31 d at laboratory temperature ( $25 \pm 2$  °C) and a relative humidity of  $53 \pm 5$  %.

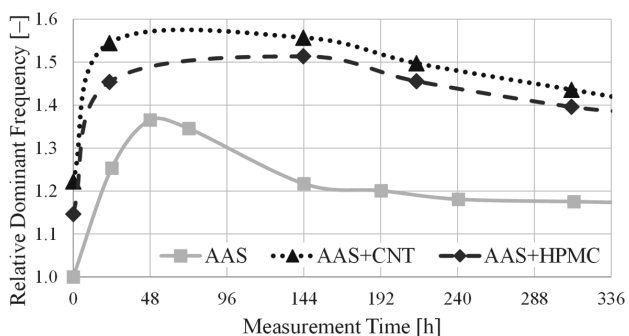


**Figure 3:** Change of relative dominant frequencies over time - without curing

**Slika 3:** Spreminjanje relativne prevladujoče frekvence s časom – brez utrjevanja

After initial curing, the specimens were dried at a temperature of 60 °C for two d. Subsequently, the specimens were subjected to gradual heating in a furnace at 200 °C, 400 °C, 600 °C, 800 °C, 1000 °C and 1200 °C. The temperature increase rate was 5 °C/min. A dwell of 60 min at each temperature was provided, in order to find out the effect of temperature on the specimens. After heat treatment, the specimens were left to cool down under laboratory conditions.

## 3 RESULTS AND DISCUSSION

### 3.1 Material for the hardening process of alkali-activated slag mortars

The experiment was employed to determine the microstructural changes during the hardening process of the alkali-activated slag composite with different admixtures. Changes in the density of the material due to the process of hardening as well as the creation of micro-cracks due to the time of curing are reflected in the shift of dominant frequencies. **Figure 3** shows the shift of the resonance frequency during 14 d after demoulding without curing. The frequency of the reference specimen (AAS) increased by about 37 % during the first 48 h from the start of the measurement and then decreased to a steady value of around 18 % from the initial value. The dominant frequency of the AAS+CNT (AAS+HPMC) specimen started 21 % (15 %) above the initial dominant frequency of the reference specimen (AAS). The dominant frequency of the AAS+CNT (AAS+HPMC) increased by about 35 % (30 %) from the initial value during the first 24 h and then decreased to a steady value of around 23 % (25 %) from the initial value. The process of hardening and the formation of a hard and dense structure caused an initial increase of the dominant frequencies. At a later time, the frequencies are again slightly shifted towards lower values. This phenomenon is probably associated with the drying process, which is followed by the shrinkage of the AAS matrix and the formation of micro-cracks. **Figure 4** shows the shift of the resonance frequency during 14 d after 28 d of curing. The dominant frequency decreased for all the measure-

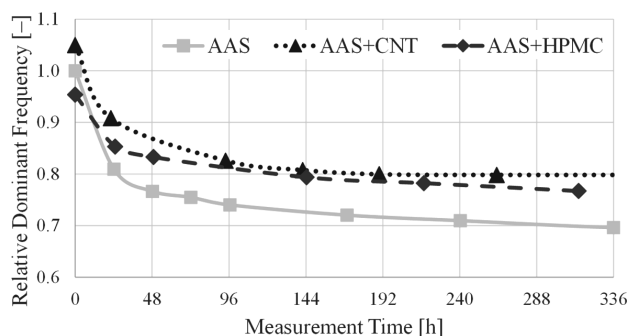


**Figure 4:** Change of relative dominant frequencies over time – after 28 d of curing

**Slika 4:** Spreminjanje relativne prevladujoče frekvence s časom – po 28 dneh utrjevanja

ment times to a stable value. For the AAS specimen there was a stable value of about 70 % of the initial value. For AAS+CNT (AAS+HPMC) there was a decline of about 25 % (20 %) from the initial value. This decline is mainly associated with the drying process, which is followed by shrinkage of the AAS matrix and probably the formation of micro-cracks. Whereas that dominant frequency obtained for specimens with admixtures was higher than for the reference sample, then both admixtures have a positive effect on the formation of a structure of alkali-activated slag composite. Both cellulose derivatives that were added to mixture are able to retain water. These admixtures prevent the material from rapidly drying and the subsequent formation of the micro-cracks caused by drying shrinkage, which generally occurs during hardening of the samples. Carbon nanotubes employed in one set of samples can act as a micro-reinforcement, it participates on the improvement of the mechanical properties.

### 3.2 Material for degradation of concrete samples by corrosion caused by the action of chlorides

Measuring the effect of corrosion on reinforced concrete samples was carried out on two sets of samples. The first set of samples was a reference and the second set of samples was subjected to corrosion by using accelerated degradation by chlorides in an aqueous NaCl solution. The measurements were always carried out after 20 cycles of alternating immersion in an aqueous NaCl solution and drying in an oven. In **Figure 5** we can see the relative change of the dominant frequencies, when the piezoelectric sensor was placed at one end of the concrete beam and hit by a steel hammer at the opposite end of the concrete beam in the longitudinal direction. **Figure 6** shows the relative change of dominant frequencies for the same samples, but measurements were carried out so that the sensor was placed at one end uncovered reinforcement and the hit was made at the opposite end of reinforcement in the longitudinal direction. The signal passing through the degraded sample changes the frequency by reflections on the inhomoge-

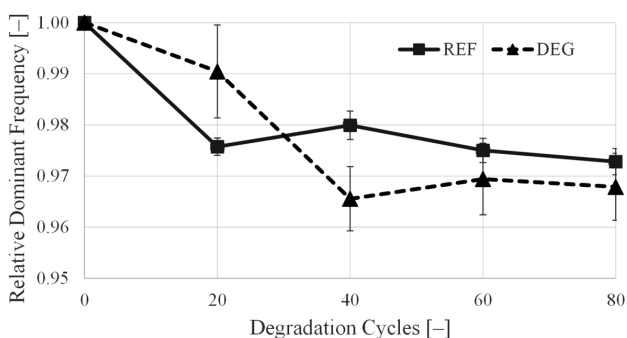


**Figure 5:** Change of the relative dominant frequencies during degradation cycles (impact and sensor on material)

**Slika 5:** Spreminjanje relativne prevladujoče frekvence med cikli propanja (udarec in senzor na materialu)

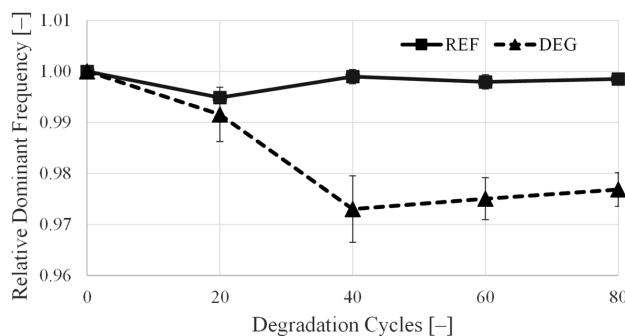


**Figure 6:** Change of relative dominant frequencies during degradation cycles (impact and sensor on reinforcement)

**Slika 6:** Spreminjanje relativne prevladujoče frekvence med cikli propanja (udarec in senzor na betonu)

neities, which is an indicator of changes in the structure. The results are referenced to a relative value and are displayed in the form of an arithmetic average (obtained from three independent measurements for reference samples and from six measurements for degraded samples) and standard deviations as error bars. In the first case, for measurements of the samples on concrete, the dominant frequencies of reference samples was a decrease of 2.4 %, which can be explained by a lack of water for the hydration of the concrete, therefore this decrease is not as significant for immersed samples, only about 1.0 %. In the case of measurements on reinforcement the phenomenon associated with hydration is not apparent, it is only within the measurement error. Between 20 and 40 cycles of degradation occurred in the samples to the formation of observable cracks due to expansion of the corrosion products. This phenomenon is reflected in a significant decrease of the monitored frequencies. For measurements on concrete the decrease was 2.5 % and for a measurement on reinforcement it was 1.9 %. Other frequency changes are no longer significant. The results obtained correspond to the processes that occur during the degradation of the reinforced concrete and reveal damage reinforced concrete.

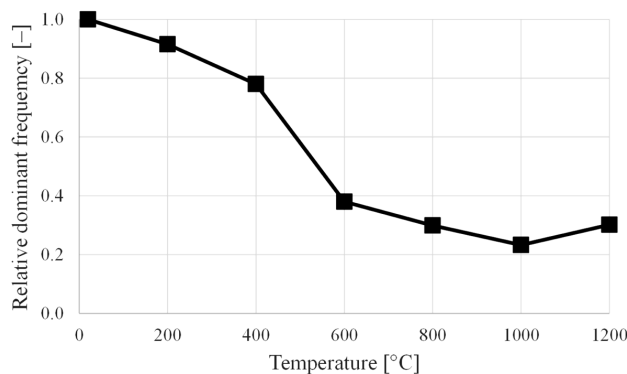


**Figure 7:** Shift of dominant frequency induced by degradation at elevated temperatures (Arrangement U0-S0)

**Slika 7:** Premik prevladujoče frekvence povzročen z razpadanjem pri povišanih temperaturah (Postavitev U0-S0)

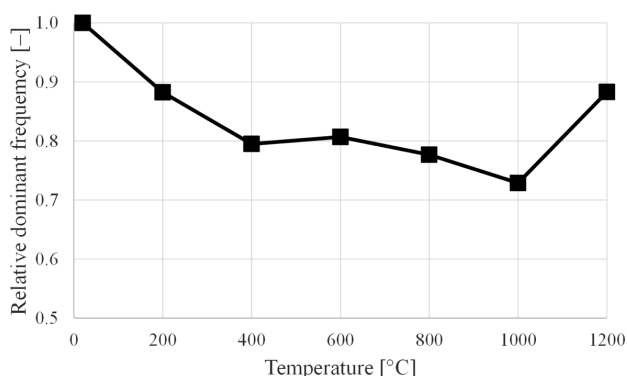


**Figure 8:** Shift of dominant frequency induced by degradation at elevated temperatures (Arrangement U1-S1)

**Slika 8:** Premik prevladujoče frekvence povzročen z razpadanjem pri povišanih temperaturah (Postavitve U1-S1)

### 3.3 Specimens intended to be subjected in a heating process

The mortar specimens of the compositions were exposed to the temperatures of 200, 400, 600, 800, 1000 and 1200 °C. The test results of impact-echo are presented below. **Figure 7** presents the change of dominant frequency versus temperature at which the specimens of mortar compositions were subjected (arrangement U0-S0; longitudinal waves). For this measurement, the sensor was placed at the specimen's end at its centre line direction, while the specimen was hit at the opposite end at the centre line direction – arrangement U0-S0. Longitudinal waves, which propagate within the sample at a speed of about 5100 m/s, can affect the mortar element oscillations. The exposure at elevated temperatures causes a decrease of the dominant frequency, leading to the conclusion that the material's elastic modulus for each composition also decreases ( $E = 4\pi \cdot (f \cdot L)^2$ ). Predominant frequencies are shifted towards the lower frequency range in the course of the degradation. The change is more rapid in the temperature range 400–600 °C, where are intense impurities changed. It is clear that the predominant frequencies shifted down towards the lower frequency region. For the specimen that underwent a thermal stress at a temperature of 1200 °C it is clear that the predominant frequencies shifted upwards towards the higher-frequency region. It is evident that a structural change, accompanied by the creation of new crystal phases, takes place in the specimen at temperatures of about 1200 °C. **Figure 8** shows the change of dominant frequency versus temperature when the arrangement was the U1-S1 one. In this case, transverse waves (gradual waves) are predominantly spread throughout the specimens. The difference between the U0-S0 and U1-S1 arrangements is that in the latter the measurement took place with the sensor being placed at the mid-point and perpendicular to the specimen. The specimen was hit at the mid-point opposite to the sensor. The dependence of frequency on temperature was similar

to that observed when the U0-S0 arrangement was used, however the frequency values were lower in the case of the U1-S1 arrangement. This is similar to the case of the U0-S0 arrangement (**Figure 7**). The comparison of **Figures 7** and **8** indicates that the frequency change is slower when the arrangement U1-S1 is applied. In general, acoustic methods illustrated the physical changes in the structure of all the tested materials. A reduction of the predominant frequency values was observed. Moreover, it was also observed in every case of elevated temperature. The heating up to 110 °C resulted in a loss of capillary water and a reduction of the cohesive forces (weakening of bonds) due to moisture evaporation. At about 170 °C decomposition of gypsum occurred, resulting in expansive spalling. Between 250 and 300 °C the hydrated cement phases were decomposed, while above 300 °C it resulted in  $\text{Ca(OH)}_2$  decomposition. Further temperature increases up to 300 °C or 400 °C intensified the cement paste's thermal decomposition and degradation. All the mentioned changes resulted in the embrittlement and hardening of the tested materials. Thus, the observed reduction of frequency values was assumed to be due to the formation of micro-cracks.

## 4 CONCLUSIONS

The paper deals with the results of measurements using the Impact-echo method on three applications in civil engineering. The aim of this paper was to study the application of the impact-echo method for the detection of flaws in composite materials during different stress situations (setting and hardening in air, degradation by corrosion caused by chlorides and exposing to elevated temperature). It is known that the impact response signal of a specimen is composed of frequencies corresponding to the modes of vibration of the specimen. A shift of the dominant frequency to a lower value is a key indication of the presence of the flaw. From the results obtained in the framework of our research group and the results demonstrated in this paper it can be summarized that the frequency inspection carried out by means of the Impact-echo method makes a convenient tool to assess the quality and lifetime of these composite materials when exposed to stress situations.

## Acknowledgement

This paper has been worked out under the project GAČR No.16-02261S supported by Czech Science Foundation and the project No. LO1408 "AdMaS UP – Advanced Materials, Structures and Technologies", supported by Ministry of Education, Youth and Sports under the "National Sustainability Programme I" and under the project No.J-16-3254 supported by Faculty of Civil Engineering of BUT.

## 5 REFERENCES

- <sup>1</sup> N. J. Carino, Structures Congress and Exposition 2001, Proceedings, American Society of Civil Engineers, Washington, DC, 2001, 1–18
- <sup>2</sup> B. Kucharczyková, P. Misák, T. Vymazal, Determination and evaluation of the air permeability coefficient using Torrent Permeability Tester, *Russian Journal of Nondestructive Testing*, 46 (2010) 3, 226–233, doi:10.1134/S1061830910030113
- <sup>3</sup> T. Vymazal, N. Žižková, P. Misák, Prediction of the risks of design and development of new building materials by fuzzy inference systems, *Ceramics-Silikáty*, 53 (2009) 3, 216–445
- <sup>4</sup> I. Plšková, M. Matysík, Z. Chobola, Evaluation of ceramic tiles frost resistance using Impact Echo Method, In 10th International Conference of the Slovenian Society for Non-Destructive Testing: Application of Contemporary Non-Destructive Testing in Engineering, Ljubljana, 2009, 333–340
- <sup>5</sup> M. Matysík, M. Kořenská, I. Plšková, NDT of freeze-thaw damaged concrete specimens by nonlinear acoustic spectroscopy method, In 10th International Conference of the Slovenian Society for Non-Destructive Testing: Application of Contemporary Non-Destructive Testing in Engineering, Ljubljana, 2009, 317–323
- <sup>6</sup> M. T. Liang, P. J. Su, Detection of the corrosion damage of rebar in concrete using impact-echo method, *Cement & Concrete Research*, 31 (2001), 1427–1436, doi:10.1016/S0008-8846(01)00569-5
- <sup>7</sup> E. Birgham, Fast Fourier Transform and Its Applications, 1st ed., Prentice Hall, New Jersey 1988, 448
- <sup>8</sup> L. Topolář, H. Šimonová, P. Rovnaník, P. Schmid, The Effect of the Carbon Nanotubes on the Mechanical Fracture Properties of Alkali Activated Slag Mortars, In Dynamic of Civil Engineering and Transport Structures and Wind Engineering, Applied Mechanics and Materials, Donovaly, 2014, 243–246, doi:10.4028/www.scientific.net/AMM.617.243



# NON-TRADITIONAL WHITEWARE BASED ON CALCIUM ALUMINATE CEMENT

## NETRADICIONALNI PORCELAN NA OSNOVI KALCIJ ALUMINATNEGA CEMENTA

**Radomir Sokolar**

Brno University of Technology, Faculty of Civil Engineering, Veveri 95, 602 00 Brno, Czech Republic  
sokolar.r@fce.vutbr.cz

*Prejem rokopisa – received: 2015-07-01; sprejem za objavo – accepted for publication: 2015-10-27*

doi:10.17222/mit.2015.182

The article introduces the differences in the properties of whiteware (porosity, strength, thermal expansion coefficient) when a non-traditional binder is used. Pure calcium aluminate cement and a mixture of kaolin and calcium aluminate cement compared with traditional plastic raw material for whiteware – kaolin – are used for the preparation of whiteware bodies with a constant content of non-plastic raw materials: K-Na feldspar and quartz sand. The results are discussed in connection with the micro-structure of the fired body of prepared whitewares (mineralogical composition). Calcium aluminate cement (CAC) in whiteware raw-material mixtures is an interesting alternative to kaolin for a higher strength of the green and fired bodies. Using calcium aluminate cement reduces the sintering temperature of the fired body and significantly changes its mineralogical composition: anorthite is the main mineralogical phase instead of mullite, which is typical for standard porcelain bodies made from raw-material mixtures based on kaolin. The coefficient of thermal expansion increases with an increasing content of CAC in the raw-materials mixture.

Keywords: calcium aluminate cement, kaolin, whiteware

Članek predstavlja razlike v lastnostih porcelana (poroznost, trdnost, koeficient toplotnega raztezka), če se uporabi neobičajno vezivo. Čisti kalcijev aluminatni cement in mešanica kaolina in kalcijevega aluminatnega cementa, v primerjavi s tradicionalno plastično sestavino porcelana – kaolina, so bili uporabljeni za keramična telesa s konstantno vsebnostjo neplastičnih surovin: K-Na glinenec in kvarčni pesek. Rezultati so razloženi v povezavi z mikrostrukturo telesa pripravljene keramike (mineraloška sestava) po žganju. Kalcijev aluminatni cement (CAC), v mešanici surovin za keramiko, je zanimivo nadomestilo za kaolin, za višjo trdnost zelenega in žganega telesa. Uporaba kalcijevega aluminatnega cementa zniža temperaturo sintranja žganega telesa in močno spremeni njegovo mineraloško sestavo; anortit je glavna mineraloška faza namesto mulita, ki je značilen v standardnih porcelanskih telesih, izdelanih iz mešanice surovin na osnovi kaolina. Koeficient toplotnega raztezka se povečuje z večanjem vsebnosti CAC v mešanici surovin.

Ključne besede: kalcijev aluminatni cement, kaolin, porcelan

## 1 INTRODUCTION

Whiteware is a traditional ceramic material that has been manufactured for centuries from a mixture of kaolin, quartz and feldspar. A new type of porcelain body – the anorthite porcelain body – from feldspar, quartz and calcium aluminate cement without using any other binders and plastic ceramic raw materials (clays, kaolins) – was fabricated at a temperature of 1300 °C and the physical and mechanical properties were investigated. The addition of calcium aluminate cement as a substitute for clays exhibits a relatively high green strength and lowers the density due to the formation of anorthite in all the fired bodies.<sup>1</sup>

Increasing the strength of the green body, reducing the coefficient of linear thermal expansion and increasing the whiteness of the fired body can be achieved primarily by replacing the kaolin for calcium aluminate cement (70 % of Al<sub>2</sub>O<sub>3</sub>). A negative aspect of using calcium aluminate cement with a high Al<sub>2</sub>O<sub>3</sub> content is reducing the sintering activity of the body and therefore the need for higher firing temperatures.<sup>2</sup>

The single-phase anorthite ceramic was fabricated (from a mixture of ball clay, quartz, calcite, feldspar and alumina) by slip casting and sintering at 1230 °C for 1 h. It has a high flexural strength of 103 MPa, which is higher than that of the conventional porcelain. The single-phase anorthite ceramic had a relatively low ( $4.9 \times 10^{-6} \text{ K}^{-1}$ ) thermal expansion coefficient, which can be easily matched with an applicable glaze and achieve an excellent thermal shock resistance.<sup>3</sup>

A new, porcelainised stoneware material based on anorthite was prepared from an undefined ratio of wollastonite, alumina, quartz, Ukrainian Ball clay and magnesia. After firing at 1220 °C we obtained a porcelainised stoneware body containing 70 % crystalline and 30 % glassy phases with a high modulus of rupture (110 MPa) that is two times higher compared to conventional porcelainised stoneware materials based on mullite.<sup>4</sup> Calcium aluminate cements are white (according to the Al<sub>2</sub>O<sub>3</sub> content), high-purity hydraulic bonding agents providing controlled setting times and strength development for today's high-performance refractory products.

There are only laboratory results in the area of replacing kaolin with CAC for the production of whiteware without any practical industrial impact. The aim of the article is to introduce the differences in the properties (porosity, strength, thermal expansion coefficient) of whiteware when pure calcium aluminate cement or a combination of the binders – a mixture of kaolin and calcium aluminate cement – instead of kaolin is used. The results will be discussed in connection with the mineralogical composition of the fired whiteware body.

## 2 CHARACTERIZATION OF USED MATERIALS

Calcium aluminate cement SECAR® 51 (CAC51) with 51 % of Al<sub>2</sub>O<sub>3</sub> content (on average) was used for the experimental study. Calcium aluminate cement contains mainly CA and C<sub>12</sub>A<sub>7</sub>, C<sub>2</sub>AS and CT as minor mineralogical phases. The chemical composition is clear from **Table 1**. SECAR®51 is a fused hydraulic binder with a mineralogy focused on mono-calcium aluminate to give a strong hydraulic activity and impart excellent mechanical properties to conventional concretes. This binder is recommended when rapid hardening properties are required. It is adapted to all types of placing methods, particularly casting and gunning at a service temperature of 1400 °C and above. The surface area is about 4 m<sup>2</sup> g<sup>-1</sup>. The equivalent mean spherical diameter (Laser PSD) of CAC51 is  $d(0.5) = 14 \mu\text{m}$ .

**Table 1:** Typical chemical composition of used binders: calcium aluminate cement CAC51 and kaolin

**Tabela 1:** Značilna kemijska sestava uporabljenih veziv: kalcijev aluminatni cement CAC51 in kaolin

Material	CaO	Al <sub>2</sub> O <sub>3</sub>	(K)Na <sub>2</sub> O	SiO <sub>2</sub>	Fe <sub>2</sub> O <sub>3</sub>	MgO	LOI
CAC51	36.9	52.2	≤0.5	4.9	1.8	≤1.0	0.0
Kaolin	0.7	36.6	1.2	46.8	0.9	0.5	13.2

LOI – lost of ignition

Kaolin Zettlitz Ia is the most renowned and the oldest product of the company Sedlecký kaolin a. s. It has been produced since 1892 when the company Zettlitz Kaolinwerke AG was founded; the present company Sedlecký kaolin a.s. is its successor. The major features of kaolin Zettlitz Ia are:

- relatively high plasticity, which enables good workability in the raw state,
- easy deflocculation with available deflocculants (addition of 0.1 % Na<sub>2</sub>CO<sub>3</sub>),

- high content of Al<sub>2</sub>O<sub>3</sub> and a low content of alkalis, which provides high stability in fire.

The original use of the kaolin Zettlitz Ia was in porcelain production. Many producers use it today as the main plastic component in bodies for plastic moulding, slip casting or isostatic pressing of tableware. Good plasticity in the raw state and high stability in fire are also employed in the production of ceramic rollers for fast firing kilns. A low content of harmful substances and plasticity play a significant role in pencil production. This feature is also important for use in cosmetics. The mineralogical composition of the used washed kaolin is 91 % of kaolinite, 2 % of quartz and about 7 % of mica minerals. The surface area of the kaolin is 17.5 m<sup>2</sup> g<sup>-1</sup>.

Industrially milled potassium-sodium feldspar rock and pure quartz sand were used for the experiments as non-plastic materials. The mineralogical composition of the sodium-potassium feldspar is potassium feldspar (microcline) 20.0 %, sodium feldspar (albite) 22.6 %, calcium feldspar (anorthite) 2.4 % and quartz 55.0 %. The chemical composition of the used feldspar rock (**Table 2**) reflects its mineralogical composition and the volume of different types of pure feldspars (potassium, sodium and calcium).

The micro-milled quartz sand ST 6 from Sklopísek Střež Company (Czech Republic) was used. The material is produced by milling in an iron-free environment, by classification with the use of air separators. The raw material used for the production of micro-milled sands, i.e., silica flour, is treated silica sand with a SiO<sub>2</sub> content above 99 %. The chemical purity, favourable particle size distribution, chemical inertness and the hardness of the micro-milled sands – silica flour – is appreciated in the production of glass fibres, ceramic enamels, glazes, as a filler in plastics, in the production of special mortar mixtures, tile adhesives and in the foundry industry for the production of moulds. The surface area of the used micro-milled quartz sand is 4.38 m<sup>2</sup> g<sup>-1</sup>.

Granulometries of the milled feldspar and milled quartz were determined according to the particle size distribution (laser particle size analyser Malvern Mastersizer 2000). The equivalent mean spherical diameters  $d(0.5) = 20.8 \mu\text{m}$  (feldspar) and  $16.0 \mu\text{m}$  (quartz sand) are suitable for the production of the porcelain body.<sup>5</sup>

## 3 METHODOLOGY

Three different raw-material mixtures on the basis of different binder bases (calcium aluminate cement

**Table 2:** Chemical composition of used non-plastic materials: K-Na feldspar rock and quartz sand

**Tabela 2:** Kemijska sestava uporabljenih neplastičnih materialov: K-Na glinenec in kvarčni pesek

	Content, in mass fractions (w/%)										
	SiO <sub>2</sub>	Al <sub>2</sub> O <sub>3</sub>	Fe <sub>2</sub> O <sub>3</sub>	MnO	TiO <sub>2</sub>	CaO	MgO	K <sub>2</sub> O	Na <sub>2</sub> O	LOI	Total
Feldspar	79.76	12.37	0.42	0.00	0.05	0.48	0.10	3.35	2.67	0.80	100.00
Quartz	99.60	0.20	0.03	–	–	0.10	0.10	0.00	–	–	100.03

LOI – lost of ignition

CAC51, washed kaolin and its mixture), industrially milled K-Na feldspar rock and industrially milled glass quartz sand were prepared (**Table 3**).

**Table 3:** Composition of raw-material mixtures (test samples) in mass fractions, (w/%)

**Tabela 3:** Sestava mešanice surovin (preizkusni vzorci), v masnih odstotkih, (w/%)

Sample	Kaolin	CAC51	Feldspar	Quartz sand
A	25		50	25
B		25		
C	15	10		

Raw-material mixtures according to **Table 3** were homogenized for 24 h in a homogenizer. The dry mixture was then moistened with 9 % mass of water. The moistened mixtures were pressed through the 1-mm sieve. The pressing granulate was thus prepared and subsequently mixed for 12 h in the closed plastic vase of the homogenizer to produce a homogenous moisture. Test samples with a green-body size of 100 mm × 50 mm × 10 mm were uniaxially pressed in a steel mould at 20 MPa with 30 s of soaking time at the maximum pressure. Drying in air at a temperature of about 21 °C was followed by final drying in a laboratory drier at 110 °C to achieve a constant weight.

The green bodies were fired in an electric laboratory furnace at different temperatures with a heating rate 10 °C/min and a 30-min soaking time at the maximum temperature to achieve the sintering temperature, which is defined as the temperature when the fired body has a water absorption  $E = 2\%$ . The subsequent cooling proceeded spontaneously, following the natural cooling rate of the furnace. After firing, the body properties (6 test samples) were defined according to the official standard EN ISO 10545 (vacuum water absorption  $E_v$ , modulus of rupture MOR). The mineralogical compositions of the pure feldspars and fired bodies were determined by X-ray diffraction (XRD). The XRD analysis was performed with a Phillips PW 1170 diffrac-

tometer using a Cu anti-cathode ( $\lambda\alpha_1 = 0.15406$  nm), accelerating voltage 40 kV, beam current 25 mA and scanning rate  $1^\circ 2\theta \text{ min}^{-1}$ .

## 4 RESULTS OF EXPERIMENTS

The mixtures containing CAC51 (B and C) show a significantly higher sintering activity (the ability of the body to create a compact body during the firing through the merging of the grains) according to dilatometric curves (**Figure 1**). The sintering activity is described by the shrinkage of the tested samples during the firing. The higher content of CAC51 in the raw-material mixture caused a lower sintering temperature of the body during the firing (**Table 4**). The sintering temperatures (temperature when the fired body has water absorption  $E = 2\%$ ) are:

- Sample A: approximately 1270 °C,
- Sample B: approximately 1150 °C
- Sample C: approximately 1250 °C

**Table 4:** Water absorption of fired bodies depending on the firing temperature

**Tabela 4:** Absorpcija vode v žganih telesih v odvisnosti od temperature žganja

Sample	Water absorption after the firing (in mass fractions, (w/%)		
	1150 °C	1250 °C	1270 °C
A	10.7	4.5	1.6
B	1.8		
C	7.6	1.5	

These are different results than when the calcium aluminate cement with a higher content of  $\text{Al}_2\text{O}_3$  (70 %) was used.<sup>2</sup> This situation reflects the different chemical composition of CA cements: CAC51 contains a higher portion of fluxing oxides ( $\text{Fe}_2\text{O}_3$  and CaO especially) to CAC70. The mineralogical composition of all the tested bodies after the firing is characterized by the existence of the quartz and the glass phase. The fired body based on

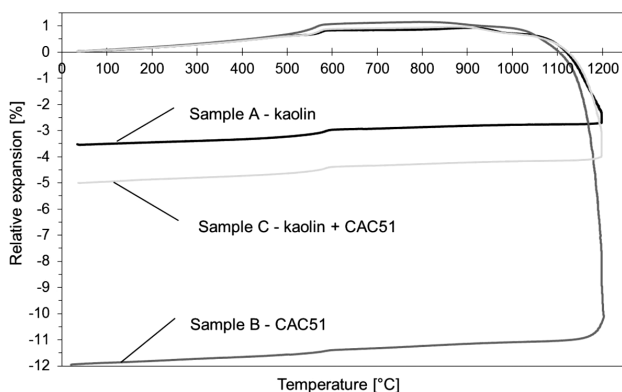


**Figure 1:** Thermal dilatometric analysis during the firing (1200 °C, 5 °C/min without soaking time)

**Slika 1:** Termična dilatometrična analiza med žganjem (1200 °C, 5 °C/min brez časa zalaganja)

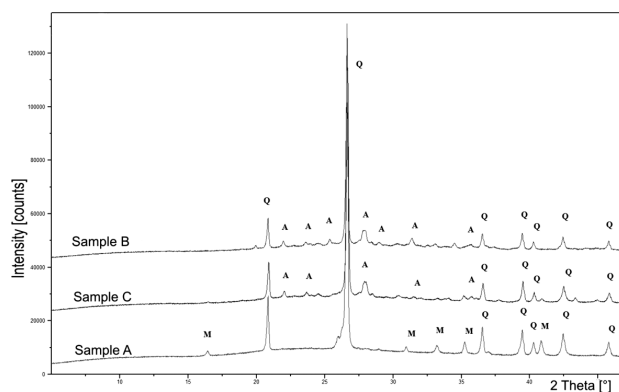


**Figure 2:** XRD of fired bodies based on different binders: kaolin or CAC51 (M-mullite, Q-quartz, A-anorthite)

**Slika 2:** Rentgenogram žganih teles na osnovi različnih veziv- kaolin ali CAC51 (M-mulit, Q- kvarc, A-anorit)

kaolin also contains mullite, while the fired bodies based on CAC51 contain anorthite without mullite (**Figure 2**). In the case of a combination of the binders, the mullite phase is missing.

By comparing the modulus of rupture (MOR) of the fired samples at their sintering temperatures (with similar porosity), it is evident that anorthitic type of body (**Figure 2**) with a lower content of glass phase (based on calcium aluminate cement) comprises a higher modulus of rupture. This confirms the results published in <sup>3,4</sup>.

**Table 5:** Modulus of rupture of tested whiteware bodies after the firing at the sintering temperatures

**Tabela 5:** Prelomni modul preizkušanih porcelanskih teles po žganju na temperaturi sintranja

Sample	Modulus of rupture (MPa)
A	34.4 (1270 °C)
B	37.4 (1150 °C)
C	33.8 (1250 °C)

The thermal expansion coefficient is the main factor when considering the thermal matching between the glaze and the body, and indirectly influences the thermal shock resistance.<sup>6</sup> The coefficient of linear thermal expansion was calculated from dilatometric curves (**Figure 3**) in the different temperature ranges from 30 °C to 1000 °C (**Table 6**). The whiteware fired body based on calcium aluminate cement CAC51 (samples B and C) shows a higher coefficient of thermal expansion compared with the kaolin-based sample A (**Figure 3**). This is an unexpected result due to the formation of anorthite in the samples B and C (**Figure 3**). A very important technical property of anorthite is its low coefficient of linear thermal expansion coefficient of  $4.82 \times 10^{-6} \text{ K}^{-1}$ <sup>7</sup> (compared with mullite  $6.00 \times 10^{-6} \text{ K}^{-1}$ ).<sup>8</sup> Different results are achieved when the CAC with 70 % of  $\text{Al}_2\text{O}_3$  has been used as the replacement for kaolin: the coefficient of linear thermal expansion decreased from  $9.24 \times 10^{-6}$  to

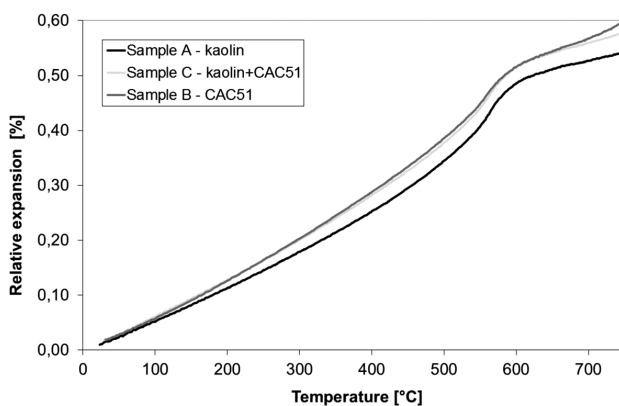


**Figure 3:** Relative expansion of the fired bodies depending on the temperature for the coefficient of linear thermal expansion determination

**Slika 3:** Relativni raztezek žganih teles v odvisnosti od temperature pri določanju linearnega toplotnega raztezka

$8.08 \times 10^{-6} \text{ K}^{-1}$ .<sup>2</sup> This may be connected with the higher content of  $\text{Fe}_2\text{O}_3$  in CAC51 (**Table 1**).

**Table 6:** The values of the coefficient of linear thermal expansion  $\alpha$  ( $\text{K}^{-1}$ ) depending on the temperature range and raw-materials mixture

**Tabela 6:** Vrednosti koeficienta linearnega toplotnega raztezka  $\alpha$  ( $\text{K}^{-1}$ ) v odvisnosti od temperaturnega območja in mešanice surovin

Temperature range	A	C	B
	$\alpha \cdot 10^{-6} (\text{K}^{-1})$	$\alpha \cdot 10^{-6} (\text{K}^{-1})$	$\alpha \cdot 10^{-6} (\text{K}^{-1})$
20-200 °C	5.73	6.43	6.35
20-300 °C	6.05	6.74	6.85
20-400 °C	6.42	7.13	7.31
20-500 °C	7.01	7.63	7.83
20-600 °C	8.25	8.71	8.73
20-700 °C	7.63	8.07	8.20
20-800 °C	7.15	7.71	8.20
20-900 °C	6.69	7.46	7.92
20-1000 °C	6.12	7.03	7.23

## 5 CONCLUSION

The presence of calcium aluminate cements in the raw-materials mixture significantly changes the mineralogical composition of a fired whiteware body, i.e., anorthite is the main mineralogical phase instead of mullite, which is typical for standard porcelain bodies made from raw-material mixtures based on kaolin. The anorthite type of porcelain body is very suitable for the high strength of the fired body. Using calcium aluminate cement with a lower content of  $\text{Al}_2\text{O}_3$  (51 %) reduces the sintering temperature of the body, impairs the whiteness of the body and increases the coefficient of linear thermal expansion.

## Acknowledgements

This work was financially supported by the Czech Science Foundation, research project No. P104/13/23051S "Anorthite porcelain body on the basis of aluminous cement".

## 6 REFERENCES

- W. Tai, K. Kimura, K. Jinnai, A new approach to anorthite porcelain bodies using nonplastic raw materials, *Journal of the European Ceramic Society*, 22 (2002) 4, 463, doi:10.1016/S0955-2219(01)00317-X
- R. Sokolář, L. Vodová, Whiteware Bodies without kaolin, *Inter-ceram.*, 63 (2014) 1–2, 19–21
- X. Cheng, S. Ke, Q. Wang, H. Wang, A. Shui, P. Liu, Fabrication and characterization of anorthite-based ceramic using mineral raw materials, *Ceramics International*, 38 (2012) 4, 3227–3235, doi:10.1016/j.ceramint.2011.12.028
- M. U. Taskiran, N. Demirkol, A. Capoglu, A new porcelainised stoneware material based on anorthite, *Journal of the European Ceramic Society*, 25 (2005) 4, 293–300, doi:10.1016/j.jeurceramsoc.2004.03.017
- A. De Noni, D. Hotza, V. C. Soler, E. Sanchez Vilchez, Effect of quartz particle size on the mechanical behaviour of porcelain tile subjected to different cooling rates, *Journal of the European Ceramic*



Society, 29 (2009) 6, 1039–1046, doi:10.1016/j.jeurceramsoc.2008.07.052

<sup>6</sup> Y. Hirata, Theoretical analyses of thermal shock and thermal expansion coefficients of metals and ceramics, *Ceramics International*, 41 (2015) 1, 1145–1153, doi:10.1016/j.ceramint.2014.09.042

<sup>7</sup> M. Potuzak, M. Solvang, D. Dingwell. Temperature independent thermal expansivities of calcium aluminosilicates melts between 1150 and 1973 K in the system anorthite–wollastonite–gehlenite (An–Wo–Geh): a density model, *Geochim. Cosmochim.*, 70 (2006) 3059–3074, doi:10.1016/j.gca.2006.03.013

<sup>8</sup> M. A. Camerucci, G. Urretavizcaya, M. S. Castro, A. L. Cavalieri, Electrical properties and thermal expansion of cordierite and cor-

dierite-mullite materials, *Journal of the European Ceramic Society*, 21 (2001) 16, 2917–2923, doi:10.1016/S0955-2219(01)00219-9



## BEHAVIOUR OF NEW ODS ALLOYS UNDER SINGLE AND MULTIPLE DEFORMATION

### OBNAŠANJE NOVIH ODS ZLITIN PRI ENOJNI IN VEČKRATNI DEFORMACIJI

**Bohuslav Mašek<sup>1</sup>, Omid Khalaj<sup>1</sup>, Zbyšek Nový<sup>2</sup>, Tomáš Kubina<sup>2</sup>, Hana Jirková<sup>1</sup>, Jiří Svoboda<sup>3</sup>, Ctibor Štádl<sup>1</sup>**

<sup>1</sup>The Research Centre of Forming Technology, University of West Bohemia, Univerzitní 22, 306 14, Pilsen, Czech Republic

<sup>2</sup>COMTES FHT a.s., Průmyslová 995, 334 41 Dobruška, Czech Republic

<sup>3</sup>Institute of Physics of Materials, Academy of Sciences Czech Republic, Žitkova 22, 616 62, Brno, Czech Republic  
khalaj@vctt.zcu.cz

*Prejem rokopisa – received: 2015-07-01; sprejem za objavo – accepted for publication: 2015-11-13*

doi:10.17222/mit.2015.156

The application of innovative processing techniques to conventional raw materials can lead to new structural materials with specific mechanical and physical properties, which open up new possibilities of use in some areas of industry. The processing is enabled by powder metallurgy, which utilizes powders consisting of a metal matrix with dispersed stable particles achieved by mechanical alloying and their hot consolidation by rolling. New oxide dispersion strengthened (ODS) Fe–Al-based alloys are tested under different single and multiple thermomechanical treatments at different temperatures. The results show that new ODS alloys are significantly affected by the thermo-mechanical treatment, leading to microstructural changes. Their analysis is performed using different analytical methods such as optical microscopy, scanning electron microscopy and X-ray diffraction analysis.

Keywords: ODS alloys, composite, steel, Fe-Al

Uporaba inovativnih tehnik preoblikovanja na običajnih materialih lahko privede do novih konstrukcijskih materialov s specifičnimi mehanskimi in fizikalnimi lastnostmi, ki odpirajo nove možnosti uporabe v industriji. Metalurgija prahov omogoča uporabo prahov s kovinsko osnovo z dispergiranimi stabilnimi delci, ki jih dobimo pri mehanskem legiranju in vroči konsolidaciji z valjanjem. Nove zlitine Fe-Al, disperzijsko utrjene z oksidi (ODS), so bile preizkušene pri različni, eno- ali večstopenjski obdelavi pri različnih temperaturah. Rezultati kažejo, da ima termomehanska obdelava novih ODS zlitin močan vpliv, ki se vidi v spremembah mikrostrukture. Analiza je bila izvedena s pomočjo različnih analitskih metod, kot so: svetlobna mikroskopija, vrstična elektronska mikroskopija in rentgenska difrakcijska analiza.

Ključne besede: ODS zlitine, kompozit, jeklo, Fe-Al

## 1 INTRODUCTION

The demand to increase the efficiency of processes in most industrial applications requires, in many cases, metallic materials that can operate at high temperatures, and often at high stresses, in corrosive environments. The presently used high-temperature Ni-, Co- and Fe-based alloys are strengthened by a combination of solid-solution and precipitation hardening, the effectiveness of which strongly decreases with increasing temperature. ODS alloys contain small amounts (0.5–1 % of weight fractions) of finely dispersed oxide phase (mostly yttrium), which is thermodynamically much more stable than other strengthening phases such as  $\gamma'$  or carbides, present in conventional high-temperature alloys.<sup>1</sup> Therefore, the strengthening imparted by the oxide dispersions is retained up to very high temperatures because only limited coarsening or dissolution of the particles occurs.<sup>2,3</sup> In addition, the presence of the fine dispersions combined with a very coarse-grained microstructure that is stable over long exposure times leads to excellent creep resistance up to higher temperatures than those that can be achieved with conventional wrought or cast alloys.<sup>4,5</sup>

The ODS alloys commercially produced at the end of the 20<sup>th</sup> century and the beginning of the 21<sup>st</sup> century are represented by MA 956 or MA 957<sup>6</sup>, PM 2000 or PM 2010<sup>6</sup>, ODM alloys<sup>7</sup> and 1DK or 1DS<sup>8</sup> with a ferritic matrix by ODS Eurofer steels with a tempered ferritic-martensitic matrix<sup>9</sup> and by austenitic Ni-ODS PM 1000 or Ni-ODS PM 3030.<sup>10</sup> ODS alloys are produced by high-energy milling of powder mixtures consisting of the alloying elements, master alloys and the oxide dispersion. The volume fraction of dispersed spherical oxides (usually Y<sub>2</sub>O<sub>3</sub>) is typically below 1 % and the oxides are typically of a mean size of 5–30 nm. The mechanically alloyed powder is then consolidated at high temperatures and pressures to produce the bulk material in the form of bar or tube stock. Afterwards, different thermomechanical treatments are applied to optimize its microstructure and mechanical properties. In the consolidation step the processing temperatures are critical in order to retain the nanocrystalline structure generated during the mechanical alloying and to impede particle coarsening and grain growth.<sup>11–14</sup> The Ni- and Fe-based ODS alloys rely on the formation of slowly growing and strongly

adherent chromium and aluminium scales for their high-temperature oxidation/corrosion resistance. Because of the lower diffusion coefficient, austenitic ODS alloys show a better creep resistance for the same oxide volume fraction and contain some minimum chromium/aluminium content to guarantee sufficient oxidation resistance. However, the resistance to the coarsening of oxides is given by the product of the solubility of oxygen in the matrix and its diffusion coefficient;<sup>16</sup> this factor is more advantageous for ferritic ODS alloys. Also, a sufficient content of Al and/or Cr in the ODS alloy is decisive for its oxidation resistance.<sup>17–19</sup> This is probably the reason why the application of ferritic ODS steels dominates.<sup>15–23</sup>

The new ODS alloys consist of a ferritic Fe-Al matrix strengthened with about 6 to 10 % volume fractions of  $\text{Al}_2\text{O}_3$  particles.<sup>24,25</sup> In order to get a more detailed insight into these new groups of materials, an experimental programme was carried out to better understand their processing behaviour and their operational properties.

## 2 EXPERIMENTAL PART

Mechanically alloyed (MA) powders were prepared in a low-energy ball mill, developed by the authors (**Figure 1**), which enables evacuation and filling by oxygen. It has two steel containers (each 24 L) and each container is filled with 80 steel balls of diameter 40 mm. The revolution speed is variable between  $20 \text{ min}^{-1}$  to  $75 \text{ min}^{-1}$ .

The mechanically alloyed powders consisting of Fe10wt%Al matrix and 6 % to 10 % volume fractions of  $\text{Al}_2\text{O}_3$  particles were deposited into a steel container of diameter 70 mm, evacuated and sealed by welding (**Figure 2**). The steel container was heated up to a temperature of 800–900 °C and rolled by a hot-rolling mill (**Figure 3**) to a thickness of 20–25 mm in the first rolling step and then heated up to a temperature of 1100 °C and rolled to a thickness of 9 mm in the second step. A

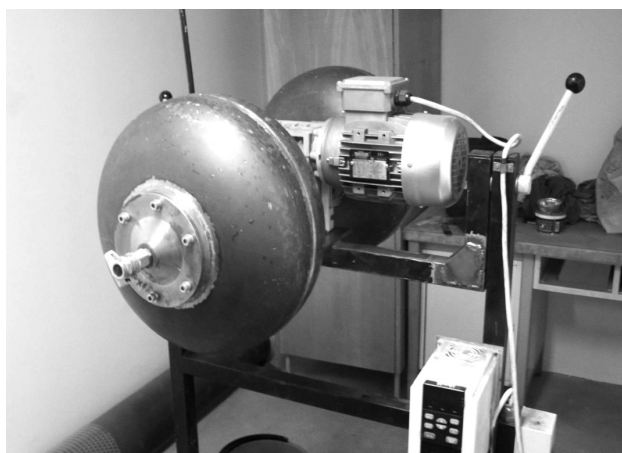


**Figure 1:** Low-energy mill for mechanical alloying  
**Slika 1:** Nizko energijski mlin za mehansko legiranje



**Figure 2:** Container for mechanical alloyed powder  
**Slika 2:** Zbirnik za mehansko legiranje prah

6-mm-thick sheet of the ODS alloy was produced in this way. Afterwards, the specimens were cut by water jet.

In order to investigate the thermomechanical treatment of specimens, a servohydraulic MTS thermomechanical simulator (**Figure 4**) was used, which allows the running of various temperature-deformation paths necessary to find conditions leading to, e.g., the most effective grain coarsening by recrystallization. Several

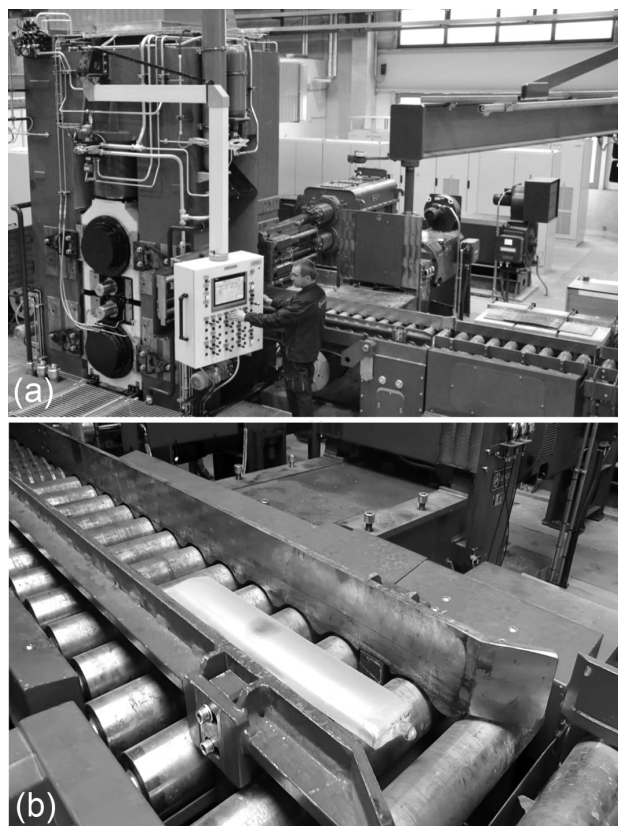


**Figure 3:** Rolling process: a) hot-rolling mill, b) steel container in rolling process

**Slika 3:** Valjanje: a) ogrodje za vroče valjanje, b) zbirnik med postopkom valjanja



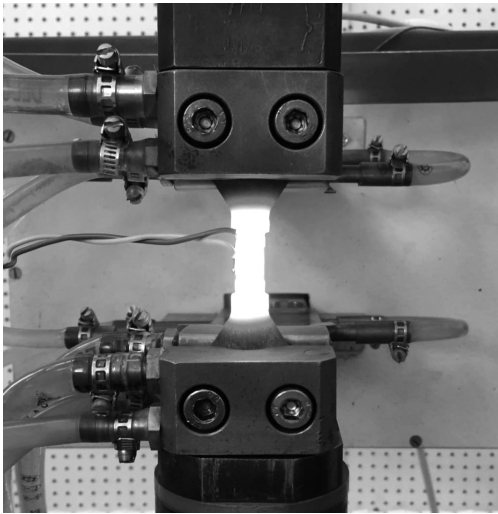


**Figure 4:** Treatment on thermomechanical simulator  
**Slika 4:** Obdelava na termomehanskem simulatorju

procedures of thermomechanical treatment were designed and carried out, which differed in the number of deformation steps characterized by different strains, strain rates and temperatures. The thermomechanical simulator also allows the combination of tensile and compressive deformation, thus accumulating a high plastic deformation (and a high dislocation density) in the specimen.

**2.1 Preparation of specimens**

One specimen (Figure 5) was selected from several examples regarding their most homogeneous temperature fields. The steel containers were removed from all the specimens that were cut by water jet in a longitudinal direction (Figure 6). The thickness of specimens was approximately 6 mm after grinding.

Six types of material were used in this research, as described in Table 1. All these materials are based on a Fe10wt%Al ferritic matrix with different particle sizes and volume fractions in % of Al<sub>2</sub>O<sub>3</sub>. Al<sub>2</sub>O<sub>3</sub> powder was

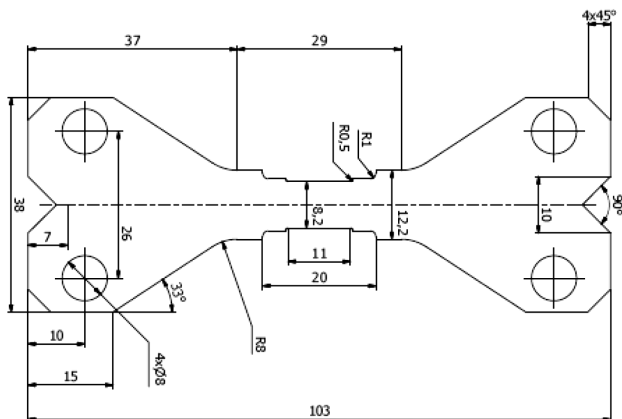


**Figure 5:** Specimen dimensions  
**Slika 5:** Dimenzije vzorca

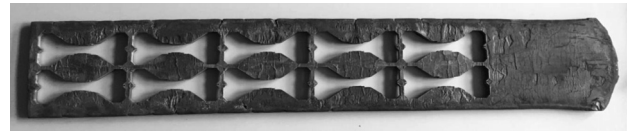


**Figure 6:** Position of specimens on rolled semi-product  
**Slika 6:** Položaj vzorcev na valjanem polproizvodu

added to prepare the composite, fine oxides in ODS alloys were obtained by internal oxidation during mechanical alloying and precipitated during hot consolidation. The microscopic SEM observations indicated several inhomogeneities due to sticking of the material during mechanical alloying on the walls of the milling container. These inhomogeneities can also influence the mechanical and fracture properties of the material, but the mechanical alloying process is steadily optimized with respect to the homogeneity of the materials.

**Table 1:** Material parameters

**Tabela 1:** Parametri materiala

Material No.	Material type	Milling time (h)	Ferritic matrix (% of mass fractions)	% of volume fractions of Al <sub>2</sub> O <sub>3</sub>	Typical particle size (nm)
1	Composite	–	Fe10%Al	10	300
2	ODS Alloy	100	Fe10%Al	6	50–200
3	ODS Alloy	150	Fe10%Al	6	50–150
4	ODS Alloy	200	Fe10%Al	6	30–150
5	ODS Alloy	245	Fe10%Al	7	20–50
6*	ODS Alloy	245	Fe10%Al	7	20–50

\* Different rolling force

**2.2 Testing programme**

The test programme was divided into six different series. The tests are summarized in Table 2.

Single deformation tests series were carried out to investigate the thermomechanical behaviour of the different materials (1 to 4) at different temperatures regarding single tensile loading with a constant strain rate of 1 s<sup>-1</sup> (Figure 7). In order to give a clearer comparison of the results, only the results at room temperature (RT), 800 °C and 1200 °C are presented.

Multiple deformation-test series were carried out to investigate the thermomechanical behaviour of Materials

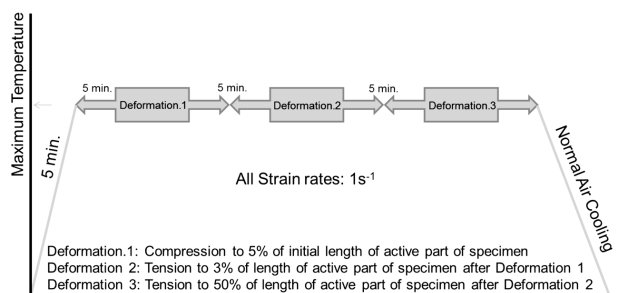


**Figure 7:** Treatment no. 1  
**Slika 7:** Obdelava št. 1

**Table 2:** Parameters of test programme  
**Tabela 2:** Parametri programa preizkusa

Test series	Material no.	Treatment no.	Treatment type	Maximum temperature (°C)	Number of tests	Purpose of tests
A	1	1	Single	1200, 1100, 1000, 900, 800, RT	6	Single deformation thermomechanical behaviour
B	2	1	Single			
C	3	1	Single			
D	4	1	Single			
E	5	2	Multiple	1200	2	Multiple deformation thermomechanical behaviour
F	6	2	Multiple			

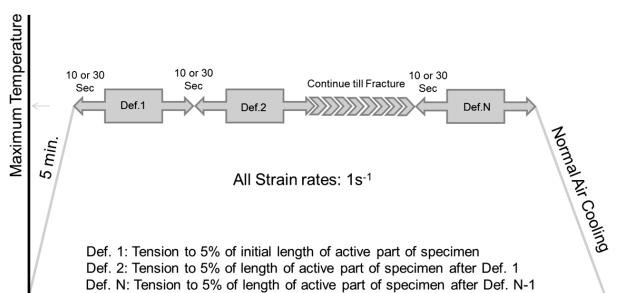


**Figure 8:** Treatment no. 2  
**Slika 8:** Obdelava št. 2

5 and 6 at 1200 °C regarding multiple tensile loading with a constant strain rate of 1 s<sup>-1</sup> (Figure 8) followed by two different holding times (10 s and 30 s).

### 3 RESULTS AND DISCUSSION

#### 3.1 Single deformation-test series

Single deformation-test series were carried out in order to investigate different materials under different conditions. Figure 9 shows the stress-strain curves for all the materials at different temperatures regarding the 5 % compression corresponding to treatment number 1. Material 2 exhibits a better strength at 30 °C and 800 °C, but at 1200 °C Material 1 shows a better strength. The hot-working behaviour of alloys is generally reflected by flow curves, which are a direct consequence of microstructural changes: the nucleation and growth of new grains, dynamic recrystallization (DRX), the generation of dislocations, work hardening (WH), the rearrangement of dislocations and their dynamic recovery (DRV). In the deformed materials, DRX seems to be the prominent softening mechanism at high temperatures. DRX occurs during the straining of metals at high temperature, characterized by nucleation of low-dislocation-density grains and their posterior growth to produce a homogeneous grain structure if a dynamic equilibrium is reached.

Material 4 showed a strange curve shape at 800 °C. The test was repeated several times and similar behaviour was observed. It could be concluded that it happens because of the inhomogeneity of the microstructure of this material.

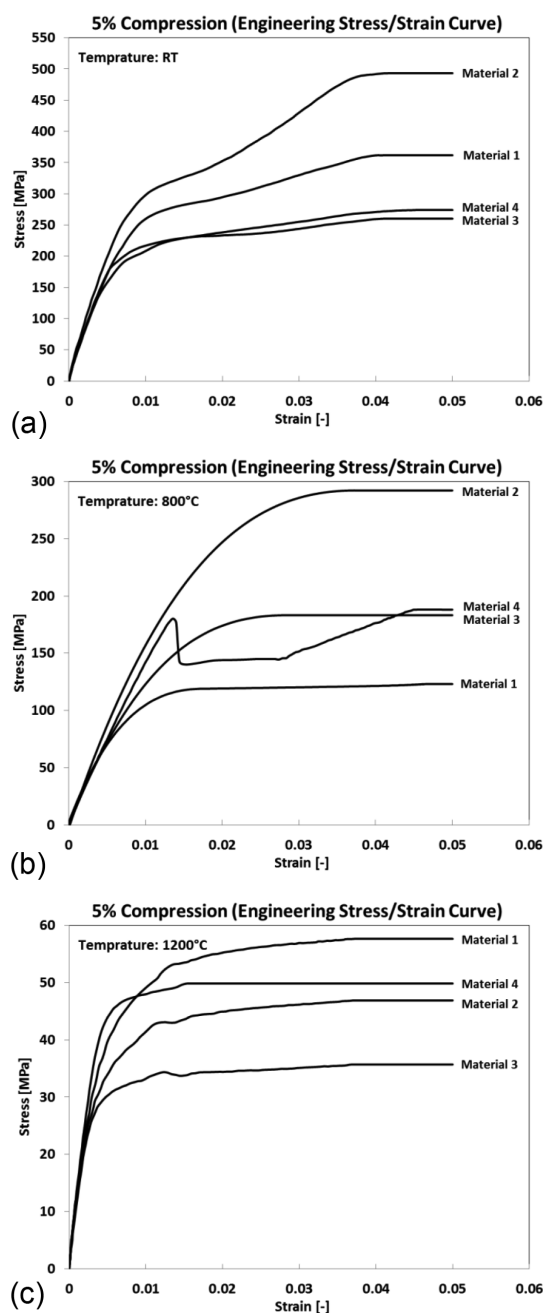


**Figure 9:** Stress-strain curves (5 % compression) for: a) RT, b) 800 °C, c) 1200 °C  
**Slika 9:** Krivulje napetost-raztezek (5 % stiskanje) za: a) RT, b) 800 °C, c) 1200 °C

Figure 10 shows the stress-strain curves for Materials 1 to 4 at different temperatures corresponding to the 3 % tension of treatment number 1 (Figure 7). As can be seen in Figure 10, Material 2 shows a higher strength at 30 °C and 800 °C, but at 1200 °C, again Material 1 shows a better strength. All four materials have almost the same elastic modulus and none of them failed during 3 % deformation. The yield stress as well as the shape of the flow curves is sensitive to temperature. Comparing all these curves, it is found that decreasing the deformation temperature increases the yield stress level, in other

words, it prevents the occurrence of softening due to dynamic recrystallization (DRX) and dynamic recovery (DRV) and allows the deformed metals to exhibit work hardening (WH). For every curve, after a rapid increase in the stress to a peak value, the flow stress decreases monotonically towards a steady-state regime with a varying softening rate, which typically indicates the onset of DRX (Figure 9c).

Figure 11 shows the stress-strain curves for Materials 1 to 4 at different temperatures corresponding to the 50 % tension of treatment number 1 (Figure 7). All four

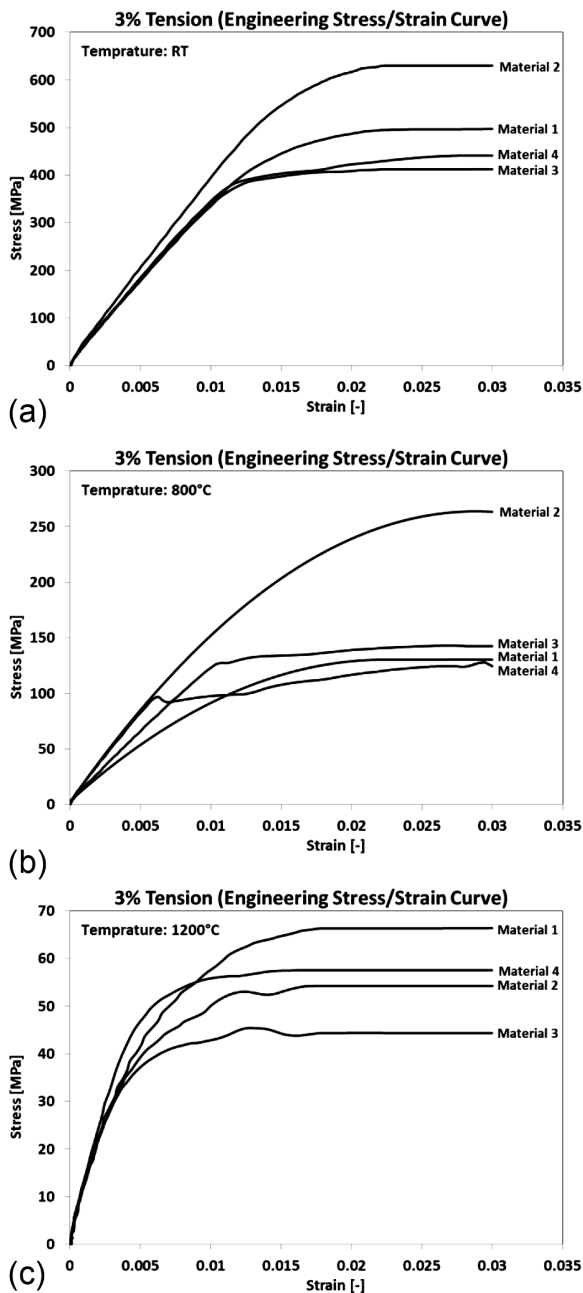


Figure 10: Stress-strain curves (3 % tension) for: a) RT, b) 800 °C, c) 1200 °C

Slika 10: Krivulja napetost-raztezek (3 % natezna obremenitev) za: a) RT, b) 800 °C, c) 1200 °C

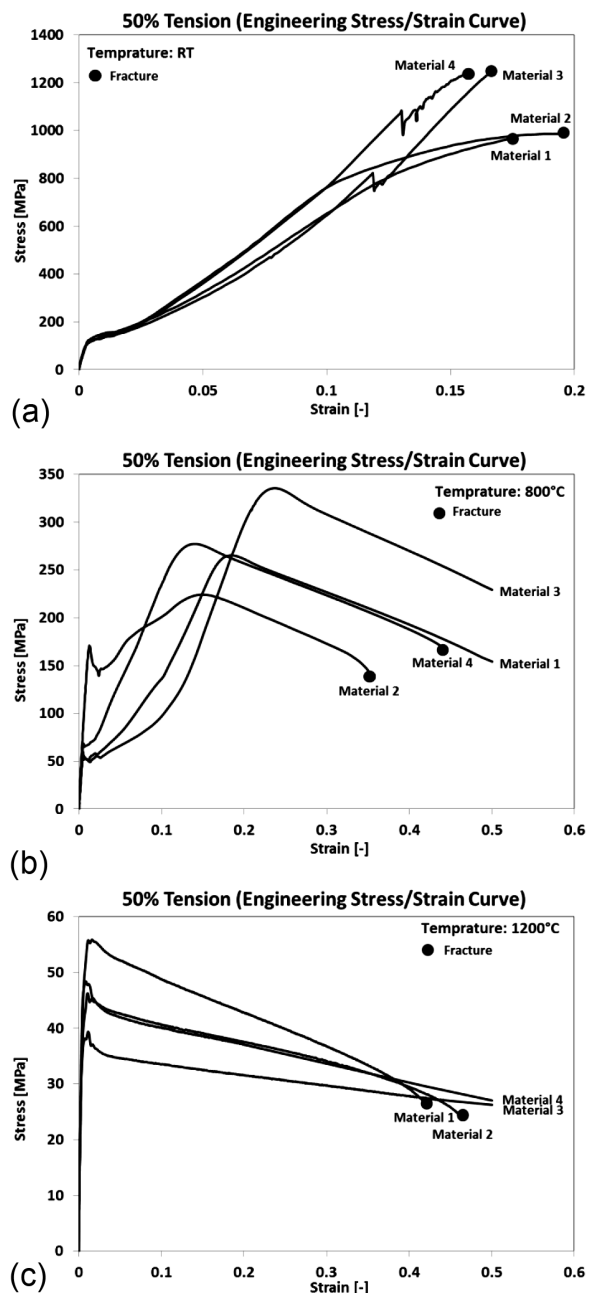


Figure 11: Stress-strain curves (50 % tension) for: a) RT, b) 800 °C, c) 1200 °C

Slika 11: Krivulja napetost-raztezek (50 % natezna obremenitev) za: a) RT, b) 800 °C, c) 1200 °C

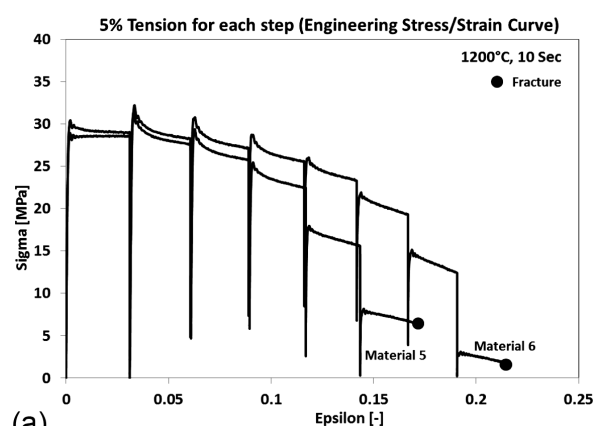
materials failed at RT, but only two materials failed below 50 % tension at higher temperatures. Material 2 failed at 34 % strain and Material 4 failed at 44 % strain at 800 °C. At 1200 °C, only Material 1 failed at 41 % and Material 2 failed at 45 % strain. From these curves, it can also be seen that the stress evolution with strain exhibits three distinct stages.

In the first stage work hardening (WH) predominates and causes dislocations to polygonize into stable subgrains. Flow stress exhibits a rapid increase with increasing strain up to a critical value. Then DRX occurs due to a large difference in dislocation density within the subgrains or grains. When the critical driving force of DRX is attained, new grains are nucleated along the grain boundaries, deformation bands and dislocations, resulting in the formation of equiaxed DRX grains.

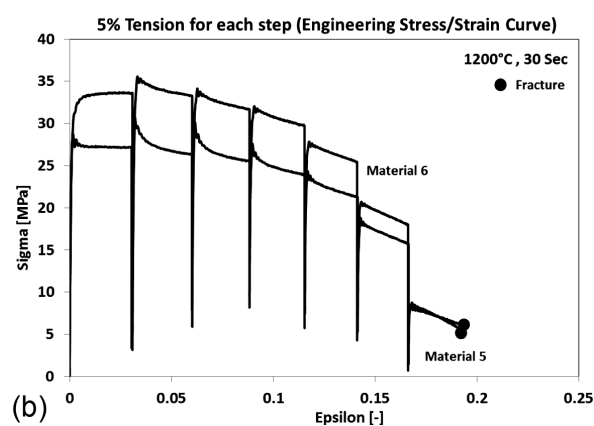
In the second stage, flow stress exhibits a smaller and smaller increase until a peak value or an inflection of the work-hardening rate is reached. This shows that the thermal softening due to DRX and dynamic recovery (DRV) becomes more and more important and it exceeds WH.

In the third stage, three types of curves can be recognized:

- Decreasing gradually to a steady state with DRX softening (Material 3 & 4 in **Figure 11c**),



(a)



(b)

**Figure 12:** Stress-strain curves (5 % tension) for: a) holding time 10 s, b) holding time 30 s

**Slika 12:** Krivulja napetost-raztezek (pri 5 % natezni obremenitvi) za: a) čas zadržanja 10 s, b) čas zadržanja 30 s

- Increasing continuously with significant work-hardening (Material 1 & 2 in **Figure 11b**),
- Decreasing continuously with significant DRX softening.

### 3.2 Multiple deformation-test series

Multiple deformation-test series were carried out in order to investigate the material behaviour under various conditions. **Figure 12** shows the stress-strain curves for both materials at different holding times following the 5 % tension during treatment number 2 (**Figure 8**). Both materials show approximately the same behaviour under the multiple tensile loading. However, Material 6 exhibits greater strength for both holding times (10 s and 30 s). It is supposed that the oxide particles prevent undesirable cyclic softening, which is observed in ferritic-martensitic steels.<sup>22</sup> Obviously, the oxide particles strengthen the material substantially, nevertheless, cyclic softening is observed at both holding times. The cyclic softening rate depends on the applied loading. A higher strain amplitude results in a higher softening rate. For instance, the softening rate was about 23 % during the second cycle in Material 5, while it decreased to 12 % during the last cycles. Although the softening in ODS steel is lower than in the ferritic-martensitic steel<sup>26</sup>, it indicates that oxide dispersion itself does not guarantee a stable cyclic behaviour and other microstructural aspects have to be taken into account. It is obvious that the stress amplitude decreased with an increasing number of cycles, while the amplitude of the plastic strain increased. The softening rate in Material 6 is lower than in Material 5, as observed for both holding times. The slight cyclic hardening is observed only during the first cycle in Material 6 with 30 s holding time (**Figure 12b**), while continuous softening behaviour is observed in the remaining part of the curve.

## 4 CONCLUSIONS

This paper outlines the results of the characterization of the single and multiple deformation thermomechanical behaviour of a new generation of ODS alloys. Six materials differing from each other in the amount and size of the oxides embedded in the ferritic matrix were tested under different conditions. The advantages of all the materials are their low-cost and creep-corrosion and oxidation-resistance due to the Fe–Al-based ferritic matrix of the ODS alloy. It can be concluded that in general the oxide dispersion significantly strengthens the material. However, the typical form of the flow curve with DRX softening, including a single peak followed by a steady state flow as a plateau, is more recognizable at high temperatures than at low temperatures. This is because at high temperatures the DRX softening compensates the WH, and both the peak stress and the onset of steady-state flow are therefore shifted to lower strain levels. The characteristics of softening flow behaviour coupled with DRX have been discussed for six materials and can be summarized as follows:



1. Decreasing deformation temperature causes the flow stress level to increase, in other words, it prevents the occurrence of softening due to DRX and dynamic recovery (DRV) and makes the deformed metals exhibit work hardening (WH).
2. For every curve, after a rapid increase in the stress to a peak value, the flow stress decreases monotonically towards a steady-state regime (a steady-state flow as a plateau due to DRX softening is more recognizable at higher temperatures). A varying softening rate typically indicates the onset of DRX, and the stress evolution with strain exhibits three distinct stages.
3. At higher temperatures, a higher DRX softening compensates the WH, and both the peak stress and the onset of steady-state flow are therefore shifted to lower strain levels.
4. The ODS alloy exhibits cyclic softening in most of the tests and its rate decreases with increasing strain.
5. The elastic part of the total strain amplitude is always higher than the plastic one in all the specimens tested, even for the highest total strain amplitudes of 15 %. This is further confirmation of the strong strengthening effect of oxide particles.

## Acknowledgements

This paper includes results created within the projects 14-24252S Preparation and Optimization of Creep Resistant Submicron-Structured Composite with Fe-Al Matrix and Al<sub>2</sub>O<sub>3</sub> Particles subsidised by the Czech Science Foundation, and LO1412 Development of West-Bohemian Centre of Materials and Metallurgy subsidised by the Ministry of Education, Youth and Sports from specific resources of the state budget of the Czech Republic for research and development.

## 5 REFERENCES

- <sup>1</sup> M. Mohan, R. Subramanian, Z. Alam, P. C. Angelo, Evaluation of the Mechanical Properties OF A Hot Isostatically Pressed Yttria-Dispersed Nickel-Based Superalloy, *Material Technology*, 48 (2014) 6, 899–904
- <sup>2</sup> W. Quadakkers. Oxidation of ODS alloys. *Journal de Physique IV*, 03 (1993), C9-177–C9-186, doi:10.1051/jp4:1993916
- <sup>3</sup> F. Pedraza, Low Energy-High Flux Nitridation of Metal Alloys: Mechanisms, Microstructures and High Temperatures Oxidation Behaviour, *Materials and technology*, 42 (2008) 4, 157–169
- <sup>4</sup> M. A. Montealegre, J. L. González-Carrasco, M. A. Morris-Muñoz, J. Chao, D. G. Morris, High Temperature Oxidation Behaviour of an ODS FeAl Alloy, *Intermetallics*, 8 (2000), 439–446, doi:10.1016/S0966-9795(99)00168-5
- <sup>5</sup> B. Šuštaršič, I. Paulin, M. Godec, S. Glodez, M. Šori, J. Flašker, A. Korošec, S. Kores, G. Abramovic, Morphological and Microstructural Features of Al-based Alloyed Powders for Powder-metallurgy Applications, *Materials and technology*, 48 (2014) 3, 439–450
- <sup>6</sup> B. Kazimierzak, J. M. Prignon, R. I. Fromont, An ODS Material with Outstanding Creep and Oxidation Resistance above 1100°C, *Materials and Design*, 13 (1992) 2, 67–70, doi:10.1016/0261-3069(92)90109-U
- <sup>7</sup> S. Ukai, M. Harada, H. Okada, M. Inoue, S. Nomura, S. Shikakura, T. Nishida, M. Fujiwara, K. Asabe, Tube Manufacturing and Mechanical Properties of Oxide Dispersion Strengthened Ferritic Steel, *Journal of Nuclear Materials*, 204 (1993), 74–80, doi:10.1016/0022-3115(93)90201-9
- <sup>8</sup> R. Schaeublin, T. Leguey, P. Spätig, N. Baluc, M. Victoria, Microstructure and Mechanical Properties of Two ODS Ferritic/Martensitic Steels, *Journal of Nuclear Materials*, 307–311 (2002), 778–782, doi:10.1016/S0022-3115(02)01193-5
- <sup>9</sup> F. D. Fischer, J. Svoboda, P. Fratzl, A thermodynamic approach to grain growth and coarsening, *Journal of Philosophical Magazine*, 83 (2003) 9, 1075–1093, doi:10.1080/0141861031000068966
- <sup>10</sup> M. J. Alinger, G. R. Odette, D. T. Hoelzer, On the role of alloy composition and processing parameters in nanocluster formation and dispersion strengthening in nanostructured ferritic alloys, *Acta Material*, 57 (2009) 2, 392–406, doi:10.1016/j.actamat.2008.09.025
- <sup>11</sup> P. Unifantowicz, Z. Oksiuta, P. Olier, Y. de Carlan, N. Baluc, Microstructure and mechanical properties of an ODS RAF steel fabricated by hot extrusion or hot isostatic pressing, *Fusion Engineering and Design*, 86 (2011), 2413–2416, doi:10.1016/j.fusengdes.2011.01.022
- <sup>12</sup> M. A. Auger, V. de Castro, T. Leguey, A. Muñoz, R. Pareja, Microstructure and mechanical behavior of ODS and non-ODS Fe-14Cr model alloys produced by spark plasma sintering, *Journal of Nuclear Materials*, 436 (2013) 5, 68–75, doi:10.1016/j.jnucmat.2013.01.331
- <sup>13</sup> M. Kos, J. Ferces, M. Brnucko, R. Rudolf, I. Anzel, pressing of Partially Oxide-Dispersion-Strengthened Copper using the ECAP Process, *Materials and technology*, 48 (2014) 3, 379–384
- <sup>14</sup> I. Kubena, B. Fournier, T. Kruml, Effect of Microstructure on Low Cycle Fatigue Properties of ODS Steels, *Journal of Nuclear Materials*, 424 (2012) 1–3, 101–108, doi:10.1016/j.jnucmat.2012.02.011
- <sup>15</sup> M. C. Brandes, L. Kovarik, M. K. Miller, G. S. Daehm, M. J. Mills, Creep Behavior and Deformation Mechanisms in a Nanocluster Strengthened Ferritic Steel, *Acta Materialia*, 60 (2012) 4, 1827, doi:10.1016/j.actamat.2011.11.057
- <sup>16</sup> M. C. Brandes, L. Kovarik, M. K. Miller, M. J. Mills, Morphology, Structure, and Chemistry of Nanoclusters in a Mechanically Alloyed Nanostructured Ferritic Steel, *Journal of Materials Science*, 47 (2012) 8, 3913–3923, doi:10.1007/s10853-012-6249-x
- <sup>17</sup> B. Fournier, A. Steckmeyer, A.-L. Rouffié, J. Malaplate, J. Garnier, M. Ratti, P. Wident, L. Ziolk, I. Tournié, V. Rabeau, J. M. Gentz-bittel, T. Kruml, I. Kubena, Mechanical Behaviour of Ferritic ODS Steels – Temperature Dependency and Anisotropy, *Journal of Nuclear Materials*, 430 (2012) 1–3, 142–149, doi:10.1016/j.jnucmat.2012.05.048
- <sup>18</sup> M. Palm, Concepts Derived from Phase Diagram Studies for the Strengthening of Fe–Al–based Alloys, *Intermetallics*, 13 (2005) 12, 1286–1295, doi: 10.1016/j.intermet.2004.10.015
- <sup>19</sup> F. Stein, M. Palm, G. Sauthoff, Mechanical Properties and Oxidation Behaviour of Two-Phase Iron Aluminium Alloys with Zr(Fe,Al) Laves Phase or Zr(Fe,Al)<sub>12</sub>τ<sub>1</sub> Phase, *Intermetallics*, 13 (2005) 12, 1275–1285, doi:10.1016/j.intermet.2004.08.013
- <sup>20</sup> D. G. Morris, M. A. Muñoz-Morris, Development of Creep-Resistant Iron Aluminides, *Materials Science and Engineering A*, 462 (2007), 45–52, doi:10.1016/j.msea.2005.10.083
- <sup>21</sup> S. Milenkovic, M. Palm, Microstructure and Mechanical Properties of Directionally Solidified Fe–Al–Nb Eutectic, *Intermetallics*, 16 (2008) 10, 1212–1218, doi:10.1016/j.intermet.2008.07.007
- <sup>22</sup> D. G. Morris, Possibilities for high-temperature strengthening in iron aluminides, *Intermetallics*, 6 (1998), 753–758, doi:10.1016/S0966-9795(98)00028-4
- <sup>23</sup> M. A. Morris-Muñoz, Creep Deformation of Oxide-Dispersion-Strengthened Fe-40Al, *Intermetallics*, 7 (1999) 6, 653–661, doi:10.1016/S0966-9795(98)00079-X

- <sup>24</sup> I. Kubena, T. Kruml, Fatigue life and microstructure of ODS steels, *Eng. Fract. Mech.*, 103 (2013), 39–47, doi:10.1016/j.engfracmech.2012.10.011
- <sup>25</sup> O. Khalaj, B. Mašek, H. Jirkova, A. Ronesova, J. Svoboda, Investigation on New Creep and Oxidation Resistant Materials, *Materials and technology*, 49 (2015) 4, 173–179, doi:10.17222/mit.2014.210
- <sup>26</sup> P. Marmy, T. Kruml, Low cycle fatigue of Eurofer 97, *Journal of Nuclear Materials*, 377 (2008) 1, 52–58, doi:10.1016/j.jnucmat.2008.02.054

# ELECTROMAGNETIC-SHIELDING EFFECTIVENESS AND FRACTURE BEHAVIOR OF LAMINATED (Ni–NiAl<sub>3</sub>) COMPOSITES

## UČINKOVITOST ELEKTROMAGNETNE ZAŠČITE IN OBNAŠANJE PRI LOMU LAMINIRANEGA KOMPOZITA (Ni–NiAl<sub>3</sub>)

Taba Yener<sup>1</sup>, Suayb Cagri Yener<sup>2</sup>, Sakin Zeytin<sup>1</sup>

<sup>1</sup>Sakarya University, Engineering Faculty, Department of Metallurgy and Materials Engineering, Serdivan, Sakarya, Turkey

<sup>2</sup>Sakarya University, Engineering Faculty, Department of Electrical and Electronic Engineering, Serdivan, Sakarya, Turkey  
syener@sakarya.edu.tr

*Prejem rokopisa – received: 2015-07-01; sprejem za objavo – accepted for publication: 2015-12-01*

doi:10.17222/mit.2015.189

In this research Ni–NiAl<sub>3</sub> multilayer composites were produced through reactive sintering in an open atmosphere using Ni and Al foils with a 250- $\mu$ m initial thickness. The sintering was performed at 700 °C under 2 MPa of pressure for 6 h. The microstructure and phase characterizations of the samples were performed. The hardness values of samples were determined using the Vickers indentation technique for the intermetallic and metallic regions as 765 $\pm$ 60 HV and 90 $\pm$ 10 HV, respectively. For the mechanical examinations, a perpendicular load was applied to the composite in order to observe the fracture behavior of the metallic-intermetallic laminate composites. SEM fracture surface analyses indicated that cracks initiated in the intermetallic region, and the crack propagation stopped when it reaches the ductile nickel phase. In addition, shielding-effectiveness measurements were performed. The MIL composite exhibits over 50 dB electromagnetic-shielding effectiveness against a very wide frequency range, from a few GHz to over 18 GHz.

Keywords: intermetallics, MIL composites, fracture behavior, electromagnetic interference shielding

V raziskavi so bili izdelani Ni–NiAl<sub>3</sub> večplastni kompoziti z reakcijskim sintranjem na atmosferi in z uporabo Ni- in Al-folij z začetno debelino 250  $\mu$ m. Sintranje je bilo 6 h na 700 °C, pri tlaku 2 MPa. Na vzorcih je bila izvedena karakterizacija mikrostrukture in faz. Trdota vzorcev je bila določena po Vickersu, 765 $\pm$ 60 HV, za področja intermetalnih faz in 90 $\pm$ 10 HV pri osnovi. Za mehanske preiskave je bila uporabljena navpična obremenitev, za opazovanje obnašanja kompozita pri lomljenju kovinskih in intermetalnih lamel. SEM-preiskave prelomov so pokazale, da je začetek razpoke v področju intermetalne faze in da se širjenje razpoke ustavi, ko pride v duktilno fazo niklja. Izvedene so bile tudi meritve učinkovitosti zaščite sevanja. MIL kompozit kaže učinkovitost pred elektromagnetnim sevanjem, višjo od 50 dB v zelo širokem območju frekvenc od nekaj GHz do preko 18 GHz.

Ključne besede: intermetalne zlitine, MIL kompoziti, obnašanje pri lomu, elektromagnetna interferenčna zaščita

## 1 INTRODUCTION

Layered metallic-intermetallic laminate (MIL) composites are a new multifunctional materials group based on open air reactive sintering of chemically active metal foils under pressure.<sup>1,2</sup> Laminate composites are being intensively studied for a number of potential applications: electronic devices, structural components, armor, etc. Ceramic–ceramic, metal–ceramic, metal–metal, metal–ceramic–intermetallic and metal–intermetallic systems have shown desirable properties.<sup>3–5</sup> They are designed to optimize the desirable mechanical properties of intermetallics by incorporating layers of ductile reinforcement.<sup>6</sup> The combination of these types of materials makes the MIL composites candidates for the armament industry as armor materials that require improved mechanical and electromagnetic properties.<sup>1,6,7</sup>

In particular, nickel–tri-nickel aluminide (Ni–NiAl<sub>3</sub>) metal–intermetallic laminate (MIL) composite systems have a great potential for aerospace, automotive and military applications because of their combination of

high strength, toughness and stiffness at a lower density than monolithic titanium or other laminate systems.<sup>7,8</sup> Intermetallics of NiAl and NiAl<sub>3</sub> have a high melting point, a low density, high strength, good corrosion and oxidation resistance at high temperature.<sup>9,10</sup> The nickel–aluminum system is one of the most well known in terms of the formation of intermetallic phases. This system is also a priority among laminate composite systems.<sup>2,5,11</sup>

The aim of the present study is to synthesize nickel–nickel aluminide metallic–intermetallic composites and analyze their mechanical, fracture and electromagnetic shielding behaviors. The organization of the paper is as follows. After this introduction, in the second section the methodology and production of materials are summarized. In the third section the experimental results are presented. In this section, the fracture behavior in terms of "physical-shielding" and then electromagnetic-shielding behavior of the composites are provided after experimental processes. Finally, the paper ends with a conclusion section.

## 2 METHODOLOGY AND EXPERIMENTAL PART

### 2.1 Materials and method

The MIL process consists of stacking commercial-purity Ni and Al foils in alternating layers. The properties of the foils are listed in **Table 1**.

**Table 1:** Properties of foils used in experiments

**Tabela 1:** Lastnosti folij, uporabljenih pri preizkusih

Foil	Ni	Al
Thickness ( $\mu\text{m}$ )	250	250
Purity (%)	99.5	99.5
Stack number	6	5

The nickel- and aluminum-foil dimensions were initially selected to completely consume the aluminum in forming the intermetallic compound with alternating layers of partially unreacted Ni metal. Each foil sheet was prepared as 10 mm  $\times$  10 mm and 60 mm  $\times$  40 mm rectangular pieces for mechanical and electromagnetic experiments, respectively. Contamination on the surface of the foils was cleaned using ethanol. After drying rapidly, they were laminated alternatively into nickel/aluminum multilayer samples. Each stack consisted of 6 nickel and 5 aluminum foils, as indicated in **Table 1**. An initial pressure of 2 MPa is applied at room temperature to ensure good contact between the foils. A schematic representation of the Ni-Al stacks is shown in **Figure 2a**. The sintering process was applied in the open air, in an electrical resistance furnace at 700 °C for 6 h. After sintering, samples were ground and polished using standard metallographic techniques.

### 2.2 Characterization

Microstructure analyses of the composites were performed with a JEOL JSM-5600 model scanning electron microscope (SEM). The presence of phases formed in the sintered samples was determined by energy-disper-

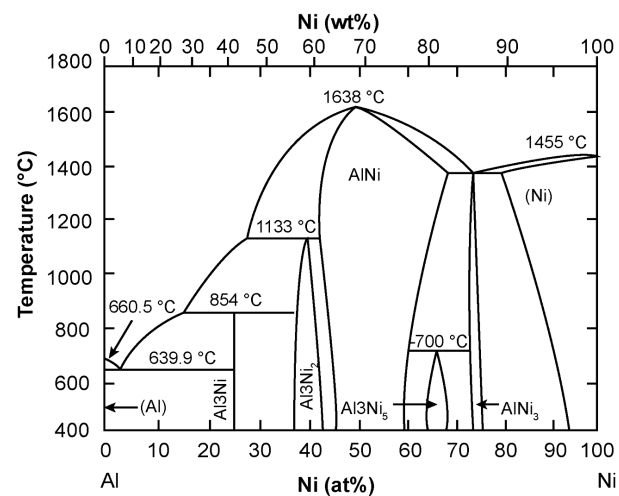


**Figure 1:** The Ni-Al binary phase diagram<sup>12</sup>

**Slika 1:** Binarni fazni diagram Ni-Al<sup>12</sup>

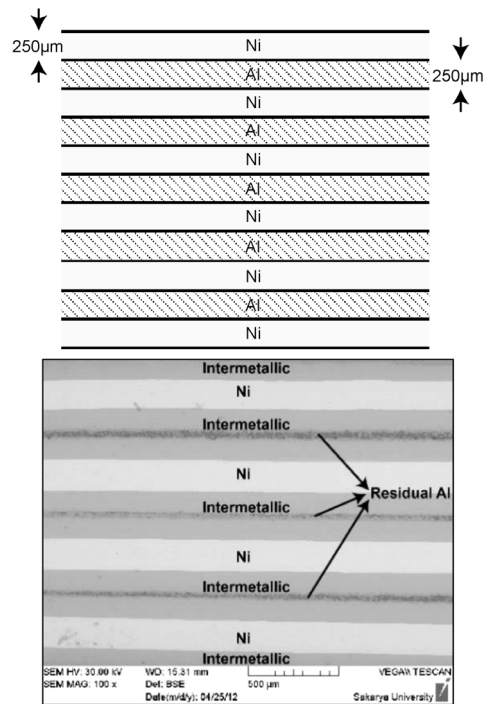


**Figure 2:** a) Nickel-aluminum foils stack, b) SEM micrograph of laminated composites produced at 700 °C/6h

**Slika 2:** a) Sestav nikelj-aluminijevih folij, b) SEM-posnetek laminiranega kompozita, izdelanega pri 700 °C/6 h

sive spectroscopy (EDS). The microhardness of composites was determined using a Leica WMHT-Mod model Vickers hardness instrument under an applied load of 300 g for the intermetallic zone, and 100 g for the metallic zone. The composition of the phases was determined by comparing the results of the microprobe analysis with the data in the binary Ni-Al phase diagram (**Figure 1**).<sup>12</sup>

## 3 EXPERIMENTAL PROCESSES AND RESULTS

### 3.1 SEM-EDS Analysis

**Figure 2b** presents the cross-sectional micrographs of representative laminated composites. The presence of

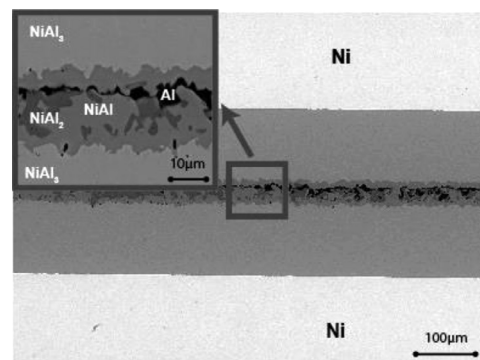


**Figure 3:** SEM-EDS analyses of Ni-NiAl<sub>3</sub> composites sintered at 700 °C/6h

**Slika 3:** SEM-EDS analize Ni-NiAl<sub>3</sub> kompozita po sintranju 6 h na 700 °C



different regions indicates the different phases in the composites. It can be seen that the laminated composites consist of unreacted Ni layers (gray regions) and the formed intermetallic NiAl<sub>3</sub> layers (dark regions). Moreover, the laminated composites are well-bonded and remain nearly fully dense. The nickel aluminide phase occurs due to the thermodynamics of the reaction between Ni and Al. The existence of liquid Al phase plays important roles in the nucleation and growth of NiAl particles and the eventual formation of continuous alternative intermetallic layers.

### 3.2 Mechanical fracture behavior and hardness

Intermetallics and ceramics, in general, have very little or no dislocation motion, and, hence, exhibit very little inherent or intrinsic crack-propagation resistance.<sup>3</sup> By using laminate design and proper composites, it is aimed to produce intermetallic NiAl<sub>3</sub> phase during the process to give a high hardness to the composite, while unreacted nickel provided moderate ductility.

Due to the deflection of cracks along the Ni/NiAl interfaces, a non-catastrophic fracture was observed in the laminated composites. A weak delamination and debonding is seen at the metallic nickel and the intermetallic layers interface. In a large number of cleavage cracks present in the brittle intermetallic layer. Despite

the severe plastic deformation, the nickel layer was not torn. This clearly demonstrates the effect of crack stopping of the ductile reinforcing phases (**Figure 4**).

When it comes to hardness, the values of samples were determined by using the Vickers indentation technique for intermetallic and metallic region as 765±60 HV, 90±10 HV, respectively, whereas the hardness of metallic aluminum and nickel, respectively, is about 45 HV and 90 HV

### 3.3 Electromagnetic-shielding effectiveness

Electromagnetic interference can lead to adverse consequences, such as malfunction or crashing of electronic systems and computers, unintentionally firing of electrically explosive devices, or be the cause of the loss of secret information to an enemy. In this respect, it is essential to protect devices from disruptive electromagnetic signals to guarantee their functionality in stable operating conditions. It is also obvious that the electromagnetic shielding is vital in military applications.<sup>13-15</sup>

Shielding effectiveness is the ratio of impinging energy to the residual energy. When an electromagnetic wave passes through a shield, absorption and reflection take place. The residual energy is part of the remaining energy that is neither reflected nor absorbed by the shield, but emerges from the shield. Shielding effectiveness (*SE*) is the ratio of the field before and after

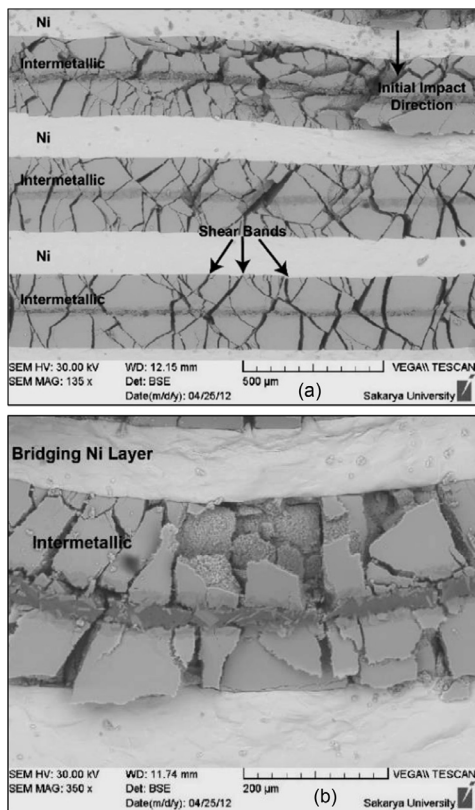


**Figure 4:** Cross-sectional micrographs of Ni-NiAl<sub>3</sub> composites after impact effect: a) 135x , b) 350x

**Slika 4:** Posnetek preseka kompozita Ni-NiAl<sub>3</sub> po udarcu: a) 135x, b) 350x

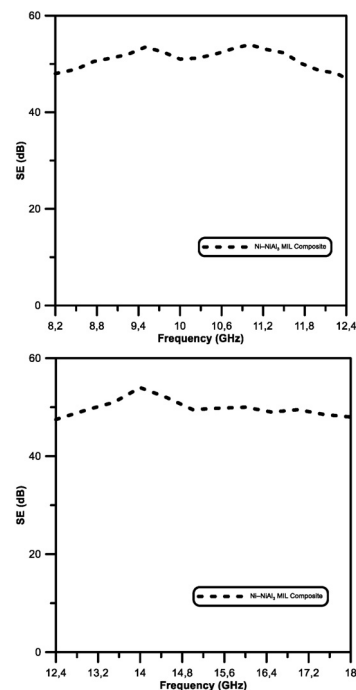


**Figure 5:** Electromagnetic-shielding effectiveness characteristics of laminated Ni-NiAl<sub>3</sub> composites a) X Band (8.2–12.4 GHz), b) Ku Band (12.4–18 GHz)

**Slika 5:** Značilnost učinkovitosti elektromagnetne zaščite laminirane Ni-NiAl<sub>3</sub> kompozita a) X-pas (8,2 GHz-12,4 GHz), b) Ku-pas (12,4 GHz – 18 GHz)

attenuation of the electric and magnetic fields and can be expressed as Equation (1):<sup>15,16</sup>

$$SE[dB] = 20 \lg \left| \frac{E_i}{E_t} \right| \quad (1)$$

Where  $E_i$  and  $E_t$  refer to the transmitted and incident waves, respectively. Shielding effectiveness is a function of frequency, and from the Equation (1) it is measured in dB.

The shielding-effectiveness characteristics of laminated Ni–NiAl<sub>3</sub> composites have been measured and the results obtained are shown in **Figures 5a** and **5b** for the X band and Ku band, respectively.

From the results, the produced MIL composites exhibit around or more 50 dB of electromagnetic-shielding effectiveness against a very wide frequency range from 8.2 GHz to over 18 GHz. That shielding level means even 99.999 % of the incident power is prevented by the produced composites. These shielding-effectiveness levels indicate that laminated composites can be remarkable candidates for shielding application also thanks to their improved mechanical properties.

#### 4 CONCLUSIONS

The conclusions of this research can be summarized as follows:

- By controlling the duration of the reactive-foil sintering process, composites can be fabricated in which a tailored amount of residual aluminum remains at the intermetallic centerline.
- Ni–NiAl<sub>3</sub> metal–intermetallic laminate (MIL) composites have been successfully synthesized by reactive-foil sintering technique in open air at 700 °C for 6 h under 2 MPa pressure. The laminated structure is well-bonded, nearly fully dense.
- Microstructural characterization by SEM and EDS indicates that NiAl, NiAl<sub>3</sub>, Ni<sub>2</sub>Al<sub>3</sub> are intermetallic phases in the composite.
- The hardness of the fabricated laminated composite was dramatically changed. Whereas the hardness of metallic aluminum and nickel, respectively, is about 45 HV and 90 HV, the hardness of intermetallic zone is approximately 765±60 HV.
- In this study the shielding effectiveness of laminated Ni–NiAl<sub>3</sub> composites was examined in a two-frequency band at GHz levels and the results obtained are shown. Around 50-dB shielding-effectiveness levels were reached experimentally from the measurements.
- Thus, experimental results obtained are promising for MIL composites to be appropriate candidate materials for military applications with their electromagnetic as well as mechanical properties.

#### 5 REFERENCES

- <sup>1</sup> K. S. Vecchio, Synthetic multifunctional metallic-intermetallic laminate composites, *JOM*, 57 (2005) 3, 25–31, doi:10.1007/s11837-005-0229-4
- <sup>2</sup> B. Besen, M. Kalayci, T. Yener, S. Zeytin, Some Properties Of Ni–AlNi Metallic-Intermetallic Laminate Material, *Journal of International Scientific Publications: Materials, Methods & Technologies*, 7 (2013) 2, 390–396
- <sup>3</sup> R. R. Adharapurapu, K. S. Vecchio, F. Jiang, A. Rohatgi, Fracture of Ti–Al3Ti metal-intermetallic laminate composites: Effects of lamination on resistance-curve behavior, *Metallurgical and Materials Transactions A*, 36 (2005) 11, 3217–3236, doi:10.1007/s11661-005-0092-5
- <sup>4</sup> L. Peng, H. Li, J. Wang, Processing and mechanical behavior of laminated titanium–titanium tri-aluminide (Ti–Al<sub>3</sub>Ti) composites, *Materials Science and Engineering A*, 406 (2005) 1, 309–318, doi:10.1016/j.msea.2005.06.067
- <sup>5</sup> X. Yang, X. Peng, F. Wang, Size effect of Al particles on the structure and oxidation of Ni/Ni3Al composites transformed from electro-deposited Ni–Al films, *Scripta Materialia*, 56 (2007) 6, 509–512, doi:10.1016/j.scriptamat.2006.11.016
- <sup>6</sup> A. Rohatgi, D. J. Harach, K. S. Vecchio, K. P. Harvey, Resistance-curve and fracture behavior of Ti–Al<sub>3</sub>Ti metal–intermetallic laminate (MIL) composites, *Acta Materialia*, 51 (2003) 10, 2933–2957, doi:10.1016/S1359-6454(03)00108-3
- <sup>7</sup> Y. Cao, C. Guo, S. Zhu, N. Wei, R. A. Javed, F. Jiang, Fracture behavior of Ti/Al3Ti metal-intermetallic laminate (MIL) composite under dynamic loading, *Materials Science and Engineering A*, 637 (2015), 235–242, doi:10.1016/j.msea.2015.04.025
- <sup>8</sup> K. H. Zuo, D. L. Jiang, Q. L. Lin, Mechanical properties of Al2O3/Ni laminated composites, *Materials Letters*, 60 (2006) 9–10, 1265–1268, doi:10.1016/j.matlet.2005.11.010
- <sup>9</sup> L. Z. Zhang, D. N. Wang, B. Y. Wang, R. S. Yu, L. Wei, Identification of lattice vacancies in the B2-phase region of Ni–Al system by positron annihilation, *Journal of Alloys and Compounds*, 457 (2008) 1–2, 47–50, doi:10.1016/j.jallcom.2007.03.065
- <sup>10</sup> F. L. Zhang, Z. F. Yang, Y. M. Zhou, C. Y. Wang, H. P. Huang, Fabrication of grinding tool material by the SHS of Ni–Al/diamond/dilute, *International Journal of Refractory Metals and Hard Materials*, 29 (2011) 3, 344–350, doi:10.1016/j.ijrmhm.2010.12.013
- <sup>11</sup> C. T. Wei, V. F. Nesterenko, T. P. Weihs, B. A. Remington, H. S. Park, M. A. Meyers, Response of Ni/Al laminates to laser-driven compression, *Acta Materialia*, 60 (2012) 9, 3929–3942, doi:10.1016/j.actamat.2012.03.028
- <sup>12</sup> ASM Handbook, Vol. 3: Alloy Phase Diagrams, ASM International, 2001
- <sup>13</sup> P. Saini, M. Aror, Microwave Absorption and EMI Shielding Behavior of Nanocomposites Based on Intrinsically Conducting Polymers, Graphene and Carbon Nanotubes, Chapter 3, In: A. De Souza Gomes (Ed.), *New Polymers for Special Applications*, InTech, 2012, doi:10.5772/48779
- <sup>14</sup> C. R. Paul, Introduction to electromagnetic compatibility, 2<sup>nd</sup> Edition, John Wiley & Sons, 2006, 184
- <sup>15</sup> S. Geetha, K. K. Satheesh Kumar, C. R. K. Rao, M. Vijayan, D. C. Trivedi, EMI shielding: Methods and materials-A review, *Journal of Applied Polymer Science*, 112 (2009) 4, 2073–2086, doi:10.1002/app.29812
- <sup>16</sup> O. Cerezci, S. Şeker, Ş. Yener, B. Kanberoğlu, M. H. Nişancı, Ev, Ofislerde GSM Frekanslı Radyasyondan Bireysel Korunma, EMANET, Yıldız Teknik Üniversitesi, Beşiktaş, İstanbul 2013, 372–376

# EFFECT OF THERMOMECHANICAL TREATMENT ON THE INTERGRANULAR CORROSION OF Al-Mg-Si-TYPE ALLOY BARS

## VPLIV TERMOMEHANSKE PREDELAVE NA INTERKRISTALNO KOROZIJO PALIC IZ ZLITIN Al-Mg-Si

**Peter Sláma, Jan Nacházek**

COMTES FHT a.s., Průmyslová 995, 33441 Dobřany, Czech Republic  
peter.slama@comtesfht.cz

*Prejem rokopisa – received: 2015-07-01; sprejem za objavo – accepted for publication: 2015-02-12*

doi:10.17222/mit.2015.170

Al-Mg-Si-type alloys (6xxx-series alloys) exhibit good mechanical properties, formability, weldability and good corrosion resistance in a variety of environments. They often find use in the automotive industry and other applications. Some alloys, however, particularly those with higher copper levels, show increased susceptibility to intergranular corrosion. Intergranular corrosion (IGC) is typically related to the formation of microgalvanic cells between cathodic, more-noble phases and depleted (precipitate-free) zones along the grain boundaries. It is encountered mainly in Al-Mg-Si alloys containing Cu, where it is thought to be related to the formation of Q-phase precipitates ( $Al_4Mg_8Si_7Cu_2$ ) along the grain boundaries. The present paper describes the effects of mechanical working (pressing, drawing and straightening) and artificial ageing on intergranular corrosion in a bar of the 6064 alloy. The resistance to intergranular corrosion was mapped using corrosion tests according to EN ISO 11846, method B. The corrosion tests showed that with continuing ageing and over-ageing, deep IGC changes into pitting corrosion with a smaller depth of attack. However, the corrosion resistance of the bars is impaired by post-quench mechanical working (drawing and straightening).

**Keywords:** Al-Mg-Si-Cu alloy, 6064 alloy, extruded bars, thermomechanical treatment, intergranular corrosion, pitting corrosion

Zlitine vrste Al-Mg-Si (6xxx-vrsta zlitin) kažejo dobre mehanske lastnosti: preoblikovalnost, varivost in dobro korozijsko odpornost v različnih okoljih. Pogosto se uporabljajo v avtomobilski industriji in tudi v druge namene. Vendar pa nekatere zlitine, posebno tiste z višjo vsebnostjo bakra, kažejo povečano občutljivost na interkristalno korozijo. Interkristalna korozija (IGC) je značilno povezana z nastankom mikrogalvanskih celic med katodno, bolj plemenito fazo in osiromašenim (brez izločkov) področjem, vzdolž meja kristalnih zrn. To se pojavlja predvsem v AlMgSi zlitinah, ki vsebujejo Cu in kjer se predpostavlja, da je to povezano z nastankom izločkov Q-faze ( $Al_4Mg_8Si_7Cu_2$ ), vzdolž meja med zrn. Članek opisuje vpliv mehanskega preoblikovanja (stiskanje, vlečenje, ravnanje) in vpliv umetnega staranja na interkristalno korozijo palic iz zlitine 6064. Odpornost na interkristalno korozijo je bila preslikana s pomočjo korozijskih preizkusov, skladno s standardom EN ISO 11846, metoda B. Korozijski preizkusi so pokazali da se z nadaljevanjem staranja in prestranem globoke interkristalne korozije, spremenijo v jamičasto korozijo, z manjšo globino napada. Vseeno pa je korozijska odpornost palic poslabšana z mehansko predelavo (vlečenje in ravnanje) po gašenju.

**Ključne besede:** zlitina Al-Mg-Si-Cu, zlitina 6064, iztiskane palice, termomehanska predelava, interkristalna korozija, jamičasta korozija

## 1 INTRODUCTION

Al-Mg-Si-type alloys (6xxx-series alloys) exhibit good mechanical properties, formability, weldability and good corrosion resistance in a variety environments. They frequently find use in automotive, aviation and other applications.<sup>1,2</sup> Some of these materials are alloyed with copper to improve their strength. In these alloys, particularly higher-copper alloys, increased susceptibility to intergranular corrosion (IGC) can be observed, most notably in the unaged condition and less often in the T6 temper condition. The effects of Cu as well as the opportunities for enhancing the resistance to intergranular corrosion have received considerable attention in a number of studies.<sup>3-11</sup> Intergranular corrosion (IGC) is typically related to the formation of microgalvanic cells between the cathodic more-noble phases and the depleted (precipitate-free) zones along the grain boundaries. It is encountered mainly in AlMgSi alloys that

contain Cu, where it is thought to be linked to the formation of cathodic Q-phase ( $Al_4Mg_8Si_7Cu_2$ ) along the grain boundaries. The occurrence of phases along the grain boundaries was observed using scanning-transmission electron microscopy (STEM).

The impact of Cu additions and heat treatment on IGC was described in several papers.<sup>3-6</sup> The alloys contained 0.5-0.6 % Mg, 0.6-0.8 % Si, 0.2 % Fe, 0.2 % Mn and Cu at 0.02 through 0.7 % of mass fractions. The occurrence of IGC was monitored in 2.5 mm × 78 mm extruded flat bars. The effects of the cooling rate from the extrusion temperature were studied<sup>3</sup>, as were the effects of artificial ageing.<sup>4,5</sup> Corrosion tests were carried out according to EN ISO 11846, method B. Corrosion was only monitored on the surface of the extruded parts. EN ISO 11846 specifies that the corrosion is monitored on the long side of the specimen. In an alloy with a Cu level of 0.02 %, no IGC was found. In an alloy with

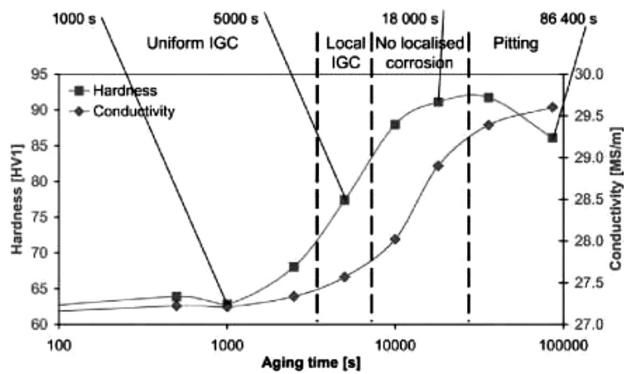


Figure 1: The dominant corrosion types in a material aged at 185 °C, according to<sup>5</sup>

Slika 1: Prevladujoče oblike korozije v materialu, staranem na 185 °C po viru<sup>5</sup>

0.2 % Cu, IGC occurred depending on the artificial ageing time, and changed into pitting corrosion. These findings suggest that between the occurrence of IGC and pitting corrosion, there is a region in which no IGC occurs (Figure 1).

Hence, over-ageing (by increasing either temperature or time) permits a transition from a region with IGC to a region with suppressed IGC.

The AA6056 material for the aviation industry is used in overaged condition. It is supplied in the T78 state with an enhanced resistance to IGC. According to<sup>6,7</sup>, the T78 temper is achieved by two-stage ageing: 175 °C/6 h + 210 °C/5 h.

Two-stage ageing was explored by the authors of the study.<sup>11</sup> The alloy had a nominal composition of 1.0 % Mg, 1.2 % Si, 0.3 % Cu, 0.6 % Mn, 0.12 % Cr, 0.12 % Fe and a balance of Al. An ageing schedule specified as 180 °C/2 h + 160 °C/120 h led to better results than 175 °C/6 h + 210 °C/5 h. However, this work was carried out using specimens of rolled sheet with a 2-mm thickness, where the corrosion attack was monitored on the sheet surface and not on its cross-section.

Thermomechanical treatment generally has a great influence on the corrosion in other types of aluminium alloys.<sup>12</sup> In this research the effect of the thermomechanical treatment (extrusion, drawing and ageing) on the intergranular corrosion in bars from EN AW-6064A (AlMg1SiBi) machineable alloy was studied. AlMgSi-type machineable alloys are used in the automotive industry. Their improved machinability is imparted by alloying with Pb (6012 alloy) or with Bi+Pb (6262 and 6064 alloys). These alloys have higher alloy levels and contain more phases than the alloys studied in<sup>3-11</sup>. These phases include Bi and Pb cathodic particles.

## 2 EXPERIMENTAL PART

The chemical composition of the EN AW-6064A bars is shown in Table 1. The bars of 17 mm diameter were made by an industrial hot-extrusion process using a multiple-hole die. The process temperature was 540–546 °C.

Right after extrusion, the bars were water-wave cooled (T1 condition). The quenched bars were then drawn to the final diameter of 15 mm at 22 % reduction and straightened in a Schumag straightening machine (T2 temper). The final operation was artificial ageing to T8. Bars in conditions corresponding to each process step were gathered for testing. The samples are listed in Table 2.

The bars that did not undergo ageing (HA1, HB2 and HF) were used in artificial ageing trials: single-stage and two-stage ageing to the under-aged, peak-aged and over-aged condition. The artificial ageing schedules are presented in Table 3.

Table 1: Chemical composition of the alloy 6064A, in mass fractions (w/%)

Tabela 1: Kemijska sestava zlitine 6064A, v masnih deležih (w/%)

Sample	Si	Fe	Cu	Mn	Mg	Cr	Pb	Bi
H	0.60	0.23	0.27	0.04	1.03	0.05	0.28	0.49

Table 2: Samples description

Tabela 2: Opis vzorcev

Sample	Diameter	Temper	Description of thermomechanical processing
HA1	17 mm	T1	Extruding, quenching
HB2	15 mm	T2	Extruding, quenching, drawing
HF	15 mm	T2	Extruding, quenching, drawing, straightening
HC	15 mm	T8	Extruding, quenching, drawing, straightening, ageing

Table 3: Heat treatment HT (artificial ageing) for samples HA1, HB2, HF

Tabela 3: Toplotna obdelava (umetno staranje) vzorcev HA1, HB2, HF

HT	One-stage	HT-A	Two-stage A	HT-B	Two-stage B
1	160 °C/4 h	1A	160 °C/4 h + 220 °C/4 h	1B	160 °C/4 h + 205 °C/4 h
2	160 °C/8 h	2A	160 °C/8 h + 220 °C/4 h	2B	160 °C/8 h + 205 °C/4 h
3	180 °C/4 h	3A	180 °C/4 h + 220 °C/4 h	3B	180 °C/4 h + 205 °C/4 h
4	180 °C/8 h				

The progress of ageing was monitored by a HV5 hardness measurement using a DURASCAN 50 hardness tester. Tests of resistance to intergranular corrosion were conducted in accordance the EN ISO 11846 standard, method B.<sup>13</sup> For these tests, specimens of 2 cm in length were made from the bars. Their cut surfaces were ground with P-1200 grinding papers. The original surface of the bar was not altered. Before testing, the specimens were degreased in acetone. In accordance with the standard requirements, they were etched with 5 % NaOH solution at 55 °C for 2 min. After a water rinse, they were placed in concentrated nitric acid for cleaning. The test itself involved submerging in a test solution for 24 h at room temperature. The solution was 30 g NaCl/L solution + 10 mL concentrated hydrochloric acid.



Following the test, the specimens were rinsed with water. Metallographic sections were prepared on longitudinal cross-sections through the specimens. The corrosion attacks on the bar surface as well as on the transverse cut surface were examined. The maximum corrosion depth was determined and documented using light microscopy. The surfaces of the specimens after corrosion testing were examined in a JEOL JSM 6380 scanning electron microscope.

### 3 RESULTS

#### 3.1 Initial microstructures

The microstructure of T8-temper HC bars upon drawing, straightening and ageing is shown in **Figure 2a**. A micrograph of the phases is in **Figure 2b**. The microstructure is fully recrystallized. The grains in the surface layer are relatively fine, with a size of 70  $\mu\text{m}$ . In the centre, the grains are coarser, of the order of several hundred  $\mu\text{m}$ . Different grain sizes in the surface and in the interior are a typical occurrence in extruded bars from Al alloys. Typically, the surface layer contains coarse grains and the interior remains unrecrystallized.<sup>1,2</sup>

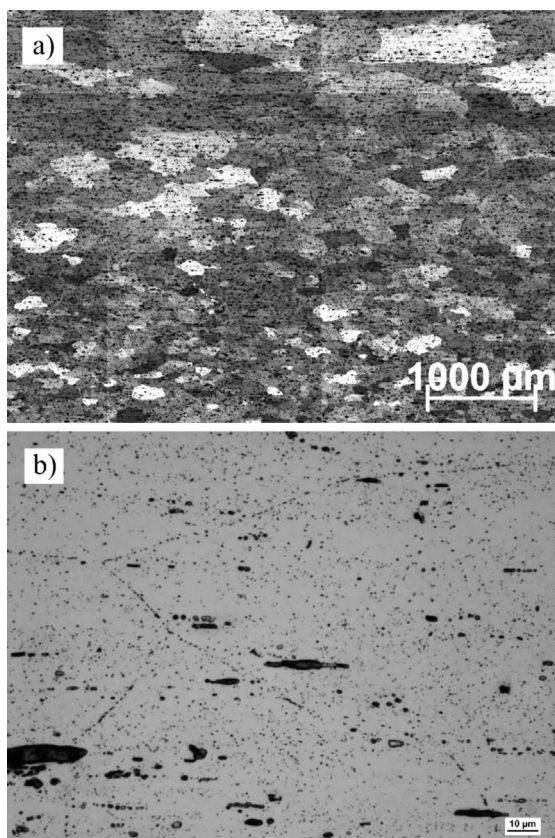


**Figure 2:** Micrographs of grains and phases in HC samples upon drawing and ageing: a) electrolytically etched with Barker's reagent, polarised light, b) etched with Dix-Keller's reagent

**Slika 2:** Posnetka zrn in faz v HC vzorcu, po vlečenju in staranju: a) elektrolitsko jedkano z Baker jedkalom, polarizirana svetloba, b) jedkano z Dix-Keller jedkalom

The phases in the microstructure are banded and aligned in the extrusion/drawing direction. Large elongated particles consist of Bi or Bi+Pb. The small ones are  $\alpha\text{-Al}_{15}(\text{Fe},\text{Mn},\text{Cu},\text{Cr})_3\text{Si}_2$  particles. Other small particles are  $\text{Mg}_2\text{Si}$  particles. The Bi, Pb and  $\alpha\text{-Al}_{15}(\text{Fe},\text{Mn},\text{Cu},\text{Cr})_3\text{Si}_2$  particles are more noble, cathodic. The  $\text{Mg}_2\text{Si}$  particles are anodic. With cathodic particles, the matrix of the aluminium solid solution is etched away preferentially when placed in a corrosion environment. With anodic particles, it is the particles that are attacked. The microstructure may also contain cathodic Q-phase particles ( $\text{Al}_4\text{Mg}_8\text{Si}_7\text{Cu}_2$ ). **Figure 2b** also shows minute particles along grain boundaries. EDS analysis revealed that they contain higher amounts of copper, which suggests that they are Q-phase particles.

#### 3.2 Corrosion tests

Specimens to be tested according to EN ISO 11846, method B, are to be alkaline pre-etched with 5-10 % NaOH solution. With this etch, the Al matrix and anodic phases are attacked. The etched surface of a specimen is shown in **Figure 3**. The large pits are the result of the Al matrix being etched away from around the Bi, Pb and  $\alpha\text{-Al}_{15}(\text{Fe},\text{Mn},\text{Cu},\text{Cr})_3\text{Si}_2$  cathodic phases. The small pits are the locations of  $\text{Mg}_2\text{Si}$  anodic particles that were

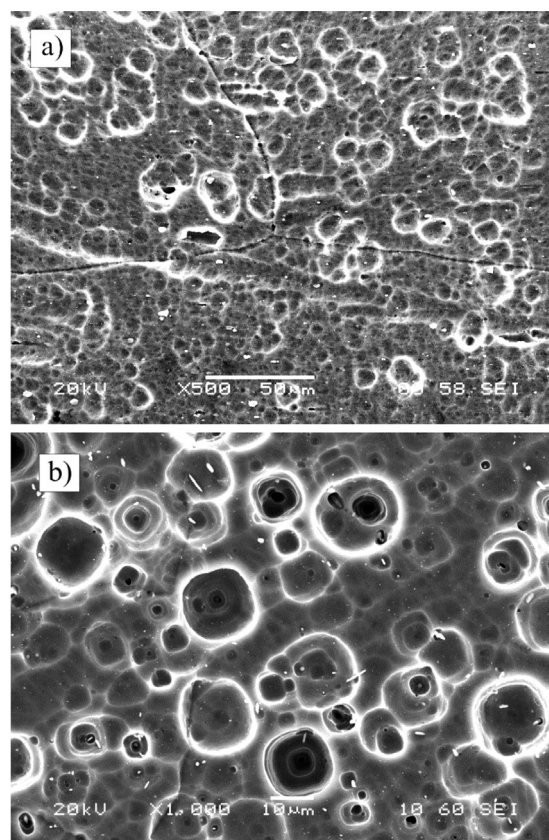


**Figure 3:** SEM micrographs of the surface of HC sample upon etching with NaOH: a) sample surface, b) transverse cut surface

**Slika 3:** SEM-posnetka površine vzorca HC, po jedkanju z NaOH: a) površina vzorca, b) prečni prerez vzorca

etched away. The grain boundaries were slightly attacked.

In order to evaluate the corrosion, the specimens were cut longitudinally after the test. On the cross-section, the type and depth of the corrosion on the bar's surface and on its transverse cut surface were examined.

### 3.2.1 Corrosion tests of materials in initial condition

The initial condition evaluation was carried out on HF samples supplied in the T2 (non-aged) condition and on the HC samples supplied in the T8 (peak-aged) condition. The HC bars were drawn and aged during the 24 h following quenching. The surface corrosion is shown in **Figure 4**. Its evaluation is detailed in **Table 4**.

**Table 4:** Evaluation of corrosion and hardness of initial samples in T2 and T8 condition

**Tabela 4:** Ocena korozije in trdota začetnih vzorcev po T2 in T8 obdelavi

Sample	Temper	HV5	Place	Corrosion depth (µm)	Corrosion type
HF	T2	108	Surface	420.5	IGC + pitting
			Transverse cut	493.2	IGC + pitting
HC	T8	124.3	Surface	217.8	Pitting, transgranular
			Transverse cut	607.7	Pitting

The surface of the non-aged HF sample shows extensive intergranular corrosion (IGC) with a depth of more than 420 µm. In the artificially-aged HC sample (T8 peak-aged temper), the corrosion changed into the pitting type, which spreads perpendicularly to the surface to a depth of more than 200 µm. The corrosion type corresponds to transgranular corrosion. On the cross-section through the HF specimen, IGC with a

depth of approximately 500 µm was found as well. The corrosion on the transverse cut surface of the HC sample is very extensive too. It is, however, pitting-type corrosion, which reached a depth of up to 600 µm. It follows the bands of coarse cathodic Bi, Pb and alpha-Al<sub>15</sub>(Fe,Mn,Cu,Cr)<sub>3</sub>Si<sub>2</sub> particles (**Figure 4d**). **Table 4** lists HV5 hardness values. The HF sample in the T2 state exhibits 108 HV5. Age-hardening to T8 increased the hardness to 124 HV5.

### 3.2.2 Corrosion tests after experimental heat treatment (artificial ageing)

Using these tests, the impact of various artificial ageing schedules (under-ageing, over-ageing) on the corrosion in bars in various conditions was monitored:

- Sample HA1 – after extruding and quenching;

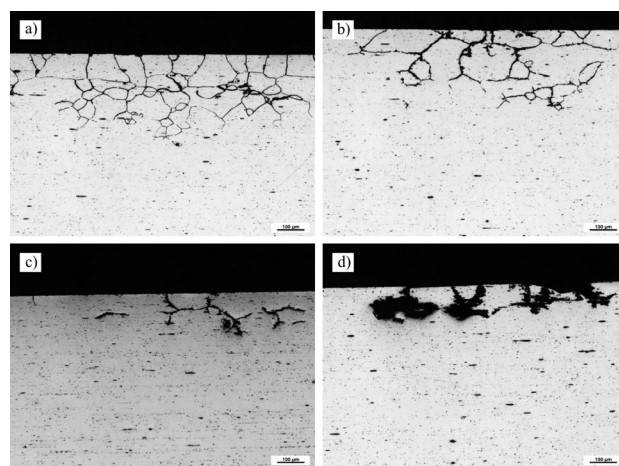


**Figure 5:** Corrosion on the HA1 bar surface upon ageing: a) 160 °C/8 h under-aged, b) 180 °C/8 h, c) 160 °C/4 h + 205 °C/4 h, d) 160 °C/4 h + 220 °C/4 h overaged

**Slika 5:** Korozija na površini HA1 palice, po staranju: a) 160 °C/8 h, podstarano, b) 180 °C/8 h, c) 160 °C/4 h – 205 °C/4 h, d) 160 °C/4 h + 220 °C/4 h, prestarano

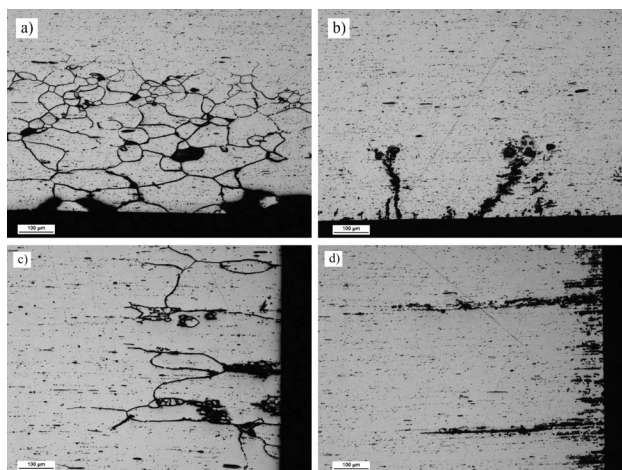


**Figure 4:** Corrosion attack in as-received bars: a) HF surface – temper T2, non-aged, b) HC surface – temper T8, peak-aged, c) HF transverse cut surface, d) HC transverse cut surface

**Slika 4:** Korozija na dobavljenih palicah: a) HF površina - žarjenje T2, nestarano, b) HC površina – žarjenje T8, starano, c) HF prečni presek, d) HC prečni presek

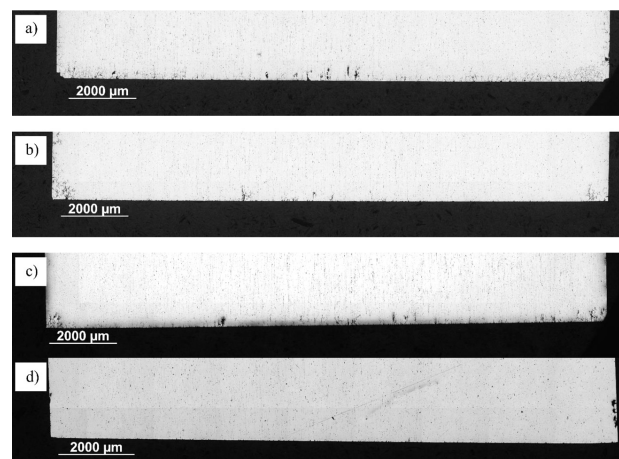


**Figure 6:** Corrosion on the HA1 transverse cut surface upon ageing: a) 160 °C/8 h under-aged, b) 180 °C/8 h, c) 160 °C/4 h + 205 °C/4 h, d) 160 °C/4 h + 220 °C/4 h overaged

**Slika 6:** Korozija na prečnem prerezu HA1 po staranju: a) 160 °C/8 h podstarano, b) 180 °C/8 h, c) 160 °C/4 h + 205 °C/4 h, d) 160 °C/4 h + 220 °C/4 h prestarano



- Sample HB2 – after extruding, quenching and drawing;
- Sample HF – after extruding, quenching, drawing and straightening
- Corrosion tests of specimens of HA1 extruded bars

The surface corrosion of selected specimens in variously aged conditions is illustrated in **Figure 5**. The corrosion of the transverse cut surface is shown in **Figure 6**. **Table 5** contains the results of the corrosion evaluation and the HV5 hardness levels, which indicate the progress of ageing. In specimens in the under-aged condition, the most extensive surface corrosion was found, involving continuous IGC with a maximum depth of more than 300 µm. In the peak-aged condition, the depth of attack decreased and IGC ceased to be continuous. In the over-aged condition, only sporadic pitting corrosion can be observed with a depth of about 120 µm.

**Table 5:** Evaluation of corrosion and hardness of samples HA1  
**Tabela 5:** Ocena korozije in trdota vzorcev HA1

Sample HV5	US	Place	Corrosion depth (µm)	Corrosion type
HA1-2 92.5	160 °C/ 8h	Surface	309.3	IGC + pitting sporadic
	Under-ageing	Transverse cut	421.1	IGC near-edge + pitting
HA1-4 113.7	180 °C/ 8 h	Surface	296.4	IGC 50 %
	peak ageing	Transverse cut	460.8	IGC near-edge + pitting
HA1-1B 114.7	160 °C/4 h + 205 °C/4 h	Surface	158.9	IGC + pitting sporadic
	peak ageing	Transverse cut	381.5	IGC + pitting
HA1-1A 109.3	160 °C/4 h + 220 °C/4 h	Surface	120.4	Pitting sporadic
	Over-ageing	Transverse cut	93.4	Pitting sporadic

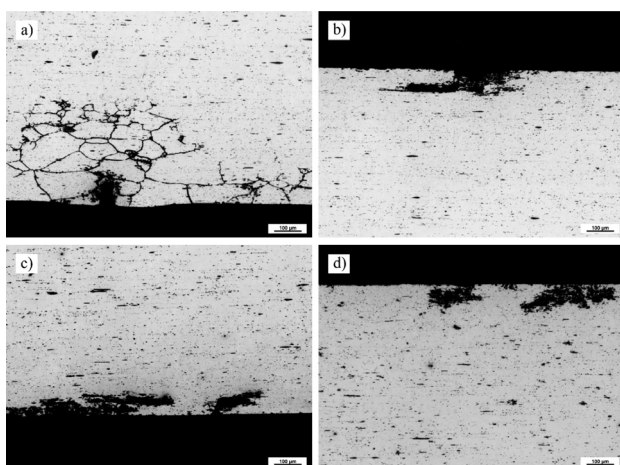


**Figure 7:** Corrosion on the HB2 transverse cut surface upon ageing: a) 180 °C/4 h under-aged, b) 180 °C/8 h, c) 180 °C/4 h + 205 °C/4 h, d) 180 °C/4 h + 220 °C/4 h overaged

**Slika 7:** Korozija na prečnem prerezu HB2 po staranju: a) 180 °C/4 h podstarano, b) 180 °C/8 h, c) 180 °C/4 h + 205 °C/4 h, d) 180 °C/4 h + 220 °C/4 h prestarano

The same type of corrosion was found on the transverse cut surface. However, the corrosion depth was larger there: more than 400 µm. The only exception was the over-aged sample where the depth was less than 100 µm.

### 3.2.3 Corrosion tests of specimens of HB2 drawn bars

The surface corrosion of selected specimens in variously aged conditions is illustrated in **Figure 7**. The corrosion of the transverse cut surface is shown in **Figure 8**. Results of the evaluation of corrosion are given in **Table 6**.

**Table 6:** Evaluation of corrosion and hardness of samples HB2  
**Tabela 6:** Ocena korozije in trdota vzorcev HB2

Sample HV5	US	Place	Corrosion depth (µm)	Corrosion type
HB2-3 120	180 °C/4 h	Surface	382.5	IGC 60 % + pitting sporadic
	Under-ageing	Transverse cut	528.4	IGC, near-edge
HB2-4 120.7	180 °C/8 h	Surface	123.6	Pitting, sporadic
	peak ageing	Transverse cut	755.6	Pitting, near-edge
HB2-3B 123.3	180 °C/4 h + 205 °C/4 h	Surface	81.8	Pitting
	peak ageing	Transverse cut	742.6	Pitting
HB2-3A 106.7	180 °C/4 h + 220 °C/4 h	Surface	88.3	Pitting
	Over-ageing	Transverse cut	678.1	Pitting, near-edge

In HB2 drawn bars, IGC was found only in the under-aged condition (**Figure 7a**). This intergranular

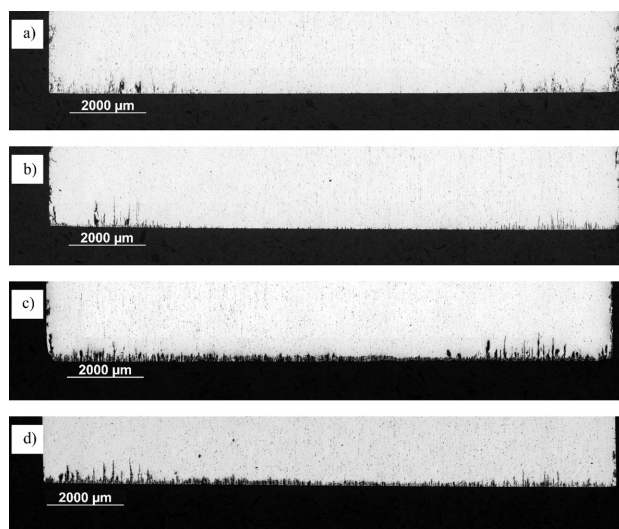


**Figure 8:** Corrosion on the HB2 transverse cut surface upon ageing: a) 180 °C/4 h under-aged, b) 180 °C/8 h, c) 180 °C/4 h + 205 °C/4 h, d) 180 °C/4 h + 220 °C/4 h overaged

**Slika 8:** Korozija na prečnem prerezu HB2 po staranju: a) 180 °C/4 h podstarano, b) 180 °C/8 h, c) 180 °C/4 h + 205 °C/4 h, d) 180 °C/4 h + 220 °C/4 h prestarano

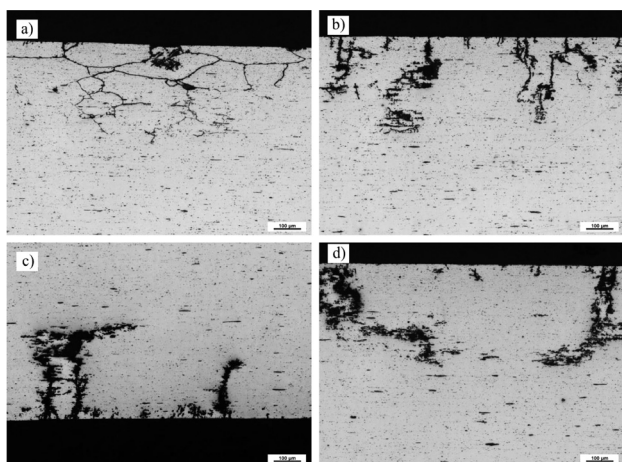


**Figure 9:** Corrosion on the HF bar surface upon ageing: a) 180 °C/4 h under-aged, b) 180 °C/8 h, c) 180 °C/4 h + 205 °C/4 h, d) 180 °C/4 h + 220 °C/4 h overaged

**Slika 9:** Korozija na površini HF palice, po staranju: a) 180 °C/4 h podstarano, b) 180 °C/8 h, c) 180 °C/4 h + 205 °C/4 h, d) 180 °C/4 h + 220 °C/4 h prestarano

corrosion is not continuous. On the surface of the bar, the corrosion depth is approx. 400 µm. On the transverse cut surface, IGC is more frequent in the fine-grained surface layer. The depth of attack exceeds 500 µm (**Figure 8**). In the peak-aged and overaged conditions, the bar’s surface only exhibits pitting corrosion with a depth of about 100 µm. Besides that, corrosion spreads parallel to and beneath the surface, along the bands of coarse cathodic phases. The authors in<sup>10</sup> describe this type of corrosion as ELA (Exfoliation-Like Attack). On the transverse cut surface, corrosion is of the pitting type as well. It is

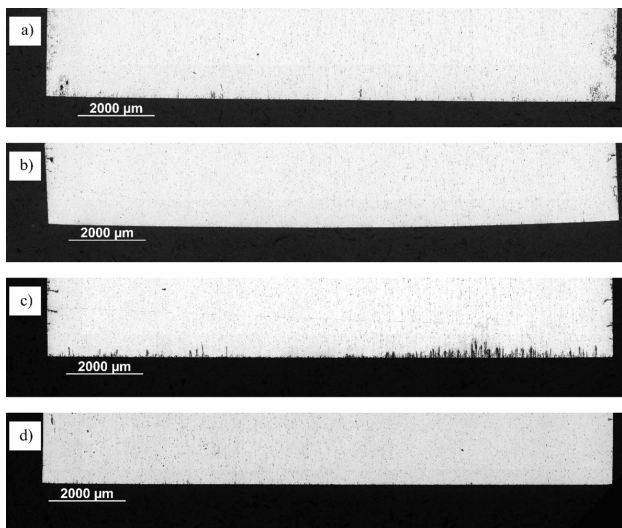


**Figure 10:** Corrosion on the HF transverse cut surface upon ageing: a) 180 °C/4 h under-aged, b) 180 °C/8 h, c) 180 °C/4 h + 205 °C/4 h, d) 180 °C/4 h + 220 °C/4 h overaged

**Slika 10:** Korozija na prečnem prerezu HF, po staranju: a) 180 °C/4 h podstarano, b) 180 °C/8 h, c) 180 °C/4 h + 205 °C/4 h, d) 180 °C/4 h + 220 °C/4 h prestarano

much deeper and, again, more frequent in the near-surface areas.

### 3.2.4 Corrosion tests of specimens of HF drawn and straightened bars

Surface corrosion of selected specimens in variously aged conditions is illustrated in **Figure 9**. The corrosion of the transverse cut surface is shown in **Figure 10**. Results of the evaluation of corrosion are given in **Table 7**.

**Table 7:** Evaluation of corrosion and hardness of samples HF  
**Tabela 7:** Ocena korozije in trdota vzorcev HF

Sample HV5	US	Place	Corrosion depth (µm)	Corrosion type
HF-3 123	180 °C/4 h	Surface	364.9	IGC
	Under-ageing	Transverse cut	545.9	IGC, near-edge
HF-4 123.3	180 °C/8h	Surface	307.1	Pitting
	peak ageing	Transverse cut	93.6	Pitting, sporadic
HF-3B 115.4	180 °C/4 h + 205 °C/4 h	Surface	348.9	Pitting, transgranular
	Over-ageing	Transverse cut	471.2	Pitting
HF-3A 110.3	180 °C/4 h + 220 °C/4 h	Surface	366.1	Pitting, transgranular
	Over-ageing	Transverse cut	122.3	Pitting, sporadic

In specimens in underaged condition, there is deep IGC on the bar’s surface, as well as on the transverse cut surface. In the peak-aged and over-aged conditions, the bar surface only exhibits pitting corrosion that spreads perpendicularly to the surface to a depth of more than 300 µm. It is transgranular corrosion, as it penetrates the grains. On the transverse cut surfaces, the least extensive corrosion was found in the peak-aged condition (**Figure 10b**). In the slightly-overaged condition, the corrosion is extensive and deep (**Figure 10c**). In increasingly overaged specimens, the number and depth of corrosion attack locations decrease (**Figure 10d**).

## 4 DISCUSSION

The main mechanism of IGC is reported to be the formation of micro-galvanic cells between cathodic more-noble phases and the depleted (precipitate-free) zones along the grain boundaries. In this case, the key cathodic phase is the Q-phase (Al<sub>4</sub>Mg<sub>8</sub>Si<sub>7</sub>Cu<sub>2</sub>), which precipitates along the grain boundaries. As a result, the grain-boundary areas become depleted of Cu and other elements. In addition, a thin Cu film forms along the grain boundaries and plays the key role in IGC growth and propagation.<sup>3-6</sup> The entire precipitation process is thermally activated and depends on the diffusion of alloying elements. Its rate is described by an Arrhenius equation. With increasing ageing temperature and time,



the Q-phase precipitates coarsen and the volume fraction of the Cu film along the grain boundaries decreases. Consequently, the susceptibility to IGC is reduced and the material typically exhibits only pitting corrosion.

The EN AW-6064 alloy contains a number of other primary cathodic phases (Bi, Pb,  $\alpha$ -Al<sub>15</sub>(Fe,Mn,Cu,Cr)<sub>3</sub>Si<sub>2</sub>). Their arrangement in bands with short distances between the phases helps the pitting corrosion to propagate to larger depths, most notably beneath the transverse cut surface (**Figure 4d**). In some cases there were great differences between the corrosion attack on the bar's surface and on the transverse cut surface.

In the extruded bars (HA1), it was found that with increasing over-ageing the large-depth IGC changes into shallower pitting corrosion, which is in agreement with the findings presented in <sup>3-6</sup>. In the overaged condition, the corrosion penetrations on the transverse cut surface were smaller. Sporadic pitting corrosion with a depth of about 100  $\mu$ m was found.

In the drawn bars (HB2), the transition from IGC to shallower pitting corrosion was observed as well. Unlike the specimens from bars that had not been drawn, all the specimens in this group showed very deep corrosion (more than 500  $\mu$ m) on their transverse cut surfaces (**Figure 8**).

In the drawn and straightened bars (HF), another type of corrosion was observed. In the under-aged bars, IGC was found on both the bar surface and the transverse cut surface. With ongoing ageing, IGC changes into pitting corrosion, which – on the bar surface – propagates perpendicularly to the surface and by transgranular mechanism to a larger depth than the pitting corrosion in the drawn bars (**Figures 9b to 9d**). This corrosion type corresponds to transgranular stress corrosion cracking (SCC).<sup>14</sup> The difference can be attributed to the variation between the internal stresses induced by drawing and straightening. Drawing typically induces tensile stress. Straightening, however, involves alternating bending loads and tensile and compressive stresses, which lead to non-uniform residual stress that promotes corrosion propagation, perpendicularly to the surface and to a larger depth. The transverse cut surface, unlike HB2 specimens, shows – in some cases – shallow sporadic pitting corrosion (**Figures 10b and 10d**).

## 5 CONCLUSION

Extruded and drawn bars from the EN AW-6064A alloy were used for exploring the impact of thermomechanical treatment on intergranular corrosion (IGC). The effects of forming (drawing and straightening) and artificial ageing were mapped, along with the type of corrosion and corrosion depth on the bar surface and its transverse cross-section. The corrosion tests were carried out in accordance with EN ISO 11486 – method B.

The results of the corrosion tests show that the thermomechanical treatment affects both the type and depth of corrosion.

The bar surface exhibited three types of corrosion:

- IGC in under-aged specimens: typically extensive corrosion with a depth of more than 300  $\mu$ m.
- Pitting corrosion in more aged and over-aged extruded/drawn bars, where the corrosion depth was approximately 100  $\mu$ m.
- Transgranular pitting corrosion in more aged and over-aged bars that had undergone final straightening. Here, the corrosion depth was larger and exceeded 300  $\mu$ m.

With more intensive ageing and over-ageing (temperature, time), IGC changed into pitting corrosion in extruded/drawn bars. There was an adverse impact of the post-drawing straightening operation on the resistance to surface corrosion in the bars, evidenced by deep transgranular pitting corrosion.

In most cases the transverse cross-sections exhibited very deep pitting corrosion with depths up to 800  $\mu$ m, which followed the bands of coarse cathodic phases. Exceptions were found in severely over-aged bars (extruded or extruded and straightened), which showed sporadic pitting corrosion with depths of approximately 100  $\mu$ m.

## Acknowledgements

This paper was created by project Development of West-Bohemian Centre of Materials and Metallurgy No.: LO1412, financed by the MEYS of the Czech Republic.

## 6 REFERENCES

- <sup>1</sup> D. G. Altenpohl, Aluminum: Technology, Applications, and Environment: A Profile of a Modern Metal, 6th ed., Minerals, Metals, and Materials Society, Warrendale, Pennsylvania 1998
- <sup>2</sup> J. E. Hatch (Ed.), Aluminium – Properties and Physical Metallurgy, ASM, Ohio 1984
- <sup>3</sup> G. Svenningsen, J. E. Lein, A. Bjorgum, J. H. Nordlien, Y. D. Yu, K. Nisancioglu, Effect of low copper content and heat treatment on intergranular corrosion of model AlMgSi alloys, Corrosion Science, 48 (2006) 1, 226–242, doi:10.1016/j.corsci.2004.11.025
- <sup>4</sup> G. Svenningsen, M. H. Larsen, J. H. Nordlien, K. Nisancioglu, Effect of high temperature heat treatment on intergranular corrosion of AlMgSi(Cu) model alloy, Corrosion Science, 48 (2006) 1, 258–272, doi:10.1016/j.corsci.2004.12.003
- <sup>5</sup> G. Svenningsen, M. H. Larsen, J. C. Walmsley, J. H. Nordlien, K. Nisancioglu, Effect of artificial aging on intergranular corrosion of extruded AlMgSi alloy with small Cu content, Corrosion Science, 48 (2006) 6, 1528–1543, doi:10.1016/j.corsci.2005.05.045
- <sup>6</sup> M. H. Larsen, J. C. Walmsley, O. Lunder, R. H. Mathiesen, K. Nisancioglu, Intergranular Corrosion of Copper-Containing AA6xxx AlMgSi Aluminum, J. Electrochem. Soc., 155 (2008) 11, C550–C556, doi:10.1149/1.2976774
- <sup>7</sup> T. Kovalčík, J. Stouřil, P. Sláma, D. Vojtěch, The Influence of Heat Treatment on Mechanical and Corrosion Properties of Wrought Aluminium Alloys 2024 and 6064, Manufacturing Technology, 15 (2015) 1, 54–61
- <sup>8</sup> V. Guillaumin, G. Mankowski, Influence of Overaging Treatment on Localized Corrosion of Al 6056, Corrosion, 56 (2000), 12–23, doi:10.5006/1.3280517

- <sup>9</sup> C. Gallais, A. Denquin, Y. Brechet, G. Lapasset, Precipitation microstructures in an AA6056 aluminium alloy after friction stir welding: Characterisation and modelling, *Mater. Sci. Eng. A*, 496 (2008), 77–89, doi:10.1016/j.msea.2008.06.033
- <sup>10</sup> F. Eckermann, T. Suter, P. J. Uggowitzer, A. Afseth, P. Schmutz, Investigation of the exfoliation-like attack mechanism in relation to Al–Mg–Si alloy microstructure, *Corrosion Science*, 50 (2008) 7, 2085–2093, doi:10.1016/j.corsci.2008.04.003
- <sup>11</sup> Z. Wang, H. Li, F. Miao, W. Sun, B. Fang, R. Song, Z. Zheng, Improving the intergranular corrosion resistance of Al–Mg–Si–Cu alloys without strength loss by a two-step aging treatment, *Mater. Sci. Eng. A*, 590 (2014), 267–273, doi:10.1016/j.msea.2013.10.001
- <sup>12</sup> A. Halap, M. Popović, T. Radetić, V. Vaščić, E. Romhanji, Influence of the thermo-mechanical treatment on the exfoliation and pitting corrosion of an AA5083-type alloy, *Mater. Tehnol.*, 48 (2014) 4, 479–483
- <sup>13</sup> EN ISO 11846, Corrosion of metals and alloys, Determination of resistance to intergranular corrosion of solution heat-treatable aluminium alloys
- <sup>14</sup> ASM Handbook, Vol. 13, Corrosion, ASM, Ohio 1987

# VALORIZATION OF BRICK WASTES IN THE FABRICATION OF CONCRETE BLOCKS

## OCENA ODPADKOV IZ OPEKE PRI PROIZVODNJI BETONSKIH ZIDAKOV

**Youcef Ghernouti<sup>1</sup>, Bahia Rabehi<sup>1</sup>, Tayeb Bouziani<sup>2</sup>, Rabah Chaid<sup>1</sup>**

<sup>1</sup>University M'Hamed Bougara of Boumerdes, Research Unit of Materials, Processes and Environment, Boumerdes, Algeria

<sup>2</sup>University Amar Telidji of Laghouat, Structures Rehabilitation and Materials Laboratory (SREML), Algeria  
y\_ghernouti@yahoo.fr

*Prejem rokopisa – received: 2015-07-05; sprejem za objavo – accepted for publication: 2015-10-30*

doi:10.17222/mit.2015.202

This work focuses on the reuse of recycled brick waste (RBW) as aggregates in the fabrication of concrete blocks. The experimental study was focused on six different concrete compositions with a  $w/c$  ratio of 0.56, a relatively constant compactness and a slump value of zero. The six compositions consist on a control concrete with natural sand and five compositions with 10 %, 20 %, 30 %, 40 % and 50 % of RBW as a partial substitute for the natural sand. The physical and mechanical properties of concrete blocks were studied, analyzed and compared. The obtained results showed that it is possible to manufacture concrete blocks based on RBW, and that the compressive strengths of these concrete blocks are comparable to that of the control concrete, but with an appreciable reduction in weight. The blocks made with 30 % of RBW showed an improvement in the compressive strength of 42 % and a reduction in weight of 11 % compared to the control concretes.

Keywords: recycled brick waste, concrete block, compactness, slump, mechanical strength

Delo je usmerjeno v ponovno uporabo recikliranih odpadkov opeke (RBW) kot sestavina pri izdelavi betonskih zidakov. Eksperimentalno delo je bilo usmerjeno v šest različnih sestav betona z razmerjem  $w/c$  je 0,56, z relativno enako kompaktnostjo in brez zmanjšanja vrednosti. Šest sestav je predstavljalo kontrolni beton z naravnim peskom in pet sestav z dodatkom 10 %, 20 %, 30 %, 40 % in 50 % RBW, kot delnim nadomestkom za naravni pesek. Proučevane, analizirane in primerjane so fizikalne in mehanske lastnosti cementnih zidakov. Dobljeni rezultati so pokazali, da je mogoča izdelava cementnih zidakov na osnovi RBW. Tlačne trdnosti teh betonskih zidakov so primerljive s tistimi iz kontrolnega betona, občutno pa je zmanjšanje teže. Zidaki izdelani z 30 % RBW so pokazali izboljšanje tlačne trdnosti za 42 % in zmanjšanje teže za 11 %, v primerjavi z zidaki iz kontrolnega betona.

Ključne besede: reciklirani odpadki iz opeke, betonski zidak, kompaktnost, padec vrednosti, mehanska trdnost

## 1 INTRODUCTION

In the past decade, Algeria has been experiencing rapid development in the construction sector. Indeed, several construction projects supported by the state have been launched. The concrete block occupied an important place in this sector; this is mainly due to the simplicities related to its prefabrication and the handling facilities on site. Like any conventional concrete, concrete block consists mostly of gravel, sand, cement and water. The concrete used for the precast blocks is characterized by a rather dry state in the fresh state (needed to confer an immediate unmolding of the block) and a delicate physico-mechanical behavior in the hardened state. The difference between this type of concrete and the conventional concrete lies mainly in the low cement and water content; that is to say a high dosage of aggregate.

In the context of the judicious use of aggregates and the development of a strategy for the sustainable development policy in the building and construction sector, the use of local resources and recycled waste, such as brick waste, is required. Indeed, the introduction of recycled brick waste (RBW) in the construction industry

was the subject of several research works in recent years. Thus, the use of RBW as alternative aggregates has a particular interest as it can considerably reduce the problem of waste storage and, on the other hand, can help in the preservation of natural aggregates.<sup>1</sup>

The use of clay brick as aggregates in concrete was proposed in the 1990s.<sup>2</sup> Only a few researchers have studied the potential of using clay brick powder as a partial cement replacement to make mortar. G. Moriconi et al.<sup>3</sup> and L. Turanli et al.<sup>4</sup> found that RBW, as a pozzolanic material, had the potential to suppress expansion due to the alkali-silica reaction. The possibility of using RBW as a replacement for cement has been investigated in the study of Nacéri et al.<sup>5</sup> The authors found that the mechanical behavior (compressive and flexural strengths) at 7 d and 28 d of hardened mortar decreased with an increasing RBW content. However, at 90 d the mortars containing up to 10 % of the waste brick will reach a resistance comparable to those of mortars without RBW.

S. Wild et al.<sup>6</sup> and M. O'Farrell et al.<sup>7</sup> reported that the presence of RBW influenced the compressive strength and the pore size distribution of mortar.

**Table 1:** Chemical and mineralogical compositions of the cement**Tabela 1:** Kemijska in mineraloška sestava cementa

Chemical composition (%)							Mineralogical composition (%)					
CaO	SiO <sub>2</sub>	Al <sub>2</sub> O <sub>3</sub>	Fe <sub>2</sub> O <sub>3</sub>	MgO	SO <sub>3</sub>	LOI	Na <sub>2</sub> O	K <sub>2</sub> O	C <sub>3</sub> S	C <sub>2</sub> S	C <sub>3</sub> A	C <sub>4</sub> AF
62.2	19.4	5.4	2.8	1.7	2.5	4.6	0.35	0.76	60	21	8	11

Recently, some researchers have studied the possibility of using RBW as aggregate to make high-strength concrete.<sup>8-14</sup>

P. B. Cachim<sup>15</sup> reported that crushed bricks could be used as a partial replacement for natural coarse aggregate without a reduction in concrete properties for a 15 % replacement ratio; however, a reduction up to 20 % has been noted for a 30 % replacement ratio.

A. K. Padmini et al.<sup>16</sup> reported that for a given strength, the modulus of elasticity of concrete made with crushed brick is between one-half and two-thirds that of normal concrete. Moreover, the water absorption and sorptivity increased for the concrete containing crushed-brick aggregates. Furthermore, concrete containing coarse crushed bricks aggregate had a relatively lower strength during the early ages than normal aggregate concrete. This is due to the higher water absorption of crushed brick aggregates compared to natural aggregates.<sup>17</sup>

A. R. Khaloo<sup>18</sup> found a decrease of 7 % in the concrete's compressive strength by using crushed clinker bricks as the coarse aggregate compared to natural aggregate.

A. A. Akhtaruzzaman and A. Hasnat<sup>19</sup> found that the tensile strength of concrete containing coarse crushed brick was higher than that of normal concrete by about 11 %. T. Kibriya and P. R. S. Speare<sup>20</sup> reported that concrete containing coarse, crushed brick had comparable compressive, tensile and flexural strengths to those of normal concrete, but the modulus of elasticity was drastically reduced.

C. S. Poon and D. S. Chan<sup>21</sup> found that the incorporation of 20 % of fine crushed brick aggregate decreased the compressive strength and the modulus of elasticity of the concrete by 18 % and 13 %, respectively.

The present experimental investigation constitutes a continuation of the work and aims to expand the use of this material in the prefabrication of concrete blocks. In this work, an optimizing of concrete block mixtures, based on natural sand and different percentages of RBW, was performed. Next, the influence of RBW on the physico-mechanical properties of the produced concrete blocks was tested.

## 2 EXPERIMENTAL PART

### 2.1 Materials

The concrete block mixtures investigated in this study were prepared with Ordinary Portland Cement (OPC) CEM II/A 42.5. The mineralogical and chemical compositions of the cement are listed in **Table 1**. The

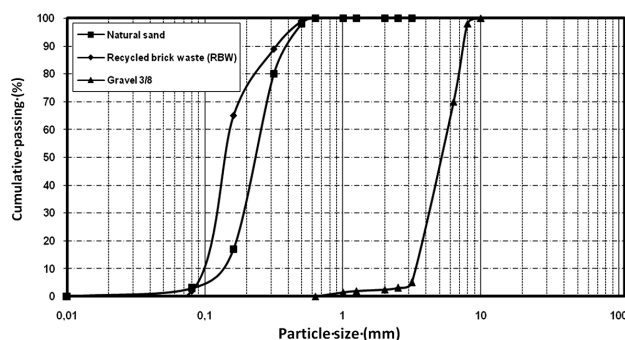
aggregates used are natural sand (NS), with a maximum particle size of 2 mm and a siliceous mineralogical nature. A crushed limestone gravel with a particle size between 3 mm and 8 mm and a recycled brick waste (RBW) aggregate resulting from crushing of the rejected bricks, composed mainly from the quartz and with a maximum particle size of 2 mm. The physical properties and granular size analysis of all the aggregates used in this work are listed and presented in **Table 2** and **Figure 1**.

**Table 2:** Physical properties of aggregates used**Tabela 2:** Fizikalne lastnosti uporabljenih sestavin

	Natural sand (NS)	Recycled brick waste (RBW)	Gravel (3/8)
Apparent density, Ad (g/cm <sup>3</sup> )	1.49	0.97	1.35
Specific gravity, SG (g/cm <sup>3</sup> )	2.59	1.21	2.64
Visual equivalent, VES (%)	72	67	/
Finesse modulus, Fm	1.05	4.7	/
Porosity (%)	26.6	34.9	33.3
Water absorption (%)	1.86	7.4	1.4

### 2.2 Formulation of concrete blocks

In the mix design of this type of concrete, the compactness criterion and maneuverability have been considered for the fresh state, since the mechanical strength of this type of concrete used in the manufacture of concrete blocks is not a very important criterion. (The mechanical strengths of the blocks are relatively low compared to traditional concrete). The first step in formulating the blocks is the optimization of the aggregates dosage (natural Sand + Gravel) by choosing the most compact mixture. Then the second step is to search the

**Figure 1:** Granular size analysis of all aggregates**Slika 1:** Analiza velikosti zrn vseh sestavin



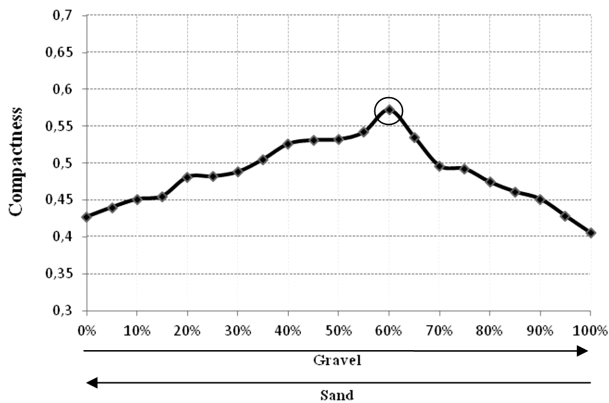


Figure 2: Compactness value depending on the percentage of sand and gravel

Slika 2: Vrednosti kompaktnosti v odvisnosti od odstotka peska in gramoza

dosage of water that verifies the criteria required for the concrete blocks (no slump and maximum compactness), while fixing the cement content (8 % to 9 % by weight of the aggregates).<sup>22</sup> The third step is to replace some natural sand in the optimized mixture by different percentages of RBW, from 10 % to 50 %, with an increment of 10 %.

2.2.1 Optimization of aggregates dosage

In our work, we started by optimizing the dosage of dry aggregates, using as criteria the maximum compactness of the mixture. We used a Modified Proctor test for determining the compactness of the mixtures (gravel and sand). Calculating the compactness is performed after a period of vibration of 30 s using a standard vibrating table. The results of the compactness of the mixture (sand + gravel) are represented in Figure 2. According to the results, the most compact mixture is that which contains 60 % gravel and 40 % sand (compactness = 0.572).

2.2.2 Optimization of water content

The second step is to find the dosage of water that verifies the criteria required for concrete blocks (no

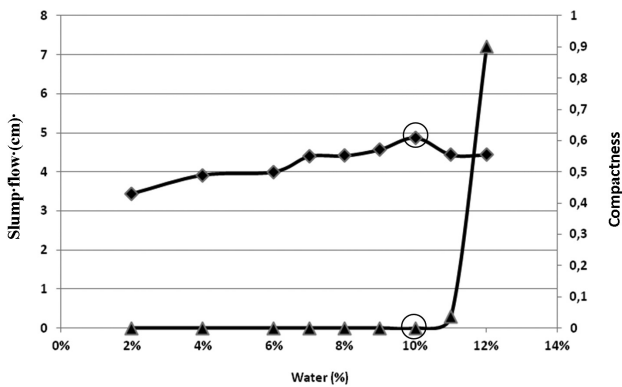


Figure 3: Compactness and slump flow values depending on the percentage of water

Slika 3: Kompaktnost in padec tekočnosti v odvisnosti od odstotka vode

Table 3: Examples of slump flow depending on the percentage (%) of water

Tabela 3: Primer zmanjšanja tekočnosti v odvisnosti od odstotka (%) vode

(%) of water	Images of slump flow test	(%) of water	Images of slump flow test
(%/w) = 2 % Slump flow = 0 mm Compactness = 0.43		(%/w) = 4 % Slump flow = 0 mm Compactness = 0.49	
(%/w) = 6 % Slump flow = 0 mm Compactness = 0.5		(%/w) = 7 % Slump flow = 0 mm Compactness = 0.55	
(%/w) = 8 % Slump flow = 0 mm Compactness = 0.55		(%/w) = 9 % Slump flow = 0 mm Compactness = 0.58	
(%/w) = 10 % Slump flow = 0 mm Compactness = 0.61		(%/w) = 12 % Slump flow = 30 mm Compactness = 0.55	

slump and maximum compactness), while fixing the cement content (8 % to 9 % of the weight of the aggregate). The water dosage ranges from 2 % to 12 % by weight of solid mixture (gravel, sand and cement). The slump is performed using the Abrams cone. In parallel the compactness of prepared fresh concrete was measured using a modified proctor mold.

The results of the measurements of the Slump flow and compactness depending on the percentage of water are shown in Figure 3. Corresponding pictures for each mixture are shown in Table 3. From the results obtained, the most compact mixture that checks a zero slump flow is the mixture containing 10 % of water.

2.2.3 Incorporation of RBW in the optimized composition

In this step, a portion of the natural sand from the optimized formulation was replaced by different percentages (10 %, 20 %, 30 %, 40 % and 50 %) of RBW aggregate.

Table 4: Formulations and dosages of the constituents in kg/m<sup>3</sup>

Tabela 4: Sestava in odmere sestavin v kg/m<sup>3</sup>







Formulation	Cement	Gravel	Water	Natural sand (NS)	Recycled brick waste (RBW)
BNS	142	875	80	564	/
BBW10				508	56
BBW20				452	113
BBW30				339	170
BBW40				508	226
BBW50				282	282

**Table 4** gives the dosages of the constituents in the mixture for the optimized formulation of the block concrete based on natural sand and block concrete based on RBW aggregate.

2.2.4 Optimization of slump flow and compactness

For each composition, the conditions for obtaining concrete blocks for a slump value of 0 are respected. The obtained results are shown in **Table 5**.

**Table 5:** Examples of slump flow for all formulations  
**Tabela 5:** Primeri zmanjšanja tekočnosti vseh sestav

Composition	Slump flow test	Composition	Slump flow test
BNS Slump flow = 0 mm Compactness = 0.52		BBW10 Slump flow = 0 mm Compactness = 0.52	
BBW20 Slump flow = 0 mm Compactness = 0.53		BBW30 Slump flow = 0 mm Compactness = 0.54	
BBW40 Slump flow = 0 mm Compactness = 0.49		BBW50 Slump flow = 0 mm Compactness = 0.42	

2.2.5 Preparation of concrete blocks

Our study was performed on hollow blocks with dimensions of (10 × 20 × 40) cm. The mixing is performed on site with a concrete mixer. The mixed concrete is then loaded into the laying machine. Excess concrete is leveled using a striking surface so that the blocks can have a rough surface. The blocks are removed from the molds immediately and thoroughly on a concrete platform (**Figure 4**). The blocks are kept on site for 24 h, and then they are transported to the laboratory and are watered every day for 28 d.

2.3 Characterization of concrete blocks

2.3.1 Dimensional variation

The tests of dimensional variation were conducted on specimens of (4× 4×16) cm with the same concrete made for the realized concrete blocks. For each formulation, four specimens were crafted. Two are left in the open air to measure the shrinkage and two are immersed in the water to measure the swelling.

2.3.2 Porosity and water absorption

The measurements of porosity and water absorption are performed according to the NF P18 554 standards, on block samples previously realized. The porosity is the amount of water absorbed using a dry sample mass. It is determined using the following Equation (1):

$$P = [(M_a - M_s) / (M_a - M_d)] \times 100 \quad (1)$$

where:

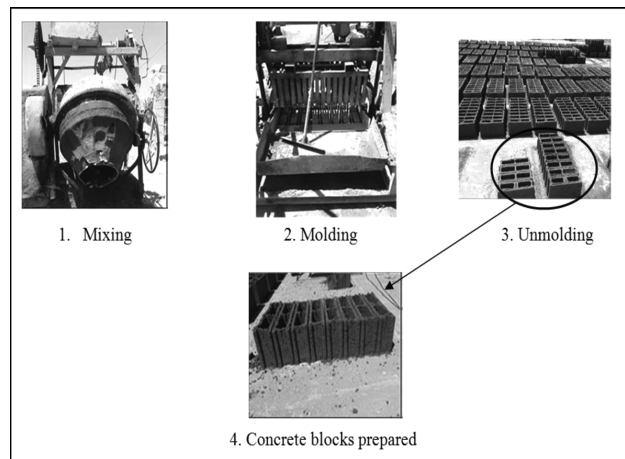


**Figure 4:** Fabrication of blocks  
**Slika 4:** Izdelava zidakov

$M_a$ : weight of sample at a dry surface.

$M_s$ : weight of the sample after drying.

$M_w$ : weight of the sample after immersion in water for 24 h.

2.3.3 Compressive strength

After surfacing of the lower and upper bearing faces of each block with sulfur, the compression test is performed by applying a continuous load without shock at a constant speed of 0.5 MPa/s. The test machine is a press for hard materials according to NFP 18-412; it is calibrated in terms of these standards (**Figure 5**). The compressive strength  $R_c$  is obtained using the following Equation (2):

$$R_c = [C / (S_b \times 10)] \times (S_a / S_n) \quad (2)$$

where:

$C$ : breaking load of the block,

$S_b$  (Gross Section): Area obtained by multiplying both dimensions, thickness and length, measured in the same horizontal section,

$S_n$  (Net Section): Area in a horizontal section concrete, empty deducted,

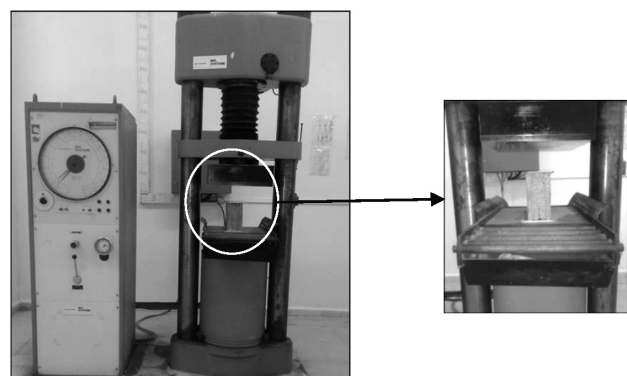


**Figure 5:** Compressive strength test  
**Slika 5:** Preizkus tlačne trdnosti

$S_a$  (Support Section): Common area of contact face and supporting face.

### 3 RESULTS AND DISCUSSION

#### 3.1 Dimensional variation of the concrete blocks

The results of shrinkage and swelling are shown in **Figure 6**. The obtained results show that for all compositions of concrete blocks, the shrinkage increases rapidly until the age of 14 d, ranges from 9.43 mm/m to 10.54 mm/m, which may result in a loss of weight due to the phenomenon of setting and hardening of concrete in the early days of hydration, subsequently a dimensional stability is recorded until 28 d. The values of the shrinkage for all compositions based on RBW are lower than the composition based on natural sand; this may be due to the improvement of compactness by the incorporation of RBW. All the specimens show a considerable swelling until the age of 14 d, ranges from 13.54 mm/m to 15.58 mm/m, due to water absorption by the concrete blocks, subsequently a dimensional stability is recorded until 28 d; this is may be due to the saturation of the pores and capillaries. The swelling of the BBW40 and BBW50 specimens was not studied because it deteriorated immediately after the immersion in water. Finally, the obtained results show that the replacement of sand by RBW until 30 % does not have a significant effect on the evolution of the shrinkage and the swelling of the concrete blocks. The maximum difference is in the order of 11 % in the case of shrinkage and 9 % in the case of swelling.

#### 3.2 Porosity and water absorption of concrete blocks

The evolution of porosity and water absorption are shown in **Figure 7**. These results show that the water absorption of all the blocks varies in the same manner as

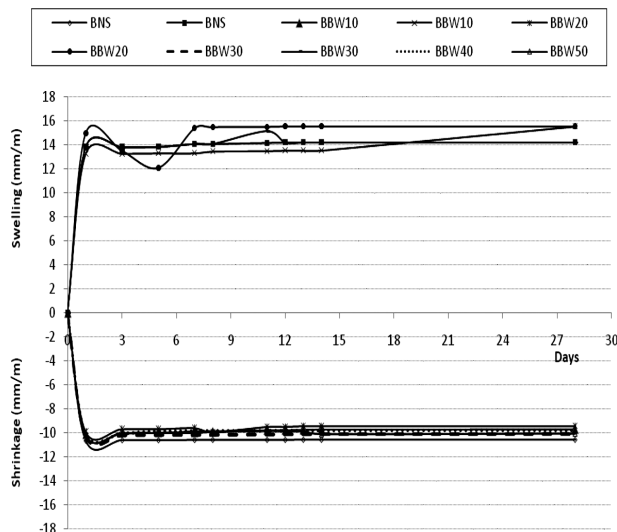


**Figure 6:** Shrinkage and swelling of concrete blocks  
**Slika 6:** Krčenje in nabrekanje betonskih zidakov

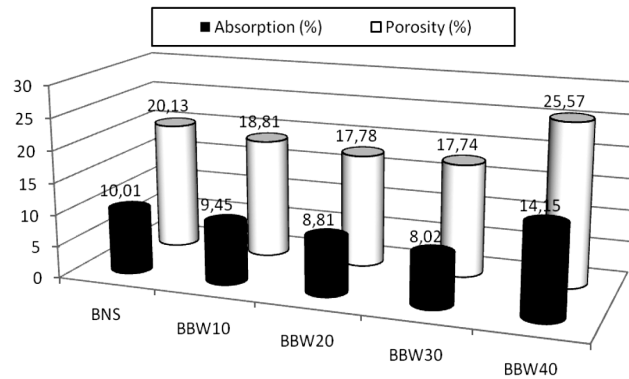


**Figure 7:** Porosity and water absorption of concrete blocks  
**Slika 7:** Poroznost in absorpcija vode v betonskih blokih

the porosity. The porosity decreases with the replacement content of sand by the RBW aggregate. However, up to a 40 % of replacement, an increase of the porosity is recorded. The decrease of the porosity and water absorption at a less than 40 % replacement of sand by RBW aggregate, can be explained by the form of the RBW aggregate (angular form), the RBW makes it possible to improve the compactness of mixture, the contact is perfect and distribution of waste brick grains, is uniform. Indeed, it fills the voids among the grains of sand. The mixtures containing less than 40 % of RBW waste aggregates having a gravel 3/8 with two sands (natural and recycled) having a size more or less identical with the presence of some fine material for the recycled aggregate, which allows for a more compact granular skeleton. The composition with 30 % RBW has a porosity of 11 % less than the composition with natural sand. The increased porosity and water absorption beyond 40 % replacement can be explained by the large amount of RBW aggregate in the mixture; it is a porous material in comparison to the natural sand, which is a less porous material.

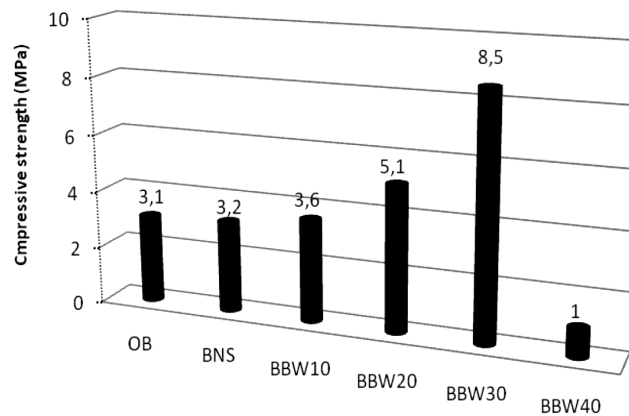


**Figure 8:** Compressive strength of concrete blocks in comparison with ordinary concrete blocks  
**Slika 8:** Tlačna trdnost cementnih zidakov v primerjavi z običajnimi cementnimi zidaki



### 3.3 Compressive strength of concrete blocks

The results of the compressive test on all the concrete blocks are shown in **Figure 8**. The blocks with RBW aggregate have a greater compressive strength than the blocks with natural sand, the concrete blocks containing 30 % of RBW have a gain of about 43 % compared to the concrete blocks with natural sand in compressive strength, which can be explained by the high compactness of this composition based on RBW, while the absorption and porosity decrease in parallel. The compressive strength of the BBW40 concrete blocks decreases; this may be due to the decrease in compactness. The compressive strengths of all the realized blocks (BNS, BBW10, BBW20 and BBW30) are better than those of the usual blocks realized in the block pre-fabrication site (ordinary concrete blocks: OCB).

## 4 CONCLUSION

This study presents the use of recycled brick waste (RBW) as sand in concrete blocks. On the basis of the obtained results, the following conclusions can be drawn:

- It is possible to use RBW as a fine aggregate for the manufacturing of concrete blocks. The shrinkage and swelling of these blocks decreases according to the increase of compactness.
- All the studied concrete blocks have the same density regardless of the replacement rate of natural sand by RBW.
- The replacement of 30 % natural sand by the RBW enabled us to achieve concrete blocks with better characteristics: a maximum compactness, an acceptable shrinkage and swelling (similar to that of concrete with natural sand), a low porosity and water absorption in comparison with other compositions, a weight reduction of 11 % and a higher compressive strength than the concrete blocks with natural sand (a gain of 43 %).

Finally, we can conclude that the RBW can be used as a fine aggregate to produce concrete blocks, which allows us to reduce the waste inventory levels in brick and limit the deficit aggregates in some areas.

## 5 REFERENCES

- <sup>1</sup> F. Debieb, S. Kenai, The use of coarse and fine crushed bricks as aggregate in concrete, *Constr. Build. Mater.*, 22 (2008) 5, 886–93, doi:10.1016/j.conbuildmat.2006.12.013
- <sup>2</sup> T. C. Hansen, *Recycling of demolished concrete masonry*, Rilem Report No. 6, E&FN Spon, London, 1992, 316
- <sup>3</sup> G. Moriconi, V. Corinaldesi, R. Antonucci, Environmentally-friendly mortars: a way to improve bond between mortar and brick, *Mater Struct*, 36 (2003) 10, 702–708, doi:10.1007/BF02479505
- <sup>4</sup> L. Turanli, F. Bektas, P. J. M. Monteiro, Use of ground clay brick as a pozzolanic material to reduce the alkali–silica reaction, *Cem. Concr. Res.*, 33 (2003) 10, 1539–1542, doi:10.1016/S0008-8846(03)00101-7
- <sup>5</sup> A. Naciri, H. M. C. Hamina, Use of waste brick as a partial replacement of cement in mortar, *Waste Management*, 29 (2009) 8, 2378–2384, doi:10.1016/j.wasman.2009.03.026
- <sup>6</sup> S. Wild, J. M. Khatib, S. D. Addis, The potential of fired brick clay as a partial cement replacement material, *International congress-concrete in the service of mankind, concrete for environment enhancement and products*, University of Dundee, Eds. Dhir and Dyer, E&FN SPON, (1996), 685–696
- <sup>7</sup> M. O'Farrell, S. Wild, B. B. Sabir, Pore size distribution and compressive strength of waste clay brick mortar, *Cem Concr Compos*, 23 (2001) 1, 81–91, doi:10.1016/S0958-9465(00)00070-6
- <sup>8</sup> B. Rabehi, Y. Ghernouti, K. Boumchedda, Strength and compressive behaviour of ultra high-performance fibre reinforced concrete (UHPC) incorporating Algerian calcined clays as pozzolanic materials and silica fume, *European Journal of Environmental and Civil Engineering*, 17 (2013) 8, 599–615, doi:10.1080/19648189.2013.802998
- <sup>9</sup> B. Safi, A. Aboutair, M. Saidi, Y. Ghernouti, C. Oubraham, Effect of the heat curing on strength development of ultra-high performance fiber reinforced concrete (UHPC) containing dune sand and ground brick waste, *J. Build. Mater. Struct.*, 1 (2014) 1, 40–46
- <sup>10</sup> M. A. Mansur, T. H. Wee, S. C. Lee, Crushed bricks as coarse aggregate for concrete, *ACI Mater. J.*, 96 (1999) 4, 478–84
- <sup>11</sup> H. L. Cheng, Study on recycled concrete made by fly-ash and waste clay-brick, *China Concr. Cem. Prod.*, (2005) 5, 48–50
- <sup>12</sup> J. M. Khatib, Properties of concrete incorporating fine recycled aggregate, *Cem. Concr. Res.*, 35 (2005) 4, 763–769, doi:10.1016/j.cemconres.2004.06.017
- <sup>13</sup> F. M. Khalaf, Using crushed clay brick as coarse aggregate in concrete, *J. Mater. Civil. Eng.*, 18 (2006) 4, 518–526, doi:10.1061/(ASCE)0899-1561(2006)18:4(518)
- <sup>14</sup> H. D. Yan, X. F. Chen, Experimental studies and analyses on properties of clay brick recycled aggregate concrete, *Tenth nation cement and concrete chemistry and application technology conference*, 2007, China
- <sup>15</sup> P. B. Cachim, Mechanical properties of brick aggregate concrete, *Constr. Build. Mater.*, 23 (2009) 3, 1292–1297, doi:10.1016/j.conbuildmat.2008.07.023
- <sup>16</sup> A. K. Padmini, K. Ramamurthy, M. S. Mathews, Relative moisture movement through recycled aggregate concrete, *Mag. Concr. Res.*, 54 (2002) 5, 77–384, doi:10.1680/macr.2002.54.5.377
- <sup>17</sup> M. Zakaria, J. G. Cabrera, Performance and durability of concrete made with demolition waste and artificial fly ash-clay aggregates, *Waste Manage*, 16 (1996) 1–3, 151–158, doi:10.1016/S0956-053X(96)00038-4
- <sup>18</sup> A. R. Khaloo, Properties of concrete using crushed clinker brick as coarse aggregate, *ACI Mater. J.*, 91 (1994) 4, 401–407
- <sup>19</sup> A. A. Akhtaruzzaman, A. Hasnat, Properties of concrete using crushed brick as aggregates, *Concr. Int.*, 5 (1983) 2, 58–63
- <sup>20</sup> T. Kibriya, P. R. S. Speare, The use of crushed brick coarse aggregate concrete, *Proceedings of international conference–concrete for environment enhancement and protection*, Scotland, University of Dundee, 1996
- <sup>21</sup> C. S. Poon, D. Chan, The use of recycled aggregate in concrete in Hong Kong, *Resour Conserv. Recycl.*, 50 (2007) 3, 293–305, doi:10.1016/j.resconrec.2006.06.005
- <sup>22</sup> T. Bouziani, A. Ferhat, M. Bederina, Optimisation des paramètres de formulation des bétons destinés à la préfabrication des blocs de béton par une approche RNA (Réseaux de Neurones Artificiels), *Revue des Sciences et Sciences de l'Ingénieur*, 2 (2011), 34–41



## POROUS MAGNESIUM ALLOYS PREPARED BY POWDER METALLURGY

### POROZNE MAGNEZIJEVE ZLITINE, IZDELANE S POMOČJO METALURGIJE PRAHOV

**Pavel Salvetr, Pavel Novák, Dalibor Vojtěch**

University of Chemistry and Technology, Department of Metals and Corrosion Engineering, Technická 5, 166 28 Prague 6, Czech Republic  
psalvetr@seznam.cz

*Prejem rokopisa – received: 2015-07-14; sprejem za objavo – accepted for publication: 2015-10-30*

doi:10.17222/mit.2015-226

This paper deals with the development of porous magnesium alloys that can be used in medicine for bone fixations and implants. The individual components of the alloys were chosen so that the biodegradability of the material is maintained. The advantage of these magnesium materials should be an ability to decompose after some time. This should reduce the number of surgeries and consequently increase the comfort of patients. All the samples were prepared using the method of powder metallurgy. The influence of particular alloying elements – aluminium, zinc, yttrium – on the structure of the alloys was explored, with changes being seen in the area of the fraction of pores, the size and the shapes of the pores, according to the alloying elements and the prolongation of the time of sintering the powders. By altering the chemical composition and the time of sintering the demanded porosity was not achieved, and that is the reason why a pore-forming agent (ammonium carbonate) was added. It was removed by thermal decomposition before the powder's sintering. By adding ammonium carbonate we managed to increase the porosity and at the same time we obtained more pores (in equivalent diameter 200–400 µm). The mechanical properties of the samples were tested in compression. In the samples without the pore-forming agent the values of the ultimate strength were larger than the values of natural bones. After adding the pore-forming agent the ultimate strength and modulus elasticity were reduced.

Keywords: magnesium alloys, powder metallurgy, porosity, biomaterial

Članek obravnava razvoj poroznih magnezijevih zlitin, ki bi lahko bile uporabne v medicini za utrjevanje kosti in vsadke. Posamezne komponente zlitin so bile izbrane tako, da je ostal material biološko razgradljiv. Prednost teh magnezijevih materialov naj bi bila zmožnost, da se s časom razgradi. To naj bi zmanjšalo število operacij in s tem povečalo ugodje pacientov. Vsi vzorci so bili pripravljani po postoku metalurgije prahov. Preiskovan je bil vpliv posameznih legirnih elementov (aluminij, cink, itrij) na mikrostrukturo zlitin. Spremembe so bile opažene pri deležu por, velikosti in obliki por glede na legirni element in podaljšanje časa sintranja prahov. S spreminjanjem kemijske sestave in časa sintranja zahtevana poroznost ni bila dosežena in to je tudi razlog, zakaj je bilo dodano sredstvo za nastajanje por (amonijev karbonat). To sredstvo je bilo odstranjeno s toplotnim razpadom pred sintranjem prahu. Z dodatkom amonijevega karbonata nam je uspelo povečati poroznost in istočasno smo dobili več por ekvivalentnega premera 200–400 µm. Mehanske lastnosti vzorcev so bile preizkušene s stiskanjem. Vzorci brez sredstva za nastajanje por so dosegli vrednosti porušne trdnosti večje od vrednosti pri naravnih kosteh. Po dodajanju sredstva za nastanek por sta se porušna trdnost in modul elastičnosti zmanjšala.

Ključne besede: magnezijeve zlitine, metalurgija prahov, poroznost, biomaterial

## 1 INTRODUCTION

Magnesium and its alloys have an import role among structural materials. They exceed other materials, especially with their low density. Magnesium is used mainly in the construction of vehicles and the aerospace industry, where it is used in mechanically less-strained components. These special applications include, for example, steering wheels, dashboards, seats and gear-boxes.<sup>1</sup> In the future, magnesium is also proposed to be a material able to store hydrogen.<sup>2</sup>

Nowadays, magnesium alloys are a subject of intensive research and development for applications in medicine as an osteosynthetic material. These materials have the ability to biodegrade, which means to decompose and be absorbed into a human body. The main advantages of these kinds of implants would be reducing the number of surgeries. The so far used biomaterials are based on bio-inert (non-reactive and corrosion-resistant

alloys). The human body may have a problem with accepting these materials. This group comprises stainless steel, titanium and cobalt alloys.<sup>3</sup> Biodegradable materials must fulfil many requirements, i.e., they must not release toxic doses of metallic ions and both the products of the corrosion reactions and the original biomaterial must not cause any allergic reaction of the organism. Therefore, the appropriate corrosion rates should be reached. The implant must not decompose too early. For example, a screw fixation of broken bones should work for 12–16 weeks, as a minimum. During this time the implant must keep its mechanical properties, which should be similar to the mechanical properties of natural bones. This requirement is met by magnesium and its alloys quite well, as you can see in **Table 1**.<sup>4,5,7–10</sup> Zinc alloys are investigated as competitive materials for biodegradable implants.<sup>6</sup>

**Table 1:** Mechanical properties of porous biomaterials**Tabela 1:** Mehanske lastnosti poroznih biomaterialov

Material	Porosity (x/%)	Pore size ( $\mu\text{m}$ )	Compressive strength (MPa)	Modulus (GPa)	Reference
Porous Mg	29–31	250–500	20–70	–	7
Porous Mg	36–55	200–400	15–31	4–18	8
Porous Mg	35–55	100–400	12–17	1–2	9
Porous Ti	78	200–500	35	5	10
Porous HA	50–77	200–400	1–17	0.1–7	8
Natural bone	–	–	2–180	0.1–20	8

Magnesium alloys mostly have better mechanical properties than pure magnesium. Corrosion resistance is increased by aluminium, zinc and rare-earth metals, but alloying elements such as iron, nickel and copper make it worse. All alloying elements in biodegradable materials must maintain the biocompatibility of the alloy. The improvement of the mechanical properties happens especially by precipitation hardening or by strengthening of a solid solution. An element that can be used is zinc, which naturally occurs in body tissue. The results of biochemical and histological investigations show that the degradation of the Mg-Zn alloy should not harm the organism.<sup>5</sup> The maximum solubility of zinc in magnesium is 6.2 % of mass fractions, and it improves the corrosion resistance and mechanical properties. The influence of aluminium on magnesium alloys is similar: it increases the strength and corrosion resistance. In a magnesium solid solution there is dissolved a maximum of 12.7 % of mass fractions of aluminium. Magnesium alloys with aluminium are heat treatable to form the  $\text{Mg}_{17}\text{Al}_{12}$  phase. Alloying with aluminium causes microporosity and according to some studies it can cause Alzheimer's disease. Other alloying elements that influence the mechanical corrosion properties in a positive way are rare-earth metals – the lanthanides, yttrium and scandium. To magnesium alloys they are usually added in relatively small amounts, where one or two elements are dominant and the rest is added only in a small amount. The rare-earth metals can be divided into a group with better solubility (Y, Gd, Tb, Dy, Ho, Er, Tm, Yb, Lu) and another group with limited solubility. Together with magnesium they create a eutectic system with limited solubility. Intermetallic phases ( $\text{Mg}_2\text{Y}$ ,  $\text{Mg}_{24}\text{Y}_5$ ) limit the movement of dislocations and increase the ultimate tensile strength.<sup>11</sup> Lanthanum and cerium could be added in a limited amount according to a biological test.<sup>12</sup> Calcium and zirconium also have a positive influence on the mechanical properties. Zirconium refines the structure, while calcium hardens the magnesium-based solid solution and forms the  $\text{Mg}_2\text{Ca}$  phase. Calcium is the main component of bones and in combination with magnesium it improves their healing.<sup>13,14</sup>

To ensure the osseointegration of the implant and the consequent substitution of the implant by the bone, the presence of pores with an average of 150–200  $\mu\text{m}$  as a minimum is important.<sup>15</sup> The porous structure can be

produced with various processes. For sample preparation by powder metallurgy a pore-forming agent (carbamide, ammonium bicarbonate) is added, which is removed by thermal decomposition.<sup>8,16</sup> With this process, pores with a random distribution and size are formed. Regular ordering of the pores is achieved by low-pressure casting of the magnesium alloy into a NaCl template.<sup>17</sup> This paper aims to prove the possibility of preparing porous magnesium alloys by sintering from elemental metallic powders with the addition of a pore-forming agent.

## 2 EXPERIMENTAL PART

All the samples were prepared by the method of powder metallurgy from Mg, Zn, and Y powders. The powders were blended manually and uniaxially pressed at a pressure of 530 MPa to form cylindrical green compacts. The samples were sintered in a tubular furnace under an argon atmosphere. The sintering temperature was chosen according to the phase diagrams of the individual alloys (MgZn5: 575 °C, MgZn10: 405 °C, MgY5: 600 °C). The duration of the sintering was 2 h. For the  $\text{MgZn}_5$  and  $\text{MgZn}_{10}$  samples, the sintering was prolonged up to 4 h or 24 h in order to observe the influence of the sintering time on the porosity and mechanical properties. The pore-forming agent  $(\text{NH}_4)_2\text{CO}_3$ , which was used in some samples, was removed before sintering by thermal decomposition. The decomposition was carried out at 230 °C for 1 h and the products of the decomposition were drained by a flow of argon. Subsequent sintering was conducted at the same temperature as for the samples without the addition of the pore-forming agent for 4 h.

To determine the porosity and to observe the microstructure, metallographic samples were prepared. The samples were mounted into methacrylate resin, ground by sandpapers P180–P4000 (abrasive elements SiC and  $\text{Al}_2\text{O}_3$ ), polished by a water-based suspension of  $\text{Al}_2\text{O}_3$  (Topol 2) or diamond paste D2. The microstructure of the samples was revealed by etching in Nital (2 mL  $\text{HNO}_3$  + 98 mL ethanol).

The microstructure was observed with an optical metallographic microscope (Olympus PME3) and documented by AxioVision image-processing software. A more detailed observation and chemical microanalysis were performed with a TESCAN VEGA 3 LMU scanning electron microscope equipped with an OXFORD Instruments INCA 350 EDS analyser.

Macrographs for the measurement of porosity were acquired with a Carl Zeiss Neophot 2 optical metallographic microscope. The porosity was evaluated with Lucia 4.8 image-analysis software as the area fraction of pores in the cross-section.

The mechanical properties of the samples were tested in compression at room temperature. The ultimate compressive strength (UCS) and modulus of elasticity E were determined from the stress-strain curves. The measure-

ments of the mechanical properties were performed using a LabTest 5.250SP1-VM universal testing machine.

### 3 RESULTS AND DISCUSSION

In the first part of the work, the alloys were prepared by sintering mixtures of the corresponding elemental powders without the addition of the pore-forming agent. The purpose of this step was to find an alloy that can be produced using this simple production route.

#### 3.1 MgZn

In the case of the Mg-Zn alloy, the influence of the sintering duration and the amount of zinc on the structure and porosity of the samples were observed. A longer duration of sintering did not cause any changes to the microstructure of the MgZn5 alloy. The effect of a longer sintering time is a decreasing number of pores with an equivalent diameter of about 30  $\mu\text{m}$  and, consequently, to a better-quality sintering of the powder. However, the decrease of the fractional area of the pores is not reached in a sample sintered for 24 h. The microstructure of the alloy MgZn5 (**Figure 1**) consists of a solid solution of Mg-Zn with a zinc content of 4 % of the mass fractions, whose grain boundaries are decorated by the intermetallic phase. This phase arises only in a thin layer and therefore its chemical composition was not determined by chemical microanalysis.

Increasing the content of zinc in the alloy up to 10 % of mass fractions (MgZn10) led to an increasing number of pores with an equivalent diameter up to 100  $\mu\text{m}$ , but the overall porosity decreased. Prolongation of the sintering duration from 2 to 4 h slightly decreased the porosity. The porosity of the alloys is written in **Table 2**. In the structure of the sample MgZn10 there are two phases: a Mg-Zn solid solution with a zinc content of 8.6 % of

mass fractions (Mg) and the phase MgZn (or Mg<sub>7</sub>Zn<sub>3</sub>) with a zinc content of approximately 45 % of mass fractions. The microstructure of the MgZn10 alloy is shown in **Figure 2**.

**Table 2:** Porosity of prepared materials

**Tabela 2:** Poroznost pripravljenih materialov

Alloy	Area fraction pores (%)
MgZn5-2h	8
MgZn5-4h	8
MgZn5-24h	10
MgZn10-2h	6
MgZn10-4h	6
MgAl5	2
MgAl3Zn1	5
MgY5	3
MgZn5+10 % of mass fractions of (NH <sub>4</sub> ) <sub>2</sub> CO <sub>3</sub>	30
MgZn5+20 % of mass fractions of (NH <sub>4</sub> ) <sub>2</sub> CO <sub>3</sub>	42
MgZn5+30 % of mass fractions of (NH <sub>4</sub> ) <sub>2</sub> CO <sub>3</sub>	48
MgAl3Zn1+20 % of mass fractions of (NH <sub>4</sub> ) <sub>2</sub> CO <sub>3</sub>	18

#### 3.2. MgAl5

The lowest porosity and pore size were determined in the alloy with 5 % of mass fractions Al. All the pores had an equivalent diameter up to 200  $\mu\text{m}$ , 94 % of them were smaller than 100  $\mu\text{m}$ . The structure is formed by the Mg-Al solid solution with an Al content of 5 % of mass fractions. At the grain boundaries, the content increases, which may be caused by the presence of a eutectic phase consisting of a Mg-based solid solution and the Mg<sub>17</sub>Al<sub>12</sub> phase. The microstructure of the alloy is shown in **Figure 3**.

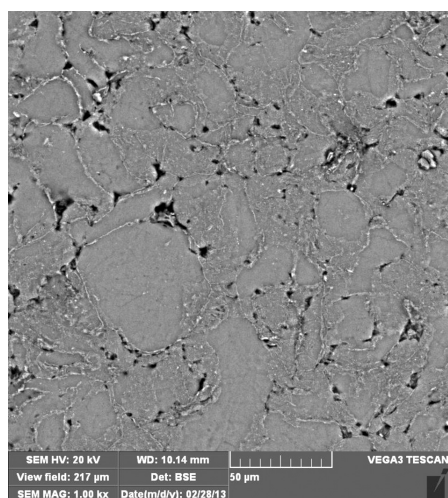


**Figure 1:** Microstructure of MgZn5 alloy  
**Slika 1:** Mikrostruktura zlitine MgZn5

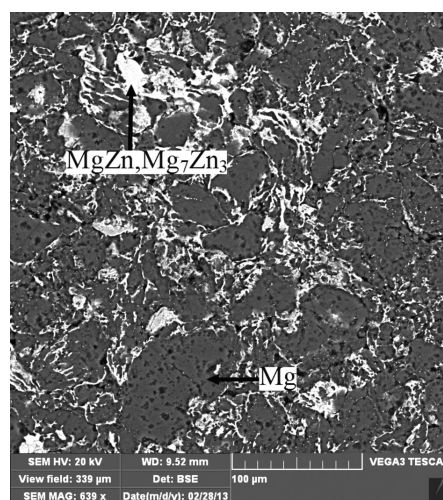


**Figure 2:** Microstructure of MgZn10 alloy  
**Slika 2:** Mikrostruktura zlitine MgZn10



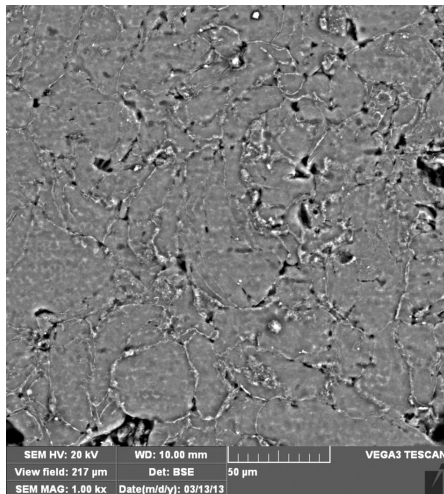


**Figure 3:** Microstructure of MgAl5 alloy  
**Slika 3:** Mikrostruktura zlitine MgAl5

### 3.3 MgAl3Zn1

In the microstructure of the MgAl3Zn1 (AZ31) alloy, there are a large number of small pores, whose amount is similar to the alloy MgZn10. The sample consists of a solid solution of alloying elements in magnesium. The microstructure of the alloy is presented in **Figure 4**, the darker parts ( $Mg^1 = 96.5\%$  of mass fractions of Mg,  $2.5\%$  of mass fractions of Al,  $1\%$  of mass fractions of Zn) have a lower content of Al, in contrast to the lighter parts ( $Mg^2 = 95\%$  of mass fractions of Mg,  $4\%$  of mass fractions of Al,  $1\%$  of mass fractions of Zn), zinc is dispersed homogeneously in the alloy.

### 3.4 MgY5

The porosity of the alloy alloyed with yttrium is  $3.1\%$ . From all the investigated samples, this alloy contains the largest amount of micropores, whose equivalent

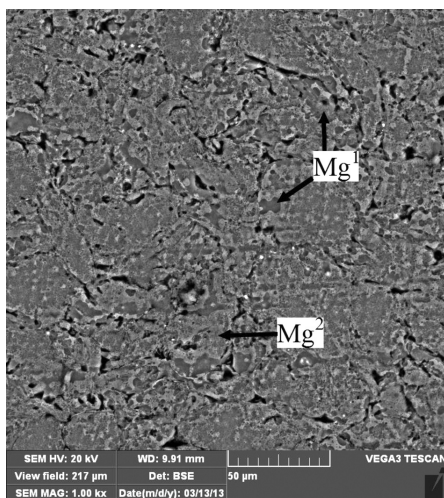


**Figure 4:** Microstructure of MgAl3Zn1 alloy  
**Slika 4:** Mikrostruktura zlitine MgAl3Zn1

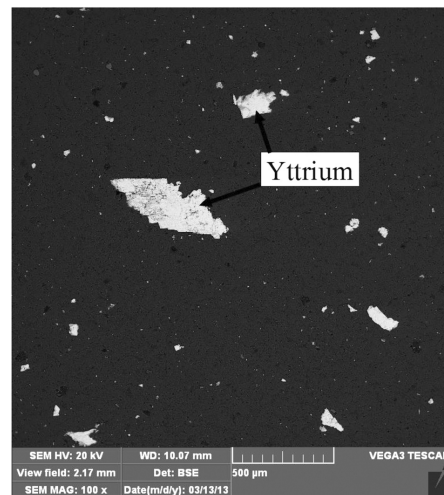


**Figure 5:** Microstructure of MgY5 alloy  
**Slika 5:** Mikrostruktura zlitine MgY5

diameter is not greater than  $10\ \mu\text{m}$ . These small pores were probably caused by the low diffusion coefficient of yttrium in magnesium. During sintering the mutual diffusion was suppressed and in the structure there were maintained the rest of the pores after pressing. In the SEM micrograph (**Figure 5**) it is obvious that particles of yttrium are not dissolved in magnesium and the solid solution is not formed.

With the addition of a pore-forming agent, the alloys MgZn5 (10, 20 and 30 % of mass fractions of ammonium carbonate) and MgAl3Zn1 (20 % of mass fractions of ammonium carbonate) were formed. With an increasing content of the pore-forming agent, the porosity of the alloy MgZn5 increased. In the structure of the alloy MgAl3Zn1+20 % mass fractions of  $(\text{NH}_4)_2\text{CO}_3$  there was a lower porosity than in the alloy MgZn5 with the same content of the pore-forming agent (**Table 2**). In **Figure 6** there are pores with the required size (equiva-

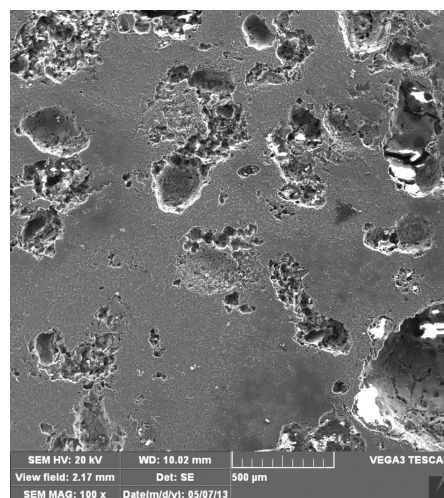


**Figure 6:** Microstructure of MgZn5 alloy with addition of 20 % of mass fractions of  $(\text{NH}_4)_2\text{CO}_3$   
**Slika 6:** Mikrostruktura zlitine MgZn5 z dodatkom 20 % masnega deleža  $(\text{NH}_4)_2\text{CO}_3$



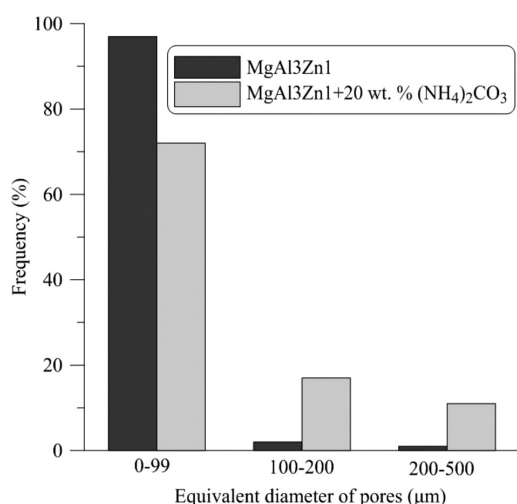


**Figure 7:** Alloy without pore-forming agent and with pore-forming agent

**Slika 7:** Zlitina brez sredstva za nastanek por in s sredstvom za nastanek por

lent diameter of more than 200–500 μm), which originated from the thermal decomposition of (NH<sub>4</sub>)<sub>2</sub>CO<sub>3</sub>. In **Figure 6** there are some cracks that may have been caused by the stress during the decomposition of the pore-forming agent.

In the samples without the pore-forming agent it was found that 85–95 % of the pores do not reach the required equivalent diameter of at least 100 μm (in the alloy MgY5, as many as 99 % of the pores). By adding the pore-forming agent the number of pores greater than 100 μm increased. In **Figure 7**, the influence of the pore-forming agent on the size of the pores in the alloy MgAl3Zn1 is presented. The most circular pores (69 %) are contained in the structure of the MgAl3Zn1 alloy. In

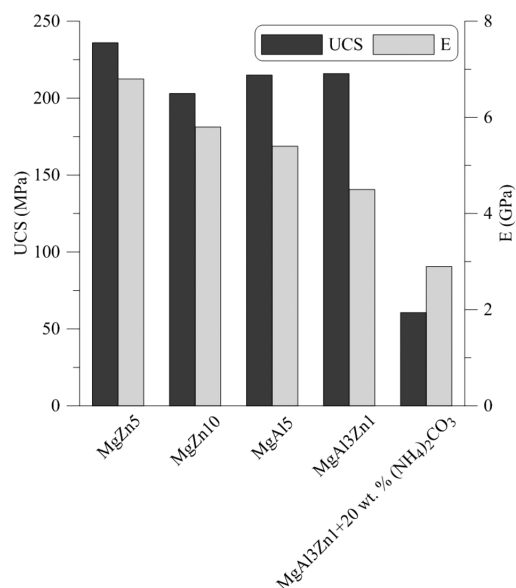


**Figure 8:** Compressive strength and modulus of elasticity of prepared samples

**Figure 8:** Tlačna trdnost in modul elastičnosti pripravljenih vzorcev

the other alloys the amount of circular pores is 45–60 %. Adding the pore-forming agent into the alloy MgAl3Zn1 decreased the quotient of the circular pores to 35 %.

The ultimate compressive strengths of the alloys are higher in comparison with the properties of natural bone (**Table 1**). The ultimate compressive strength is between 203 MPa and 236 MPa. The modulus of elasticity is comparable with natural bone. A slightly lower modulus of elasticity was found in the case of the MgAl3Zn1 alloy, in contrast with the other alloys. Increased porosity and the presence of large pores cause a significant decrease in the mechanical properties. The results of the compression test (UCS, E) are shown in **Figure 8**.

## 4 CONCLUSION

Magnesium alloys prepared by powder metallurgy without a pore-forming agent have an adequate modulus of elasticity and a higher ultimate compressive strength than natural bones. In the microstructure of magnesium alloys alloyed with zinc and aluminium, the solid solution dominates. An exception is the microstructure of the alloy MgY5, where the particles of yttrium did not dissolve in magnesium. The porosity of the samples without the pore-forming agent is up to 10 % of the volume fractions. Approximately 90 % of pores have an equivalent diameter of less than 100 μm. The addition of the pore-forming agent – (NH<sub>4</sub>)<sub>2</sub>CO<sub>3</sub> – to the alloys MgZn5 and MgAl3Zn1, increases the quantity of pores with an equivalent diameter of 200 μm and an area fraction of pores to 18–48 % of the volume fractions. The ultimate compressive strength reached 203–236 MPa. With an increasing porosity after adding the (NH<sub>4</sub>)<sub>2</sub>CO<sub>3</sub> it decreases to 61 MPa.

## Acknowledgement

This research was financially supported by Czech Science Foundation, project No. P108/12/G043.

## 5 REFERENCES

- B. L. Mordike, T. Ebert, Magnesium: Properties – applications – potential, *Materials Science and Engineering A*, 302 (2001) 1, 37–45, doi:10.1016/S0921-5093(00)01351-4
- D. Vojtěch, V. Knotek, Magnesium alloys for hydrogen storage, *Mater. Tehnol.*, 46 (2012) 3, 247–250
- G. Klačnik, M. Zdovc, U. Kovšca, B. Praček, J. Kovač, J. Rozman, Osseointegration and rejection of a titanium screw, *Mater. Tehnol.*, 44 (2010) 5, 261–264
- D. Vojtěch, V. Knotek, J. Čapek, J. Kubásek, Hořčík - kov pro medicínu i pro skladování vodíku, *Chemické listy*, 105 (2011) 9, 678–683
- N. Li, Y. Zheng, Novel Magnesium Alloys Developed for Biomedical Application: A Review, *Journal of Materials Science & Technology*, 29 (2013) 6, 489–502, doi:10.1016/j.jmst.2013.02.005
- J. Kubásek, I. Pospíšilová, D. Vojtěch, E. Jablonská, T. Ruml, Structural, mechanical and cytotoxicity characterization of as-cast biodegradable Zn-xMg (x = 0.8–8.3 %) alloys, *Mater. Tehnol.*, 48 (2014) 5, 623–629

- <sup>7</sup> J. Čapek, D. Vojtěch, Effect of sintering conditions on the microstructural and mechanical characteristics of porous magnesium materials prepared by powder metallurgy, *Materials Science and Engineering C*, 35 (2014), 21–28, doi:10.1016/j.msec.2013.10.014
- <sup>8</sup> H. Zhuang, Y. Han, A. Feng, Preparation, mechanical properties and in vitro biodegradation of porous magnesium scaffolds, *Materials Science and Engineering C*, 28 (2008) 8, 1462–1466, doi:10.1016/j.msec.2008.04.001
- <sup>9</sup> C. E. Wen, Y. Yamada, K. Shimojima, Y. Chino, H. Hosokawa, M. Mabuchi, Compressibility of porous magnesium foam: dependency on porosity and pore size, *Materials Letters*, 58 (2004) 3–4, 357–360, doi:10.1016/S0167-577X(03)00500-7
- <sup>10</sup> C. E. Wen, M. Mabuchi, Y. Yamada, K. Shimojima, Y. Chino, T. Asahina, Processing of biocompatible porous Ti and Mg, *Scripta Materialia*, 45 (2001) 10, 1147–1153, doi:10.1016/S1359-6462(01)01132-0
- <sup>11</sup> M. Socjusz-Podosek, L. Lityńska, Effect of yttrium on structure and mechanical properties of Mg alloys, *Materials Chemistry and Physics*, 80 (2003) 2, 472–475, doi:10.1016/S0254-0584(02)00549-7
- <sup>12</sup> F. Feyerabend, J. Fischer, J. Holtz, F. Witte, R. Willumeit, H. Drücker, C. Vogt, N. Hort, Evaluation of short-term effects of rare earth and other elements used in magnesium alloys on primary cells and cell lines, *Acta Biomaterialia*, 6 (2010) 5, 1834–1842, doi:10.1016/j.actbio.2009.09.024
- <sup>13</sup> K. U. Kainer, P. Bala Srinivasan, C. Blawert, W. Dietzel, 3.09 - Corrosion of Magnesium and its Alloys, In *Shreir's Corrosion*, Elsevier, Oxford 2010, 2011–2041, doi:10.1016/B978-044452787-5.00096-2
- <sup>14</sup> F. Witte, N. Hort, C. Vogt, S. Cohen, K. U. Kainer, R. Willumeit, F. Feyerabend, Degradable biomaterials based on magnesium corrosion, *Current Opinion in Solid State and Materials Science*, 12 (2008) 5–6, 63–72, doi:10.1016/j.cossms.2009.04.001
- <sup>15</sup> V. Karageorgiou, D. Kaplan, Porosity of 3D biomaterial scaffolds and osteogenesis, *Biomaterials*, 26 (2005) 27, 5474–5491, doi:10.1016/j.biomaterials.2005.02.002
- <sup>16</sup> J. Čapek, D. Vojtěch, Properties of porous magnesium prepared by powder metallurgy, *Materials Science and Engineering C*, 33 (2013) 1, 564–569, doi:10.1016/j.msec.2012.10.002
- <sup>17</sup> N. T. Kirkland, I. Kolbeinsson, T. Woodfield, G. J. Dias, M. P. Staiger, Synthesis and properties of topologically ordered porous magnesium, *Materials Science and Engineering B*, 176 (2011) 20, 1666–1672, doi:10.1016/j.mseb.2011.04.006

# INFLUENCE OF NANO-SIZED COBALT OXIDE ADDITIONS ON THE STRUCTURAL AND ELECTRICAL PROPERTIES OF NICKEL-MANGANITE-BASED NTC THERMISTORS

## VPLIV DODATKA NANODELCEV KOBALTOVEGA OKSIDA NA ZGRADBO IN ELEKTRIČNE LASTNOSTI NTC TERMISTORJEV NA OSNOVI NIKLJEVEGA MANGANITA

Gökhan Hardal, Berat Yüksel Price

Istanbul University, Engineering Faculty, Metallurgical and Materials Engineering Department, Avcılar, Istanbul, Turkey  
berat@istanbul.edu.tr

Prejem rokopisa – received: 2015-07-15; sprejem za objavo – accepted for publication: 2015-12-15

doi:10.17222/mit.2015.228

The structural and electrical properties of  $\text{NiMn}_2\text{O}_4$  and  $\text{Ni}_{0.5}\text{Co}_x\text{Mn}_{2.5-x}\text{O}_4$  (where  $x = 0.5, 0.8$  and  $1.1$ ) NTC thermistors have been investigated. The samples, prepared by conventional ceramic processing techniques, were calcinated at  $900^\circ\text{C}$  for 2 h and then sintered at  $1100^\circ\text{C}$  and  $1200^\circ\text{C}$  for 5 h. The cubic spinel phase was observed by XRD analysis in the  $\text{NiMn}_2\text{O}_4$  and  $\text{Ni}_{0.5}\text{Co}_{0.8}\text{Mn}_{1.7}\text{O}_4$  samples sintered at  $1100^\circ\text{C}$  for 5 h. The sintering at  $1200^\circ\text{C}$  resulted in much denser microstructures with a larger grain size. The room-temperature electrical resistivity ( $\rho_{25}$ ) and material constant ( $B$ ) value of the  $\text{NiMn}_2\text{O}_4$  sample sintered at  $1100^\circ\text{C}$  were  $7710\ \Omega\ \text{cm}$  and  $3930\ \text{K}$ , respectively. The electrical resistivity of the samples decreased significantly with the addition of  $\text{Co}_3\text{O}_4$ . The  $B_{25/85}$  values of the  $\text{Ni}_{0.5}\text{Co}_x\text{Mn}_{2.5-x}\text{O}_4$  (where  $x = 0.5, 0.8$  and  $1.1$ ) samples sintered at  $1100^\circ\text{C}$  were found to be  $3820\ \text{K}$ ,  $3525\ \text{K}$  and  $3270\ \text{K}$ , respectively.

Keywords: cobalt oxide, electrical properties, microstructure, NTC thermistor

Preiskovana je bila zgradba in električne lastnosti  $\text{NiMn}_2\text{O}_4$  in  $\text{Ni}_{0.5}\text{Co}_x\text{Mn}_{2.5-x}\text{O}_4$  (kjer je  $x = 0.5, 0.8$  in  $1.1$ ) NTC termistorjev. Vzorci, pripravljani po običajni tehniki priprave keramike, so bil kalcinirani 2 h na  $900^\circ\text{C}$  in potem 5 h sintrani na  $1100^\circ\text{C}$  in  $1200^\circ\text{C}$ . Kubična spinelna faza je bila opažena pri XRD-analizi, v vzorcih  $\text{NiMn}_2\text{O}_4$  in  $\text{Ni}_{0.5}\text{Co}_{0.8}\text{Mn}_{1.7}\text{O}_4$ , sintranih 5 h na  $1100^\circ\text{C}$ . Sintranje na  $1200^\circ\text{C}$  je povzročilo mnogo bolj gosto mikrostrukturo z večjimi zrni. Vrednosti za električno upornost pri sobni temperaturi ( $\rho_{25}$ ) in materialne konstante ( $B$ ) vzorca  $\text{NiMn}_2\text{O}_4$ , sintrane na  $1100^\circ\text{C}$ , sta bili  $7710\ \Omega\ \text{cm}$  in  $3930\ \text{K}$ . Električna upornost vzorcev se je občutno zmanjšala po dodatku  $\text{Co}_3\text{O}_4$ . Vrednosti  $B_{25/85}$  pri vzorcih  $\text{Ni}_{0.5}\text{Co}_x\text{Mn}_{2.5-x}\text{O}_4$  (kjer je bil  $x = 0.5, 0.8$  in  $1.1$ ) sintranih na  $1100^\circ\text{C}$  so bile:  $3820\ \text{K}$ ,  $3525\ \text{K}$  in  $3270\ \text{K}$ .

Ključne besede: kobaltov oksid, električne lastnosti, mikrostruktura, NTC termistor

## 1 INTRODUCTION

Sensors for monitoring and controlling temperature are very important, not only in our daily life but also in many industrial and laboratory applications such as aerospace and automotive industries, circuit compensation, cryogenic systems etc.<sup>1,2</sup> NTC thermistors are useful for precision temperature measurements as their resistance decreases with increasing temperature.<sup>3</sup> The most extensively used negative temperature coefficient (NTC) thermistor materials are nickel-manganite-based semiconducting materials which exhibit the spinel-type crystal structure with the general formula  $\text{AB}_2\text{O}_4$ .<sup>4</sup> In the spinel structure, there are two sites available for the cations, i.e., the tetrahedral site, A-site, and the octahedral site, B-site. The distribution of the ions over the sites is as follows:  $\text{Mn}^{3+}$  will predominantly occupy the B-site, while  $\text{Mn}^{2+}$  will be placed on the A-site and the majority  $\text{Ni}^{2+}$  will go to the B-site.<sup>5</sup> The electrical resistivity,  $\rho$ , of NTC thermistors varies exponentially with temperature,  $T$ , by the well-known Arrhenius equation  $\rho = \rho_0 \exp(B/T)$ , where  $\rho_0$  is the resistivity of the material at infinite

temperature and  $B$  is a constant, which is a measure of the sensitivity of the materials over a given temperature.<sup>6</sup> The material constant  $B$ , can be calculated using Equation (1):

$$B_{T_1} = \frac{\ln \rho_1 - \ln \rho_2}{\frac{1}{T_1} - \frac{1}{T_2}} \quad (1)$$

where  $\rho_1$  and  $\rho_2$  are the electrical resistivity at temperatures  $T_1$  and  $T_2$ , respectively. The activation energy  $E_a$  can also be found by the equation  $B = E_a/k_B$ , where  $k_B$  is the Boltzmann constant.<sup>7</sup>

The electrical properties of nickel-manganite-based NTC thermistors closely depend on the ratio of the compositions (type and amount of additives), initial particle size of raw materials and processing conditions (selected synthesis method, calcination and sintering temperature, sintering time etc.). Attainment of high-density, controlled-grain-size microstructures and appropriate dimensional designs are important factors in good sensor design.<sup>8</sup> Previous studies have been focused on the effect

of composition ratios and different production routes on the electrical properties of various metal-oxide-doped NTC thermistors. In this study, nano-sized cobalt-oxide-added, nickel-manganite-based NTC thermistors were fabricated by the solid-state reaction method, the effect of dopant concentration and sintering temperature on the structural and electrical properties of NTC materials were investigated.

## 2 EXPERIMENTAL PART

The particle size of  $\text{Co}_3\text{O}_4$  powder was less than 50 nm, purchased from Sigma-Aldrich.  $\text{NiO}$  (99 % purity, Alfa Aesar),  $\text{Co}_3\text{O}_4$  (99.5 % purity, Sigma-Aldrich) and  $\text{Mn}_2\text{O}_3$  (99 % purity, Sigma-Aldrich) powders were weighed according to the compositions of  $\text{NiMn}_2\text{O}_4$  and  $\text{Ni}_{0.5}\text{Co}_x\text{Mn}_{2.5-x}\text{O}_4$  (where  $x=0.5, 0.8$  and  $1.1$ ). The molar ratios of these compositions are given in **Table 1**. The raw powder mixture was ball-milled using  $\text{ZrO}_2$  balls as a grinding media with ethyl alcohol in a jar for 5 h. The obtained slurries were dried and powders were calcinated at  $900^\circ\text{C}$  for 2 h. The powders were pressed to form disc-shaped specimens and then sintered at  $1100$  and  $1200^\circ\text{C}$  for 5 h employing a  $360^\circ\text{C/h}$  heating rate in the air and then cooled naturally in the furnace. The bulk density ( $\rho$ ,  $\text{g cm}^{-3}$ ) of the sintered samples was calculated from their weights and dimensions. The phases in the sintered samples were determined by X-ray diffraction (XRD, Rigaku D/Max-2200/PC) analysis using  $\text{Cu-K}\alpha$  radiation at  $60\text{ kV}/2\text{ kW}$ .

**Table 1:** Molar ratio of Ni, Mn and Co in all compositions

**Tabela 1:** Molarno razmerje Ni, Mn in Co v vseh spojinah

Composition code	Ni (moles)	Mn (moles)	Co (moles)
A1	1	2	-
A2	0.5	2	0.5
A6	0.5	1.7	0.8
A10	0.5	1.4	1.1

In order to calculate the lattice parameter of the samples Equation (2) was applied:

$$a = d\sqrt{h^2 + k^2 + l^2} \quad (2)$$

where  $h$ ,  $k$  and  $l$  are the miller indices,  $a$  (nm) is the lattice parameter of cubic structure,  $d$  is the interplanar spacing of the peaks corresponding to (311).

The volume of the unit cell ( $V$ ,  $\text{nm}^3$ ) for the cubic system is obtained from Equation (3):

$$V = a^3 \quad (3)$$

The average values of the crystallite size ( $D$ , nm) of the samples were calculated by means of X-ray line broadening method, using the Debye Scherrer formula:

$$D = \frac{0.9\lambda}{\beta \cos \theta} \quad (4)$$

where 0.9 is a constant related to crystallite shape,  $\lambda$  is the X-ray radiation wavelength in nanometres (nm),  $\beta$  is the full width at half-maximum (FWHM) of the peaks corresponding to (311) and  $\theta$  is Bragg's angle.<sup>9</sup> The value of  $\beta$  from the  $2\theta$  axis of the diffraction profile must be in radians.<sup>10</sup> The microstructure of the samples was observed using scanning electron microscopy (SEM, JEOL, JSM 5600) on fracture surfaces. The sintered samples were coated with silver paste to form electrodes. The electrical resistance was measured in a temperature programmable furnace between  $25^\circ\text{C}$  and  $85^\circ\text{C}$  in steps of  $0.1^\circ\text{C}$ . The material constant,  $B$ , the activation energy,  $E_a$ , and the sensitivity coefficient,  $\alpha$ , values were calculated for the NTC thermistors.

## 3 RESULTS

The XRD patterns of the  $\text{NiMn}_2\text{O}_4$  and  $\text{Ni}_{0.5}\text{Co}_{0.8}\text{Mn}_{1.7}\text{O}_4$  samples sintered at  $1100^\circ\text{C}$  for 5 h are given in **Figure 1**. The calculated lattice parameter, unit-cell volume,  $\beta$ , peak position corresponding to (311) and crystallite size of the samples are given in **Table 2**. The XRD analysis of these samples demonstrated only the cubic spinel phase (PDF No: 71-0852). A comparison of the XRD patterns of the sintered samples and the data is given in **Table 2**, the diffraction peaks of the  $\text{Ni}_{0.5}\text{Co}_{0.8}\text{Mn}_{1.7}\text{O}_4$  sample shifted to higher  $2\theta$  angles, and

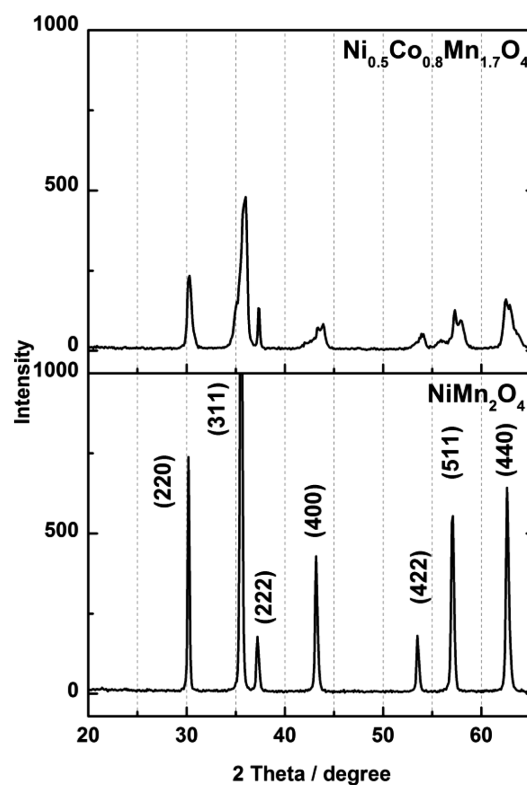


**Figure 1:** XRD patterns of  $\text{NiMn}_2\text{O}_4$  (A1) and  $\text{Ni}_{0.5}\text{Co}_{0.8}\text{Mn}_{1.7}\text{O}_4$  (A6) samples in the  $2\theta$  range  $20$ – $65^\circ$

**Slika 1:** Rentgenogram vzorcev  $\text{NiMn}_2\text{O}_4$  (A1) in  $\text{Ni}_{0.5}\text{Co}_{0.8}\text{Mn}_{1.7}\text{O}_4$  (A6) v področju  $2\theta$  med  $20^\circ$  in  $65^\circ$



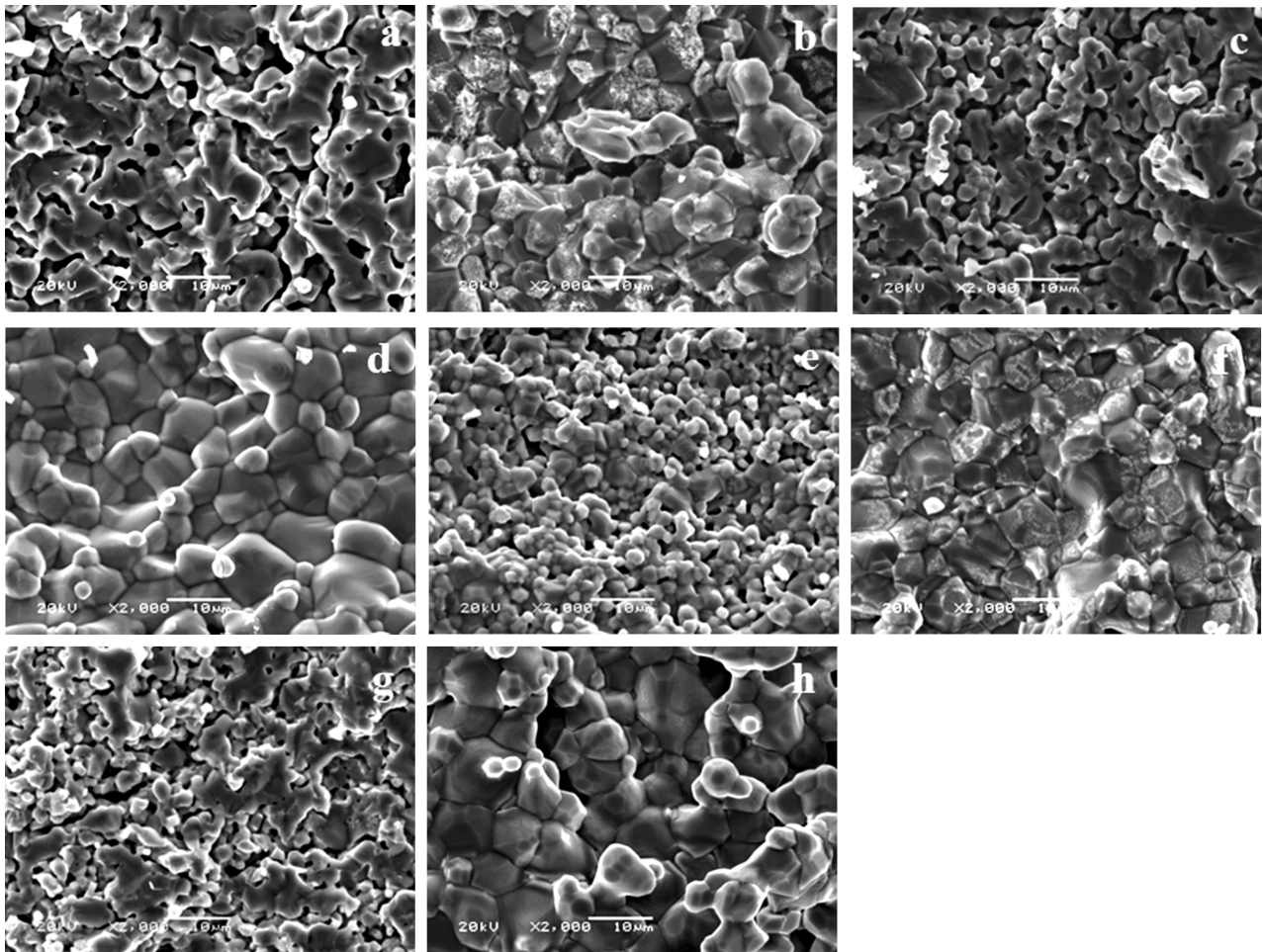


**Figure 2:** SEM micrographs of sintered samples: A1 a) 1100 °C, b) 1200 °C, A2 c) 1100 °C, d) 1200 °C, A6 e) 1100 °C, f) 1200 °C, A10 g) 1100 °C, h) 1200 °C

**Slika 2:** SEM-posnetki sintranih vzorcev: A1 a) 1100 °C, b) 1200 °C, A2 c) 1100 °C, d) 1200 °C, A6 e) 1100 °C, f) 1200 °C, A10 g) 1100 °C, h) 1200 °C

as a result the lattice parameters and the unit-cell volume decreased. The value of  $\beta$  increased to  $0.7692^\circ$  and the value of average crystallite size decreased to 10.86 nm.

**Table 2:** The lattice parameter, unit-cell volume,  $\beta$ , peak position and crystallite size of samples sintered at 1100 °C

**Tabela 2:** Parameter mreže, prostornina enotne celice,  $\beta$ , položaj vrhov in velikost kristalnih zrn vzorcev sintranih na 1100 °C

Composition	$a$ (L)	$V$ (L <sup>3</sup> )	$\beta$ (311) (°)	$2\theta$ (311) (°)	$D$ (nm)
NiMn <sub>2</sub> O <sub>4</sub> (A1)	0.8365	0.585	0.2538	35.6	32.87
Ni <sub>0.5</sub> Co <sub>0.8</sub> Mn <sub>1.7</sub> O <sub>4</sub> (A6)	0.8273	0.566	0.7692	36	10.86

The bulk densities of the sintered NiMn<sub>2</sub>O<sub>4</sub> and Ni<sub>0.5</sub>Co<sub>x</sub>Mn<sub>2.5-x</sub>O<sub>4</sub> samples are shown in **Table 3**. The bulk density of the A1 sample sintered at 1100 °C was found to be 4.23 g cm<sup>-3</sup> and it increased to 4.78 g cm<sup>-3</sup> when the sample was sintered at 1200 °C. The bulk density of the samples decreased first and then increased with the addition of Co<sub>3</sub>O<sub>4</sub>.

**Table 3:** The bulk density of samples sintered at 1100 °C and 1200 °C for 5 h

**Tabela 3:** Gostota osnove po 5 urnem sintranju na 1100 °C in 1200 °C

Composition code	$\rho$ (g cm <sup>-3</sup> )	
	1100 °C	1200 °C
A1	4.23	4.78
A2	4.05	4.43
A6	4.27	4.63
A10	4.30	4.72

The SEM micrographs of the A1, A2, A6, A10 samples sintered at 1100 and 1200 °C for 5 h are given in **Figure 2**. It can be seen in this figure that all the samples sintered at 1100 °C had a fine-grained microstructure with most of the pores at the grain boundaries. The grain size of A1 was larger relative to the A2, A6 and A10 samples sintered at 1100 °C. When the sintering temperature was increased to 1200 °C, all the samples had a much denser microstructure and larger grains with a number of small grains on their surface. In addition,

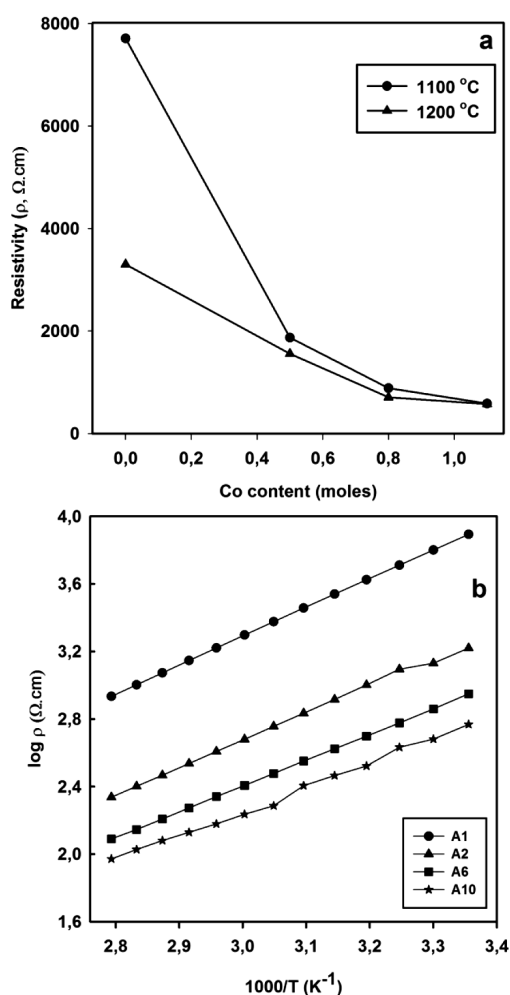


**Figure 3:** a) The change of resistivity as a function of cobalt content, b) the relationship between  $\log \rho$  and  $1000/T$  ( $\text{K}^{-1}$ ) for A1, A2, A6 and A10 samples

**Slika 3:** a) Sprememba upornosti v odvisnosti od vsebnosti kobalta, b) odvisnost med  $\log \rho$  in  $1000/T$  ( $\text{K}^{-1}$ ) pri vzorcih A1, A2, A6 in A10

the A10 sample had much bigger grains in comparison with the A2 and A6 samples sintered at 1200 °C.

The plot of resistivity versus Co content (moles) and the plots of  $\log \rho$  versus  $1000/T$  are given in **Figures 3a** and **3b** for all the sintered samples. The plots of  $\log \rho$  versus  $1000/T$  exhibited a linear dependence in the range 25–85 °C, indicating semiconducting NTC thermistor characteristics. The activation energy, the sensitivity coefficient and the material constant can also be calculated from this plot. The room-temperature electrical resistances,  $R_{25}$ , of the A1, A2, A6 and A10 samples sintered at 1100 °C were 1487, 360, 167 and 107  $\Omega$ , respectively. For the same sintering temperature, the room temperature electrical resistivity of the A1, A2, A6 and A10 samples were calculated as 7710, 1870, 890 and 590  $\Omega \cdot \text{cm}$ , respectively.

The relationship between the  $B_{25/85}$  constant of the samples and the increase in  $\text{Co}_3\text{O}_4$  content is given in **Figure 4**. The activation energy and sensitivity coefficient value of the samples is given in **Table 4**. With in-

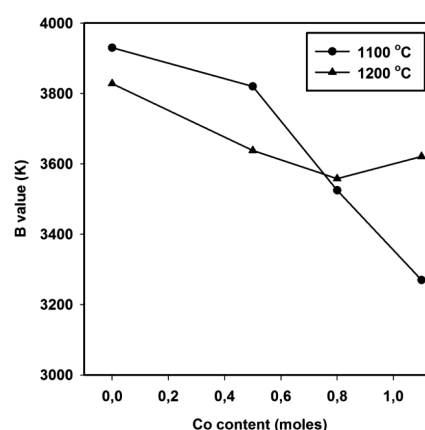


**Figure 4:** Effect of cobalt content on  $B_{25/85}$  value of A1, A2, A6 and A10 samples sintered at 1100 and 1200 °C

**Slika 4:** Vpliv vsebnosti kobalta na vrednost  $B_{25/85}$  vzorcev A1, A2, A6 in A10, sintranih na 1100 °C in na 1200 °C

creasing Co content, the  $B_{25/85}$  constant and activation energy of the samples sintered at 1100 °C decreased from 3930 K to 3270 K and from 0.338 to 0.282 eV, respectively. A similar tendency was also seen in the A1, A2 and A6 samples sintered at 1200 °C. For the A10 sample, the  $B_{25/85}$  constant and activation energy values were found to be 3620 K and 0.312 eV, respectively. The sensitivity coefficient value of all samples sintered at 1100 °C decreased from -4.426 to -3.683 %/K. When the sintering temperature increased to 1200 °C, the sensitivity coefficient value of all samples decreased from -4.311 to -4.078 %/K.

**Table 4:** The activation energy and sensitivity coefficient of A1, A2, A6 and A10 samples sintered at 1100 °C and 1200 °C for 5 h

**Tabela 4:** Aktivacijska energija in koeficient občutljivosti A1, A2, A6 in A10 vzorcev, sintranih 5 ur na 1100 °C in 1200 °C

Composition code	$E_a$ (eV)		$\alpha_{25}$ (%/K)	
	1100 °C	1200 °C	1100 °C	1200 °C
A1	0.338	0.330	-4.426	-4.311
A2	0.329	0.313	-4.301	-4.097
A6	0.303	0.306	-3.970	-4.007
A10	0.282	0.312	-3.683	-4.078

## 4 DISCUSSION

The cubic spinel phase was found by XRD analysis in  $\text{NiMn}_2\text{O}_4$  and  $\text{Ni}_{0.5}\text{Co}_{0.8}\text{Mn}_{1.7}\text{O}_4$  samples sintered at 1100 °C for 5 h. No secondary phase was found in these samples. As it is well known from the binary phase diagram of Mn-Ni-O, the spinel phase can only form when the ratio of Ni/(Ni+Mn) is less than 0.35 at a calcination temperature of 900 °C.<sup>11</sup> The diffraction peaks of  $\text{Ni}_{0.5}\text{Co}_{0.8}\text{Mn}_{1.7}\text{O}_4$  samples shift to the higher  $2\theta$  angles, indicating a decrease in the lattice parameter with the addition of  $\text{Co}_3\text{O}_4$  due to the differences between the ionic radii of the Mn and Co ions. Wu et al.<sup>12</sup> reported that the peak shift toward higher  $2\theta$  angles with the increasing of Co content indicates lattice constriction when

Co substitutes Mn. It was also reported that the decrease in the lattice parameter with the addition of Co should be attributed to the fact that the ionic radius of  $\text{Co}^{2+}$  (0.072 nm) is smaller than that of  $\text{Mn}^{2+}$  (0.080 nm) for occupying the tetrahedral sites and/or  $\text{Co}^{3+}$  (0.068 nm) is smaller than  $\text{Mn}^{3+}$  (0.072 nm) for occupying the octahedral sites.<sup>12,13</sup> As can be seen in Figure 1, we observed a significant broadening and a decrease of the diffraction peak intensities in the XRD pattern of the  $\text{Ni}_{0.5}\text{Co}_{0.8}\text{Mn}_{1.7}\text{O}_4$  sample. This could be attributed to a decrease in the average crystallite size as given in Table 2 due to the nano-size of the  $\text{Co}_3\text{O}_4$  starting powder. Savic et al. reported that the increase in the diffraction peak width and the decrease in the peak intensities in the XRD patterns are associated with a decreasing of the crystallite size and an increasing of the strain.<sup>14</sup>

Since the desired NTC thermistor properties strongly depend on the densification and grain size, we also investigated the microstructure properties of these samples. The bulk density and grain size of the A1, A2, A6 and A10 samples sintered at 1100 °C were less than the samples sintered at 1200 °C. Smaller grains result in a large number of grain boundaries, which act as scattering centres for the flow of electrons and therefore higher electrical resistivity values were obtained when the samples were sintered at 1100 °C.<sup>15</sup> As expected, the increasing of the sintering temperature gave rise to an increase in the bulk density and the grain size of these samples, thus the room-temperature resistivity of the samples decreased. In addition, the cation distribution in the octahedral and tetrahedral sites changes with an increasing sintering temperature in the spinel ceramics. The ratio of  $\text{Mn}^{3+}/\text{Mn}^{4+}$  in the octahedral sites increases with the increasing sintering temperature and also results in a decrease in the resistivity.<sup>16</sup> The electrical resistivity of the samples decreased significantly with the increasing of the  $\text{Co}_3\text{O}_4$  content. Muralidharan et al. observed that the resistivity and B-value decreased with the increasing Co content. Their observation is expected as the  $\text{Co}^{2+}$  and  $\text{Co}^{3+}$  ions can also occupy the octahedral sites and contribute to the electrical conductivity along with  $\text{Mn}^{3+}/\text{Mn}^{4+}$  ion pairs in the octahedral sites. This gives rise to a decrease of the resistivity, B-value and temperature coefficient of resistance.<sup>2</sup> This phenomenon is prominent for all samples sintered at 1100 °C, while the Co content was increasing in the samples. Similar trends were also observed for the A1, A2 and A6 compositions when the samples were sintered at 1200 °C. When the sintering temperature was increased from 1100 to 1200 °C for the A10 sample, similar resistivity values were found, but the B-values and activation energy of samples were nearly constant. Moreover, the lattice parameters were found to be 0.8365 nm and 0.8273 nm for the  $\text{NiMn}_2\text{O}_4$  and  $\text{Ni}_{0.5}\text{Co}_{0.8}\text{Mn}_{1.7}\text{O}_4$  samples, respectively. This may be due to the fact that the hopping distance of the charge carriers becomes easier with the decreasing lattice parameter, thus the resistivity value decreases.<sup>17</sup> The sensitivity coefficient and the activation-energy values of all the samples were found in the range -4.426

to -3.683 %/K and 0.282 eV to 0.338 eV, respectively. It is well known that the desired sensitivity coefficient,  $\alpha_{25}$ , and the activation energy of the NTC thermistors are in the range -2.2 %/K to -5.5 %/K and 0.1–1.5 eV, respectively.<sup>18,19</sup>

## 5 CONCLUSION

The influence of nano-sized cobalt oxide additions on the structural and electrical properties of nickel-manganite-based NTC thermistors was investigated. Our results in this work indicate that a wide range of electrical properties of nickel-manganite-based NTC thermistors can be obtained by the addition of nano-sized cobalt oxide. The particularly interesting finding in this study demonstrated that the  $\text{Ni}_{0.5}\text{Co}_{1.1}\text{Mn}_{1.4}\text{O}$  sample sintered at 1200 °C for 5 h has a low electrical resistivity and a high B-constant.

## Acknowledgements

This study is supported by TÜBİTAK (The Scientific and Technical Research Council of Turkey), Project number 3001-114M860. We would like to thank TÜBİTAK for its financial support.

## 6 REFERENCES

- R. N. Jadhav, S. N. Mathad, V. Puri, Studies on the properties of  $\text{Ni}_{0.6}\text{Cu}_{0.4}\text{Mn}_2\text{O}_4$  NTC ceramic due to Fe doping, *Ceramics International*, 38 (2012), 5181–5188, doi:10.1016/j.ceramint.2012.03.024
- M. N. Muralidharan, P. R. Rohini, E. K. Sunny, K. R. Dayas, A. Seema, Effect of Cu and Fe addition on electrical properties of Ni–Mn–Co–O NTC thermistor compositions, *Ceramics International*, 38 (2012), 6481–6486, doi:10.1016/j.ceramint.2012.05.025
- J. Fraden, *Handbook of Modern Sensors Physics, Designs, and Applications*, Springer Science+Business Media, New York 2010
- E. D. Macklen, *Thermistors*, Electrochemical Publications Limited, Scotland 1979
- K. Park, Fabrication and Electrical Properties of Mn-Ni-Co-Cu-Si Oxides Negative Temperature Coefficient Thermistors, *Journal of the American Ceramic Society*, 88 (2005), 862–866, doi:10.1111/j.1551-2916.2005.00170.x
- J. Wang, J. Zhang, Effects of Mg substitution on microstructure and electrical properties of  $\text{NiMn}_{2-x}\text{Mg}_x\text{O}_4$  NTC ceramics, *Journal of Materials Research*, 27 (2012), 928–931, doi:10.1557/jmr.2012.29
- K. Park, S. J. Kim, J. G. Kim, S. Nahm, Structural and electrical properties of MgO-doped  $\text{Mn}_{1.4}\text{Ni}_{1.2}\text{Co}_{0.4-x}\text{Mg}_x\text{O}_4$  ( $0 < x < 0.25$ ) NTC thermistors, *Journal of the European Ceramic Society*, 27 (2007), 2009–2016, doi:10.1016/j.jeurceramsoc.2006.07.002
- M. Hosseini, B. Yasaei, Effect of Grain Size and Microstructures on Resistivity of Mn-Co-Ni Thermistor, *Ceramics International*, 24 (1998), 543–545
- S. Talam, S. R. Karumuri, N. Gunnam, Synthesis, Characterization, and Spectroscopic Properties of ZnO Nanoparticles, *ISRN Nanotechnology*, 2012 (2012) 372505, 1–6, doi:10.5402/2012/372505
- A. Monshi, M. R. Foroughi., M. R. Monshi, Modified Scherrer Equation to Estimate More Accurately Nano-Crystallite Size Using XRD, *World Journal of Nano Science and Engineering*, 2 (2012), 154–160, doi:10.4236/wjnse.2012.23020

- <sup>11</sup> M. N. Muralidharan, E. K. Sunny, K. R. Dayas, A. Seema, K. R. Resmi, Optimization of process parameters for the production of Ni–Mn–Co–Fe based NTC chip thermistors through tape casting route, *Journal of Alloys and Compounds*, 509 (2011), 9363–9371, doi:10.1016/j.jallcom.2011.07.037
- <sup>12</sup> J. Wu, Z. Huang, Y. Hou, Y. Gao, J. Chu, Structural, electrical, and magnetic properties of  $\text{Mn}_{2.52-x}\text{Co}_x\text{Ni}_{0.48}\text{O}_4$  films, *Journal of Applied Physics*, 107 (2010) 053716, 1–6, doi:10.1063/1.3309780
- <sup>13</sup> R. D. Shannon, Revised Effective Ionic Radii and Systematic Studies of Interatomic Distances in Halides and Chalcogenides, *Acta Crystallography*, A32 (1976), 751–767
- <sup>14</sup> S. M. Savic, L. Mancic, K. Vojisavljevic, G. Stojanovic, Z. Brankovic, O. S. Aleksic, G. Brankovic, Microstructural and electrical changes in nickel manganite powder induced by mechanical activation, *Materials Research Bulletin*, 46 (2011), 1065–1071, doi:10.1016/j.materresbull.2011.03.008
- <sup>15</sup> S. A. Kanade, V. Puri, Electrical properties of thick-film NTC thermistor composed of  $\text{Ni}_{0.8}\text{Co}_{0.2}\text{Mn}_2\text{O}_4$  ceramic: Effect of inorganic oxide binder, *Materials Research Bulletin*, 43 (2008), 819–824, doi:10.1016/j.materresbull.2007.05.008
- <sup>16</sup> W. Kong, L. Chen, B. Gao, B. Zhang, P. Zhao, G. Ji, A. Chang, C. Jiang, Fabrication and properties of  $\text{Mn}_{1.56}\text{Co}_{0.96}\text{Ni}_{0.48}\text{O}_4$  free-standing ultrathin chips, *Ceramics International*, 40 (2014), 8405–8409, doi:10.1016/j.ceramint.2014.01.049
- <sup>17</sup> C. Ma, Y. Liu, Y. Lu, H. Gao, H. Qian, J. Ding, Preparation and characterization of  $\text{Ni}_{0.6}\text{Mn}_{2.4}\text{O}_4$  NTC ceramics by solid-state coordination reaction, *Journal of Materials Science: Materials in Electronics*, 24 (2013), 5183–5188, doi:10.1007/s10854-013-1542-2
- <sup>18</sup> A. Feteira, Negative Temperature Coefficient Resistance (NTCR) Ceramic Thermistors: An Industrial Perspective, *Journal of the American Ceramic Society*, 92 (2009), 967–983, doi:10.1111/j.1551-2916.2009.02990.x
- <sup>19</sup> K. Park, I. H. Han, Effect of  $\text{Cr}_2\text{O}_3$  addition on the microstructure and electrical properties of Mn–Ni–Co oxides NTC thermistors, *Journal of Electroceramics*, 17 (2006), 1069–1073, doi:10.1007/s10832-006-8317-6



## DURABILITY OF ALUMINA SILICATE CONCRETE BASED ON SLAG/FLY-ASH BLENDS AGAINST ACID AND CHLORIDE ENVIRONMENTS

### ZDRŽLJIVOST BETONA NA OSNOVI GLINICE IN SILIKATOV IZ MEŠANICE ŽLINDRA/LETEČI PEPEL NA KISLO IN KLORIDNO OKOLJE

Rajagopalan Gopalakrishnan<sup>1</sup>, Komarasamy Chinnaraju<sup>2</sup>

<sup>1</sup>Sri Venkateswara College of Engineering, Department of Civil Engineering, 602 117 Sriperumbudur, India

<sup>2</sup>Anna University, Division of Civil and Structural Engineering, 600 025 Chennai, India  
gopalakrishnan@svce.ac.in, rajagopalan.gopalakrishnan0@gmail.com

*Prejem rokopisa – received: 2015-07-19; sprejem za objavo – accepted for publication: 2015-12-02*

doi:10.17222/mit.2015.230

The durability of a concrete mainly depends on its resistance against acid and chloride environments. This article presents an investigation of the durability of geopolymer concrete with GBFS (Granulated Blast Furnace slag), Fly ash (class F) and alkaline activators when exposed to 5 % sulphuric acid and chloride solutions. GBFS was replaced by fly ash with different replacement levels from 0 % to 50 % in a constant concentration of 12-M alkaline activator solution. The main parameters of this study are the evaluation of the change in weight, strength and microstructural changes. The degradation was studied using Scanning Electron Microscopy (SEM) with EDAX. From the test results it is observed that the strength of the geopolymer concrete with GBFS in ambient curing performs compared well to geopolymer concrete with GBFS blended with fly ash. The acid resistance in terms of the rate of reduction of strength of GPC with GBFS is 85 %, while for 40 % replacement of fly ash to GBFS performs well with a reduction of only 53 %. Similar observations are also observed in a chloride environment in which 40 % replacement of fly ash to GBFS performs well when compared to GPC with GBFS. Hence, geopolymer concrete with 40 % replacement of fly ash for GBFS is the appropriate level of replacement, satisfying the above durability properties.

Keywords: durability, geopolymer concrete, acid and chloride environment

Zdržljivost betona je predvsem odvisna od odpornosti na kislino in kloridno okolje. Članek predstavlja preiskavo zdržljivosti geopolimernega betona z GBFS (granulirana žlindra iz plavža), letečega pepela (razred F) in alkalnih aktivatorjev med izpostavitvijo 5 % žvepleni kislini in kloridnim raztopinam. V GBFS je bila dodana različna količina: od 0 % do 50 % letečega pepela pri konstantni koncentraciji 12 M raztopine alkalnega aktivatorja. Glavni parametri v študiji so bili sprememba teže, trdnost in mikrostrukturne spremembe. Degradacija je bila preučevana z uporabo vrstičnega elektronskega mikroskopa (SEM) z EDAX. Iz rezultatov preizkusov je opaziti, da je pri izpostavitvi trdnost geopolimernega betona z GBFS dobra, v primerjavi z geopolimernim betonom z GBFS s primešanim letečim pepelom. Odpornost na kislino, izraženo s hitrostjo zmanjševanja trdnosti GPC z GBFS je 85 %, medtem ko se pri 40 % nadomestitvi letečega pepela v GBFS, ta ponaša dobro, s samo 53 % zmanjšanjem trdnosti. Podobna opažanja so bila tudi v kloridnem okolju, v katerem se 40 % nadomestilo letečega pepela v GBFS obnaša dobro, v primerjavi z GPC, ki vsebuje tudi GBFS. Torej je geopolimerni beton, s 40 % nadomestitvijo letečega pepela z GBFS, primeren za zgornji omenjeni zdržljivost.

Ključne besede: zdržljivost, geopolimerni beton, kislino in kloridno okolje

## 1 INTRODUCTION

The durability of concrete structures, especially those built in corrosive environments, starts to deteriorate after 20 to 30 years, even though they have been designed for more than 50 years of service life. Although the use of Portland cement is unavoidable in the foreseeable future, many efforts are being made to reduce the use of Portland cement in concrete.<sup>1</sup> Inorganic polymer concretes, or geopolymers have been emerging as novel engineering materials with the potential to form an alternative element for the construction industry.<sup>2-4</sup> Geopolymers show substantially superior resistance to fire<sup>5</sup> and acid attack<sup>6</sup> and much less shrinkage than OPC Concrete. The tensile strength of geopolymer concrete falls within the range observed for OPC-based concrete. Also, the flexural strengths are generally higher than the standard

model line for OPC-based concrete. This favourable behaviour can be attributed to the type of matrix formation in the geopolymer concrete.<sup>7</sup> It has been reported that the stress strain relationship of fly-ash-based geopolymer concrete is almost similar to that of ordinary portland cement concrete.<sup>1</sup> These advantages make the geopolymer concrete a strong alternative for replacing ordinary Portland cement concrete.

Geopolymers are produced by a polymerization reaction of strong alkali liquids such as sodium hydroxide (NaOH), potassium hydroxide (KOH), sodium silicate and potassium silicate with a source material of geological origin or by a product material such as fly ash, GBFS, metakaolin. The mixture can be cured at room temperature or heat cured. Under a strong alkali solution, an alumina silicate material dissolves and forms SiO<sub>4</sub> and AlO<sub>4</sub> tetrahedral units.

Three common types of geopolymer are the polysialate Al-O-Si chain, polysialate siloxo Al-O-Si-Si chain and polysialate disiloxo Al-O-Si-Si-Si chain.<sup>8,9</sup> The raw materials commonly used for preparing geopolymers are clay and metakaolin. Studies are under progress recently are using the waste and byproducts for geopolymerization from waste materials.<sup>10-18</sup> A number of research publications related to geopolymers have been published, with some reports on chemical composition or reaction processes, others relating to mechanical properties and durability. The compressive strength depends on both the Si/Al ratio and the type of raw materials used.<sup>19-22</sup> To improve the performance of these binders, a number of recent investigations have been published, giving attention to producing mixes based on blends with reactive precursors. The blends commonly involve a Ca-rich precursor such as granulated blast furnace slag (GBFS), and an alumino silicate source such as low calcium fly ash or metakaolin, to form the stable coexistence of calcium silicate hydrate (C-S-H) gels formed from the activation of GBFS and geopolymer gel (also expressed as N-A-S-H) produced from the activation of alumina silicate, which is a cementitious paste that improves the setting and strength properties.<sup>23-25</sup>

Fly ash contains mainly alumina and silica, along with other impurities like iron oxide, lime and magnesia. Due to increased industrial growth fly ash is generated in huge amounts and its accumulation over the years has become a threat to the environment. The utilization of fly ash for preparing geopolymers not only conserves the nature, but also reduces the ever-increasing burden of fly ash on the environment. GBFS is a glassy granular material essentially consisting of oxides like CaO, SiO<sub>2</sub> and Al<sub>2</sub>O<sub>3</sub>. It is formed when molten blast-furnace slag, a byproduct in the extraction of iron is cooled, usually by immersion in water and then ground fine to improve its reactivity.<sup>18,26-30</sup> There is a relatively small number of research reports expressing the structure and performance of alkali-activated GBFS/Fly ash blends cured at ambient environment, and have been mainly discussed where fly ash is added to GBFS to enhance the strength and microstructure, which leads to a good durability. The durability of these binders in an acid and chloride environment was not investigated before; however, there is an opinion that geopolymer materials have excellent resistance in acid and chloride environments. The above resistance against acid and chloride is an important durability property concerned with serviceability for geopolymer materials used in the construction industry. T. Bakerev<sup>31</sup> studied the resistance of geopolymer materials prepared

from fly ash against 5 % sulphuric acid up to 5 months exposure and concluded that geopolymer materials have better resistance than ordinary cement concretes. Portland cement and blended cement concretes show a deterioration when exposed to acid and chloride environments. The demand of standard methods to evaluate the performance of cements in acid environments has led to research in different exposure conditions by various researchers making it difficult to correlate the results.<sup>32</sup>

This paper presents an investigation of acid and chloride attack on geopolymer materials prepared using GBFS blended with low calcium fly ash in different percentages and sodium hydroxide, sodium silicate as activators and cured in ambient conditions (25±5 °C). The effects of the fly ash addition to GBFS, weight change, visual appearance, microstructure and strength properties have also been studied. To study the microstructure methods such as SEM with EDAX have been employed. An attempt has been made to correlate the structure with reaction and properties.

## 2 EXPERIMENTAL PART

### 2.1 Materials

The class F fly ash (as per ASTM C618-99) obtained from Ennore power plant and GBFS obtained from M/s Jindal, Karnataka were used for the study. The chemical analysis of GBFS and fly ash were made using the XR fluorescence method and the results were shown in **Table 1**. Coarse aggregate of maximum 20 mm with a specific gravity of 2.67 was used. Locally available river sand conforming to Zone II (as per IS 383) with a specific gravity of 2.52 was used for the study. Sodium hydroxide in the form of flakes having a purity of 90 % and sodium silicate in the liquid having a chemical composition of Na<sub>2</sub>O = 14.7 % SiO<sub>2</sub> = 29.4 % H<sub>2</sub>O = 55.9 % by mass. To improve the workability of fresh concrete a superplasticizer Glenium supplied by BASF, a polycarboxylic ether is added with the ingredients.

### 2.2 Test variables

Fly ash with GBFS of various mixture proportions were subjected to geopolymerization. However the ratio of SiO<sub>2</sub> to Al<sub>2</sub>O<sub>3</sub> is maintained at approximately 2, which is a typical ratio for a geopolymer structure. Details of the batch compositions are given in **Table 2**. The ratio of sodium silicate solution to sodium hydroxide by mass was kept as 2.5, the ratio of alkaline liquid to the geopolymer solids was kept as 0.4 and water to geopolymer

**Table 1:** Raw materials chemical properties

**Tabela 1:** Kemijske lastnosti sestavnih materialov

Materials	Chemical composition, in mass fractions (w/%)								
	SiO <sub>2</sub>	Al <sub>2</sub> O <sub>3</sub>	CaO	Fe <sub>2</sub> O <sub>3</sub>	MgO	SO <sub>3</sub>	Na <sub>2</sub> O	K <sub>2</sub> O	LOI
GBFS	34.60	17.40	33.01	1.50	8.70	0.05	1.25	0.83	1.39
Fly ash	53.80	21.20	0.90	17.00	3.50	1.50	–	–	0.48

**Table 2:** Batch composition**Tabela 2:** Sestava posamezne serije

Test variables	Batch composition ratio <i>GBFS</i> & fly ash, in mass fractions (w/%)		SiO <sub>2</sub> / Al <sub>2</sub> O <sub>3</sub> ratio	CaO %
	<i>GBFS</i>	Fly ash		
GPCA	100	0	1.99	33.01
GPCB	90	10	2.05	29.80
GPCC	80	20	2.12	26.59
GPCD	70	30	2.18	23.38
GPCE	60	40	2.23	20.17
GPCF	50	50	2.28	16.96

**Table 3:** Designation of test variables and mix proportions**Tabela 3:** Oznaka preizkusnih spremenljivk in razmerja mešanic

Test variables ID in different environment			Binder composition		Ingredient contents kg/m <sup>3</sup>					
Ambient curing	Sulphuric acid	Sodium chloride	<i>GBFS</i> %	Fly ash %	<i>GBFS</i>	Fly ash	Sodium hydroxide solution	Sodium silicate solution	Coarse aggregate	Fine aggregate
GPCA	GPCAA	GPCAC	100	0	400	0	46	115	1200	645
GPCB	GPCBA	GPCBC	90	10	360	40	46	115	1200	645
GPCC	GPCCA	GPCCC	80	20	320	80	46	115	1200	645
GPCD	GPCDA	GPCDC	70	30	280	120	46	115	1200	645
GPCE	GPCEA	GPCEC	60	40	240	160	46	115	1200	645
GPCF	GPCFA	GPCFC	50	50	200	200	46	115	1200	645

solids as 0.24. The properties of various concrete mixes are shown in **Table 3**.

### 2.3 Sample preparation for physical testing

Solutions of NaOH (12-M concentration) and Na<sub>2</sub>SiO<sub>3</sub> were separately prepared 24 h before casting. Both the solutions were mixed together at the time of mixing. A weighed quantity of *GBFS*, fly ash, fine aggregate and coarse aggregate were dry mixed in a pan for about 3 min to 5 min. Wet mixing was done for another 3 mins and the required quantity of super plasticizer and water was added to obtain the required consistency. The samples were then cast into the steel moulds of size 100 mm × 100 mm × 100 mm. Compaction was done by manual strokes, followed by a compaction on a vibrating table for 20 s. The cubes were remoulded after 24 h and cured at a relative humidity of 25±5 °C to prevent drying effects. The required number of samples for each mix was prepared and cured under ambient conditions and were reported as the mean of the three samples.

### 2.4 Test procedure

The resistance of the materials to acid and chloride attack was studied by immersion of the cubical specimens of size (100 mm × 100 mm × 100 mm) in a 5 % solution of concentrated sulphuric acid for acid attack and with a proportion of 4 % NaCl with 1 % magnesium sulphate solution for chloride attack for a period up to 180 d. The compressive strength was determined before

the test and after (28, 60, 120 and 180) d of exposure. The choice of acid solution and its concentration was based on the practical application of concrete as a construction material mainly in the sewage pipe and mining industries. The volume of solution was kept not less than four times the volume of the specimens immersed and maintained throughout the test period. The testing solutions were replaced with new solutions after 30 d until the completion of the test period. The samples were compared with all the grades of concrete that were ambient cured.

The deterioration of samples was studied by SEM with EDAX. For this testing, the samples were taken from the surface at a 0–5-mm depth, exposed to the solutions of 120 d and compared with conventional ambient cured samples. The SEM analysis was done using a microscope having a magnification of 5× to 3,00,000× with a voltage of 0.3–30 kV. The coating of the samples for the analysis was done using an ion sputter with a gold target and the system was attached with the latest PIV. The resolution of the equipment varied from 3 nm, 4 nm to 10 nm. The change in mass before and after the immersion was observed for all the samples.

## 3 RESULTS AND DISCUSSION

### 3.1 Visual appearance

Visual appearances of geopolymer specimens after immersion in a solution of concentrated sulphuric acid after 180 d are shown in the **Figure 1**. Its appearance



**Figure 1:** GPC samples after 180 d in sulphuric acid  
**Slika 1:** Vzorci GPC po 180 dneih v žvepleni kislini

seems to be very slightly changed after 28 d, but there is a distinct change in the appearance of the deterioration after 180 d. The surface became softer as the duration of the test period prolonged, but could not be scratched with finger nails. The deterioration of the surface increased with the duration, but the amount of deterioration could not be determined through a visual inspection.<sup>31</sup>

The geopolymer specimens immersed in chloride solution did not reveal any changes in the surface after 28 d. Even after 180 d also, there is no severe deterioration.

### 3.2 Change in weight

**Table 4** and **Figure 2** give the comparative weight changes for the specimens exposed to sulphuric acid and chloride solution with the ambient cured samples after 180 d. In ambient cured samples there is a loss of weight with the replacement of fly ash to GBFS. The percentage of loss increases with the percentage of replacement. The loss of weight at 10 % replacement of fly ash to GBFS is 1.512 % and 1.678 % with 50 % replacement (GBFC). But at 40 % replacement there is loss of weight of only 1.369 %, which shows the optimum replacement of fly ash. This may be due to the limitations of the SiO<sub>2</sub>/Al<sub>2</sub>O<sub>3</sub> ratio. The geopolymer samples (GPCA) immersed in sulphuric acid solution show a little loss of weight 0.05 %. The samples with the replacement of fly ash to GBFS show a loss of 0.43 % at 10 % with a gain of 0.88 % at

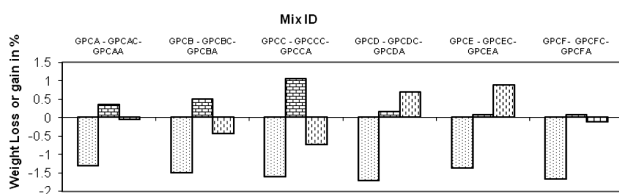


**Figure 2:** Weight change in % ambient curing with NaCl & H<sub>2</sub>SO<sub>4</sub> after 180 d  
**Slika 2:** Spreminjanje teže v % pri 180 dnevni izpostavitvi okolju z NaCl in H<sub>2</sub>SO<sub>4</sub>

40 % replacement. Similar observations have been reported by<sup>31</sup>. The mass change was calculated according to ASTM C267. All the geopolymer concrete mixes show a very low mass loss of less than 3 %.

**Table 4:** Weight change in % ambient curing with NaCl & sulphuric acid after 180 d

**Tabela 4:** Sprememba teže v % po 180 dneih izpostavitve okolju z NaCl in žvepleno kislino

Test variables Id	Weight change, %		
GPCA - GPCAC - GPCAA	-1.32	0.35	-0.05
GPCB - GPCBC - GPCBA	-1.512	0.49	-0.43
GPCC - GPCCC - GPCCA	-1.622	1.05	-0.73
GPCD - GPCDC - GPCDA	-1.715	0.16	0.69
GPCE - GPCEC - GPCEA	-1.369	0.08	0.88
GPCF - GPCFC - GPCFA	-1.678	0.08	-0.12

The geopolymer samples with GBFS (GPCA) immersed in chloride solution gain weight to 0.35 %. When it is replaced by fly ash to GBFS it gains weight, which varied from 0.35 % at 10 % replacement to a very low gain of 0.08 % at 50 % replacement. The gain in % increases with the increase of the replacement. But it shows a low value in 40 % and 50 % of 0.08 %. A minimal change in nominal weight loss has been observed with 40 % fly ash in the geopolymer composite, which indicates that 40 % fly ash composite with geopolymer performs the best, compared to all the other compositions. The specimens were damaged beyond this 40 % fly ash and longer durations of immersion, which is in good agreement with<sup>33</sup>. Interaction of geopolymer in the acid solution may result in replacement of exchangeable cations such as Na<sup>+</sup> in the polymer by hydrogen ion or hydronium ion.<sup>31</sup>

### 3.3 Compressive strength

**Figure 3** shows the variation of compressive strength of samples for different duration periods in ambient curing. The compressive strength increases with time in all the mixes. The geopolymer concrete with 100 % GBFS (GPC-A) shows a higher compressive strength of 74 MPa at 180 d. Its strength varies from 37 MPa at 3 d to 74 MPa at 180 d. The increase in percentage was 100, which is in good agreement with S. A. Bernal.<sup>34</sup> The geopolymer concrete GBFS blended with fly ash at 10 % replacement (GPC-B) strength varies from 32.4 MPa at 3

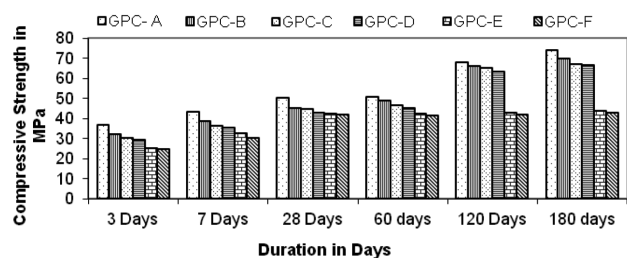


**Figure 3:** Compressive strength of GPC  
**Slika 3:** Tlačna trdnost GPC



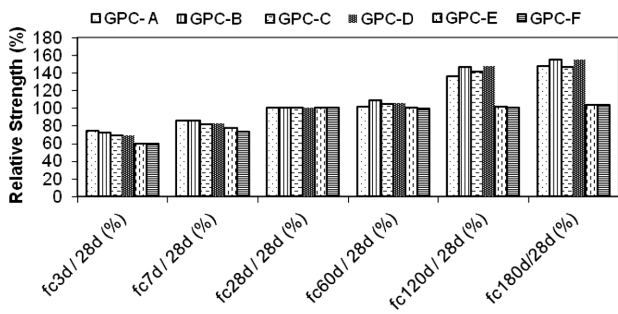


Figure 4: Compressive strength development  
Slika 4: Razvoj tlačne trdnosti

d to 69.8 MPa at 180 d. Similarly, other replacement levels 20 %, 30 % (GPC-C, GPC-D) strength varies 30.5, 29.6 MPa at 3 d to 67, 66 MPa at 180 d, respectively. In the above, replacement levels of fly ash to GBFS the percentage increase is 120 %. But at 40 % and 50 % (GPC-E, GPC-F) replacement levels its strength at 180 d was 44 MPa and 43 MPa, respectively, with a percentage increase of 73 %. The rate of development of strength at 180 d with reference to 28 d is 150 % in all the mixes, except in the mixes of GPC-E, GPC-F, which show only 100 %, as in Figure 4.

3.4 Effect of sulphuric acid and chloride

Figure 5 show the evaluation of compressive strength for different duration periods for the samples immersed in a solution sodium chloride. It reveals that the reduction of strength is more with an increase in the percentage of replacement of fly ash to GBFS in the geopolymer concrete. The strength reduction rate increases with the duration period in all the mixes. The reduction rate from 28 d to 60 d is more and it is further increased at 120 d. The reduction of strength of geopolymer concrete with 100 % GBFS (GPC-A) is 42 % compared to the ambient cured samples at 180 d. There is a minimum reduction of strength from 120 d to 180 d. The GPC blended with fly ash at 10 % replacement (GPC-B) shows a reduction of strength 40 % at 180 d. Similarly, other replacement levels 20 %, 30 % (GPC-C, GPC-D) show a strength reduction of 47 % and 45 % respectively at 180 d. In the replacement of fly ash to GBFS, 40 % replacement performs well and shows a reduction rate of 24 %. This shows that GBFS can be replaced by 40 % of fly ash as

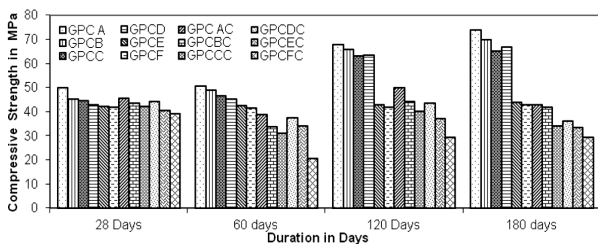


Figure 5: Compressive strength comparison of ambient curing with NaCl

Slika 5: Primerjava tlačne trdnosti pri utrjevanju v okolju z NaCl

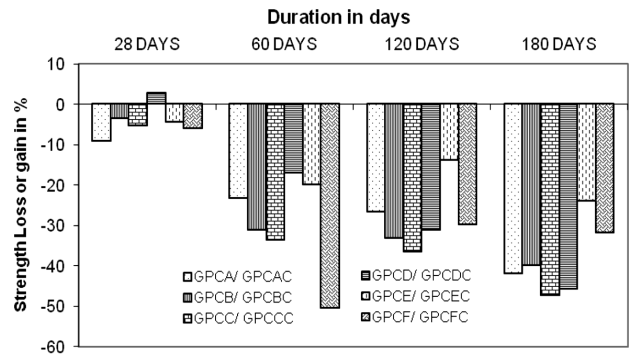


Figure 6: Strength change in % ambient curing with NaCl

Slika 6: Spreminjanje trdnosti v % pri utrjevanju v okolju z NaCl

the reduction rate is less compared to GPC with 100 % GBFS. The reactivity of fly ash in the chloride environment is good. The detailed loss or gain in % is shown in Table 5 and Figure 6.

Table 5: Strength change in % ambient curing with NaCl

Tabela 5: Spreminjanje trdnosti v % pri utrjevanju v okolju z NaCl

Days	GPCA/ GPCAC	GPCB/ GPCBC	GPCC/ GPCCC	GPCD/ GPCDC	GPCE/ GPCEC	GPCF/ GPCFC
28	-9.2	-3.54		2.8	-4.3	-6
60	-23.3	-31.2	-33.6	-17	-20	-50.4
120	-26.7	-33.1	-36.5	-31.2	-13.9	-29.8
180	-42	-40	-47.4	-45.7	-24	-31.86

Figure 7 shows the evaluation of compressive strength for the different duration periods for the test samples immersed in 5 % solution of sulphuric acid. The reduction rate continuously increases with the duration period. There is a strength reduction of 85 % compared to ambient cured samples for the geopolymer concrete prepared with 100 % GBFS at 180 d. The GPC blended with fly ash at 10 % replacement (GPC-B) shows an 83 % reduction of strength at 180 d. Similarly, other replacement levels 20 %, 30 % (GPC-C, GPC-D) show a strength reduction of 81 % and 77 %, respectively, at 180 d. In the replacement of fly ash to GBFS, 40 % replacement performs well and it shows a reduction rate of 53 %. This shows that the replacement of 40 % of fly ash is the optimum. The strength reduction is proportional to the replacement of fly ash. The detailed loss or gain in % is shown in Table 6 and in Figure 8. Com-

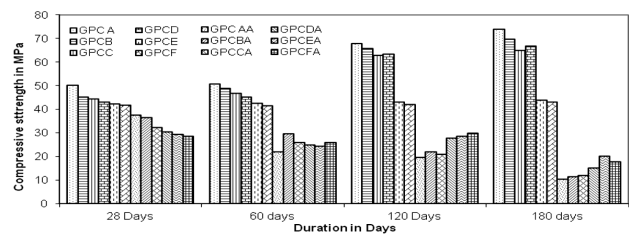
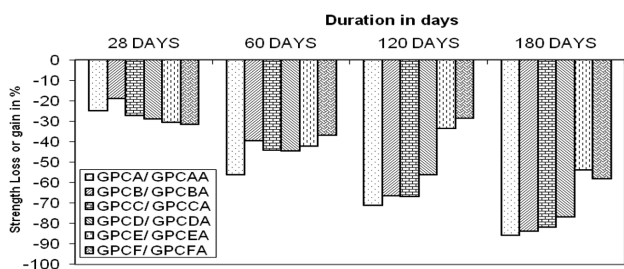
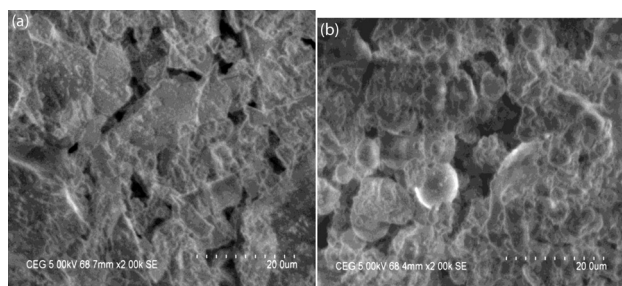


Figure 7: Compressive strength comparison of ambient curing with sulphuric acid

Slika 7: Primerjava tlačne trdnosti po utrjevanju v okolju z žvepleno kislino



**Figure 8:** Strength change in % ambient curing with sulphuric acid  
**Slika 8:** Spreminjanje trdnosti v % pri utrjevanju v okolju z žvepleno kislino



**Figure 9:** SEM images of: a) GBFS and b) fly ash  
**Slika 9:** SEM-posnetek: a) GBFS in b) leteči pepel

pressive strength appears to increase for a set of samples with curing time for ambient curing, whereas for the set cured in the NaCl solution it appears to decrease. This improvement in compressive strength is attributed to the leaching of silica and aluminium at a higher Ca of NaOH.<sup>36</sup>

**Table 6:** Strength change in % ambient curing with sulphuric acid

**Tabela 6:** Spreminjanje trdnosti v % pri utrjevanju v okolju z žvepleno kislino

Days	GPCA / GPCAA	GPCB / GPCBA	GPCC / GPCCA	GPCCD / GPCDA	GPCE / GPCEA	GPCF / GPCFA
28	-25.1	-19.1	-27.4	-29.1	-30.5	-31.7
60	-56.4	-39.6	-44.1	-44.7	-42.3	-37.1
120	-71.2	-66.6	-66.8	-56.2	-33.5	-28.5
180	-85.8	-83.7	-81.7	-77	-53.9	-58.4

The development of the strength of specimens is suppressed due to the hydration of Ca-Al- silicates from the dissolution of the CAS phase by the hydroxyl ion (OH<sup>Φ</sup>) contributed by water and aqueous NaOH so that the Al and Si become penta-valent due to the attachment of (OH<sup>Φ</sup>). Due to this, Al–O–Al and Si–O–Si tend to

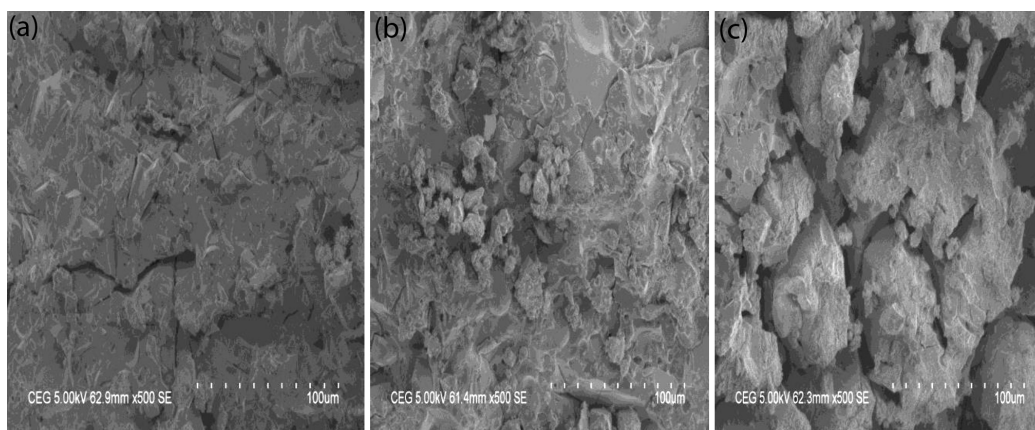


**Figure 10:** SEM images before immersion: a) GPCA, b) GPCC, c) GPCE  
**Slika 10:** SEM-posnetki pred namakanjem: a) GPCA, b) GPCC, c) GPCE

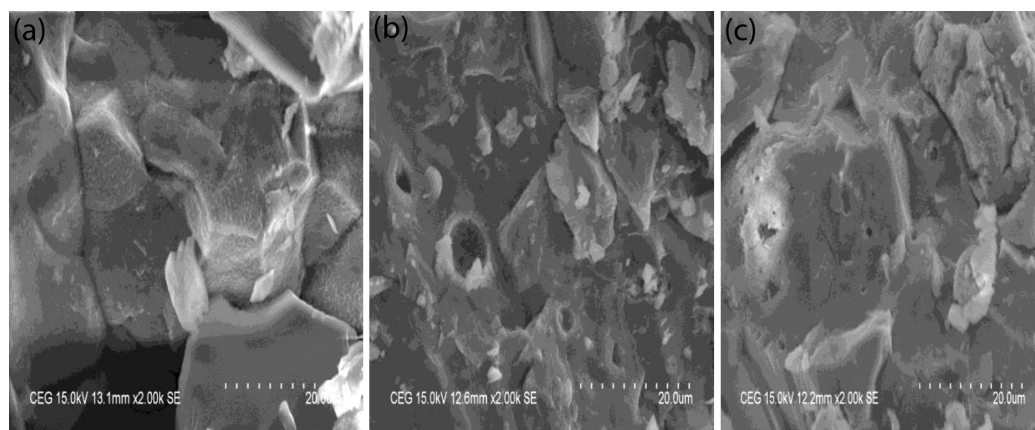


**Figure 11:** SEM images after immersion in solution of NaCl for 120 d: a) GPCAC, b) GPCCC, c) GPCEC  
**Slika 11:** SEM-posnetki po 120 dnevnem namakanju v raztopini NaCl: a) GPCAC, b) GPCCC, c) GPCEC

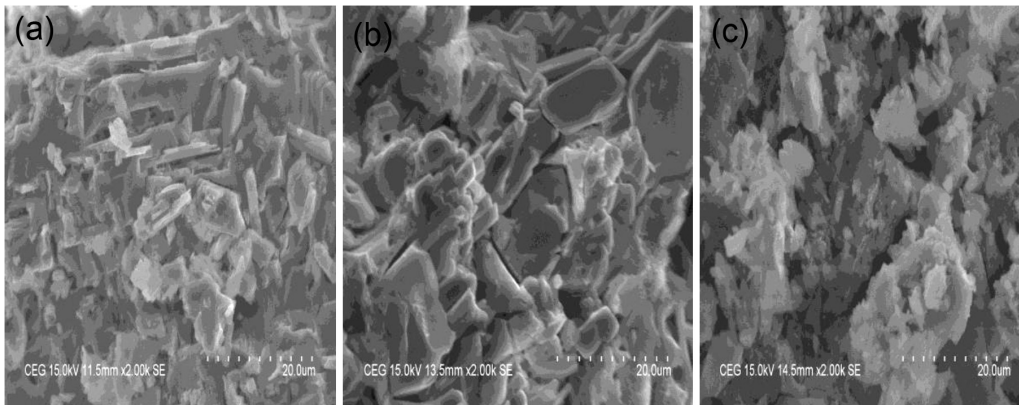
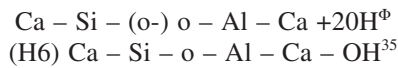


**Figure 12:** SEM images after immersion in solution of H<sub>2</sub>SO<sub>4</sub> for 120 d: a) GPCAA, b) GPCCA, c) GPCEA  
**Slika 12:** SEM-posnetki po 120 dnevnom namakanju v raztopini H<sub>2</sub>SO<sub>4</sub>: a) GPCAA, b) GPCCA, c) GPCEA

strengthen the bands. This can be schematically represented as:



### 3.5 SEM with EDAX

**Figure 9** shows the SEM images of GBFS and fly ash. **Figure 10** shows the SEM images of the specimens before immersion into the solutions of sulphuric acid and chloride. It is evident that the appearance of gel-like

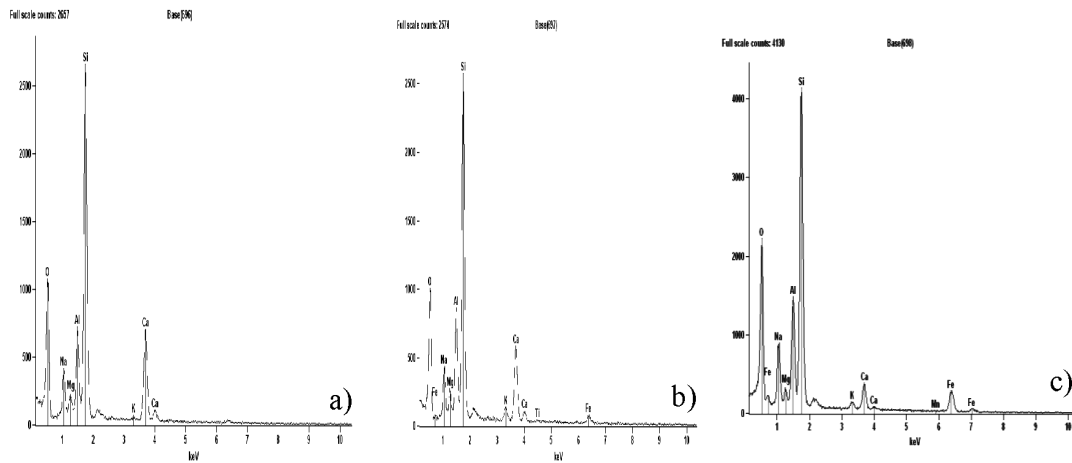


**Figure 13:** EDAX spectrum before immersion: a) GPCA, b) GPCC, c) GPCE  
**Slika 13:** EDAX-spekter pred namakanjem: a) GPCA, b) GPCC, c) GPCE

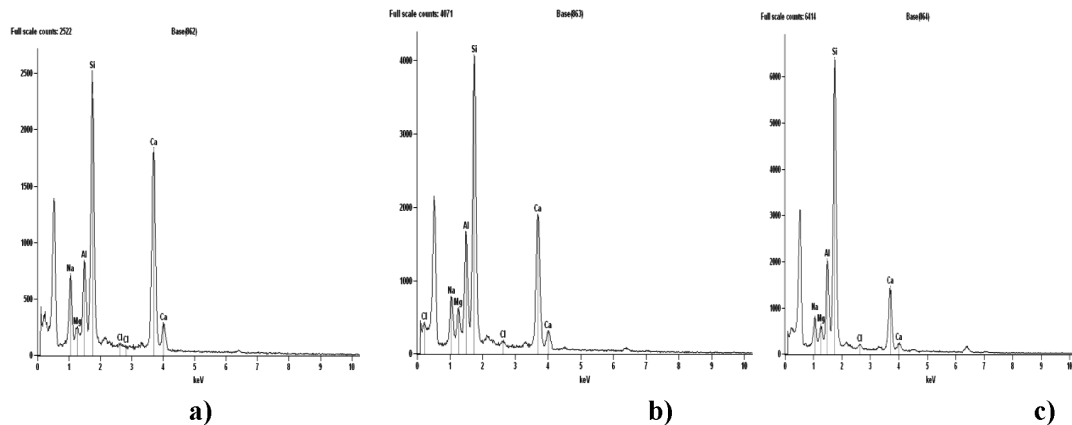


**Figure 14:** EDAX spectrum after immersion in solution of NaCl for 120 d: a) GPCA, b) GPCCC, c) GPCE  
**Slika 14:** EDAX-spekter po 120 dnevnom namakanju v NaCl: a) GPCA, b) GPCCC, c) GPCE



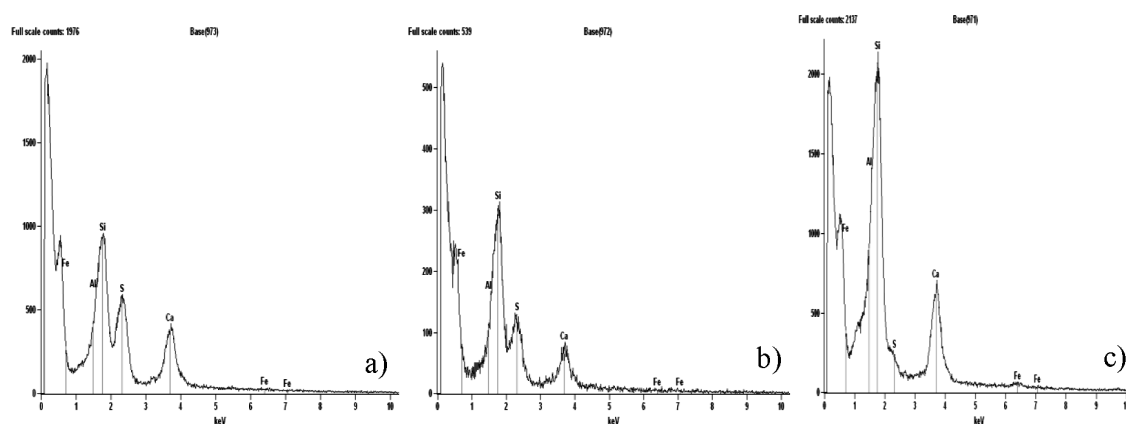


**Figure 15:** EDAX spectrum after immersion in solution  $H_2SO_4$  for 120 d: a) GPCAA, b) GPCCA, c) GPCEA

**Slika 15:** EDAX-spekter po 120 dnevnom namakanju v raztopini  $H_2SO_4$ : a) GPCAA, b) GPCCA, c) GPCEA

phases in the microstructure (of the SEM) can be attributed to the development of the microstructure particularly in the GBFS phases.<sup>6</sup>

The immersion in NaCl for the 120 d period appears to cause a decrease in Na content of the samples, which may be due to the migration of  $Na^+$  ions from the specimen samples to NaCl. The microstructures of the specimen samples after 120 d of immersion in a solution of NaCl were studied using SEM and the results are shown in **Figure 11**.

SEM images of the samples after immersion in  $H_2SO_4$  for 120 d (**Figure 12**) indicate that there is a formation of light-coloured precipitates in the sample after immersion in  $H_2SO_4$  solution. The formation of light-coloured precipitates is indicative of the degradation of the cured specimen.<sup>36</sup> The appearance of lightly coloured precipitates in a low distribution may be attributed to a more amorphous, less-crystalline layer formation.<sup>6</sup>

A comparison of the EDAX patterns of the samples before immersion and also after immersion in the NaCl and  $H_2SO_4$  media indicates the following:

The parent samples as prepared contain Magnesium as is evident from **Figure 13**, but this magnesium content is retained even after immersion in NaCl, as evident from the **Figure 14** after immersion.

The magnesium content of the samples was found to be lost during immersion in the solution of  $H_2SO_4$  after 120 d, which is shown in **Figure 15**. This fall is in the magnesium content of the samples in  $H_2SO_4$ . Immersion may be attributed to the migration of  $Mg^{2+}$  from the samples to the  $H_2SO_4$  medium forming  $MgSO_4$  (soluble). The results are good agreement with previous literatures.<sup>36</sup>

#### 4 CONCLUSION

From the experimental investigation the following conclusions can be drawn. There is an improvement in strength with respect to the age observed for a maximum period of 180 d in all the mixes. The geopolymer con-

crete with GBFS (100 %) performed better than the other mixes with fly ash and GBFS combination during ambient curing. A geopolymer concrete mix with 40 % replacement of fly ash to GBFS performed well in chloride environment with a reduction of 24 % in comparison to the geopolymer concrete with GBFS (100 %) having a reduction rate of 42 %. The geopolymer concrete mix with 40 % replacement of fly ash to GBFS performed well in the acid environment with a reduction rate of 53 % in comparison to geopolymer concrete prepared with GBFS (100 %) has a reduction rate of 85 %. In general, the reduction rate increases with the increase in replacement levels of fly ash to GBFS in the geopolymer concrete in both the chloride and acid environment. The SEM and EDAX images after 120 d of immersion in acid and chloride environment show the deterioration, same as that of previous researchers. The geopolymer concrete prepared with GBFS can be replaced by fly ash (40 %) as it performs equally well and satisfies all the durability properties in both the chloride and acid environments.

#### Acknowledgement

The authors are very thankful to the management of Sri Venkateswara college of Engineering, Sri Perumbudur and College of Engineering Guindy, Anna University, Chennai for providing facilities to carry out the work.

#### 5 REFERENCES

- <sup>1</sup> B. V. Rangan, D. Hardjito, Development and properties of low calcium fly ash based Geopolymer concrete, Research report GC-1, Faculty of Engineering, Curtin's University of Technology, Perth, Australia 2005
- <sup>2</sup> P. Duxson, A. Fernandez-Jimenez, J. L. Provis, G. C. Lukey, A. Palomo, J. S. J. Van Deventer, Geopolymer technology: the current state of the art, *Journal of Materials Science*, 42 (2007) 9, 2917–2933, doi:10.1007/s10853-006-0637-z
- <sup>3</sup> J. L. Provis, G. C. Lukey, J. S. J. van Deventer, Do geopolymers actually contain nanocrystalline zeolites? A reexamination of existing results, *Chem. Mater.*, 17 (2005) 12, 3075–3085, doi:10.1021/cm050230i



- <sup>4</sup> P. Duxson, J. L. Provis, G. C. Lukey, J. S. J. Van Deventer, The role of inorganic polymer technology in the development of "Green Concrete", *Cement and Concrete Research*, 37 (2007) 12, 1590–1597, doi:10.1016/j.cemconres.2007.08.018
- <sup>5</sup> T. W. Cheng, J. P. Chiu, Fire-resistant geopolymer produced by granulated blast furnace slag, *Minerals Engineering*, 16 (2003) 3, 205–210, doi:10.1016/S0892-6875(03)00008-6
- <sup>6</sup> T. Bakharev, Durability of Geopolymer Materials in Sodium and Magnesium Sulfate Solutions, *Cement and Concrete Research*, 35 (2005) 6, 1233–1246, doi:10.1016/j.cemconres.2004.09.002
- <sup>7</sup> M. Sofi, J. S. J. van Deventer, P. A. Mendis, G. C. Lukey, Engineering properties of inorganic polymer concretes (IPCs), *Cement and Concrete Research*, 37 (2007) 2, 251–57, doi:10.1016/j.cemconres.2006.10.008
- <sup>8</sup> J. Davidovits, *Geopolymer chemistry and application*, Institute of Geopolymer, 16 rue GalileeF-02100 Saint Quentin, France, 2008, 585
- <sup>9</sup> K. Somna, C. Jaturapitakkul, P. Kajitvichyanukul, P. Chindaprasirt, NAOH-activated ground fly ash geopolymer cured at ambient temperature, *Fuel*, 90 (2011) 6, 2118–2124, doi:10.1016/j.fuel.2011.01.018
- <sup>10</sup> S. Ahmari, L. Zhang, Production of eco-friendly bricks from copper mine tailings through geopolymerization, *Construction and Building Materials*, 29 (2012), 323–331, doi:10.1016/j.conbuildmat.2011.10.048
- <sup>11</sup> T. Tho-in, V. Sata, P. Chindaprasirt, C. Jaturapitakkul, Pervious high-calcium fly ash geopolymer concrete, *Construction and Building Materials*, 30 (2012), 366–371, doi:10.1016/j.conbuildmat.2011.12.028
- <sup>12</sup> W. D. A. Rickard, J. Temuujin, A. van Riessen, Thermal analysis of geopolymer pastes synthesised from five fly ashes of variable composition, *Journal of Non-Crystalline Solids*, 358 (2012) 15, 1830–1839, doi:10.1016/j.jnoncrysol.2012.05.032
- <sup>13</sup> F. Škvara, L. Kopecky, J. Nemeček, Z. Bittnar, Microstructure of geopolymer materials based on fly ash, *Ceramics - Silikaty*, 50 (2006) 4, 208–215
- <sup>14</sup> A. Fernandez-Jimenez, I. Garcia-Lodeiro, A. Palamo, Durability of alkali-activated fly ash cementitious materials, *Journal of Materials Science*, 42 (2007) 9, 3055–3065, doi:10.1007/s10853-006-0584-8
- <sup>15</sup> N. W. Chen-Tan, A. van Riessen, C. V. Ly., D. C. Southam, Determining the reactivity of a fly ash for production of geopolymer, *J. Am. Ceram. Soc.*, 92 (2009) 4, 881–887, doi:10.1111/j.1551-2916.2009.02948x
- <sup>16</sup> X. Guo, H. Shi, W. Dick, Use of heat treated water treatment residuals in fly ash-based geopolymers, *J. Am. Ceram. Soc.*, 93 (2010) 1, 272–278, doi:10.1111/j.1551-2916.2009.03331x
- <sup>17</sup> M. Guerrieri, J. G. Sanjayan, Behaviour of combined fly ash/slag-based geopolymers when exposed to high temperatures, *Fire and Materials*, 34 (2010) 4, 163–175, doi:10.1002/fam.1014
- <sup>18</sup> S. K. Nath, S. Kumar, Influence of iron making slags on strength and microstructure of fly ash geopolymer, *Construction and Building Materials*, 38 (2013), 924–930, doi:10.1016/j.conbuildmat.2012.09.070
- <sup>19</sup> P. Duxson, S. W. Mallicoat, G. C. Lukey, W. M. Kriven, J. S. J. van Deventer, The effect of alkali and Si/Al ratio on the development of mechanical properties of metakaolin-based geopolymers, *Colloids and Surfaces A*, 292 (2007) 1, 8–20, doi:10.1016/j.colsurfa.2006.05.044
- <sup>20</sup> P. Chindaprasirt, C. Jaturapitakkul, W. Chalee, U. Rattanasak, Comparative study on the characteristics of fly ash and bottom ash geopolymers, *Waste Management*, 29 (2009) 2, 539–543, doi:10.1016/j.wasman.2008.06.023
- <sup>21</sup> P. Duxson, J. L. Provis, G. C. Lukey, S. W. Mallicoat, W. M. Kriven, J. S. J. van Deventer, Understanding the relationship between geopolymer composition, microstructure and mechanical properties, *Colloids and Surfaces A*, 269 (2005) 1–3, 47–58, doi:10.1016/j.colsurfa.2005.06.060
- <sup>22</sup> J. Wongpa, K. Kiattikomol, C. Jaturapitakkul, P. Chindaprasirt, Compressive strength, modulus of elasticity, and water permeability of inorganic polymer concrete, *Materials and Design*, 31 (2010) 10, 4748–4754, doi:10.1016/j.matdes.2010.05.012
- <sup>23</sup> C. Shi, A. Fernandez-Jimenez, A. Palomo, New cements for the 21<sup>st</sup> Century: The pursuit of an alternative to Portland cement, *Cement and Concrete Research*, 41 (2011) 7, 750–763, doi:10.1016/j.cemconres.2011.03.016
- <sup>24</sup> S. A. Bernal, D. Herfort, J. Skibsted, Hybrid binders based on sulphate-activated Portland clinker and metakaolin, In: *Proceedings of XII international congress on the chemistry of cement*, Madrid, Spain, 2011 (CD-Rom)
- <sup>25</sup> S. A. Bernal, R. Mejia de Gutierrez, J. L. Provis, Engineering and durability properties of concretes based on alkali-activated granulated blast furnace slag/metakaolin blends, *Construction and Building Materials*, 33 (2012), 99–108, doi:10.1016/j.conbuildmat.2012.01.017
- <sup>26</sup> S. Kumar, R. Kumar, S. P. Mehrotra, Influence of granulated blast furnace slag on the reaction, structure and properties of fly ash based geopolymer, *Journal of Materials Science*, 45 (2010) 3, 607–615, doi:10.1007/s10853-009-3934-5
- <sup>27</sup> C. Shi, R. L. Day, Early strength development and hydration of alkali-activated blast furnace slag/fly ash blends, *Advances in Cement Research*, 11 (1999) 4, 189–196, doi:10.1680/adcr.1999.11.4.189
- <sup>28</sup> A. Buchwald, H. Hilbig, Ch. Kaps, Alkali-activated metakaolin-slag blends - performance and structure in dependence of their composition, *Journal of Materials Science*, 42 (2007) 9, 3024–3032, doi:10.1007/s10853-006-0525-6
- <sup>29</sup> Z. Li, S. Liu, Influence of slag as additive on compressive strength of fly ash-based geopolymer, *J. Mater. Civ. Eng.*, 19 (2007) 6, 470–474, doi:10.1061/(ASCE)0899-1561(2007)19:6(470)
- <sup>30</sup> F. Puertas, A. Fernandez-Jimenez, Mineralogical and microstructural characterisation of alkali-activated fly ash/slag pastes, *Cement and Concrete Composites*, 25 (2003) 3, 287–292, doi:10.1016/s0958-9465(02)00059-8
- <sup>31</sup> T. Bakharev, Resistance of geopolymer materials to acid attack, *Cement and Concrete Research*, 35 (2005) 4, 658–670, doi:10.1016/j.cemconres.2004.06.005
- <sup>32</sup> S. Thokchom, P. Ghosh, S. Ghosh, Resistance of fly ash based geopolymer mortars in sulfuric acid, *ARPN Journal of Engineering and Applied Sciences*, 4 (2009) 1, 65–70
- <sup>33</sup> V. Sata, A. Sathonsaowaphak, P. Chindaprasirt, Resistance of lignite bottom ash geopolymer mortar to sulfate and sulfuric acid attack, *Cement and Concrete Composites*, 34 (2012) 5, 700–708, doi:10.1016/j.cemconcomp.2012.01.010
- <sup>34</sup> S. A. Bernal, Carbonatacion de concretos producidos en sistemas binarios de unaescoria siderurgica, Ph.d. Thesis, Universidad dei valle, Cali, Colombia, 2009
- <sup>35</sup> M. O. Yusuf, M. A. M. Johari, Z. A. Ahmad, M. Maslehuddin, Strength and microstructure of alkali-activated binary blended binder containing palm oil fuel ash and ground blast-furnace slag, *Construction and Building Materials*, 52 (2014), 504–510, doi:10.1016/j.conbuildmat.2013.11.012
- <sup>36</sup> K. Kannapiran, T. Sujatha, S. Nagan, Resistance of reinforced geopolymer concrete beams to acid and chloride migration, *Asian Journal of Civil Engineering*, 14 (2013) 2, 225–238



## THE SIZE EFFECT OF HEAT-TRANSFER SURFACES ON BOILING

### VPLIV VELIKOSTI POVRŠIN, KI PRENAŠAJO TOPLOTO NA VRENJE

**Petr Kracík, Marek Balas, Martin Lisy, Jiří Pospíšil**

Brno University of Technology, Institute of Power Engineering, Faculty of Mechanical Engineering,  
Technická 2896/2, 616 69 Brno, Czech Republic  
kracik@fme.vutbr.cz

*Prejem rokopisa – received: 2015-07-31; sprejem za objavo – accepted for publication: 2015-12-14*

doi:10.17222/mit.2015.245

A sprinkled tube bundle is frequently used in technology processes where an increase or decrease of a liquid temperature in a very low-pressure environment is required. Phase transitions of the liquid very often occur at low temperatures at pressures ranging in the thousands of pascals, which enhances the heat transfer. This paper focuses on the issue of a heat-transfer coefficient that is experimentally examined at the surface of a tube bundle. The tube is located in a low-pressure chamber where the vacuum is generated using an exhaustor via an ejector. The tube consists of smooth copper tubes of 12 mm diameter placed horizontally one above another. Heating water flows in the bundle from the bottom towards the top at an average input temperature of approximately 40 °C and an average flow rate of approximately 7.2 L min<sup>-1</sup>. A falling film liquid at an initial temperature of approximately 15 °C at an initial tested pressure of approximately 97 kPa (atmospheric pressure) is sprinkled onto the tubes' surface. Afterwards, the pressure in the chamber is gradually decreased. When reaching the minimum pressure of approximately 3 kPa (abs) the water partially evaporates at the lower part of the bundle. Consequently, the influence of the falling film liquid temperature increase is tested. This gradually leads to the boiling of water in a significant part of the bundle and the residual cooling liquid that drops back to the bottom of the vessel is almost not heated anymore. In this paper we present the influences of the size of the heat-transfer surfaces.

Keywords: sprinkled tube bundle, water, under pressure, heat transfer

Pršenje po snopu cevi se pogosto uporablja v tehnoloških procesih, kjer se zahteva povišanje ali zmanjšanje temperature tekočine v okolju z nizkim tlakom. Fazni prehod tekočine se pogosto pojavi pri nizkih temperaturah in tlakih v območju nekaj tisoč paskalov, kar vpliva na prenos toplote. Članek se nanaša na koeficient prenosa toplote, ki je eksperimentalno določen na površini snopa cevi. Cev je nameščena v nizkotlačni komori, kjer se vakuum ustvarja s pomočjo aspiratorja preko ejetorja. Snop cevi sestavljajo gladke bakrene cevi, premera 12 mm, ki so nameščene horizontalno ena nad drugo. Voda za ogrevanje teče v snop od spodaj proti vrhu s povprečno temperaturo okrog 40 °C in povprečno hitrostjo pretoka okrog 7,2 L min<sup>-1</sup>. Padajoč vodni film z začetno temperaturo okrog 15 °C in z začetnim tlakom okrog 97 kPa (atmosferski tlak) prši po površini cevi. Tlak se v komori postopno znižuje. Ko doseže minimalni tlak okrog 3 kPa (absolutni tlak) voda delno izhlapi na spodnjem delu snopa. Posledično je preizkušen vpliv naraščanja temperature padajoče vode. To postopno privede do vrenja vode na večjem delu površine snopa in preostala hladilna tekočina, ki kaplja na dno posode, se skoraj ne segreje več. Članek predstavlja vpliv velikosti površine kjer se prenaša toplota.

Ključne besede: pršenje po snopu cevi, podtlak, prenos toplote

## 1 INTRODUCTION

Due to a decreasing supply of fossil fuels and their increasing price, the minimization of energy consumption becomes an important priority, followed by saving the primary fuel entering energy processes that are supposed to achieve the maximum efficiency possible, and last but not least, using so-called renewable sources of energy. Among these renewable sources, a biomass combustion technology is mainly used to generate thermal energy and electricity in the Czech Republic. Current research aims to reflect these demands well. For instance, research is conducted in the field of optimization of technology for wood mass preparation<sup>1,2</sup> before combustion or further utilization for pellets' production. At the Department of Power Engineering long-term research focuses, apart from other things, on the utilization of waste thermal energy, which is found, for example, in

condensers at large energy units, for the possible generation of cool in absorption units.

One of the basic elements of an absorption circuit is an evaporator, inside of which the heat-carrier substance is sprayed onto a tube bundle. Due to a low pressure environment inside the container where the bundle is located the falling film liquid at the tube bundle boils. The heat necessary for boiling is derived from a cooled substance flowing inside the tube bundle.

Under ideal conditions water boils at the whole surface of an exchanger, but in practice it must be considered that in original spots of contact between the water and the exchanger wall the water will not boil at the tubes' surface, but the cooling liquid will merely be heated-up. This paper deals with this very situation – heat transfer behaviour when heating a sprinkled water film that boils in a low-pressure environment for a real tube bundle.

Research in the area of sprinkled exchangers can be divided into two major parts. The first part is research on heat transfer and a determination of the heat-transfer coefficient with respect to sprinkled tube bundles for various liquids, whether boiling or not. For water as the falling film liquid, they were, for example<sup>3-7</sup>. The second part is testing of the sprinkle modes for various tube diameters, tube pitches and tube materials and a determination of individual modes' interface. This area is mainly researched in<sup>8-10</sup>.

All the results published so far for water as the falling film liquid apply to one to three tubes, for which the mentioned relations studied are determined in rigid laboratory conditions, defined strictly in advance. The sprinkled tubes were not viewed from the operational perspective where there are more tubes and various modes can occur in different parts with various heat-transfer values.

## 2 EXPERIMENTAL PART

For the purposes of examination of the heat transfer for sprinkled tube bundles a test apparatus was constructed (**Figure 1**). A tube bundle at which a heat transfer from a heated water flowing inside the tubes into a falling film liquid is studied is placed in a vessel where the low pressure is created by an exhaustor through an ejector.

The test apparatus chamber is a cylindrical vessel with a length of 1.2 m with three apertures in which the tube bundle of an examined length of 940.0 mm is inserted. The tube bundle is installed in two fitting metal sheets which define the sprinkled area. The bundle consists of eight copper tubes of diameter 12.0 mm situated horizontally, one above another, with a distribution tube above them, with apertures of the diameter from 1.0 mm to 9.2 mm. The bundle can be operated using only the first four or six tubes too.

Two closed loops are connected to the chamber. A heating one and a sprinkling one. The heating liquid flowing inside the tubes is intended for an overpressure up to 1.0 MPa. The second loop contains flowing falling film liquid. There is a pump, a regulation valve, a flow meter and plate heat exchangers attached to both loops.

The plate heat exchanger at the heating loop is connected to a gas boiler, which supplies heat to the heating liquid. The sprinkling loop uses two plate heat exchangers. In the first one the falling film liquid is cooled by cold drinking water from the water mains and the falling film liquid is cooled in the second exchanger by drinking water cooled in a cooler, which regulates the temperature up to 1.0 °C. In order to enable visual control, the heating loop also includes a manometer and a thermometer. The thermal status in individual loops is measured by wrapped unearthed T-type thermocouples on the agents' input and output from the vessel. All the thermocouples were calibrated in the CL1000 Series calibration furnace, which maintains a given temperature with an accuracy of ±0.15 °C. None of the thermocouples exceeded the error ±0.5 °C within the studied range from 28 °C to 75 °C. That is why the total error for the temperature measurement is set uniformly for all the thermocouples along the whole studied range ±0.65 °C.

There are three vacuum gauges measuring the low pressure. The first vacuum gauge is designed for visual control and is a mercury meter, the second one is a

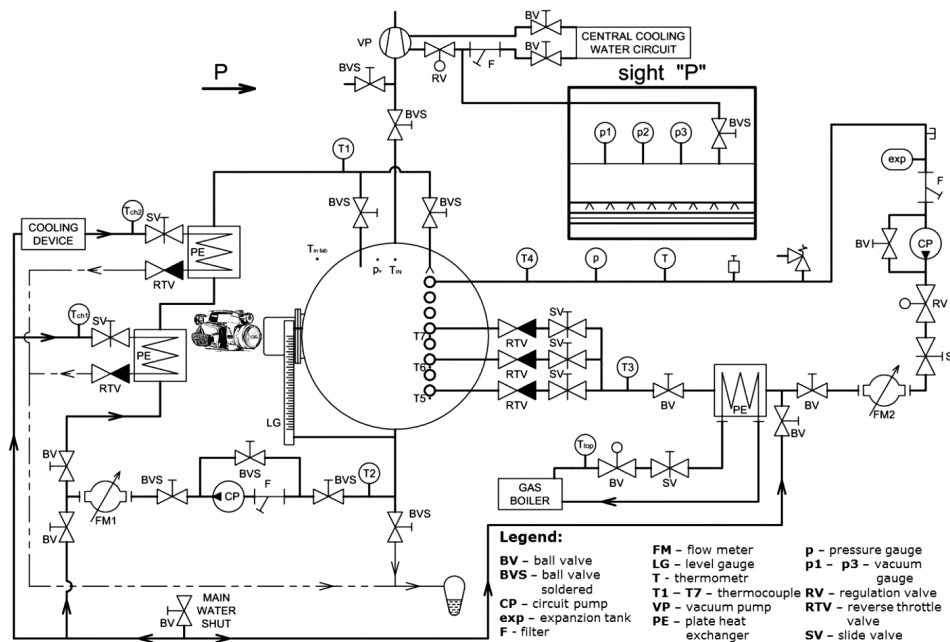


Figure 1: Measurement apparatus diagram

Slika 1: Shema merilnih naprav



digital vacuum gauge Baumer TED6 and enables measurements within the whole desired low-pressure range, but it is less accurate with lower pressure values. To allow a precise measuring of the low spectrum, a third digital vacuum gauge in the range 2.0 kPa to 0 Pa is used. The accuracy of a vacuum gauge, the results of which have been used for the assessment, is 0.5 % from the measured range, i.e.,  $\pm 0.5$  kPa.

Electromagnetic flow meters Flomag 3000 attached to both loops measure the flow rate. The flow meters' range is 0.0078 to 0.9424 L s<sup>-1</sup>, where the accuracy is 0.5 % from the measured range, i.e.  $\pm 0.00467$  L s<sup>-1</sup>. All the examined quantities are either directly (thermocouples) or via transducers scanned by measuring cards DAQ 56 with a frequency of 0.703 Hz.

### 3 METHODOLOGY OF THE DATA ASSESSMENT

The assessment of the measured data is based on the thermal balance between the operating liquid circulating inside the tubes and a sprinkling loop according to the law of conservation of energy. Heat transfer is realized by convection, conduction and radiation. At lower temperatures the heat transferred by radiation is negligible; therefore, it is excluded from further calculations. The calculation of the studied heat-transfer coefficient is based on Newton's heat-transfer law and Fourier's heat-conduction law that have been used to form the following relation in Equation (1):

$$\alpha_0 = \frac{1}{2\pi r_0 \left[ \frac{1}{k_s} - \frac{1}{2\pi\alpha_i r_i} - \frac{1}{2\pi\lambda_s} \cdot \ln\left(\frac{r_0}{r_i}\right) \right]} \quad (1)$$

where  $\alpha_0$  [W m<sup>-2</sup>K<sup>-1</sup>] is the heat transfer coefficient at the sprinkled tubes' surface

$\alpha_i$  [W m<sup>-2</sup> K<sup>-1</sup>] is the heat-transfer coefficient at the inner side of a tube set for a fully developed turbulent flow according to<sup>11</sup>,

$r_o$ ;  $r_i$  [m] are the outer and inner tube radii

$\lambda_s$  [W m<sup>-1</sup> K<sup>-1</sup>] is the thermal conductivity

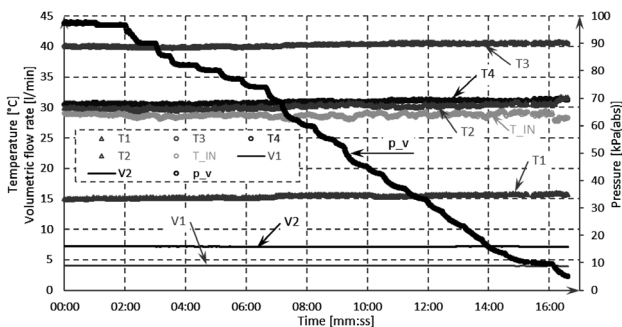


Figure 2: Record of the main measured quantities

Slika 2: Zapis glavnih izmerjenih količin

$k_s$  [W m<sup>-1</sup> K<sup>-1</sup>] is the heat admittance based on the above-mentioned laws governing heat transfer, which is calculated from the heat balance of the heating side of the loop, which is why the following Equation (2) must be valid:

$$\dot{Q}_s = k_s L \Delta T_{ln} = \dot{M}_{34} c_p \left( \frac{t_3 + t_4}{2} \right) (t_3 - t_4) \quad (2)$$

where  $M_{34}$  [kg s<sup>-1</sup>] is the mass flow of heating water  
 $c_p$  [J kg<sup>-1</sup> K<sup>-1</sup>] is the specific heat capacity of water at constant pressure related to the mean temperature inside the loop

$L$  [m] is the total length of the bundle

$\Delta T_{ln}$  [K] is a logarithmic temperature gradient where a counter-current exchanger was considered

The final heat-transfer coefficient for various falling film liquid flow rates is recalculated into the Nusselt number, due to its more common application for a results comparison. For sprinkled exchangers the following form is normally used<sup>3,4</sup> for the recalculation of the heat-transfer coefficient into the Nusselt number:

$$Nu = \alpha_0 \sqrt[3]{\frac{v^2}{g\lambda^3}} \quad [-] \quad (3)$$

where  $\nu$  [m<sup>2</sup> s<sup>-1</sup>] is the kinematic viscosity,

$g$  [m s<sup>-2</sup>] is the acceleration due to gravity and

$\lambda$  [W m<sup>-1</sup> K<sup>-1</sup>] is the liquid film's thermal conductivity.

### 4 RESULTS

Tube bundles comprising four, six and eight copper tubes were tested and the results are given in this paper. Constant flow rates of the sprinkling liquid and the heating liquid of the required temperature were set first; the pressure in the chamber was then slowly lowered. The initial pressure in the chamber at that moment always equaled the atmospheric pressure.

Three temperature gradients of sprinkling water and heating water 20/40, 15/40 and 20/50 were tested. The first number designates the temperature of the sprinkling water in the distribution tube; the other number designates the temperature of the heating water entering the bundle. The thermal differences were (20, 25 and 30) °C. The flow rate of the heating water in all the experiments was kept at approximately 7.2 L min<sup>-1</sup>. The flow rates of the sprinkling liquid were carefully selected and remained "constant" throughout the experiments.

Figure 2 shows a recording of the main quantities measured in one of the experiments. Only four tubes were heated in this experiment, which lasted 16 min and 37 s (horizontal axis of the chart). The average temperature of the heating water entering the bottom tube (T3) was 40.2 °C  $\pm$  0.3 °C, and the average flow rate of the heating water (V2) was 7.16  $\pm$  0.03 L min<sup>-1</sup>. The temperature of the heating water leaving the exchanger is designated as (T4) in the chart. The average temperature

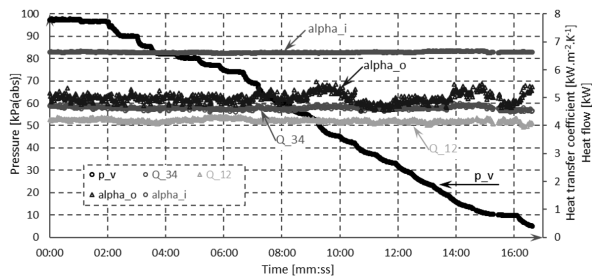


**Figure 3:** Quantities derived from the measurements  
**Slika 3:** Količine pridobljene iz meritev

of the sprinkling water entering the distribution tube was  $15.4\text{ }^{\circ}\text{C} \pm 0.3\text{ }^{\circ}\text{C}$ , and average flow rate ( $V_1$ ) was  $4.03 \pm 0.02\text{ L min}^{-1}$ . The mass flow of the sprinkling liquid related to the length of the sprinkled area (which is 0.940 mm for all three exchangers) is more commonly used for the comparison. The said mass flow was  $0.0713 \pm 0.0004\text{ kg/(s m)}$ , i.e., the average Reynolds number was  $304.4 \pm 2.1 [-]$ . Other values in the chart include the current pressure in the testing chamber ( $p$ ) (in absolute values), and the temperature of the sprinkling water ( $T_2$ ) beyond the tube bundle where the water was heated.

**Figure 3** shows the quantities derived from the measurements presented in the previous figure. The quantities in the chart depend on the duration of the experiment. The quantities represented in the chart include the current heat flow extracted from the heating water ( $Q_{34}$ ), the current heat flow absorbed by the sprinkling liquid ( $Q_{12}$ ), the heat-transfer coefficient on the inside tube wall ( $\alpha_i$ ) and the analyzed heat-transfer coefficient on the surface of the tube ( $\alpha_o$ ). The chart also presents the current pressure in the testing

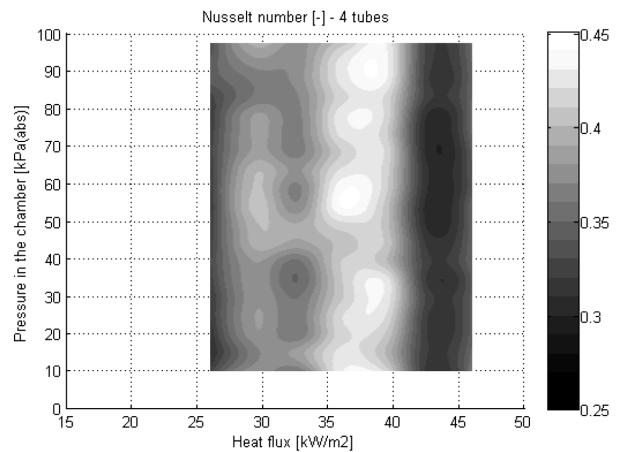


**Figure 4:** Dependency of the Nusselt number on the pressure in the testing chamber and the heat flow extracted from the heating liquid – four tubes

**Slika 4:** Odvisnost Nusseltovega števila od tlaka v preizkusni komori in toplotni tok pridobljen z tekočine za ogrevanje – štiri cevi

chamber. The course of the analysed heat-transfer coefficient clearly shows that decrease in pressure in the chamber results in a slightly increased coefficient. The coefficient depends mostly on the temperature of the heating water and the sprinkling water, and not so much on their flow rates.

Altogether 21 experiments on tube bundles with four, six and eight tubes were performed, that is seven experiments for each bundle. **Table 1** presents the measured parameters that helped identify, among others, the mass flow of the sprinkling liquid. The parameters were related to the length of the sprinkled area, the corresponding Reynolds number, and the heat flow extracted from the

**Table 1:** Core values of the experiments

**Tabela 1:** Temeljne vrednosti eksperimentov

tubes	$T_1$ (°C)	$T_2$ (°C)	$T_3$ (°C)	$T_4$ (°C)	$V_1$ (L/min)	$V_2$ (L/min)	$\Gamma$ (kg/(s.m))	Re [-]	$q$ (kW/m <sup>2</sup> )
4	$19.7 \pm 0.1$	$32.1 \pm 0.2$	$40.1 \pm 0.1$	$32.7 \pm 0.1$	$4 \pm 0$	$7.2 \pm 0$	$0.0711 \pm 0.0005$	$326 \pm 2.4$	$26.03 \pm 0.38$
	$20.2 \pm 0.1$	$29.4 \pm 0.3$	$40.3 \pm 0.3$	$31.7 \pm 0.2$	$6 \pm 0$	$7.2 \pm 0$	$0.1065 \pm 0.0004$	$476.9 \pm 2.9$	$30.26 \pm 0.64$
	$15.4 \pm 0.2$	$30.2 \pm 0.4$	$40.2 \pm 0.3$	$30.9 \pm 0.3$	$4 \pm 0$	$7.2 \pm 0$	$0.0713 \pm 0.0004$	$304.3 \pm 1.5$	$32.66 \pm 0.29$
	$15.7 \pm 0.1$	$28.5 \pm 0.3$	$39.9 \pm 0.4$	$29.9 \pm 0.2$	$5 \pm 0$	$7.2 \pm 0$	$0.0889 \pm 0.0003$	$373.4 \pm 1.4$	$34.97 \pm 0.78$
	$15.5 \pm 0.2$	$27.3 \pm 0.2$	$40.6 \pm 0.1$	$29.8 \pm 0.1$	$6 \pm 0$	$7.1 \pm 0$	$0.1065 \pm 0.0006$	$440.3 \pm 3.3$	$37.57 \pm 0.4$
	$19.7 \pm 0.2$	$38.4 \pm 0.4$	$50.2 \pm 0.2$	$38.8 \pm 0.2$	$4 \pm 0$	$7.2 \pm 0$	$0.0709 \pm 0.0005$	$348.4 \pm 2.7$	$39.76 \pm 0.48$
6	$20.1 \pm 0.2$	$33.6 \pm 0.2$	$50.2 \pm 0.2$	$37.1 \pm 0.1$	$6 \pm 0$	$7.2 \pm 0$	$0.1064 \pm 0.0005$	$498.9 \pm 2.3$	$46.08 \pm 0.46$
	$20.2 \pm 0.1$	$35.6 \pm 0.2$	$40.6 \pm 0.1$	$32.1 \pm 0.1$	$4 \pm 0$	$7.2 \pm 0$	$0.0709 \pm 0.0002$	$339.8 \pm 1.6$	$19.94 \pm 0.21$
	$19.6 \pm 0.2$	$32.0 \pm 0.2$	$39.7 \pm 0.2$	$29.6 \pm 0.3$	$6 \pm 0$	$7.2 \pm 0$	$0.1065 \pm 0.0003$	$487.2 \pm 2.9$	$23.8 \pm 0.33$
	$15.4 \pm 0.1$	$33.2 \pm 0.3$	$40.4 \pm 0.3$	$30.3 \pm 0.2$	$4 \pm 0.1$	$7.1 \pm 0$	$0.0713 \pm 0.0017$	$309.3 \pm 7.9$	$23.71 \pm 0.49$
	$15.5 \pm 0.2$	$32.3 \pm 0.2$	$40.2 \pm 0.3$	$28.2 \pm 0.2$	$5 \pm 0$	$7.2 \pm 0$	$0.0888 \pm 0.0002$	$389.1 \pm 1.7$	$28.2 \pm 0.36$
	$15.4 \pm 0.3$	$31.3 \pm 0.5$	$40.5 \pm 0.2$	$28.0 \pm 0.3$	$6 \pm 0$	$7.2 \pm 0$	$0.1065 \pm 0.0003$	$444.4 \pm 3.5$	$29.03 \pm 0.38$
8	$20.2 \pm 0.2$	$40.8 \pm 0.8$	$50.4 \pm 0.3$	$36.0 \pm 0.2$	$5 \pm 0$	$7.2 \pm 0$	$0.0885 \pm 0.0005$	$448.8 \pm 5.2$	$34.03 \pm 0.38$
	$19.9 \pm 0.1$	$38.5 \pm 0.5$	$49.5 \pm 0.1$	$34.2 \pm 0.1$	$6 \pm 0$	$7.2 \pm 0$	$0.1063 \pm 0.0003$	$524.7 \pm 3.6$	$35.64 \pm 0.28$
	$20.3 \pm 0.1$	$37.2 \pm 0.4$	$40.3 \pm 0.2$	$31.1 \pm 0.1$	$4 \pm 0$	$7.2 \pm 0$	$0.0709 \pm 0.0005$	$346.5 \pm 3.2$	$16.28 \pm 0.31$
	$20.2 \pm 0.1$	$34.7 \pm 0.2$	$40.3 \pm 0.1$	$28.9 \pm 0.1$	$6 \pm 0$	$7.2 \pm 0$	$0.1064 \pm 0.0004$	$505 \pm 2.3$	$19.94 \pm 0.13$
	$15.3 \pm 0.2$	$36.3 \pm 0.3$	$40.2 \pm 0.1$	$28.7 \pm 0.2$	$4 \pm 0$	$7.2 \pm 0$	$0.071 \pm 0.0003$	$324.7 \pm 2.5$	$20.25 \pm 0.22$
	$15.6 \pm 0.3$	$34.1 \pm 0.4$	$39.9 \pm 0.4$	$27.1 \pm 0.3$	$5 \pm 0$	$7.2 \pm 0$	$0.0887 \pm 0.0003$	$397 \pm 2.9$	$22.3 \pm 0.53$
8	$15.3 \pm 0.5$	$32.8 \pm 0.6$	$39.7 \pm 0.3$	$26.1 \pm 0.5$	$6 \pm 0$	$7.2 \pm 0$	$0.1063 \pm 0.0006$	$467.4 \pm 6.5$	$23.82 \pm 0.51$
	$20.0 \pm 0.2$	$45.8 \pm 1.2$	$50.4 \pm 0.2$	$36.3 \pm 0.4$	$4 \pm 0$	$7.2 \pm 0$	$0.0709 \pm 0.0003$	$378 \pm 3.5$	$24.93 \pm 0.81$
	$20.2 \pm 0.1$	$41.2 \pm 0.7$	$50.0 \pm 0.3$	$33.0 \pm 0.3$	$6 \pm 0$	$7.2 \pm 0$	$0.1065 \pm 0.0003$	$542.2 \pm 4.2$	$29.73 \pm 0.27$

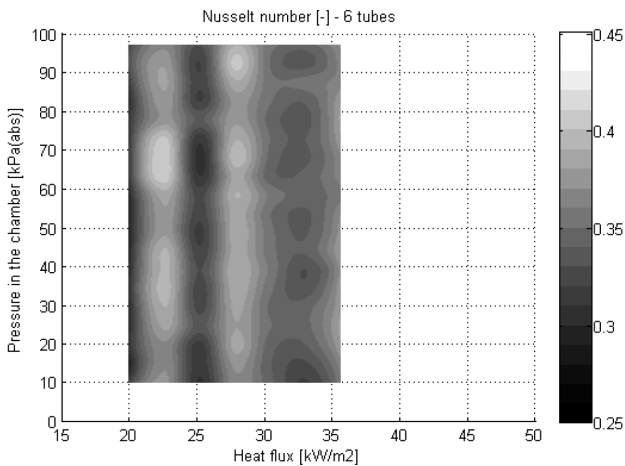


**Figure 5:** Dependency of the Nusselt number on the pressure in the testing chamber and heat flow extracted from the heating liquid – six tubes

**Slika 5:** Odvisnost Nusseltovega števila od tlaka v preizkusni komori in toplota pridobljena iz tekočine za ogrevanje – šest cevi

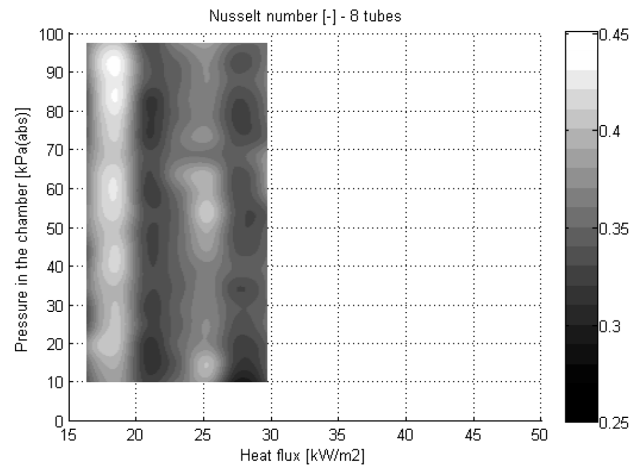


**Figure 6:** Dependency of the Nusselt number on the pressure in the testing chamber and the heat flow extracted from the heating liquid – eight tubes

**Slika 6:** Odvisnost Nusseltovega števila od tlaka v preizkusni komori in toplota pridobljena iz tekočine za ogrevanje – osem cevi

heating water, which was related to the size of the heat-exchanging surface.

The heat-transfer coefficient on the surface of the tube bundle was later converted to the Nusselt number. Values acquired at pressures ranging from 5.0 kPa(abs) to 95.0 kPa(abs) in 5.0 kPa increments, and values acquired at atmospheric pressure were selected from the data measured in each experiment. The values were then averaged for each pressure. This helped us to develop matrices of the same sizes for a particular bundle length. The matrices were interpolated using a cubic curve in Matlab software. Contour graphs, shown in **Figures 4 to 6**, were developed using these new matrices. The presented Nusselt number in the figures is dependent on the pressure in the chamber (vertical axis) and the extracted heat flow of the heating water (horizontal axis). The range of the Nusselt number is identical for all three charts, i.e., 0.15 to 0.46 [-], so that individual phases can be compared. However, this procedure was disabled to observe slight increases in the Nusselt number as the pressure decreases in particular measurement sessions.

All three analysed sizes of the tube bundle clearly show three vertical zones that do not connect; these are a result of a different temperature gradient. The temperature gradient is 20/40 in the zone 1, 15/40 in the zone 2, and 20/50 in the zone 3. Temperature gradient 15/40 with the highest Nusselt number seems to be the best option for all three analysed lengths of the bundle. The Nusselt number dropped by almost 0.2 [-] when the temperature of heating water increased. The Nusselt number also drops at very low pressures. The decrease is caused by the fact that heat extracted from the heating liquid is also used for evaporation and not only for heating the heating water. However, the decrease is not very significant and the boiling occurs only at the bottom section of the tube bundle.

Concerning a tube bundle with four tubes, the maximum Nusselt number was attained at a specific heat flow of approximately 35 kW m<sup>-2</sup> and 38 kW m<sup>-2</sup>, which corresponds to a temperature gradient of 15/40 °C. The maxima ranged at values around 0.44 [-]. The larger the surface area and the lower the specific loading, the higher the values. In the case of a tube bundle with six tubes, the heat flow is approximately 28 kW m<sup>-2</sup>. In the case of a tube bundle with eight tubes, the maximum reached almost 0.46 [-] at a thermal load of approximately 24 kW m<sup>-2</sup>.

## 5 CONCLUSIONS

Sprinkled tube bundles are most commonly used as evaporators since they quickly separate the vapor phase and the liquid phase thanks to a thin liquid film. However, the practice proves that there is no boiling on the first affected tubes, only the liquid is heated. We describe in this paper how the surface area of the tubes affects the heat transfer coefficient on the tube surface. This effect was tested at three thermal differences: (15, 20 and 30) °C. After the flow rate of the heating and sprinkling liquids and their temperatures were set, only the pressure in the testing chamber was changed during the experiment. The initial pressure in the chamber was atmospheric pressure.

The pressure in the chamber and the exhaustion of the air-vapour mixture from the chamber (vapour was formed at the bottom part of the tube bundle at low pressures) had no major impact on the coefficient. It was the exhaustion itself which affected the boundary layers on the tube bundle. A significant change of the coefficient may come only if the boiling on the tube bundle increases.

The impact of the heat-exchanging surface area on the heat-transfer coefficient is evident in zone 3 of parti-

cular bundles where the thermal gradient was 20/50 °C. The increase in the surface area results in a decrease in the specific loading of the area but the heat-transfer coefficient increases.

### Acknowledgement

Presented results were obtained in frame of the project NETME CENTRE PLUS (LO1202), created with financial support from the Ministry of Education, Youth and Sports of the Czech Republic under the "National Sustainability Programme I".

### 6 REFERENCES

- <sup>1</sup> J. Beniák, J. Ondruška, V. Čáčko, Design Process of Energy Effective Shredding Machines for Biomass Treatment, *Acta Polytechnica*, 52 (2012) 5, 1210–2709
- <sup>2</sup> J. Beniák, P. Križan, M. Matúš, M. Kováčová, The Operating Load of a Disintegration Machine, *Acta Polytechnica*, 54 (2014) 1, 1210–2709, doi:10.14311/AP.2014.54.0001
- <sup>3</sup> L. H. Chien, Ch. H. Cheng, A Predictive Model of Falling Film Evaporation with Bubble Nucleation on Horizontal Tubes, *HVAC*, 12 (2006) 1, 1078–9669, doi:10.1080/10789669.2006.10391168
- <sup>4</sup> J. J. Lorenz, D. Yung, A Note on Combined Boiling and Evaporation of Liquid Films on Horizontal Tubes, *Journal of Heat Transfer*, 101 (1979) 1, 0022–1481, doi:10.1115/1.3450914
- <sup>5</sup> W. L. Owens, Correlation of Thin Film Evaporation Heat Transfer Coefficients for Horizontal Tubes, Proceedings of the Fifth Ocean Thermal Energy Conversion Conference, Miami Beach, Florida, 1978
- <sup>6</sup> W. H. Parken, L. S. Fletcher, V. Sernas, J. C. Han, Heat Transfer Through Falling Film Evaporation and Boiling on Horizontal Tubes, *Journal of Heat Transfer*, 112 (1990) 3, 0022–1481, doi:10.1115/1.2910449
- <sup>7</sup> V. Sernas, Heat Transfer Correlation for Subcooled Water Films on Horizontal Tubes, *Journal of Heat Transfer*, 101 (1979) 1, 0022–1481, doi:10.1115/1.3450913
- <sup>8</sup> R. Armbruster, J. Mitrovic, Patterns of Falling Film Flow over Horizontal Smooth Tubes, Proceedings of the 10th international heat transfer conference, Brighton, UK, 1994, 3
- <sup>9</sup> X. Hu, A. M. Jacobi, The Intertube Falling Film: Part 1 - Flow Characteristics, Mode Transitions, and Hysteresis, *Journal of Heat Transfer*, 118 (1996) 3, 0022–1481, doi:10.1115/1.2822678
- <sup>10</sup> J. F. Roques, V. Dupont, J. R. Thome, Falling Film Transitions on Plain and Enhanced Tubes, *Journal of Heat Transfer*, 124 (2002) 3, 0022–1481, doi:10.1115/1.1458017
- <sup>11</sup> M. Jícha, Heat and mass transfer, Brno, CERM, 2001, 1, 160



# EFFECT OF GAS ATMOSPHERE ON THE NON-METALLIC INCLUSIONS IN LASER-WELDED TRIP STEEL WITH Al AND Si ADDITIONS

## VPLIV PLINSKE ATMOSFERE NA NEKOVINSKE VKLJUČKE V LASERSKO VARJENEM TRIP JEKLU Z DODATKOM Al IN Si

Adam Grajcar<sup>1</sup>, Maciej Róžański<sup>2</sup>, Małgorzata Kamińska<sup>3</sup>,  
Barbara Grzegorzczak<sup>1</sup>

<sup>1</sup>Silesian University of Technology, Institute of Engineering Materials and Biomaterials, Konarskiego Street 18a, 44100 Gliwice, Poland

<sup>2</sup>Institute of Welding, Bl. Czesława Street 16-18, 44100 Gliwice, Poland

<sup>3</sup>Institute of Non Ferrous Metals, Sowinskiego Street 5, 44100 Gliwice, Poland  
adam.grajcar@polsl.pl

*Prejem rokopisa – received: 2015-08-12; sprejem za objavo – accepted for publication: 2015-11-04*

doi:10.17222/mit.2015.253

The present study aims to characterize the weldability of a multiphase, automotive steel containing Al and Si additions from the point of view of its tendency to form non-metallic inclusions. Laser welding tests of 2-mm-thick sheets were performed using the keyhole-welding mode and a solid-state laser. The tests were carried out in air and with the use of an argon atmosphere. The distribution, type and chemical composition of the non-metallic inclusions formed in the base metal and fusion zones were analysed. The effect of applying the protective gas on the type and amount of non-metallic inclusions was determined using light and scanning electron microscopy. The chemical composition of the identified particles was assessed using the EDS method. It was found that a protective gas has a beneficial effect on reducing the non-metallic inclusions, but only to a limited extent. The boundary between the complex oxides and the pure aluminium oxides was determined to be 2–3  $\mu\text{m}$ .

Keywords: TRIP steel, laser welding, non-metallic inclusions, protective gas, Ar atmosphere, oxidation

Namen te študije je opredeliti varivost s stališča tvorbe nekovinskih vključkov v večfaznem jeklu, ki vsebuje Al in Si, za avtomobilsko industrijo. Izvedeni so bili varilni preizkusi z laserjem na 2 mm debelih pločevinah z V zarez. Preizkusi so bili izvedeni na zraku in v zaščitni atmosferi argona. Analizirana je bila razporeditev, vrsta in kemijska sestava nekovinskih vključkov v osnovnem materialu in v coni zlivanja. Vpliv uporabe zaščitnega plina na vrsto in količino nekovinskih vključkov je bil določen s pomočjo svetlobne in vrstične elektronske mikroskopije. Kemijska sestava najdenih delcev je bila ugotovljena z metodo EDS. Ugotovljeno je bilo, da ima zaščitni plin ugoden vpliv na zmanjšanje nekovinskih vključkov le v omejenem obsegu. Meja med kompleksnimi oksidi in čistimi oksidi aluminija je bila določena kot 2-3  $\mu\text{m}$ .

Ključne besede: TRIP jeklo, lasersko varjenje, nekovinski vključki, zaščitni plin, atmosfera Ar, oksidacija

## 1 INTRODUCTION

Multiphase steels with a transformation-induced plasticity (TRIP) effect belong to the advanced high-strength steels (AHSS) used in the modern automotive industry. The beneficial balance between strength and ductility requires increased contents of Mn, Al and Si. Their total content in TRIP steels can reach 4 %.<sup>1-3</sup> Medium-Mn and high-Mn alloys require an even higher concentration of alloying elements.<sup>4-8</sup> Whereas a lot of efforts focus on the relationships between hot-working, heat-treatment, microstructure and mechanical properties, the weldability of AHSS has not received much attention so far.

M. S. Węglowski et al.<sup>9</sup> reported that the maximum hardness in the fusion zone of 0.07C-1Mn-0.4Cr dual-phase steel (which belongs to the 1<sup>st</sup> generation of AHSS) reaches 340 HV. The hardness increases to approximately 430 HV with increasing carbon and manganese contents in the 0.13C-1.3Mn-0.2Cr-0.2Cu steel.<sup>10</sup> Another problem in high-strength, multiphase

steels is the heat-affected zone (HAZ) softening because of the tempering of the pre-existing martensite. Since the AHSS contain a high alloying content their weldability should also be affected by the presence of non-metallic inclusions. Different sulphide and oxide particles have been identified by M. Amirthalingam et al.<sup>11</sup> and A. Grajcar et al.<sup>12</sup> in different types of TRIP steels containing Mn, Si and Al additions. It is well known that brittle oxides and ductile manganese sulphides affect the fatigue endurance limit, the fatigue-crack propagation rate, the fracture toughness, the anisotropy of the tensile properties with respect to the rolling direction and the weld quality, too.<sup>13,14</sup>

Recently, A. Grajcar et al.<sup>12</sup> analysed various types of non-metallic inclusions in laser-welded Fe-1.5Mn-0.9Si-0.4Al TRIP steel. Numerous oxide-type particles have been revealed in the fusion zone formed under air conditions. Therefore, the aim of the present work is to investigate the effect of a protective gas on the quantity, type and chemical composition of non-metallic inclusions in Si- and Al-alloyed TRIP steel.

## 2 EXPERIMENTAL PART

The work addresses the laser welding of thermo-mechanically processed, 2-mm-thick, TRIP steel sheets with the following chemical composition: 0.24 % C, 1.55 % Mn, 0.87 % Si, 0.4 % Al, 0.03 % Nb, 0.023 % Ti, 0.004 % S, 0.01 % P and 0.0028 % N. Rare-earth elements (REE) such as mischmetal (~50 % Ce, ~20 % La, ~20 % Nd) were added to modify the chemical composition and the shape of the non-metallic inclusions. The 25-kg, vacuum-melted ingot was cast using a protective atmosphere of argon. The Si+Al addition is required in TRIP steels to prevent carbide precipitation because C is needed to enrich the retained austenite.<sup>1,2,11</sup> The Nb+Ti micro-additions are added to increase the strength level as a result of the precipitation strengthening and grain refinement. These phenomena are especially useful for thermo-mechanically processed steels.<sup>15,16</sup>

The initial hot-working included the hot forging and rough rolling of the ingot to a thickness of 5 mm. The fundamental thermo-mechanical rolling consisted of 3 passes with a finishing rolling temperature of 850 °C. The major step of the controlled cooling following the hot rolling was isothermal holding of the sheets at a temperature of 350 °C within 600 s. The final thickness of the sheets was 2 mm.

Laser welding generally includes two major modes: keyhole welding and conductive welding.<sup>17</sup> The conductive welding utilizes the natural thermal conduction into the material. The welds obtained in this welding mode have good quality and do not contain pores and spalls. However, the keyhole welding is more efficient. Because of this the present tests were carried out using keyhole welding. In this treatment mode the power density is much higher compared to the conductive welding and the fusion depth is much higher compared to the diameter of the liquid pool. The welding tests were performed using a solid-state laser integrated with a robotized laser-treatment system. The welding station is equipped with the TruDisk 12002 solid-state laser type Yb:YAG characterized by a maximum power of 12 kW. The heat input value of 0.048 kJ/mm was applied. The welding tests were performed using an Ar atmosphere. To assess the effect of the protective atmosphere, tests under air conditions were performed too.

The distribution, type and chemical composition of the non-metallic inclusions formed in the base metal (BM) and fusion zone (FZ) of both types of samples (using Ar gas and without any protective gas) were compared. Samples for light microscopy (LM) and scanning electron microscopy (SEM) were prepared. The chemical composition of the non-metallic inclusions was assessed using EDS point analyses. The distribution of the particular alloying elements was revealed using mapping. The quantitative measurements of the chemical composition for the identified inclusions were carried out using a JCSA 8230 X-ray micro-analyser with an accelerating voltage of 15 kV. The microstructures of the BM, the heat-affected zone (HAZ) and the FZ were revealed

using the SUPRA 25 SEM at an accelerating voltage of 20 kV after nital etching.

## 3 RESULTS AND DISCUSSION

### 3.1 Distribution of non-metallic inclusions

The use of different gas atmospheres influences the quantity of non-metallic inclusions. The distributions of non-metallic inclusions formed in the fusion zones under the conditions of an air atmosphere and Ar protective gas are compared in **Figure 1**. The intense oxidation takes place when the laser welding was conducted without any protective gas. As a result numerous particles of different sizes can be observed in the fusion zone. The clear boundary near the fusion line is easily visible in **Figure 2** for both the air- and Ar-treated samples. The amount of particles in the heat-affected zone is a few times lower when compared to the fusion zones.

The size of the non-metallic inclusions is similar when the protective gas was applied. The quantity of particles is lower compared to the laser treatment without any protective atmosphere. However, the amount of non-metallic inclusions for Ar-protected samples is higher than would be expected. This means that the Ar atmosphere has a limited efficiency in the reduction of harmful, non-metallic inclusions formed in the fusion zone. The explanation is the essence of the keyhole-welding technique. The high-density power in the region of the laser beam's exposure creates a gas-dynamic

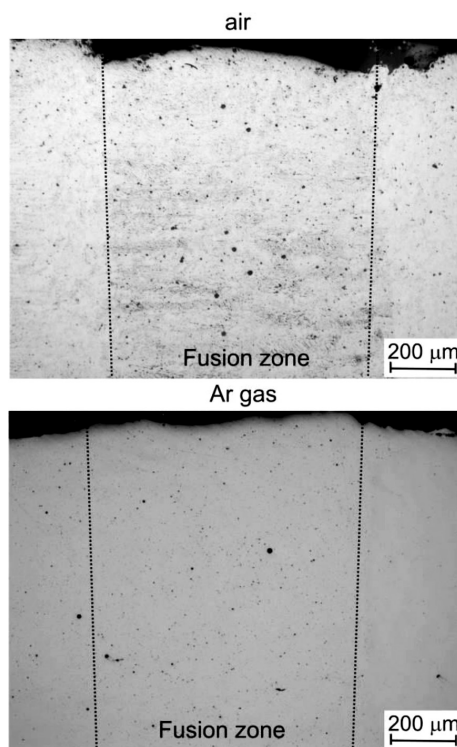


**Figure 1:** Distribution of non-metallic inclusions in the fusion zones formed under conditions of air atmosphere and Ar protective gas  
**Slika 1:** Razporeditev nekovinskih vključkov v področju zlitvanja, nastalih na zraku in v zaščitni atmosferi Ar

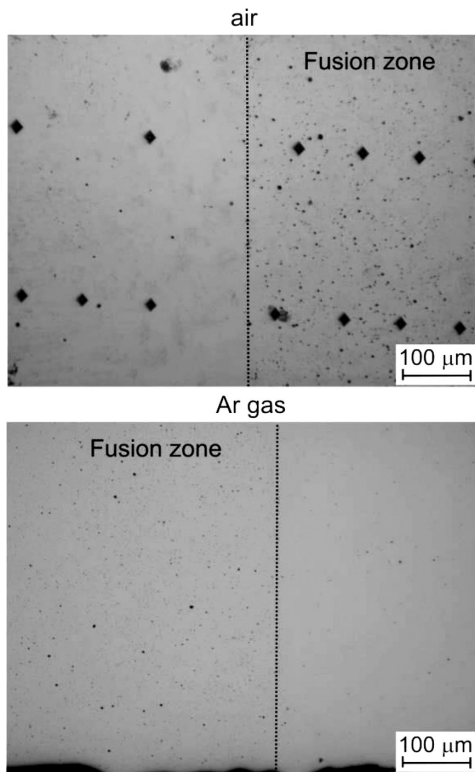


**Figure 2:** Distribution of non-metallic inclusions near the fusion line in the fusion zones and heat-affected zones formed under conditions of air atmosphere and Ar protective gas

**Slika 2:** Razporeditev nekovinskih vključkov blizu linije področja zlivanja in toplotno vplivane cone, nastalih na zraku in v zaščitni atmosferi Ar

channel, i.e., a deep and narrow capillary filled with gases and metal steams.<sup>17,18</sup> These turbulent gases partially break the protective atmosphere of the argon. That is why the amount of non-metallic inclusions for laser welding tests with the use of Ar gas is higher than expected.

### 3.2 Microstructure of the steel

The microstructure of the base metal consists of polygonal ferrite (F) grains elongated along the hot-rolling direction, bainite and retained austenite (**Figure 3**). Retained austenite (RA) is the most favourable structural constituent of TRIP steels due to its beneficial effect on increasing the steel's plasticity. This phase is usually found as small, blocky, granules along ferrite grain boundaries or between bainitic ferrite laths. Hence, a large fraction of the microstructure constitutes bainite-austenite (BA) constituents.

The rapid cooling rate typical for laser welding influences the microstructure of the fusion zone. Typical SEM microstructures of the fusion zone are shown in **Figure 4**. Both microstructures are characterized by the presence of martensite laths. Due to the chemical contrast typical for observations using back-scattered electrons (BSE) white interlath retained austenite (RA) can also be observed. The amount of non-metallic inclusions

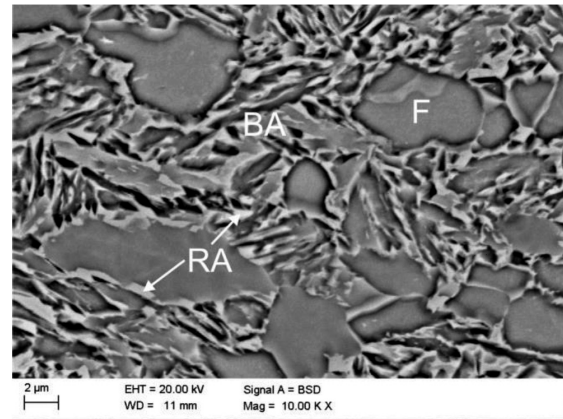


**Figure 3:** SEM microstructure of the base metal consisting of ferrite (F), bainite-austenite constituents (BA) and retained austenite (RA)

**Slika 3:** SEM-posnetek mikrostrukture osnovnega materiala, ki jo sestavljajo ferit (F), bainit-avstenit (BA) in zaostali avstenit (RA)

is slightly smaller for the samples welded using the argon gas. Moreover, a lot of sub-micron-sized particles are formed in this steel.

### 3.3 Non-metallic inclusions

The amount of non-metallic inclusions in the base metal is very small (**Figures 1 and 2**). It is related to the high metallurgical cleanliness of the laboratory-melted steel and the use of rare-earth elements. A result of the mischmetal addition is a partial or total substitution of

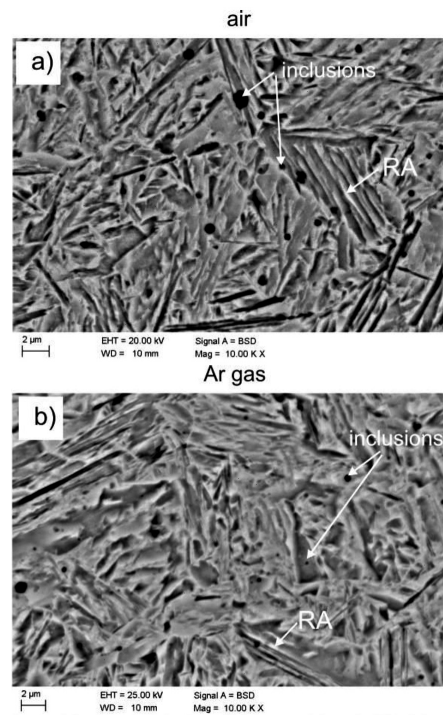


**Figure 4:** Martensite laths and globular non-metallic inclusions formed in the fusion zones under conditions of: a) air atmosphere and b) Ar protective gas

**Slika 4:** Martenzitne late in globularni nekovinski vključki, nastali v coni zlivanja: a) na zraku in b) v zaščitni atmosferi Ar



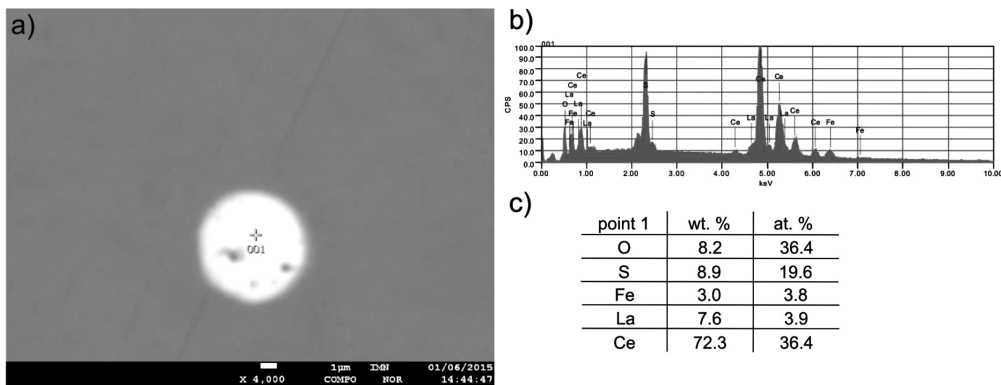
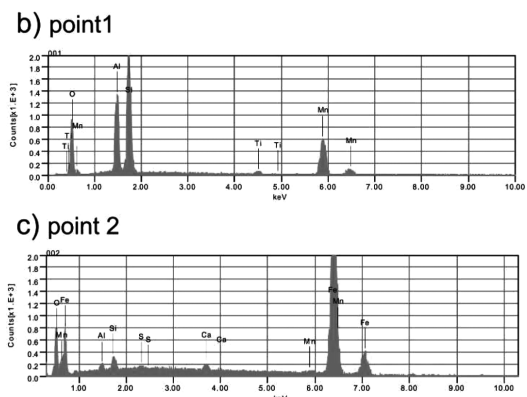
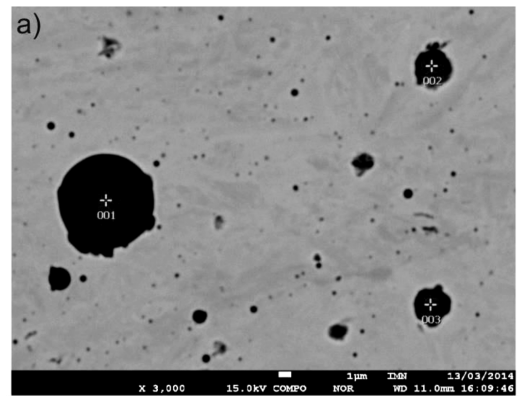


**Figure 5:** Complex oxysulphide containing La and Ce: a) formed in the base metal, b) spectrum of the inclusion and c) its chemical composition determined using EDS

**Slika 5:** Sestavljeni oksisulfid, ki vsebuje La in Ce: a) nastal v osnovnem material, b) spekter vključka in c) njegova kemijska sestava, določena s pomočjo EDS

Mn in sulphide inclusions and Al in oxide inclusions by the REE. These elements have a higher chemical affinity for sulphur and oxygen compared to Mn and Al. The example of such a particle is shown in **Figure 5**. In this case Ce and La totally replaced Mn and Al, forming a globular oxysulphide. Such particles are hardly deformed during hot rolling and reduce the anisotropy of the mechanical properties of flat products.<sup>4,15</sup> The mapping of the globular inclusions indicates that Ce and La as well as S and O are distributed uniformly within the particle (**Figure 6**).

**Figure 7** presents typical non-metallic inclusions formed in the fusion zone of the sample laser-welded in



point 1	wt. %	at. %
O	42.7	62.7
Al	11.0	9.6
Si	19.4	16.2
Ti	0.8	0.4
Mn	26.1	11.1

**Figure 7:** Complex oxides of various size formed in the fusion zone of the sample welded in the air atmosphere: a), b) spectrum of the particle from point 1, c) spectrum of the particle from point 2 and d) the chemical composition of the large particle (point 1) determined using EDS

**Slika 7:** Sestavljeni oksidi različnih velikosti: a) nastali v coni zlivanja vzorca zvarjenega na zraku, b) spekter delca v točki 1, c) spekter delca v točki 2 in d) kemijska sestava velikega delca (točka 1), določena s pomočjo EDS

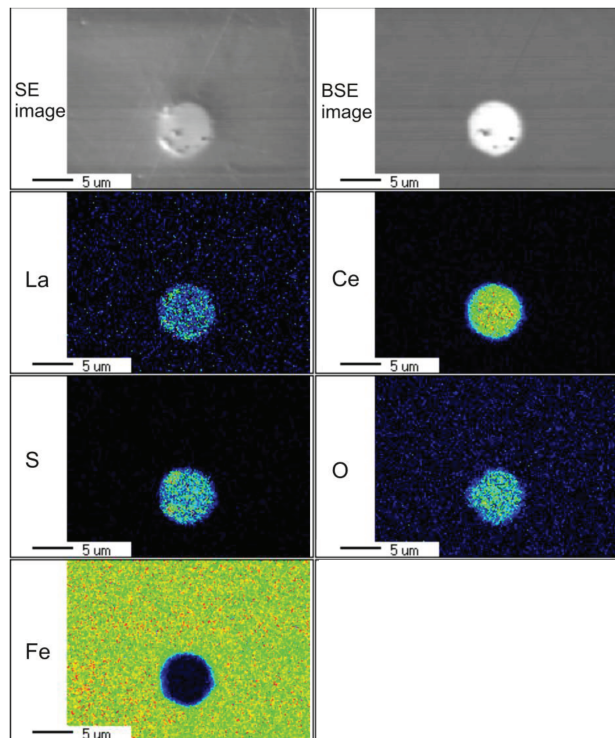


**Figure 6:** Elemental mapping of the particle from **Figure 5**

**Slika 6:** Razporeditev elementov v delcu prikazanem na **Sliki 5**



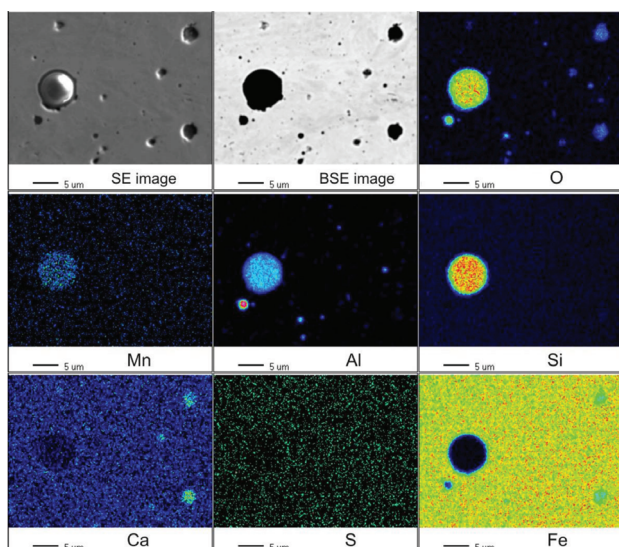


**Figure 8:** Elemental mapping of the particles from **Figure 7**  
**Slika 8:** Razporeditev elementov v delcih, prikazanih na **Sliki 7**

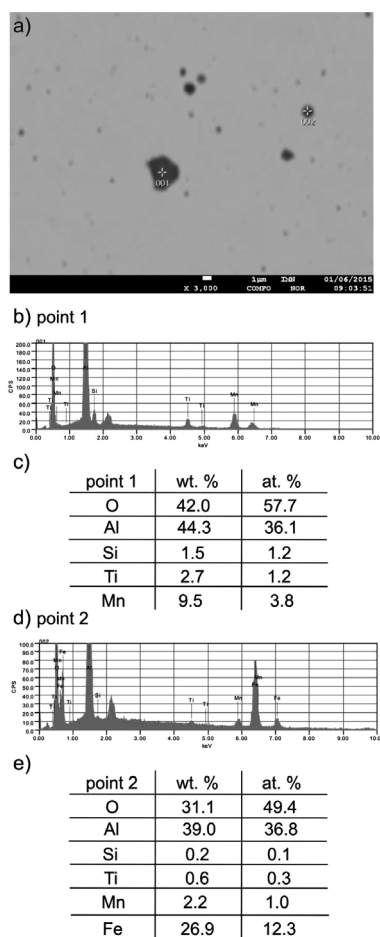


**Figure 9:** Complex oxides of various sizes formed in the fusion zone of the sample: a) welded in the Ar atmosphere, b), d) spectra of the particles from points 1 and 2, c) the chemical composition of the particles from point 1 and e) point 2 determined using EDS

**Slika 9:** Sestavljeni oksidi različnih velikosti nastalih v coni zlivanja: a) vzorca zvarjenega v atmosferi Ar, b), d) spekter delcev iz točke 1 in 2, c) kemijska sestava delcev iz točke 1 in e) točke 2, določenih s pomočjo EDS

the air atmosphere. There are a few large inclusions with a size ranging from approximately 3 µm to 7 µm and numerous small particles smaller than 1 µm. All the inclusions have a globular shape. EDS analyses of the large particles indicate that these are complex oxides containing Al, Mn and Si (**Figures 7b to 7d**). It indicates that there is a strong oxidation of the alloying elements in the air atmosphere. Elemental mapping indicates that there is no sulphur in the inclusions. Moreover, it should be noted that Mn and Si are located only at the largest inclusions, whereas the smaller ones are pure aluminium oxides (**Figure 8**).

The use of a protective atmosphere of argon causes a decrease in the amount of non-metallic inclusions. It is especially true for large particles, the quantity of which is much smaller (**Figure 9a**). As previously, the spectral lines in **Figures 9b** and **9d** do not contain sulphur peaks. The intense evaporation during the keyhole welding results in the partial oxidation of the same alloying elements, like for the samples welded in the air atmosphere. Hence, many oxides can be identified in **Figure 9**. The analysis of the chemical composition indicates that the concentrations of Mn and Si decrease with a decrease in the particle diameter (**Figures 9c** and **9e**). The presence of Fe in the spectrum of the smaller particle (point 2 in **Figure 9**) is caused by a similar diameter of the inclusion and a beam diameter. The occurrence of Mn and Si only in the largest inclusions is confirmed by **Figure 10**, where these elements are located in the largest particle of a diameter of approximately 4 µm. Some content of titanium was also revealed.

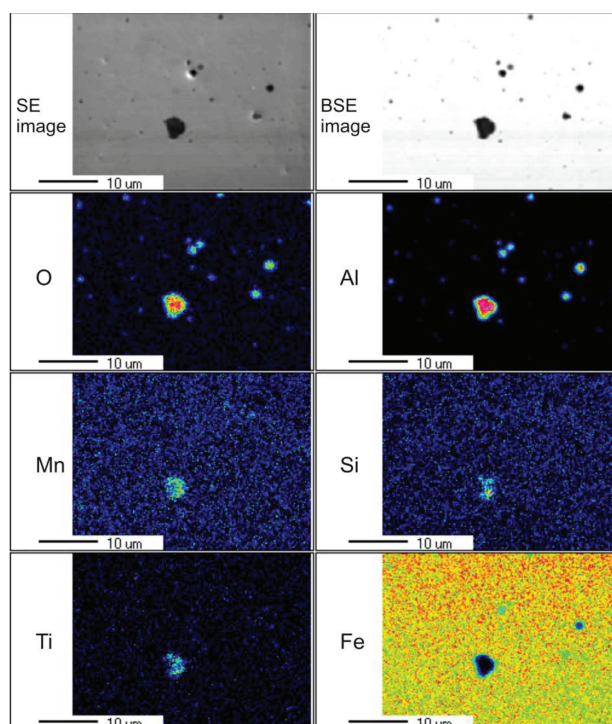


**Figure 10:** Elemental mapping of the particles from **Figure 9**  
**Slika 10:** Razporeditev elementov v delcih, prikazanih na **Sliki 9**

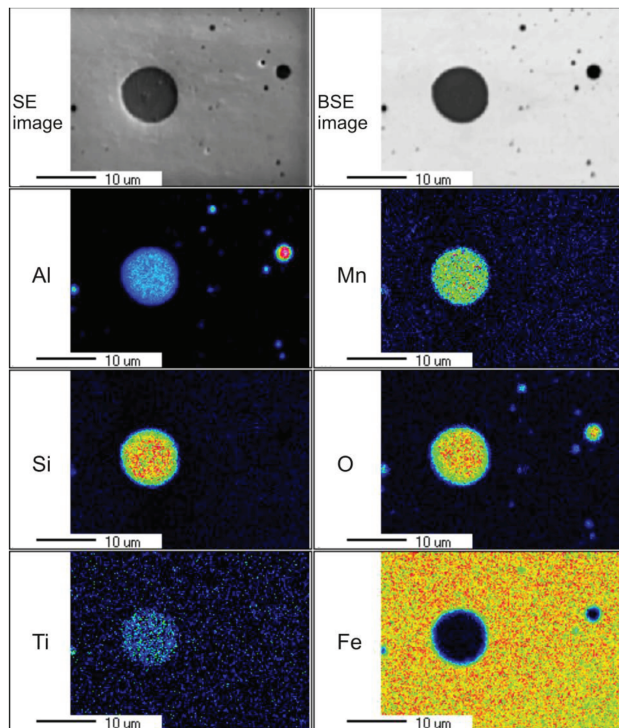


**Figure 11:** Elemental mapping of the complex oxides formed in the fusion zone of the sample welded in the Ar atmosphere

**Slika 11:** Razporeditev elementov v sestavljenih oksidih, nastalih v coni zlivanja, vzorca zvarjenega v atmosferi Ar

Ti, Al, Si and Mn are also located in the largest inclusion in **Figure 11**. However, the amount of such large inclusions is reduced compared to the samples welded in the air atmosphere. The region around such large inclusions is usually free of any other particles. The limit between Mn- and Si-containing large inclusions and small pure aluminium oxides can be assessed as 2–3 µm.

#### 4 CONCLUSIONS

The effect of the use of an Ar atmosphere during laser welding in the keyhole-welding mode was assessed for the Al-Si-bearing TRIP steel. It was found that the intense evaporation of gases and metal steams partially destroys the protective atmosphere of the argon. As a result, some oxidation of the weld pool takes place. The amount of non-metallic inclusions in the fusion zone of the samples welded using Ar is smaller compared to the samples treated without a protective gas. It concerns especially the large inclusions with a diameter between 3 µm and 7 µm. The Ar atmosphere has no effect on the chemical composition of the formed particles. In both cases globular oxides of various sizes are formed in the fusion zone. The particles with a diameter ranging from 3 µm to 7 µm constitute the complex inclusions containing Al, Si and Mn (sometimes also Ti). The numerous particles smaller than 2–3 µm are pure aluminium oxides.

#### Acknowledgment

This work was financially supported with statutory funds of Faculty of Mechanical Engineering of Silesian University of Technology in 2015.

#### 5 REFERENCES

- <sup>1</sup> B. Masek, C. Stadler, H. Jirkova, P. Feuser, M. Selig, Transformation-induced plasticity in steel for hot stamping, *Mater. Tehnol.*, 48 (2014), 555–557
- <sup>2</sup> A. Kokosza, J. Pacyna, Formation of medium carbon TRIP steel microstructure during annealing in the intercritical temperature range, *Archives of Metallurgy and Materials*, 59 (2014), 1017–1022
- <sup>3</sup> S. Wiewiorowska, Analysis of the influence of drawing process parameters on the mechanical properties of TRIP-structure steel wires, *Archives of Metallurgy and Materials*, 58 (2013), 573–576
- <sup>4</sup> A. Grajcar, M. Opiela G. Fojt-Dymara, The influence of hot-working conditions on a structure of high-manganese steel, *Archives of Civil and Mechanical Engineering*, 9 (2009), 49–58
- <sup>5</sup> S. Lasek, E. Mazancova, Influence of thermal treatment on structure and corrosion properties of high manganese triplex steels, *Metallurgija*, 52 (2013), 441–444
- <sup>6</sup> L. A. Dobrzański, A. Grajcar, W. Borek, Microstructure evolution of C-Mn-Si-Al-Nb high-manganese steel during the thermomechanical processing, *Materials Science Forum*, 638-642 (2010), 3224–3229, doi:10.4028/MSF.638-642.3224
- <sup>7</sup> M. Jabłońska, G. Niewielski, R. Kawalla, High-manganese TWIP steel – technological plasticity and selected properties, *Solid State Phenomena*, 212 (2014), 87–90, doi:10.4028/SSP.212.87
- <sup>8</sup> A. Grajcar, R. Kuziak, Dynamic recrystallization behavior and softening kinetics in 3Mn-1.5 Al TRIP steels, *Advanced Materials Research*, 314–316 (2011), 119–122, doi:10.4028/AMR.314-316.119
- <sup>9</sup> M.S. Wegłowski, S. Stano, G. Michta, W. Osuch, Structural characterization of Nd:YAG laser welded joint of dual phase steel, *Archives of Metallurgy and Materials*, 55 (2010), 211–220
- <sup>10</sup> F. Nikoosohbat, S. Kheirandish, M. Goodarzi, M. Pouranvari, Effect of tempering on the microstructure and mechanical properties of resistance-spot-welded DP980 dual-phase steel, *Mater. Tehnol.*, 49 (2015), 133–138
- <sup>11</sup> M. Amirthalingam, M. J. M. Hermans, I. M. Richardson, Microstructural development during welding of silicon- and aluminum-based transformation-induced plasticity steels - inclusion and elemental partitioning analysis, *Metallurgical and Materials Transactions A*, 40 (2009), 901–909, doi:10.1007/s11661-008-9761-5
- <sup>12</sup> A. Grajcar M. Różański M. Kamińska B. Grzegorzczak, Study on non-metallic inclusions in laser-welded TRIP-aided Nb-microalloyed steel, *Archives of Metallurgy and Materials*, 59 (2014), 1163–1169, doi:10.2478/amm-2014-0203
- <sup>13</sup> J. Maciejewski, The effects of sulfide inclusions on mechanical properties and failures of steel components, *Journal of Failure Analysis and Prevention*, 15 (2015), 169–178, doi:10.1007/s11668-015-9940-9
- <sup>14</sup> I.J. Park, S.M. Lee, M. Kang, S. Lee, Y.K. Lee, Pitting corrosion behavior in advanced high strength steels, *Journal of Alloys and Compounds*, 619 (2015), 205–210, doi:10.1016/j.jallcom.2014.08.243
- <sup>15</sup> J. Górka, Weldability of thermomechanically treated steels having a high yield point, *Archives of Metallurgy and Materials*, 60 (2015), 469–475, doi:10.1515/amm-2015-0076
- <sup>16</sup> R. Celin, J. Bernetic, D.A. Skobir Balantic, Welding of the steel grade S890QL, *Mater. Tehnol.*, 48 (2014), 931–935
- <sup>17</sup> A. Lisiecki, Welding of thermomechanically rolled fine-grain steel by different types of lasers, *Archives of Metallurgy and Materials*, 59 (2014), 1625–1631, doi:10.2478/amm-2014-0276

# MACHINING PARAMETERS INFLUENCING IN ELECTRO CHEMICAL MACHINING ON AA6061 MMC

## PARAMETRI STROJNE OBDELAVE, KI VPLIVAJO NA ELEKTROKEMIJSKO STROJNO OBDELAVO AA6061 MMC

Chenthil Jegan Thankaraj Mariapushpam<sup>1</sup>, Durairaj Ravindran<sup>2</sup>, Manaharan Dev Anand<sup>3</sup>

<sup>1</sup>St. Xavier's Catholic College of Engineering, Department of Mechanical Engineering, Kanyakumari District, India

<sup>2</sup>National Engineering College, Department of Mechanical Engineering, K.R.Nagar, Kovilpatti, Thuthukoodi District, India

<sup>3</sup>Noorul Islam Centre for Higher Education, Department of Mechanical Engineering, Kumaracoil, Kanyakumari District, India  
oprtrajegan@yahoo.co.in

*Prejem rokopisa – received: 2015-08-18; sprejem za objavo – accepted for publication: 2015-11-05*

doi:10.17222/mit.2015.260

In this study the mechanical and microstructural behaviours of AA6061 reinforced with silicon carbide (SiC) and AA6061 reinforced with boron carbide (B<sub>4</sub>C), obtained from the enhanced stir-casting process, were investigated using scanning electron microscopy (SEM) and X-ray diffraction (XRD) with various weight percentages, i.e., 2.5 %, 5 % and 7.5 %. The testing shows that the tensile and microhardness properties of the AA6061 were improved in both the reinforced aluminium-matrix composites. The influence of the electrochemical machining process parameters like current, voltage, electrolyte concentration, feed rate, gap and flow rate were considered as the input parameters. The output responses are the material removal rate (*MRR*), the surface roughness (*SR*) and the radial overcut (*ROC*). The study shows that the dominant output parameter *MRR* was directly proportional to the input parameters current, voltage and feed rate. The *SR* was significantly influenced by the input parameters current, feed rate and gap. The *ROC* was considerably balanced by the input parameters current and feed rate.

Keywords: metal-matrix composites, material removal rate, electrochemical machining, surface roughness, radial overcut

V študiji so bile preiskovane mehanske lastnosti in mikrostruktura AA6061, izdelanega z naprednim postopkom ulivanja s premešavanjem in ojačanjem z različnim masnim deležem silicijevega karbida (SiC) ali borovega karbida (B<sub>4</sub>C) (2,5 %, 5 % in 7,5 %). Preiskave so bile izvedene s pomočjo vrstičnega elektronskega mikroskopa (SEM) in z rentgensko difrakcijo (XRD). Preizkušanje kaže, da sta natezna trdnost in mikrotrdnost AA6061 narasli pri obeh vrstah kompozita na osnovi aluminija. Za vpliv vhodnih procesnih parametrov pri elektrokemijski strojni obdelavi so bili upoštevani: tok, napetost, koncentracija elektrolita, hitrost podajanja, reza in hitrost pretoka. Izhodni odgovori so bili: hitrost odstranjevanja materiala (*MRR*), hrapavost površine (*SR*) in povečanje radiusa (*ROC*). Študija kaže, da je prevladujoči izhodni parameter *MRR* neposredno soracionalen vhodnim parametrom; toku, napetosti in hitrosti podajanja. Na *SR* so močno vplivali vhodni parametri: tok, hitrost podajanja in reza. *ROC* je bil posebej uravnotežen z vhodnima parametroma, tokom in hitrostjo podajanja.

Ključne besede: kompoziti na kovinski osnovi, hitrost odstranjevanja materiala, elektrokemijska strojna obdelava, hrapavost površine, povečanje radiusa

## 1 INTRODUCTION

Electrochemical machining (ECM) is a well-known process used for the manufacture of various sophisticated parts, such as turbine blades, rifle bores, hip-joint implants, micro-components as well as many other applications. ECM provides an economical and effective method for shaping high-strength, heat-resisting materials into complex shapes and producing high-quality products from composites and other hard materials.<sup>1</sup> In ECM the machining is done at low voltage compared to other processes with a high metal removal rate. It is suitable for mass production work and low labour requirements. ECM is one of the most widely used advanced machining processes to make complicated shapes of varying sizes with electrically conducting, but difficult to machine, materials such as super alloys, Ti alloys, alloy steel, tool steel, stainless steel, etc.<sup>2</sup> These materials are extensively used in aerospace, automobile, space, nuclear, defence, cutting tools, dies and mould making applications. The material used for ECM tools should be

electrically conductive and easily machinable to the required geometry. The various materials used for this purpose include copper, brass, stainless steel, titanium, and copper-tungsten. Tool insulation controls the side electrolyzing current and hence the amount of oversize. Spraying or dipping is generally the simplest method of applying insulation. Teflon, urethane, phenol, epoxy, and powder coatings are commonly used for tool insulation.<sup>3</sup>

The material removal rate of an aluminium work-piece has been obtained by electrochemical machining using a NaCl electrolyte at different current densities and compared with the theoretical values.<sup>4</sup> It has been observed that the resistance of the electrolyte solution decreases sharply with increasing current densities. The increase in the peak current increases the *MRR*, *TWR* and *ROC* significantly in a nonlinear fashion, *MRR* and *ROC* increased with the increase in the pulse on time and the gap voltage was found to have some effect on the three responses.<sup>5,6</sup> The influence of electrochemical process parameters such as the applied voltage, electrolyte



concentration, electrolyte flow rate and tool feed rate on the metal removal rate and surface roughness to fulfil the effective utilization of electrochemical machining can be used.<sup>7</sup>

For non-passivating electrode systems, the reduction in electrolyte concentration and an increase in its temperature improve the quality of surfaces.<sup>8</sup> The use of a gap voltage between 20 V and 25 V saves energy and reduces the production cost.<sup>9</sup> The machining current increases linearly with the tool feed rate. Sparking causes damage to both the tool and the workpiece due to the critical feed rate, which is because of the rapid moment of the tool towards the workpiece. The feed rate was the main parameter affecting the material removal rate.<sup>10</sup> So it is better to maintain the feed rate according to the anodic dissolution rate for proper machining.<sup>11</sup> The electrolyte temperature, pressure variations in the inter electrode gap and the choice of an optimum gap voltage also avoid the occurrence of sparking and the consequent loss of the tool and workpiece.<sup>12</sup>

A metal-matrix composite (MMC) contains matrix materials where reinforcements can be made from polymers, ceramics or metals. MMCs are divided into composites reinforced by fibres (fibrous composites) and composites filled with fine particles that are insoluble in the base-metal-strengthened composites.<sup>13</sup> Aluminium-matrix composites consist of a uniform distribution of strengthening ceramic particles embedded within an aluminium matrix. Many researchers discovered aluminium materials and found they exhibit higher strength and stiffness, in addition to isotropic behaviour at a lower density, when compared to the un-reinforced aluminium matrix.<sup>14-16</sup> The ceramic's ability to withstand high velocity impacts and the high toughness of the metal matrix, which helps in preventing total shattering, are one of the main reason for AMC strength. The composites possess good mechanical properties at high temperature and thus an AMC can be a favourite choice for cost-effective alternatives and shows potential in large-scale applications such as automotive, aerospace and airframe applications. It is proved that among the aluminium alloys, AA6061 was quite a popular choice as a matrix material.<sup>17</sup> In our previous work the ductile and microhardness properties of silicon-carbide, boron-carbide-based AMCs were analysed and it was reported that both AMCs are suitable for unconventional machining.<sup>18</sup> The fabrication of a MMC with various ceramic particles such as  $\text{Si}_3\text{N}_4$ ,  $\text{TiB}_2$ ,  $\text{B}_4\text{C}$  and machining the fabricated MMC individually was analysed by many researchers.<sup>19-21</sup>

Fabrication by the pressure-less infiltration process under a nitrogen gas atmosphere and the grinding of the aluminium-based MMC reinforced with SiC particles show that the physical and chemical compatibility between the SiC particles and the Al matrix is the main concern in the preparation of SiC/Al composites.<sup>22</sup> Due to the low coefficients of thermal expansion for maxi-

mizing heat dissipation and minimizing thermal stress, high-performance thermal management materials are most commonly used in the packaging of microprocessors, power semiconductors, high-power laser diodes, light-emitting diodes and micro-electromechanical systems.<sup>23,24</sup>

Limited research work has been reported on AMCs reinforced with  $\text{B}_4\text{C}$  due to higher raw-material costs and poor wetting. Stir casting is accepted as a general commercial technique for producing MMCs.<sup>25</sup> Boron carbide was an attractive reinforcement for aluminium and its alloys, showing many of the mechanical and physical properties required of an effective reinforcement, in particular high stiffness and hardness. These factors combined with a density less than that of solid aluminium indicate that large specific property improvements are possible.<sup>26</sup> Boron-carbide-particulate-reinforced aluminium composites possessed a unique combination of high specific strength, high elastic modulus, good wear resistance and good thermal stability compared to the corresponding non-reinforced matrix alloy system.<sup>27</sup>

This study covers the fabrication and machining of an aluminium-based MMC reinforced with SiC particles. The mechanical properties of the fabricated MMC and the influence on the ECM machining process parameters were analysed with experiments. The mechanical and microstructural properties of AA6061 reinforced with silicon carbide and AA6061 reinforced with boron carbide attained from the enhanced stir casting method were discussed. The influence of the ECM process parameters current, voltage, electrolyte concentration, feed rate, gap and flow rate on the predominant output parameters material removal rate, surface roughness and radial overcut were also analysed.

## 2 SPECIMEN PREPARATION USING AA6061

The matrix material for the study was AA6061. The composite material consists of AA6061 alloy as a matrix material reinforced with three different weight percentage of SiC and varying weight percentages of  $\text{B}_4\text{C}$  (2.5 %, 5 % and 7.5 %) prepared through the enhanced stir-casting technique. The SiC has better mechanical properties such as high hardness, low density and retains its properties even at higher temperatures. The  $\text{B}_4\text{C}$  is a hard reinforcement particle that has neutron absorbing characteristics in nature. The percentage of silicon content in AA6061 is high compared to other aluminium alloys and its melting point is low. The chemical composition of AA 6061 by weight percentage is Cu 0.1 %, Mg 0.4 %, Si 10 %, Mn 0.3 %, Ni 0.1 %, Zn 0.1 %, Pb 0.05 % and Sn 0.2 %. The average particle size of the SiC is 200 mesh, with a density of  $3.2 \text{ g/cm}^3$  and a thermal conductivity  $3.2 \text{ W cm}^{-1} \text{ K}^{-1}$  and also an average particle size of the  $\text{B}_4\text{C}$  is 200 mesh.

The test specimens were prepared using the simplest and most commercially used technique known as



enhanced stir-casting technique. In the stir-casting process the pre-heated ceramic particles were mixed with a vortex of molten alloy created by the rotating impeller. As a result of the interaction between the suspended ceramic particles and the moving solid-liquid interface during solidification, there was a possibility of inhomogeneity in the reinforcement distribution. Generally, it is possible to incorporate up to 30 % of ceramic particles in the size range 5  $\mu\text{m}$  to 100  $\mu\text{m}$  in a variety of molten aluminium alloys. AA6061 was placed inside the crucible and the temperature was set 1000  $^{\circ}\text{C}$ . Some 1 % of the degasser Hexa Chloro Ethane was added to the melted AA6061. The molten metal was stirred and the crucible was held with forks to eliminate the gases. The same process was repeated for various weight percentages of SiC-reinforced AMC and B<sub>4</sub>C-reinforced AMC.

### 3 ELECTROCHEMICAL MACHINING

For this experiment the whole work was carried out with an ECM set up having a power supply of 415 V, 3-phase AC, 50 Hz and it consists of three major sub systems: the machining cell, the control panel and the electrolyte circulation tank. The parameter that is able to change the output parameters by increasing and decreasing the level is known as the controlling parameters or the input parameters. In this paper the considered input parameters are the current, voltage, electrolyte concentration, feed rate, gap and flow rate. The output parameters considered are the *MRR*, *SR* and *ROC*. The various levels of input parameters selected for the machining are listed in **Table 1**.

**Table 1:** Input parameters and levels

**Tabela 1:** Vhodni parametri in njihovi nivoji

Variables	Values of different levels				
	1	2	3	4	5
Current (A)	90	120	150	180	210
Voltage (V)	8	10	12	14	16
Electrolyte concentration (g/L)	3.34	6.67	10	13.34	16.67
Feed rate (mm/min)	0.1	0.2	0.3	0.4	0.5
Gap (mm)	0.1	0.2	0.3	0.4	0.5

#### 3.1 Machining process

The machine cell has a tool area of 300 mm<sup>2</sup>, a cross-head stroke 150 mm, a job holder 100 mm opening, 50 mm depth and 100 mm width. A DC servo-type tool feed motor was used for the tool movement. The control panel consists of an electrical output rating ranging from 0 A to 300 A DC for any voltage from 0  $\mu\text{m}$  to 20 V, tool feed of 0.2 to 2 mm/min, while the supply given to the machining was 3-phase AC with 50 Hz. The specimen to be machined was fixed in the machine vice. The tool was brought near the job with the help of press buttons provided on the control panel and a table-lifting arrangement, maintaining a particular gap.

The tool progress was maneuvered vertically by the servomotor and is governed by a microcontroller-based programmable drive. The c cathode tool is made of non-reacting copper material. The process parameters like current, voltage, electrolyte concentration, feed rate, gap and flow rate were set. The process was started in the presence of an electrolyte flow. This electrolyte flow was adjusted using a flow-control valve. After the desired time interval, a hooter gives an indication of the completion of the time and the process. The specimen prepared was a cylindrical blank of 16 mm in diameter and 32 mm in height. The electrolyte composition used was NaCl solution.

### 4 RESULTS AND DISCUSSION

The hardness of the specimens was measured by a Rockwell hardness and a tensile test. The Rockwell hardness number measures the overall response of the material and it is relatively insensitive to localized effects. The Rockwell scale is a hardness scale based on the indentation hardness of a material. The Rockwell test determines the hardness by measuring the depth of the penetration of an indenter under a large load compared to the penetration made by a preload. The chief advantage of Rockwell hardness is its ability to display hardness values directly, thus obviating tedious calculations involved in other hardness-measurement techniques. The Rockwell Hardness number for AA 6061 and the other experimental MMC are shown in **Figure 1**. It is clear that the hardnesses of the MMCs are closer to one another, but the values are high compared with AA 6061.

For microstructure analysis the machined samples were polished using silicon carbide paper (60, 80, 120, 220 and 400) grit and finally using a soft cloth with fine alumina powder as a slurry. Kerosene was used for cleaning and polishing to prevent the embedding of foreign particles in the sample. The samples were then etched using the modified diamond paste for 140 s. The long etching time was due to the large oxide content of

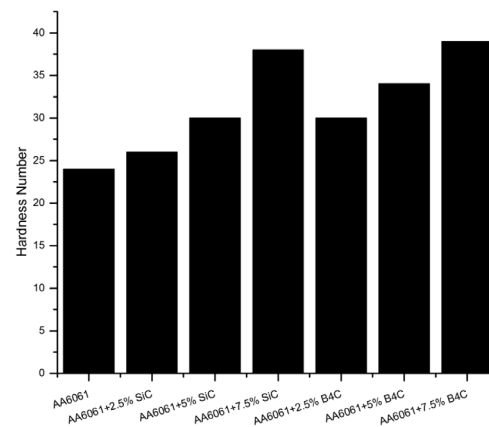


**Figure 1:** Rockwell hardness number for experimental samples  
**Slika 1:** Rockwell trdota preizkusnih vzorcev

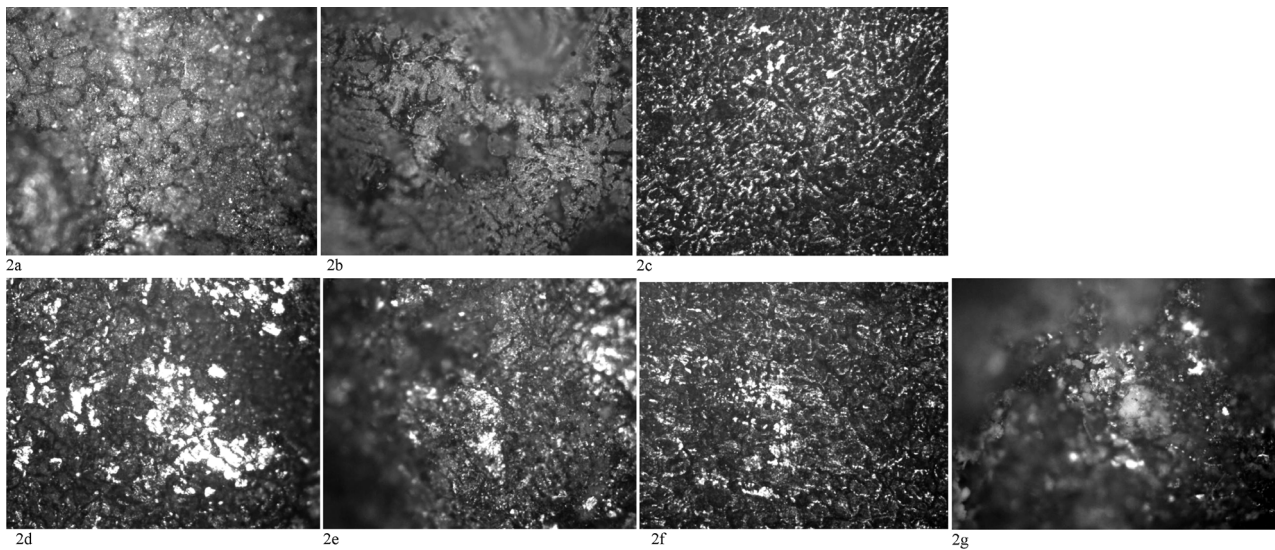


**Figure 2:** Light microscope (20 $\times$ ) images of seven samples showing the distribution of the reinforcement in the matrix: a) AA6061, b) AA6061 + 2.5 % SiC, c) AA6061 + 5 % SiC, d) AA6061 + 7.5 % SiC, e) AA6061 + 2.5 % B<sub>4</sub>C, f) AA6061 + 5 % B<sub>4</sub>C, g) AA6061 + 7.5 % B<sub>4</sub>C  
**Slika 2:** Svetlobna mikroskopija (20 $\times$ ) sedmih vzorcev, ki kaže razporeditev delcev za utrditev v osnovi: a) AA6061, b) AA6061 + 2,5 % SiC, c) AA6061 + 5 % SiC, d) AA6061 + 7,5 % SiC, e) AA6061 + 2,5 % B<sub>4</sub>C, f) AA6061 + 5 % B<sub>4</sub>C, g) AA6061 + 7,5 % B<sub>4</sub>C

the aluminium powder. The light microscope photographs of the seven combinations of composite samples using an optical microscope of 20 $\times$  lens are shown in **Figure 2**. **Figure 2a** shows various elements present in AA6061. **Figures 2b to 2d** represents AA6061+ reinforced silicon carbide particles. AA6061+ reinforced boron carbide particles are shown in **Figures 2d to 2f**. It can be shown that the silicon carbide particles and boron carbides are homogeneously distributed in the aluminium matrix.

Scanning electron microscopy (SEM) was used to reveal the morphological features in the machined samples. For the study of their microstructure the specimen preparation or polishing is important. The procedure for preparing the specimen involved the selection of the specimen and the mounting of the specimen in the machine, obtaining a flat specimen surface, intermediate and fine grinding, rough polishing using diamond powder with an oil-soluble paste, fine polishing with alumina powder along with distilled water and etching using dilute hydrofluoric acid. The morphological structure of the AMC was obtained using a ZEISS (NIIST) SEM at an accelerating voltage of 20 kV. The AA6061 specimens were mounted with conductive adhesives and coated with gold powder. Then, the SEM images were taken at the centre of the machined surface of the sample specimen.

From the above examination both MMCs exhibited similar microstructural features in terms of homogeneous particle distributions associated with similar carbide particle sizes. The SEM analysis of the B<sub>4</sub>C-reinforced composites and SiC-reinforced composites exhibited very similar microstructures. However, it was possible to observe some large size pores that were not in the B<sub>4</sub>C-reinforced composites. The distribution of the

particles was also altered by the growth of the grains. In the B<sub>4</sub>C-reinforced MMC microstructure both coarser grains and finer grains were identified, but the grain size

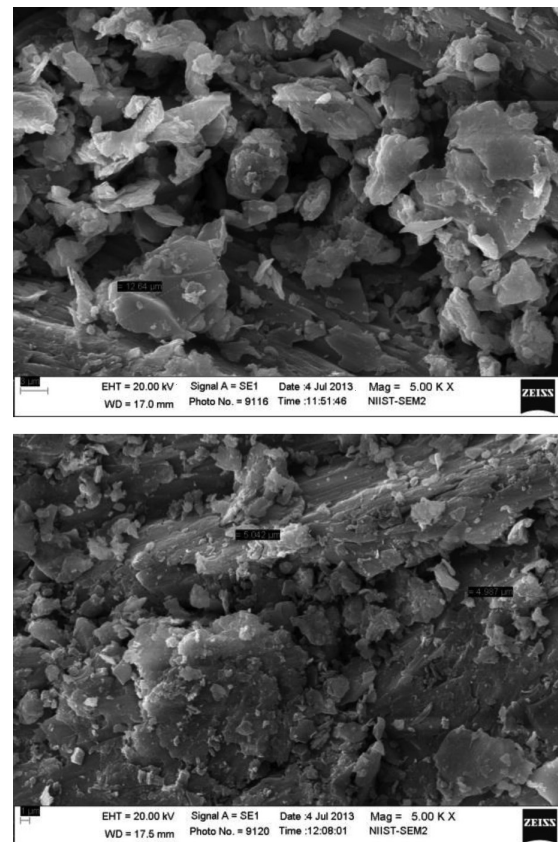


**Figure 3:** SEM microstructure of: a) SiC-reinforced AA6061 and b) B<sub>4</sub>C-reinforced AA6061

**Slika 3:** SEM-posnetek mikrostrukture: a) AA6061, ojačan s SiC in b) AA6061, ojačan z B<sub>4</sub>C

was less compared to that of SiC. Similarly, the pore size was also less for the B<sub>4</sub>C-reinforced MMC.

The SEM microstructure of the AMCs is shown in **Figure 3**. From the **Figures 3a** and **3b** it is evident that the distributions of the SiC and B<sub>4</sub>C particles were homogeneous in the AA6061. Most of the ceramic particles were found within the grain boundaries. The distribution of the particles becomes intra granular. The basic atomic structure of AA6061 is body-centred cubic, so that the B<sub>4</sub>C particles were bonded together in reinforcement. Good wettability was also seen in both MMCs, but it was especially high in the B<sub>4</sub>C.

To determine the rate of penetration of each aluminium alloy, a series of partial infiltrations were performed in order to study the growth rate at short times (less than 2 h). XRD micro-diffraction of the SiC-reinforced AMC and the B<sub>4</sub>C-reinforced AMC was shown in **Figure 4**.

The XRD peak list of the SiC-reinforced AA6061 and B<sub>4</sub>C-reinforced AA6061 are listed in **Tables 2** and **3**, respectively.

**Table 2:** Peak list for SiC reinforced AA6061

**Tabela 2:** Seznam vrhov pri AA6061, ojačanjem s SiC

Pos. 2θ (°)	Height (cm)	FWHM 2θ (°)	d-spacing (nm)	Rel. Int. (%)
28.4044	59.37	0.0816	0.313967	8.57
38.4426	692.59	0.1632	0.233979	100.00
44.6516	307.84	0.1632	0.202778	44.45
47.2508	38.12	0.1224	0.192212	5.50
49.0100	4.93	0.0816	0.185716	0.71
56.0546	19.32	0.2856	0.163931	2.79
57.6437	0.75	0.2448	0.159784	0.11
65.0870	156.16	0.1224	0.143194	22.55
78.1848	161.46	0.2448	0.122159	23.31
82.3912	47.66	0.2040	0.169540	6.88
87.9251	6.83	0.4896	0.110964	0.99

**Table 3:** Peak List for B<sub>4</sub>C reinforced AA6061

**Tabela 3:** Seznam vrhov pri AA6061, ojačanjem z B<sub>4</sub>C

Pos. 2θ (°)	Height (cm)	FWHM 2θ (°)	d-spacing (nm)	Rel. Int. (%)
28.5168	55.08	0.1632	0.312755	5.71
36.5506	6.86	0.1224	0.245644	0.71
38.5654	963.85	0.1632	0.233262	100.00
44.8543	372.10	0.1836	0.201909	38.61
47.3974	42.42	0.1632	0.191651	4.40
56.2284	12.82	0.3264	0.163466	1.33
65.2212	206.18	0.0816	0.142932	21.39
76.4518	7.85	0.3264	0.124490	0.81
78.3073	240.23	0.1632	0.121998	24.92
82.5530	64.93	0.2448	0.116766	6.74
83.4711	3.89	0.4080	0.115714	0.40
88.0604	10.43	0.3264	0.110828	1.08

From **Figure 4** it was observed that the waves were almost the same and symmetrical. The ambiguous structure was available in both AMCs. As compared to the

SiC-reinforced particle, the other one possessed good hardness and an even distribution of particles. The starting angle was also high for the B<sub>4</sub>C-reinforced AA6061. In the SiC-reinforced AA6061, the SiC particle peaks were identified at angles of 28.4044, 44.6516, 49.0100, 57.6437, 65.0870 and 87.9251. The remaining peak values in **Table 3** and **4** were related to the AA6061 alloy. Similarly, in the B<sub>4</sub>C-reinforced AA6061, the B<sub>4</sub>C particle peaks were obtained at angles of 28.5168, 36.5506, 44.8543, 56.2284, 65.2212, 76.4518 and 88.0604.

The ductility of the MMC was improved by the addition of ceramic particles with AA6061. The stress vs. elongation analyses of the AA6061 samples were compared with the AA6061 + SiC MMC, and it was shown in **Figure 5**. From **Figure 5a** it was noted that the strength of the specimen increases with an increase in the addition of silicon carbide particles. The maximum strength was obtained for sample 3, with aluminium and SiC, in a ratio of 100:7.5. Similarly, for the AA6061 + B<sub>4</sub>C MMC samples the results were shown in **Figure 5b**. In AA6061 + B<sub>4</sub>C MMC also better tensile strength was obtained with high percentage of B<sub>4</sub>C reinforcement. From the analysis it was concluded that the ductile nature of AA6061 increased with the addition of SiC and B<sub>4</sub>C particles.

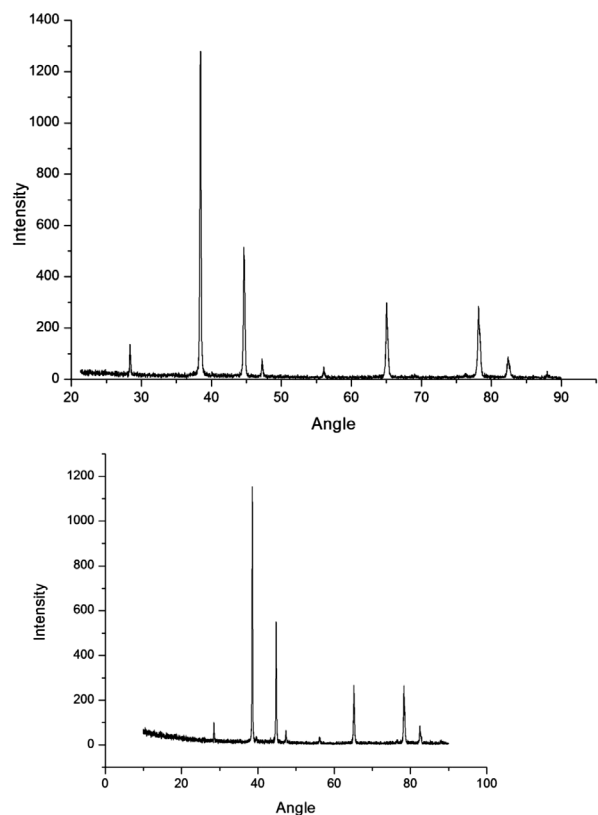


**Figure 4:** XRD patterns of: a) SiC-reinforced AA6061 and b) B<sub>4</sub>C-reinforced AA6061

**Slika 4:** Rentgenograma: a) AA6061, ojačanega z SiC in b) AA6061, ojačanega z B<sub>4</sub>C



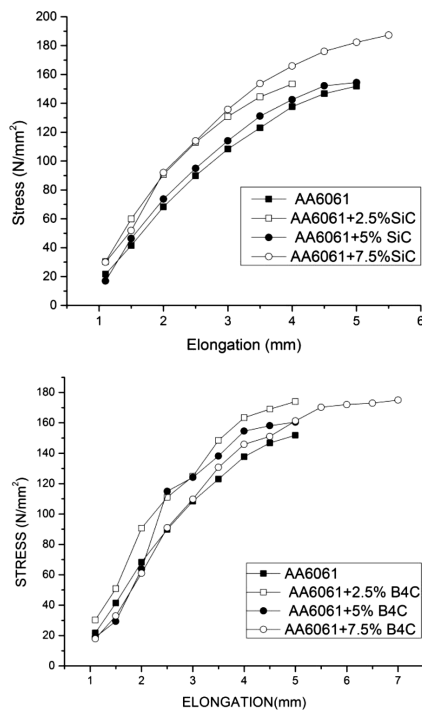


**Figure 5:** Stress vs. elongation of: a) SiC-reinforced AA6061 and b) B<sub>4</sub>C-reinforced AA6061

**Slika 5:** Napetost v odvisnosti od raztezka: a) AA6061, ojačan z SiC in b) AA6061 ojačan z B<sub>4</sub>C

The tensile strength vs. strain analysis of the samples is shown in **Figure 6** from which it is noted that the ultimate strength, plasticity and elasticity increased with the percentage of added ceramics. The ultimate point and yield point of the B<sub>4</sub>C + AA6061 MMC were high compared to those of the SiC + AA6061 MMC. The ductility of both MMCs were high and it can be treated using unconventional machining process as well as conventional machining, and also the workability of the material was very good. Thus SiC-reinforced AA6061 and B<sub>4</sub>C-reinforced AA6061 MMC were suited for metal-forming processes such as hot and cold forging, rolling, drawing and spinning.

#### 4.1 Factors affecting ECM process parameters

##### 4.1.1 Factors influencing the material removal rate

In ECM the current is the major influencing parameter on the *MRR* of aluminium-based alloys. The values of the *MRR* obtained in experimentation with different levels of current for the selected samples were shown in **Figure 7a**. From **Figure 7a** it was observed that when the current was less the *MRR* was also less. The AA6061 + 7.5 % B<sub>4</sub>C gave a lower *MRR* compared to AA6061 + 7.5 % SiC. When the current was low the material removal rate was low and it gradually increased with increases in the current. A high current will lead to more material removal and optimum material removal appeared at a current value of 150 A. For better ECM indices, higher accuracy, and a better surface finish, it is

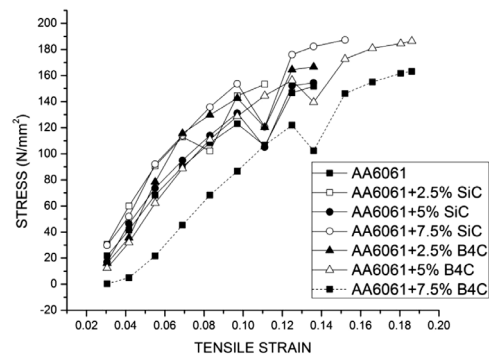


**Figure 6:** Stress strain diagram of MMC samples

**Slika 6:** Diagram odvisnosti napetost-raztezka MMC vzorcev

essential to choose the proper current density. Low values of current efficiency may indicate a failure to choose the optimum machining conditions that lead to high removal rates and surface roughness.

The influence of voltage over *MRR* for different samples is shown in **Figure 7b**. From the graph it was clear that the material removal rate was proportional to rate of change of voltage. When the maximum voltage was applied in between the workpiece and the tool, the maximum material can be removed from the workpiece. If the potential differences in between the copper electrode and aluminium alloys were very low, minimum material removal occurred from the workpiece.

The influence of electrolyte concentration over *MRR* is shown in **Figure 7c**. For the consideration of electrolyte concentration, best material removal occurred at a 10 g/L concentration. A very low electrolyte concentration produced minimum material removal due to the lack of ionic particles present in the electrolyte. At high range values the ionic concentration was high and the reaction phase at this stage was lagging. Hence, a lower rate of material removal was caused at a high concentration of electrolyte than with the medium electrolyte concentration of 10 g/L.

The influence of feed rate on *MRR* is shown in **Figure 7d**. The directly proportional effect was shown in discussion of the feed rate of the tool on the aluminium alloys. When the feed rate was 0.1 mm/min, then material removal was minimum. This process gradually increased with increases in the feed rate. It was a maximum at the maximum feed rate of 0.5 mm/min.

The influence of the gap on *MRR* is shown in **Figure 7e**. The gap plays a vital role in electrochemical machining. In electrochemical machining there is no direct physical contact in between the copper electrode and the aluminium workpiece. The reaction was carried out in the presence of an electrolyte that was circulated in between the tool and the workpiece. Therefore, to set the correct gap is an important factor to produce high material removal from the workpiece. In our experiment the maximum material removal could be obtained from the gap with an optimal value at 0.3 mm. Only a minimum amount of material was removed from the workpiece at a



gap of 0.5 mm. If the gap is a maximum then a lack of reaction will be carried out in between the tool and the minimum *MRR* will be obtained in the workpiece.

The influence of flow rate on *MRR* is shown in **Figure 7f**. The electrolyte flow rate across the tool and the workpiece stamped the noted impressions. During machining the chips were formed on the surface of the workpiece. Electrolyte flow plays the major role in the material removal process with the removal of contaminated chip particles presented on the surface of the machining area. If the flow rate of the electrolyte is too low to splash out the removed chips material on the machined surface, then the minimum amount of material will be removed from the workpiece. From **Figure 7f** it is clear that the material removal rate was increased by increasing the flow of electrolyte. The maximum flow rate can be obtained from 8 L/min. Beyond this level it was slightly reduced due to the high flow of electrolyte, which will cause a lean electrolyte concentration.

4.1.2 Factors influencing surface roughness

Generally the ECM process is used for the machining of hard materials with good surface finish. But material removal rate and surface roughness are inversely proportional to each other. Therefore, if the material removal rate is high, a poor surface finish will be obtained in the machining process.

The influence of current on the *SR* for the selected samples is shown in **Figure 8a**. It was found that there

was an inverse effect between the surface roughness and the current. At low current conditions a good surface finish was obtained and it was gradually decreased with an increase in the current. At high current conditions the least surface roughness was obtained. The best value of surface roughness was achieved at minimum material removal and with respect to the hardness of material.

The influence of voltage on the *SR* for AMCs is shown in **Figure 8b**. If the potential difference in between the electrode and the workpiece is very high, then a poor surface roughness can be achieved from the aluminium workpiece. At low voltage the surface finish was high, and it was slightly increased at 10 V. Then it was smoothly reduced with an increase in the voltage and finally poor surface roughness occurred due to the maximum voltage level.

The *SR* obtained at the different levels of electrolyte concentration for selected samples is shown in **Figure 8c**. In the figure the surface roughness and electrolyte concentration were directly proportional to each other. If the electrolyte concentration was less, a poor surface finish obtained. It is increased with increasing the concentration of electrolyte. A high range of surface roughness can be achieved at a high electrolyte concentration. It was mainly due to the lubrication and good reaction between the electrode and the workpiece.

The influence of feed rate on *SR* is shown in **Figure 8d**. For considering the surface roughness feed rate and inter electrode gap plays the same role. A good surface

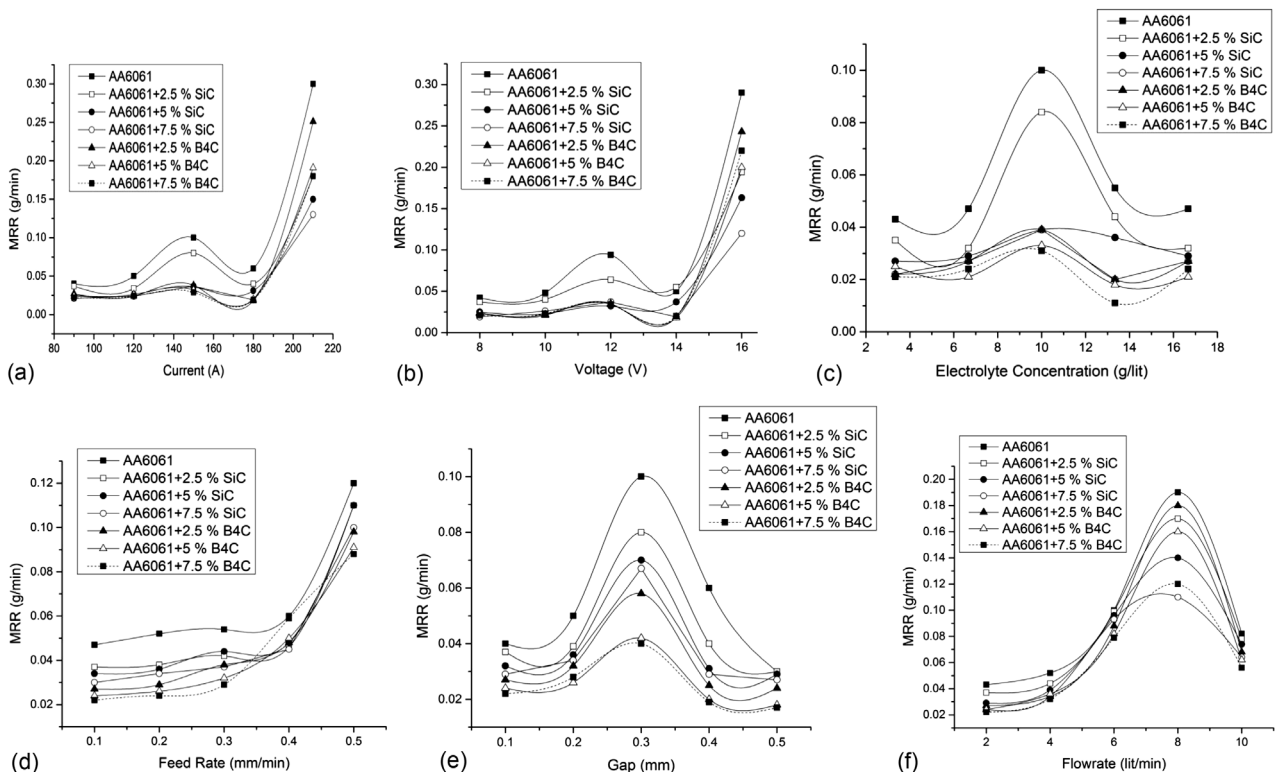


**Figure 7:** Influencing parameters with *MRR*: a) current, b) voltage, c) electrolyte concentrations, d) feed rate, e) gap, f) flow rate  
**Slika 7:** Parametri, ki vplivajo na *MRR*: a) tok, b) napetost, c) koncentracija elektrolita, d) hitrost podajanja, e) reza, f) hitrost pretoka

finish was obtained with a proper gap and a minimum feed rate. The feed rate was increased when the surface roughness of the workpiece was reduced.

The value of *SR* for different levels of gap is plotted and shown in **Figure 8e**. The optimal value of the inter electrode gap was maintained for a better surface roughness. The minimum electrode gap produced the minimum material removal rate and hence provided a good surface finish. A high surface roughness was obtained for a 0.2 mm gap and the surface finish was reduced with increases in the gap between the tool and the workpiece.

The electrolyte flow rate governs the surface finish in the right way. The influence of flow rate on *SR* was shown in **Figure 8f**. A very low flow rate creates a poor surface finish due to the non-flushing of the chip materials on the surface of the workpiece. A good surface roughness was obtained at a 6 L/min flow of electrolyte. The flushing pressure was high for very high electrolyte flow conditions like 10 L/min. A very high flushing pressure tends to produce a vertex on the machining zone, and it will produce abrasive action on the surface of the machined zone. Hence, under high flow rate conditions, the surface roughness was comparatively low.

#### 4.1.3 Factors influencing radial overcut

The *ROC* values obtained at different levels of current for the selected samples are shown in **Figure 9a**. The *ROC* was increased with an increase in the current. If the current was low then the minimum material was removed from the surface of the machined zone. Hence, the *ROC* was low. When the current was increased gradually, then the *ROC* was increased. When a high current

was applied in between the tool and the workpiece, then the maximum amount of material was removed from the workpiece and a high *ROC* was produced.

The influence of the applied voltage on the *ROC* is shown in **Figure 9b**. When the applied voltage between the electrodes was high, a high *ROC* was obtained. The optimal value of the *ROC* was achieved at a 12 V potential difference. At very low and very high voltages the flow of electrons through the electrodes is improper and hence it will tend to produce a variable machining rate. So the extreme levels of voltages were produced maximum *ROC* and minimum *ROC* was happened at mid-range values.

The effects of the electrolyte concentration on radial overcut for different AMCs are shown in **Figure 9c**. When the electrolyte concentration was high, the *ROC* was low. High lubrication was provided in a high concentration of electrolyte solutions and hence a better surface finish was obtained. The concentrated electrolyte solution has a good number of ions that will act as the catalyst to improve the reaction between the electrode and the workpiece. In the above condition an enormous amount of hydrogen was generated and an unwanted reaction in the machining zone was avoided. So, the minimum *ROC* was obtained with high electrolyte concentrations.

The influence of feed rate on the *ROC* is shown in **Figure 9d**. The material removal rate and the *ROC* were directly proportional to each other. The higher feed rate of the tools produced a poor surface roughness and a high material removal rate. The higher rate of material removal from the workpiece increased the *ROC*. The

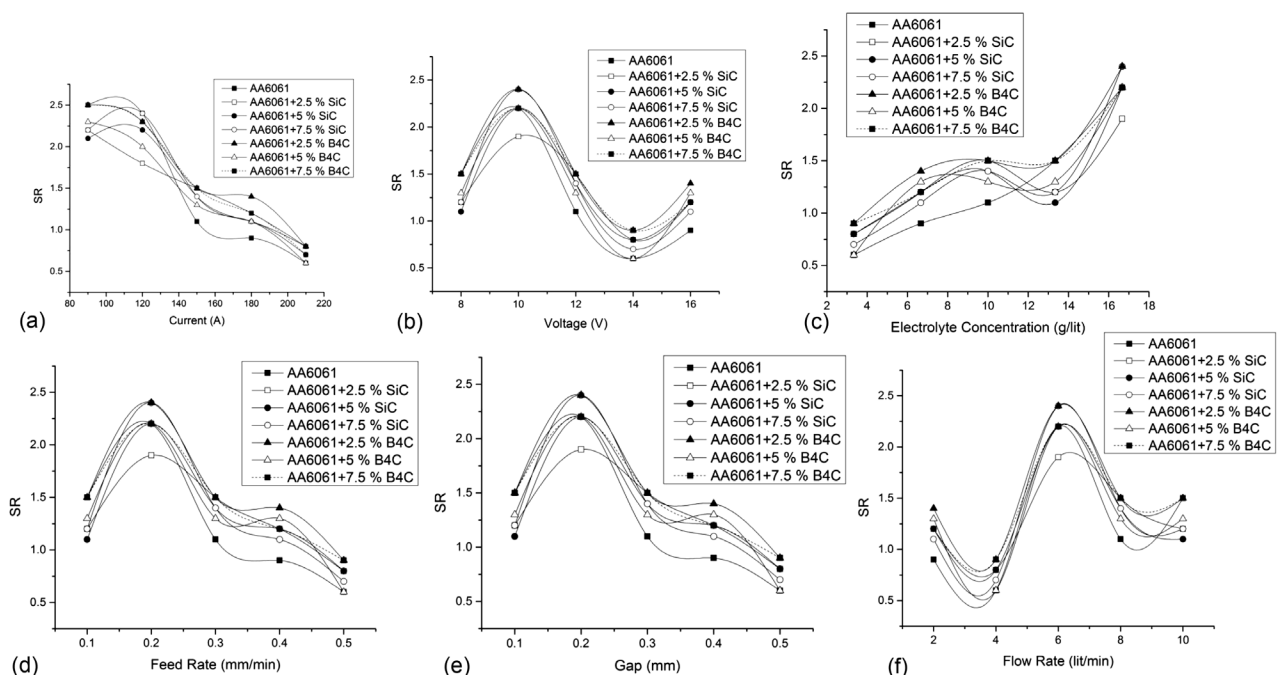


**Figure 8:** Influencing parameters with *SR*: a) current, b) voltage, c) electrolyte concentrations, d) feed rate, e) gap, f) flow rate  
**Slika 8:** Parametri, ki vplivajo na *SR*: a) tok, b) napetost, c) koncentracija elektrolita, d) hitrost podajanja, e) reža, f) hitrost pretoka

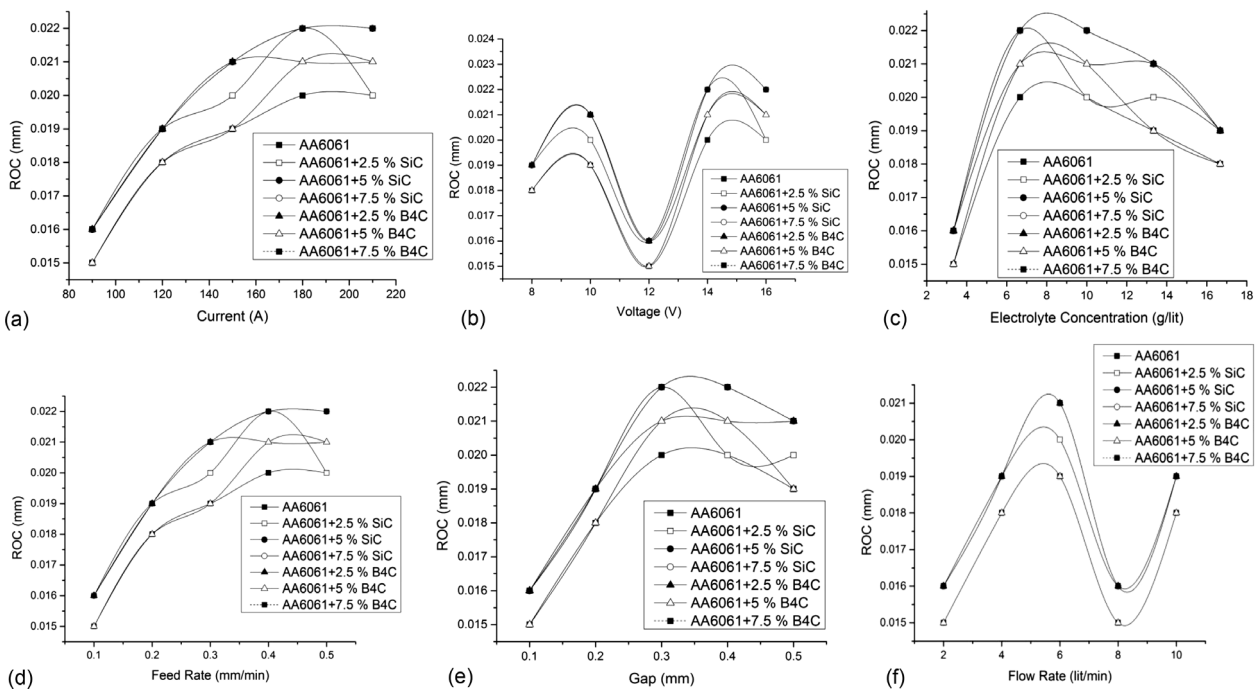


**Figure 9:** Influencing parameters with ROC: a) current, b) voltage, c) electrolyte concentrations, d) feed rate, e) gap, f) flow rate  
**Slika 9:** Parametri, ki vplivajo na ROC: a) tok, b) napetost, c) koncentracija elektrolita, d) hitrost podajanja, e) reža, f) hitrost pretoka

ROC was high at a very high range of the tool feed on the workpiece. The ROC values obtained in the different gaps for the selected samples were plotted in **Figure 9e**. The inter electrode gap was maintained with an optimal range of values. If the gap between the tool and the workpiece was too low, then the contact took place and the very minimum material was removed from the workpiece. Hence, the ROC in the low gap was a minimum. The spark in between the tool and the workpiece material might be produced because of an improper gap and irregular machining on the workpiece. Due to the irregular machining the ROC was very high.

The influence of flow rate on ROC is shown in **Figure 9f**. When the flow of the electrolyte was very low then the sludge was stagnated at the machining zone. Further machining was on the chip with a new machining surface and a poor surface finish leads to high ROC. Similarly, the high velocity of the stream of electrolyte created the flow of the abrasive action with sludge chips and hence the ROC was increased. The optimal flow of electrolyte was needed for the proper removal of sludge formation and good machining accuracy.

## 5 CONCLUSION

In this paper the microstructure and mechanical properties of AA6061 reinforced with silicon carbide and AA6061 reinforced with boron carbide obtained from an enhanced stir-casting method was investigated. Three different weight percentages, i.e., 2.5 %, 5 % and 7.5 %, of silicon carbide and boron carbide were used for the reinforcement. The presence of silicon- and boron-based

particles employs a key role in the microstructure development of the composites. The ductility of the AA6061 was increased in both the reinforced AMCs with significantly good tensile properties. The microhardness was markedly influenced by both the alloying elements. From the study it was observed that the selected AMCs were suitable for unconventional machining process like electrochemical machining. In ECM the input parameters influence the output variables Material Removal Rate (MRR), Surface Roughness (SR) and Radial Overcut (ROC). The higher input parameters increased the Material Removal Rate. The higher value of Material Removal Rate during the machining produced poor-surface-quality materials. The RO was also in close agreement with the SR.

## Acknowledgement

The author gratefully acknowledges the contributions of National Institute for Interdisciplinary Science and Technology Trivandrum, National Institute of Technology Trichy and Annamalai University Chithambaram.

## 6 REFERENCES

- 1 K. P. Rajurkar Sekar. T. Marappan, R. Experimental investigations into the influencing parameters of electrochemical machining of AISI 202, Journal of Advanced Manufacturing Systems, 7 (2008) 2, 337-43, doi:10.1142/S0219686708001486
- 2 A. DeBarr, D. A. Eand Oliver, Electro-chemical Machining, Macdonald & Co. Ltd, 1968
- 3 Metals Handbook, Vol. 16, Machining, ASM International, Materials Park, OH 1989

- <sup>4</sup> S. K. Mukherjee, S. Kumar, P. Shrivastava, A. Kumar, Effect of valency on material removal rate in electrochemical machining of aluminium, *Journal of Materials Processing Technology*, 202 (2008), 398–401, doi:10.1016/j.jmatprotec.2007.09.065
- <sup>5</sup> J. A. Westley, J. Atkinson, A. Duffield, Generic aspects of tool design for electrochemical machining, *Journal of Materials Processing Technology*, 149 (2004), 384–392, doi:10.1016/j.jmatprotec.2004.02.046
- <sup>6</sup> S. Dhar, R. Purohit, N. Saini, A. Sharma, G. H. Kumar, Mathematical modelling of electric discharge machining of cast Al-4Cu-6Si alloy-10 wt.% SiCp composites, *Journal of Materials Processing Technology*, 194 (2007), 24–29, doi:10.1016/j.jmatprotec.2007.03.121
- <sup>7</sup> C. Senthilkumar, G. Ganesan, R. Karthikeyan, Study of electrochemical machining characteristics of Al/SiCp composites, *Journal of Materials Processing Technology*, 43 (2009), 256–263, doi:10.1007/s00170-008-1704-1
- <sup>8</sup> T. Masuzawa, H. K. Tonshof, Three Dimensional Micro Machining by Machine Tools, *Annals of CIRP*, 42 (1997) 2, 621–628, doi:10.1016/S0007-8506(07)60882-8
- <sup>9</sup> A. F. Rashed, H. Youssef, H. El-Hofy, Effect of Some Process Parameters on the Side Machining During Electrolytic Sinking, PEDAC-3 Conf., Alexandria, 1986, 733–746
- <sup>10</sup> J. C. da Silva Neto, E. M. da Silva, M. B. da Silva, Intervening variables in electrochemical machining, *Journal of Materials Processing Technology*, 179 (2006) 1–3, 92–96, doi:10.1016/j.jmatprotec.2006.03.105
- <sup>11</sup> H. Youssef, H. El-Hofy, Y. El-Mehdawy, Sparking Phenomena and Hole Oversize by ECM, Effect of Some Process Parameters, *Alexandria Engineering Journal*, 28 (1989) 4, 247–259
- <sup>12</sup> M. Datta, R. V. Shenoy, L. T. Romatkiw, Recent Advances in the Study of Electrochemical Micromachining, *Journal of Engineering for Industry*, 118 (1996), 29–36, doi:10.1115/1.2803644
- <sup>13</sup> T. W. Clyne, P. J. Withers, An introduction to metal matrix composites, Cambridge University Press, 1993
- <sup>14</sup> K. K. Chawla, Composite materials-science and engineering, Springer-Verlag, New York (1998) 2, 165–211, doi:10.1007/978-0-387-74365-3\_1
- <sup>15</sup> D. L. McDanel, Analysis of stress–strain, fracture, and ductility behavior of aluminium matrix composites containing discontinuous silicon carbide reinforcement, *Metall Trans A*, 16 (1985), 1105–15, doi:10.1007/BF02811679
- <sup>16</sup> F. Toptan, A. Kilicarslan, M. Cigdem, I. Kertil, Processing and micro structural characterization of AA 1070 and AA 6063 matrix B4C reinforced composites, *Advanced Component Manufacture from Light Materials International Conference on Materials for Advanced Technologies*, 31 (2010) 1, 87–91, doi:10.1016/j.matdes.2009.11.064
- <sup>17</sup> C. San Marchia, M. Kouzelia, R. Raoc, J. A. Lewisc, D. C. Dunanda, Alumina-Aluminum Interpenetrating Phase Composites With Three Dimensional Periodic Architecture, *Journal of Scripta Materialia*, 49 (2003) 9, 861–866, doi:10.1016/S1359-6462(03)00441-X
- <sup>18</sup> T. M. Chenthil Jegan, D. Ravindran, M. Dev Anand, Material Characterization Study on Aluminium Metal Matrix Composites by Enhanced Stir Casting Method, *Advanced Materials Research*, 984–985 (2014), 326–330, doi:10.4028/www.scientific.net/AMR.984-985.326
- <sup>19</sup> K. M. Shorowordi, T. Laoui, A. S. M. A. Haseeb, J. P. Celis, L. Froyen, Microstructure and interface characteristics of B<sub>4</sub>C, SiC, Al<sub>2</sub>O<sub>3</sub> reinforced Al matrix composites: a comparative study, *J. Mater. Process. Technol.*, 142 (2003), 738–743, doi:10.1016/S0924-0136(03)00815-X
- <sup>20</sup> L. E. G. Cambroner, E. Sanchez, J. M. Ruiz-Roman, J. M. Ruiz-Prieto, Mechanical characterization of AA7015 aluminum alloy reinforced with ceramics, *Proceedings of the International Conference on the Advanced Materials Processing Technology*, 143–144 (2003), 378–383, doi:10.1016/S0924-0136(03)00424-2
- <sup>21</sup> E. Mart, A. Forn, R. Nogue, Strain hardening behaviour and temperature effect on Al-2124/SiCp, *Proceedings of the International Conference on the Advanced Materials Processing Technology*, 143–144 (2003), 1–4, doi:10.1016/S0924-0136(03)00292-9
- <sup>22</sup> J. S. Kwak, Y. S. Kim, Mechanical properties and grinding performance on aluminum-based metalmatrix composites, *Journal of Materials Processing Technology*, 201 (2008) 1–3, 596–600, doi:10.1016/j.jmatprotec.2007.11.139
- <sup>23</sup> M. Tan, Q. Xin, L. Zhenghua, B. Y. Zong, Influence of SiC and Al<sub>2</sub>O<sub>3</sub> particulate reinforcements and heat treatments on mechanical properties and damage evolution of Al-2618 metal matrix composites, *Journal of Materials Science*, 36 (2001), 2045–2053, doi:10.1023/A:1017591117670
- <sup>24</sup> D. T. Chung, Development of new actuators for flapping wing flight, *Materials Science Forum*, 543 (2007), 36–41, doi:10.4028/www.scientific.net/MSF.539-543.36
- <sup>25</sup> P. T. B. Shaffer, *Engineered Materials Handbook*, 4, 1991, 804–810
- <sup>26</sup> I. Kerti, F. Toptan, Microstructural variations in cast B<sub>4</sub>C-reinforced aluminium matrix composites (AMCs), *Journal of Materials Letters*, 62 (2008) 8–9, 1215–1218, doi:10.1016/j.matlet.2007.08.015
- <sup>27</sup> J. Hashim, L. Looney, M. S. J. Hashmi, Metal matrix composites: production by the stir casting method, *Journal of Materials Processing Technology*, 92–93 (1999), 1–7, doi:10.1016/S0924-0136(99)00118-1



# MODELING THE DEEP DRAWING OF AN AISI 304 STAINLESS-STEEL RECTANGULAR CUP USING THE FINITE-ELEMENT METHOD AND AN EXPERIMENTAL VALIDATION

## MODELIRANJE GLOBOKEGA VLEKA PRAVOKOTNE ČAŠE IZ AISI 304 NERJAVNEGA JEKLA Z METODO KONČNIH ELEMENTOV IN Z EKSPERIMENTALNIM PREVERJANJEM

**Bora Sener<sup>1</sup>, Hasan Kurtaran<sup>2</sup>**

<sup>1</sup>Yildiz Technical University, Department of Mechanical Engineering, Istanbul, Turkey

<sup>2</sup>Gebze Technical University, Department of Mechanical Engineering, Kocaeli, Turkey  
borasener84@gmail.com, borasen@yildiz.edu.tr

*Prejem rokopisa – received: 2015-09-06; sprejem za objavo – accepted for publication: 2015-11-16*

doi:10.17222/mit.2015.278

In this paper the deep drawing of a rectangular cup from AISI 304 stainless steel sheet was investigated numerically and experimentally. The finite-element method was used for computer modeling of the deep-drawing process. The thickness distribution predicted from the finite-element analysis was compared with experimental measurements. It was observed that the numerical results agree well with the experimental values. The minimum thickness was observed at the punch radius in both the simulation and experiment.

Keywords: deep drawing, rectangular cup, finite element, stainless steel

V članku je bil numerično in eksperimentalno preiskovan globoki vlek pravokotne čaše iz pločevine iz nerjavnega jekla AISI 304. Za računalniško modeliranje procesa globokega vleka je bila uporabljena metoda končnih elementov. Iz analize končnih elementov napovedana razporeditev debeline je bila primerjana z eksperimentalnimi meritvami. Preiskava je pokazala, da se numerični rezultati dobro ujemajo z eksperimentalnimi vrednostmi. Najmanjša debelina je bila opažena na radiusu pestiča, tako pri simulaciji kot tudi pri eksperimentu.

Ključne besede: globoki vlek, pravokotna čaša, končni element, nerjavno jeklo

## 1 INTRODUCTION

The rectangular/square-cup deep-drawing process has specific forming characteristic. Non-uniform material flow and quite complicated deformation mechanism are seen in this process. Therefore, the deep drawing of square and rectangular cups is more difficult than that of some other shapes, such as circular cups. Many researchers investigated the rectangular/square-cup deep-drawing process experimentally and numerically. A. G. Marmalis et al.<sup>1</sup> investigated the effect of material and forming characteristics on the simulation of the deep drawing of square cups by using the explicit non-linear finite-element code DYNA-3D. They considered the effect of material density, punch velocity and friction coefficient. L. F. Menezes and C. Teodosiu<sup>2</sup> studied the square-cup deep-drawing process numerically and experimentally. They modeled the process by using solid elements and compared the numerical results with the experiment. E. Bayraktar and S. Altintas<sup>3</sup> investigated the square-cup deep-drawing process and 2D-draw bending process of Hadfield steel experimentally. They evaluated the draw-in values of the flange, the principal strains in the square-cup deep drawing and compared the experimental results with that those of mild steel. Y. Ma-

rumo and H. Saiki<sup>4</sup> studied differential lubrication methods in the square-cup deep-drawing process in order to prevent any deformation concentration on the corners. Y. Harada and M. Ueyama<sup>5</sup> investigated the drawability of pure titanium sheets in the square-cup deep-drawing process. Titanium sheets were coated by heat oxide and formed into a square with a punch. L. M. A. Hezam et al.<sup>6</sup> developed a new technique for the deep drawing of square cups made from brass and pure aluminum. They improved the material flow by using a conical die with a square aperture at its end without a blank holder. M. Gavas and M. Izciler<sup>7</sup> designed a blank holder with a spiral spring to reduce the friction area between the blank and the blank holder during the deep drawing of square cups. A higher drawing height, a homogenous thickness distribution and minimum earing cups were obtained in their study. M. A. Hassan et al.<sup>8</sup> have developed a new divided blank holder with a tapered base and eight tapered segments to increase the deep drawability of the square cups. They improved the drawability of thin sheets and foils and increased the limiting drawing ratio with this technique over the conventional techniques. L. P. Lei et al.<sup>9</sup> studied the square-cup deep-drawing process for 304 stainless-steel sheet numerically and experimentally. They evaluated the effect of the blank

shape on the material flow. J. H. Lee and B. S. Chun<sup>10</sup> investigated the effect of temperature, blank shape and holding pressure on the deep drawability of a square cup from 304 stainless-steel sheet experimentally and numerically. F. K. Chen and S. Y. Lin<sup>11</sup> examined the effects of process parameters such as punch radius, die radius, die corner radius, die gap and the length-to-width ratio by both the finite-element method and the experimental approach. The authors formulated a formability index that serves as a design rule for the rectangular cup drawing from 304 stainless-steel sheet. Although many significant studies are carried out about the rectangular/square-cup deep-drawing process, they are generally limited to the forming of Al and Al alloys. Very little of the literature is devoted to the rectangular-cup deep drawing of 304 stainless-steel sheets. The available literature on the rectangular-cup deep drawing of 304 stainless steel sheets is limited to warm forming. Therefore, the cold forming of a rectangular cup from 304 stainless steel sheet is investigated numerically and experimentally in this study.

## 2 EXPERIMENTAL PROCEDURE

A die with a rectangular aperture, a conical punch and a circular blank holder that has a rectangular cavity are used in this study. The dimensions of the rectangular-cup tooling are given in **Table 1**. Deep-drawing experiments were carried out on a 160-ton-capacity double-action

hydraulic press. The punch is mounted to the lower shoe. The blank holder slides around the punch in the lower shoe. The upper shoe consists of the die. In the press, the lower shoe is mounted on the press bed and the upper shoe is attached to the press ram. The blank holder is supported by the cushion pins that apply the blank holding force to the blank holder during the forming process. During the deep-drawing process, the blank holder is raised to the top-most level. The blank is positioned on the blank holder. The clamped blank with the die and blank holder moves further down and forms the blank against the stationary punch under the action of the blank holder force through the cushion pins. The experimental set-up is shown in **Figure 1**.

**Table 1:** Tool dimensions

**Tabela 1:** Dimenzije orodja

Die	Radius, mm	35
	Edge length of rectangular cavity, mm	129 × 143
	Corner radius of the rectangular cavity, mm	47
	Depth of the rectangular portion, mm	27
Punch	Radius, mm	20
	Rectangular side length, mm	120 × 134
	Cone angle, deg	2
Blank holder	Diameter, mm	351
	Edge length of rectangular cavity, mm	127.5 × 142
	Corner radius of the rectangular cavity, mm	45.5

An austenitic grade AISI 304 stainless steel was used in this study. The thickness of the material was 0.8 mm. The mechanical properties of the material are explained in Section 3. The initial blank of diameter 335 mm was drawn to a rectangular cup of height 80 mm. A 340-kN blank holder force was applied in the experiments. The operating speed was 20 mm/s. A rectangular cup from 304 stainless-steel sheet was successfully drawn using the this blank holder force as shown in **Figure 2**.

## 3 FINITE ELEMENT MODEL

In the present work, the explicit non-linear finite-element (FE) code DYNIFORM 5.9.2 software is used for

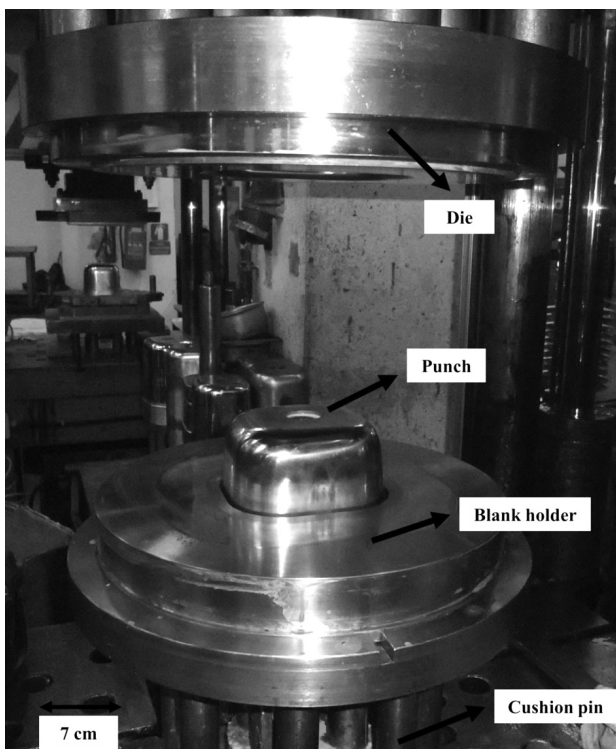


**Figure 1:** Experimental set-up  
**Slika 1:** Eksperimentalni sestav

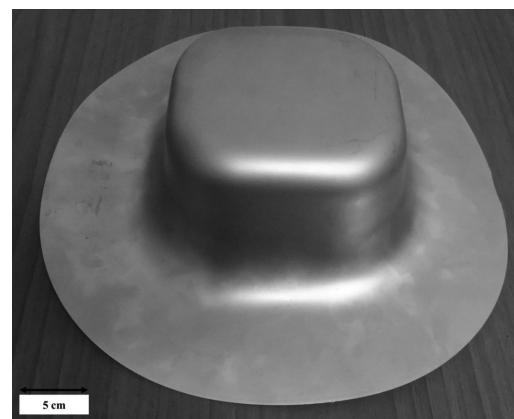


**Figure 2:** Rectangular cup  
**Slika 2:** Pravokotna čaša

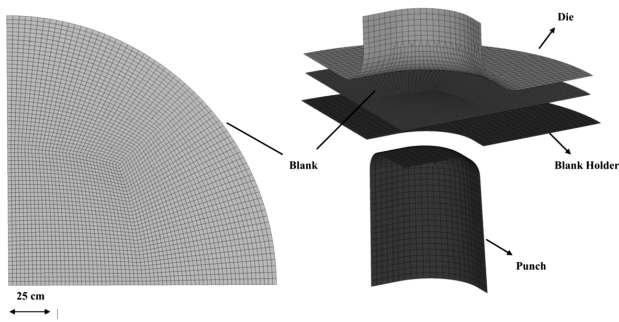


**Figure 3:** Finite-element model  
**Slika 3:** Model končnega elementa

simulating the rectangular-cup deep-drawing process. The blank is meshed with 3333 quadrilateral elements and 3434 nodes. A Belytschko-Tsay shell element with five integration points across the thickness is used for the shell mesh of the blank. Because of the symmetry, only a quarter model is employed in the numerical simulation, as shown in **Figure 3**. The punch, die and the blank holder were modeled as rigid objects because of their high stiffness, while the blank was modeled as a deformable body. A forming-one-way-surface-to-surface contact algorithm is used in the analysis. The friction coefficients are assumed to be 0.11 for the contact between the tools (die, punch and blank holder) and the blank. This value was recommended by a previous investigation.<sup>12</sup> The die speed employed is 1000 mm/s, which is extremely slow compared to the typical wave speeds in the materials to be formed (the wave speed in steel is approximately 5000 m/s). In general, inertia forces will not play a dominant role for forming rates that are considerably higher than the nominal 1000 mm/s rates in the physical problem.<sup>13</sup> The displacement of the die was taken as 80 mm, which is decided by the height of the cup. A 85-kN constant blank holder force is applied in the model (quarter of the experimental value). AISI 304 stainless-steel sheet is used in the simulation work. It is assumed that the material is isotropic and homogeneous. The strain-hardening model used is isotropic hardening. The mechanical properties of the material were determined by tensile testing. Different constitutive

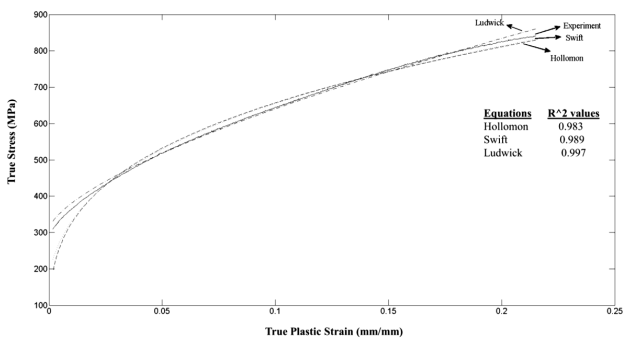


**Figure 4:** Comparison of the hardening models with experimental data

**Slika 4:** Primerjava modelov utrjevanja z eksperimentalnimi podatki

equations, such as Holloman, Swift, and Ludwick, were evaluated in order to represent the plastic behavior of the AISI 304 stainless steel. The nonlinear least-squares method and a trust-region algorithm were used in determining the material parameters. It was found that the Ludwick equation was the best fit to the experimental data for the AISI 304 stainless steel. This result agrees with the literature<sup>14</sup>. The flow curve was extrapolated to higher strains using this equation and was used in the simulation. A comparison of these different hardening models with experimental data is shown in **Figure 4**.

The mechanical properties of the materials are reported in **Table 2**.

**Table 2:** Mechanical properties of the material

**Tabela 2:** Mehanske lastnosti materiala

Parameters	Units	Value
Young's modulus ( $E$ )	GPa	256.86
Poisson's ratio ( $\nu$ )		0.28
Yield strength ( $\sigma_y$ )	MPa	308.94
Strain hardening ( $n$ )		0.3
Coefficient of strength ( $K$ )		1528

#### 4 RESULTS AND DISCUSSION

The thickness distribution is one of the major quality characteristics in the sheet-metal formed part. Therefore, the thickness distribution of the AISI 304 stainless-steel sheet in the deep-drawing process was investigated theoretically and experimentally. The drawn component was cut along the diagonal direction and the thickness of the part along this direction was measured using a micrometer, as shown in **Figure 5**.

For the verification of the FEM results, the thickness variations predicted by the numerical simulation were compared with the experimental results. **Figure 6** shows the comparison of the FE predictions with the experiment for the formed part along section YO (diagonal). It could be observed from **Figure 6** that the thickness

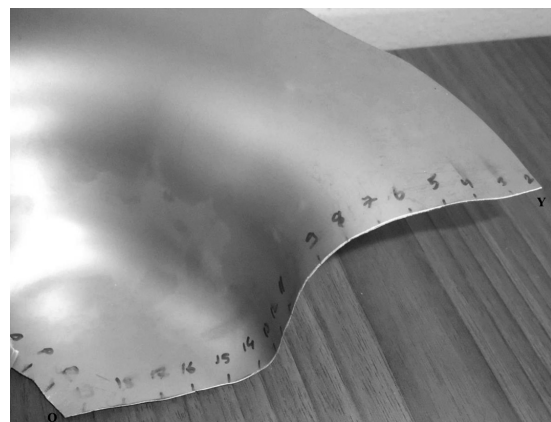


**Figure 5:** Location of the diagonal section in the formed part for evaluation of the thickness distribution

**Slika 5:** Prikaz diagonalnega preseka preoblikovanega dela za oceno razporeditve debeline

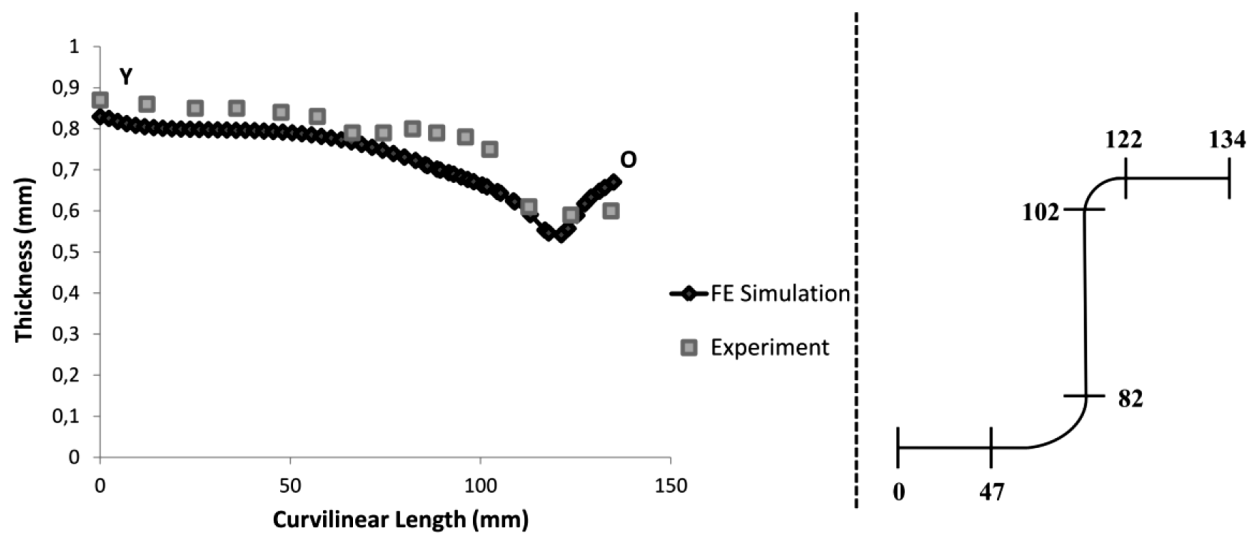


Figure 6: Comparison of the thickness distribution along section YO (diagonal) from FE simulation with experiments

Slika 6: Primerjava razporeditve debeline vzdolž preseka YO (diagonalno) iz FE simulacije z eksperimentalnimi podatki

distribution predicted by the FE simulation along section YO agrees with the experiment.

A minimum thickness was observed at the punch radius for both the simulation and the experiment. This is due to the appearance of the biaxial stretching state in this region. Hence, it is obvious that the potential failure site in the deep drawing of the part is located in the vicinity of the punch radius where the thinning is a maximum. This phenomenon is also observed by S. Gallée<sup>12</sup> during the deep drawing of stainless-steel sheet.

Although the trend of thickness distribution predicted by the simulation matches with the experiment, more thinning was observed in the simulation (32 %) than in the experiments (26 %). The difference in thinning could be attributed to the insufficiency of the tensile test. The flow stress available from the tensile test was limited to small strains at low strain rates. The flow curve of the material was obtained up to the 0.21 plastic strain value in the tensile test. Beyond this value, the hardening curve was extrapolated to high strains using the Ludwick equation. These values were probably overestimated. Thus, more restraining force to draw the material from the flange resulted in a localized thinning of 32 % in the simulation.

## 5 CONCLUSIONS

Finite-element simulations and deep-drawing experiments of the AISI 304 stainless-steel sheet were carried out. The conclusions can be summarized as follow:

- Different constitutive equations were evaluated to represent the plastic behavior of the AISI 304 stainless steel sheet. The Ludwick equation was the best fit to the experimental data for this steel.
- Good agreement was obtained between the experimental and finite-element results. Maximum thinning was observed at the punch radius in both the simula-

tion and experiment. This is because of the appearance of the biaxial stretch state at the punch radius.

- Predicted thinning values were larger than the experimental data at the punch radius. More thinning observed in the simulation could be due to the extrapolation of the flow stress to higher strains in the software and overestimated.

## Acknowledgements

The authors would like to thank Mr. Kani Yilmaz for his help with the experimental set-up.

## 6 REFERENCES

- <sup>1</sup> A. G. Mamalis, D. E. Manolacos, A. K. Baldoukas, Simulation of sheet metal forming using explicit finite element techniques: effect of material and forming characteristics, *Journal of Materials Processing Technology*, 72 (1997), 110–116, doi:10.1016/S0924-0136(97)00137-4
- <sup>2</sup> L. F. Menezes, C. Teodosiu, Three-dimensional numerical simulation of the deep-drawing process using solid finite elements, *Journal of Materials Processing Technology*, 97 (2000), 100–106, doi:10.1016/S0924-0136(99)00345-3
- <sup>3</sup> E. Bayraktar, S. Altintas, Square cup deep drawing and 2D-draw bending analysis of Hadfield steel, *Journal of Materials Processing Technology*, 60 (1996), 183–190, doi:10.1016/0924-0136(96)02326-6
- <sup>4</sup> Y. Marumo, H. Saiki, Evaluation of the forming limit of aluminum square cups, *Journal of Materials Processing Technology*, 80-81 (1998), 427–432, doi:10.1016/S0924-0136(98)00196-4
- <sup>5</sup> Y. Harada, M. Ueyama, Formability of Pure Titanium Sheet in Square Cup Deep Drawing, *Procedia Engineering*, 81 (2014), 881–886, doi:10.1016/j.proeng.2014.10.092
- <sup>6</sup> L. M. A. Hezam, M. A. Hassan, I. M. Hassab-Allah, M. G. El-Sebaie, Development of a new process for producing deep square cups through conical dies, *International Journal of Machine Tools & Manufacture*, 49 (2009), 773–780, doi:10.1016/j.ijmactools.2009.04.001



- <sup>7</sup> M. Gavas, M. Izciler, Design and application of blank holder system with spiral spring in deep drawing of square cups, *Journal of Materials Processing Technology*, 171 (2006), 274–282, doi:10.1016/j.jmatprotec.2005.06.082
- <sup>8</sup> M. A. Hassan, K. I. E. Ahmed, N. A. Takakura, A developed process for deep drawing of metal foil square cups, *Journal of Materials Processing Technology*, 212 (2012), 295–307, doi:10.1016/j.jmatprotec.2011.09.015
- <sup>9</sup> L. P. Lei, S. M. Hwang, B. S. Kang, Finite element analysis and design in stainless steel sheet forming and its experimental comparison, *Journal of Materials Processing Technology*, 110 (2001), 70–77, doi:10.1016/S0924-0136(00)00735-4
- <sup>10</sup> J. H. Lee, B. S. Chun, Investigation on the variation of deep drawability of STS304 using FEM simulations, *Journal of Materials Processing Technology*, 159 (2005), 389–396, doi:10.1016/j.jmatprotec.2004.05.029
- <sup>11</sup> F. K. Chen, S. Y. Lin, A formability index for the deep drawing of stainless steel rectangular cups, *International Journal of Advanced Manufacturing Technology*, 34 (2007), 878–888, doi:10.1007/s00170-006-0659-3
- <sup>12</sup> S. Gallée, P. Pilvin, Deep drawing simulation of a metastable austenitic stainless steel using a two-phase model, *Journal of Materials Processing Technology*, (2010), 835–843, doi:10.1016/j.jmatprotec.2010.01.008
- <sup>13</sup> F. Ayari, E. Bayraktar, *Journal of Achievements in Materials and Manufacturing Engineering*, 48 (2011) 1, 64–86
- <sup>14</sup> N. C. Da Silva, S. A. G. De Oliveria, E. H. Guimaraes, A Comparative Study of the Constitutive Equations to Predict Work Hardening Characteristics of Stainless Steels 304 and ACE P439A, 20th International Congress of Mechanical Engineering, Brazil, 2009, 1–7



# SURFACE AND ANTICORROSION PROPERTIES OF HYDROPHOBIC AND HYDROPHILIC TiO<sub>2</sub> COATINGS ON A STAINLESS-STEEL SUBSTRATE

## POVRŠINSKE IN PROTİKOROZIJSKE LASTNOSTI HIDROFOBNIH IN HIDROFILNIH TiO<sub>2</sub> PREVLEK NA JEKLENI PODLAGI

Marjetka Conradi, Aleksandra Kocijan

Institute of Metals and Technology, Lepi pot 11, 1000 Ljubljana, Slovenia  
marjetka.conradi@imt.si

Prejem rokopisa – received: 2016-04-21; sprejem za objavo – accepted for publication: 2016-05-03

doi:10.17222/mit.2016.068

We compare the wetting, morphology and anticorrosion properties of fluorosilane-modified TiO<sub>2</sub> (FAS-TiO<sub>2</sub>/epoxy) and as-received TiO<sub>2</sub>/epoxy coatings. An array of double-layer TiO<sub>2</sub> nanoparticles of two sizes (30 nm and 300 nm) were spin coated onto a steel substrate AISI 316L. The static water contact angles were measured to evaluate the wetting properties of the FAS-TiO<sub>2</sub>/epoxy (hydrophobic) and the as-received TiO<sub>2</sub>/epoxy (hydrophilic) coatings. The morphology of the coatings was analyzed with average surface roughness ( $S_a$ ) measurements and SEM imaging. We show that the order of the deposition in a double layer composed of dual-size nanoparticles plays an important role in the surface roughness and hence the wettability. SEM images reveal a typical morphology and  $S_a$  difference between the FAS-TiO<sub>2</sub>/epoxy and the as-received TiO<sub>2</sub>/epoxy coatings, reflected in the discrepancy of the average size of the agglomerates that are coating the substrate. Potentiodynamic measurements show an enhanced corrosion resistance for the FAS-TiO<sub>2</sub>/epoxy-coated AISI 316L stainless steel compared to the as-received TiO<sub>2</sub>/epoxy-coated AISI 316L.

Keywords: TiO<sub>2</sub>, epoxy, coatings, wetting, corrosion

V članku primerjamo omočitvene lastnosti, morfologijo in antikorozijske lastnosti s fluorosilanom oblečenih TiO<sub>2</sub> (FAS-TiO<sub>2</sub>/epoksi) in čistih TiO<sub>2</sub>/epoksi prevlek. TiO<sub>2</sub> nanodelce dveh velikosti (30 nm in 300 nm) smo na jekleno podlago tipa AISI 316L nanesli s "spin coaterjem". Omočitvene lastnosti prevlek smo določili z meritvami statičnih kontaktnih kotov. Le-te so pokazale hidrofobno naravo FAS-TiO<sub>2</sub>/epoksi prevlek in hidrofobno naravo čistih TiO<sub>2</sub>/epoksi prevlek. Morfološke lastnosti prevlek smo analizirali z meritvami povprečne hrapavosti površine ( $S_a$ ) ter SEM-mikroskopijo. Pokazali smo pomen vrstnega reda nalaganja nanodelcev dveh velikosti na hrapavost površine in njeno omočljivost. SEM-posnetki prikazujejo razliko v morfologiji in hrapavosti površin FAS-TiO<sub>2</sub>/epoksi in čistih TiO<sub>2</sub>/epoksi prevlek, ki se odraža v tvorbi aglomeratov različnih velikosti na eni in drugi površini. Potenciodinamske meritve kažejo izboljšano odpornost proti koroziji FAS-TiO<sub>2</sub>/epoksi prevlek v primerjavi s čistimi TiO<sub>2</sub>/epoksi prevlekami na jekleni podlagi tipa AISI 316L.

Ključne besede: TiO<sub>2</sub>, epoksi, prevleke, omočitvene lastnosti, korozija

## 1 INTRODUCTION

Austenitic (AISI) stainless steel is an important engineering material because of its generally high corrosion resistance combined with favourable mechanical properties, such as its high tensile strength.<sup>1,2</sup> Its high corrosion resistance is attributed to the presence of a passive film, which is stable, invisible, thin, durable and extremely adherent and self-repairing.<sup>3</sup> However, in many aggressive environments, such as a chloride-ion-rich environment, AISI 316L stainless steel is still observed to suffer from pitting corrosion.<sup>4</sup> Therefore, the modification of metallic surfaces using various coatings is an important subject in the field of enhancing particular surface properties, mechanical as well as anticorrosion properties.

Epoxy coatings have been widely used for metallic-surface protection because of their good mechanical and electrical-insulating properties, chemical resistance and strong adhesion to heterogeneous substrates. However, the highly cross-linked structure of an epoxy resin often makes epoxy coatings susceptible to the propagation of

cracks and damage due to surface abrasion and wear.<sup>5</sup> Therefore, a lot of research has been done to improve the performance of epoxy coatings by adding various nanoparticles, like SiO<sub>2</sub>, TiO<sub>2</sub>, ZnO, CuO etc.<sup>6</sup> In addition, nanoparticles also enhance the corrosion-protection properties of the epoxy coatings by decreasing the porosities due to the small size and high specific area. TiO<sub>2</sub> nanoparticles are well-known anticorrosion additives used in several applications, such as aerospace, marine, bio-medicine, etc. because of their unique physiochemical properties and good chemical stability.<sup>7-9</sup>

Here we report on a comparison of the surface and anticorrosion properties of double-layer, dual-size (30 nm and 300 nm) FAS-TiO<sub>2</sub>/epoxy and as-received TiO<sub>2</sub>/epoxy coatings. We show that the order of the nanoparticle deposition plays an important role in the wetting and the morphological properties of the coatings. Potentiodynamic measurements reveal that the hydrophobic coating has better anticorrosion properties than the hydrophilic coating.

## 2 EXPERIMENTAL PART

**Materials** – Epoxy resin (Epikote 816, Momentive Specialty Chemicals B.V.) was mixed with a hardener Epikure F205 (Momentive Specialty Chemicals B.V.) in the ratio of mass fractions of 100:53 %. TiO<sub>2</sub> nanoparticles with mean diameters of 30 nm were provided by Cinkarna Celje, whereas the 300-nm particles were provided by US Research Nanomaterials, Inc.

Austenitic stainless steel AISI 316L (17 % Cr, 10 % Ni, 2.1 % Mo, 1.4 % Mn, 0.38 % Si, 0.041 % P, 0.021 % C, <0.005 % S in mass fraction) was used as a substrate.

**Surface functionalization** – For the hydrophobic effect, TiO<sub>2</sub> particles were functionalized in 1 % of volume fractions of ethanolic fluoroalkylsilane or FAS17 (C<sub>16</sub>H<sub>19</sub>F<sub>17</sub>O<sub>3</sub>Si) solution.

**Steel substrate preparation** – Prior to the application of the coating, the steel discs of 25 mm diameter and with a thickness of 1.5 mm were diamond polished following a standard mechanical procedure and then cleaned with ethanol in an ultrasonic bath.

**Coating preparation** – To improve the TiO<sub>2</sub> nanoparticles' adhesion, the diamond-polished AISI 316L substrate was spin-coated with a 300-nm layer of epoxy (as determined by ellipsometry)<sup>10</sup> and then cured for 1 h at 70 °C and post-cured at 150 °C for another hour. The nanoparticles were then coated onto the AISI 316L + epoxy (AISI + E) surface by spin-coating 20 µL of 3 % of mass fractions of TiO<sub>2</sub> nanoparticle ethanolic solution. We prepared dual-size, double-layer coatings consisting of 30 nm and 300 nm FAS-TiO<sub>2</sub> nanoparticles. Both possibilities of the order of TiO<sub>2</sub> nanoparticles were analyzed for the FAS-TiO<sub>2</sub>/epoxy coatings' preparation: AISI+E+30+300 and AISI+E+300+30. Finally, the coatings were dried in an oven for approximately 20 min at 100 °C.

The same procedure was repeated with the as-received, non-functionalized, TiO<sub>2</sub> nanoparticles to prepare the TiO<sub>2</sub>/epoxy coatings.

**Scanning electron microscopy (SEM)** – SEM analysis using a FE-SEM Zeiss SUPRA 35VP was employed to investigate the morphology of the TiO<sub>2</sub> coatings' surfaces, which were sputtered with gold prior to imaging.

**Contact-angle measurements** – The static contact-angle measurements of water (W) on the TiO<sub>2</sub>/epoxy-coated AISI 316L substrates and on the FAS-TiO<sub>2</sub>/epoxy-coated AISI 316L substrates were performed using a surface-energy evaluation system (Advex Instruments s.r.o.). Liquid drops of 5 µL were deposited on different spots of the substrates to avoid the influence of roughness and gravity on the shape of the drop. The drop contour was analysed from an image of the deposited liquid drop on the surface and the contact angle was determined by using Young-Laplace fitting. To minimize the errors due to roughness and heterogeneity, the average values of the contact angles of the drop were calculated approximately 30 s after the deposition from at least five measurements on the studied coated steel. All the contact-angle measurements were carried out at 20 °C and ambient humidity.

**Surface roughness** – Optical 3D metrology system, model Alicona Infinite Focus (Alicona Imaging GmbH) was employed for the surface-roughness analysis. At least three measurements per sample were performed at a magnification of 20× with a lateral resolution of 0.9 µm and a vertical resolution of about 50 nm. IF-Measure-Suite (Version 5.1) software was used for the roughness analysis. The software offers the possibility to calculate the average surface roughness, S<sub>a</sub>, for each sample, based on the general surface roughness equation (Equation 1):

$$S_a = \frac{1}{L_x} \frac{1}{L_y} \int_0^{L_x} \int_0^{L_y} |z(x, y)| dx dy \quad (1)$$

where L<sub>x</sub> and L<sub>y</sub> are the acquisition lengths of the surface in the x and y directions and z(x,y) is the height. The size of the analyzed area was (714×542) µm. To level the profile, corrections were made to exclude the general geometrical shape and possible measurement-induced misfits.

**Electrochemical measurements** – Electrochemical measurements were performed on the TiO<sub>2</sub>/epoxy-coated AISI 316L stainless steel and on the FAS-TiO<sub>2</sub>/epoxy-coated AISI 316L stainless steel. The experiments were carried out in a simulated physiological Hank's solution, containing 8 g/L NaCl, 0.40 g/L KCl, 0.35 g/L NaHCO<sub>3</sub>, 0.25 g/L NaH<sub>2</sub>PO<sub>4</sub>×2H<sub>2</sub>O, 0.06 g/L Na<sub>2</sub>HPO<sub>4</sub>×2H<sub>2</sub>O, 0.19 g/L CaCl<sub>2</sub>×2H<sub>2</sub>O, 0.41 g/L MgCl<sub>2</sub>×6H<sub>2</sub>O, 0.06 g/L MgSO<sub>4</sub>×7H<sub>2</sub>O and 1 g/L glucose, at pH = 7.8 and 37 °C. All the chemicals were from Merck, Darmstadt, Germany. The measurements were performed by using BioLogic Modular Research Grade Potentiostat/Galvanostat/FRA Model SP-300 with EC-Lab Software and a three-electrode flat corrosion cell, where the working electrode (WE) was the investigated specimen, the reference electrode (RE) was a saturated calomel electrode (SCE, 0.242 V vs. SHE) and the counter electrode (CE) was a platinum net. The specimens were immersed in the solution 1 h prior to the measurement in order to stabilize the surface at the open-circuit potential (OCP). The potentiodynamic curves were recorded, starting the measurement at 250 mV vs. SCE more negative than the open-circuit potential (OCP). The potential was then increased, using a scan rate of 1 mV s<sup>-1</sup>, until the transpassive region was reached.

## 3 RESULTS AND DISCUSSION

### 3.1 Wetting properties

To analyze the surface wettability, we performed five static contact-angle measurements with water (W) on different spots all over the sample and used them to determine the average contact-angle values of the coating with an estimated error in the reading of θ±1.0°.

To fabricate a surface that is as hydrophobic as possible we followed the trend of increasing hydrophobicity based on dual-scale roughness.<sup>11,12</sup> For this purpose, the surface roughness was adjusted via spin-coating 30-nm



and 300-nm FAS-TiO<sub>2</sub> nanoparticles onto the flat AISI+E surface. The substrate was consequently modified by self-assembled FAS-TiO<sub>2</sub> nanoparticles resulting in micro- to nanoparticle-textured surfaces with a refined roughness structure. The static water contact angles,  $\theta^w$ , and average surface roughness,  $S_a$ , for both possibilities of the dual-size, double-layer, FAS-TiO<sub>2</sub>/epoxy coatings, (30 + 300) nm and reversed, (300 + 30) nm, are listed in **Table 1**. The measured contact angles indicate that the surface is more hydrophobic when the bottom layer is composed of 30-nm and the top layer of 300-nm FAS-TiO<sub>2</sub>. The difference in  $\theta^w$  between the two coatings is approximately 11° and this behavior can be attributed to the increased roughness implemented by the larger nanoparticles on the top, which is reflected in the average surface-roughness measurements,  $S_a$  (**Table 1**).

**Table 1:** Comparison of static water contact angles ( $\theta^w$ ) and average surface roughness ( $S_a$ ) of dual-size, double-layer FAS-TiO<sub>2</sub>/epoxy and as-received TiO<sub>2</sub>/epoxy coatings

**Tabela 1:** Primerjava statičnih kontaktnih kotov ( $\theta^w$ ) in povprečne površinske hrapavosti ( $S_a$ ) dvoplastnih FAS-TiO<sub>2</sub>/epoksi in čistih TiO<sub>2</sub>/epoksi prevlek

	Contact angle	Roughness	Contact angle	Roughness
	FAS-TiO <sub>2</sub>		TiO <sub>2</sub>	
Substrate	$\theta^w/^\circ$	$S_a/\text{nm}$	$\theta^w/^\circ$	$S_a/\text{nm}$
AISI+E+30+300	126.0	250.9	80.3	89.8
AISI+E+300+30	115.2	160.2	79.2	95.1

We prepared, in the same manner, a double-layer of (30 + 300) nm and (300 + 30) nm with as-received TiO<sub>2</sub> nanoparticles. These coatings are hydrophilic due to the hydroxyl groups on the surface of the as-received TiO<sub>2</sub> nanoparticles. The static water contact angles of both possibilities were comparable, around 80°. In addition, the average surface roughness,  $S_a$ , was much lower compared to the FAS-TiO<sub>2</sub>/epoxy coatings (**Table 1**). This result indicates that FAS functionalization significantly changes not only the wetting properties of the coating but also its morphology, as will be shown in the following section.

### 3.2 Surface morphology

**Figure 1** compares the morphology of the double-layer FAS-TiO<sub>2</sub>/epoxy (a, b) and the as-received TiO<sub>2</sub>/epoxy (c, d) coatings. SEM images reveal an obvious difference in the morphology between layers of FAS-TiO<sub>2</sub> and as-received TiO<sub>2</sub> nanoparticles, which is reflected mostly in the different length scale of the average size of the nanoparticle agglomerates and consequently in a discrepancy of the average surface roughness,  $S_a$ , as reported in **Table 1**. FAS functionalization apparently does not homogenize the particle distribution as the formation of large agglomerates up to a few tenths of microns is observed (**Figure 1a** and **1b**). In contrast, for the as-received TiO<sub>2</sub> nanoparticle coatings, the nanoparticles are more finely dispersed and agglomerates of

the order of few microns are observed (**Figure 1c** and **1d**).

SEM images also reveal that TiO<sub>2</sub> nanoparticles were not able to cover completely the underlying substrate. This might additionally influence the contact-angle values and the wetting properties of the FAS-TiO<sub>2</sub> and the as-received TiO<sub>2</sub> layers as the epoxy substrate is hydrophilic with a static water contact angle of 74.3°. This effect is, however, probably more pronounced in coatings prepared with hydrophobic FAS-TiO<sub>2</sub> nanoparticles, as the uncovered fractions allow the water to impregnate between the nanoparticles and the agglomerates to come into contact with the exposed hydrophilic epoxy and, consequently, reduce the static water contact angle. On the other hand, this effect does not play an important role in the as-received TiO<sub>2</sub>/epoxy coatings as both the as-received TiO<sub>2</sub> nanoparticles and the epoxy are hydrophilic.

The role of the order of nanoparticle deposition seems to be more pronounced in the FAS-TiO<sub>2</sub>/epoxy coatings (**Figure 1a** and **1b**), which is also reflected in the discrepancy in static water contact angles and the average surface roughness between AISI+E+30+300 and AISI+E+300+30, as reported in **Table 1**. Larger particles on the top seem to create larger agglomerates and consequently a rougher surface.

The morphology of the as-received TiO<sub>2</sub>/epoxy coatings, AISI+E+30+300 and AISI+E+300+30 (**Figure 1c** and **1d**) is, however, comparable, as are the static water contact angles and the average surface roughness (**Table 1**).

### 3.3 Potentiodynamic measurements

For an analysis of the anticorrosion properties we chose the more hydrophobic coating, FAS-TiO<sub>2</sub>/epoxy coating, AISI+E+30+300. The comparison was made

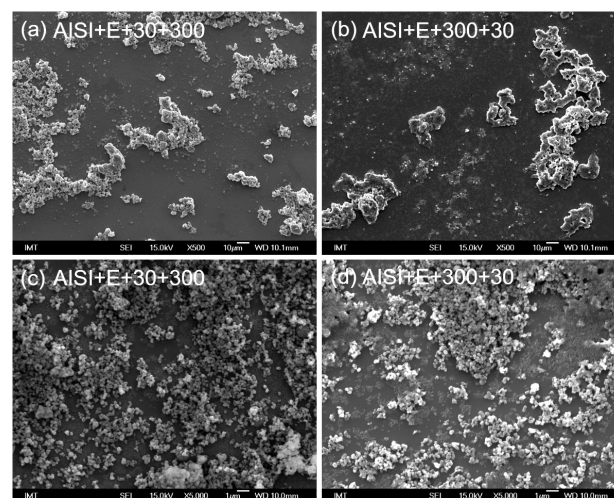


**Figure 1:** Comparison of surface morphology of double-layer, FAS-TiO<sub>2</sub>/epoxy (a, b) and as-received, TiO<sub>2</sub>/epoxy (c, d) coatings

**Slika 1:** Primerjava morfologije dvoplastnih FAS-TiO<sub>2</sub>/epoksi (a, b) in čistih TiO<sub>2</sub>/epoksi (c, d) prevlek

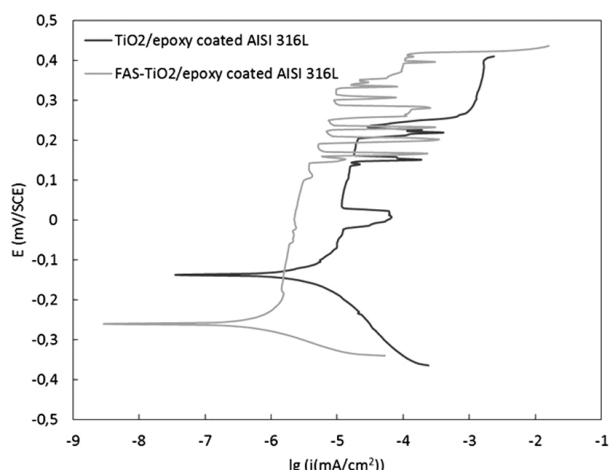


**Figure 2:** Potentiodynamic curves for as-received  $\text{TiO}_2$ /epoxy- and FAS- $\text{TiO}_2$ /epoxy-coated AISI 316L substrate in a simulated physiological Hank's solution

**Slika 2:** Potenciodinamske krivulje čistih  $\text{TiO}_2$ /epoksi in FAS- $\text{TiO}_2$ /epoksi prevlek na AISI 316L podlagi, izmerjene v simulirani fiziološki Hankovi raztopini

with the as-received  $\text{TiO}_2$ /epoxy coating using the same order of particle deposition (30+300). **Figure 2** shows the potentiodynamic behaviour of the as-received  $\text{TiO}_2$ /epoxy-coated AISI 316L and FAS- $\text{TiO}_2$ /epoxy-coated AISI 316L stainless steel in a simulated physiological Hank's solution. We studied the polarization and the passivation behaviour of the tested material after the surface modification. After 1 h of stabilization at the OCP, the corrosion potential ( $E_{\text{corr}}$ ) for the as-received  $\text{TiO}_2$ /epoxy-coated AISI 316L in Hank's solution was approximately  $-0.13$  V vs. SCE. Following the Tafel region, the alloy exhibited a broad range of passivity. The breakdown potential ( $E_b$ ) was approximately  $0.25$  V vs. SCE. In the case of the FAS- $\text{TiO}_2$ /epoxy-coated AISI 316L stainless steel, the  $E_{\text{corr}}$  in Hank's solution was approximately  $-0.27$  V vs. SCE. The passivation range was significantly broader, i.e.,  $0.4$  V vs. SCE, and at lower corrosion-current densities compared to  $\text{TiO}_2$ /epoxy-coated AISI 316L specimen. The results show an enhanced corrosion resistance for the FAS- $\text{TiO}_2$ /epoxy-coated AISI 316L stainless steel compared to as-received  $\text{TiO}_2$ /epoxy coated AISI 316L.

#### 4 CONCLUSIONS

We analyzed the wettability behavior of double-sized, double-layer, FAS-functionalized  $\text{TiO}_2$  and as-received  $\text{TiO}_2$  nanostructured surfaces. We showed that the order of the  $\text{TiO}_2$  nanoparticle deposition determines the surface roughness and hence the wettability, as confirmed by the average surface-roughness measurements and the SEM imaging. This effect was more pronounced in coatings with FAS- $\text{TiO}_2$  nanoparticles. The morphology analysis also revealed a typical morphology and  $S_a$  difference between the FAS- $\text{TiO}_2$ /epoxy and the as-received  $\text{TiO}_2$ /epoxy coatings reflected in a discrepancy in the

average size of the agglomerates that are coating the substrate. The corrosion stability of double-sized, double-layer, FAS-functionalized  $\text{TiO}_2$  and the as-received  $\text{TiO}_2$  nanostructured coatings on the surface of the AISI 316L stainless steel was studied in a simulated physiological Hank's solution. The results showed the superior corrosion stability of the FAS- $\text{TiO}_2$ /epoxy-coated AISI 316L stainless steel compared to the as-received  $\text{TiO}_2$ /epoxy-coated AISI 316L.

#### Acknowledgement

This work was carried out within the research project J2-7196: "Antibakterijske nanostrukturirane zaščitne plasti za biološke aplikacije" of the Slovenian Research Agency (ARRS).

#### 5 REFERENCES

- M. A. M. Ibrahim, S. S. A. El Rehim, M. M. Hamza, Corrosion behavior of some austenitic stainless steels in chloride environments, *Mat. Chem. Phys.*, 115 (2009), 80–85, doi:10.1016/j.matchemphys.2008.11.016
- T. Hryniewicz, R. Rokicki, K. Rokosz, Corrosion characteristics of medical-grade AISI Type 316L stainless steel surface after electropolishing in a magnetic field, *Corrosion*, 64 (2008), 660–665, doi: http://dx.doi.org/10.5006/1.3279927
- C. Perez, A. Collazo, M. Izquierdo, P. Merino, X. R. Novoa, Characterisation of the barrier properties of different paint systems, Part II. Non-ideal diffusion and water uptake kinetics, *Prog. Org. Coat.*, 37 (1999), 169–177, doi:10.1016/s0300-9440(99)00073-9
- C. G. Oliveira, M. G. S. Ferreira, Ranking high-quality paint systems using EIS, Part 1: intact coatings, *Corrosion Science*, 45 (2003), 123–138, doi:10.1016/s0010-938x(02)00088-4
- B. Wetzel, F. Hauptert, M. Q. Zhang, Epoxy nanocomposites with high mechanical and tribological performance, *Comp. Sci. Technol.*, 63 (2003), 2055–2067, doi:10.1016/s0266-3538(03)00115-5
- Y. Qing, C. Yang, Y. Sun, Y. Zheng, X. Wang, Y. Shang, L. Wang, C. Liu, Facile fabrication of superhydrophobic surfaces with corrosion resistance by nanocomposite coating of  $\text{TiO}_2$  and polydimethylsiloxane, *Colloids and Surfaces A-Physicochemical and Engineering Aspects*, 484 (2015), 471–477, doi:10.1016/j.colsurfa.2015.08.024
- V. N. Moiseev, Titanium in Russia, *Metal Science and Heat Treatment*, 47 (2005), 371–376, doi:10.1007/s11041-005-0080-9
- I. Gurrappa, Characterization of titanium alloy Ti-6Al-4V for chemical, marine and industrial applications, *Mat. Charact.*, 51 (2003), 131–139, doi:10.1016/j.matchar.2003.10.006
- F. Samanipour, F. M. R. Bayati, F. Golestani-Fard, H. R. Zargar, A. R. Mirhabibi, V. Shoaie-Rad, S. Abbasi, Innovative fabrication of  $\text{ZrO}_2$ -HAp- $\text{TiO}_2$  nano/micro-structured composites through MAO/EPD combined method, *Materials Letters*, 65 (2011), 926–928, doi:10.1016/j.matlet.2010.11.039
- M. Conradi, G. Intihar, M. Zorko, Mechanical and wetting properties of nanosilica/epoxy-coated stainless steel, *Mater. Tehnol.*, 49 (2015), 613–618, doi:10.17222/mit.2015.060
- L. Xu, R. G. Karunakaran, J. Guo, S. Yang, Transparent, Superhydrophobic Surfaces from One-Step Spin Coating of Hydrophobic Nanoparticles, *ACS Appl. Mat. & Interfaces*, 4 (2012), 1118–1125, doi:10.1021/am201750h
- T. J. Athauda, W. Williams, K. P. Roberts, R. R. Ozer, On the surface roughness and hydrophobicity of dual-size double-layer silica nanoparticles, *J. Mat. Sci.*, 48 (2013), 6115–6120, doi:10.1007/s10853-013-7407-5

# ELECTROSLAG REMELTING: A PROCESS OVERVIEW

## ELEKTROPRETALJEVANJE POD ŽLINDRO – PREGLED PROCESA

**Boštjan Arh, Bojan Podgornik, Jaka Burja**

Institute of Metals and Technology, Lepi pot 11, Ljubljana, Slovenia  
bostjan.arh@imt.si

*Prejem rokopisa – received: 2016-06-15; sprejem za objavo – accepted for publication: 2016-09-02*

doi:10.17222/mit.2016.108

The electroslag remelting process (ESR) is important because it provides better control of the solidification microstructure and chemical homogeneity; it also enables greater cleanliness and better mechanical properties. The manufactured high-alloyed steels and other alloys with a controlled chemical composition are used in aerospace, in thermal- and nuclear-power plants, in chemical engineering, for military equipment, special tools, etc. An overview and the basics of the ESR process are presented in this paper.

**Keywords:** electroslag remelting, solidified microstructure, chemical homogeneity, clean steel

Postopek elektropretaljevanja kvalitetnih jekel pod žlindro (EPŽ) ima velik pomen zaradi sposobnosti nadzora strjevalne strukture in kemijske homogenosti saj postopek omogoča doseganje večje čistosti jekla in boljše mehanske lastnosti. Tako izdelana visokolegirana jekla, in zlitine z garantirano kemijsko sestavo in lastnostmi, se namensko uporabljajo v letalstvu, termoelektrarnah in jedrskih elektrarnah, v kemični industriji, v medicini, za vojaško opremo, za specialna orodja, itd. V prispvku so opisane osnove tehnologije pretaljevanja zlitin pod žlindro.

**Ključne besede:** elektropretaljevanje pod žlindro, strjevalna struktura, kemijska homogenost, čisto jeklo

### 1 INTRODUCTION

Nowadays, steelmaking technology enables the production of high-purity steel melts. However, during ingot casting the reoxidation of the melt occurs, thus increasing the inclusion content. Segregations on the macro and micro scales are also characteristic for ingot casting. These cause anisotropy in the mechanical properties of the steel. The ESR process almost completely removes the macro-segregation phenomenon in heavy steel ingots, thus ensuring a more homogeneous chemical composition and a finer microstructure with fewer and more evenly distributed non-metallic inclusions than in cast ingots.<sup>1</sup> The influence of ESR on remelted steel is shown in **Figure 1**.<sup>2</sup> This is why the ESR process is essential for heavy steel ingots that are used for the manufacturing of large generator and turbine shafts.<sup>3</sup>

The ESR process is suitable for high-quality materials such as:

- steel ball bearings, steel rollers, tool steels, wear-resistant steels for low and high working temperatures, high-speed steels for high performance,
- highly alloyed stainless steels, corrosion- and acid-resistant steels and steels for high-temperature applications,
- steels for aviation and aerospace technology, for medical, pharmaceutical and chemical industries,
- Ni superalloys, Ti and Zr alloys for aerospace, medical and chemical industry, components,
- off-shore, power and aerospace engineering, reactor comp.

ESR is a continuous process, where during the remelting of the consumable electrode, refining and solidification of the steel occur simultaneously. Cast, rolled or forged ingots can be used as a consumable electrode.

The ESR process is based on an electrical current running via an electrode through the molten slag and ingot. Due to the high electrical resistance of the slag, the slag heats up and melts. The consumable electrode is immersed in the liquid slag where the slag heat gradually melts the tip of the electrode. Liquefied steel is dripping

	Worse	Same	Better	Much better
<b>Quality of ingot</b>				
Surface			↔	
Porosity, density			↔↔	
Yield of metal			↔↔↔	
<b>Chemical composition</b>				
Basic elements	↔↔			
Hydrogen	↔↔↔			
Oxygen			↔↔↔↔	
Sulfur			↔↔↔	
Oligoelements		↔↔		
<b>Degree of purity</b>				
Microscopic			↔↔↔↔	
Macroscopic			↔↔	
<b>Structure of ingot</b>				
Block segregation			↔↔↔↔	
Crystal segregation		↔↔↔↔		
<b>Mechanical properties</b>				
Hardness	↔↔↔			
Tensile strength	↔↔↔			
Toughness			↔↔↔↔	
Isotropy			↔↔↔↔	

**Figure 1:** Effect of ESR on the properties of remelted steels<sup>2</sup>

**Slika 1:** Vpliv ESR na lastnosti pretaljenih jekel<sup>2</sup>



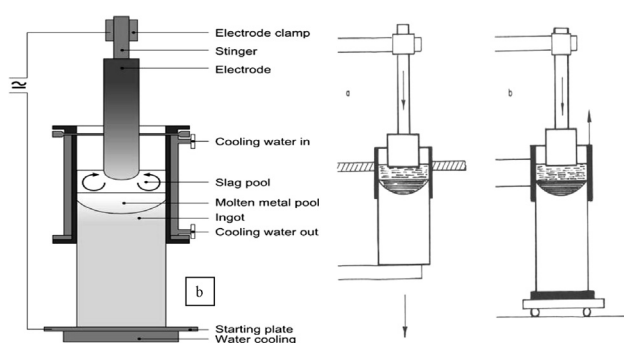


**Figure 2:** Schematic representation of the ESR unit: a) retracting ingot, b) rising mould<sup>5,6</sup>

**Slika 2:** Shematski prikaz ESR naprave: a) navzdol vlečen ingot, b) dvigajoča kokila<sup>5,6</sup>

from the electrode tip and is refined when passing through the liquid slag, with oxides and sulphur being bound in the slag. After passing through the slag, the steel cools down and solidifies again into a remelted ingot.<sup>3,4</sup> The whole remelting process takes place in a water-cooled copper mould, which allows the remelted ingot to solidify quickly and very uniformly.

The mould with the slag pool is moving upwards as the new ingot is formed. The design of the mould can be in the form of fixed long moulds or collar-type moulds. The use of collar-type moulds with movable moulds or a movable base plate, gives the possibility of producing ingots of any required length (**Figure 2**).<sup>5,6</sup> Furthermore, the ESR enables the production of ingots with the desired shape, i.e., round, square, rectangular.

In Slovenia, among other steelmaking processes, ESR technology is used in the Metal Ravne steelworks.

## 2 ATMOSPHERE CONTROL

Due to the ever-increasing demands for material properties, different variations of the ESR process were developed to ensure these demands.<sup>6-8</sup>

IESR (electroslag remelting under a protective atmosphere of inert gas at atmospheric pressure) is a variation of the ESR where an inert gas (argon) protects the slag and metal from oxidation and the absorption of nitrogen and hydrogen from the air. The oxidation of the electrode is almost entirely avoided, thus providing better cleanliness of the ingot. However, due to the absence of oxygen in the furnace atmosphere, desulphurization is not optimal.

PESR (electroslag remelting under increased pressure) is a variation of the ESR with an increased pressure of nitrogen and the melt solidifies under pressure. In this way a large amount of nitrogen can be introduced into the steel melt. The pressure depends on the alloy composition and the desired nitrogen content in the remelted ingot.

VAC-ESR (electroslag remelting under vacuum) is a variation of the ESR that provides vacuum degassing of

the melt. Dissolved gases such as hydrogen and nitrogen are removed, and the remelted metal is protected from oxidation. The process is suitable for the remelting of superalloys and titanium alloys.

## 3 PROCESS PARAMETERS

The heat required to run the ESR process is generated by the Joule effect in the slag bath. The electrical characteristics, heat balance and electrode/ingot diameter, influence the quality of the remelted ingot.<sup>7,9</sup> An energy input of between 1000 kWh/t and 1500 kWh/t of steel is usually required for ESR. The slag bath is considered to be a variable resistor, whose resistance is determined by the electrode distance, the effective slag resistivity and by the electrical current path. The usual slag depth is of the order of 100 mm.

The shape of the liquid pool is influenced by the heat input in the process.<sup>10,11</sup> The greater the distance between the consumable electrode and the remelted ingot, the smoother the heat distribution in the slag. When determining the electrode distance, it is important to take into consideration that a shorter current path means a higher current with concentrated heat generation under the electrode tip and an undesirable deepening of the metal pool. On the other hand, a longer current path demands a high voltage, which causes more even heat generation and a flatter, more favourable pool profile. ESR operating voltages are usually in the region of 40 V or less.

A choice of AC versus DC circuit ESR<sup>9</sup> is possible. For ingots of 20 cm in diameter or more, single phase AC gives optimum refinement and melt rate. The DC-ESR requires a lower melt rate for metal refinement. However, when the metal refinement is not the main criterion, the DC-ESR provides the highest melting rates per unit of power consumption. The present practice is to utilize a single-phase AC power supply and low electrode/ingot diameter ratio (0.4 to 0.7).<sup>11</sup> Typically, a frequency of 50 Hz or 60 Hz is used in AC operation. However, for the largest ingots, where reactivity becomes more important, it is better to use low-frequency power (5-10 Hz) for improved efficiency.

Optimum melting rates and energy inputs depend on the ingot diameter. A. S. Ballantyne and A. Mitchell<sup>12</sup> considered the optimum conditions for the maximum permissible melt rate at the lowest possible power with the Equation (1):

$$\text{Melt rate} = \text{constant} \times \text{power} \times \text{fill ratio (area)} \times \frac{\text{mould area}}{\text{electrode distance}} \quad (1)$$

Many operators considered melt rate as proportional to the ingot diameter, which is obtained at a melt rate of the order of 0.004 kg/min/mm.<sup>7</sup> The relationships between the melt rate, current and voltage for a 240-mm diameter ingot are shown in **Figure 3**. For a given



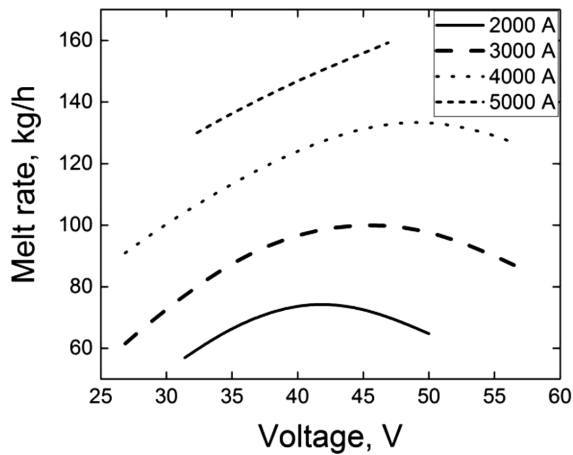


Figure 3: Effect of current and voltage on melt rates<sup>7</sup>  
 Slika 3: Vpliv toka in napetosti na hitrost taljenja<sup>7</sup>

current and ingot size there is an optional voltage that corresponds to a maximum melt rate.<sup>7</sup>

The ESR process can be controlled by a computer: from melt initiation, through power build-up, steady melt rate period, reduced melt rate period to maintain pool profile, hot-tapping sequences and melting termination.<sup>13</sup>

4 SLAG

The slag plays an important role in the ESR process; it generates Joule heat for the melting of the electrode, refines the liquid metal through the absorption of non-metallic inclusions, desulphurization, protects the metal from contamination, provides lubrication for the copper mould/solidifying steel shell interface, and controls the horizontal heat transfer between solidifying metal and mould.

Slags for ESR are usually based on calcium fluoride (CaF<sub>2</sub>), lime (CaO) and alumina (Al<sub>2</sub>O<sub>3</sub>). Silica (SiO<sub>2</sub>), magnesia (MgO) and titania (TiO<sub>2</sub>) may be present, depending on the alloy to be remelted and refined. The CaF<sub>2</sub> content increases the solubility of basic components in the slag (CaO and MgO) and thus increases the effective sulphide capacity of the slag.<sup>7</sup> In order to perform its intended functions, the slag must have some well-defined properties, which are:

- its melting point must be lower than that of the metal to be remelted,
- it must be electrically efficient,
- its composition must ensure the desired chemical reactions,
- it must have suitable viscosity at the remelting temperature.

As presented in Table 1 the concentrations of calcium fluoride may vary from 0 % to 100 % of mass fractions.<sup>7</sup> The remaining slag constituents are mostly used for decreasing the basicity.

The slag chemical composition is changed during the ESR process, due to the formation of volatile fluoride,

the precipitation of high-melting-point phases and the reaction in the ESR process.<sup>14</sup> The changes in composition affect the slag’s metallurgical properties and eventually affect the quality of the final product. The quantity of consumed slag steel depends on the remelted ingot diameter.<sup>6</sup>

Table 1: Composition of some ESR slags, in mass fractions (w/%)<sup>7</sup>  
 Tabela 1: Sestava nekaterih ESR žlinder, v masnih odstotkih (w/%)<sup>7</sup>

CaF <sub>2</sub>	CaO	MgO	Al <sub>2</sub> O <sub>3</sub>	SiO <sub>2</sub>	Comments
100					Electrically inefficient, use where oxides are not permissible
70	30				Difficult starting, high conductivity, use where Al not allowed, risk of H <sub>2</sub> pick-up
70	20		10		Good all-round slags, medium resistivity
70	15	0	15		
50	20		30		Good all-round slag, higher resistivity
70			30		Some risk of Al pick-up, good for avoidance of H <sub>2</sub> pick-up, higher resistivity
40	30		30		Good general-purpose slags
60	20		20		
80		10	10		Moderate resistivity, relatively inert
60	10	10	10	10	Low melting point, "long" slag
	50		50		Difficult starting, efficient electrically

Many of the slags used in ESR can be described with the ternary fluorspar-lime-alumina system.<sup>7</sup> The phase diagram shown in Figure 4 has been extensively investigated and defined by K. Mills.<sup>15</sup> The main feature is an eutectic corresponding to compositions with roughly

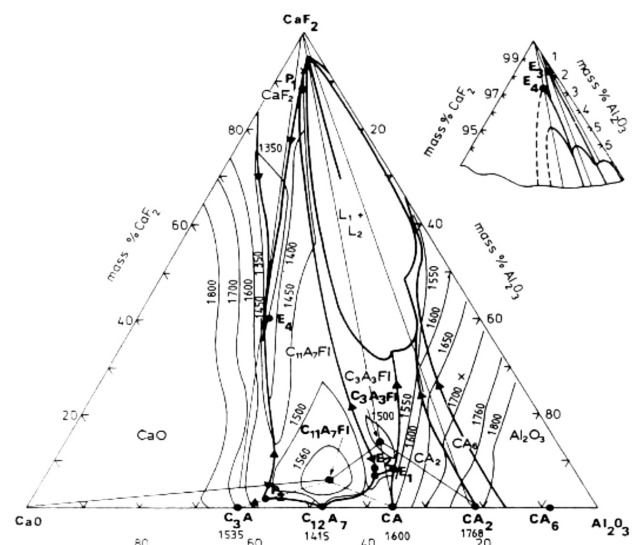
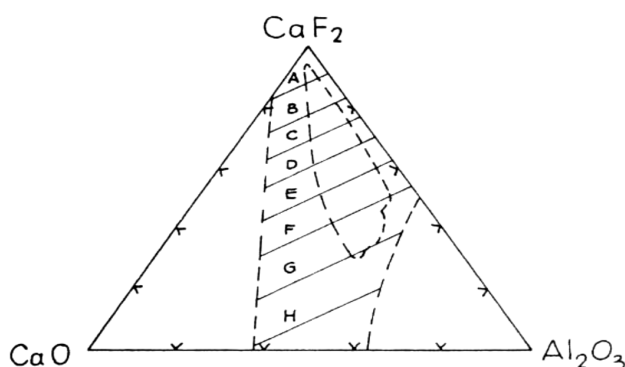


Figure 4: Phase diagram of the CaF<sub>2</sub>-Al<sub>2</sub>O<sub>3</sub>-CaO system according to K. Mills<sup>15</sup>

Slika 4: Fazni diagram sistema CaF<sub>2</sub>-Al<sub>2</sub>O<sub>3</sub>-CaO po K. Millsu<sup>15</sup>

**Table 2:** Phase diagram of the  $\text{CaF}_2\text{-Al}_2\text{O}_3\text{-CaO}$  system and the physical properties of slag at 1600 °C, according to K. Mills<sup>19</sup>**Tabela 2:** Fazni diagram sistema  $\text{CaF}_2\text{-Al}_2\text{O}_3\text{-CaO}$  in fizikalne lastnosti žlindre pri 1600 °C, po K. Millsu<sup>19</sup>

Contour	Electrical conductivity $\kappa$ ( $\Omega^{-1}\text{cm}^{-1}$ )	Viscosity $\eta$ ( $10^{-1}\text{Ns m}^{-1}$ )	Density $\rho$ ( $\text{g cm}^{-3}$ )	Surface tension $\sigma_s$ ( $\text{mN m}^{-1}$ )	Total normal emissivity $\epsilon_{\text{TN}}$
A	6	0.15	2.47	285	0.96
B	5	0.2	2.48	300	
C	4	0.25	2.49	310	
D	3.5	0.3	2.5	320	0.9
E	3	0.4	2.55	335	
F	2.5	0.6	2.6	350	0.85
G	2	0.8	2.7	400	
H	1	1.0	2.8	450	

equal proportions of lime and alumina. This identifies the slags with liquidus temperatures in the range 1350–1500 °C, which make them suitable for melting of a wide range of alloys, including steels and super alloys. In the case of slag with 70 % fluoride and 30 % alumina the lime is excluded as much as possible in order to prevent hydrogen pick-up, while there are no problems with the presence of the two liquids. The binary lime-alumina system on the other hand, has only a limited range of slags with suitable melting characteristics, while the binary calcium fluoride-lime system is used in cases

where a high degree of desulphurization is required. However, its disadvantage is having a low resistivity. High lime contents also increase the risk of moisture retention or hydrogen pick-up.

According to the tendency to reduce  $\text{CaF}_2$  in slags, the investigations of the slag S 2015 (Wacker Chemie) with 30 %  $\text{CaF}_2$  were performed. The results also showed that tested slags with 4.7 %  $\text{CaF}_2$  can be satisfactorily applied in the ESR-process of UTOP Mo6 steel.<sup>16</sup>

A certain amount of  $\text{SiO}_2$  addition into the ESR slag in the case of the drawing-ingot-type ESR process is important for improving the lubrication performance, controlling silicon and aluminium content in the liquid steel and modifying oxide-type inclusions.<sup>17</sup> Furthermore, the addition of  $\text{SiO}_2$  suppresses the crystallization temperature of  $\text{CaF}_2\text{-Al}_2\text{O}_3\text{-CaO}$  slags. Furthermore, the  $\text{MgO}$  and  $\text{SiO}_2$  in fluoride-containing slags affect the slag's surface tension.<sup>18</sup>

Although  $\text{CaF}_2$  is a crucial component in any ESR slag and it greatly decreases the melting temperature of the slag systems, it is insoluble in oxide phases. An example of an ESR slag microstructure is shown in **Figure 5**, where the lighter dendrite-like phase is a stable  $\text{CaO-Al}_2\text{O}_3$  phase, the darker phase is fluorspar, and the small white dots the undissolved magnesia particles. The fluorspar phase contains only calcium and fluoride and is not dissolved in other microstructural constituents.

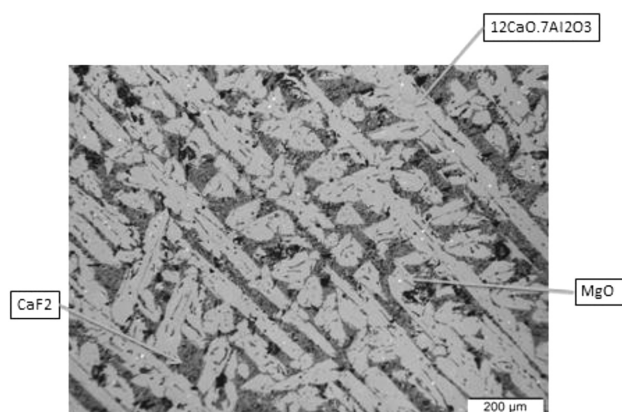
Slag properties, such as electrical conductivity, thermal conductivity, density, viscosity and surface tension play an important role in effective melting and metal refining. K. Mills<sup>19</sup> has produced a table of the physical properties of slags for practical purposes (**Table 2**). Slag resistivity affects the operating characteristics and economics of ESR. Alumina increases the resistivity of the slag and promotes good heat generation, thus enabling a reduction of the slag bulk content, which also reduces the heat loss due to the reduced area of contact between the slag and the mould wall.

L. A. Kamenski et al.<sup>20</sup> refer to "long" and "short" slags when discussing slag viscosity. Long slags remain fluid over a wide range of temperatures and are likely to give thin slag skins and therefore good ingot surfaces. Short slags rapidly become viscous on cooling and are likely to give thick slag skins and poor ingot surfaces. High calcium fluoride contents promote short slags, whereas silica and magnesia favour long slags.

The slag plays an important role in ESR, from the control-of-inclusions point of view.<sup>21</sup> The chemical and physical properties of slag also have a great effect on the removal of inclusions.

## 5 THERMODYNAMICS

In the case of ESR of steel in an air atmosphere, chemical reactions take place and change the chemical composition of the as-cast ingot.<sup>22</sup> The levels of some

**Figure 5:** Microstructure of ESR slag**Slika 5:** Mikrostruktura ESR žlindre

elements, such as Co, Ni, Cr, Mo, W, C remain unchanged after remelting. However, the content of Si, O, and S can be changed from 10 % to 80 %, while the content of Al and Ti can vary depending on the melting conditions (decrease or increase). Therefore, some measures need to be taken to prevent the losses of elements. This can be achieved by using special ESR variations as discussed before. Another way is control of the slag composition and regular additions to the slag, which is desirable due to steady melting conditions. The oxidation of the elements can be prevented by deoxidation of the slag during the melting process by additions of aluminium.

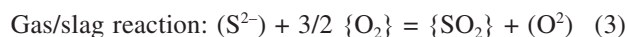
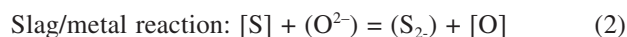
The oxygen potential of the slag determines the chemistry of the ESR process.<sup>7</sup> It affects the non-metallic inclusions and sulphur removal. Oxygen reacts with some elements in the metal and suppresses hydrogen pick up. In the slag oxygen is mostly bound as FeO, MnO and SiO<sub>2</sub>. To estimate the oxygen content in the steel it is necessary to find the relationship between FeO in the slag and oxygen in the remelted ingot.<sup>22,23</sup> However, due to the very low solubility of FeO in CaF<sub>2</sub> slags, its activity is extremely high. The oxygen content can be estimated by thermodynamic analyses of the reactions between active components and oxygen. Silicon and manganese are elements that can react with the oxygen present in the steel and from the slag.<sup>23,24</sup> When silicon is the strongest deoxidizer, the oxygen content of the steel is determined by the Si content.<sup>23</sup> At constant temperature and Si content in the steel, the oxygen content of the metal is higher at higher activity of the SiO<sub>2</sub> in the slag, or by lowering the basicity of the slag.

Aluminium losses in the remelted ingot are small, especially at high alumina content in the slag. On the other hand, the presence of Al<sub>2</sub>O<sub>3</sub> in the slag reduces the oxidation of silicon. The reaction between the silicon in the electrode and Al<sub>2</sub>O<sub>3</sub> in the slag also controls the oxidation of aluminium in the remelted ingot.<sup>25</sup> Thus, Al

content in the remelted ingot depends on the content of Al<sub>2</sub>O<sub>3</sub> in the slag and the content of silicon in the electrode, temperature and chemical composition of the steel.<sup>7,25</sup> The content of Al in the remelted ingot decreases when CaF<sub>2</sub>-Al<sub>2</sub>O<sub>3</sub>-CaO slags with increased SiO<sub>2</sub> content are used. When aluminium is used for deoxidation, up to 15 % of added Al is transferred to the molten steel. The content of titanium in the remelted steel will depend on the content of Al and Ti in the consumable electrode, the content of Al<sub>2</sub>O<sub>3</sub> and TiO<sub>2</sub> in the slag and the oxygen potential in the gas phase above the slag (**Figure 6**).<sup>26</sup> The equilibrium between the Al and Ti content in the electrode at different TiO<sub>2</sub> contents is presented in **Figure 6**.

For the content of Al in electrode, the titanium loss can be minimized by the addition of TiO<sub>2</sub> to the slag. At high contents of Al, aluminium reduces TiO<sub>2</sub> in the slag and also regulates the ratio of Ti:TiO<sub>2</sub>.

In the early stages of ESR development, the removal of sulphur was considered as one of the major objectives. The rate of desulphurization increases with the basicity of the slag. Sulphur transfer takes place mainly at two interfaces, according to the following two reactions:<sup>23</sup>



A thermodynamic analysis of the reactions shows that the desulphurisation is related to the concentration of O<sup>2-</sup> ions in the slag, the partial pressure of oxygen in the gas phase and the chemical composition of the steel.<sup>27</sup> The transfer of sulphur from the metal to the slag is promoted by the high slag basicity and low concentration of oxygen in the metal. On the other hand, the sulphur transfer from slag to gas is promoted by a high partial pressure of oxygen in the atmosphere and the low basicity of the slag. The ability of the slag to take sulphur is defined in terms of its sulphur capacity. The sulphur capacity for the fluorspar-lime-alumina system increases as the CaF<sub>2</sub> content is increased and by increasing the amount of lime to the saturation point.<sup>28</sup>

In the case of ESR under inert gas, the sulphur remains in the slag and builds up there as the process continues. In such cases the sulphur capacity is the ruling factor, and the slag bulk must be adjusted in order to continue its desulphurising action to the end of the process, i.e., the slag/metal ratio assumes greater importance.<sup>7</sup>

## 6 SOLIDIFICATION AND STRUCTURE

The solidification structure of an ESR ingot is a function of the local solidification time and the temperature gradient at the liquid/solid interface.<sup>4,7</sup> To achieve a directed dendrite primary structure, a relatively high temperature gradient at the solidification front must be maintained during the entire remelting period.

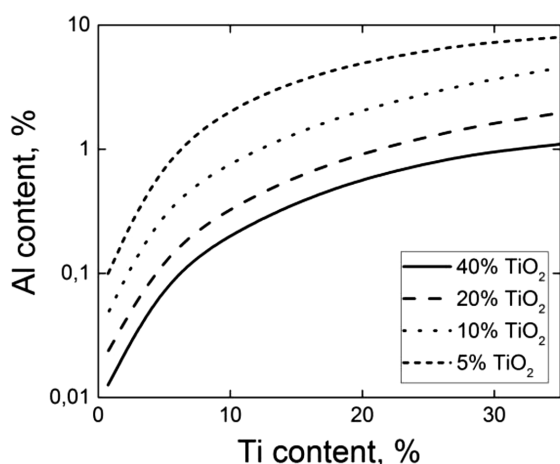


**Figure 6:** Effect of Al:Ti ratio in the electrode on TiO<sub>2</sub> content in the slag.<sup>26</sup>

**Slika 6:** Vpliv odvisnosti Al:Ti v elektrodi na vsebnost TiO<sub>2</sub> v žlindri.<sup>26</sup>



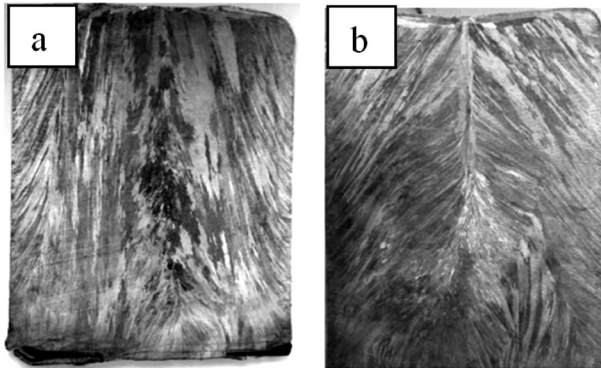


**Figure 7:** The ingot grain growth at a melting rate of: a) 0.9 kg/min and b) 1.2 kg/min<sup>32</sup>

**Slika 7:** Rast zrna v ingotu pri hitrostih taljenja: a) 0,9 kg/min in b) 1,2 kg/min<sup>34</sup>

Macrostructure of the ESR ingots is different from the macrostructure of conventionally cast ingots due to the different heat transfer and heat removal. The growth direction of the dendrites is a function of the metal pool during solidification. Thus, the gradient of dendrites with respect to the ingot axis increases with melting rate. In extreme cases the growth of directed dendrites can come to a stop. The ingot core then solidifies non-directionally in equiaxed grains, which leads to segregation and micro shrinkage. Even in the case of directional dendritic solidification, the micro segregation increases with the dendrite arm spacing. A solidification structure with dendrites parallel to the ingot axis yields optimal results. However, this is not always possible. A good ingot surface requires a minimum energy input and accordingly a minimum melting rate.

Increasing the melting rate increases the difference between the gradient of the solidus and liquidus isotherms and leads to increased pool depth.<sup>29</sup> Hence, grains grow in radial direction instead of vertical direction. **Figure 7** shows the direction of the grain growth dependent on the melting rate, which affects the pool depth.

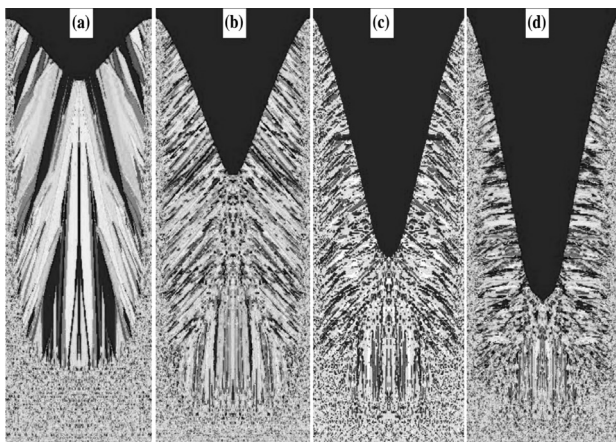


**Figure 8:** The predicted grain structure of ESR ingot<sup>30</sup> for different melting rates; a) 136 kg/h, b) 271 kg/h, c) 407 kg/h and d) 542 kg/h

**Slika 8:** Napovedana zrnatost ESR-ingota<sup>30</sup> pri različnih hitrostih taljenja: a) 136 kg/h, b) 271 kg/h, c) 407 kg/h in d) 542 kg/h

**Figure 8** presents the predicted grain structures for different melting rates up to 600 kg/h.<sup>30</sup> Increasing the melting rate causes a finer grain structure and changes the growth direction of the columnar structure from the axial to radial growth and deeper liquid pool at very high melting rates. Increasing the molten slag temperature also results in a coarser columnar grain structure and a reduced thickness of the refined equiaxed grain layer, both at the surface and the bottom of the ESR ingot.

In spite of directional dendritic solidification, defects such as tree-ring patterns, freckles and white spots can occur in a remolten ingot.<sup>4,7,31</sup> Macro-segregation and porosity structures in the middle of the ingot are very uncommon for ESR ingots.

A major attribute of ESR is its ability to produce material with reduced micro-segregation. This is linked with the local solidification time and dendrite-arm spacing.<sup>7</sup> ESR material normally freezes in a columnar manner, which gives less micro-segregation than equiaxed structures. The greater the temperature gradient, the smaller is the distance between the dendritic arm spacing and the lower is the chemical heterogeneity in the micro areas. In ESR, temperature gradients are greater than for conventional casting. Therefore, the secondary dendrite-arm spacing will be smaller in ESR than in conventional

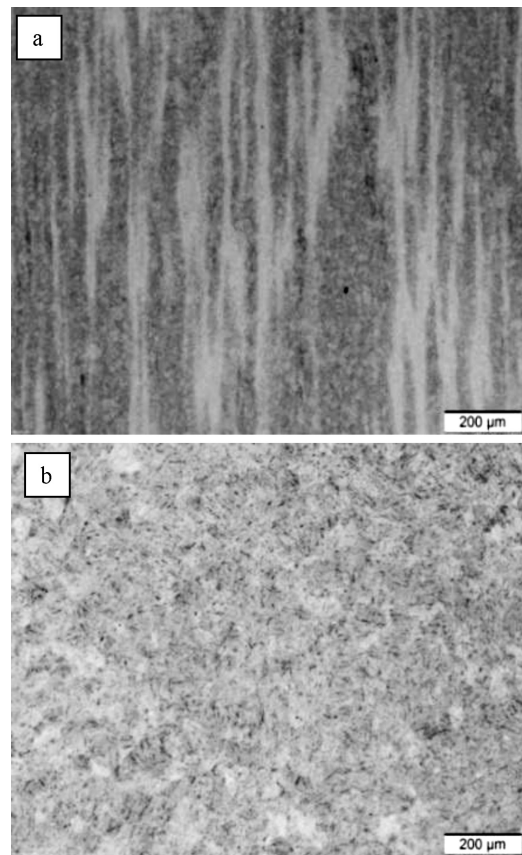


**Figure 9:** Segregations in the hot-work tool steel: a) consumable electrode, b) remelted ingot

**Slika 9:** Izceje v orodnem jeklu za delo v vročem: a) elektroda pred pretaljevanjem, b) pretaljen ingot



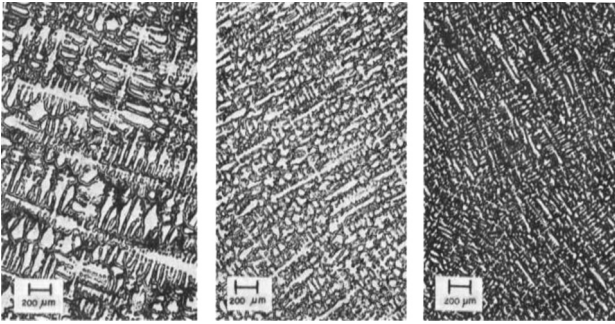


**Figure 10:** Microstructures of ingots of ESR nickel alloy 718, with dendrite-arm spacing at different cooling rates: a) slower cooling, b) faster cooling and c) fastest cooling<sup>32</sup>

**Slika 10:** Mikrostruktura EPŽ ingota nikljeve zlitine 718 in razdalj med dendritnimi vejami: a) počasnejše ohlajanje, b) hitrejše ohlajanje in c) najhitrejše ohlajanje<sup>32</sup>

ingots. The effect of decreasing the segregation effect is shown in **Figure 9**, where a comparison of microstructures before (**Figure 9a**) and after (**Figure 9b**) ESR processing was made for a hot-work tool steel. The microstructure in both cases is tempered martensite. The difference in segregation bands is obvious. While the segregations are evident in the consumable electrode (**Figure 9a**) they are almost completely eliminated in the remelted ingot (**Figure 9b**).

**Figure 10** shows the effect of local solidification time on the dendrite spacing.<sup>32</sup> The dendrite-arm spacing is decreased as the cooling rate is increased.

Besides a more homogeneous composition and compact solidification structure, the removal of non-metallic inclusions is an important characteristic of ESR.<sup>33</sup> Normally, inclusions easily initiate micro-voids and

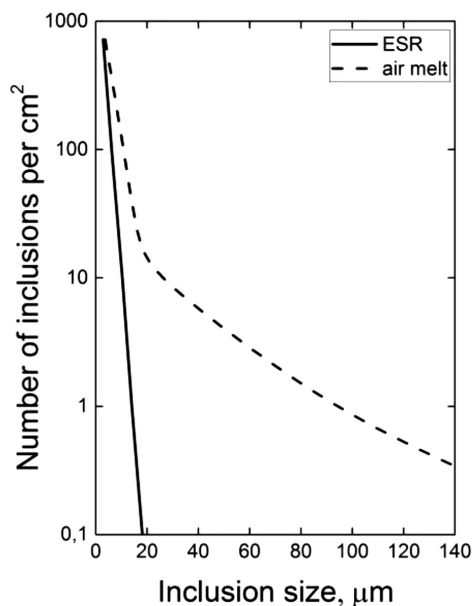


**Figure 11:** Inclusion size and frequency for inclusions >2.5 µm in air-melted and ESR with 3 % Cr-Mo-V steels<sup>38</sup>

**Slika 11:** Velikost in število vključkov > 2,5 µm po ESR-pretaljevanju in pretaljevanju na zraku jekla 3 % Cr-Mo-V<sup>38</sup>

cracks at the inclusion/steel interface, which can be the origin of fatigue fracture or other defects. Also, ESR steel is not an exception.<sup>34</sup> Many factors influence the formation of non-metallic inclusions in ESR steel, including furnace atmosphere, content of inclusions in the consumable electrode, slag amount and its composition, power input, melting rate, filling ratio, etc. Most non-metallic inclusions occur due to the reactions between oxygen and elements such as manganese, silicon and aluminium.<sup>35</sup> Deoxidization of the slag during electroslag remelting<sup>36</sup> has an important influence on the non-metallic inclusions formation in the ESR ingot. The results of the experimental work show that the lowest number of inclusions is attained in ESR with the lowest viscosity and the highest interfacial tension.<sup>37</sup> However, the absence of large inclusions is typical for ESR, as shown in **Figure 11**.<sup>38</sup>

The removal of non-metallic inclusions during ESR takes place at the tip of the electrode, where mainly absorption and dissolution of non-metallic inclusions in the slag take place.<sup>6,39</sup> As the electrode tip is heated towards its melting point, the inclusions in the electrode are re-dissolved before the metal melts. Any other inclusions, such as larger exogenous inclusions in the electrode, are not dissolved in the solid metal and will be exposed to the slag when the electrode tip becomes molten. If the slag composition is suitable, the temperature is high enough and the dwell time is long enough the non-metallic inclusions will dissolve in the slag.<sup>40</sup> However, at this point there may be further reactions due to the difference in equilibrium constants, as well as the possibility of the flotation of large inclusions. The metal at this point is free from non-metallic inclusions, but may have in solution elements that produce inclusions by reaction during the freezing time (sulphur removal reaction).<sup>41,42</sup> The removal efficiency of inclusions increases with the reduced melting speed.<sup>43</sup>

The research work of Y.-W. Dong et al.<sup>44</sup> was focused on the impact of fluoride-containing slag and interactions at the slag-metal interface on the non-metallic inclusions in steel. Results indicate that a multi-component slag (CaF<sub>2</sub>, CaO, Al<sub>2</sub>O<sub>3</sub>, SiO<sub>2</sub>, MgO) has a better capacity for controlling the amount of inclusions. Most non-metallic inclusions for multi-component slag are MgO-Al<sub>2</sub>O<sub>3</sub> inclusions, while mainly Al<sub>2</sub>O<sub>3</sub> inclusions exist when using conventional 70 % CaF<sub>2</sub> – 30 % Al<sub>2</sub>O<sub>3</sub> slag. Furthermore, the maximum inclusion size for multi-component slags was found to be smaller than for conventional binary slag.

## 7 CONCLUSION

The main purpose of the remelting process is to control the non-metallic inclusions in the steel, remove segregations and shrinkage, and produce more homogeneous ingots. The low speed of remelting, combined with the water-cooled mould, ensures a particularly homoge-

neous and balanced, stable solidification. The segregations within a remolten ingot are thus much lower (or even eliminated) compared to open cast continuous cast billets or conventional cast ingots. For this reason most segregation-sensitive steels are ESR processed for homogenisation.

The slag plays an important role in the ESR process, as it absorbs non-metallic inclusions, removes sulphur, influences the ingot surface and the melting rate as well as the overall economics of the process. That is why the chemical composition and physical properties of the chosen ESR slag is of paramount importance for a high-quality ESR ingot.

In order to further improve non-metallic inclusion reduction, specialised versions of the ESR process like IESR, PESR and VAC-ESR have been developed.

The application of the ESR process is appropriate for tool and high-speed steels as well as special stainless steels and special alloys intended for the most demanding applications.

## 8 REFERENCES

- R. C. Reed, *The Superalloys: Fundamentals and Applications*, Cambridge University Press, 2006
- J. Rodič, Razvoj električnega pretaljevanja jekel pod žlindro v Železarni Ravne, *ŽEZB*, 18 (1984) 4, 105
- R. H. Nafziger, *The electroslag melting process*, United States Bureau of Mines, Bulletin 669, Washington, 1976
- A. Hauf, General overview of secondary metallurgy including subsequent refining by ESR, VAR, EB and Plasma, Special melting and processing technologies, Proceedings Conference San Diego, California, April 11–15, 1988, 402–443
- P. J. Wooding, ESR: Static crucible versus moving mould, Third Int. Iron and steel Congress, April 1978, 727
- W. Holzhruber, Današnje stanje razvoja in razvojne smeri postopka električnega pretaljevanja pod žlindro, *ŽEZB* 18 (1984) 4, 105
- G. Hoyle, *Electroslag processes, Principle and Practice*, Applied Science Publishers LTD, England 1983
- U. Betz, H. Kemmer, D. Schleich, W. Schwarz, New developments in equipment design and control of remelting processes ESR, VAR, and VAR-ESR, Special melting and processing technologies, Proceedings Conference San Diego, California, April 11–15, 1988, 444–457
- A. K. Vaish, G. V. R. Iyer, P. K. De, B. A. Lakra, A. K. Chakrabarti, P. Ramachandrarao, Electroslag remelting-Its status, mechanism and refining aspects in the production of quality steels, *J. Metall. Mater. Sci.*, 42 (2000) 11–29, <http://eprints.nmlindia.org/1448/>
- W. Holzhruber, Results of operation of ESR equipment, Sixth International Congress on Electro Heat, Brighton, 1967, N 139
- M. Kawakami, Profiles of temperature, voltage and local heat generation in slag phase and metal pool of ESR unit, *Testu To Hagane*, 63 (1977) 13, 2162–2171
- A. S. Ballantyne, A. Mitchell, Computation in ESR furnace control, Fifth International Symposium on Electroslag and Other Special Melting Technologies, Oct. 11–15, 1976, Leybold-Heraeus GmbH, 449
- J. H. Chen et al., Computer control of ESR, Proceedings of Sixth International Conference on Special Melting, April 1979, 831, American Vacuum Society
- J. X. Zhao, Y. M. Chen, X. M. Li, Y. R. Cui, X. T. Lu, Mechanism of Slag Composition Change During Electroslag Remelting Process, *J. Iron Steel Res. Int.*, 18 (2011) 24–28, doi:10.1016/S1006-706X(12)60017-X
- K. Mills, *The estimation of slag properties*, Sautheren African Pyrometallurgy, March, 2011
- J. Medved, A. Rosina, J. Ilievski, Raziskave električne prevodnosti žlindra pri postopku EPŽ, *Kovine, zlitine, tehnologije*, 28 (1994) 1–2, 111–114
- C. B. Shi, J. Li, J. W. Cho, F. Jiang, I. H. Jung, Effect of SiO<sub>2</sub> on the Crystallization Behaviors and In-Mold Performance of CaF<sub>2</sub>-CaO-Al<sub>2</sub>O<sub>3</sub> Slags for Drawing-Ingot-Type Electroslag Remelting, *Metall. Mater. Trans. B Process Metall. Mater. Process. Sci.*, 46 (2015) 2110–2120, doi:10.1007/s11663-015-0402-2
- Y. Dong, Z. Jiang, Y. Cao, H. Zhang, H. Shen, Effect of MgO and SiO<sub>2</sub> on surface tension of fluoride containing slag, *J. Cent. South Univ.*, 21 (2014) 4104–4108, doi:10.1007/s11771-014-2404-7
- K. Mills, B. J. Keene, Physical Chemical properties of molten calcium fluoride based slags, *Int. Met. Rev.*, 26, (1981) 1
- L. A. Kamenski et al., Electroslag casting of forging ingots, *Sbornik Trud. Mosk. Vech. Met. Inst.*, 10 (1971), 146
- Y. – W. Dong, Z.- H. Jiang, Z.- X. Xiao, Z.- B. Li, Influence of ESR Process Parameters on Solidification Quality of Remelting Ingots, *Journal of Northeastern University (Natural Science)*, (2009) 11, 1598-1607
- B. Kouroušič, Izboljšanje kvalitete legiranih jekel s pretaljevanjem pod žlindro (EPŽ-postopek), *ŽEZB*, 8 (1974) 2, 89–98
- B. Kouroušič, Metalurške reakcije pri pretaljevanju kvalitetnih jekel pod žlindro (EPŽ), *ŽEB*, 7 (1973) 1, 23–29
- B. Kouroušič, Vpliv elektropretaljevanja pod žlindro na kvaliteto jekla za kroglične ležaje (OCR-4 ex.sp.), *ŽEZB*, 7 (1973) 1, 193–198
- B. Kouroušič, Prispevek k termodinamiki reakcij, ki nastopajo pri EPŽ – procesu, *ŽEZB*, 14 (1980) 1/2, 65–72
- G. Pateisky, H. Biele, H.J. Fleischer, The Reactions of Titanium and Silicon with Al<sub>2</sub>O<sub>3</sub>-CaO-CaF<sub>2</sub>, Slags in the ESR Process, *J. Vac. Sci. Technol.*, 9 (1972) 1318–1321, doi:10.1116/1.1317029
- A. Mitchell, F. Reyes-Carmona, E. Samuelsson, The Deoxidation of Low-alloy during ESR, *Trans. Iron Steel Inst. Japan.*, 24 (1984) 547–556
- G. J. W. Kor, F. D. Rihardson, Sulphide capacities of basic slags containing calcium fluoride, *Trans. met. Soc. AIME*, 245 (1969), 139
- S. Ahmadi, H. R. Shahverdi, H. Arabi, Effects of electro-slag remelting process (ESR) on macrostructure and refinement of a medical grade of stainless steel, *Iron Journal of Materials Science & Engineering*, 11 (2014), 3
- X. Wang, Y. Li, Numerical Simulation Structure of ESR Ingot Using Cellular Automation Method, *Metallurgical and Materials transactions B*, 46B (2015) 04, 800–812, doi:10.1007/s11663-0140227-4
- K. O. Yu, J. A. Domingue, Control of solidification structure in VAR and ESR processed alloy 718 ingots, *The Minerals, Metals & Materials Society*, (1989), 33–47
- W. V. Venal et al., The effect of electroslag remelting on the properties of AISI 4330 MOD, Proceedings of 5th International conference Vacuum metallurgy and Electroslag remelting processes, 1976, 173
- Y.-W. Dong, Z.-H. Jiang, Y.-L. Cao, A. Yu, D. Hou, Effect of Slag on Inclusions During Electroslag Remelting Process of Die Steel, *Metall. Mater. Trans. B.*, 45 (2014) 1315–1324, doi:10.1007/s11663-014-0070-7
- A. Sabih, P. Wanjara, J. Nemes, *ISIJ Int.*, 45 (2005), 1179–1186, doi:10.2355/isij
- B. Kouroušič, A. Rozman, F. Tehovnik, Advanced technologies for the production of high-quality steels at Metal-Ravne., *Mater. in Tehnol.*, 34 (2000) 6, 401–407
- Z. B. Li, J. W. Zhang, and X. Q. Che, Control of content and composition of non-metallic inclusion in ESR steel, *J. Iron Steel Res.*, 9 (1997) 2, 7
- H. Hossam, Behavior of nitrogen-rich inclusions in new developed 12 % maraging steel during active slag ESR refining, 23. International Conference on Metallurgy and Materials, may 2014, Brno, Czech Republic

- <sup>38</sup> E. M. Lowe, A. Hogg, Application of ESR to alloy steel forgings, Proceedings of conference on Electroslag refining, Iron and Steel Institute, Sheffield, 1973, 68
- <sup>39</sup> B.-H. Yoon, K.-H. Heo, J.-S. Kim, H.-S. Sohn, Improvement of steel cleanliness by controlling slag composition, Ironmaking Steelmak., 29 (2002) 214–217, doi:10.1179/030192302225004160
- <sup>40</sup> A. Mitchell, Oxide inclusion behavior during consumable electrode remelting, Ironmaking and Steelmaking, 1 (1974) 3, 172
- <sup>41</sup> M. E. Fraser, A. Mitchell, Mass transfer in the electroslag process, Part 1, Mass transfer model, Ironmaking and Steelmaking, 3 (1976) 5, 279
- <sup>42</sup> M. E. Fraser, A. Mitchell, Mass transfer in the electroslag process, Part 2, Mass transfer coefficients, Ironmaking and Steelmaking, 3 (1976) 5, 288
- <sup>43</sup> C. Chen, J. Wang, D. Shu, B. Sun, Removal of Iron Impurity from Aluminum by Electroslag Refining, Mater. Trans., 52 (2011) 1320–1323, doi:10.2320/matertrans.M2010435
- <sup>44</sup> Y. - W. Dong, Z. - H. Jiang, Y. - L. Cao, A. Yu, D. Hou, Effect of slag on inclusions during electroslag remelting process of die steel, Metallurgical and Materials Transactions B, 45B (2014) 8, 1315–1324, <http://dx.doi.org/10.1007/s11663-014-0070-7>





# CONTINUOUS VERTICAL CASTING OF A NiTi ALLOY

## VERTIKALNO KONTINUIRNO LITJE NiTi ZLITINE

**Aleš Stambolić<sup>1,2</sup>, Ivan Anžel<sup>3</sup>, Gorazd Lojen<sup>3</sup>, Aleksandra Kocijan<sup>1</sup>,  
Monika Jenko<sup>1,2</sup>, Rebeka Rudolf<sup>3,4</sup>**

<sup>1</sup>Institute of Metals and Technology, Lepi pot 11, 1000 Ljubljana, Slovenia

<sup>2</sup>Jožef Stefan International Postgraduate School, Jamova 39, 1000 Ljubljana, Slovenia

<sup>3</sup>University of Maribor, Faculty of Mechanical Engineering, Smetanova 17, 2000 Maribor, Slovenia

<sup>4</sup>Zlatarna Celje d.d., Kersnikova 19, 3000 Celje, Slovenia

ales.stambolic@imt.si

*Prejem rokopisa – received: 2016-06-17; sprejem za objavo – accepted for publication: 2016-06-27*

doi:10.17222/mit.2016.111

In this paper we present research that is connected to the performance of a series of experiments combined with the vacuum-induction melting and continuous vertical casting of a NiTi alloy in order to produce the strand. The theoretical chosen parameters made it possible to obtain a continuously cast strand with a diameter of 11 mm. The strand microstructures were investigated with a light and scanning electron microscope, while the chemical composition of the single phase was identified with the semi-quantitative micro-analysis energy-dispersive X-ray spectroscopy and inductively coupled plasma – optical emission spectrometry. The research showed that the microstructure is dendritic, where in the inter-dendritic region the eutectic is composed of a dark NiTi phase and a bright TiNi<sub>3-x</sub> phase. In some areas we found Ti carbides and phases rich in Fe. The micro-chemical analysis of the NiTi strand showed that the composition changed over the cross and longitudinal sections, which is proof that the as-cast alloys are inhomogeneous. In the final part, the electrochemical behaviours of NiTi strand samples were compared to a commercially available NiTi cast alloy with the same composition.

**Keywords:** NiTi alloy, continuous vertical casting, microstructure, potentiodynamic and impedance test

V tem prispevku predstavljamo raziskavo, ki je povezana z izvedbo niza preizkusov vakuumskega pretaljevanja in sočasnega kontinuirnega vertikalnega litja NiTi zlitine s ciljem odliti palico. Teoretično izbrani parametri so omogočili, da smo uspeli kontinuirno odliti NiTi palico s premerom 11 mm. Dobljeno mikrostrukturo palice smo raziskali s svetlobnim in vrstičnim elektronskim mikroskopom, kemijsko sestavo posameznih faz pa smo identificirali s semi-kvantitativno mikro-kemično analizo Energijsko disperzijsko spektrometrijo in z optičnim emisijskim spektrometrom z induktivno sklopljeno plazmo. Preiskave so pokazale, da je mikrostruktura dendritska, medtem ko s v meddendritskem prostoru nahaja evtektik, sestavljen iz temne NiTi faze in svetle TiNi<sub>3-x</sub> faze. Mestoma smo identificirali tudi Ti karbide in fazo bogato s Fe. Mikro-kemična analiza NiTi palice je odkrila, da se sestava spreminja po prerezu in po dolžini, kar nakazuje, da je zlitina po strjevanju nehomogena. V zaključnem delu smo primerjali elektrokemijsko obnašanje vzorcev NiTi palice s komercialno dostopno valjano NiTi zlitino enake sestave.

**Ključne besede:** NiTi zlitina, vertikalno kontinuirno litje, mikrostruktura, potenciodinamični in impedančni test

## 1 INTRODUCTION

NiTi alloys are an attractive group that also include nitinol. Nitinol is a group of nearly equiatomic alloys of nickel and titanium which is located in the central region of the NiTi phase diagram and bounded by the Ti<sub>2</sub>Ni and TiNi<sub>3</sub> phases.<sup>1</sup> It exhibits a unique combination of good functional properties and a high mechanical strength, such as super-elasticity and a shape-memory effect, good corrosion resistance, an unusual combination of strength and ductility and excellent biomechanical compatibility.<sup>2,3</sup> This alloy was developed in the 1970s and its properties have enabled its use especially for biomedical purposes, first in orthodontic treatments, and later on in cardiovascular surgery for stents, guide wires, filters, etc., in orthopaedic surgery for various staples and rods, and in maxillofacial and reconstructive surgery.<sup>4</sup> In addition to bio-engineering, nitinol has been used in aerospace, automotive, civil and structural engineering.<sup>5</sup> Super-elastic NiTi is capable of recovering large inelastic strains spontaneously upon unloading. On the other hand, shape memory is exhibited when NiTi recovers

large strain deformation upon heating. Both the super-elasticity and shape-memory effect are induced in nitinol by reversible, displacive, diffusionless, solid–solid phase transformations from a high-temperature parent phase (austenite) with a highly ordered crystal structure to a low temperature, stress-free martensite that has a less ordered structure. Nitinol is hysteretic, and there are several transformation temperatures, including the austenite start temperature ( $A_s$ ), the austenite finish temperature ( $A_f$ ) during heating and the martensite start temperature ( $M_s$ ) and the martensite finish temperature ( $M_f$ ) during cooling. Super-elastic behaviour will only occur if the material is loaded above its  $A_f$  temperature.<sup>6-8</sup>

The common production route for a NiTi alloy with a shape-memory effect is known and has been experimented on laboratory equipment with the technological aspects of vacuum induction melting, hot and cold working operations. The process is still being optimized with a particular focus on obtaining a small dimension in the cross-section and with stabilisation of its functional properties over its lifetime.<sup>9</sup> Vacuum induction melting

(VIM) is often used as the first technique in the preparation of a melt. Basically, it is a typical melting technique for the production of different NiTi-based alloys. This is appreciated particularly for NiTi alloy due to the strong influence of the chemical composition on the reactivity with oxygen and other elements, leading to oxidation of the NiTi melt. In the second step, such a prepared melt is cast, which enables pouring the molten metal into a mould of the desired shape, and allowing it to solidify. When the molten metal is poured into the mould, chill crystals nucleate on the cold walls of the mould and grow inwards. Conventional casting is a batch process that produces large ingots requiring significant subsequent processing. Large mechanical equipment with high construction and operational costs is necessary to break down most ingots. These problems can be solved by using continuous vertical casting (CVC).<sup>10–13</sup> With CVC the raw material is placed into a VIM furnace, in which the material melts. After melting, the melt is, based on gravity force, moved against the nozzle, which adjusts the rate and direction of the melt flow. The melt flows through the nozzle into a water-chilled mould, where the melt is solidified, and obtains the final strand shape.

Nitinol is often subjected to deformations or stresses that result in some kinds of mechanical failures. Two very important factors must be considered when using various materials in medicine, i.e., the toxicity of the material and the failure of material. The main problem of NiTi alloys is the high Ni content. Ni releasing can induce toxic, allergic and hypersensitive reactions or tissue necrosis after long-term implantation. To prevent failure and Ni release, a coating of appropriate thickness must be formed on the NiTi surface. Titanium oxide coatings effectively suppress the nickel ions outleaching. The nitinol surface is spontaneously covered by Ti dioxide because of the gain in free energy of formation for this

oxide compared to the Ni oxides. However, the oxides formed on the nitinol surface always contain a certain fraction of Ni.<sup>14–19</sup>

The main goal of this work was the performance of the series of experiments combined with vacuum-induction melting and continuous vertical casting of NiTi alloy in order to produce the strand. This was followed by the characterization of the obtained microstructure and finally we compared the electrochemical behaviour between a NiTi strand and commercially available nitinol.

## 2 EXPERIMENTAL PART

### 2.1 Continuous vertical casting of NiTi alloy

The NiTi alloy composed of 50 % of amount fractions of Ni and 50 % of amount fractions of Ti was prepared with the combination of techniques: VIM and CVC. A clay-graphite crucible was filled up to 2/3 of its volume due to the high metallostatic pressure (pressure that occurs within a molten metal) with Ti pellets (99.99 % purity) and Ni tablets (99.99 % purity). By remelting the NiTi alloy with VIM at a temperature of about 1450 °C a pressure lower than  $10^{-2}$  mbar was achieved in the system. The induction power during heating was for first 10 min 10 kW, then next 10 min 20 kW and in final 5 min 30 kW, while during casting it was between 25 and 30 kW. Continuous casting was operating in the mid range frequency (4 kHz). In the experiments a Cu-mould (**Figure 1**), a ZrO<sub>2</sub> nozzle stabilized with Y<sub>2</sub>O<sub>3</sub> and an Fe starter bar were applied.

### 2.2 Preparing of the samples for further investigation

The samples for characterization were cut longitudinally (according to the direction of casting) and across the cross-section. For this purpose, an Accutom 50 electronic saw was used for precision cutting. The grinding was performed with 320 grit SiC abrasive paper, mechanical polishing with MD-Largo discs with 9- $\mu$ m diamond suspension and with peroxide grains in a chemically aggressive suspension – OP-S (colloidal silica). The sample was then etched with Kroll's reagent (3 mL HF, 6 mL HNO<sub>3</sub> and 100 mL of distilled water).

### 2.3 Analytical techniques

The microstructure was investigated with a light microscope – Microphot FXA, Nikon 3CCD-Hitachi Camcorder HV-C20A and Thermal Field Emission SEM JEOL JSM-6500F equipped with energy-dispersive X-ray spectroscopy (EDS) analytical technique. Chemical analyses were performed by inductively coupled plasma – optical emission spectrometry ICP-OES (Agilent 720).

Potentiodynamic polarisation measurements and electrochemical impedance spectrometry (EIS) have been used to study the electrochemical behaviour of

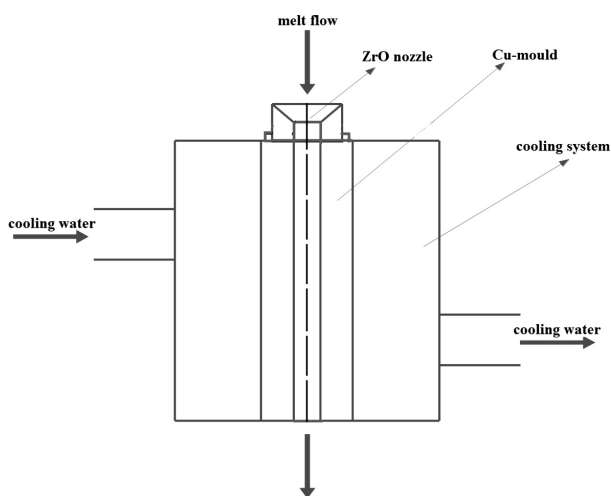


**Figure 1:** Schematic presentation of copper mould with cooling system at the Faculty of Mechanical Engineering, Maribor, Slovenia

**Slika 1:** Shema bakrene kokile s hladilnim sistemom na Strojni fakulteti v Mariboru, Slovenija

samples. All the measurements were recorded by BioLogic Modular Research Grade Potentiostat/Galvanostat/FRA Model SP-300 with an EC-Lab Software and a three-electrode cell. In this cell, the sample was the working electrode, saturated calomel electrode (SCE, 0,242 V vs. SHE) was used as reference electrode and the counter electrode (CE) was a platinum net. The experiment was held in simulated physiological Hank's solution, containing 8 g/L NaCl, 0.40 g/L KCl, 0.35 g/L NaHCO<sub>3</sub>, 0.25 g/L NaH<sub>2</sub>PO<sub>4</sub>×2H<sub>2</sub>O, 0.06 g/L Na<sub>2</sub>HPO<sub>4</sub>×2H<sub>2</sub>O, 0.19 g/L CaCl<sub>2</sub>×2H<sub>2</sub>O, 0.41 g/L MgCl<sub>2</sub>×6H<sub>2</sub>O, 0.06 g/L MgSO<sub>4</sub>×7H<sub>2</sub>O and 1 g/L glucose, at pH = 7.8 and 37 °C. All the chemicals were from Merck, Darmstadt, Germany. The potentiodynamic curves were recorded after 1 h of sample stabilisation at the open-circuit potential (OCP), starting the measurement at 250 mV vs. SCE more negative than the OCP. The potential was then increased, using a scan rate of 1 mV s<sup>-1</sup>, until the transpassive region was reached. Long-term open circuit potentiostatic electrochemical impedance spectra were obtained for the investigated samples. The impedance was measured at the OCP, with sinus amplitude of 5 mV peak to peak and a frequency range of 65 kHz to 1 mHz, in the sequence of directly after immersion after 1h, 2 h, 6 h, 12 h, 24 h, 48 h, 72 h, 96 h, 120 h, 144 h, 168 h and 192 h. The impedance data are presented in terms of Nyquist plots. For the fitting process Zview v3.4d Scribner Associates software was used.

### 3 RESULTS AND DISCUSSION

#### 3.1 Continuous vertical casting of a NiTi alloy

The CVC of a NiTi alloy is a complex process that requires precise process parameters. Accurate measurement and regulation of temperature was very difficult because the thermocouple was not in constant contact with the melt due to the potential contamination of the melt and the temperature at the crucible wall is quite different from the actual temperature of the melt. The

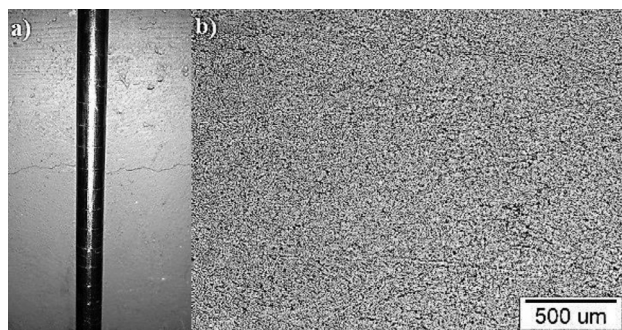


**Figure 2:** a) NiTi strand, produced at Faculty of Mechanical Engineering, Maribor, Slovenia and b) light microscope image of cross-section of the strand

**Slika 2:** a) NiTi palica, lita na Strojni fakulteti v Mariboru, Slovenija in b) posnetek prečnega prereza palice, narejen s svetlobnim mikroskopom

frequency of induction is also very important for the casting, as a high frequency enables the temperature to rise and low frequency means more intensive stirring. In this case the casting was operated at a mid-range frequency of induction that does not provide adequate mixing power, causing an undesirable chemical composition in some places of the strand. The drawing of the strand was carried out in the sequence of pull – pause, as this reduces the possibility of a reaction between the alloy and the mould, as well as the porosity of the material or the occurrence of cracks in the material. The drawing stroke had a length of between 0 and 10 mm and the pause lasted between 0 and 1 s. The drawing rate is also an important factor. When the drawing is too slow, the temperature decreases, which leads to solidification of the alloy in the nozzle and retraction of further drawing. This leads to fracture of the strand and the process ends without the desired result. The strand also breaks when the drawing rate is too fast due to the adhesion to the mould and the weakness of the thin solidified skin.

With CVC a strand with diameter of 11 mm was obtained (**Figure 2**). ICP analysis for the first attempt of CVC NiTi strand showed a constant material composition of 59.8 % of amount fractions of Ni, 38.9 % of amount fractions of Ti and 0.3 % of amount fractions of C, EDS analysis showed approximately 1 % of amount fractions of Fe. Deviation from the desired value (50 % of amount fractions of Ni) is probably caused by complications with stirring of the melt (better mixing takes place at a lower frequency induction, Ti is very difficult to mix). The source of Fe could be attributed to the Fe screw that was used as a starter bar. During further attempts the chemical composition of the strand varied during casting. At the beginning of drawing XRF analysis showed that the strand was rich in nickel (70.6 % of amount fractions of Ni; 27.1 % of amount fractions of Ti) and with the increasing length of the strand the nickel content decreased. Chemical composition during the fracture of the strand was 52 % of amount fractions of Ni and 47 % of amount fractions of Ti.

#### 3.2 Microstructure

##### 3.2.1 Continuously vertical cast NiTi alloy

The light microscopy of the strand cross-section reveals the dendritic microstructure (**Figure 3**), where inside the primary phase NiTi is located. This is according to the Ni-Ti phase diagram where the first solidified phase is NiTi. Dendrites grew in the direction from the coldest location (from the walls of the nozzle) to the middle of the strand. The orientation of dendrites is random. These dendrites are arranged in the matrix of eutectic (composed with NiTi eut + TiNi<sub>3-x</sub>). In the microstructure there are no visible defects such as cracks and porosity.



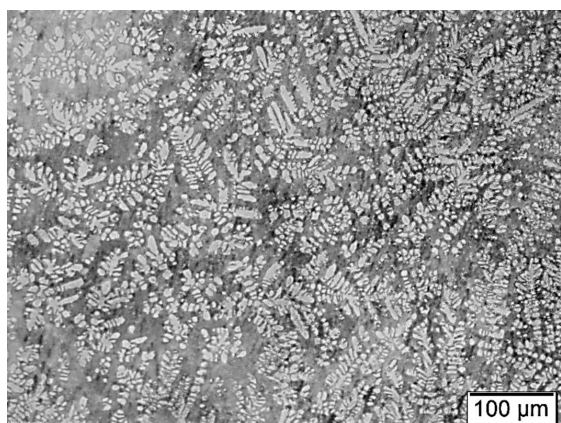


**Figure 3:** Light microscope image of NiTi strand at 100x magnification

**Slika 3:** Posnetek NiTi palice na svetlobnem mikroskopu pri 100x povečavi

The NiTi strand contains between 50 % and 60 % of amount fractions of Ni. From the phase diagram (**Figure 4**) it is clear that this is a hypo-eutectic alloy (according to the eutectic reaction at 1118 °C:  $L \rightarrow \text{NiTi} + \text{TiNi}_3$ ). With an ideal cooling the melt would begin to solidify in the temperature range between 1310 °C and 1118 °C. From the melt firstly the primary NiTi phase solidifies that would be continuously generated and grew until the eutectic temperature (1118 °C) is reached. At this temperature, the remaining melt solidifies into a eutectic structure composed of a NiTi phase and TiNi<sub>3</sub> phase in the form of lamellas.

In the real case, the cooling is non-equilibrium. Solidifying rates are large, but the diffusion rates in the solid state are too small to make it possible to achieve a homogeneous solid phase. A backscattered electrons image (**Figure 5**) shows a typical dendritic structure (tree-like form) that are solidified primarily (NiTi phase). At the eutectic temperature (1118 °C) solidifies typical

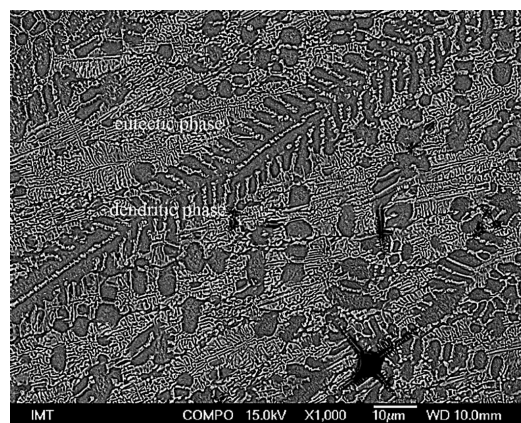


**Figure 5:** Backscattered-electron image of NiTi strand at 1000x magnification

**Slika 5:** Posnetek povratno-sipanih elektronov NiTi palice pri 1000x povečavi

lamellar eutectic structure (NiTi + TiNi<sub>3-x</sub>) from the residue of the melt. EDS analysis at 5 keV showed that both the dendritic phase and the dark lamellas of eutectic, have a composition of approximately 50 % of amount fractions of Ni and 50 % of amount fractions of

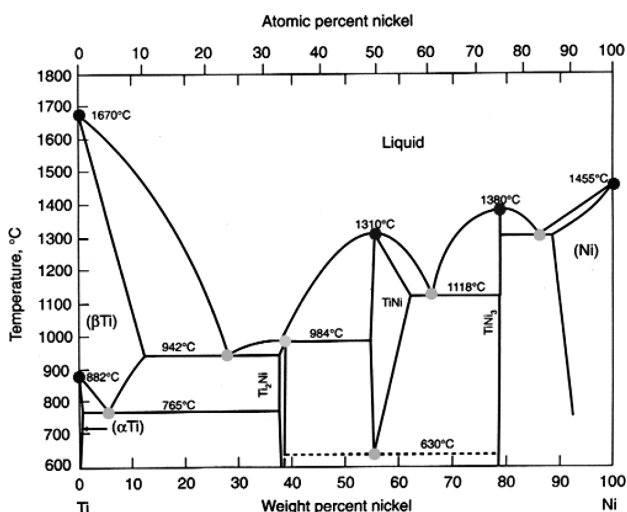


**Figure 4:** Ni-Ti phase diagram

**Slika 4:** Fazni diagram Ni-Ti

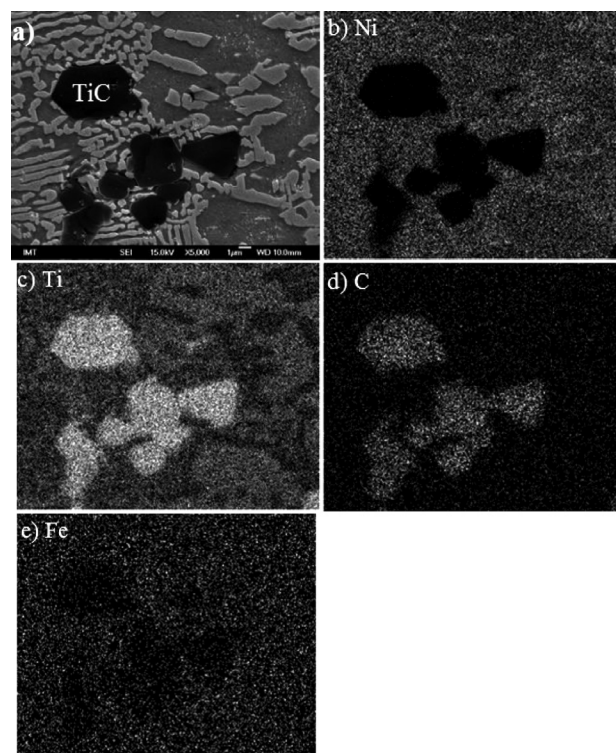


**Figure 6:** a) SE image of NiTi strand at 5000x magnification of area where the TiC inclusions are present, b), c), d) and e) elemental mapping at the microstructural level by scanning electron microscopy (SEM) with energy dispersive X-ray spectrometry (EDS) in the area with TiC inclusions

**Slika 6:** a) SE-posnetek NiTi palice pri 5000x povečavi v območju, kjer so prisotni TiC vključki, b), c), d) in e) elementna analiza na mikrostrukturni ravni z vrstičnim elektronskim mikroskopom (SEM) z energijo disperzijsko rentgensko spektrometrijo (EDS) v območju s TiC vključki



Ti, while bright lamellas of eutectic have a composition of 33 % of amount fractions of Ti and 67 % of amount fractions of Ni.

The secondary electron (SE) image (**Figure 6**) reveals in addition to the dendritic structure also the presence of the individual inclusions. The EDS analysis showed that the inclusions are titanium carbide (TiC). Carbon originates from the clay-graphite crucible and diffuses into the melt during the melting and reacts there with the Ti. The Gibbs free energy for the formation of TiC is very low, so the conditions for the formation of TiC are very favourable. From the results of the EDS analysis it appears that the carbon is located only in the form of carbides, and there is none in the other phases. Ni and Fe are located in the dendrites and the matrix, but not in the carbides, while titanium is present in all the phases. Another important fact is that, during CVC, there was no contamination with oxygen because no dissolved oxygen or oxides were observed in the strand. In this manner it could be concluded that the vacuum was appropriate.

So far several VIM + CVC experiments for the production of NiTi strand were made. In the first attempt the chemical composition of the strand was constant, but incorrect. During further attempts it varied during drawing in the direction of reducing the nickel content. It was concluded that the mixing of the melt was inappropriate. Insufficient stirring was attributed to the 4-kHz inductor. To achieve better stirring, a low-frequency generator should be modulated. Costs for something like that are too high and therefore the remelting method will be further used. CVC will be held with an in advance prepared NiTi alloy. Instead of Fe starter bar, that probably introduced Fe impurities in the alloy, a starter bar with a Ti-tip will be applied. The vacuum by VIM was appropriate, because no oxygen or oxides were found in the strand, but the crucible will also need to be modified due to some concentration of TiC phase in the strand.

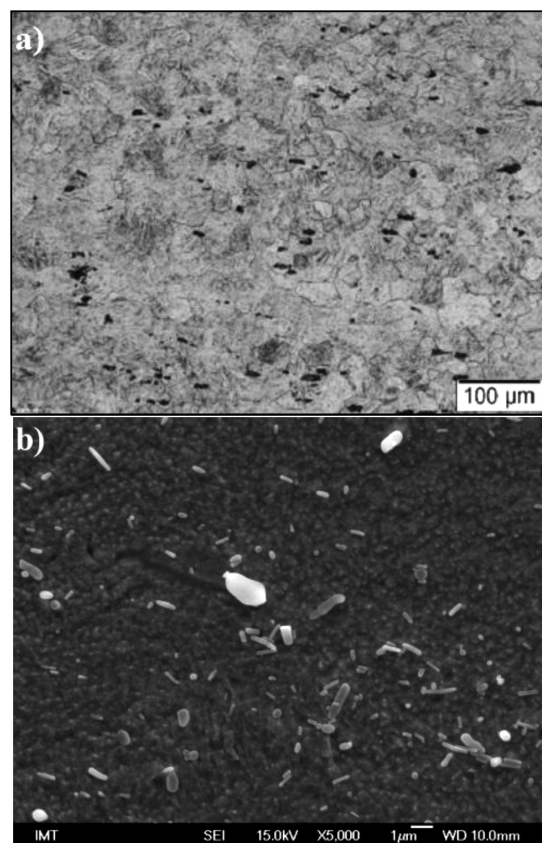


**Figure 7:** a) Light microscope image of commercially available NiTi alloy at 100× magnification and b) SE image of commercially available NiTi alloy at 5000× magnification

**Slika 7:** a) Posnetek komercialno dostopne NiTi zlitine na svetlobnem mikroskopu pri 100× povečavi in b) SE slika komercialno dostopne NiTi zlitine pri 5000× povečavi

### 3.2.2 Commercially available NiTi alloy

The light microscope image (**Figure 7a**) reveals relatively large grains (> 20 μm); the grain boundaries are clearly noticeable and the grains have different shapes and sizes.

The secondary-electron image made with SEM (**Figure 7b**) reveals that the commercially available NiTi

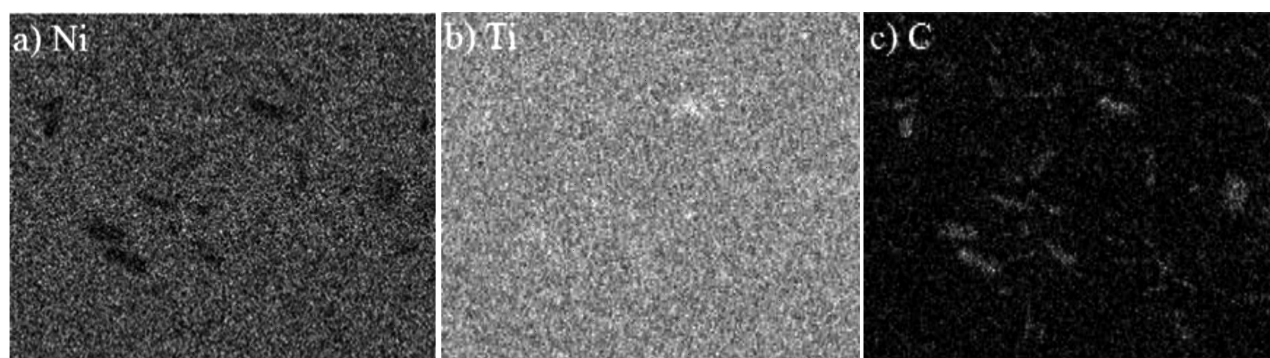


**Figure 8:** a), b) and c) Elemental mapping at the microstructural level by scanning electron microscopy (SEM) with energy-dispersive X-ray spectrometry (EDS) of commercial NiTi alloy

**Slika 8:** a), b) in c) Elementna analiza komercialne NiTi zlitine na mikrostrukturni ravni z vrstičnim elektronskim mikroskopom (SEM) z energijsko disperzijsko rentgensko spektrometrijo (EDS)

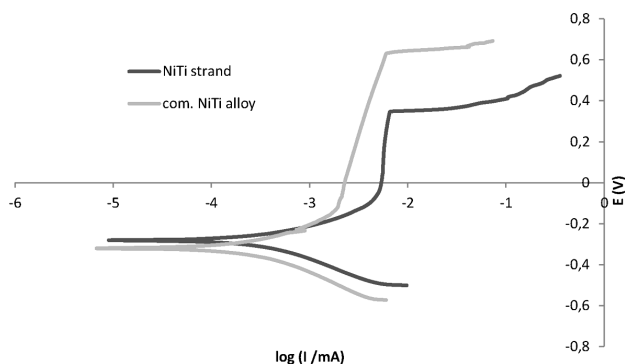


**Figure 9:** Potentiodynamic curves for NiTi strand and commercially available NiTi alloy

**Slika 9:** Potenciodinamske krivulje NiTi palice in komercialno dostopne NiTi zlitine

**Table 1:** Electrochemical parameters determined from the potentiodynamic curves measured for the NiTi strand and the commercially available NiTi alloy

**Tabela 1:** Elektrokemijski parametri, določeni iz potenciodinamskih krivulj, izmerjenih za NiTi palico in komercialno dostopno NiTi zlitino

	$E_{\text{corr}}$ (mV)	$I_{\text{corr}}$ ( $\mu\text{A}$ )	$E_{\text{bd}}$ (mV)	$I_{\text{bd}}$ ( $\mu\text{A}$ )	$v_{\text{corr}}$ (mmpy)
NiTi strand	-287.1	0.343	348.5	6.767	$3.201 \cdot 10^{-3}$
com. NiTi alloy	-324.9	0.328	625.8	5.948	$2.828 \cdot 10^{-3}$

$E_{\text{corr}}$  – corrosion potential determined from potentiodynamic curves;  $I_{\text{corr}}$  – corrosion current;  $E_{\text{bd}}$  – breakdown potential;  $I_{\text{bd}}$  – breakdown current; and  $v_{\text{corr}}$  – corrosion rate

alloy consist of two phases. EDS analysis showed that the prevailing phase is NiTi, containing 50 % of amount fractions of Ni and 50 % of amount fractions of Ti. The second phase is carbon rich phase (33.3 % of amount fractions of C, 40.12 % of amount fractions of Ti, 26.59 % of amount fractions of Ni). **Figure 8** shows the distribution of elements in the individual phases.

### 3.3 Potentiodynamic test

**Figure 9** shows the potentiodynamic curves for NiTi strand and commercially available NiTi alloy, while **Table 1** contains the quantitative results of the measurements. Corrosion potential and current, and breakdown

potential and current values were obtained by graphic extrapolation.

The corrosion potential of the NiTi strand is 38 mV higher than for the commercially available NiTi alloy, which means that the passive layers spontaneously developed on the NiTi strand are less affected by environmental factors. The presence of a wider passivation range was observed for the commercially available NiTi alloy, while for the NiTi strand the passivity occurs in a narrower range of potentials, indicating a higher tendency for localized corrosion. On the surface of the nitinol a double layer is formed. The outer layer is  $\text{TiO}_2$  and the inner layer is  $\text{TiNi}_3$ . When the thickness of the  $\text{TiO}_2$  layer increases, two phenomena play a competing role. First, since Ni atoms are diffusing further away from the surface, they accumulate in the region with the lowest oxidation state (close to the oxide–metal interface). Second, as  $\text{TiNi}_3$  appears as a line phase in the Ni–Ti phase diagram, the amount of Ni in the intermetallic  $\text{TiNi}_3$  layer becomes saturated upon formation of this layer. As a result it will be more energetically favourable to form metallic particles within the  $\text{TiO}_2$  layer than increase the thickness of the intermetallic layer.<sup>20</sup> Breakdown of the passive film occurs as a result of thickening of the oxide layer, leading to an increase in the size of the nickel particles in the outer oxide layer. These particles cause local stress, so the layer cracks, which facilitates the progress of corrosion. The commercially available NiTi alloy has higher breakdown potential, meaning it will form thicker oxide layer before the collapse. The corrosion rate of the commercially available NiTi alloy is lower, so it is more corrosion resistant.

### 3.4 Impedance test

Electrochemical impedance spectroscopy (EIS) measurements were performed at open circuit potential conditions in a simulated physiological fluid for 8 days. **Figure 10** shows the Nyquist impedance diagrams for the NiTi strand and the commercially available NiTi alloy. The analysed spectra proposed an equivalent circuit, considering an outer titanium oxide layer with

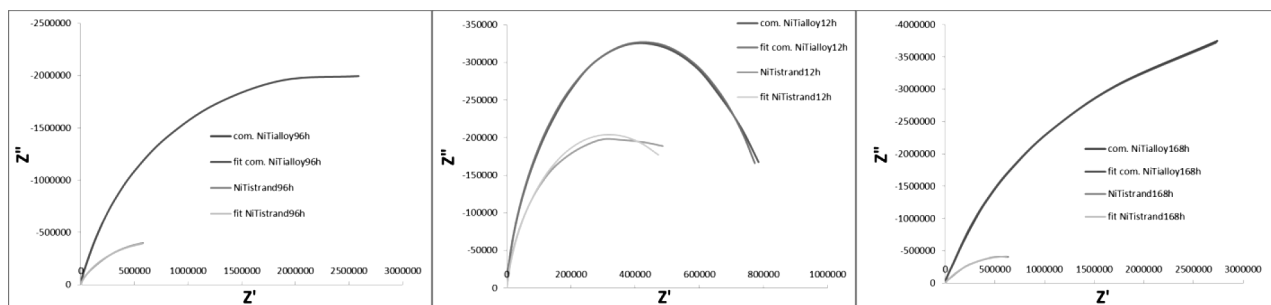


**Figure 10:** Nyquist diagrams for the NiTi strand and the commercially available NiTi alloy with corresponding fit after a) 12 h, b) 96 h, and c) 168 h of immersion

**Slika 10:** Nyquistovi diagrami NiTi palice in komercialno dostopne NiTi zlitine, z ustreznimi prilegajočimi krivuljami po času izpostavljenosti: a) 12 h, b) 96 ur, in c) 168 h

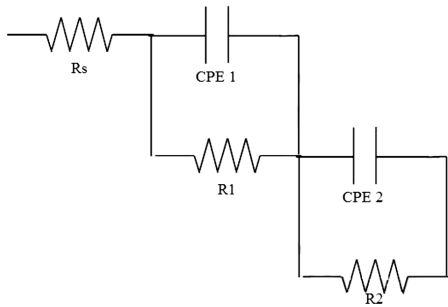


**Figure 11:** Equivalent circuit of two-layer model used for the interpretation of the measured impedance spectra of NiTi alloy

**Slika 11:** Ekvivalentno vezje uporabljeno za razlago izmerjenih impedančnih spektrov NiTi zlitine na osnovi dvoslojnega modela

corrosion resistance  $R_1$  and an inner  $TiNi_3$  layer with resistance  $R_2$  (**Figure 11**), where  $R_s$  is the resistance of the solution. The use of a constant phase element (CPE) was required to account for the non-ideal capacitive response observed as a depressed semicircle when the spectra were plotted in the corresponding Nyquist diagrams. The CPE originates from the surface roughness and inhomogeneities present in the titanium oxide layers at the microscopic level.<sup>21</sup>

**Table 2:** Corrosion resistance of NiTi strand and commercially available NiTi alloy in outer ( $R_1$ ) and inner ( $R_2$ ) oxide layer, and total corrosion resistance  $R_p$  at certain time of immersion

**Tabela 2:** Korozijska odpornost NiTi palice in komercialno dostopne NiTi zlitine v zunanji ( $R_1$ ) in notranji ( $R_2$ ) plasti oksida ter skupna odpornost proti koroziji  $R_p$  pri določenem času izpostavljenosti

t/h	$R_{1com} / \Omega$	$R_{2com} / \Omega$	$R_{1strand} / \Omega$	$R_{2strand} / \Omega$	$R_{p,com} / \Omega$	$R_{p,strand} / \Omega$
1	180400	328850	10110	457060	509250	467170
2	170510	640510	10812	638590	811020	649402
12	265080	603270	11854	736850	868350	748704
24	333940	695490	12652	764400	1029430	777052
48	387740	1048800	12903	939500	1436540	952403
72	544540	1919700	28966	1206800	2464240	1235766
96	702330	3989100	9377	1470000	4691430	1479377
120	798180	5642300	5493	1500600	6440480	1506093
144	843170	6984000	25020	1511900	7827170	1536920
168	917140	8901100	96538	1526000	9818240	1622538
192	1018900	8101300	35321	1447100	9120200	1482421

As shown in **Table 2**, the resistances of the outer and inner oxide layers in the commercial NiTi alloy are very similar and very high, while the difference in resistance between the outer and the inner layer by the NiTi strand is very high. This means that the outer layer of the NiTi strand has Ni particles, which are the weakest link in the corrosion resistance of the NiTi alloy. Resistance values in the outer layer of NiTi strand are so low ( $< 10000 \Omega$ ), that they present no obstacle in the progress of corrosion that can occur hazardous nickel ions outleaching from this layer into the surrounding area. Corrosion has slower progress in the inner  $TiNi_3$  layer.

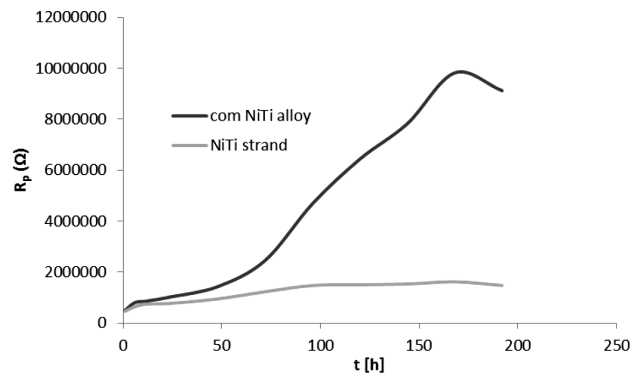


**Figure 12:**  $R_p$  vs time diagram for NiTi strand and commercially available NiTi alloy

**Slika 12:** Diagram  $R_p$  proti času NiTi palice in komercialno dostopne NiTi zlitine

**Figure 12** represents the polarization or a totally corrosion resistance  $R_p$  as a function of time.  $R_p$  can be calculated according to Equation (1):

$$R_p = R_1 + R_2 \quad (1)$$

as a function of time. The slope of the commercial NiTi alloy increases rapidly with time, while the slope of NiTi strand increases slightly with time. It is clear that the corrosion resistance of the commercial NiTi alloy is much greater than that of the NiTi strand at any time. The main reasons for the poorer corrosion resistance of the NiTi strand are a lower homogeneity and a lower titanium content.

## 4 CONCLUSIONS

From this study the following conclusions can be drawn:

- a dendritic microstructure of the NiTi strand was formed while VIM+CVC,
- the chemical composition of the NiTi strand varied through the cross and longitudinal sections, so the drawing process by CVC is not optimal,
- TiC and Fe phases were identified in the NiTi strand,
- the commercially available NiTi alloy has a higher breakdown potential than the NiTi strand, meaning it will have thicker, more stable oxide layer before the collapse,
- the corrosion resistance of the commercial NiTi alloy is much greater than that of NiTi strand at any time,
- 10% deficit of titanium in NiTi strand is reflected in poorer corrosion resistance properties,
- despite the fact that the corrosion resistance of the NiTi strand is not sufficient, we have successfully cast NiTi strand by VIM + CVC processes, so it is evident that it is possible to produce such an alloy in this way.

## 5 REFERENCES

- <sup>1</sup> A. Tuissi, P. Bassani, A. Mangioni, L. Toia, F. Butera, Fabrication process and characterization of NiTi wires for actuators, SMST-2004: Proceedings of the International Conference on Shape Memory and Superelastic Technologies, Baden-Baden, 2004, 501–508
- <sup>2</sup> P. R. Halani, I. Kaya, Y. C. Shin, H. E. Karaca, Phase transformation characteristics and mechanical characterization of nitinol synthesized by laser direct deposition, *Materials Science & Engineering A*, 559 (2013), 836–843, doi:10.1016/j.msea.2012.09.031
- <sup>3</sup> J. Frenzel, Z. Zhang, K. Neuking, G. Eggeler, High quality vacuum induction melting of small quantities of NiTi shape memory alloys in graphite crucibles, *Journal of Alloys and Compounds*, 385 (2004) 1–2, 214–223, doi:10.1016/j.jallcom.2004.05.002
- <sup>4</sup> I. Milošev, B. Kapun, The corrosion resistance of Nitinol alloy in simulated physiological solutions Part 1: The effect of surface preparation, *Materials Science and Engineering C*, 32 (2012) 5, 1087–1096, doi:10.1016/j.msec.2011.11.007
- <sup>5</sup> C. H. Fu, M. P. Sealy, Y. B. Guo, X. T. Wei, Finite element simulation and experimental validation of pulsed laser cutting of nitinol, *Journal of Manufacturing Processes*, 19 (2015), 81–86, doi:10.1016/j.jmapro.2015.06.005
- <sup>6</sup> B. Lin, K. Gall, H. J. Maier, R. Waldron, Structure and thermomechanical behavior of NiTiPt shape memory alloy wires, *Acta Biomaterialia*, 5 (2009) 1, 257–267, doi: 10.1016/j.actbio.2008.07.015
- <sup>7</sup> J. M. McNaney, V. Imbeni, Y. Jung, P. Papadopoulos, R. O. Ritchie, An experimental study of the superelastic effect in a shape-memory Nitinol alloy under biaxial loading, *Mechanics of Materials*, 35 (2003), 969–986, doi:10.1016/S0167-6636(02)00310-1
- <sup>8</sup> A. Saigal, M. Fonte, Solid, shape recovered “bulk” Nitinol: Part I – Tension – compression asymmetry, *Materials Science and Engineering A*, 528 (2011) 16–17, 5536–5550, doi:10.1016/j.msea.2011.03.060
- <sup>9</sup> K. Otsuka, X. Ren, Physical metallurgy of Ti-Ni based shape memory alloys. *Progress in Materials science*, 50 (2005) 5, 511–678, doi:10.1016/j.pmatsci.2004.10.001
- <sup>10</sup> F. M. Ashby, R. H. D. Jones, *Engineering Materials 2: An Introduction to Microstructures, Processing and Design*, Second Edition, Butterworth-Heinemann, 1998
- <sup>11</sup> J. Beddoes, M. J. Bibby, *Principles of Metal Manufacturing Processes*, Second Edition, Butterworth-Heinemann, 2003
- <sup>12</sup> H. Fredriksson, U. Åkerlind, *Materials Processing during Casting*, First Edition, Wiley, 2006
- <sup>13</sup> M. Ferry, *Direct Strip Casting of Metals and Alloys*, First Edition, Woodhead Publishing Limited and CRC Press LLC, 2006
- <sup>14</sup> M. J. Mahtabi, N. Shamsaei, M. R. Mitchell, Fatigue of Nitinol: The state-of-the-art and ongoing challenges, *Journal of the mechanical behavior of biomedical materials*, 50 (2015), 228–254, doi:10.1016/j.jmbbm.2015.06.010
- <sup>15</sup> J. Ferčec, R. Rudolf, Theoretical calculation of stress for the start of stress induced martensitic phase transformation in the Shape Memory Alloys NiTi, *Anali Pazu*, 3 (2013) 2, 75–78
- <sup>16</sup> T. Hu, C. Chu, L. Yin, Y. Pu, Y. Dong, C. Guo, X. Sheng, J.-CY Chung, P.-K. Chu, In vitro biocompatibility of titanium-nickel alloy with titanium oxide film by H<sub>2</sub>O<sub>2</sub> oxidation, *Trans. Nonferrous Met. Soc. China*, 17 (2007), 553–557
- <sup>17</sup> D. Vojtěch, M. Voděrová, J. Fojt, P. Novák, T. Kubásek, Surface structure and corrosion resistance of short-time heat-treated NiTi shape memory alloy, *Applied Surface Science*, 257 (2010) 5, 1573–1582, doi:10.1016/j.apsusc.2010.08.097
- <sup>18</sup> S. A. Shabalovskaya, H. Tian, J. W. Anderegg, D. U. Schryvers, W. U. Carroll, J. Van Humbeeck, The influence of surface oxides on the distribution and release of nickel from Nitinol wires, *Biomaterials*, 30 (2009) 4, 468–477, doi:10.1016/j.biomaterials.2008.10.014
- <sup>19</sup> S. A. Shabalovskaya, G. C. Rondelli, A. L. Undisz, J. W. Anderegg, T. D. Burleigh, M. E. Rettenmayr, The electrochemical characteristics of native Nitinol surfaces, *Biomaterials*, 30 (2009) 22, 3662–3672, doi:10.1016/j.biomaterials.2009.03.034
- <sup>20</sup> H. Tian, D. Schryvers, D. Liu, Q. Jiang, J. Van Humbeeck, Stability of Ni in nitinol oxide surfaces, *Acta Biomaterialia*, 7 (2011) 2, 892–899, doi:10.1016/j.actbio.2010.09.009
- <sup>21</sup> J. Izquierdo, M. B. González-Marrero, M. Bozorg, B. M. Fernández-Pérez, H. C. Vasconcelos, J. J. Santana, R. M. Souto, Multi-scale electrochemical analysis of the corrosion of titanium and nitinol for implant applications, *Electrochimica Acta*, 203 (2016), 366–378, doi:10.1016/j.electacta.2016.01.146



# HOT TENSILE TESTING OF SAF 2205 DUPLEX STAINLESS STEEL

## VROČI NATEZNI PRESKUSI DUPELEKS NERJAVNEGA JEKLA SAF 2205

**Franc Tehovnik, Borut Žužek, Jaka Burja**

Institute of Metals and Technology, Lepi pot 11, 1000 Ljubljana, Slovenia  
franc.tehovnik@imt.si

*Prejem rokopisa – received: 2016-08-04; sprejem za objavo – accepted for publication: 2016-09-06*

doi:10.17222/mit.2016.242

The changes to the microstructure of the duplex stainless steel SAF 2205 during hot tensile tests were investigated. The dominant restoration mechanisms for ferrite and austenite were dynamic recovery (DRV) and dynamic recrystallization (DRX), respectively. Also, the effect of temperature on the deleterious phase precipitation was investigated. The specimens were tested with hot tensile deformation tests in the temperature range from 800 °C to 1100 °C. The tensile strength of the investigated steel decreased rapidly in the temperature range from 800 °C to 950 °C and slowly at the testing temperatures from 1000 °C to 1100 °C. It was found that SAF 2205 has excellent hot-working properties at temperatures between 950 °C and 1100 °C. The differences in the mechanical properties of austenite and ferrite along with the precipitation of the  $\sigma$ -phase represent the most important restrictions during hot working. Optical microscopy was used for the microstructure-evolution analysis in the duplex stainless steel during the hot tensile tests.

**Keywords:** duplex stainless steel, hot tensile test, microstructural evolution, intermetallic phases,  $\sigma$ -phase

Preiskovali smo spremembe mikrostrukture dupleks nerjavnega jekla SAF 2205 med vročimi nateznimi preskusi. Prevladujoča mehanizma mehčanja v feritu in avstenitu sta bila dinamična poprava in/ali dinamična rekristalizacija. V dupleks nerjavnem jeklu je bil raziskan vpliv temperature na izločanje škodljivih faz. Vzorce smo vroče natezno preskušali v temperaturnem območju med 800 °C in 1100 °C. Natezna trdnost preiskanega jekla se je hitro znižala v temperaturnem območju med 800 °C in 950 °C ter počasneje pri temperaturah preskusov med 1000 °C in 1100 °C. Ugotovili smo, da ima SAF 2205 odlične vroče preoblikovalne lastnosti v temperaturnem območju med 950 °C in 1100 °C. Največje omejitve pri preoblikovanju predstavljajo razlike v mehanskih lastnostih med avstenitom in feritom ter izločanje  $\sigma$ -faze. V raziskavi je bila uporabljena optična mikroskopija za analizo razvoja mikrostrukture v dupleks nerjavnem jeklu med vročimi nateznimi preskusi.

**Ključne besede:** dupleks nerjavno jeklo, vroči natezni preskusi, razvoj mikrostrukture, intermetalne faze,  $\sigma$ -faza

## 1 INTRODUCTION

Duplex stainless steels (DSS) have the advantage of low price, pitting-corrosion resistance, stress-corrosion-cracking resistance, resistance to intergranular corrosion, high mechanical strength, corrosion-fatigue resistance, wear resistance, super plastic behaviour and good weldability.<sup>1-8</sup> But they have a severe disadvantage in being difficult to hot work.<sup>2,9,10</sup> The DSS microstructure generally consists of around 50 %  $\delta$ -ferrite and 50 %  $\gamma$ -austenite, which gives them excellent properties, but also provides for a narrow window in the hot-working process. During hot working, ferrite and ferritic stainless steels undergo dynamic recovery (DRV),<sup>11</sup> which means that subgrains develop in the microstructure, as is the case for the hot working of duplex stainless steels,<sup>12</sup> while austenite and austenitic stainless steels undergo a high degree of strain hardening and then dynamic recrystallization (DRX).<sup>8</sup>

While the austenite is dominated by high-angle grain boundaries (HAB), ferrite shows a substantial amount of subgrain boundaries, i.e., low-angle grain boundaries (LAB). Such a contrasting behaviour of austenite and ferrite phases is due to the different stacking-fault ener-

gies of these phases, which imposes different deformation mechanisms.<sup>13</sup>

Therefore, when hot working duplex stainless steels, DRV is the initial softening mechanism. But austenite undergoes DRV only at high temperatures and low strain rates. At low strain rates and high temperatures DSS exhibit superplasticity; therefore, allowing elongations that exceed 1000 %.<sup>6</sup> Superplasticity can be linked to grain-boundary sliding, but grain-boundary sliding also causes cavity formation, which in turn causes stress concentration, and if these stresses cannot be released at sufficient rates, the cavities nucleate.<sup>14</sup> The cavities, provided with appropriate conditions, then undergo the processes of growth and coalescence and form larger cavities that can lead to failure.<sup>14</sup> Another factor that negatively influences the mechanical properties is the precipitation of secondary phases,<sup>15</sup> especially the  $\sigma$ -phase, which occurs in the temperature range from 700 °C to 1000 °C and is promoted by Cr, Mo and Si.<sup>12,16,17</sup> The  $\sigma$ -phase reduces the ductility and toughness of the steel.<sup>12</sup> Increased steel hardness is an indicator of  $\sigma$ -phase precipitation.<sup>12</sup> The precipitation phenomena in duplex stainless steels occur mainly in the  $\delta$ -ferrite,

**Table 1:** Chemical composition SAF 2205 in mass fractions, (w/%)**Tabela 1:** Kemijska sestava jekla SAF 2205 v masnih odstotkih, (w/%)

C	Si	Mn	P	S	Cr	Ni	Cu	Mo	V	Ti	Nb	Al	N
0.021	0.32	1.58	0.026	0.002	22.95	5.3	0.26	2.742	0.15	0.005	0.008	0.012	0.141

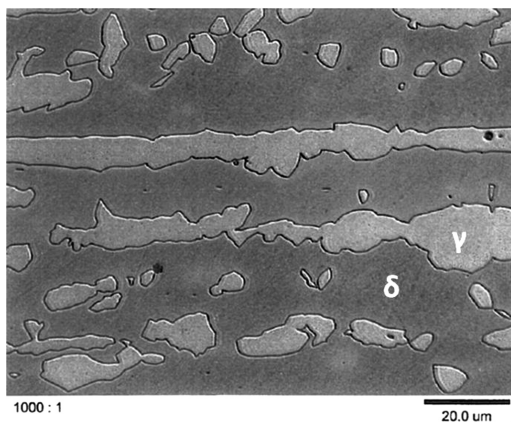
because the diffusion rates are much faster than in the austenite. The genesis of the precipitates can be attributed to the large amount of alloying element and is promoted by the instability of the ferritic matrix at the high temperatures. The morphology and location of the secondary phases are well known and described,<sup>18</sup> they precipitate both at triple points and grain boundaries, and their growth occurs towards the unstable ferrite, also due to the diffusion behaviour of the involved elements.

## 2 MATERIALS AND EXPERIMENTAL PART

Duplex stainless-steel grade SAF 2205, with the chemical composition given in **Table 1**, was used in the experimental work.

The initial microstructure is presented in **Figure 1**. Both phases have an almost fully recrystallized microstructure produced by the annealing treatment at 1050 °C before deformation testing.

The tensile test specimens of SAF 2205 were made according to DIN 50125. The specimens were cut out from the hot-rolled plates longitudinal to the rolling direction. Tensile tests were performed at elevated temperatures of (800, 850, 900, 950, 1000, 1050 and 1100) °C on a 500-kN INSTRON tensile test machine with a special furnace mounted to ensure high-temperature conditions. The specimens were heated at a rate of 700 °C/h, and were held at the deformation temperature for 15 min. The deformation speed was 5 mm/min, which gives a logarithmic strain rate of 0.0014 s<sup>-1</sup>. During the hot tensile tests the force and extension were recorded simultaneously. At the end of the tensile tests, the specimens were air cooled.

**Figure 1:** Initial microstructure of SAF 2205 duplex stainless steel, austenite (light) and ferrite (dark), light microscopy**Slika 1:** Začetna mikrostruktura dupleks nerjavnega jekla SAF 2205, avstenit (svetel) in ferit (temen), svetlobna mikroskopija

The samples for metallographic analysis of the tensile specimens were taken 10 mm from the fracture surface in the contraction area, longitudinal to the testing direction. The samples were etched with a solution of 30 g KOH, 30 g K<sub>3</sub>Fe(CN)<sub>6</sub> and 100 mL distilled water. The etching causes the phases in the microstructure to colour differently: the  $\sigma$ -phase is dark, the  $\delta$ -ferrite is lighter and the  $\gamma$ -austenite is the brightest in colour. The metallographic samples were observed with an optical microscope (Microphot FXA, Nikon). The content of the magnetic  $\delta$ -ferrite was determined by a ferritoscope instrument FISCHER MP30.

## 3 RESULTS AND DISCUSSION

The initial microstructure of the steel is composed from austenitic grains (light) that are oriented in the rolling direction and recrystallized ferrite grains (dark). Individual "islands" of austenite grains are located in the ferrite areas. Specimens that were tested at (800, 850 and 900) °C contain  $\sigma$ -phase, while those that were tested at higher temperatures contain no  $\sigma$ -phase.

The specimen's microstructures after the tensile tests are shown in **Figures 2a** to **2g**. Cavitations or cracks that formed at high deformations are visible in **Figures 2d** to **2f** at temperatures from 950 °C to 1050 °C. The **Figures 2d** to **2f** show some cracks that nucleated at the austenite/ferrite interfaces and propagated along the interface towards the softer ferrite phase. The same phenomenon was also found by M. Faccoli and R. Roberti.<sup>19</sup> Due to a notable difference in strength between the ferrite and austenite, voids are formed at the austenite/ferrite interfaces. Deformation at high temperatures, however, allows dynamic restoration (DRV and DRX) to take affect and reduce the work hardening, thus reducing the probability of void formation.

It is clear that the hot tensile strength of the steel at deformations up to  $\varphi = 0.5$  gradually increases at temperatures around 800 °C, and this can be partially said for the test at 850 °C. But at the temperature of 900 °C the tensile strength does not change significantly due to the established equilibria between the strain hardening and the softening effects. **Figure 2a** shows the microstructure of the sample tested at the lowest temperature. The austenite phase appears in the form of elongated islands. In the sample tested at the lowest temperature (**Figure 2a, 2b**) their distribution is not homogeneous and the austenite/ferrite interfaces are affected by  $\sigma$ -phase precipitation.

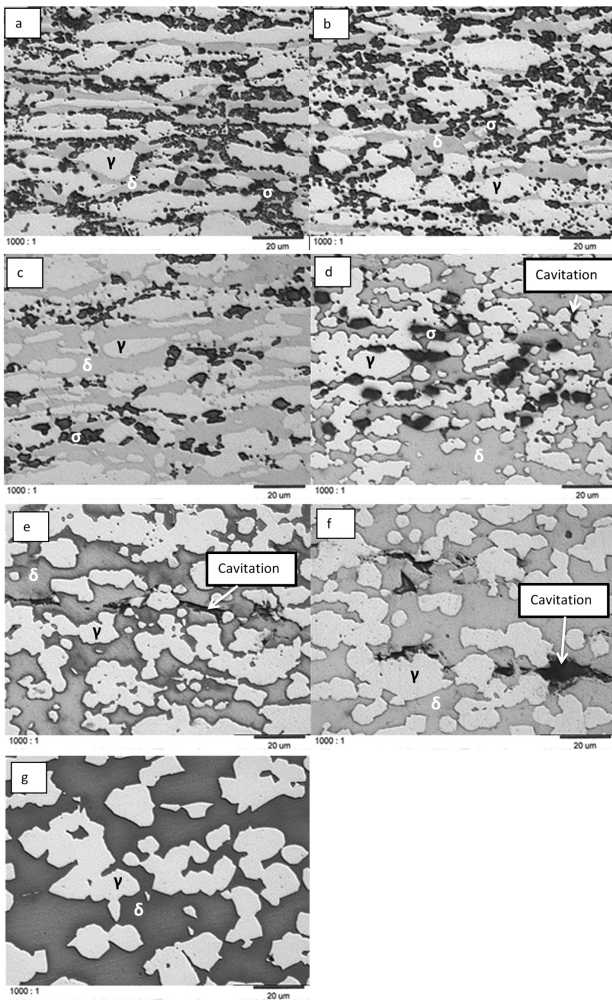


**Figure 2:** Microstructures of specimens after tensile tests at different temperatures, light microscopy

**Slika 2:** Mikrostruktura preskušancev po vročih nateznih testih pri različnih temperaturah, svetlobna mikroskopija

At higher temperatures from 950 °C to 1100 °C there is a significant drop in tensile strength due to the softening effects, and the initial strengths are not reached.

**Figures 2d to 2g** show more equiaxed austenitic grains, a sign of the recrystallization process.

As the temperature increases, the austenite volume fraction decreases and the austenite phase islands are progressively reduced in length and appear more discontinuous;  $\gamma$ -islands which are almost totally dissolved assume a globular shape. According to A. Iza-Mendia et al.,<sup>20</sup> austenite produces non-deformed regions at this temperature. The strain difference between the two phases is, therefore, responsible for the severe shear strains at the phase boundaries, sliding or even cracks.

The stress-strain curves for the tests at different temperatures (from 800 °C to 1100 °C) at the strain rate of 0.0014 s<sup>-1</sup> are shown in **Figure 3**. According to **Figure 3**, the optimum hot-working temperature range at the strain rate of 0.0014 s<sup>-1</sup> should be between 950 °C and 1100 °C.

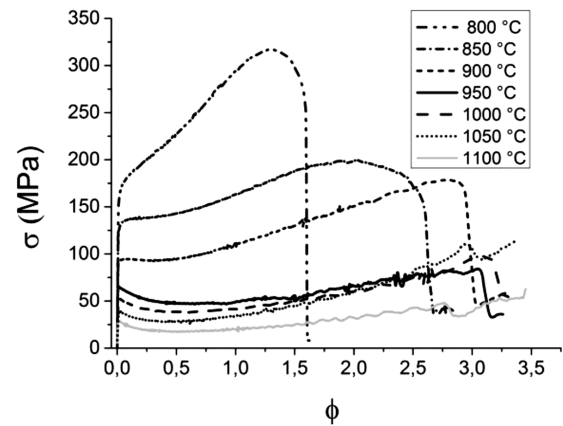


**Figure 3:** Stress-strain (logarithmic) diagram for hot tensile tests at different temperatures

**Slika 3:** Graf napetost – (logaritemska) deformacija vročih nateznih preskusov pri različnih temperaturah

The worst hot-working properties are at 800 °C. Generally, the flow stress rises to a maximum at the commencement of the straining before dropping to a steady-state level. The shape of the curves also changes as the material and deformation conditions are altered. At high temperatures, above 950 °C, the flow curves have the characteristic shape expected for materials that show dynamic recovery. As the deformation temperature is decreased the shape changes with rapid work hardening, followed by extensive flow softening. These changes become more dramatic when the austenite volume fraction is further increased. As the volume fraction of austenite in the ferrite matrix is increased, the ductility also decreases

The results of the tensile strength and the reduction of area that were obtained from hot tensile tests are summed up in **Figure 4**. The best hot-working properties are achieved at higher temperatures, as the material has the lowest tensile strengths and the highest contractions and elongations (**Figure 4**).

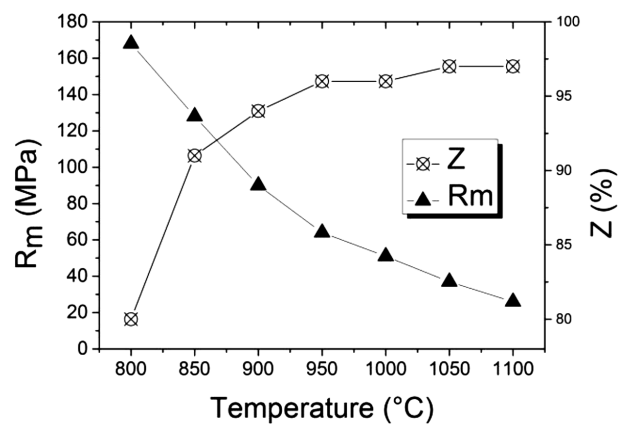


**Figure 4:** Tensile strength and contraction of SAF 2205, depending on the testing temperature in the range from 800 °C to 1100 °C

**Slika 4:** Natezna trdnost in kontrakcija SAF 2205 v odvisnosti od temperature preizkušanja v temperaturnem območju od 800 °C do 1100 °C



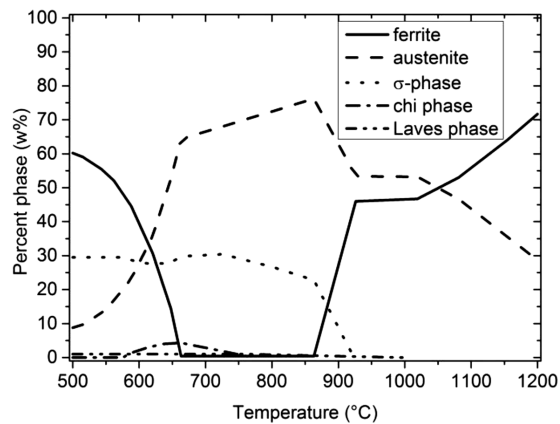


**Figure 5:** Calculated weight fractions of equilibrium phases in SAF 2205 in the temperature range from 500 °C to 1250 °C

**Slika 5:** Izračunani masni deleži ravnotežnih faz v SAF 2205 v temperaturnem območju od 500 °C do 1250 °C

There is a rapid increase in the reduction area as the temperature rises from 800 °C to 850 °C, from 850 °C on it gradually increases with temperature, while the fall in tensile strength is more continuous.

The high-temperature mechanical properties and hot-working properties depend mostly on the microstructural changes. DRV can be observed as a polygonisation of the subgrains; it is more pronounced at high temperatures and lower deformation speeds and lower loads. DRX can be observed as the formation of new, equiaxed grains. Another process that can influence the hot-working properties is the precipitation of the intermetallic phases from the matrix, namely the  $\sigma$ -phase.

The equilibrium phase composition for SAF 2205 was calculated with Thermo-Calc, the results are presented in **Figure 5**.

As shown in **Figure 5**,  $\sigma$ -phase formation does not occur at temperatures above 930 °C, while the sample at 950 °C still contains some  $\sigma$ -phase. With a decrease of temperature, the austenite weight fraction increases significantly from 28 % at 1200 °C up to 67 % at 860 °C. The change in austenite volume fraction influences the mechanical behaviour of the duplex stainless steel because of the large difference in strength between the ferrite and austenite.

The content of ferrite in the samples was measured with the ferritoscope. The results of the measurements are presented in **Figure 6**.

**Figure 6** shows the evolution of the  $\delta$ -ferrite volume fraction at different test temperatures; the amount of  $\delta$ -ferrite increases between 850 °C and 1000 °C. According to **Figure 5**, the amount of  $\sigma$ -phase formed is at least a factor of 5 greater than the amount of chi phase. Predictions by Thermo-Calc are relatively good for the amount of ferrite at 1000 °C; the predicted value is about 48 % compared to 46 % measured. Above 850 °C, the amount of austenite decreases considerably with the deformation temperature, which is attributed to the  $\gamma \rightarrow \delta$  transformation. The content of ferrite rises at

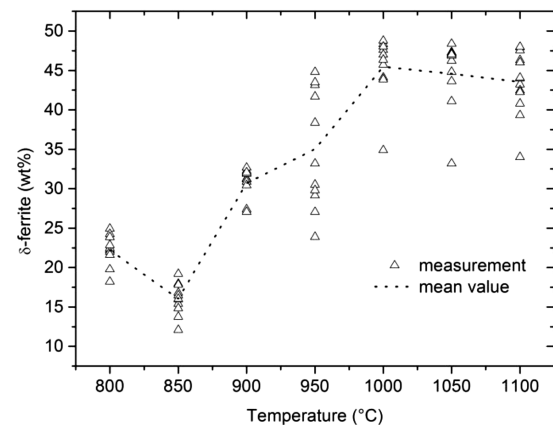


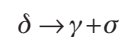
**Figure 6:** Measured  $\delta$ -ferrite weight fraction and mean values at different temperatures in the range from 800 °C to 1100 °C

**Slika 6:** Izmerjen masni delež  $\delta$ -ferita in srednje vrednosti pri različnih temperaturah v območju od 800 °C do 1100 °C

temperatures from 950 °C to 1100 °C; it is about 45 % at 1100 °C, the rest is austenite.

The hot-working properties greatly depend on the austenite and ferrite content in the steel microstructure; their ratio depends on the temperature, as shown on **Figure 5**. The softening mechanism in ferrite is DRV; it can be observed as the subgrain formation, while the softening mechanism in austenite is the DRX, which is discontinuous, and it mostly occurs on ferrite–austenite phase grain boundaries. The lower driving force for ferrite strain softening is compensated with a higher diffusion rate and a higher mobility of dislocations in a cubic body-centred lattice, that contribute to a faster strain softening process in ferrite.

Another important factor that contributes to the difficult hot-working properties of DSS is the occurrence of the  $\sigma$ -phase. The  $\sigma$ -phase is formed by the eutectoid transformation:



The presence of the  $\sigma$ -phase is the most prominent at 900 °C. Long exposure times at temperatures up to 900 °C and deformation are sufficient conditions for  $\sigma$ -phase formation during hot tensile tests. Duplex stainless steels are more susceptible to the precipitation of intermetallic phases than austenitic steels due to the high Cr and Mo contents and higher diffusion rates in the ferrite phase. The precipitation reaction of  $\sigma$ -phase in austenite is sluggish due to the slow diffusivity of the solute atoms. As the precipitation continues, Cr and Mo diffuse to the  $\sigma$ -phase, leading to the depletion of these elements in the ferrite, especially the Mo content. Therefore, Mo from the inner region of the ferrite diffuses to the  $\sigma$ -phase. The  $\sigma$ -phase nucleates preferentially at the ferrite/ferrite and ferrite/austenite boundaries, and then grows into the adjacent ferritic grains. Mo is the main element controlling secondary-phase precipitation. The  $\sigma$ -phase is a hard, brittle, non-magnetic intermetallic phase, with high Cr and Mo contents.



The partitioning of the elements between the ferrite and austenite takes place during DSS and contributes to the difference in hot strength between the ferrite and austenite. This means that some alloying elements can dissolve preferentially in one phase compared to the other, depending on the nature of the considered chemical element: austenite or ferrite stabilizer. At both extremes, Mo is the element that segregates mostly to ferrite, whereas C and N tend to leave the ferrite. The high N content in austenite is important, as the solute-strengthening effect tends to increase the hot strength of the austenite. The partition of elements changes with temperature. The content of ferrite-forming elements in the austenite phase decreases with temperature, whereas the austenite stabilizer content increases. As a consequence the hot-deformation behaviour of duplex steels can be different at the beginning and at the end of the hot-deformation process. The higher the temperature, the more uniform the element partitioning is between ferrite and austenite.

#### 4 CONCLUSIONS

The following conclusions can be drawn from the experimental work:

The SAF 2205 duplex stainless steel has excellent hot-working properties at temperatures between 950 °C and 1100 °C, while hot working is not recommended at 800 °C.

Difficulties in hot working due to  $\sigma$ -phase precipitation can be accurately predicted by Thermo-Calc software.

The  $\sigma$ -phase is mostly observed below 950 °C. The microstructure of the steel is ferrite + austenite at room temperature, ferrite + austenite +  $\sigma$  from 800 °C to 950 °C and ferrite + austenite at higher temperatures 1000 °C to 1100 °C. The specimens that were tensile tested at lower temperatures (800–900 °C) broke at lower strains due to severe  $\sigma$ -phase precipitation and diminished softening mechanisms. These specimens did not show cavity occurrence 10 mm from the fracture surface, as the fracture was more localized, while the higher temperature tests from 950 °C to 1050 °C had cavities occurring even 10 mm from the fracture surface. The highest testing temperature, however, resulted in a microstructure that showed no apparent damage. This suggests that the dominant reason for failures at temperatures from 950 °C to 1050 °C is the difference in mechanical properties between the ferrite and austenite that are further increased by the differences in the softening mechanisms.

#### 5 REFERENCES

- <sup>1</sup> Z. Y. Liu, C. F. Dong, X. G. Li, Q. Zhi, Y. F. Cheng, Stress corrosion cracking of 2205 duplex stainless steel in H<sub>2</sub>S–CO<sub>2</sub> environment, *J. Mater. Sci.*, 44 (2009) 4228–4234, doi: 10.1007/s10853-009-3520-x
- <sup>2</sup> A. Momeni, K. Dehghani, Hot working behavior of 2205 austenite-ferrite duplex stainless steel characterized by constitutive equations and processing maps, *Mater. Sci. Eng. A*, 528 (2011) 1448–1454, doi:10.1016/j.msea.2010.11.020
- <sup>3</sup> G. W. Fan, J. Liu, P. D. Han, G. J. Qiao, Hot ductility and microstructure in casted 2205 duplex stainless steels, *Mater. Sci. Eng. A*, 515 (2009), 108–112, doi:10.1016/j.msea.2009.02.022
- <sup>4</sup> N. Ortiz, F. F. Curiel, V. H. López, A. Ruiz, Evaluation of the intergranular corrosion susceptibility of UNS S31803 duplex stainless steel with thermoelectric power measurements, *Corros. Sci.*, 69 (2013), 236–244, doi:10.1016/j.corsci.2012.12.008
- <sup>5</sup> C. Allen, A. Ball, B. E. Protheroe, The Abrasive-Corrosive Wear of Stainless Steels, *Wear* 74 (1981), 287–305
- <sup>6</sup> S. Li, X. Ren, X. Ji, Y. Gui, Effects of microstructure changes on the superplasticity of 2205 duplex stainless steel, *Mater. Des.*, 55 (2014), 146–151, doi:10.1016/j.matdes.2013.09.042
- <sup>7</sup> S. N. Patankar, C. T. Lim, M. J. Tan, Superplastic forming of duplex stainless steel, *Metall. Mater. Trans. A*, 31 (2000), 2394–2396, doi: 10.1007/s11661-000-0158-3
- <sup>8</sup> A. Moreira Jorge, G. Silva Reis, O. Balancin, Influence of the microstructure on the plastic behaviour of duplex stainless steels, *Mater. Sci. Eng. A*, 528 (2011), 2259–2264, doi:10.1016/j.msea.2010.11.087
- <sup>9</sup> L. Chen, X. Ma, X. Liu, L. Wang, Processing map for hot working characteristics of a wrought 2205 duplex stainless steel, *Mater. Des.*, 32 (2011), 1292–1297, doi:10.1016/j.matdes.2010.09.030
- <sup>10</sup> H. Farnoush, A. Momeni, K. Dehghani, J. A. Mohandesi, H. Keshmiri, Hot deformation characteristics of 2205 duplex stainless steel based on the behavior of constituent phases, *Mater. Des.*, 3 (2010), 220–226, doi:10.1016/j.matdes.2009.06.028
- <sup>11</sup> B. K. Choudhary, D. P. R. Palaparti, E. I. Samuel, Analysis of tensile stress-strain and work-hardening behavior in 9Cr-1Mo ferritic steel, *Metall. Mater. Trans. A*, 44 (2013), 212–223, doi:10.1007/s11661-012-1385-0
- <sup>12</sup> F. Tehovnik *et al.* Microstructure evolution in SAF 2507 super duplex stainless steel, *Mater. Tehnol.*, 45 (2011), 339–345
- <sup>13</sup> A. Eghlimi, M. Shamanian, M. Eskandarian, A. Zabolian, J. A. Szpunar, Characterization of microstructure and texture across dissimilar super duplex/austenitic stainless steel weldment joint by super duplex filler metal, *Mater. Charact.*, 106 (2015), 27–35, doi:10.1016/j.matchar.2015.05.017
- <sup>14</sup> D. Pulino-Sagradi, A. M. M. Nazar, J.-J. Ammann, R. E. Medrano, Effect of temperature and strain rate on cavitation in a superplastic duplex stainless steel, *Acta Mater.*, 45 (1997), 4663–4666, doi:10.1016/S1359-6454(97)00134-1
- <sup>15</sup> N. Pettersson, R. F. A. Pettersson, S. Wessman, Precipitation of Chromium Nitrides in the Super Duplex Stainless Steel 2507, *Metall. Mater. Trans. A*, 46 (2015), 1062–1072, doi:10.1007/s11661-014-2718-y
- <sup>16</sup> J. Y. Maetz, S. Cazottes, C. Verdu, X. Kleber, Precipitation and Phase Transformations in 2101 Lean Duplex Stainless Steel During Isothermal Aging, *Metall. Mater. Trans. A*, 47 (2015) 239–253, doi:10.1007/s11661-014-2718-y
- <sup>17</sup> D. C. Dos Santos, R. Magnabosco, Kinetic Study to Predict Sigma Phase Formation in Duplex Stainless Steels, *Metall. Mater. Trans. A*, 47 (2016) 1–12, doi:10.1007/s11661-016-3323-z
- <sup>18</sup> I. Calliari, M. Breda, E. Ramous, M. Magrini, Effect of isothermal heat treatments on Duplex Stainless Steels impact toughness. in *Convegno Nazionale IGF XXII*, Rome, 2013, 56–65
- <sup>19</sup> M. Faccoli, R. Roberti, Study of hot deformation behaviour of 2205 duplex stainless steel through hot tension tests, *J. Mater. Sci.*, 48 (2013), 5196–5203, doi:10.1007/s10853-013-7307-8
- <sup>20</sup> A. Iza-Mendia, A. Pinol-Juez, J. J. Urcola, I. Gutiérrez, Microstructural and Mechanical Behavior of a Duplex Stainless Steel under Hot Working Conditions, *Metall. Mater. Trans. A*, 29 (1998), 2975–2986



# A HIGH-EFFICIENCY AUTOMATIC DE-BUBBLING SYSTEM FOR LIQUID SILICONE RUBBER

## VISOKOZMOGLJIV SISTEM ZA ODPRAVLJANJE MEHURČKOV V TEKOČI SILIKONSKI GUMI

**Chil-Chyuan Kuo, Chuan-Ming Huang**

Ming Chi University of Technology, Department of Mechanical Engineering, No. 84, Gungjuan Road, Taishan Dist. New, Taipei City 24301, Taiwan  
jacksonk@mail.mcut.edu.tw

*Prejem rokopisa – received: 2014-06-13; sprejem za objavo – accepted for publication: 2016-10-27*

doi:10.17222/mit.2014.089

The silicone-rubber mold is regarded as an important method for reducing the cost and time to market a new product by shortening the development phase. A commercial, automatic, vacuum machine is widely used to degas in the manufacturing of a silicone-rubber mold, but the hardware is costly. A low-cost, high-efficiency degassing system was designed and implemented from a regular vacuum machine. The control style was based on a human-machine interface. It was found that the whole degassing-process sequences consist of the explosive phase, the balanced phase and the convergence phase. The time saving in the degassing process can be at least 42 %. Six predicted equations for both the balanced phase and the convergence phase are investigated and the maximum relative error of these equations can be controlled to within 6.34 %. The advantages of the developed de-bubbling system include saving labor, reducing the human error of the operator and a higher degassing efficiency.

Keywords: air bubbles, de-bubbling, silicone rubber mold, rapid tooling

Forma iz silikonske gume je pomembna pri zmanjševanju stroškov in skrajšanju časa razvojne faze pri uvajanju novega izdelka na trg. Pri izdelavi forme iz silikonske gume se za razplinjevanje uporabljajo drage komercialne vakuumske avtomatske naprave. Iz običajne vakuumske naprave je bil izdelan poceni in učinkovit razplinjevalni sistem. Kontrola stroja temelji na povezavi človek-naprava. Ugotovljeno je, da razplinjevanje sestoji iz eksplozivne faze, faze uravnoveženja in iz faze konvergence. Postopek razplinjevanja omogoča 42 % prihranek časa. Preiskanih je bilo šest predvidenih enačb pri obeh uravnoveženih fazah in pri konvergenčni fazi in maksimalna napaka znaša 6,34 %. Prednosti razvitega sistema razplinjevanja so: prihranek dela, zmanjšanje človeških napak operaterja in večja učinkovitost razplinjevanja.

Gljučne besede: zračni mehurčki, odprava mehurčkov, forma iz silikonske gume, hitra izdelava orodij

## 1 INTRODUCTION

To reduce the time and the cost of product development, rapid prototyping (RP) was developed.<sup>1</sup> This offers the potential to completely revolutionize the process of manufacture. However, the features of the prototype do not usually meet the needs of the end product with the required material. Rapid tooling (RT) technologies are then developed because it is the technology that uses RP technologies and applies them to the manufacturing of mold inserts.<sup>2</sup> Since the importance of RT goes far beyond component performance testing, RT is regarded as an important method of reducing the costs and the time to market in a new-product development process. Several RT technologies are commonly available in industry now. RT is divided into direct tooling and indirect tooling.<sup>3</sup> Direct tooling means fabricating mold inserts directly from an RP machine, such as selective laser sintering.<sup>4,5</sup> Indirect tooling means fabricating the mold insert by a master pattern fabricated using various RP technologies. Soft tooling is used for low-volume production. The materials used for soft tooling have low hardness levels, such as silicone-rubber<sup>6</sup> and epoxy-resin composites.<sup>7</sup> Conversely, hard tooling is associated with

higher volumes of production. Materials used for hard tooling often have high hardness levels. Soft tooling is easier to work with than tooling steels because these tools are created from materials such as epoxy-based composites with aluminum particles, silicone rubber or low-melting-point alloys. It is well known that RT is capable of replacing conventional steel tooling, saving costs and time in the manufacturing process.<sup>8</sup> Indirect soft tooling is used more frequently in the development of new products than direct tooling, because it is fast, simple and cost-effective. It is a well-known fact that a silicone rubber mold is employed frequently because it has flexible and elastic characteristics, so that parts with sophisticated geometries can be fabricated.<sup>9</sup> A silicone-rubber mold can be used for producing low-melting-point metal parts, wax patterns and plastic parts. Air bubbles in the silicone-rubber mold are one of the most common types of defects, especially in the vicinity of the master pattern. A silicone-rubber mold with air bubbles appearing in the vicinity of the master pattern will change the appearance and dimensional accuracy of the part duplicated from this silicone-rubber mold using vacuum casting. Conventionally, de-bubbling the air bubbles with a purely manual operation mode depends

significantly on the experiences of the operator. The drawbacks of this method include human error and noise pollution derived from the vacuum pump. A commercially available automatic vacuum machine was widely employed to degas in the manufacturing of silicone-rubber molds, but the hardware is costly.<sup>10</sup> In addition, the programmable logic controller mode lacks the flexibility to modify the program. Hence, developing a low-cost and easy-to-operate automated de-bubbling system is a major concern. To meet this requirement, the objective of this work is to develop a low-cost and high-efficiency automatic de-bubbling system with a human-machine interface (HMI).<sup>11</sup> Three vessels were used for filling the liquid silicone rubber for de-bubbling. The de-bubbling process sequences were investigated in detail. The effect of the pressure-relief process in the explosive phase on the de-bubbling efficiency for manual and automatic modes was also analyzed. Trend equations for predicting the balance phase duration and convergence phase duration for three vessels were investigated. The performance of the automatic de-bubbling system developed was evaluated. Comparisons of the de-bubbling efficiencies for automatic and manual modes were compared.

## 2 EXPERIMENTAL PART

Figure 1 shows a low-cost, automated de-bubbling system with an HMI. This system consists of a photoelectric sensor (EX-11EB; SUNX, Inc.), a programmable logic controller (PLC) (FX 2N-32MR, Mitsubishi), an HMI (GP37W2-BG41-24V; Pro-face, Inc.), an electromagnetic valve (SUG 15-24VDC; Chelic, Inc.) and an



Figure 1: A low-cost, automated, de-bubbling system with an HMI  
 Slika 1: Stroškovno ugoden in avtomatiziran sistem za odpravo mehurčkov s HMI

electronic buzzer (TS2BCL; Tend, Inc.). A photoelectric sensor (response time 0.5 ms) was used for detecting the air bubbles during the de-bubbling process. A PLC was used as a key component of the electric control module. An HMI was used for operating the automatic de-bubbling system. The HMI consists of all the aspects of the interaction and communication between the operators and machines by using a graphical HMI unit. The electromagnetic valve (on-off reaction time < 15 ms) was used to break the vacuum automatically. An electronic buzzer was used to alert the operator when the de-bubbling process is completed. Considering the practical requirements for the different operators, the de-bubbling method of this system includes an automation mode and a manual control mode. This system can be equipped with manual and automatic modes. Three different volumes (250 mL, 500 mL and 1000 mL) of vessels were used for filling the liquid silicone rubber in this study. The silicone rubber (KE-1310ST; ShinEtsu, Inc.) in the liquid state was mixed with a hardener (CAT-1310S; ShinEtsu, Inc). Generally, the curing agent and silicone

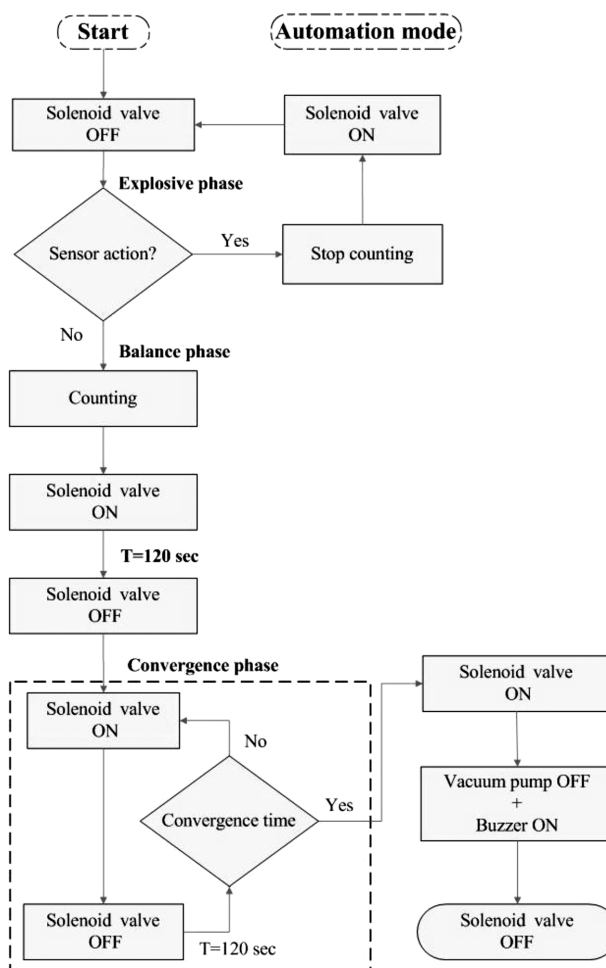
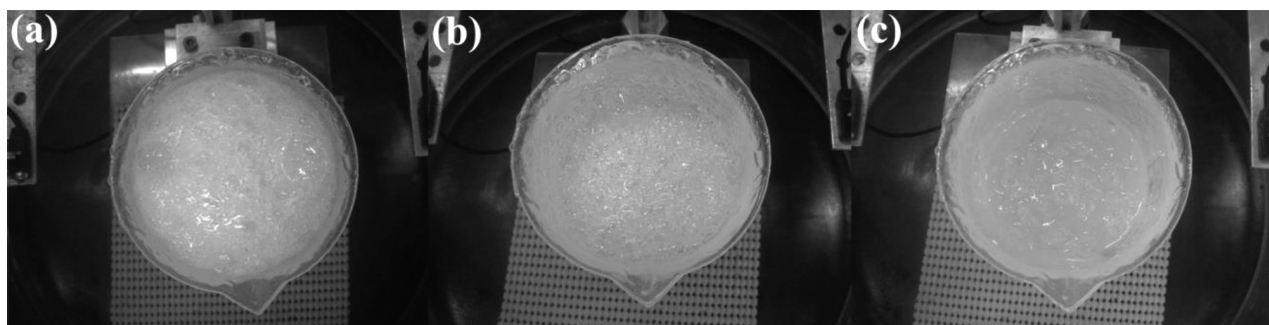


Figure 2: Brief flowchart of the automatic vacuum degassing process using an HMI

Slika 2: Shema poteka postopka avtomatskega vakuumskega razplinjavanja s pomočjo HMI





**Figure 3:** Three phases of the de-bubbling process: a) explosive phase, b) balance phase and c) convergence phase  
**Slika 3:** Tri faze postopka razplinjevanja: a) eksplozivna faza, b) ravnotežna faza in c) konvergenčna faza

rubber in a weight ratio of 10:1 were mixed thoroughly with a stirrer. After the de-bubbling process, the pressure inside the vacuum machine was changed by breaking the vacuum atmosphere. Thus, a silicone-rubber mold can be fabricated with defects caused by the air bubbles derived from the mixing process. To reduce the difference caused by the different operators in the amount of air bubbles, while mixing the liquid silicone rubber, an agitation blade for mixing the liquid silicone rubber was designed and fabricated. To confirm the center of the vessel is aligned with the center of the agitation blade, a positioning fixture was designed and fabricated. **Figure 2** shows a brief flowchart of the automatic vacuum degassing process using an HMI. Due to the experimental limitations, the solenoid valve does not work when the break vacuum duration is set less than 0.03 s. Thus, the break vacuum duration was set to be 0.03 s.

### 3 RESULTS AND DISCUSSION

The center of the vessel can be aligned with the center of the agitation blade using the positioning fixture. **Figure 3** shows the three phases of the de-bubbling process sequences. In general, the liquid silicone rubber has a large number of air bubbles because of the mixing reaction of the materials. As can be seen from this figure,

the first phase is the explosive phase, where the volume of liquid silicone rubber is drastically increased because the pressure in the vacuum chamber is lower than the atmospheric pressure, as shown in **Figure 4a**. The second phase is the balance phase, where the air bubbles in the liquid silicone rubber are eliminated gradually, as shown in **Figure 4b**. The final phase is the convergence phase, where the number and the size of the air bubbles in the liquid silicone rubber are eliminated significantly, as shown in **Figure 4c**. Schematic illustrations of the three phases of the de-bubbling process are shown in **Figure 5**. A number of air bubbles less than 15 is defined as the end of balance phase. In addition, no more air bubbles inside the liquid silicone rubber is defined as the end of convergence. A stopping vacuum of 120 s between convergence phase and convergence phase is required for reducing the convergence phase's duration. This is because air bubbles inside the liquid silicone rubber can reach the top of the liquid silicone rubber during 120 s. The air bubbles can be eliminated completely by an automatic de-bubbling system with an HMI based on the criteria discussed above.

**Table 1:** Time saving of the explosive phase for different volumes of silicone rubber

**Table 1:** Prihranek časa pri eksplozivni fazi, pri različnih prostorninah silikonske gume

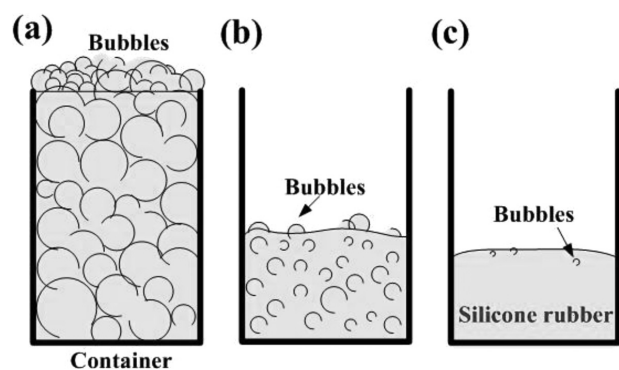


**Figure 4:** Schematic illustrations of the three phases of the de-bubbling process: a) explosive phase, b) balance phase and c) convergence phase

**Slika 4:** Shematski prikaz treh faz postopka razplinjevanja: a) eksplozivna faza, b) ravnotežna faza in c) konvergenčna faza

Volume of silicone rubber (mL)	Percentage of volume (%)	Mode	Explosive phase duration (s)	Time saving (%)
350	70	Manual	5335	61.46
		Automatic	2056	
300	60	Manual	3952	81.12
		Automatic	746	
250	50	Manual	2883	82.59
		Automatic	502	
200	40	Manual	706	70.00
		Automatic	233	
150	30	Manual	283	61.48
		Automatic	109	
100	20	Manual	0	0
		Automatic	0	

**Table 1** shows the time saving of the explosive phase for different volumes of silicone rubber. As can be seen,

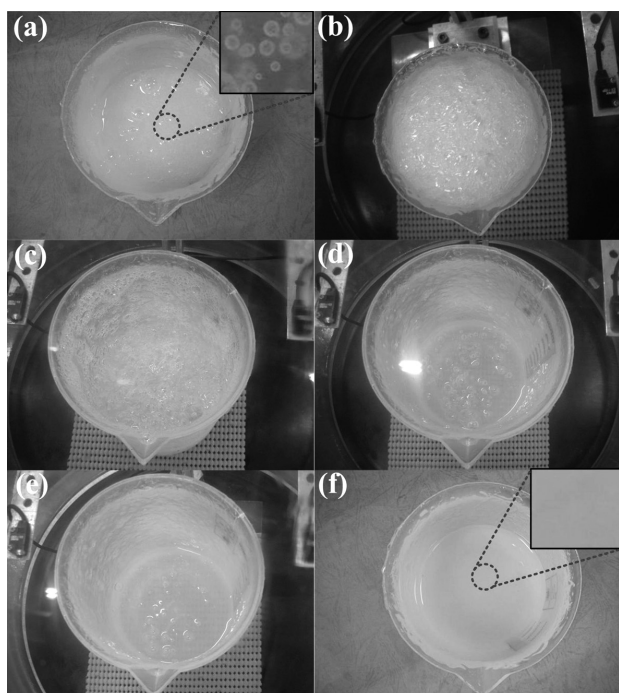


**Figure 5:** Sequential procedures of the automatic operation mode: a) liquid silicone rubber before de-bubbling process, b) explosive phase, c) balance phase, d) pause 120 s, e) convergence phase and f) de-bubbling process was completed

**Slika 5:** Sekvenčni postopki pri avtomatskem načinu dela: a) tekoča silikonska guma pred razplinjevanjem, b) eksplozivna faza, c) ravnotežna faza, d) pavza 120 s, e) konvergenčna faza in f) zaključen postopek razplinjevanja

the maximum time saving of the explosive phase is about 81.12 %. The time savings of the explosive phase increase with the increasing percentage of volume, ranging from 30 % to 60 %. The time saving of the explosive phase decreases when the percentage of volume exceeds 60 %. These results show that the vessel with a percentage of volume of 60% of silicone rubber is the optimum value.

**Figure 5** shows the sequential procedures of the automatic de-bubbling process. **Figure 6** shows the sequential procedures of the de-bubbling process with manual operation. It is obvious that the results for the two operation modes are the same, showing no air bubbles inside the liquid silicone rubber. This result shows that the air bubbles inside the liquid silicone rubber can be eliminated completely with the automatic operation mode. This means the system can be used for the production of a high-quality, bubble-free, silicone-rubber mold.<sup>12</sup>

Precise determination the balance phase's duration and the convergence duration is an absolute requirement for a high-efficiency, automatic, de-bubbling process. **Figure 7** shows the trend equations for the balance duration and convergence duration for vessel volumes of 250 mL, 500 mL and 1000 mL. For a vessel volume of 250 mL, the balance phase's duration ( $y$ ) can be predicted from the trend equation of  $y = 3.316x - 30.8$  by

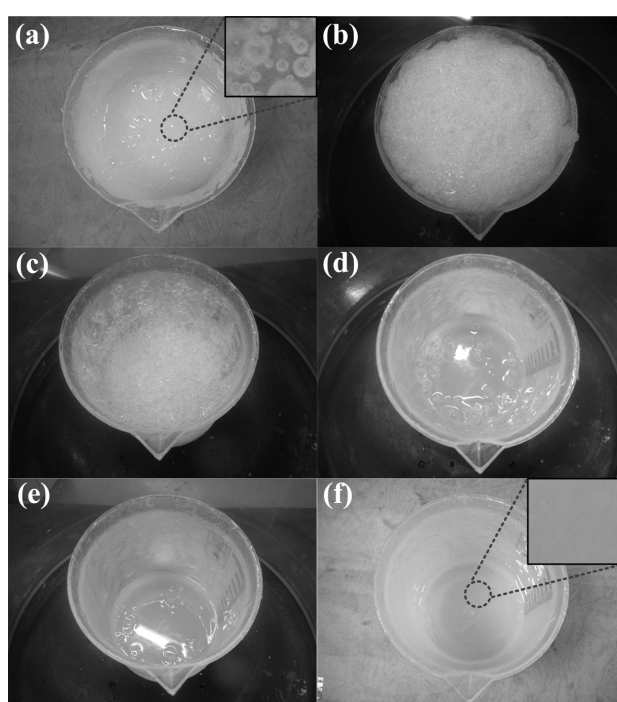


**Figure 6:** Sequential procedures of the de-bubbling process with the manual de-bubbling mode: a) liquid silicone rubber before de-bubbling process, b) explosive phase, c) balance phase, d) pause 120 s, e) convergence phase and f) de-bubbling process was completed

**Slika 6:** Sekvenčni postopki postopka razplinjevanja pri ročnem vodenju razplinjevanja: a) tekoča silikonska guma pred razplinjevanjem, b) eksplozivna faza, c) ravnotežna faza, d) pavza 120 s, e) konvergenčna faza in f) zaključen postopek razplinjevanja

the volume of silicone rubber ( $x$ ). Note that the  $R^2$  represents the correlation coefficient. Generally, a higher  $R^2$  value (maximum value =1) means a better accuracy of the trend equation.<sup>16</sup> Six predicted equations for both the balanced phase and the convergence phase are investigated, and the maximum relative error of these equations can be controlled within 6.34 %. This means that both the balanced phase duration and the convergence phase duration can be calculated from these equations.

To evaluate the performance of the automatic degassing system developed, each test was carried out three times with the mean and the deviation determined. **Table 2** shows the time saving of the total degassing time for three different volumes of silicone rubber. **Figure 8** shows the total degassing time as a function of silicone rubber for the manual and automatic operation modes. As can be seen, a reduction in the degassing time of at least 42 % can be observed using the automatic degassing system with a human-machine interface. It is obvious that there is an increase in time saving of degassing with an increase in the volume of silicone rubber. Three phases are important for the degassing process, but the explosive phase is the most critical one. This is because the pressure-relief process in the automatic operation mode is significantly different from that in the manual operation mode, as shown in **Figure 9**. The recovery

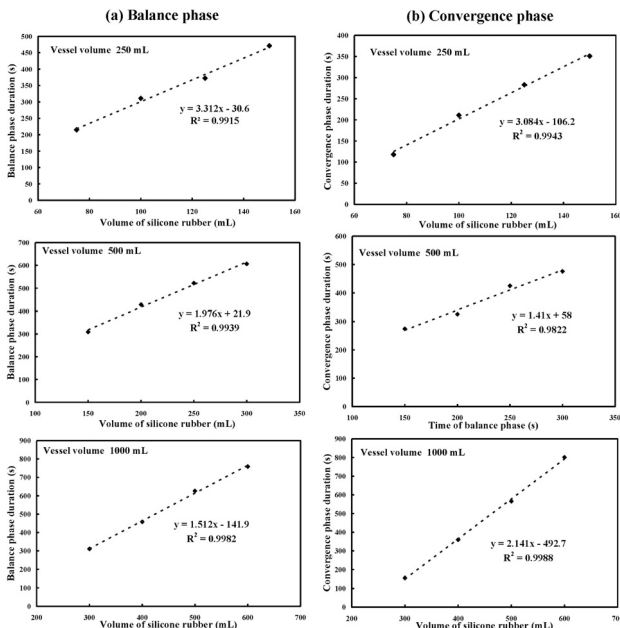


Figure 7: Trend equations of: a) balance phase duration and b) convergence phase duration for vessel volumes of 250 mL, 500 mL and 1000 mL.

Slika 7: Trend enačb za: a) trajanje ravnotežne faze in b) trajanje konvergenčne faze pri prostornini posode 250 mL, 500 mL in 1000 mL.

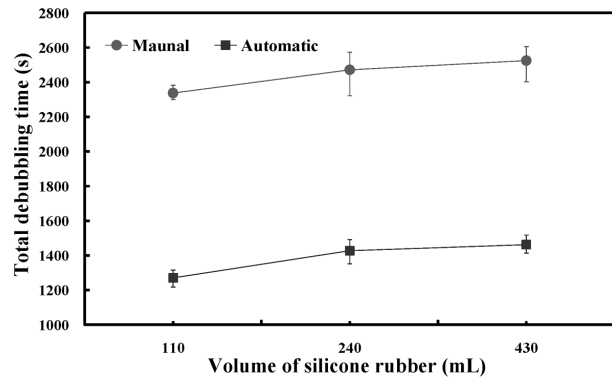


Figure 8: Total degassing time as a function of silicone-rubber volume for manual and automatic operation modes.

Slika 8: Celotni čas razplinjevanja (v odvisnosti od volumna) silikonske gume pri avtomatskem in ročnem načinu upravljanja.

time needed for the pressure of the chamber reaching the degassing pressure with the automatic operation mode is

Table 2: Time saving of the total degassing time for three different volumes of silicone rubber

Tabela 2: Prihranek časa od vsega časa razplinjevanja, pri treh različnih prostorninah silikonske gume

Volume of silicone rubber (mL)	Mode	Explosive phase duration (s)	Balance phase duration (s)	Pause (s)	Convergence phase duration (s)	Total (s)	Time saving (%)
110	Manual	1642	338	120	237	2337	45.64
	Automatic	583	334	120	233	1270	
240	Manual	1415	509	120	427	2471	42.24
	Automatic	416	496	120	396	1428	
430	Manual	1409	530	120	465	2525	42.07
	Automatic	406	508	120	428	1462	

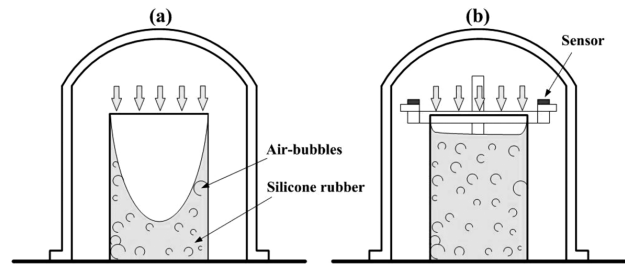


Figure 9: Schematic illustrations of the pressure relief process in the explosive phase: a) manual operation mode and b) automatic operation mode.

Slika 9: Shematski prikaz postopka sproščanja tlaka v eksplozivni fazi: a) ročni način vodenja in b) avtomatski način vodenja.

shorter than that with the manual operation mode. Based on the experimental results, the advantages of this system include saving labor, reducing the human error of the operator and a higher degassing efficiency. This system has broad application prospects in the development of new products using a silicone-rubber mold.

#### 4 CONCLUSIONS

A low-cost, high-efficiency degassing system has been designed, implemented and tested in this study. The entire degassing-process sequences consist of the explosive phase, the balance phase and the convergence phase. The automatic degassing method provides three decisive advantages compared with the manual degassing method. The explosive phase has been proved to be a key process for a high-efficiency degassing process. A reduction of the degassing time by at least 42 % can be gained. This system has broad application prospects in the development stage for new products using rapid-tooling technology.

#### Acknowledgement

This work was financially supported by the Ministry of Science and Technology of Taiwan under contract nos. NSC 102-2221-E-131-012 and NSC 101-2221-E-131-007.

## 5 REFERENCES

- <sup>1</sup> M. Laub, H. P. Jennissen, Identification of the anthelix motif in the TGF- $\beta$  superfamily by molecular 3D-Rapid Prototyping, *Materialwissenschaft und Werkstofftechnik*, 34 (2003) 12, 1113–1119, doi:10.1002/mawe.200300715
- <sup>2</sup> A. Iftikhar, M. Khan, K. Alam, S. H. I. Jaffery, L. Ali, Y. Ayaz, A. Khan, Turbine blade manufacturing through rapid tooling (RT) process and its quality inspection, *Materials and Manufacturing Processes*, 28 (2013) 5, 534–538, doi:10.1080/10426914.2012.746698
- <sup>3</sup> D. K. Pal, B. Ravi, Rapid tooling route selection and evaluation for sand and investment casting, *Virtual and Physical Prototyping Journal*, 2 (2007) 4, 197–207, doi:10.1080/17452750701747088
- <sup>4</sup> S. Singh, V. S. Sharma, A. Sachdeva, S. K. Sinha, Optimization and analysis of mechanical properties for selective laser sintered polyamide parts, *Materials and Manufacturing Processes*, 28 (2013) 2, 163–172, doi:10.1080/10426914.2012.677901
- <sup>5</sup> J. Liu, H. Hu, P. Li, C. Shuai, S. Peng, Fabrication and characterization of porous 45S5 glass scaffolds via direct selective laser sintering, *Materials and Manufacturing Processes*, 28 (2013) 6, 610–615, doi:10.1080/10426914.2012.736656
- <sup>6</sup> D. Juarez, R. Balart, T. Boronat, M. J. Reig, S. Ferrandiz, Validation of the use of SEBS blends as a substitute for liquid silicone rubber in injection processes, *Materials and Manufacturing Processes*, 28 (2013) 11, 1215–1222, doi:10.1080/10426914.2013.811732
- <sup>7</sup> R. Azim, M. T. Islam, Design of a wideband planar antenna on an epoxy-resin-reinforced woven-glass material, *Mater. Tehnol.*, 49 (2015) 2, 193–196, doi:10.17222/mit.2013.169
- <sup>8</sup> C. C. Kuo, A cost-effective approach to the rapid fabrication of functional metal prototypes, *Mater. Tehnol.*, 48 (2014) 4, 581–585
- <sup>9</sup> C. C. Kuo, C. Y. Lin, Development of bridge tooling for fabricating mold inserts of aspheric optical lens, *Materialwissenschaft und Werkstofftechnik*, 42 (2011) 11, 1019–1024, doi:10.1002/mawe.201100819
- <sup>10</sup> Y. Tang, W. K. Tan, J. Y. H. Fuh, H. T. Loh, Y. S. Wong, S. C. H. Thian, L. Lu, Micro-mould fabrication for a micro-gear via vacuum casting, *Journal of Materials Processing Technology*, 192-193 (2007), 334–339, doi:10.1016/j.jmatprotec.2007.04.098
- <sup>11</sup> A. Jaklič, F. Vode, R. Robič, F. Perko, B. Strmole, J. Novak, J. Trip-lat, The implantation of an online mathematical model of slab reheating in a posher-type furnace, *Mater. Tehnol.*, 39 (2005) 6, 215–220
- <sup>12</sup> C. C. Kuo, Y. J. Wang, Development of a micro-hot embossing mold with high replication fidelity using surface modification, *Materials and Manufacturing Processes*, 29 (2014) 9, 1101–1110, doi:10.1080/10426914.2014.912312



# IMPACT TOUGHNESS OF WMD AFTER MAG WELDING WITH MICRO-JET COOLING

## UDARNA ŽILAVOST WMD PO MAG VARJENJU Z MIKRO-JET HLAJENJEM

**Tomasz Wegrzyn<sup>1</sup>, Jan Piwnik<sup>2</sup>, Aleksander Borek<sup>3</sup>, Agnieszka Kurc-Lisiecka<sup>4</sup>**

<sup>1</sup>Silesian University of Technology, Faculty of Transport, Krasińskiego 8, 40-019 Katowice, Poland

<sup>2</sup>Białystok University of Technology, Mechanical Faculty, Wiejska 45c, 16-351 Białystok, Poland

<sup>3</sup>Plasma-system, Towarowa 14, 41-103 Siemianowice Śląskie, Poland

<sup>4</sup>University of Dąbrowa Górnicza, Rail Transport Department, Ciepłaka 1c, 41-300 Dąbrowa Górnicza, Poland  
a.kurc@wp.pl

*Prejem rokopisa – received: 2015-06-30; sprejem za objavo – accepted for publication: 2015-11-05*

doi:10.17222/mit.2015.159

The MAG welding process with micro-jet cooling of the weld during the cooling stage was investigated. For micro-jet gases the mixtures of argon with carbon dioxide, oxygen, and nitrogen were tested. This paper presents a piece of information about a new proposal for gas mixtures during micro-jet cooling after welding. Presented is the main information about the influence of various micro-jet gas mixtures on the metallographic structure of the weld metal. The mechanical properties of the welds were presented in terms of various gas mixtures selection for micro-jet cooling. The influence of argon gas mixtures with oxygen and nitrogen for micro-jet cooling after welding are reported for the first time in the technical literature.

Keywords: welding, micro-jet cooling, weld, metallographic structure, gas mixtures, GMA welding

Preiskovana je bila začetna faza postopka MAG varjenja z mikro-jet hlajenjem zvara. Za mikro-jet so bile preizkušene mešanice argona z ogljikovim dioksidom, kisikom in dušikom. Članek predstavlja del informacije o predlogu novih mešanic plinov za mikro-jet hlajenje po varjenju. Dane so informacije o vplivu različnih plinskih mešanic za mikro-jet na metalografske strukture zvarjenega materiala. Mehanske lastnosti zvarov so prikazane v smislu izbranih različnih vrst mešanic plinov za mikro-jet hlajenje. Vpliv mešanice argona s kisikom in dušikom za mikro-jet hlajenje po varjenju je prvič prikazan tudi v tehniški literaturi.

Ključne besede: varjenje, mikro-jet hlajenje, zvar, metalografska struktura, mešanice plinov, GMA varjenje

## 1 INTRODUCTION

MAG is an important industrial welding process, preferred for its versatility, speed and the relative ease of adapting the process to robotic automation. Developments in arc welding processes are strongly related with the need to increase productivity without losing the quality of the weld.<sup>1-5</sup> The reduction of costs and competitive pricing are each day more strongly related with technological innovations.<sup>6-11</sup> The properties of steel welded structures depend on many factors such as welding technology, filler materials, state of stress. The main role of these conditions is also connected with the materials, the chemical composition of steel and the weld metal deposit (WMD).<sup>12-16</sup> The chemical composition of metal weld deposit could be regarded as a very important factor influencing the properties of the weld metal deposit (WMD). In particular, the oxygen, titanium, manganese and aluminium are regarded as the main elements that positively effect the mechanical properties and the metallographic structure of low-alloy welds. This is because of the non-metallic inclusions in weld (**Figure 1**) that have similar lattice parameter as the ferrite (TiO, TiN, MnO, Al<sub>2</sub>O<sub>3</sub>).

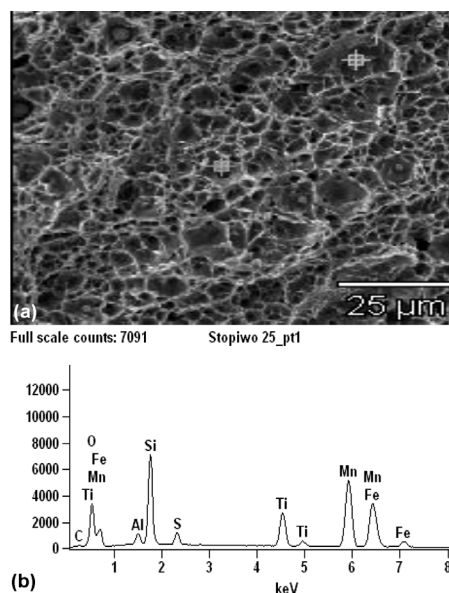


**Figure 1:** a) SEM micrographs showing the oxide inclusions in low-alloy WMD after welding with basic electrodes and b) EDS analysis of the WMD<sup>1</sup>

**Slika 1:** a) SEM-posnetek prikazuje oksidne vključke v malo legiranem WMD po varjenju z bazičnimi elektrodami in b) EDS analiza WMD<sup>1</sup>

The welding parameters, metallographic structure and chemical composition of the weld metal deposit are regarded as important factors that influence the impact toughness properties of the deposits.<sup>9–12</sup> In a typical low-alloy steel weld structure the best mechanical properties correspond with the maximum amount of acicular ferrite (AF) in the weld metal deposit (WMD) and the minimum amount of MAC phases (self-tempered martensite, retained austenite, carbide). This article focuses on mild-steel welding and covers the new possibilities of that method. Since 2011, innovative welding technology based on micro-jet cooling just after welding has been investigated. The weld metal deposit (WMD) was carried out for the standard MAG process and for the innovative welding method with micro-jet cooling. A very high percentage of acicular ferrite (AF) in WMD was obtainable (55–73 %) for low-alloy steel welding only for micro-jet cooling after the MIG process with argon or helium.<sup>13–18</sup> Argon and helium, as micro-jet gases, could provide a better impact toughness of the WMD (0.08 % C, 0.8 % Mn) than in the case of the classic MAG process (**Table 1**). **Table 1** shows that argon is a more beneficial micro-jet cooling gas than helium. Also, it is shown that micro-jet cooling improves the amount of acicular ferrite in the weld. Helium is not such a beneficial micro-jet gas as argon and its mixtures in the MAG process (because of the high percentage of MAC phases). In that paper gas mixtures of argon with a small amount of oxygen and nitrogen were mainly tested because of the positive influence of some oxide and nitride inclusions of acicular ferrite forming and thus the very good impact toughness of the welds.

**Table 1:** Metallographic structure of MAG welds<sup>1</sup>

**Tabela 1:** Metalografske strukture MAG zvarov<sup>1</sup>

Micro-jet gases	Ferrite AF	MAC phases
without micro-jet	43%	4%
He	59%	6%
Ar	63%	2%

## 2 EXPERIMENTAL PART

The weld metal deposit was prepared by welding with micro-jet cooling with gas mixtures both for the standard MAG process and the MAG welding with micro-jet cooling. The MAG welding process was based on a shielded gas mixture of 79 % Ar and 21 % CO<sub>2</sub>. To obtain various amounts of acicular ferrite in the WMD the installed micro-jet injector was close to the MAG welding head. The main parameters of the micro-jet cooling were slightly varied:

- cooling steam diameter (40 μm and 50 μm),
- gas pressure (0.4 MPa and 0.5 MPa),
- gas mixtures of argon (82 % Ar/18 % CO<sub>2</sub> and 98 % Ar/2 % O<sub>2</sub> and 98 % Ar + 2 % N<sub>2</sub>) were chosen as the micro-jet gases.

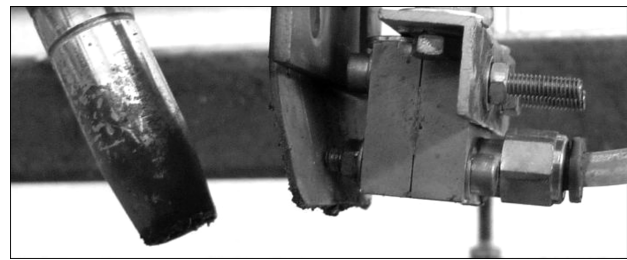


**Figure 2:** Montage of welding head and micro-jet injector (on the right)

**Slika 2:** Namestitev varilne glave in mikro-jet injektor (na desni)

A montage of the welding head and the micro-jet injector is illustrated in **Figure 2**. The main data about the parameters of the welding are shown in **Table 2**. The weld metal deposit was prepared by welding with micro-jet cooling using a larger number of parameters (**Table 3**).

**Table 2:** Parameters of the welding process

**Tabela 2:** Parametri procesa varjenja

No.	Parameter	Value
1.	Diameter of wire	1.2 mm
2.	Standard current	220 A
3.	Voltage	24 V
4.	Shielding welding gases	82% Ar/18% CO <sub>2</sub>
5.	Kind of tested micro-jet cooling gases	Ar, 82% Ar/18% CO <sub>2</sub> ; 98% Ar/2% O <sub>2</sub> ; 98% Ar/2% N <sub>2</sub>
6.	Gas pressure	0.4 MPa; 0.5 MPa
7.	Number of micro-jets	1
8.	Cooling stream diameter	40 μm; 50 μm

**Table 3:** Chemical composition of WMD

**Tabela 3:** Kemijska sestava WMD

Comment	Element	Amount
in all tested cases	C	0.08%
in all tested cases	Mn	0.79%
in all tested cases	Si	0.39%
in all tested cases	P	0.017%
in all tested cases	S	0.018%

## 3 RESULTS AND DISCUSSION

We tested and compared various welds of the standard MAG process connected with those of the innovative micro-jet cooling. A typical weld metal deposit had a similar chemical composition in all the tested cases. The micro-jet gas could only have an influence on more or less intensive cooling conditions, but it does not have any influence on the chemical WMD composition (**Table 3**), except for the oxygen and nitrogen amounts in the WMD (**Table 4**).

It is easy to deduce that the amount of oxygen and nitrogen was slightly increased in terms of the chemical composition of the micro-jet gas mixtures. After the chemical analyses the metallographic structure of the WMD

(with and without micro-jet cooling) was carried out. An example of this structure was shown in **Table 5**.

**Table 4:** Content of oxygen and nitrogen in WMD

**Tabela 4:** Vsebnost kisika in dušika v WMD

Micro-jet gases	Element	Amount (%)
Ar	O	0.0350
82% Ar / 18% CO <sub>2</sub>	O	0.0380
98% Ar / 2% O <sub>2</sub>	O	0.0380
98% Ar / 2% N <sub>2</sub>	O	0.0350
Ar	N	0.0055
82% Ar / 18% CO <sub>2</sub>	N	0.0055
98% Ar / 2% O <sub>2</sub>	N	0.0055
98% Ar / 2% N <sub>2</sub>	N	0.0060

**Table 5:** Metallographic structure of (MAG method 82% Ar/18% CO<sub>2</sub>) welds

**Tabela 5:** Metalografska struktura zvarov (metoda MAG z 82 % Ar/18 % CO<sub>2</sub>)

Micro-jet gas	Gas pressure, MPa	Cooling steam diameter, $\mu\text{m}$	Ferrite AF	MAC phases
without micro-jet	-	-	55%	3%
Ar	0.4	40	60%	2%
Ar	0.4	50	63%	2%
Ar	0.5	40	63%	2%
Ar	0.5	50	61%	2%
98% Ar/2% O <sub>2</sub>	0.4	40	64%	2%
98% Ar/2% O <sub>2</sub>	0.4	50	66%	2%
98% Ar/2% O <sub>2</sub>	0.5	40	67%	2%
98% Ar/2% O <sub>2</sub>	0.5	50	65%	2%
82% Ar/18% CO <sub>2</sub>	0.4	40	58%	2%
82% Ar/18% CO <sub>2</sub>	0.4	50	60%	2%
82% Ar/18% CO <sub>2</sub>	0.5	40	61%	2%
82% Ar/18% CO <sub>2</sub>	0.5	50	59%	3%
98% Ar/2% N <sub>2</sub>	0.4	40	58%	2%
98% Ar/2% N <sub>2</sub>	0.4	50	59%	2%
98% Ar/2% N <sub>2</sub>	0.5	40	59%	2%
98% Ar/2% N <sub>2</sub>	0.5	50	57%	3%

**Table 5** shows that in all cases a gas mixture of argon with oxygen is the most beneficial choice. We also observed MAC (self-tempered martensite, retained austenite, carbide) phases on various levels. In the standard MAG welding process (without micro-jet cooling) there are usually gettable larger amounts of grain-boundary ferrite (GBF) and site-plate ferrite (SPF) fraction, meanwhile in micro-jet cooling WMD both of the GBF and SPF structures were not so dominant. Ferrite with a percentage above 60 % was gettable only in one case after MAG welding with micro-jet gas mixtures: argon/oxygen or argon/carbon dioxide (**Figure 3**).

The larger amount of MAC phases was especially gettable for the more intensive micro-jet cooling with a gas mixture of argon-oxygen (**Tables 5 and 6**). The heat-transfer coefficient of the various micro-jet gas mixtures influences the cooling conditions of the welds (and consequently the rise in the content of the MAC

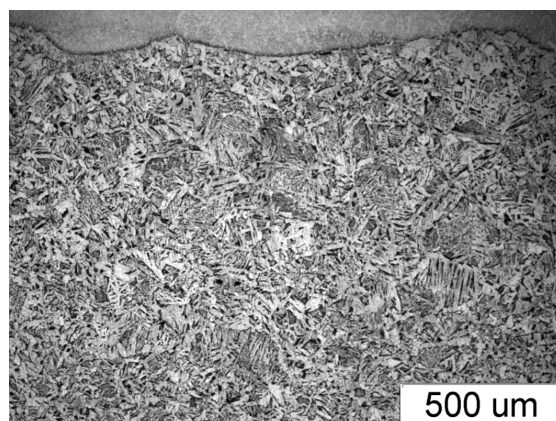


**Figure 3:** Microstructure weld metal with large amount of acicular ferrite in weld (67 %) after Ar/CO<sub>2</sub> micro-jet cooling

**Slika 3:** Mikrostruktura zvara z velikim deležem igličastega ferita v zvaru (67 %), po mikro-jet hlajenju z Ar/CO<sub>2</sub>

phases). This is due to the conductivity coefficients ( $\lambda \cdot 10^5$ ), as shown in **Table 6**.

**Table 6:** Heat-transfer coefficient of various gases used in micro-jet cooling

**Tabela 6:** Koeficient prenosa toplote različnih plinov, uporabljenih pri mikro-jet hlajenju

Gas	Conductivity coefficients, mW/mK
Ar	17.9
CO <sub>2</sub>	16.8
O <sub>2</sub>	26.3
N <sub>2</sub>	26
He	156.7

**Table 7:** Metallographic structure of MAG (82 % Ar/18 % CO<sub>2</sub>) welds

**Tabela 7:** Metalografska struktura MAG zvarov (82 % Ar/18 % CO<sub>2</sub>)

Welding method	Micro-jet gas	Test temperature, °C	Impact toughness KCV, J
MAG	without	-40	below 40
MAG with micro-jet cooling	Ar	-40	55
MAG with micro-jet cooling	82% Ar/18% CO <sub>2</sub>	-40	53
MAG with micro-jet cooling	98% Ar/2% O <sub>2</sub>	-40	57
MAG with micro-jet cooling	98% Ar/2% N <sub>2</sub>	-40	below 40
MAG	without	+20	177
MAG with micro-jet cooling	Ar	+20	191
MAG with micro-jet cooling	82% Ar/18% CO <sub>2</sub>	+20	189
MAG with micro-jet cooling	98% Ar/2% O <sub>2</sub>	+20	194
MAG with micro-jet cooling	98% Ar/2% N <sub>2</sub>	+20	183

Analysing **Table 6**, it is possible to deduce that helium could give the strongest cooling conditions, but helium was not tested in this investigation. The cooling



conditions after welding using other micro-jet gases are on a similar level. After the microscope tests, the Charpy V impact toughness of the deposited metal was assessed with 5 specimens. The Charpy tests were carried out at temperatures of  $-40\text{ }^{\circ}\text{C}$  and  $+20\text{ }^{\circ}\text{C}$  only. The impact toughness results are given in **Table 7**.

It is easy to deduce that the impact toughness, especially at the negative temperature of the weld metal deposit, is apparently affected by the kind of micro-jet cooling gas mixtures. Micro-jet technology always strongly improves the impact toughness of the WMD. Argon with oxygen and argon with carbon dioxide must be treated as good choices. Argon as the main element of the gas mixture with a small amount of oxygen gives better results than gas mixtures of argon with carbon dioxide and argon with nitrogen. Nevertheless, micro-jet cooling with gas mixture of argon with 2 % of nitrogen gives better results than the simple MAG welding without micro-jet cooling. This can be explained by the presence of nitride inclusions in the weld (for instance TiN) that facilitate the nucleation of ferrite AF.

#### 4 CONCLUSIONS

In low-alloy steel welding there are two general types of tests performed: impact toughness and structure. Acicular ferrite and MAC phases (self-tempered martensite, upper and lower bainite, retained austenite, carbides) were analysed and counted for each weld metal deposit. These two tests (microstructure and impact toughness) proved that micro-jet technology gives a beneficial modification to the mechanical properties of the welds. The innovative micro-jet technology was firstly recognized with great success for MIG welding only with argon as a micro-jet gas. In this paper micro-jet cooling technology was for the first time described and tested for MAG welding process with various micro-jet gas mixtures of argon.

Final conclusions:

- micro-jet cooling could be treated as an important element of MAG welding process,
- micro-jet cooling after welding can improve the amount of ferrite AF, the most beneficial phase in low-alloy steel WMD,
- gas mixture of argon with carbon dioxide and gas mixture of argon with oxygen could be treated as better micro-jet cooling media than gas mixture of argon with nitrogen,
- micro-jet cooling after welding can seriously improve the impact toughness of low-alloy steel WMD,
- micro-jet cooling after welding practically does not have an influence on the MAC amount in low-alloy steel WMD.

#### 5 REFERENCES

- <sup>1</sup> T. Węgrzyn, Gas mixtures for welding with micro-jet cooling, *Arch. Metall. Mater.*, 47 (2011), 57–61, doi: 10.1515/amm-2015-0017
- <sup>2</sup> B. Słazak, J. Słania, T. Węgrzyn, A.P. Silva, Process stability evaluation of manual metal arc welding using digital signals, *Mater. Sci. Forum*, 730-732 (2013), 847–852, doi:10.4028/www.scientific.net/MSF.730-732.847
- <sup>3</sup> P. Folega, FEM analysis of the options of using composite materials in flexsplines, *Arch. Mater. Sci. Eng.*, 51 (2011) 1, 55–60
- <sup>4</sup> T. Węgrzyn, J. Mirosławski, A. Silva, D. Pinto, M. Miros, Oxide inclusions in steel welds of car body, *Mater. Sci. Forum* 6 (2010), 585–591, doi:10.4028/www.scientific.net/MSF.636-637.585
- <sup>5</sup> T. Kasuya, Y. Hashiba, S. Ohkita, M. Fuji, Hydrogen distribution in multipass submerged arc weld metals, *Sci. Tech. Weld. Join.*, 6 (2011) 4, 261–266, doi:http://dx.doi.org/10.1179/136217101101538767
- <sup>6</sup> J. Słania, Influence of phase transformations in the temperature ranges of 1250–1000 °C and 650–350 °C on the ferrite content in austenitic welds made with T 23 12 LRM3 tubular electrode, *Arch. Metall. Mater.*, 50 (2005), 757–767
- <sup>7</sup> W. Tarasiuk, B. Szczucka–Lasota, J. Piwnik, W. Majewski, Hydrogen distribution in multipass submerged arc weld metals, *Adv. Mat. Res.*, 1036 (2014), 452–457, doi: 10.4028/www.scientific.net/AMR.1036.452
- <sup>8</sup> T. Węgrzyn, Mathematical equations of the influence of molybdenum and nitrogen in welds, *Conference of International Society of Offshore and Polar Engineers ISOPE'2002, Kita Kyushu, Japan, 2002*, Copyright by International Society of Offshore and Polar Engineers, vol. IV, ISBN 1-880653-58-3, Cupertino – California – USA 2002
- <sup>9</sup> R. Burdzik, Z. Stanik, J. Warczek, Method of assessing the impact of material properties on the propagation of vibrations excited with a single force impulse, *Arch. Metall. Mater.*, 57 (2012) 2, 409–416
- <sup>10</sup> R. Burdzik, Monitoring system of vibration propagation in vehicles and method of analysing vibration modes, *Comm. Comp. Inorm. Scie.*, 329 (2012), 406–413
- <sup>11</sup> R. Burdzik, P. Folega, B. Łazarz, Z. Stanik, J. Warczek, Analysis of the impact of surface layer parameters on wear intensity of friction pairs, *Arch. Metall. Mater.*, 57 (2012) 4, 987–993
- <sup>12</sup> K. Lukaszewicz, A. Kriz, J. Sondor, Structure and adhesion of thin coatings deposited by PVD technology on the X6CrNiMoTi17-12-2 and X40CrMoV5-1 steel substrates, *Arch. Mater. Sci. Eng.*, 51 (2011), 40–47
- <sup>13</sup> A. Lisiecki, Diode laser welding of high yield steel, *Proc. of SPIE 8703 Vol.8703, Laser Technology 2012: Applications of Lasers*, 87030S (January 22, 2013), doi:10.1117/12.2013429
- <sup>14</sup> A. Lisiecki, Welding of titanium alloy by Disk laser, *Proc. of SPIE Vol. 8703, Laser Technology 2012: Applications of Lasers*, 87030T (January 22, 2013), doi: 10.1117/12.2013431
- <sup>15</sup> A. Lisiecki, Welding of thermomechanically rolled fine-grain steel by different types of lasers, *Arch. Metall. Mater.*, 59 (2014), 1625–1631, doi: 10.2478/amm-2014-0276
- <sup>16</sup> A. Kurc-Lisiecka, W. Ozgowicz, W. Ratuszek, J. Kowalska, Analysis of deformation texture in AISI 304 steel sheets, *Sol. St. Phenom.*, 203-204 (2013), 105–110, doi: 10.4028/www.scientific.net/SSP.203-204.105
- <sup>17</sup> G. Golański, J. Słania, Effect of different heat treatments on microstructure and mechanical properties of the martensitic GX12CrMoVNbN91 cast steel, *Arch. Metall. Mater.*, 58 (2012) 1, 25–30, doi: 10.2478/v10172-012-0145-x
- <sup>18</sup> T. Węgrzyn, J. Piwnik, D. Hadryś, R. Wieszała, Car body welding with micro-jet cooling, *J. Arch. Mater. Sci. Eng.*, 49 (2011), 90–94



# FORMING-LIMIT DIAGRAMS AND STRAIN-RATE-DEPENDENT MECHANICAL PROPERTIES OF AA6019-T4 AND AA6061-T4 ALUMINIUM SHEET MATERIALS

## MEJNI DIAGRAMI PREOBLIKOVANJA IN ODVISNOST MEHANSKIH LASTNOSTI OD HITROSTI PREOBLIKOVANJA ALUMINIJEVIH PLOČEVIN IZ AA6019-T4 IN AA6061-T4

Onur Çavuşoğlu<sup>1,2</sup>, Alan Gordon Leacock<sup>2</sup>, Hakan Gürün<sup>1</sup>

<sup>1</sup>Gazi University, Faculty of Technology, Department of Manufacturing Engineering, Ankara, Turkey  
<sup>2</sup>University of Ulster, Advanced Metal Forming Research Group (AMFOR), Newtonabbey, Northern Ireland  
onur.cavusoglu@gazi.edu.tr

*Prejem rokopisa – received: 2015-08-17; sprejem za objavo – accepted for publication: 2015-27-10*

doi:10.17222/mit.2015.259

The mechanical properties and formability behaviour of sheet materials depend on the deformation conditions. In this study, the variance of AA6019-T4 and AA6061-T6 aluminium sheet materials related to the strain rate of their mechanical properties was studied by applying uniaxial tensile tests on these materials at different semi-static strain rates ( $0.3 \text{ s}^{-1}$ ,  $0.03 \text{ s}^{-1}$ ,  $0.003 \text{ s}^{-1}$ ,  $0.0003 \text{ s}^{-1}$ ,  $0.00003 \text{ s}^{-1}$ ). In addition, forming-limit diagrams of these materials were determined by applying Nakajima tests. When the results were analysed, it was found that the strain rate developed some mechanical properties in the AA6019-T4 and AA6061-T4 sheet materials and that the AA6061-T4 sheet material has a higher formability capability in comparison with the AA6019-T4 sheet material.

Keywords: FLD, strain rate, aluminium alloy 6061, aluminium alloy 6019

Mehanske lastnosti in obnašanje pri preoblikovanju pločevine sta odvisna od pogojev deformacije. V študiji je bilo proučevano spreminjanje AA6019-T4 in AA6061-T6 aluminijeve pločevine glede na hitrost preoblikovanja in proučevane so bile njihove mehanske lastnosti z uporabo enosnih nateznih preizkusov teh materialov pri različnih semi-statičnih hitrostih preoblikovanja ( $0.3 \text{ s}^{-1}$ ,  $0.03 \text{ s}^{-1}$ ,  $0.003 \text{ s}^{-1}$ ,  $0.0003 \text{ s}^{-1}$ ,  $0.00003 \text{ s}^{-1}$ ). Dodatno so bili določeni še diagrami mejnega preoblikovanja teh materialov z uporabo Nakajima preizkusov. Analiza dobljenih rezultatov je pokazala, da hitrost preoblikovanja vpliva na mehanske lastnosti AA6019-T4 in AA6061-T4 pločevin in da ima AA6061-T4 pločevina večjo sposobnost preoblikovanja v primerjavi s pločevino AA6019-T4.

Ključne besede: FLD, hitrost deformacije, aluminijeva zlitina 6061, aluminijeva zlitina 6019

## 1 INTRODUCTION

Great importance is attached to weight-reduction technology at the present time. For this reason, studies on the reduction of the amount of vehicle fuel consumption and CO<sub>2</sub> emissions have been analysed. It has been observed in the studies conducted for this purpose that improved high-strength steels and light-metal materials such as aluminium and magnesium alloys have an important place.<sup>1,2</sup> When the usage applications of aluminium alloys are analysed, it is clear that they have been commonly preferred in the automotive and aerospace industries on account of their superior characteristics, such as their low density, high strength, formability, corrosion resistance and high availability as a source.<sup>2,3</sup>

Tensile testing is a method commonly used for determining a plurality of mechanical properties and the deformation behaviour of the materials. Many parameters obtained from the tensile test may vary, based on the material's deformation conditions, such as friction, deformation speed and temperature.<sup>4</sup> It is known that the strain rate changes many metallic materials' properties

by affecting the relation between the tensile and deformation.<sup>3</sup> Studies about the effects of the strain rate on the mechanical properties of aluminium alloys are available in the literature. J. Q. Tan et al.<sup>5</sup> analysed the tensile behaviour at high strain rates by using 7050-T7451 aluminium alloy, and they determined that an increasing deformation rate increases the amount of tensile. M. Vural and J. Caro<sup>6</sup> observed, by analysing the tensile behaviour of 2139-T8 aluminium alloy at different temperatures and deformation rates, that a significant change in the behaviour of materials at low strain rates does not occur and that the yield stress at high deformation rates increases. By applying tensile tests on the AA5754 and AA5182 aluminium alloys, Smerd and others have found that when high deformation rates subtract from the semi-static strain rates of the AA5754 aluminium alloy, there is no change among the high strain rates, while a significant increase in the yield stress occurs, and they also found that the AA5182 alloy is not completely affected by changes in the strain rates. However, the increasing strain rate increases the amount of stretching in both alloys.<sup>7</sup> In their study O. G. Lademo et al.<sup>8</sup>

determined that an increase in the tensile strength and elongation occurs by analysing the strain rate sensitivity of the AA1200 and AA3103 aluminium alloys, although the yield strength is not affected, depending on the increase in the deformation rate. In their study, D. Li and A. Ghosh<sup>9</sup> determined the mechanical properties of aluminium alloys at different temperatures and strain rates.

Forming-limit diagrams (FLDs) must be determined in order to assess the behaviour of the sheet's formability during the sheet material's characterization. The Nakajima test is widely preferred for the determination of the forming-limit diagram. Deforming the sheet with a hemispherical punch until the sheet material, for different geometries, starts to neck in the Nakajima test and measuring changes to the shape occurring in a predetermined grid on the sheet material can be obtained using forming-limit diagrams. In this process, deformations of uniaxial plane strain and biaxial stretching deformations occur in the sheet material.<sup>10,11</sup>

The parameters of the deformation, such as the temperature and strain rate, affecting the mechanical properties of materials affect the formability of sheet material and therefore also affect the forming-limit diagrams. In their studies, C. Zang et al.<sup>12,13</sup> determined, by analysing the FLDs of AA5086 and AA5083 aluminium alloys at elevated temperatures and at different strain rates, that the ability of formability decreases due to the increase in the strain rate. T. Naka et al.<sup>14</sup> in their study looked at the 5083 magnesium-aluminium alloy at different temperatures and strain rates and reported that the strain rates decrease the formability at high temperatures, but a significant effect is not observed at room temperature.

Considering the studies in the literature; it has been seen in the majority of aluminium alloys that an increase in the strain rate improves some of the mechanical pro-

perties, whereas analysing its effects on the forming-limit diagrams and the strain rate at room temperature is understood not to have a significant effect.<sup>4-8,12-14</sup>

In this study, it is intended to bring in the literature AA6019-T4 and AA6061-T4 aluminium alloy sheet materials whose mechanical properties have been determined, and whose forming-limit diagram has been obtained.

## 2 MATERIAL AND EXPERIMENTAL METHODS

### 2.1 Material

AA6061-T4 and AA6019-T4 sheet metal materials that are Al-Mg-Si-based are used in the study conducted. The chemical composition of these materials is given in **Table 1**. Also, microstructure photographs taken during the rolling, transverse and diagonal directions of the sheet materials are shown in **Figures 1** and **2**. The specimens for the optical investigations were etched using a mixture of acetic acid (7 mL), picric acid (25 g), ethanol (140 mL), and purified water (40 mL) for 15 s to reveal the microstructure.

Tensile test samples were prepared according to ASTM E517 standards in order to determine the mechanical properties of the material depending on the strain rate. The standard size is shown for the tensile test in **Figure 3**. It is carried out according to the Nakajima test method for forming-boundary limits. Thus, test samples that have been prepared according to the ASTM E 2218-02 standard are used. The Nakajima test-sample dimensions are shown in **Table 2**. The cutting process was performed in a water-jet machine in order to minimize the thermal impacts that may occur on the sheet material during the preparation of the test samples. Also, the notch effect, which may occur during deformation,

**Table 1:** Chemical composition of AA6019-T4 and AA6061-T4 sheet metal material, in mass fractions (w%)

**Tabela 1:** Kemijska sestava AA6019-T4 in AA6061-T4 pločevin, v masnih odstotkih (w%)

Material	Mg	Si	Fe	Cu	Cr	Mn	Ti	Zn	Al
AA 6061-T4	0.8	0.4	0.5	0.15	0.15	<0.15	<0.15	<0.25	balance
AA 6019-T4	1.2	0.1	<0.5	0.6	0.35	<0.1	<0.15	0.1	balance

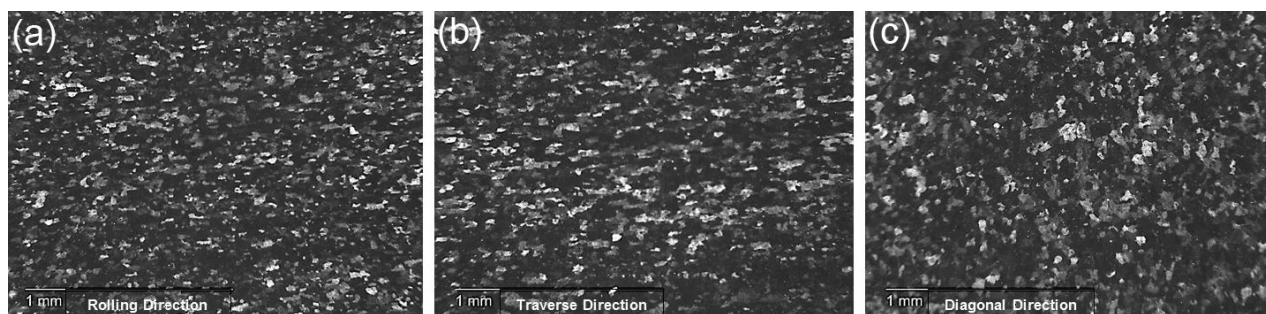


**Figure 1:** Microstructure photos of AA6061-T4

**Slika 1:** Posnetki mikrostrukture AA6061-T4

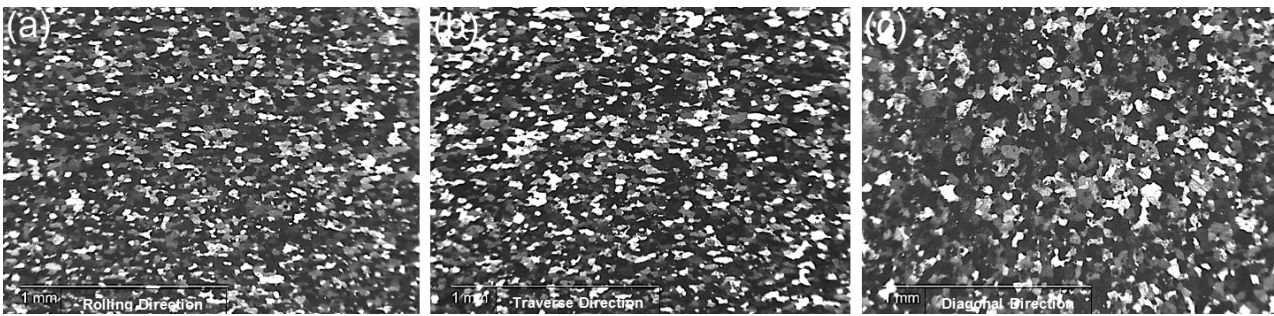


**Figure 2:** Microstructure photos of AA6019-T4  
**Slika 2:** Posnetki mikrostrukture AA6019-T4

was eliminated by polishing the side surface of the test sample.

**Table 2:** Nakajima test sample sizes

**Tabela 2:** Velikost vzorcev za Nakajima preizkus

Nakajima specimen	Sample No.	R (mm)
	1	0
	2	20
	3	40
	4	50
	5	57.5
	6	65
	7	72.5
	8	80

## 2.2 Experimental methods

### 2.2.1 Tensile test

Tensile test samples of the AA6019-T4 and AA6061-T4 metal material sheet were prepared according to ASTM E517 standards. The tensile tests were carried out at room temperature using a mechanical deformation meter in an Instron 5500 tensile test device.

Tensile tests were carried out for three different directions (RD, TD, DD) and five different strain rates ( $0.3 \text{ s}^{-1}$ ,  $0.03 \text{ s}^{-1}$ ,  $0.003 \text{ s}^{-1}$ ,  $0.0003 \text{ s}^{-1}$ ,  $0.00003 \text{ s}^{-1}$ ). The average values were taken by repeating each test three times for each sheet material and each different deformation rate in order to reduce the margin of error. As a result of these tests, the yield strength, tensile strength, strain-hardening coefficient, total elongation and anisotropy values were obtained, depending on the strain rates from the the true stress vs. true strain curves of the sheet material.

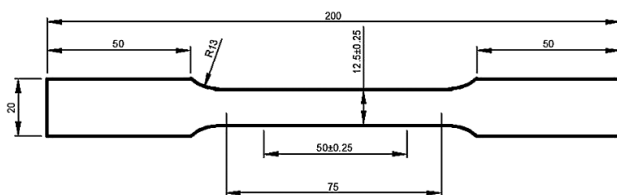


**Figure 3:** ASTM E517 tensile test specimen dimensions  
**Slika 3:** Dimenzije nateznega preizkušanca po ASTM E517

### 2.2.2 Forming-limit diagrams (FLDs)

In the second part of the study, the forming-limit diagrams were obtained using the Nakajima test method in order to determine the formability capabilities of AA6019-T4 and AA6061-T4 sheet metal. A schematic view of the Nakajima test method is presented in **Figure 4**.

A 2.4-mm-diameter circular gridding process using an electrochemical etching method was performed on the upper surfaces of the samples for these tests. Then, the hydraulic bulging process was applied on the test samples with a hemispherical punch until the fracture on

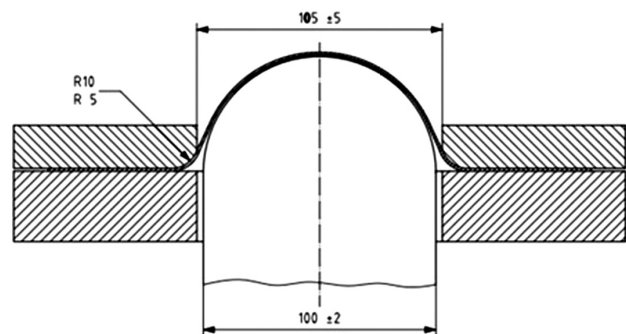


**Figure 4:** Nakajima test method's schematic display of forming limit diagram

**Slika 4:** Shematski prikaz Nakajima preizkusa za mejni diagram preoblikovanja



**Figure 5:** The measurement of the grid  
**Slika 5:** Merjenje mreže



the sheet material occurred. The measurement process of the samples proceeded in order to determine the plastic deformation occurring in the grid. The measurement processes was carried out by means of the measuring system at the University of Ulster, Northern Ireland. A photograph of the performed measurement process is presented in **Figure 5**. The grids in which the deformation occurs on the sheet material were computerized by measuring with the help of a camera and a 3.0 GPA program. After this, the forming-limit diagrams were determined by processing the data.

### 3 RESULTS AND DISCUSSION

#### 3.1 Tensile test results

The variance of the sheet materials' mechanical properties depending on the strain rate is determined by applying the tensile tests at (0.3 s<sup>-1</sup>, 0.03 s<sup>-1</sup>, 0.003 s<sup>-1</sup>, 0.0003 s<sup>-1</sup>, 0.00003 s<sup>-1</sup>) strain rates. The data obtained from the tensile-test results are given in **Tables 3** and **4**.

**Table 3:** AA6019-T4 tensile test results

**Tabela 3:** Rezultati nateznega preizkusa AA6019-T4

Strain rate	Yield strength	Tensile strength	Hardening coefficient	Elongation	R value
0.3	224	399	0.23	0.15	0.291
0.03	221	397	0.24	0.17	0.316
0.003	219	396	0.23	0.17	0.384
0.0003	220	397	0.24	0.17	0.446
0.00003	219	390	0.22	0.18	0.469

**Table 4:** AA6061-T4 tensile test results

**Tabela 4:** Rezultati nateznega preizkusa AA6061-T4

Strain rate	Yield strength	Tensile strength	Hardening coefficient	Elongation	R value
0.3	165	325	0.25	0.18	0.46
0.03	165	322	0.24	0.18	0.468
0.003	162	324	0.25	0.19	0.479
0.0003	164	325	0.24	0.20	0.555
0.00003	155	310	0.25	0.21	0.649

The relationship between the strain rate of the AA6019-T4 and AA6061-T4 sheet materials and the yield strength is given in **Figure 6**. An increase in the yield strength of the sheet materials occurs with an increased strain rate.<sup>5-7</sup> Upon analysing **Figure 6**, it is seen that the yield strength of both sheet materials shows an upward tendency with the strain rate. By considering the amounts of increase in the yield strength, the AA6019-T4 sheet material's yield strength was determined to be between 220 MPa and 225 MPa at the lowest (0.00003 s<sup>-1</sup>) and the highest (0.3 s<sup>-1</sup>) strain rates. It is determined that the AA6061-T4 sheet material has the lowest yield strength at the lowest (0.00003 s<sup>-1</sup>) strain-rate value. At the other strain rates it is clear that the detected values of the yield strength were between 163 MPa and 166 MPa. According to these results, it is

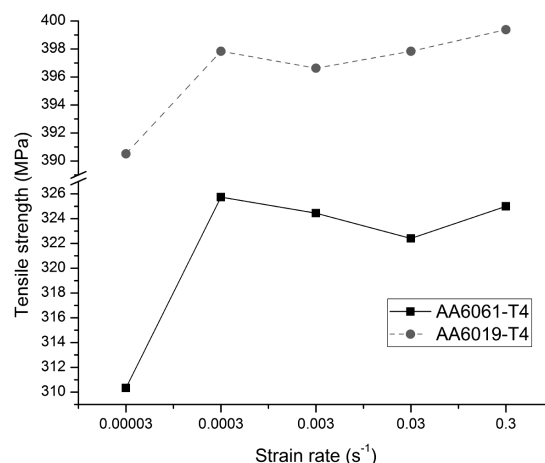


**Figure 6:** Strain rate vs. yield strength

**Slika 6:** Odvisnost med hitrostjo preoblikovanja in mejo plastičnosti

observed that the yield strength of AA6019-T4 and AA6061-T4 sheet materials was not significantly affected by the increase in the strain rate.

Tensile strength is one of the most important parameters in the classification of sheet materials. The strain rate vs. tensile strength relationship is shown in **Figure 7**. Analysing the effects of the strain rate on the tensile strength, it is determined that both sheet materials have the lowest tensile strength at the lowest deformation rate. The tensile strength also increased with an increase in the strain rate. However, very small amounts of change in the tensile strength were seen at the other strain rates. In studies in the literature, it is determined that an increase occurred in the tensile strength with an increasing strain rate, but this increase was very small at room temperature.<sup>5,8</sup> Also in this study, when the tensile strength obtained at the lowest deformation rate for the AA6019-T4 and AA6061-T4 sheet materials used in the experiments was compared with the other strain rates in the tensile strength values, it is clear that the tensile strength of both sheet materials increased by a small amount.

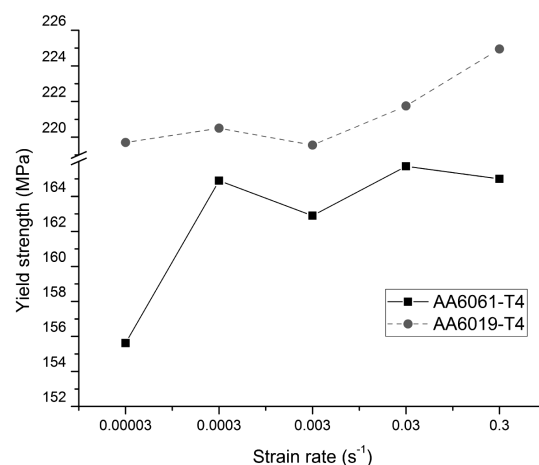


**Figure 7:** Strain rate vs. tensile strength

**Slika 7:** Odvisnost med hitrostjo preoblikovanja in natezno trdnostjo



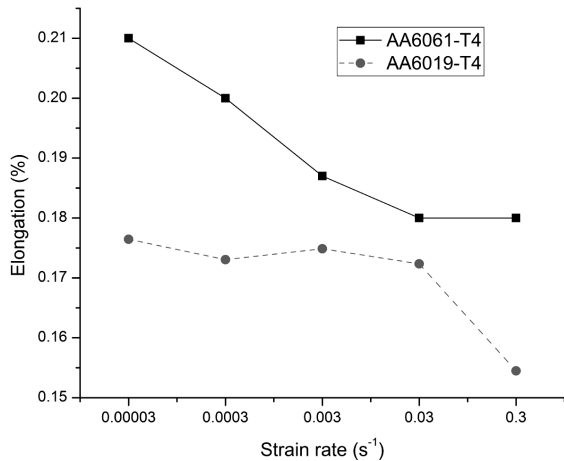


Figure 8: Strain rate vs. elongation

Slika 8: Odvisnost med hitrostjo deformacije in razteznost

As a result of the performed tensile tests, the strain rate vs. total elongation graphs of the AA6019-T4 and AA6061-T4 sheet materials are given in Figure 8. When the graphics are analysed, the maximum elongation of the AA6019-T4 sheet material occurred at the lowest strain rate of the total elongation. For the other deformation rates, it is seen to be unaffected by the changes at the strain rates. When the AA6061-T4 sheet material's elongation behaviour was analysed, it is clear that the increasing strain rate and total elongation have a downward tendency. Upon comparing the elongation behaviour of the two materials, it is seen that the AA6019-T4 sheet material has elongated less than the AA6061-T4 sheet material. Upon analysing sheet materials in the same series, it is seen that sheet materials having a high tensile strength elongated less.

The materials gain strength through strain hardening during the plastic deformation of the sheet-metal material. Upon analysing graphs of the strain rate vs. strain hardening coefficient in Figure 9, it is clear that strain-hardening coefficient was in the range 0.22–0.24 for the

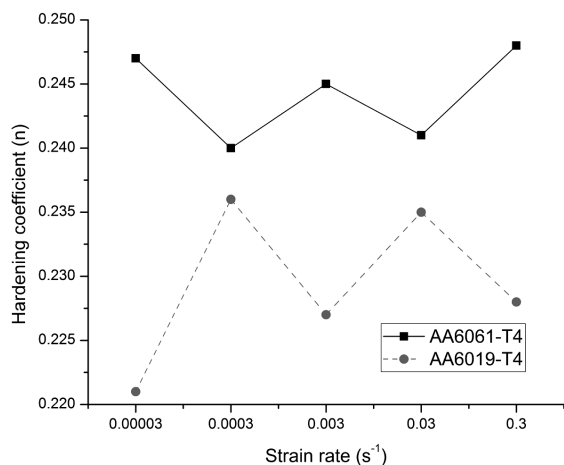


Figure 9: Strain rate vs. hardening coefficient

Slika 9: Odvisnost med hitrostjo preoblikovanja in koeficientom utrjevanja

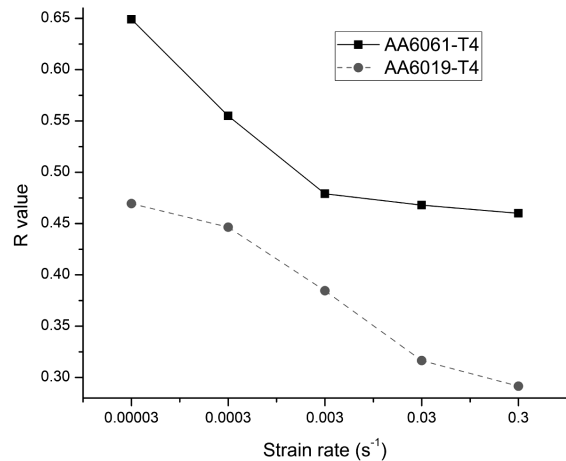


Figure 10: Strain rate vs. anisotropy

Slika 10: Odvisnost med hitrostjo preoblikovanja in anizotropijo

AA6019-T4 sheet material, and 0.24–0.25 for the AA6061-T4 sheet material. Also, it is clear that the strain-hardening coefficient of both sheet materials was not significantly affected by the variance in the deformation rate. The strain-hardening coefficient results in the study of D. Li and A. Ghosh<sup>9</sup> shows that it has changed over a very small range. Therefore, the results obtained were found to be consistent with the literature.

When analysing the average planer anisotropy values in Figure 10, it is seen that an amount of decrease has occurred in the plane anisotropy and increasing deformation speed. However, when evaluating the plane anisotropy coefficients, the values were found to be close to each other. It was concluded that the plane anisotropy coefficient in both sheet materials shows a slight downward tendency.

### 3.2 Forming-limit diagram

Upon analysing the results obtained from tensile tests, both experimental sheet materials used in this study were determined not to have been significantly affected by the variance in the strain rate. Therefore, the forming-limit diagrams of the AA6019-T4 and AA6061-T4 sheet materials were determined by Nakajima Tests by considering the strain rate 0.003 s<sup>-1</sup> (10 mm/s). Forming-limit diagrams are shown in Figure 11.

The area under the forming-limit diagrams represents a safety forming area. The upper parts of the curve show the areas occurring for the fracture in the sheet material.<sup>11–13</sup> Upon evaluating the forming-limit diagram in Figure 11, it is clear that the AA6061-T4 sheet material has higher deformation limits than the AA6019-T4 sheet material, by showing higher elongation behaviour than the latter. Thus, it provides that the forming-limit curve obtained for the AA6061-T4 sheet material was above the AA6019-T4 sheet metal's forming-limit curve. This case shows that the AA6061-T4 sheet material had better formability. And this case constitutes solid-solu-

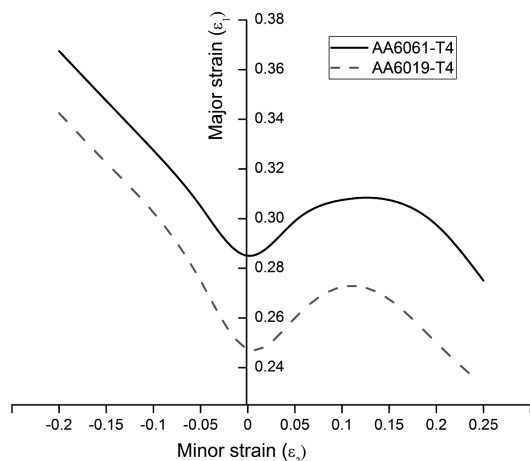


**Figure 11:** Forming-limit diagrams

**Slika 11:** Diagrami meje preoblikovanja

tion strengthening, owing to the fact that the rate of alloying elements in the chemical composition of the AA6019-T4 sheet material was higher than the AA6061-T4 sheet material. This also ensures that it has a higher yield and tensile strength and causes the ability of formability to decrease. Furthermore, the AA6061-T4 sheet material had greater elongation and anisotropy ( $R$ ) values than the AA6019-T4 sheet material, which is another sign that the former has a higher formability than the latter.

#### 4 CONCLUSIONS

The results obtained from this study are summarized below.

The lowest values for both the yield and tensile strength of the sheet material are obtained at the lowest deformation rate ( $0.00003 \text{ s}^{-1}$ ). It is found that as long as the strain rate increases, the yield and tensile strengths show a slight increase.

A very small range of change in the strain-hardening coefficient is observed with an increase in the strain rate.

A downward tendency is seen in both sheet materials' elongation, the plane anisotropy upon the increase of the strain rate. However, the exchange range of the elongation and the plane anisotropy are found to be too narrow. Therefore, it can be said that the AA6061-T4 and AA6019-T4 sheet materials are insensitive to the strain rate.

AA6061-T4 aluminium alloy is found to have higher formability limits than the AA6019-T4 aluminium alloy.

#### Acknowledgement

The authors would like to thank Turkish Council of Higher Education for the research grant and University

of Ulster, Advanced Metal Forming Research Group (AMFOR) for the necessary equipment and material support.

#### 5 REFERENCES

- O. Çavuşoğlu, H. Gürün, Investigation of the effects of deformation speed on the mechanical properties and deep drawing process of DP600 and DP780 sheet metal, *Journal of the Faculty of Engineering and Architecture of Gazi University*, 29 (2014) 4, 777–784, doi:10.17341/gummfd.76140
- N. Wang, Z. Zhou, G. Lu, Microstructural evolution of 6061 alloy during isothermal heat treatment, *J. Mater. Sci. Technol.*, 27 (2011) 1, 8–14, doi:10.1016/S1005-0302(11)60018-2
- B. M. Dariani, H. G. Liaghat, M. Gerdooei, Experimental investigation of sheet metal formability under various strain rates, *Proc. IMechE Part B: J. Engineering Manufacture*, 223 (2009), 703–712, doi:10.1243/09544054JEM1430
- C. Kubat, A. Kiraz, The modeling of tensile test in virtual laboratory design using artificial intelligence *Journal of the Faculty of Engineering and Architecture of Gazi University*, 27 (2012) 1, 205–209, doi:10.17341/gummfd.04550
- J. Q. Tan, M. Zhan, S. Liu, T. Huang, J. Guo, H. Yang, A modified Johnson–Cook model for tensile flow behaviors of 7050-T7451 aluminum alloy at high strain rates, *Materials Science & Engineering A*, 631 (2015), 214–219, doi:10.1016/j.msea.2015.02.010
- M. Vural, J. Caro, Experimental analysis and constitutive modeling for the newly developed 2139-T8 alloy, *Materials Science and Engineering A*, 520 (2009), 56–65, doi:10.1016/j.msea.2009.05.026
- R. Smerd, S. Winklera, C. Salisbury, M. Worswicka, D. Lloydb, M. Finn, High strain rate tensile testing of automotive aluminum alloy sheet, *International Journal of Impact Engineering*, 32 (2005), 541–560, doi:10.1016/j.ijimpeng.2005.04.013
- O. G. Lademo, O. Engler, J. Aegerter, T. Berstad, A. Benallal, O. S. Hopperstad, Strain-rate sensitivity of aluminum alloys AA1200 and AA3103, *J. Eng. Mater. Technol.*, 132 (2010) 4, 041007–8, doi:10.1115/1.4002160
- D. Li, A. Ghosh, Tensile deformation behavior of aluminum alloys at warm forming temperatures, *Materials Science and Engineering A*, 352 (2003), 279–286, doi:10.1016/S0921-5093(02)00915-2
- Material Properties: Determination of Process Limitations in Sheet Metal Forming - Forming Limit Diagram, *gom Optical Measuring Techniques*, [http://www.gom.com/fileadmin/user\\_upload/industries/flc\\_fid\\_EN.pdf](http://www.gom.com/fileadmin/user_upload/industries/flc_fid_EN.pdf), 18.06.2015
- O. Anket, T. Koruvatan, İ. Ay, The use of forming limit diagrams in forming sheet metal materials, *Journal of Polytechnic*, 14 (2011) 1, 39–47
- C. Zhang, X. Chuc, D. Guinesd, L. Leotoing, J. Dinga, G. Zhao, Effects of temperature and strain rate on the forming limit curves of AA5086 sheet, *Procedia Engineering*, 81 (2014), 772–778, doi:10.1016/j.proeng.2014.10.075
- C. Zhang, L. Leotoing, D. Guines, E. Ragneau, Theoretical and numerical study of strain rate influence on AA5083 formability, *Journal of Materials Processing Technology*, 209 (2009), 3849–3858, doi:10.1016/j.jmatprotec.2008.09.003
- T. Naka, G. Torikai, R. Hino, F. Yoshida, The effects of temperature and forming speed on the forming limit diagram for type 5083 aluminum–magnesium alloy sheet, *Journal of Materials Processing Technology*, 113 (2001), 648–653, doi:10.1016/S0924-0136(01)00650-1

## EFFECT OF ALTERNATIVE HEAT-TREATMENT PARAMETERS ON THE AGING BEHAVIOR OF SHORT-FIBER-REINFORCED 2124 Al COMPOSITES

### VPLIV ALTERNATIVNIH PARAMETROV TOPLOTNE OBDELAVE NA STARANJE 2124 Al KOMPOZITA, OJAČANEGA S KRATKIMI VLAKNI

Yahya Altunpak<sup>1</sup>, Serdar Aslan<sup>2</sup>, Mehmet Oğuz Güler<sup>2</sup>, Hatem Akbulut<sup>2</sup>

<sup>1</sup>Abant İzzet Baysal University, Faculty of Engineering and Architecture, Mechanical Engineering, 14280 Bolu, Turkey

<sup>2</sup>Sakarya University, Faculty of Engineering, Department of Metallurgy and Materials Engineering, Esentepe Campus, 54187 Adapazarı, Turkey  
altunpak\_y@ibu.edu.tr

*Prejem rokopisa – received: 2015-09-10; sprejem za objavo – accepted for publication: 2015-11-24*

doi:10.17222/mit.2015.287

The 2124 Al alloy and a composite of the 2124 Al alloy reinforced with 20 % of volume fractions of  $\delta$ -Al<sub>2</sub>O<sub>3</sub> short fibers made by squeeze casting were subjected to controlled and systematic aging treatments. The materials were solution treated at (495, 525 and 555) °C. After quenching, the matrix alloy and the composite were artificially aged at (160, 170, 180 and 190) °C up to 36 h. The aging was monitored with hardness measurements and differential scanning calorimetry. The time required to reach the peak hardness of the composite matrix during a precipitation treatment was shorter than that for the unreinforced 2124 Al. An increase in the solution-treatment temperature resulted in an increase of the composite-matrix hardness. The  $\delta$ -Al<sub>2</sub>O<sub>3</sub>-reinforced composite exhibits no grain-boundary melting, but appears to show incipient melting around short alumina fiber interfaces at temperatures above 525 °C. The highest HV value was obtained after solutionizing at 495 °C for 6 h, followed by water quenching and aging at 190 °C for 10 h for the unreinforced matrix alloy. In the case of the reinforced alloy the highest HV value was found after solutionizing at 555 °C for 6 h, quenching and aging at 170 °C for 12 h.

Keywords: aluminum matrix composite, alumina, solution temperature, aging kinetics

Al zlitina 2124 in kompozit Al zlitine 2124, ojačane z 20 % volumenskega deleža kratkih vlaken  $\delta$ -Al<sub>2</sub>O<sub>3</sub>, ulitih z iztiskanjem, so bile kontrolirano in sistematično starane. Materiali so bili raztopno žarjeni na (495, 525 in 555) °C. Po hitrem ohlajanju sta bili osnovna zlitina in kompozit umetno starani 36 h na (160, 170, 180 in 190) °C. Staranje je bilo kontrolirano z merjenjem trdote in z diferenčno vrstično kalorimetrijo. Čas za doseganje najvišje trdote kompozitnega materiala med postopkom izločanja je bil krajši kot pri osnovnem materialu Al 2124. Povišanje temperature raztopnega žarjenja se je odrazilo na povečanju trdote kompozita. Kompozit, ojačan z  $\delta$ -Al<sub>2</sub>O<sub>3</sub>, ne kaže nataljevanja po mejah zrn, vendar pa kaže zametke taljenja na stiku s kratkimi vlakni, pri temperaturah nad 525 °C. Najvišja vrednost HV neojačane zlitine je bila dobljena po 6 urnem raztopnem žarjenju na 495 °C, ki mu je sledilo hlajenje v vodi in 10 urno staranje na 190 °C. V primeru kompozitne zlitine je bila zabeležena najvišja HV vrednost po raztopnem žarjenju 6 h na 555 °C, ohlajanju v vodi in 12 urnem staranju na 170 °C.

Ključne besede: kompozit na osnovi aluminija, aluminijev oksid, temperatura raztapljanja, kinetika staranja

## 1 INTRODUCTION

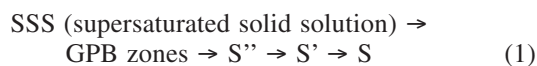
Research efforts on aluminum alloys are focused on precipitation phenomena in which the precipitates formed from a supersaturated solution are responsible for the hardening by natural or artificial ageing in an alloy. The response of an aluminum-matrix composite to aging can be completely different from that of the unreinforced alloy.<sup>1-8</sup> Hence, the age-hardening behavior of particulate-reinforced aluminum composites has been the subject of great interest from the scientific and technological viewpoints. The nature of the change in the hardening kinetics during the aging of composites depends on the matrix material, the type of reinforcement including their size, morphology and volume fraction, composite processing route, solution and aging temperatures.<sup>9-12</sup>

The pressure applied during solidification in the squeeze-casting technique results in excellent feeding

during solidification shrinkage. The commercialization of squeeze casting has only been used to fabricate high-integrity engineering components with reinforcement very recently.<sup>13-15</sup>

Different types of intermetallics were reported in the solidified 2xxx Al alloys. K. C. Chen and C. G. Chao<sup>3</sup> found Cu<sub>2</sub>Mn<sub>3</sub>Al<sub>20</sub> intermetallic particles in the 2024 matrix alloy and its  $\delta$ -Al<sub>2</sub>O<sub>3</sub> short-fiber-reinforced composites. The same intermetallic phase was also reported by T. Christman and S. Suresh<sup>16</sup> in a 2014 Al alloy. On the other hand, C. Badini et al.<sup>17</sup> showed the possibility of the formation of Cu<sub>2</sub>FeAl<sub>7</sub> and (CuFeMn)Al<sub>6</sub> in the 2618 Al SiC particle-reinforced composite. The same authors detected (CuFeMn)Al<sub>6</sub> in the 2024 Al alloy and its composite derived from MnAl<sub>6</sub>. They pointed out that this precipitate did not grow during aging and was not affected by the solution treatment because of its large size. Aluminum alloys with a copper:magnesium weight ratio of 2:1 and higher are used for manufacturing a

variety of age-hardenable structural alloys. The structural changes that occur during the aging of these alloys have been extensively studied.<sup>16-19</sup> According to S. K. Varma et al.<sup>18</sup> and A. P. Sanino and H. J. Rack<sup>19</sup>, the precipitation sequence in the pseudo-binary Al-Al<sub>2</sub>CuMg alloy (Al-3 % of mass fractions of Cu-1.5 % of mass fractions of Mg) can be represented as follows in Equation (1):



The solutionizing at 495 °C for 2-6 h, subsequent quenching and precipitation at 190 °C for 8-12 h, is defined as the standard heat treatment for the 2124 Al alloy.<sup>20</sup> It is an age-hardenable alloy, whose mechanical properties are mainly controlled with the hardening precipitates contained in the material. Accordingly, the present work was undertaken to study the effect of the  $\delta$ -Al<sub>2</sub>O<sub>3</sub> short fibers on the aging response of the composite matrix. Particular emphasis was given to examine the effect of the solution treatment and aging temperature on the age-hardening kinetics.

## 2 EXPERIMENTAL PART

The 2124 aluminum matrix alloy and the Saffil fiber/2124 aluminum (4.2 Cu, 1.5 Mg, 0.6 Mn, 0.3 Fe, 0.25 Zn, in mass fractions) composite were produced by squeeze casting using 20 % volume fractions of  $\delta$ -Al<sub>2</sub>O<sub>3</sub> preforms supplied by I.C.I. The preform cohesion was ensured by the addition of 3-4 % silica binder. The preform was supplied in the form of discs with 100 mm in diameter and 10 mm in thickness. The liquid aluminum alloy was squeezed into the preform at 800 °C with a 60 MPa hydraulic press to produce the composites. The pressure holding time was 75 s, to eliminate shrinkage during the solidification. Specimens were solution treated at three different temperatures of (495, 525 and 555) °C for 6 h. Thereafter, all the specimens were quenched into the water ice brine (-15 °C). The aging treatment was carried out in an electrical furnace at (160, 170, 180 and 190) °C up to 36 h. Microhardness measurements of the matrix and the composites (between the fibers) were performed using a diamond pyramid indenter and a 25-g mass. At least 6 hardness

measurements were carried out for each aging condition to ensure accurate results.

A group of specimens from the alloy solution treated 2124 Al matrix and the 2124 + 20 % of volume fractions of  $\delta$ -Al<sub>2</sub>O<sub>3</sub> composite were immediately stored in a refrigerator at -15 °C. Discs (5 mm diameter and 0.3 mm thickness) for DSC measurements were prepared. The differential scanning calorimetry (DSC) analyses of these samples were performed using a Perkin-Elmer DSC 1700 thermal analyzer. All the samples were loaded in a DSC cell at room temperature and equilibrated for a few minutes. The heating rate was 10 K/min from 25 °C to 550 °C. Dry pure nitrogen was purged through the cell at a rate of 55 cm<sup>3</sup>/min to avoid oxidation. The data for all the DSC runs were recorded in the instrument memory. At least two samples of each heat treatment were analyzed.

Microstructural observations were performed on mechanically polished and etched samples of the unreinforced alloy and composite. Surface-characterization studies were carried out using a Hitachi HHS-2R scanning electron microscope (SEM) with energy-dispersive spectroscopy (EDS).

## 3 RESULTS AND DISCUSSION

### 3.1 Microstructural aspects

At 525 °C and 555 °C the solution treatment both alloys showed surface blistering. However, the amount of blistering was more pronounced on the solution treated and quenched unreinforced alloy. These blisters were caused by a high internal gas pressure. Typical representative microstructures of the unreinforced alloy solution treated at (495, 525 and 555) °C and subsequently quenched are shown in **Figures 1a to 1c** and **Figures 2a to 2c** shows the light-microscope microstructures of the reinforced composite. All the polished samples were slightly etched with Kellers' agent to reveal grain boundaries and the dissolved intermetallics. Light microscope investigations of the samples of unreinforced alloy have revealed that significant incipient melting along the grain boundaries occurred when the solution heat treatment was at 525 °C and 555 °C (**Figures 1b** and **1c**). The  $\delta$ -Al<sub>2</sub>O<sub>3</sub>-reinforced composite exhibits no such grain-

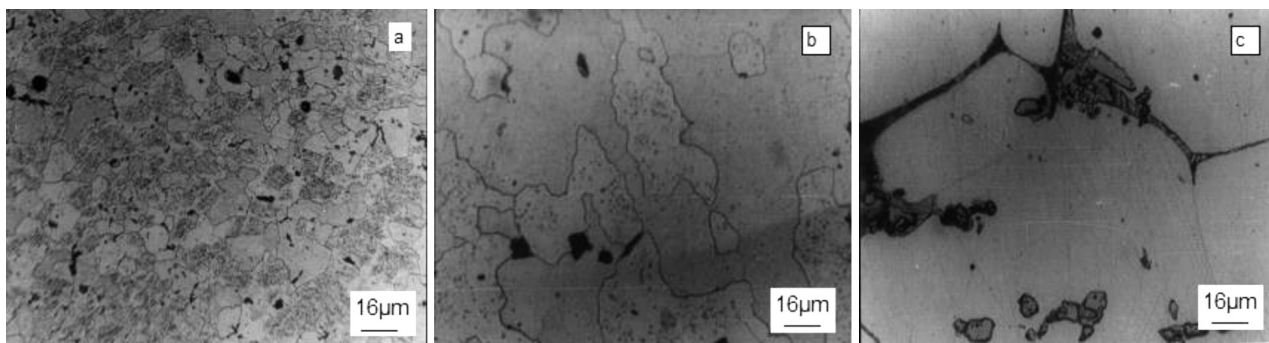


**Figure 1:** Light micrographs of the unreinforced 2124 Al matrix solution treated at: a) 495 °C, b) 525 °C, and c) 555 °C  
**Slika 1:** Mikrostrukture neojačane Al zlitine 2124, raztopno žarjene na: 495 °C, b) 525 °C in c) 555 °C



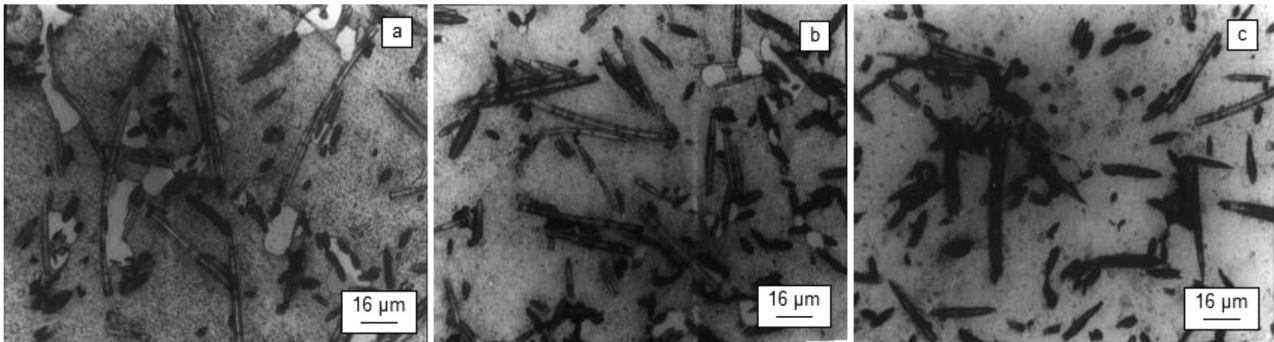


**Figure 2:** Light micrographs of the 2124 Al + 20 % volume fractions of  $\delta$ -Al<sub>2</sub>O<sub>3</sub> composite solution treated at: a) 495 °C, b) 525 °C, and c) 555 °C  
**Slika 2:** Mikrostrukture Al kompozita 2124 +20 % volumenskega deleža  $\delta$ -Al<sub>2</sub>O<sub>3</sub>, raztopno žarjenega na: a) 495 °C, b) 525 °C in c) 555 °C

boundary melting, but appears to show incipient melting around the short alumina-fiber interfaces (**Figures 2b** and **2c**). There are low-melting-point constituents, which melt first at temperatures above the initial melting point of an alloy producing incipient melting and embrittlement. Thus, it appears that whilst these low-melting-point constituents segregate to the grain boundaries in the unreinforced alloy they may segregate to  $\delta$ -Al<sub>2</sub>O<sub>3</sub> short fiber interfaces. **Figures 1** and **2** show that as the solution treatment temperature is increased the amount of intermetallic appearing on the polished and etched surface decreases. The unreinforced alloy does not exhibit a visible intermetallic at any of the solution temperatures studied. The reduction in the intermetallics appearing on the polished surface as the solution temperature increase (**Figure 2**) is due to the dissolution of intermetallic particles. In order to clarify the undissolved phase, an SEM-EDS study was undertaken. **Figure 3** shows a typical EDS spectrum performed on the undissolved phase in the composite matrix. From the EDS analysis copper, magnesium, aluminum, manganese, and iron peaks were observed on the undissolved phase in the heat-treated, unreinforced and composite matrix. For the EDS analysis of the undissolved phase the average elemental concentrations of these undissolved phases and the spectral analyses of the matrix material (2124 Al) were given in **Table 1**. It is clear that the contents of copper and manganese of the undissolved

phase are much higher than those of the matrix material. The undissolved phase in the literature was identified as Cu<sub>2</sub>Mn<sub>3</sub>Al<sub>20</sub>, which was also found in 2024 Al by K. C. Chen and C. G. Chao<sup>3</sup> and in 2014 Al by T. Christman and S. Suresh.<sup>16</sup>

**Table 1:** Spectral analysis and EDS analysis results, in mass fractions (w/%)

**Tabela 1:** Rezultati spektralne in EDS-analiz, v masnih deležih (w/%)

	Cu	Mg	Mn	Fe	Zn	Al
2124 Al alloy spectral analyses results	4.2	1.5	0.6	0.3	0.25	Bal- ance
EDS analysis results of the undissolved phase in unreinforced matrix	7.55	0.15	9.05	0.04		83.2
EDS analysis results of the undissolved phase in the composite matrix	7.52	0.13	9.20	0.05		83.1

### 3.2 DSC analysis

The DSC scans of the unreinforced 2124 alloy and 2124 Al + 20 % volume fractions of  $\delta$ -Al<sub>2</sub>O<sub>3</sub> composite are shown in **Figure 4**. For comparison purposes, results from the DSC scans of the unreinforced matrix and the composite quenched into ice brine after the solution treatment at 495 °C and 555 °C are presented in **Figures 4a** and **4b**, respectively. The DSC traces of the composites were different from each other. However, the DSC

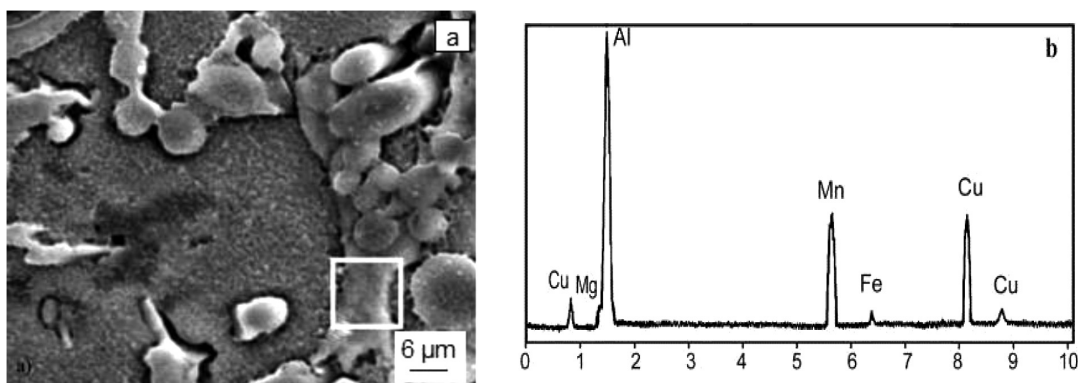


**Figure 3:** a) SEM micrograph of the 2124 Al + 20 % volume fractions of  $\delta$ -Al<sub>2</sub>O<sub>3</sub> composite and b) an EDS spectrum taken from the undissolved intermetallic phase

**Slika 3:** a) SEM-posnetek Al kompozita 2124 + 20 % volumenskega deleža  $\delta$ -Al<sub>2</sub>O<sub>3</sub> in b) EDS- spekter neraztopljene intermetalne faze

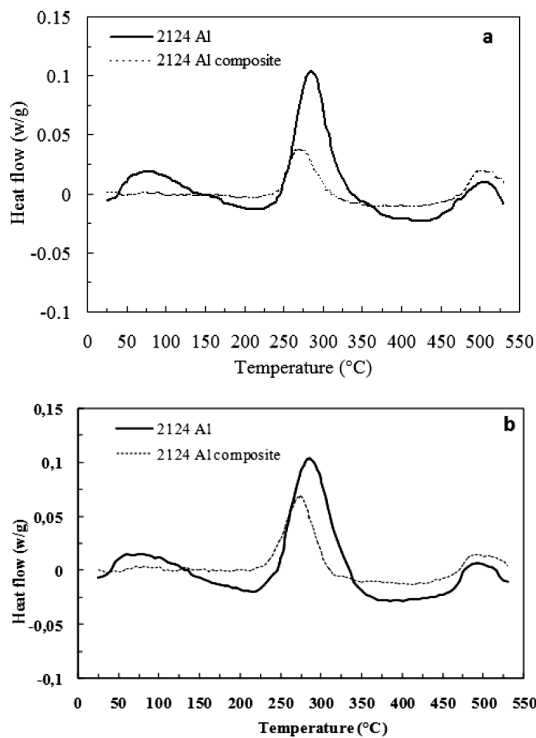


**Figure 4:** Results of DSC for 2124 Al alloy and 2124 Al alloy + 20 % volume fractions of  $\delta$ -Al<sub>2</sub>O<sub>3</sub> composite solution treated at: a) 495 °C and b) 555 °C

**Slika 4:** Rezultati DSC Al zlitine 2124 in Al kompozita 2124 + 20 % volumenskega deleža  $\delta$ -Al<sub>2</sub>O<sub>3</sub>, po raztopnem žarjenju na: a) 495 °C in b) 555 °C

traces of the matrix alloy do not exhibit significant differences depending on the solutionizing temperatures. The curve of the unreinforced matrix alloy shows four zones: an exothermic reaction between 40 °C and 135 °C due to the formation of Guiner-Preston zones followed by an endothermic between 135 °C and 245 °C due to the dissolution of the Guiner-Preston zones; an exothermic reaction between 245 °C and 335 °C due to formation of S' precipitates and finally the endothermic reaction between 335 °C and 485 °C due to the dissolution of these S' precipitates (**Figures 4a** and **4b**). However, the DSC curves for the composite do not have obvious Guiner-Preston zone formation and dissolution peaks. Increasing the solution temperature to 555 °C resulted in an increase in the amount of S' precipitate for the composite, as shown in **Figures 4a** and **4b**. Additionally, the figure also shows an acceleration of S' precipitate formation in the case of the reinforced alloy. For example, the S' precipitates are formed at 245 °C in the unreinforced 2124 Al matrix (**Figure 4a**), but this temperature is approximately 230 °C for the composite material (**Figure 4b**). This shows that the short  $\delta$ -Al<sub>2</sub>O<sub>3</sub> ceramic phase shifted the S' precipitate-formation temperature.

### 3.3 Matrix microhardness

**Figure 5** shows the microhardness (HV) as a function of aging time at 190 °C for both alloys. For all con-

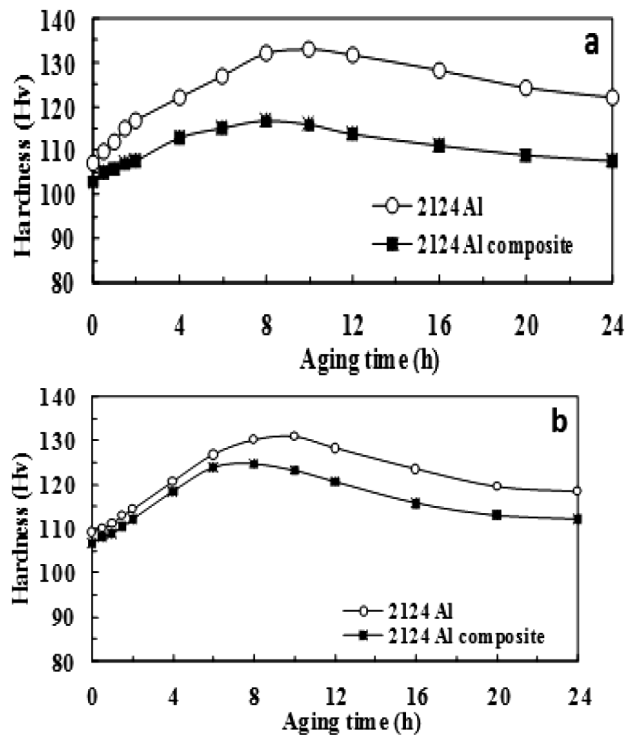


**Figure 5:** Microhardness variation of 2124 Al alloy and 2124 Al alloy + 20 % volume fractions of  $\delta$ -Al<sub>2</sub>O<sub>3</sub> composite as a function of aging time at 190 °C after solution treatment at: a) 495 °C and b) 555 °C

**Slika 5:** Spreminjanje mikrotvrdote Al zlitine 2124 in Al kompozita 2124 + 20 % volumenskega deleža  $\delta$ -Al<sub>2</sub>O<sub>3</sub>, v odvisnosti od časa staranja na 190 °C, po raztopnem žarjenju na: a) 495 °C in b) 555 °C

ditions, the unreinforced 2124 Al matrix alloy and the composite reached a peak hardness after aging for 10–12 h and 7–9 h, respectively, at 190 °C. A reduced hardness of the matrix was observed in the case of the reinforced alloy.

The times required to attain the peak hardness for both alloys artificially aged between 160 °C and 190 °C are summarized in **Table 2**. First, the peak of the matrix microhardness values of the composite samples increase with increasing solutionizing temperature, while these values show a slight decrease in the unreinforced 2124 Al matrix. Second, the presence of short alumina fibers in the matrix decreases the time needed to achieve the peak microhardness. This suggests that the addition of 20 % volume fractions of  $\delta$ -Al<sub>2</sub>O<sub>3</sub> short fibers for the matrix causes considerable acceleration in the aging kinetics of the matrix alloy. Third, a decrease in the aging temperature from 190 °C to 170 °C leads to an increase of the peak microhardness of the composite matrix. From **Table 2**, solutionizing at 495 °C for 6 h, followed by water quenching and aging at 190 °C for 10 h, seems to be the best aging procedure for the unreinforced matrix alloy. In the case of the reinforced alloy the highest HV value was formed after solutionizing at 555 °C for 6 h, quenching and aging at 170 °C for 12 h.

**Table 2:** Times (h) required to attain peak hardness for 2124 Al and 2124 Al + 20 % volume fractions of  $\delta$ -Al<sub>2</sub>O<sub>3</sub> composite matrices at different aging temperatures**Tabela 2:** Čas (h) potreben za doseganje najvišje trdote Al zlitine 2124 in kompozita Al zlitine 2124+ 20 % volumenskega deleža  $\delta$ -Al<sub>2</sub>O<sub>3</sub> pri različnih temperaturah staranja

Solution temp. (°C)	Time (h) / Microhardness (HV <sub>0.025</sub> )				
	Material	160 °C	170 °C	180 °C	190 °C
495	2124 Al	20/132.0	17/130.4	12/133.0	10/133.3
	2124 Al composite	12/118.8	12/119.6	10/117.9	8/116.7
525	2124 Al	20/130.6	16/129.6	12/130.7	8/132.5
	2124 Al composite	12/124.5	12/125.4	10/122.9	8/121.3
555	2124 Al	20/127.5	16/129.1	10/129.6	8/130.5
	2124 Al composite	12/128.4	12/130.4	8/125.8	8/124.5

### 3.4 Discussion

The use of an Al-Cu-Mg alloy for fabricating an aluminum matrix composite leads to the formation of intermetallic particles of Cu<sub>2</sub>Mn<sub>3</sub>Al<sub>20</sub> type. Increasing the solution treatment temperature caused greater dissolution of the Cu-Mn-Al-based intermetallic particles, and this is related to a decrease in the number of particles on the metallographic polished and etched sample surfaces. At 525 °C and 555 °C for the solution-treated unreinforced alloy and the composites, surface blistering was observed after quenching. However, the amount of blistering was observed to be more in the unreinforced alloy when compared with the composite. These blisters were suggested to form due to a high internal gas pressure. Above the solution treatment of 495 °C for the unreinforced alloy, grain-boundary melting was detected. For 2124 Al + 20 % volume fractions of  $\delta$ -Al<sub>2</sub>O<sub>3</sub> the composite specimens intermetallic dissolution was almost complete at 555 °C.

Regarding the heat-treated samples, the extensive dissolution of the Cu<sub>2</sub>Mn<sub>3</sub>Al<sub>20</sub>-type intermetallics and the formation of coherent precipitates after aging, indicate an apparently good solution and precipitation treatment that improves the hardness values of the 2124 Al matrix. At solution-treatment temperatures above 495 °C the peak hardness values of the matrix alloy decrease, probably as a result of increasing the amount of gas porosity due to hydrogen absorption from a moist atmosphere. The increment in the peak hardness values of the composite was observed by increasing the solution-treatment temperature.

The thermal analysis technique was employed to study the change in the enthalpy, which is associated with the formation and dissolution of the precipitates. The area of the peak in the DSC curve gives the reaction enthalpy, which is directly related to the molar heat of reaction and the volume fraction of the precipitating or dissolving phase. The corresponding temperature is related to the stability of the precipitates and to the reaction kinetics. The DSC curves show that the GP zone's formation peak is suppressed in the composite matrix.

This inhibition of the GP zone's formation and its effect on the age hardening are similar to the observation of sintered aluminum powder (SAP) alloys.<sup>3</sup> In SAP alloys, these phenomena have been attributed to a lack of quenched-in vacancies that were soaked up by the grain boundaries in the fine-grain matrix and by the Al/Al<sub>2</sub>O<sub>3</sub> particle interfaces. The observations in the present work suggest that a similar mechanism is responsible for the inhibition of the GP zone's formation in aluminum matrix composite matrices. From the DSC scans and microhardness measurements, it was observed that the S' formation temperature is lower in the composite than in the unreinforced matrix alloy. In general, the addition of  $\delta$ -Al<sub>2</sub>O<sub>3</sub> fibers decreases the time required to attain peak hardness. These features encourage the nucleation of precipitates by reinforcing the ceramic phase. The addition of  $\delta$ -Al<sub>2</sub>O<sub>3</sub> fibers to the 2124 alloy was also resulted to obtain lower age-hardening temperatures to attain time to require peak aging. It is well known that  $\delta$ -Al<sub>2</sub>O<sub>3</sub> fibers lead to acceleration in the aging kinetics and some possible reasons for the acceleration of the aging kinetics are given in<sup>21,22</sup>. Composite matrix has finer grains than that of the unreinforced alloy. As also evidenced from the transmission electron microscopy studies by C. M. Friend and S. D. Luxton<sup>23</sup>, the dislocation densities are almost similar in the aluminum matrix alloy and its  $\delta$ -Al<sub>2</sub>O<sub>3</sub> short-fiber-reinforced composites. The dislocations in the matrix are in the form of long lines and short lines in the composite. However, the short dislocations are agglomerated close to the fiber matrix interfaces. In this study, it is suggested that these dislocations can also accelerate the formation of the S' phase. In addition, fiber matrix interfaces are well-known heterogeneous nucleation sites for precipitation.

In the as-quenched condition, the microhardness of the composite matrix is lower than that of the unreinforced matrix. The result is similar to the 2024 Al- $\delta$ -Al<sub>2</sub>O<sub>3</sub> composites and 2124 Al-SiC composites that were reported by K. C. Chen and C. G. Chao<sup>3</sup> and T. S. Christman and Suresh<sup>16</sup>, respectively. When the composite is cooled from the elevated temperature of the aging process, misfit strains occur due to differential thermal contraction at the reinforcement/matrix interface, which are sufficient to generate dislocations. The dislocation density is able to influence the microhardness. B. Dutta and M. K. Surappa<sup>11</sup> suggested an enhanced dislocation density in the 6061 Al-Al<sub>2</sub>O<sub>3</sub> composite matrix that contributes to higher microhardness values compared to the unreinforced matrix alloy. K. C. Chen and C. G. Chao<sup>3</sup> reported that a very low dislocation density was observed in a 2024 Al alloy that was reinforced with  $\delta$ -Al<sub>2</sub>O<sub>3</sub> short fibers when compared with Al-SiC systems. They pointed out that the coefficient of thermal expansion difference between Al and  $\delta$ -Al<sub>2</sub>O<sub>3</sub> is 3:1, but this ratio is 10:1 for Al and SiC. Thus, a lower dislocation density is established in the matrix of Al- $\delta$ -Al<sub>2</sub>O<sub>3</sub> short-fiber composites. Moreover, the porosity level is expected to be higher in the composite matrix due to poor wetting of the short fiber by the



matrix during the squeeze-casting process route since the fibers are agglomerated in some regions. Since the artificial age hardening of 2124 Al is attributed to the GP zone and the S' phase, the microhardness of the composites is smaller due to the suppression of the GP zones. Consequently, the number of S' precipitates in the composite matrix decreases. The increasing number of precipitates are expected to result in high strength in the age-hardenable alloys and their composites. The response of the  $\delta$ -Al<sub>2</sub>O<sub>3</sub> short-fiber-reinforced 2124 Al alloy matrix to aging is significantly different to that of the unreinforced alloy in the 495 °C solution-treated condition. The grain boundaries and the addition of fiber-matrix interfaces were thought to be the preferred site for pore nucleation for the following reasons; i) the incipient melting that occurs there (incipient melting is particularly prone to gas porosity because of the higher solubility in the liquid phase<sup>9</sup> and, ii) the observation that when an aluminum matrix composite was charged with hydrogen, the gas migrates to the clusters in addition to the  $\delta$ -Al<sub>2</sub>O<sub>3</sub> fiber interfaces.<sup>24</sup>

#### 4 CONCLUSIONS

Increasing the solution treatment temperature led to an increase in the dissolution of the intermetallic particles in the composite matrix. At temperatures above 525 °C, samples of the unreinforced alloy experienced significant incipient melting along the grain boundaries. The  $\delta$ -Al<sub>2</sub>O<sub>3</sub> reinforced composite exhibits no grain-boundary melting, but appears to show incipient melting around the short alumina fiber interfaces.

The microhardness values of the matrix of the composite were lower than that of the 2124 unreinforced matrix in their peak-aged conditions. The highest microhardness value was obtained after solutionizing at 495 °C for 6 h, and aging at 190 °C for 10 h for the unreinforced matrix alloy. The highest HV value was found after solutionizing at 555 °C for 6 h and aging at 170 °C for 12 h for the composite.

#### 5 REFERENCES

- 1 A. Daoud, W. Reif, Influence of Al<sub>2</sub>O<sub>3</sub> particulate on the aging response of A356 Al-based composites, *J. Mater. Process. Tech.*, 123 (2002) 2, 313–318, doi:10.1016/S0924-0136(02)00103-6
- 2 J. S. Lin, P. X. Li, R. J. Wu, Aging evaluation of cast particulate-reinforced SiC/Al (2024) composites, *Scr. Metall. Scr. Metall. Mater.*, 28 (1993) 3, 281–286, doi:10.1016/0956-716X(93)90428-U
- 3 K. C. Chen, C. G. Chao, Effect of  $\delta$  alumina fibers on the aging characteristics of 2024-based metal-matrix composites, *Metall. Mater. Trans. A.*, 26 (1995), 1035–1043, doi:10.1007/BF02670599
- 4 K. Sukumaran, K. K. Ravikumar, S. G. K. Pillai, T. P. D. Rajan, M. Ravi, R. M. Pillai, B. C. Pai, Studies on squeeze casting of Al 2124 alloy and 2124-10% SiCp metal matrix composite, *Mater. Sci. Eng. A.*, 490 (2008), 235–241, doi:10.1016/j.msea.2008.01.054
- 5 J. Peng, D. H. W. Li, J. Du, Y. Xie, G. Liu, Study on the yield behavior of Al<sub>2</sub>O<sub>3</sub>-SiO<sub>2</sub> (sf)/Al-Si metal matrix composites, *Mater. Sci. Eng. A.*, 486 (2008), 427–432, doi:10.1016/j.matchar.2007.08.007
- 6 J. Wang, D. Yi, X. Su, F. Yin, Influence of deformation ageing treatment on microstructure and properties of aluminum alloy 2618, *Mater. Charact.*, 59 (2008), 965–968, doi:10.1016/j.matchar.2007.08.007
- 7 M. Emamy, A. Razaghian, H. R. Lashgari, R. Abbasi, The effect of Al-5Ti-1B on the microstructure, hardness and tensile properties of Al<sub>2</sub>O<sub>3</sub> and SiC-containing metal-matrix composites, *Mater. Sci. Eng. A*, 485 (2008), 210–217, doi:10.1016/j.msea.2007.07.090
- 8 S. C. Sharma, S. Sastry, M. Krishna, Effect of aging parameters on the micro structure and properties of ZA-27/aluminate metal matrix composites, *J. Alloy Compd.*, 346 (2002), 292–301, doi:10.1016/S0925-8388(02)00528-5
- 9 M. P. Thomas, J. E. King, Effect of thermal and mechanical processing on tensile properties of powder formed 2124 aluminium and 2124 Al-SiC<sub>p</sub> metal matrix composite, *Mater. Sci. Technol.*, 9 (1993), 742–753
- 10 S. Suresh, T. Christman, S. Sugimura, Accelerated aging in cast Al alloy-SiC particulate composites, *Scr. Metall. Mater.*, 23 (1989), 1599–1602, doi:10.1016/0036-9748(89)90136-1
- 11 B. Dutta, M. K. Surappa, Age-hardening behaviour of Al-Cu-SiCp composites synthesized by casting route, *Scr. Metall. Mater.*, 32 (1995) 5, 731–736, doi:10.1016/0956-716X(95)91594-F
- 12 V. Massardier, L. Pelletier, P. Merle, Influence of the introduction of ceramic particles in Al-Cu alloys on GP zone formation, *Mater. Sci. Eng. A.*, 2491 (1998), 21–133, doi:10.1016/S0921-5093(98)00577-2
- 13 A. Mazahery, M. O. Shabani, Mechanical properties of squeeze-cast A356 composites reinforced with B<sub>4</sub>C particulates, *JMPEG*, 21 (2011), 247–252, doi:10.1007/s11665-011-9867-6
- 14 I. Sahin, A. A. Eker, Analysis of microstructures and mechanical properties of particle reinforced AlSi<sub>7</sub>Mg<sub>2</sub> matrix composite materials, *JMPEG*, 20 (2010), 1090–1096, doi:10.1007/s11665-010-9738-6
- 15 S. J. Qu, L. Geng, G. J. Cao, T. Q. Lei, Fabricating a 15 vol. %-3.5  $\mu$ m-SiCp/Al composite by a squeeze casting technique, *J. Mater. Sci.*, 39 (2004), 2967–2969, doi:10.1023/B:JMSE.0000021494.55123.e1
- 16 T. Christman, S. Suresh, Microstructural development in aluminum alloy-SiC whisker composite, *Acta Metall.*, 36 (1988) 7, 1691–1704, doi:10.1016/0001-6160(88)90236-2
- 17 C. Badini, F. Marino, E. Verne, Calorimetric study on precipitation path in 2024 alloy and its SiC composite, *Mater. Sci. Eng. A.*, 191 (1995), 185–191, doi:10.1016/0921-5093(94)09637-C
- 18 S. K. Varma, D. Salas, E. Corral, E. Esquivel, K. K. Chawla, R. Mahapatra, Microstructural development during aging of 2014 aluminum alloy composite, *J Mater. Sci.*, 34 (1999), 1855–1863, doi:10.1023/A:1004527729424
- 19 A. P. Sanino, H. J. Rack, Effect of reinforcement size on age hardening of PM 2009 Al-SiC 20 vol% particulate composites, *J. Mater. Sci.*, 30 (1995), 4316–4322, doi:10.1007/BF00361511
- 20 Heat Treatment of Aluminum Alloys, ASM Handbook, 4th ed., ASM International, 1997, 845
- 21 Y. Song, T. N. Baker, Accelerated aging processes in ceramic reinforced AA 6061 composites, *Mater. Sci. & Tech.*, 10 (1994), 406–413, doi:10.1179/mst.1994.10.5.406
- 22 K. Chen, C. Chao, Effect of  $\delta$  alumina fibers on the aging characteristics of 2024-based metal-matrix composites, *Metall. & Mater. Trans. A.*, 26a (1995), 1035–1043, doi:10.1007/BF02670599
- 23 C. M. Friend, S. D. Luxton, The effect of  $\delta$  alumina fibre arrays on the age-hardening characteristics of an Al-Mg-Si alloy, *J. Mater. Sci.*, 23 (1988), 3173–3180, doi:10.1007/BF0055129
- 24 C. P. You, M. Dollar, A. W. Thompson, Microstructure property relationships and hydrogen effects in a particulate-reinforced aluminum composite, *Metall. Trans. A.*, 22 (1991), 2445–2450, doi:10.1007/BF02665010



# MATERIALI IN TEHNOLOGIJE

MATERIALS AND TECHNOLOGY

Letnik / Volume 50 2016

ISSN 1580-2949

© Materiali in tehnologije  
IMT Ljubljana, Lepi pot 11, 1000 Ljubljana, Slovenija

**MATERIALI IN TEHNOLOGIJE / MATERIALS AND TECHNOLOGY****VSEBINA / CONTENTS****LETNIK / VOLUME 50, 2016/1, 2, 3, 4, 5, 6****2016/1****Improvement of the casting of special steel with a wide solid-liquid interface**

Izboljšanje ulivanja posebnega jekla s širokim intervalom trdno-tekoče

T. Mauder, J. Stetina . . . . . 3

**Non-traditional non-destructive testing of the alkali-activated slag mortar during the hardening**

Netradicionalno neporušno preizkušanje z alkalijami aktivirane malte med strjevanjem

L. Topolář, P. Rypák, K. Timčáková-Šamárková, L. Pazdera, P. Rovnaník . . . . . 7

**Multi-walled carbon nanotubes effect in polypropylene nanocomposites**

Vpliv večstenskih ogljikovih nanocevk v nanokompozitih iz polipropilena

C. E. Ban, A. Stefan, I. Dinca, G. Pelin, A. Ficai, E. Andronescu, O. Oprea, G. Voicu . . . . . 11

**Experimental and numerical study of hot-steel-plate flatness**

Eksperimentalni in numerični študij ravnosti vročih plošč iz jekla

J. Hrabovský, M. Pohanka, P. J. Lee, J. H. Kang . . . . . 17

**Investigation of hole effects on the critical buckling load of laminated composite plates**

Preiskava vpliva luknje na kritično upogibno obremenitev laminiranih kompozitnih plošč

A. Kurşun, E. Topal . . . . . 23

**Corrosion of the refractory zirconia metering nozzle due to molten steel and slag**

Korozija ognjeodporne cirkonske dozirne šobe s staljenim jeklom in žlindro

K. Wiśniewska, D. Madej, J. Szczerba . . . . . 29

**Effects of an epoxy-resin-fiber substrate for a  $\Omega$ -shaped microstrip antenna**Vpliv z vlakni ojačane epoksi podlage pri  $\Omega$ -obliki mikrotrakaste antene

Md. M. Islam, M. R. I. Faruque, M. Tariqul Islam, H. Arshad . . . . . 33

**X-ray radiography of AISI 4340-2205 steels welded by friction welding**

Rentgenski pregled jekel AISI 4340-2205, varjenih s trenjem

U. Caligulu, M. Yalcinoz, M. Turkmen, S. Mercan . . . . . 39

**Thermodynamic properties and microstructures of different shape-memory alloys**

Termodinamične lastnosti in mikrostruktura različnih zlitin z oblikovnim spominom

L. Gomidželović, E. Požega, A. Kostov, N. Vuković, D. Živković, D. Manasijević . . . . . 47

**The relationship between thermal treatment of serpentine and its reactivity**

Ovisnost med toplotno obdelavo serpentina in njegovo aktivnostjo

G. Sučik, A. Szabóová, L. Popović, D. Hršak . . . . . 55

**Deformations and velocities during the cold rolling of aluminium alloys**

Defamacija in hitrosti pri hladnem valjanju aluminijevih zlitin

M. Mišović, N. Tadić, M. Jaćimović, M. Janjić . . . . . 59

**Prediction of the chemical non-homogeneity of 30MnVS6 billets with genetic programming**

Napovedovanje nehomogenosti kemijske sestave pri gredicah 30MnVS6 s pomočjo genetskega programiranja

M. Kovačič, D. Novak . . . . . 69

**Effect of the TiBN coating on a HSS drill when drilling the MA8M Mg alloy**

Vpliv TiBN prevleke na HSS svedru pri vrtanju MA8M Mg zlitine

F. Karaca, B. Aksakal . . . . . 75

**Application of the Taguchi method to select the optimum cutting parameters for tangential cylindrical grinding of AISI D3 tool steel**

Uporaba Taguchi metode za izbiro optimalnih parametrov odrezavanja pri tangencialnem cilindričnem brušenju orodnega jekla AISI D3

C. Ozay, H. Ballıkaya, V. Savas . . . . . 81

**Effects of friction-welding parameters on the morphological properties of an Al/Cu bimetallic joint**

Vpliv parametrov tornega varjenja na morfološke lastnosti Al/Cu bimetalnega spoja

V. D. Milašinović, R. V. Radovanović, M. D. Milašinović, B. R. Gligorijević . . . . . 89

**Characterisation of the mechanical and corrosive properties of newly developed glass-steel composites**

Karakterizacija mehanskih in korozijskih lastnosti novo razvitih kompozitov steklo-jeklo

O. Lyubimova, E. Gridasova, A. Gridasov, G. Frieling, M. Klein, F. Walther . . . . . 95

<b>Phase analysis of the slag after submerged-arc welding</b> Analiza faz v žlindri pri obločnem varjenju pod praškom M. Prijanovič Tonkovič, J. Lamut . . . . .	101
<b>Optimizing the parameters for friction welding stainless steel to copper parts</b> Optimiranje parametrov pri tornem varjenju nerjavnega jekla na bakrene dele M. Sahin . . . . .	109
<b>WEDM cutting of Inconel 718 nickel-based superalloy: effects of cutting parameters on the cutting quality</b> WEDM rezanje nikljeve superzlitine Inconel 718: vpliv parametrov rezanja na kvaliteto rezanja U. Çaydaş, M. Ay . . . . .	117
<b>Influence of dredged sediment on the shrinkage behavior of self-compacting concrete</b> Vpliv izkopanih sedimentov na krčenje samozgoščevalnega betona N. E. Bouhamou, F. Mostefa, A. Mebrouki, K. Bendani, N. Belas . . . . .	127
<b>Study of the properties and hygrothermal behaviour of alternative insulation materials based on natural fibres</b> Študij lastnosti in higrotermalno obnašanje alternativnih izolacijskih materialov na osnovi naravnih vlaken J. Zach, M. Reif, J. Hroudová . . . . .	137
<b>Prediction of the elastic moduli of chicken-feather-reinforced PLA and a comparison with experimental results</b> Napovedovanje modulov elastičnosti PLA, ojačanega s piščančjim perjem in primerjava z eksperimentalnimi rezultati U. Özmen, B. Okutan Baba . . . . .	141
<b>Composites based on inorganic matrices for extreme exposure conditions</b> Kompoziti z anorgansko osnovo za izpostavitvev ekstremnim razmeram A. Dufka, T. Melichar . . . . .	147
<b>The effect of EO and steam sterilization on the mechanical and electrochemical properties of titanium Grade 4</b> Vpliv EO in sterilizacije s paro na mehanske in elektrokemijske lastnosti titana Grade 4 M. Basiaga, W. Walke, Z. Paszenda, A. Kajzer . . . . .	153
<b>Influence of the carbide-particle spheroidisation process on the microstructure after the quenching and annealing of 100CrMnSi6-4 bearing steel</b> Vpliv procesa sferoidizacije karbidnih delcev na mikrostrukturo jekla 100CrMnSi6-4 za ležaje po kaljenju in popuščanju J. Dlouhy, D. Hauserova, Z. Novy . . . . .	159
<b>2016/2</b>	
<b>Corrosion behavior and the weak-magnetic-field effect of aluminum packaging paper</b> Vpliv šibkega magnetnega polja na korozijo aluminijeve embalažne folije N. Zazi, J.-P. Chopart, A. Bilek . . . . .	165
<b>Characteristics of the AlTiCrN+DLC coating deposited with a cathodic arc and the PACVD process</b> Značilnosti AlTiCrN+DLC prevleke, nanešene s katodnim oblokom in PACVD postopkom K. Lukaszowicz, E. Jonda, J. Sondor, K. Balin, J. Kubacki . . . . .	175
<b>Implicit numerical multidimensional heat-conduction algorithm parallelization and acceleration on a graphics card</b> Paralelizacija in pospešitev implicitnega numeričnega večdimenzijskega algoritma prevajanja toplote na grafični kartici M. Pohanka, J. Ondroušková . . . . .	183
<b>Magnetic properties and microstructure of a bulk amorphous Fe<sub>61</sub>Co<sub>10</sub>Ti<sub>3</sub>Y<sub>6</sub>B<sub>20</sub> alloy, fabricated as rods and tubes</b> Magnetne lastnosti in mikrostruktura masivne amorfne zlitine Fe <sub>61</sub> Co <sub>10</sub> Ti <sub>3</sub> Y <sub>6</sub> B <sub>20</sub> v obliki palic in cevi M. Nabałek, K. Bloch, K. Szlązak, M. Szota . . . . .	189
<b>Effect of the skin-core morphology on the mechanical properties of injection-moulded parts</b> Vpliv morfologije skorja-jedro na mehanske lastnosti vbrizganih delov E. Hnatkova, Z. Dvorak . . . . .	195
<b>Recrystallization behaviour of a nickel-based superalloy</b> Obnašanje superzlitine na osnovi niklja pri rekristalizaciji P. Podany, Z. Novy, J. Dlouhy . . . . .	199
<b>Estimation of the number of forward time steps for the sequential Beck approach used for solving inverse heat-conduction problems</b> Ugotavljanje števila vnaprejšnjih časovnih korakov za sekvenčni Beckov približek pri reševanju problemov inverzne toplotne prevodnosti J. Komínek, M. Pohanka . . . . .	207
<b>Enhanced stability and electrochemical performance of a BaTiO<sub>3</sub>/PbO<sub>2</sub> electrode via a layer obtained with layer electrodeposition</b> Izboljšana stabilnost in elektrokemijska zmogljivost elektrode BaTiO <sub>3</sub> /PbO <sub>2</sub> , izdelane z elektrodepozicijo plast na plast G. Muthuraman, K. Karunakaran, I. S. Moon . . . . .	211
<b>Deformation behaviour of amorphous Fe-Ni-W/Ni bilayer-confined bulk metallic glasses</b> Obnašanje deformiranega, amorfnega, na dve plasti omejenega kovinskega stekla Fe-Ni-W/Ni H. K. Lau, N. Yip, S. H. Chen, W. Chen, K. C. Chan . . . . .	217
Materiali in tehnologije / Materials and technology 50 (2016) 6, 1017–1040	1019

<b>Synergistic effect of organic- and ceramic-based ingredients on the tribological characteristics of brake friction materials</b> Sinergističen vpliv sestavin z organsko in keramično osnovo na tribološke značilnosti materialov za torne zavore R. Ertan .....	223
<b>Optimization of the parameters for the surfactant-added EDM of a Ti–6Al–4V alloy using the GRA-Taguchi method</b> Optimizacija površinsko aktivnih mešanih EDM parametrov na Ti-6Al-4V zlitini z uporabo GRA-Taguchi metode M. Kollı, K. Adepu .....	229
<b>Determination of the cutting-tool performance of high-alloyed white cast iron (Ni-Hard 4) using the Taguchi method</b> Določanje zmogljivosti rezalnih orodij na močno legiranem belem litem železu (Ni-Hard 4) z uporabo Taguchi metode D. Kir, H. Öktem, M. Çöl, F. Gül Koç, F. Erzincanlı .....	239
<b>Use of the ABI technique to measure the mechanical properties of aluminium alloys: effect of chemical composition on the mechanical properties of the alloys</b> Uporaba tehnike ABI za merjenje mehanskih lastnosti aluminijevih zlitin: vpliv kemijske sestave na mehanske lastnosti zlitin M. Puchnin, O. Trudonoshyn, O. Prach .....	247
<b>Fe-Zn intermetallic phases prepared by diffusion annealing and spark-plasma sintering</b> Fe-Zn intermetalne faze, pripravljene z difuzijskim žarjenjem in s sintranjem v iskreči plazmi P. Pokorný, J. Cinert, Z. Pala .....	253
<b>High-temperature oxidation of silicide-aluminide layer on the TiAl6V4 alloy prepared by liquid-phase siliconizing</b> Visokotemperaturna oksidacija plasti silicid-aluminid, pripravljene s silikoniziranjem s tekočo fazo zlitine TiAl6V4 T. F. Kubatık .....	257
<b>Characterization and kinetics of plasma-paste-borided AISI 316 steel</b> Karakterizacija in kinetika plazma boriranja s pasto jekla AISI 316 R. Chegroune, M. Keddou, Z. Nait Abdellah, S. Ulker, S. Taktak, I. Gunes .....	263
<b>Investigation of the adhesion and wear properties of borided AISI H10 steel</b> Preiskava adhezije in obrabnih lastnosti boriranega jekla AISI H10 I. Gunes, M. Ozcatıl .....	269
<b>The effects of cutting conditions on the cutting torque and tool life in the tapping process for AISI 304 stainless steel</b> Vpliv pogojev rezanja na moment pri rezanju in zdržljivost navojnega vreznika pri vrezovanju notranjih navojev v nerjavno jeklo AISI 304 G. Uzun, I. Korkut .....	275
<b>Chemical synthesis and densification behavior of Ag/ZnO metal-matrix composites</b> Obnašanje Ag/ZnO kompozita s kovinsko osnovo pri kemijski sintezi in zgoščevanju M. Ardestani .....	281
<b>2016/3</b>	
<b>Experimental verifications and numerical thermal simulations of automobile lamps</b> Eksperimentalna preverjanja in numerične toplotne simulacije avtomobilskih žarometov M. Guzej, J. Horský .....	289
<b>Tensile and compressive tests of textile composites and results analysis</b> Natezni in tlačni preizkusi tekstilnih kompozitov in analiza rezultatov K. Kunc, T. Kroupa, R. Zemčík, J. Krystek .....	295
<b>Deformation behaviour of a natural-shaped bone scaffold</b> Obnašanje naravno oblikovanega ogrodja kosti pri deformaciji D. Kytýř, T. Doktor, O. Jiroušek, T. Fíla, P. Koudelka, P. Zlámal .....	301
<b>Printed microstrip line-fed patch antenna on a high-dielectric material for C-band applications</b> Tiskana mikrotrakasta linijsko napajana krpasta antena na visoko dielektričnem materialu za uporabo v C-pasu Md. M. Islam, M. R. I. Faruque, M. F. Mansor, M. T. Islam .....	307
<b>Compressive properties of auxetic structures produced with direct 3D printing</b> Stiskanje struktur materialov z negativnim Poissonovim razmerjem, proizvedenih z neposrednim tridimenzionalnim tiskanjem P. Koudelka, O. Jiroušek, T. Fíla, T. Doktor .....	311
<b>Model of progressive failure for composite materials using the 3D Puck failure criterion</b> Model postopnega popuščanja kompozitnega materiala z uporabo Puckovega tridimenzionalnega kriterija porušitve L. Bek, R. Zemčík .....	319
<b>Physicochemical properties of a Ti67 alloy after EO and steam sterilization</b> Fizikalno kemijske lastnosti zlitine Ti67 po EO in parni sterilizaciji W. Walke, M. Basiaga, Z. Paszenda, J. Marciniak, P. Karasinski .....	323
<b>Surface properties of a laser-treated biopolymer</b> Lastnosti površine biopolimera, obdelanega z laserjem I. Michaljaničová, P. Slepíčka, S. Rimpelová, P. Sajdl, V. Švorčík .....	331
<b>Analyzing the heat-treatment effect on the mechanical properties of free-cutting steels</b> Analiza vpliva toplotne obdelave na mehanske lastnosti avtomatnih jekel M. K. Kulekci, U. Esme, F. Kahraman, R. Ozgun, A. Akkurt .....	337



<b>Analysis of the cutting temperature and surface roughness during the orthogonal machining of AISI 4140 alloy steel via the Taguchi method</b>	
Analiza temperature rezanja in hrapavosti površine s Taguchi metodo pri ortogonalni strojni obdelavi legiranega jekla AISI 4140	
A. R. Motorcu, Y. Isik, A. Kus, M. C. Cakir . . . . .	343
<b>Weldability of Ti6Al4V to AISI 2205 with a nickel interlayer using friction welding</b>	
Preizkušanje varivosti pri varjenju s trenjem Ti6Al4V in AISI 2205 z vmesno plastjo niklja	
I. Kirik . . . . .	353
<b>Effect of activated flux and nitrogen addition on the bead geometry of borated stainless-steel GTA welds</b>	
Vpliv aktiviranega topila in dodatka dušika na geometrijo kopeli pri GTA zvarih boriranega nerjavnega jekla	
G. R. Kumar, G. D. J. Ram, S. R. Koteswara Rao . . . . .	357
<b>Microstructural evolution during the transient liquid-phase bonding of dissimilar nickel-based superalloys of IN738LC and NIMONIC 75</b>	
Razvoj mikrostrukture med spajanjem s prehodno tekočo fazo neenakih superzlitin na osnovi niklja IN738LC in NIMONIC 75	
M. G. Khakian, S. Nategh, S. Mirdamadi . . . . .	365
<b>Workability behaviour of Cu-TiB<sub>2</sub> powder-metallurgy preforms during cold upsetting</b>	
Preoblikovalnost Cu-TiB <sub>2</sub> predoblik izdelanih z metalurgijo prahov med hladnim kovalnim preizkusom	
S. Gadakary, A. Kumar Khanra, M. J. Davidson . . . . .	373
<b>Effects of extrusion shear on the microstructures and a fracture analysis of a magnesium alloy in the homogenized state</b>	
Vplivi striženja med iztiskanjem homogenizirane magnezijeve zlitine na mikrostrukturo in na analizo preloma	
H. J. Hu, Z. Sun, D. F. Zhang . . . . .	381
<b>FSW welding of Al-Mg alloy plates with increased edge roughness using square pin tools of various shoulder geometries</b>	
FSW varjenje plošč iz Al-Mg zlitine s povečano hrapavostjo robov z orodjem s kvadratno konico in različno geometrijo bokov	
S. Balos, L. Sidjanin, M. Dramicanin, D. Labus Zlatanovic, A. Antic . . . . .	387
<b>Improvement of selective copper extraction from a heat-treated chalcopyrite concentrate with atmospheric sulphuric-acid leaching</b>	
Izboljšanje selektivne ekstrakcije bakra iz toplotno obdelanega koncentrata halkopirita z luženjem z žvepleno kislino na zraku	
E. Uzun, M. Zengin, İ. Atilgan . . . . .	395
<b>Homogenization of an Al-Mg alloy and alligating failure: alloy ductility and fracture</b>	
Homogenizacija Al-Mg zlitine in krokodiljenje: duktilnost zlitine in prelom	
E. Romhanji, T. Radetić, M. Popović . . . . .	403
<b>Assessment of tubular light guides with respect to building physics</b>	
Ocena cevastih vodnikov svetlobe glede na gradbeno fiziko	
F. Vajkay, D. Bečkovský, V. Tichomirov . . . . .	409
<b>Creep behaviour of a short-fibre C/PPS composite</b>	
Vedenje kratkih vlaken C/PPS kompozitov pri lezenju	
T. Fíla, P. Koudelka, D. Kytýř, J. Hos, J. Šleichrt . . . . .	413
<b>Increasing micro-purity and determining the effects of the production with and without vacuum refining on the qualitative parameters of forged-steel pieces with a high aluminium content</b>	
Povečanje mikročistoče in določitev učinka proizvodnje, z vakuumskim rafiniranjem ali brez, na kvalitativne parametre kovanega jekla z visoko vsebnostjo aluminija	
V. Kurka, J. Pindor, J. Kosňovská, Z. Adolf . . . . .	419
<b>Use of the ABI technique to measure the mechanical properties of aluminium alloys: effect of heat-treatment conditions on the mechanical properties of alloys</b>	
Uporaba ABI tehnike za merjenje mehanskih lastnosti aluminijevih zlitin: vpliv pogojev toplotne obdelave na mehanske lastnosti zlitin	
O. Trudonoshyn, M. Puchnin, O. Prach . . . . .	427
<b>Investigation of the effect of holding time and melt stirring on the grain refinement of an A206 alloy</b>	
Preiskava vpliva časa zadrževanja in mešanja taline na zmanjšanje velikosti zrn zlitine A206	
N. Akar, Z. Tanyel, K. Kocatepe, R. Kayikci . . . . .	433
<b>Investigating the influence of cutting speed on the tool life of a cutting insert while cutting DIN 1.4301 steel</b>	
Preiskava vpliva hitrosti rezanja na zdržljivost vložka za rezanje pri rezanju jekla DIN 1.4301	
R. Dubovská, J. Majerfk, R. Čep, K. Kouřil . . . . .	439
<b>NiAl intermetallic prepared with reactive sintering and subsequent powder-metallurgical plasma-sintering compaction</b>	
Reakcijsko sintranje in zgoščevanje s plazemskim sintranjem NiAl intermetalne zlitine	
A. Michalcová, D. Vojtěch, T. F. Kubatík, P. Novák, P. Dvořák, P. Svobodová, I. Marek . . . . .	447
<b>Microscopic characterization and particle distribution in a cast steel matrix composite</b>	
Mikroskopska karakterizacija in razporeditev delcev v kompozitu z matrico litega jekla	
A. Kračun, M. Torkar, J. Burja, B. Podgornik . . . . .	451
<b>A comparison of as-welded and simulated heat affected zone (HAZ) microstructures</b>	
Primerjava mikrostrukture toplotno vplivanega področja varjenega in simuliranih vzorcev	
R. Celin, J. Burja, G. Kosec . . . . .	455
Materiali in tehnologije / Materials and technology 50 (2016) 6, 1017–1040	1021

<b>Degradation of an AISI 304 stainless-steel tank</b> Degradacija rezervoarja iz AISI 304 nerjavnega jekla M. Torkar, I. Paulin, B. Podgornik. . . . .	461
<b>2016/4</b>	
<b>Predgovor urednika/Editor's preface</b> Matjaž Torkar . . . . .	469
<b>Organosoluble xanthone-based polyimides: synthesis, characterization, antioxidant activity and heavy-metal sorption</b> Organsko topni poliamidi na osnovi ksantona: sinteza, karakterizacija, antioksidativna aktivnost in sorpcija težkih kovin M. M. Lakouraj, G. Rahpaima, R. Azimi . . . . .	471
<b>Correlation of the heat-transfer coefficient at sprinkled tube bundle</b> Korelacija koeficienta prenosa toplote pri potresenem snopu cevi P. Kracik, L. Šnajdárek, M. Lisý, M. Baláš, J. Pospíšil. . . . .	479
<b>Mathematical modeling of a cement raw-material blending process using a neural network</b> Matematično modeliranje postopka mešanja sestavin cementa s pomočjo nevronske mreže A. Egrisogut Tiryaki, R. Kozan, N. Gokhan Adar . . . . .	485
<b>Possibilities of determining the air-pore content in cement composites using computed tomography and other methods</b> Možnosti določanja vsebnosti zračnih por v cementnih kompozitih z uporabo računalniške tomografije in drugih metod B. Moravcová, P. Pössl, P. Misák, M. Blažek. . . . .	491
<b>Material and technological modelling of closed-die forging</b> Materialno-tehnološko modeliranje kovanja v zaprtem utopu I. Vorel, Š. Jeníček, H. Jirková, B. Mašek . . . . .	499
<b>Investigation of wear behavior of borided AISI D6 steel</b> Preiskava obrabe boriranega jekla AISI D6 I. Gunes, S. Kanat. . . . .	505
<b>Investigation of Portevin-Le Chatelier effect of hot-rolled Fe-13Mn-0.2C-1Al-1Si TWIP steel</b> Preiskava Portevin-Le Chatelier učinka pri vročem valjanju Fe-13Mn-0.2C-1Al-1Si TWIP jekla B. Aydemir, H. Kazdal Zeytin, G. Guven. . . . .	511
<b>The influence of surface coatings on the tooth tip deflection of polymer gears</b> Vpliv površinskih prevlek na povse vrha zoba polimernih zobnikov B. Trobentar, S. Glodež, J. Flašker, B. Zafošnik. . . . .	517
<b>Vapour-phase condensed composite materials based on copper and carbon</b> Kompoziti na osnovi bakra in ogljika, kondenzirani iz plinske faze V. Bukhanovsky, M. Rudnytsky, M. Grechanyuk, R. Minakova, C. Zhang . . . . .	523
<b>Homogenization of an Al-Mg alloy and alligating failure: influence of the microstructure</b> Homogenizacija Al-Mg zlitine in krokodiljenje: vpliv mikrostrukture E. Romhanji, T. Radetić, M. Popović. . . . .	531
<b>Metal particles size influence on graded structure in composite Al<sub>2</sub>O<sub>3</sub>-Ni</b> Vpliv velikosti kovinskih delcev na gradientno strukturo kompozita Al <sub>2</sub> O <sub>3</sub> -Ni J. Zyguntowicz, A. Miazga, K. Konopka, W. Kaszuwara . . . . .	537
<b>Static and dynamic tensile characteristics of S420 and IF steel sheets</b> Statične in dinamične natezne lastnosti pločevine iz S420 in IF jekla M. Mihaliková, V. Girman, A. Lišková . . . . .	543
<b>Acoustic and electromagnetic emission of lightweight concrete with polypropylene fibers</b> Akustična in elektromagnetna emisija lahkega betona s polipropilenskimi vlakni R. Štoudek, T. Trčka, M. Matysík, T. Vymazal, I. Plšková . . . . .	547
<b>Multi-criteria analysis of synthesis methods for Ni-based catalysts</b> Večkriterijska analiza sinteznih metod na osnovi Ni katalizatorja V. Nikolić, B. Agarski, Ž. Kamberović, Z. Anđić, I. Budak, B. Kosec . . . . .	553
<b>Influence of structural defects on the magnetic properties of massive amorphous Fe<sub>60</sub>Co<sub>10</sub>Mo<sub>2</sub>W<sub>x</sub>Y<sub>8</sub>B<sub>20-x</sub> (x = 1, 2) alloys produced with the injection casting method</b> Vpliv strukturnih napak na magnetne lastnosti masivne amorfne zlitine Fe <sub>60</sub> Co <sub>10</sub> Mo <sub>2</sub> W <sub>x</sub> Y <sub>8</sub> B <sub>20-x</sub> (x = 1, 2), izdelane z metodo litja z vbrizgavanjem J. Gondro, K. Bloch, M. Nabiałek, S. Garus . . . . .	559
<b>Possibilities of NUS and Impact-Echo methods for monitoring steel corrosion in concrete</b> Možnosti metod NUS in Udarec-odmev za kontrolo korozije jekla v betonu K. Timčaková-Šamárková, M. Matysík, Z. Chobola . . . . .	565
<b>Characterization of heterogeneous arc welds through miniature tensile testing and Vickers-hardness mapping</b> Karakterizacija heterogenih zvarov s pomočjo miniaturnih nateznih preizkusov in matričnimi meritvami trdote po Vickersu S. Hertelé, J. Bally, N. Gubeljak, P. Štefane, P. Verleysen, W. De Waele. . . . .	571

<b>Overcooling in overlap areas during hydraulic descaling</b> Podhladitev in prekrivanje področij med hidravličnim razškajanjem M. Pohanka, H. Votavová . . . . .	575
<b>Investigation of the mechanical properties of a cork/rubber composite</b> Raziskava mehanskih lastnosti kompozita pluta/guma R. Kottner, J. Kocáb, J. Heczko, J. Krystek . . . . .	579
<b>Fabrication and properties of SiC reinforced copper-matrix-composite contact material</b> Izdelava in lastnosti s SiC utrjenega kompozitnega materiala na osnovi bakra G. F. Celebi Efe, M. İpek, S. Zeytin, C. Bindal . . . . .	585
<b>Investigation of the cutting forces and surface roughness in milling carbon-fiber-reinforced polymer composite material</b> Preiskava sil rezanja in hrapavosti površine pri rezkanju kompozitnega polimernega materiala, ojačanega z ogljikovimi vlakni S. Bayraktar, Y. Turgut . . . . .	591
<b>Development of aluminium alloys for aerosol cans</b> Razvoj aluminijevih zlitin za aerosol doze S. Kores, J. Turk, J. Medved, M. Vončina . . . . .	601
<b>Computer tools to determine physical parameters in wooden houses</b> Določanje fizikalnih parametrov z računalniškimi orodji v lesenih hišah D. Bečkovský, F. Vajkay, V. Tichomirov . . . . .	607
<b>Impression relaxation and creep behavior of Al/SiC nanocomposite</b> Sprostitev vtisa in obnašanje Al/SiC nanokompozita pri lezenju Y. S. Kakhki, S. Nategh, T. S. Mirdamadi . . . . .	611
<b>Microstructure and properties of the high-temperature (HAZ) of thermo-mechanically treated S700MC high-yield-strength steel</b> Mikrostruktura in lastnosti visoko temperaturnega območja zvara (HAZ) termo-mehansko obdelanega jekla S700MC z visoko mejo plastičnosti J. Górká . . . . .	617
<b>New concept for manufacturing closed die forgings of high strength steels</b> Nov koncept izdelave odkovkov iz visokotrnostnih jekel v zaprtih utopih K. Ibrahim, I. Vorel, D. Publíková, B. Mašek . . . . .	623
<b>Helium atom scattering – a versatile technique in studying nanostructures</b> Sipanje atomov helija – vsestranska tehnika za študij nanostruktur G. Bavdek, D. Cvetko . . . . .	627
<b>2016/5</b>	
<b>Predgovor urednika/Editor's preface</b> P. J. McGuinness . . . . .	639
<b>Effect of the addition of niobium and aluminium on the microstructures and mechanical properties of micro-alloyed PM steels</b> Vpliv dodatka niobija in aluminija na mikrostrukturo in mehanske lastnosti mikrolegiranih PM jekel S. Gündüz, M. A. Erden, H. Karabulut, M. Türkmen . . . . .	641
<b>Characteristics of dye-sensitized solar cells with carbon nanomaterials</b> Značilnosti na fiksirano barvo občutljivih solarnih celic z ogljikovimi nanomateriali L. A. Dobrzański, A. Mucha, M. Prokopiuk vel Prokopowicz, M. Szindler, A. Drygała, K. Lukaszkoicz . . . . .	649
<b>The effect of the welding parameters and the coupling agent on the welding of composites</b> Vpliv parametrov varjenja in sredstva za spajanje na varjenje kompozitov S. E. Erdogan, U. Huner . . . . .	655
<b>Chemical cross-linking of chitosan/polyvinyl alcohol electrospun nanofibers</b> Kemijsko zamreženje elektro spredeni nanovlaken iz hitosan/polivinil alkohola S. Pouranvari, F. Ebrahimi, G. Javadi, B. Maddah . . . . .	663
<b>Investigation of hole profiles in deep micro-hole drilling of AISI 420 stainless steel using powder-mixed dielectric fluids</b> Preiskava profilov luknje pri globokem vrtnanju mikroluknje v AISI 420 nerjavnem jeklu s pomočjo dielektrične tekočine s primešanim prahom V. Yılmaz . . . . .	667
<b>The phenomenon of reduced plasticity in low-alloyed copper</b> Pojav zmanjšanja plastičnosti malo legiranega bakra W. Ozgowicz, E. Kalinowska-Ozgowicz, B. Grzegorzcyk, K. Lenik . . . . .	677
<b>The effect of high-speed grinding technology on the properties of fly ash</b> Vpliv tehnologije hitrega mletja na lastnosti letečega pepela K. Dvořák, I. Hájková . . . . .	683
<b>Investigation of the mechanical properties of electrochemically deposited Au-In alloy films using nano-indentation</b> Preiskava mehanskih lastnosti elektrokemijsko nanešenega filma zlitine Au-In z nanovtiskovanjem S. Cherneva, R. Iankov, M. Georgiev, T. Dobrovolska, D. Stoychev . . . . .	689
Materiali in tehnologije / Materials and technology 50 (2016) 6, 1017–1040	1023

<b>Growth of K<sub>2</sub>CO<sub>3</sub>-doped KDP crystal from an aqueous solution and an investigation of its physical properties</b> Rast KDP kristalov z dodatkom K <sub>2</sub> CO <sub>3</sub> iz vodne raztopine in preiskava njihovih fizikalnih lastnosti A. Roust, H. R. Dizaji .....	695
<b>Surface treatment of heat-treated cast magnesium and aluminium alloys</b> Obdelava površine toplotno obdelanih magnezijevih in aluminijevih livnih zlitin T. Tański, M. Wiśniowski, W. Matysiak, M. Staszuk, R. Szklarek .....	699
<b>Analysis of the structural-defect influence on the magnetization process in and above the Rayleigh region</b> Analiza vpliva strukturnih defektov na proces magnetizacije v in nad Rayleigh področjem K. Gruszka .....	707
<b>Effect of sulphide inclusions on the pitting-corrosion behaviour of high-Mn steels in chloride and alkaline solutions</b> Vpliv sulfidnih vključkov na jamičasto korozijo jekel z visoko vsebnostjo Mn v raztopinah kloridov in alkalij A. Grajcar, A. Plachcińska .....	713
<b>Influence of Na<sub>2</sub>SiF<sub>6</sub> on the surface morphology and corrosion resistance of an AM60 magnesium alloy coated by micro arc oxidation</b> Vpliv Na <sub>2</sub> SiF <sub>6</sub> na morfologijo površine in korozijsko odpornost magnezijeve zlitine AM60, prekrte z mikrooblačno oksidacijo A. Ayday .....	719
<b>Mechanical properties of polyamide/carbon-fiber-fabric composites</b> Mehanske lastnosti kompozitne tkanine iz poliamid/ogljikovih vlaken C.-E. Pelin, G. Pelin, A. Ștefan, E. Andronescu, I. Dincă, A. Ficăi, R. Trușcă .....	723
<b>Evaluation of the grindability of recycled glass in the production of blended cements</b> Ocena sposobnosti drobljenja recikliranega stekla pri proizvodnji mešanih cementov K. Dvořák, D. Dolák, D. Všíanský, P. Dobrovolný .....	729
<b>Rheological properties of alumina ceramic slurries for ceramic shell-mould fabrication</b> Reološke lastnosti gošče iz glinice za izdelavo keramičnih kalupov J. Szymańska, P. Wiśniewski, M. Małek, J. Mizera .....	735
<b>Effect of mechanical activation on the synthesis of a magnesium aluminate spinel</b> Vpliv mehanske aktivacije na sintezo magnezij-aluminatnega špinela D. Kirsever, N. K. Karabulut, N. Canikoğlu, H. Ö. Toplan .....	739
<b>Phase and microstructure development of LSCM perovskite materials for SOFC anodes prepared by the carbonate-coprecipitation method</b> Razvoj kristalnih faz in mikrostrukture LSCM perovskitnih materialov za SOFC anode, pripravljenih s karbonatno metodo koprecipitacije K. Zupan, M. Marinšek, T. Skalar .....	743
<b>Artificial aggregate from sintered coal ash</b> Umetni agregat iz sintranega pepela premoga V. Cerny, R. Drochytka .....	749
<b>Investigation studies involving wear-resistant ALD/PVD hybrid coatings on sintered tool substrates</b> Preiskave obrabne odpornosti hibridnega nanosa ALD/PVD na sintranem orodju M. Staszuk, D. Pakuła, T. Tański .....	755
<b>Dissimilar spot welding of DQSK/DP600 steels: the weld-nugget growth</b> Točkasto varjenje jekel DQSK/DP600: rast jedra zvara S. P. Hoveida Marashi .....	761
<b>Armour plates from Kozlov rob – analyses of two unusual finds</b> Oklepni plošči s Kozlovega roba – analize dveh nenavadnih najdb T. Lazar, P. Mrvar, M. Lamut, P. Fajfar .....	767
<b>Numerical and experimental investigation of the effect of hydrostatic pressure on the residual stress in boiler-tube welds</b> Numerična in eksperimentalna preiskava vpliva hidrostatskega tlaka na zaostale napetosti v zvaru na kotlovski cevi D. Danyali, E. Ranjbarneh .....	775
<b>Effect of direct cooling conditions on the microstructure and properties of hot-forged HSLA steels for mining applications</b> Vpliv pogojev ohlajanja na mikrostrukturo in lastnosti vroče kovanih HSLA jekel za uporabo v rudarstvu P. Skubisz, Ł. Lisiecki, T. Skowronek, A. Żak, W. Zalecki .....	783
<b>Influence of the tool rotational speed on the microstructure and joint strength of friction-stir spot-welded pure copper</b> Vpliv hitrosti vrtenja orodja na mikrostrukturo in trdnost torno vrtilno točkasto zvarjenega spoja čistega bakra I. Dinaharan, E. T. Akinlabi .....	791
<b>Measurement of bio-impedance on an isolated rat sciatic nerve obtained with specific current stimulating pulses</b> Meritev bioimpedance na izoliranem živcu Ischiadicus pri podgani, vzbujenem s posebnimi tokovnimi stimulacijskimi impulzi J. Rozman, M. C. Žužek, R. Frangež, S. Ribarič .....	797
<b>Influence of different production processes on the biodegradability of an FeMn17 alloy</b> Vpliv različnih procesov izdelave na biorazgradljivost zlitine FeMn17 A. Kocijan, I. Paulin, Č. Donik, M. Hočevar, K. Zelič, M. Godec .....	805



<b>Effect of a combination of fly ash and shrinkage-reducing additives on the properties of alkali-activated slag-based mortars</b> Vpliv kombinacije letečega pepela in dodatka za zmanjšanje krčenja na lastnosti malte iz z alkalijami aktivirane žindre V. Bílek, L. Kalina, J. Koplík, M. Mončeková, R. Novotný . . . . .	813
<b>Cutting-tool performance in the end milling of carbon-fiber-reinforced plastics</b> Zmogljivost rezilnega orodja pri rezkanju plastike, ojačane z ogljikovimi vlakni O. Bílek, S. Rusnáková, M. Žaludek . . . . .	819
<b>Influence of solidification speed on the structure and magnetic properties of Nd<sub>10</sub>Fe<sub>81</sub>Zr<sub>1</sub>B<sub>6</sub> in the as-cast state</b> Vpliv hitrosti strjevanja na strukturo in magnetne lastnosti zlitine Nd <sub>10</sub> Fe <sub>81</sub> Zr <sub>1</sub> B <sub>6</sub> v litem stanju M. Došpiał, M. Nabiałek . . . . .	823
<b>Metalografska preiskava in korozijska odpornost zvarov feritnega nerjavnega jekla</b> Metallographic investigation and corrosion resistance of welds of ferritic stainless steels M. Torkar, A. Kocijan, R. Celin, J. Burja, B. Podgornik . . . . .	829
<b>2016/6</b>	
<b>The microstructure of metastable austenite in X5CrNi18-10 steel after its strain-induced martensitic transformation</b> Mikrostruktura metastabilnega avstenita po pretvorbi v napetostno inducirani martenit v jeklu X5CrNi18-10 A. Kurc-Lisiecka, W. Ozgowicz, E. Kalinowska-Ozgowicz, W. Maziarz . . . . .	837
<b>The structure and morphology of the surface of duplex layers after saturation of the base layer with carbon</b> Struktura in morfologija površine dupleks plasti po nasičenju osnovne plasti z ogljikom W. Skoneczny . . . . .	845
<b>Modeling of shot-peening effects on the surface properties of a (TiB + TiC)/Ti-6Al-4V composite employing artificial neural networks</b> Modeliranje vpliva hladnega površinskega kovanja na lastnosti površine (TiB + TiC)/Ti-6Al-4V kompozita s pomočjo umetnih nevronske mreže E. Maleki, A. Zabihollah . . . . .	851
<b>Analysis of twin-roll casting AA8079 alloy 6.35-<math>\mu</math>m foil rolling process</b> Analiza procesa valjanja 6,35 $\mu$ m folije iz zlitine AA8079 ulite med dvema valjema A. Can, H. Arikán, K. Çınar . . . . .	861
<b>Antimicrobial modification of polypropylene with silver nanoparticles immobilized on zinc stearate</b> Protimikrobno spreminjanje polipropilena z nanodelci srebra, imobiliziranih na cinkovem stearatu G. Jandikova, P. Holcapkova, M. Hrabalikova, M. Machovsky, V. Sedlarik . . . . .	869
<b>A new wideband negative-refractive-index metamaterial</b> Novi širokopasovni metamaterial z negativnim lomnim količnikom S. S. Islam, M. R. Iqbal Faruque, M. J. Hossain, M. T. Islam . . . . .	873
<b>Evaluation of the degree of degradation using the impact-echo method in civil engineering</b> Ocena stopnje degradacije v gradbeništvu z uporabo metode odmeva zvočnih valov D. Štefková, K. Timčáková, L. Topolář, P. Cikrle . . . . .	879
<b>Non-traditional whiteware based on calcium aluminate cement</b> Netradicionalni porcelan na osnovi kalcij aluminatnega cementa R. Sokolar . . . . .	885
<b>Behaviour of new ODS alloys under single and multiple deformation</b> Obnašanje novih ODS zlitin pri enojni in večkratni deformaciji B. Mašek, O. Khalaj, Z. Nový, T. Kubina, H. Jirkova, J. Svoboda, C. Štádlér . . . . .	891
<b>Electromagnetic-shielding effectiveness and fracture behavior of laminated (Ni-NiAl<sub>3</sub>) composites</b> Učinkovitost elektromagnetne zaščite in obnašanje pri lomu laminiranega kompozita (Ni-NiAl <sub>3</sub> ) T. Yener, S. C. Yener, S. Zeytin . . . . .	899
<b>Effect of thermomechanical treatment on the intergranular corrosion of Al-Mg-Si-Type alloy bars</b> Vpliv termomehanske predelave na interkristalno korozijo palic iz zlitin Al-Mg-Si P. Sláma, J. Nacházal . . . . .	903
<b>Valorization of brick wastes in the fabrication of concrete blocks</b> Ocena odpadkov iz opeke pri proizvodnji betonskih zidakov Y. Ghernouti, B. Rabehi, T. Bouziani, R. Chaid . . . . .	911
<b>Porous magnesium alloys prepared by powder metallurgy</b> Porozne magnezijeve zlitine, izdelane s pomočjo metalurgije prahov P. Salvetr, P. Novák, D. Vojtěch . . . . .	917
<b>Influence of nano-sized cobalt oxide additions on the structural and electrical properties of nickel-manganite-based NTC thermistors</b> Vpliv dodatka nanodelcev kobaltovega oksida na zgradbo in električne lastnosti NTC termistorjev na osnovi nikljevega manganita G. Hardal, B. Y. Price . . . . .	923

<b>Durability of alumina silicate concrete based on slag/fly-ash blends against acid and chloride environments</b> Zdržljivost betona na osnovi glinice in silikatov iz mešanice žlindra/leteči pepel na kislino in kloridno okolje R. Gopalakrishnan, K. Chinnaraju . . . . .	929
<b>The size effect of heat-transfer surfaces on boiling</b> Vpliv velikosti površin, ki prenašajo toploto na vrenje P. Kracik, M. Balas, M. Lisy, J. Pospíšil . . . . .	939
<b>Effect of gas atmosphere on the non-metallic inclusions in laser-welded trip steel with Al and Si additions</b> Vpliv plinske atmosfere na nekovinske vključke v lasersko varjenem trip jeklu z dodatkom Al in Si A. Grajcar, M. Róžański, M. Kamińska, B. Grzegorzczak . . . . .	945
<b>Machining parameters influencing in electro chemical machining on AA6061 MMC</b> Parametri strojne obdelave, ki vplivajo na elektrokemijsko strojno obdelavo AA6061 MMC C. J. Thankaraj Mariapushpam, D. Ravindran, M. D. Anand . . . . .	951
<b>Modeling the deep drawing of an AISI 304 stainless-steel rectangular cup using the finite-element method and an experimental validation</b> Modeliranje globokega vleka pravokotne čaše iz AISI 304 nerjavnega jekla z metodo končnih elementov in z eksperimentalnim preverjanjem B. Sener, H. Kurtaran . . . . .	961
<b>Surface and anticorrosion properties of hydrophobic and hydrophilic TiO<sub>2</sub> coatings on a stainless-steel substrate</b> Površinske in protikorozijske lastnosti hidrofobnih in hidrofilnih TiO <sub>2</sub> prevlek na jekleni podlagi M. Conradi, A. Kocijan . . . . .	967
<b>Electroslag remelting: A process overview</b> Elektropretaljevanje pod žlindro – pregled procesa B. Arh, B. Podgornik, J. Burja . . . . .	971
<b>Continuous vertical casting of a NiTi alloy</b> Vertikalno kontinuirno litje NiTi zlitine A. Stambolić, I. Anžel, G. Lojen, A. Kocijan, M. Jenko, R. Rudolf . . . . .	981
<b>Hot tensile testing of SAF 2205 duplex stainless steel</b> Vročni natezni preskusi dupleks nerjavnega jekla SAF 2205 F. Tehovnik, B. Žužek, J. Burja . . . . .	989
<b>A high-efficiency automatic de-bubbling system for liquid silicone rubber</b> Visokozmogljiv sistem za odpravljanje mehurčkov v tekoči silikonski gumi C.-C. Kuo, C.-M. Huang . . . . .	995
<b>Impact toughness of WMD after MAG welding with micro-jet cooling</b> Udarna žilavost WMD po MAG varjenju z mikro-jet hlajenjem T. Wegrzyn, J. Piwnik, A. Borek, A. Kurc-Lisiecka . . . . .	1001
<b>Forming-limit diagrams and strain-rate-dependent mechanical properties of AA6019-T4 and AA6061-T4 aluminium sheet materials</b> Mejni diagrami preoblikovanja in odvisnost mehanskih lastnosti od hitrosti preoblikovanja aluminijevih pločevin iz AA6019-T4 in AA6061-T4 O. Çavuşoğlu, A. G. Leacock, H. Gürün . . . . .	1005
<b>Effect of alternative heat-treatment parameters on the aging behavior of short-fiber-reinforced 2124 Al composites</b> Vpliv alternativnih parametrov toplotne obdelave na staranje 2124 Al kompozita, ojačanega s kratkimi vlakni Y. Altunpak, S. Aslan, M. Oğuz Güler, H. Akbulut . . . . .	1011
<b>Letnik 50 (2016), 1–6 – Volume 50 (2016), 1–6 . . . . .</b>	1017

## MATERIALI IN TEHNOLOGIJE / MATERIALS AND TECHNOLOGY

## AVTORSKO KAZALO / AUTHOR INDEX

## LETNIK / VOLUME 50, 2016, 1–6, A–Ž

- A**  
 Adepu K. 229  
 Adolf Z. 419  
 Agarski B. 553  
 Akar N. 433  
 Akbulut H. 1011  
 Akinlabi E. T. 791  
 Akkurt A. 337  
 Aksakal B. 75  
 Altunpak Y. 1011  
 Anand M. D. 951  
 Andronescu E. 11  
 Andronescu E. 723  
 Anđić Z. 553  
 Antic A. 387  
 Anžel I. 981  
 Ardestani M. 281  
 Arh B. 971  
 Arikan H. 861  
 Arshad H. 33  
 Aslan S. 1011  
 Atýlgan Ý. 395  
 Ay M. 117  
 Ayday A. 719  
 Aydemir B. 511  
 Azimi R. 471
- B**  
 Baláš M. 479, 939  
 Balin K. 175  
 Ballikaya H. 81  
 Bally J. 571  
 Balos S. 387  
 Ban C. E. 11  
 Basiaga M. 153, 323  
 Bavdek G. 627  
 Bayraktar S. 591  
 Bečkovský D. 409, 607  
 Bek L. 319  
 Belas N. 127  
 Bendani K. 127  
 Bilek A. 165  
 Bílek O. 819  
 Bílek V. 813  
 Bindal C. 585  
 Blažek M. 491
- Błoch K. 189, 559  
 Borek A. 1001  
 Bouhamou N. E. 127  
 Bouziani T. 911  
 Bublíková D. 623  
 Budak I. 553  
 Bukhanovsky V. 523  
 Burja J. 451, 455, 829, 971, 989
- C**  
 Cakir M. C. 343  
 Caligulu U. 39  
 Can A. 861  
 Canikoğlu N. 739  
 Çavuşoğlu O. 1005  
 Çaydaş U. 117  
 Celebi Efe G. F. 585  
 Celin R. 455, 829  
 Cerny V. 749  
 Chaid R. 911  
 Chan K. C. 217  
 Chegroune R. 263  
 Chen S. H. 217  
 Chen W. 217  
 Cherneva S. 689  
 Chinnaraju K. 929  
 Chobola Z. 565  
 Chopart J.-P. 165  
 Cikrle P. 879  
 Cinert J. 253  
 Conradi M. 967  
 Cvetko D. 627  
 Çınar K. 861  
 Çöl M. 239
- Č**  
 Čep R. 439
- D**  
 Danyali D. 775  
 Davidson M. J. 373  
 Dinaharan I. 791  
 Dincă I. 11, 723  
 Dizaji H. R. 695  
 Dlouhy J. 159, 199  
 Dobrovolný P. 729  
 Dobrovolska T. 689
- Dobrzański L. A. 649  
 Doktor T. 301, 311  
 Dolák D. 729  
 Donik Č. 805  
 Došpiał M. 823  
 Dramicanin M. 387  
 Drochytka R. 749  
 Drygała A. 649  
 Dubovská R. 439  
 Dufka A. 147  
 Dvořák K. 683, 729  
 Dvořák P. 447  
 Dvorak Z. 195
- E**  
 Ebrahimi F. 663  
 Egrisogut Tiryaki A. 485  
 Erden M. A. 641  
 Erdogan S. E. 655  
 Ertan R. 223  
 Erzincanlı F. 239  
 Esme U. 337
- F**  
 Fajfar P. 767  
 Faruque M. R. I. 33, 307  
 Ficaí A. 11, 723  
 Fíla T. 301, 311, 413  
 Flašker J. 517  
 Frangež R. 797  
 Frieling G. 95
- G**  
 Gadakary S. 373  
 Garus S. 559  
 Georgiev M. 689  
 Ghernouti Y. 911  
 Girman V. 543  
 Gligorijević B. R. 89  
 Glodež S. 517  
 Godec M. 805  
 Gokhan Adar N. 485  
 Gomidželović L. 47  
 Gondro J. 559  
 Gopalakrishnan R. 929  
 Górká J. 617  
 Grajcar A. 713, 945

Grechanyuk M. 523  
 Gridasov A. 95  
 Gridasova E. 95  
 Gruszka K. 707  
 Grzegorzczak B. 677, 945  
 Gubeljak N. 571  
 Gunes I. 263, 269, 505  
 Guven G. 511  
 Guzej M. 289  
 Gül Koç F. 239  
 Gündüz S. 641  
 Gürün H. 1005

**H**

Hájková I. 683  
 Hardal G. 923  
 Hauserova D. 159  
 Heczko J. 579  
 Hertelé S. 571  
 Hnatkova E. 195  
 Hočevar M. 805  
 Holcapkova P. 869  
 Horsky J. 289  
 Hos J. 413  
 Hossain M. J. 873  
 Hoveida Marashi S. P. 761  
 Hršak D. 55  
 Hrabalikova M. 869  
 Hrabovský J. 17  
 Hroudová J. 137  
 Hu H. J. 381  
 Huang C.-M. 995  
 Huner U. 655

**I**

Iankov R. 689  
 Ibrahim K. 623  
 İpek M. 585  
 Iqbal Faruque M. R. 873  
 Isik Y. 343  
 Islam M. T. 307, 873  
 Islam Md. M. 33, 307  
 Islam S. S. 873

**J**

Jaćimović M. 59  
 Jandikova G. 869  
 Janjić M. 59  
 Javadi G. 663  
 Jeníček Š. 499  
 Jenko M. 981  
 Jirková H. 499, 891  
 Jiroušek O. 301, 311  
 Jonda E. 175

**K**

Kahraman F. 337  
 Kajzer A. 153  
 Kakhki Y. S. 611  
 Kalina L. 813  
 Kalinowska-Ozgowicz E. 677, 837  
 Kamberović Ž. 553  
 Kamińska M. 945  
 Kanat S. 505  
 Kang J. H. 17  
 Karabulut H. 641  
 Karabulut N. K. 739  
 Karaca F. 75  
 Karasinski P. 323  
 Karunakaran K. 211  
 Kaszuwara W. 537  
 Kayikci R. 433  
 Kazdal Zeytin H. 511  
 Keddám M. 263  
 Khakian M. G. 365  
 Khalaj O. 891  
 Kir D. 239  
 Kirik I. 353  
 Kirsever D. 739  
 Klein M. 95  
 Kocáb J. 579  
 Kocatepe K. 433  
 Kocijan A. 805, 829, 967, 981  
 Kolli M. 229  
 Komínek J. 207  
 Konopka K. 537  
 Koplík J. 813  
 Kores S. 601  
 Korkut I. 275  
 Kosec B. 553  
 Kosec G. 455  
 Kosňovská J. 419  
 Kostov A. 47  
 Koteswara Rao S. R. 357  
 Kottner R. 579  
 Koudelka P. 301, 311  
 Koudelka P. 413  
 Kouřil K. 439  
 Kovačič M. 69  
 Kozan R. 485  
 Kračun A. 451  
 Kracík P. 479, 939  
 Kroupa T. 295  
 Krystek J. 295, 579  
 Kubacki J. 175  
 Kubatík T. F. 257, 447  
 Kubina T. 891  
 Kulekci M. K. 337

Kumar G. R. 357  
 Kumar Khanra A. 373  
 Kunc K. 295  
 Kuo C.-C. 995  
 Kurc-Lisiecka A. 837, 1001  
 Kurka V. 419  
 Kurşun A. 23  
 Kurtaran H. 961  
 Kus A. 343  
 Kytýř D. 301, 413

**L**

Labus Zlatanovic D. 387  
 Lakouraj M. M. 471  
 Lamut J. 101  
 Lamut M. 767  
 Lau H. K. 217  
 Lazar T. 767  
 Leacock A. G. 1005  
 Lee P. J. 17  
 Lenik K. 677  
 Lišková A. 543  
 Lisiecki Ł. 783  
 Lisý M. 479, 939  
 Lojen G. 981  
 Lukaszewicz K. 175, 649  
 Lyubimova O. 95

**M**

Mašek B. 499, 623, 891  
 Machovsky M. 869  
 Maddah B. 663  
 Madej D. 29  
 Majerík J. 439  
 Małek M. 735  
 Maleki E. 851  
 Manasijević D. 47  
 Mansor M. F. 307  
 Marciniak J. 323  
 Marek I. 447  
 Marinšek M. 743  
 Matysiak W. 699  
 Matysík M. 565, 547  
 Mauder T. 3  
 Maziarz W. 837  
 Mebrouki A. 127  
 Medved J. 601  
 Melichar T. 147  
 Mercan S. 39  
 Mišović M. 59  
 Miazga A. 537  
 Michalčová A. 447  
 Michaljaníčova I. 331  
 Mihalíková M. 543



- Milašinović M. D. 89  
Milašinović V. D. 89  
Minakova R. 523  
Mirdamadi S. 365  
Mirdamadi T. S. 611  
Misák P. 491  
Mizera J. 735  
Mončeková M. 813  
Moon I. S. 211  
Moravcová B. 491  
Mostefa F. 127  
Motorcu A. R. 343  
Mrvar P. 767  
Mucha A. 649  
Muthuraman G. 211
- N**  
Nabiałek M. 189, 559, 823  
Nacházal J. 903  
Nait Abdellah Z. 263  
Nategh S. 365, 611  
Nikolić V. 553  
Novak D. 69  
Novák P. 447, 917  
Novotný R. 813  
Nový Z. 159, 199, 891
- O**  
Oğuz Güler M. 1011  
Okutan Baba B. 141  
Ondroušková J. 183  
Oprea O. 11  
Ozay C. 81  
Ozcatal M. 269  
Ozgowicz W. 677, 837  
Ozgun R. 337  
Öktem H. 239  
Özmen U. 141
- P**  
Pakuła D. 755  
Pala Z. 253  
Paszenda Z. 153, 323  
Paulin I. 461, 805  
Pazdera L. 7  
Pelín C.-E. 723  
Pelín G. 11, 723  
Pindor J. 419  
Piwnik J. 1001  
Plšková I. 547  
Płachcińska A. 713  
Požega E. 47  
Podany P. 199  
Podgornik B. 451, 461, 829, 971
- Pohanka M. 17, 183, 207, 575  
Pokorný P. 253  
Popović M. 403, 531  
Popović L'. 55  
Pospíšil J. 479, 939  
Pouranvari S. 663  
Prach O. 247, 427  
Price B. Y. 923  
Prijanović Tonkovič M. 101  
Prokopiuk vel Prokopowicz M. 649  
Puchnin M. 247, 427  
Pössl P. 491
- R**  
Rabehi B. 911  
Radetić T. 403, 531  
Radovanović R. V. 89  
Rahpaima G. 471  
Ram G. D. J. 357  
Ranjbarnodeh E. 775  
Ravindran D. 951  
Reif M. 137  
Ribarič S. 797  
Rimpelova S. 331  
Romhanji E. 403, 531  
Rousta A. 695  
Rovnaník P. 7  
Róžański M. 945  
Rozman J. 797  
Rudnytsky M. 523  
Rudolf R. 981  
Rusnáková S. 819  
Rypák P. 7
- S**  
Sahin M. 109  
Sajdl P. 331  
Salvetr P. 917  
Savas V. 81  
Sedlarik V. 869  
Sener B. 961  
Sidjanin L. 387  
Skalar T. 743  
Skoneczny W. 845  
Skowronek T. 783  
Skubisz P. 783  
Sláma P. 903  
Slepička P. 331  
Sokolar R. 885  
Sondor J. 175  
Stambolić A. 981  
Staszuk M. 699, 755  
Ştefan A. 11, 723  
Stetina J. 3
- Stoychev D. 689  
Sučík G. 55  
Sun Z. 381  
Svoboda J. 891  
Svobodová P. 447  
Szabóová A. 55  
Szczerba J. 29  
Szindler M. 649  
Szkłarek R. 699  
Szlązak K. 189  
Szota M. 189  
Szymańska J. 735
- Š**  
Šleichrt J. 413  
Šnajdárek L. 479  
Štádlér C. 891  
Štefane P. 571  
Štefková D. 879  
Štoudek R. 547  
Švorčík V. 331
- T**  
Tadić N. 59  
Taktak S. 263  
Tański T. 699, 755  
Tanyel Z. 433  
Tariqul Islam M. 33  
Tehovnik F. 989  
Thankaraj Mariapushpam C. J. 951  
Tichomirov V. 409, 607  
Timčaková K. 879  
Timčaková-Šamárková K. 7, 565  
Topal E. 23  
Toplan H. Ö. 739  
Topolář L. 7, 879  
Torkar M. 451, 461, 469, 829  
Trčka T. 547  
Trobentar B. 517  
Trudonoshyn O. 247, 427  
Truşcă R. 723  
Turgut Y. 591  
Turk J. 601  
Turkmen M. 39, 641  
Ulker S. 263  
Uzun E. 395  
Uzun G. 275
- U**  
Všianský D. 729  
Waele De W. 571  
Vajkay F. 409, 607
- W**  
Walke W. 153, 323

Walther F. 95  
Wegrzyn T. 1001  
Wiśniewska K. 29  
Wiśniewski P. 735  
Wiśniowski M. 699

**V**

Verleysen P. 571  
Voicu G. 11  
Vojtěch D. 447, 917  
Vončina M. 601  
Vorel I. 499, 623  
Votavová H. 575  
Vuković N. 47  
Vymazal T. 547

**Y**

Yalcinoz M. 39  
Yener S. C. 899  
Yener T. 899  
Yip N. 217  
Yılmaz V. 667

**Z**

Zabihollah A. 851  
Zach J. 137  
Zafošnik B. 517  
Žak A. 783  
Zalecki W. 783  
Zazi N. 165  
Zelič K. 805

Zemčík R. 295, 319  
Zengin M. 395  
Zeytýn S. 585, 899  
Zhang C. 523  
Zhang D. F. 381  
Zlámal P. 301  
Zupan K. 743  
Zygmuntowicz J. 537

**Ž**

Žaludek M. 819  
Živković D. 47  
Žužek B. 989  
Žužek M. C. 797

# MATERIALI IN TEHNOLOGIJE / MATERIALS AND TECHNOLOGY

## VSEBINSKO KAZALO / SUBJECT INDEX

### LETNIK / VOLUME 50, 2016, 1–6

#### Kovinski materiali – Metallic materials

<b>Improvement of the casting of special steel with a wide solid-liquid interface</b> Izboljšanje ulivanja posebnega jekla s širokim intervalom trdno-tekoče T. Mauder, J. Stetina . . . . .	3
<b>Corrosion of the refractory zirconia metering nozzle due to molten steel and slag</b> Korozija ognjeodporne cirkonske dozirne šobe s staljenim jeklom in žlindro K. Wiśniewska, D. Madej, J. Szczerba . . . . .	29
<b>X-ray radiography of AISI 4340-2205 steels welded by friction welding</b> Rentgenski pregled jekel AISI 4340-2205, varjenih s trenjem U. Caligulu, M. Yalcinoz, M. Turkmen, S. Mercan . . . . .	39
<b>Thermodynamic properties and microstructures of different shape-memory alloys</b> Termodinamične lastnosti in mikrostruktura različnih zlitin z oblikovnim spominom L. Gomidželović, E. Požega, A. Kostov, N. Vuković, D. Živković, D. Manasijević . . . . .	47
<b>The relationship between thermal treatment of serpentine and its reactivity</b> Ovisnost med toplotno obdelavo serpentina in njegovo aktivnostjo G. Sučik, A. Szabóová, L. Popović, D. Hršak . . . . .	55
<b>Deformations and velocities during the cold rolling of aluminium alloys</b> Deformacija in hitrosti pri hladnem valjanju aluminijevih zlitin M. Mišović, N. Tadić, M. Jaćimović, M. Janjić . . . . .	59
<b>Prediction of the chemical non-homogeneity of 30MnVS6 billets with genetic programming</b> Napovedovanje nehomogenosti kemijske sestave pri gredicah 30MnVS6 s pomočjo genetskega programiranja M. Kovačič, D. Novak . . . . .	69
<b>Effect of the TiBN coating on a HSS drill when drilling the MA8M Mg alloy</b> Vpliv TiBN prevleke na HSS svodru pri vrtanju MA8M Mg zlitine F. Karaca, B. Aksakal . . . . .	75
<b>Effects of friction-welding parameters on the morphological properties of an Al/Cu bimetallic joint</b> Vpliv parametrov tornega varjenja na morfološke lastnosti Al/Cu bimetalnega spoja V. D. Milašinović, R. V. Radovanović, M. D. Milašinović, B. R. Gligorijević . . . . .	89
<b>Optimizing the parameters for friction welding stainless steel to copper parts</b> Optimiranje parametrov pri tornem varjenju nerjavnega jekla na bakrene dele M. Sahin . . . . .	109
<b>WEDM cutting of Inconel 718 nickel-based superalloy: effects of cutting parameters on the cutting quality</b> WEDM rezanje nikljeve superzlitine Inconel 718: vpliv parametrov rezanja na kvaliteto rezanja U. Çaydaş, M. Ay . . . . .	117
<b>The effect of EO and steam sterilization on the mechanical and electrochemical properties of titanium Grade 4</b> Vpliv EO in sterilizacije s paro na mehanske in elektrokemijske lastnosti titana Grade 4 M. Basiaga, W. Walke, Z. Paszenda, A. Kajzer . . . . .	153
<b>Influence of the carbide-particle spheroidisation process on the microstructure after the quenching and annealing of 100CrMnSi6-4 bearing steel</b> Vpliv procesa sferoidizacije karbidnih delcev na mikrostrukturo jekla 100CrMnSi6-4 za ležaje po kaljenju in popušcanju J. Dlouhy, D. Hauserova, Z. Novy . . . . .	159
<b>Corrosion behavior and the weak-magnetic-field effect of aluminum packaging paper</b> Vpliv šibkega magnetnega polja na korozijo aluminijeve embalažne folije N. Zazi, J.-P. Chopart, A. Bilek . . . . .	165
<b>Characteristics of the AlTiCrN+DLC coating deposited with a cathodic arc and the PACVD process</b> Značilnosti AlTiCrN+DLC prevleke, nanešene s katodnim oblokrom in PACVD postopkom K. Lukaszkwicz, E. Jonda, J. Sondor, K. Balin, J. Kubacki . . . . .	175

<b>Magnetic properties and microstructure of a bulk amorphous Fe<sub>61</sub>Co<sub>10</sub>Ti<sub>3</sub>Y<sub>6</sub>B<sub>20</sub> alloy, fabricated as rods and tubes</b> Magnetne lastnosti in mikrostruktura masivne amorfne zlitine Fe <sub>61</sub> Co <sub>10</sub> Ti <sub>3</sub> Y <sub>6</sub> B <sub>20</sub> v obliki palic in cevi M. Nabiałek, K. Bloch, K. Szlązak, M. Szota . . . . .	189
<b>Recrystallization behaviour of a nickel-based superalloy</b> Obnašanje superzlitine na osnovi niklja pri rekristalizaciji P. Podany, Z. Novy, J. Dlouhy . . . . .	199
<b>Use of the ABI technique to measure the mechanical properties of aluminium alloys: effect of chemical composition on the mechanical properties of the alloys</b> Uporaba tehnike ABI za merjenje mehanskih lastnosti aluminijevih zlitin: vpliv kemijske sestave na mehanske lastnosti zlitin M. Puchnin, O. Trudonoshyn, O. Prach . . . . .	247
<b>Fe-Zn intermetallic phases prepared by diffusion annealing and spark-plasma sintering</b> Fe-Zn intermetalne faze, pripravljene z difuzijskim žarjenjem in s sintranjem v iskreči plazmi P. Pokorný, J. Cinert, Z. Pala . . . . .	253
<b>High-temperature oxidation of silicide-aluminide layer on the TiAl6V4 alloy prepared by liquid-phase siliconizing</b> Visokotemperaturna oksidacija plasti silicid-aluminid, pripravljene s silikoniziranjem s tekočo fazo zlitine TiAl6V4 T. F. Kubatík . . . . .	257
<b>Characterization and kinetics of plasma-paste-borided AISI 316 steel</b> Karakterizacija in kinetika plazma boriranja s pasto jekla AISI 316 R. Chegroune, M. Keddou, Z. Nait Abdallah, S. Ulker, S. Taktak, I. Gunes . . . . .	263
<b>The effects of cutting conditions on the cutting torque and tool life in the tapping process for AISI 304 stainless steel</b> Vpliv pogojev rezanja na moment pri rezanju in zdržljivost navojnega vreznika pri vrezovanju notranjih navojev v nerjavno jeklo AISI 304 G. Uzun, I. Korkut . . . . .	275
<b>Physicochemical properties of a Ti67 alloy after EO and steam sterilization</b> Fizikalno kemijske lastnosti zlitine Ti67 po EO in parni sterilizaciji W. Walke, M. Basiaga, Z. Paszenda, J. Marciniak, P. Karasinski . . . . .	323
<b>Analyzing the heat-treatment effect on the mechanical properties of free-cutting steels</b> Analiza vpliva toplotne obdelave na mehanske lastnosti avtomatnih jekel M. K. Kulekci, U. Esme, F. Kahraman, R. Ozgun, A. Akkurt . . . . .	337
<b>Analysis of the cutting temperature and surface roughness during the orthogonal machining of AISI 4140 alloy steel via the Taguchi method</b> Analiza temperature rezanja in hrapavosti površine s Taguchi metodo pri ortogonalni strojni obdelavi legiranega jekla AISI 4140 A. R. Motorcu, Y. Isik, A. Kus, M. C. Cakir . . . . .	343
<b>Weldability of Ti6Al4V to AISI 2205 with a nickel interlayer using friction welding</b> Preizkušanje varivosti pri varjenju s trenjem Ti6Al4V in AISI 2205 z vmesno plastjo niklja I. Kirik . . . . .	353
<b>Effect of activated flux and nitrogen addition on the bead geometry of borated stainless-steel GTA welds</b> Vpliv aktiviranega topila in dodatka dušika na geometrijo kopeli pri GTA zvarih boriranega nerjavnega jekla G. R. Kumar, G. D. J. Ram, S. R. Koteswara Rao . . . . .	357
<b>Microstructural evolution during the transient liquid-phase bonding of dissimilar nickel-based superalloys of IN738LC and NIMONIC 75</b> Razvoj mikrostrukture med spajanjem s prehodno tekočo fazo neenakih superzlitin na osnovi niklja IN738LC in NIMONIC 75 M. G. Khakian, S. Nategh, S. Mirdamadi . . . . .	365
<b>Workability behaviour of Cu-TiB<sub>2</sub> powder-metallurgy preforms during cold upsetting</b> Preoblikovalnost Cu-TiB <sub>2</sub> predoblik izdelanih z metalurgijo prahov med hladnim kovalnim preizkusom S. Gadakary, A. Kumar Khanra, M. J. Davidson . . . . .	373
<b>Effects of extrusion shear on the microstructures and a fracture analysis of a magnesium alloy in the homogenized state</b> Vplivi striženja med iztiskanjem homogenizirane magnezijeve zlitine na mikrostrukturo in na analizo preloma H. J. Hu, Z. Sun, D. F. Zhang . . . . .	381
<b>FSW welding of Al-Mg alloy plates with increased edge roughness using square pin tools of various shoulder geometries</b> FSW varjenje plošč iz Al-Mg zlitine s povečano hrapavostjo robov z orodjem s kvadratno konico in različno geometrijo bokov S. Balos, L. Sidjanin, M. Dramicanin, D. Labus Zlatanovic, A. Antic . . . . .	387
<b>Homogenization of an Al-Mg alloy and alligating failure: alloy ductility and fracture</b> Homogenizacija Al-Mg zlitine in krokodiljenje: duktilnost zlitine in prelom E. Romhanji, T. Radetić, M. Popović . . . . .	403
<b>Increasing micro-purity and determining the effects of the production with and without vacuum refining on the qualitative parameters of forged-steel pieces with a high aluminium content</b> Povečanje mikročistoče in določitev učinka proizvodnje, z vakuumskim rafiniranjem ali brez, na kvalitativne parametre kovanega jekla z visoko vsebnostjo aluminija V. Kurka, J. Pindor, J. Kosňovská, Z. Adolf . . . . .	419



<b>Use of the ABI technique to measure the mechanical properties of aluminium alloys: effect of heat-treatment conditions on the mechanical properties of alloys</b>	
Uporaba ABI tehnike za merjenje mehanskih lastnosti aluminijevih zlitin: vpliv pogojev toplotne obdelave na mehanske lastnosti zlitin	
O. Trudonoshyn, M. Puchnin, O. Prach . . . . .	427
<b>Investigation of the effect of holding time and melt stirring on the grain refinement of an A206 alloy</b>	
Preiskava vpliva časa zadrževanja in mešanja taline na zmanjšanje velikosti zrn zlitine A206	
N. Akar, Z. Tanyel, K. Kocatepe, R. Kayikci . . . . .	433
<b>Investigating the influence of cutting speed on the tool life of a cutting insert while cutting DIN 1.4301 steel</b>	
Preiskava vpliva hitrosti rezanja na zdržljivost vložka za rezanje pri rezanju jekla DIN 1.4301	
R. Dubovská, J. Majerík, R. Čep, K. Kouřil . . . . .	439
<b>NiAl intermetallic prepared with reactive sintering and subsequent powder-metallurgical plasma-sintering compaction</b>	
Reakcijsko sintranje in zgoščevanje s plazemskim sintranjem NiAl intermetalne zlitine	
A. Michalčová, D. Vojtěch, T. F. Kubatík, P. Novák, P. Dvořák, P. Svobodová, I. Marek . . . . .	447
<b>Microscopic characterization and particle distribution in a cast steel matrix composite</b>	
Mikroskopska karakterizacija in razporeditev delcev v kompozitu z matrico litega jekla	
A. Kračun, M. Torkar, J. Burja, B. Podgornik . . . . .	451
<b>A comparison of as-welded and simulated heat affected zone (HAZ) microstructures</b>	
Primerjava mikrostrukture toplotno vplivanega področja varjenega in simuliranih vzorcev	
R. Celin, J. Burja, G. Kosec . . . . .	455
<b>Degradation of an AISI 304 stainless-steel tank</b>	
Degradacija rezervoarja iz AISI 304 nerjavnega jekla	
M. Torkar, I. Paulin, B. Podgornik . . . . .	461
<b>Correlation of the heat-transfer coefficient at sprinkled tube bundle</b>	
Korelacija koeficienta prenosa toplote pri potresnem snopu cevi	
P. Kracík, L. Šnajdárek, M. Lisý, M. Baláš, J. Pospíšil . . . . .	479
<b>Investigation of wear behavior of borided AISI D6 steel</b>	
Preiskava obrabe boriranega jekla AISI D6	
I. Gunes, S. Kanat . . . . .	505
<b>Investigation of Portevin-Le Chatelier effect of hot-rolled Fe-13Mn-0.2C-1Al-1Si TWIP steel</b>	
Preiskava Portevin-Le Chatelier učinka pri vročem valjanju Fe-13Mn-0.2C-1Al-1Si TWIP jekla	
B. Aydemir, H. Kazdal Zeytin, G. Guven . . . . .	511
<b>Homogenization of an Al-Mg alloy and alligatoring failure: influence of the microstructure</b>	
Homogenizacija Al-Mg zlitine in krokodiljenje: vpliv mikrostrukture	
E. Romhanji, T. Radetić, M. Popović . . . . .	531
<b>Static and dynamic tensile characteristics of S420 and IF steel sheets</b>	
Statične in dinamične natezne lastnosti pločevine iz S420 in IF jekla	
M. Mihaliková, V. Girman, A. Lišková . . . . .	543
<b>Multi-criteria analysis of synthesis methods for Ni-based catalysts</b>	
Večkriterijska analiza sinteznih metod na osnovi Ni katalizatorja	
V. Nikolić, B. Agarški, Ž. Kamberović, Z. Anđić, I. Budak, B. Kosec . . . . .	553
<b>Influence of structural defects on the magnetic properties of massive amorphous Fe<sub>60</sub>Co<sub>10</sub>Mo<sub>2</sub>W<sub>x</sub>Y<sub>8</sub>B<sub>20-x</sub> (x = 1, 2) alloys produced with the injection casting method</b>	
Vpliv strukturnih napak na magnetne lastnosti masivne amorfnе zlitine Fe <sub>60</sub> Co <sub>10</sub> Mo <sub>2</sub> W <sub>x</sub> Y <sub>8</sub> B <sub>20-x</sub> (x = 1, 2), izdelane z metodo litja z vbrizgavanjem	
J. Gondro, K. Bloch, M. Nabiałek, S. Garus . . . . .	559
<b>Possibilities of NUS and Impact-Echo methods for monitoring steel corrosion in concrete</b>	
Možnosti metod NUS in Udarec-odmev za kontrolo korozije jekla v betonu	
K. Timčaková-Šamárková, M. Matysík, Z. Chobola . . . . .	565
<b>Characterization of heterogeneous arc welds through miniature tensile testing and Vickers-hardness mapping</b>	
Karakterizacija heterogenih zvarov s pomočjo miniaturnih nateznih preizkusov in matričnimi meritvami trdote po Vickersu	
S. Hertelé, J. Bally, N. Gubeljak, P. Štefane, P. Verleysen, W. De Waele . . . . .	571
<b>Overcooling in overlap areas during hydraulic descaling</b>	
Podhladitev in prekrivanje področij med hidravličnim razškajanjem	
M. Pohanka, H. Votavová . . . . .	575
<b>Development of aluminium alloys for aerosol cans</b>	
Razvoj aluminijevih zlitin za aerosol doze	
S. Kores, J. Turk, J. Medved, M. Vončina . . . . .	601

<b>Microstructure and properties of the high-temperature (HAZ) of thermo-mechanically treated S700MC high-yield-strength steel</b> Mikrostruktura in lastnosti visoko temperaturnega območja zvara (HAZ) termo-mehansko obdelanega jekla S700MC z visoko mejo plastičnosti J. Górka . . . . .	617
<b>New concept for manufacturing closed die forgings of high strength steels</b> Nov koncept izdelave odkovkov iz visokotrnostnih jekel v zaprtih utopih K. Ibrahim, I. Vorel, D. Bublíková, B. Mašek . . . . .	623
<b>Effect of the addition of niobium and aluminium on the microstructures and mechanical properties of micro-alloyed PM steels</b> Vpliv dodatka niobija in aluminija na mikrostrukturo in mehanske lastnosti mikrolegiranih PM jekel S. Gündüz, M. A. Erden, H. Karabulut, M. Türkmen . . . . .	641
<b>The effect of the welding parameters and the coupling agent on the welding of composites</b> Vpliv parametrov varjenja in sredstva za spajanje na varjenje kompozitov S. E. Erdogan, U. Huner . . . . .	655
<b>Investigation of hole profiles in deep micro-hole drilling of AISI 420 stainless steel using powder-mixed dielectric fluids</b> Preiskava profilov luknje pri globokem vrtnanju mikroluknje v AISI 420 nerjavnem jeklu s pomočjo dielektrične tekočine s primešanim prahom V. Yilmaz . . . . .	667
<b>The phenomenon of reduced plasticity in low-alloyed copper</b> Pojav zmanjšanja plastičnosti malo legiranega bakra W. Ozgowicz, E. Kalinowska-Ozgowicz, B. Grzegorzcyk, K. Lenik . . . . .	677
<b>Investigation of the mechanical properties of electrochemically deposited Au-In alloy films using nano-indentation</b> Preiskava mehanskih lastnosti elektrokemijsko nanešenega filma zlitine Au-In z nanovtiskovanjem S. Cherneva, R. Iankov, M. Georgiev, T. Dobrovolska, D. Stoychev . . . . .	689
<b>Surface treatment of heat-treated cast magnesium and aluminium alloys</b> Obdelava površine toplotno obdelanih magnezijevih in aluminijevih livnih zlitin T. Tański, M. Wiśniowski, W. Matysiak, M. Staszuk, R. Szklarek . . . . .	699
<b>Analysis of the structural-defect influence on the magnetization process in and above the Rayleigh region</b> Analiza vpliva strukturnih defektov na proces magnetizacije v in nad Rayleigh področjem K. Gruszka . . . . .	707
<b>Effect of sulphide inclusions on the pitting-corrosion behaviour of high-Mn steels in chloride and alkaline solutions</b> Vpliv sulfidnih vključkov na jamičasto korozijo jekel z visoko vsebnostjo Mn v raztopinah kloridov in alkalij A. Grajcar, A. Plachcińska . . . . .	713
<b>Influence of Na<sub>2</sub>SiF<sub>6</sub> on the surface morphology and corrosion resistance of an AM60 magnesium alloy coated by micro arc oxidation</b> Vpliv Na <sub>2</sub> SiF <sub>6</sub> na morfologijo površine in korozijsko odpornost magnezijeve zlitine AM60, prekrte z mikrooblačno oksidacijo A. Ayday . . . . .	719
<b>Investigation studies involving wear-resistant ALD/PVD hybrid coatings on sintered tool substrates</b> Preiskave obrabne odpornosti hibridnega nanosa ALD/PVD na sintranem orodju M. Staszuk, D. Pakuła, T. Tański . . . . .	755
<b>Dissimilar spot welding of DQSK/DP600 steels: the weld-nugget growth</b> Točkasto varjenje jekel DQSK/DP600: rast jedra zvara S. P. Hoveida Marashi . . . . .	761
<b>Armour plates from Kozlov rob – analyses of two unusual finds</b> Oklepni plošči s Kozlovega roba – analize dveh nenavadnih najdb T. Lazar, P. Mrvar, M. Lamut, P. Fajfar . . . . .	767
<b>Numerical and experimental investigation of the effect of hydrostatic pressure on the residual stress in boiler-tube welds</b> Numerična in eksperimentalna preiskava vpliva hidrostatskega tlaka na zaostale napetosti v zvaru na kotlovski cevi D. Danyali, E. Ranjbarnodeh . . . . .	775
<b>Effect of direct cooling conditions on the microstructure and properties of hot-forged HSLA steels for mining applications</b> Vpliv pogojev ohlajanja na mikrostrukturo in lastnosti vroče kovanih HSLA jekel za uporabo v rudarstvu P. Skubisz, Ł. Lisiecki, T. Skowronek, A. Żak, W. Zalecki . . . . .	783
<b>Influence of the tool rotational speed on the microstructure and joint strength of friction-stir spot-welded pure copper</b> Vpliv hitrosti vrtenja orodja na mikrostrukturo in trdnost torno vrtilno točkasto zvarjenega spoja čistega bakra I. Dinaharan, E. T. Akinlabi . . . . .	791
<b>Influence of different production processes on the biodegradability of an FeMn17 alloy</b> Vpliv različnih procesov izdelave na biorazgradljivost zlitine FeMn17 A. Kocijan, I. Paulin, Č. Donik, M. Hočevár, K. Zelič, M. Godec . . . . .	805

<b>Influence of solidification speed on the structure and magnetic properties of Nd<sub>10</sub>Fe<sub>81</sub>Zr<sub>1</sub>B<sub>6</sub> in the as-cast state</b> Vpliv hitrosti strjevanja na strukturo in magnetne lastnosti zlitine Nd <sub>10</sub> Fe <sub>81</sub> Zr <sub>1</sub> B <sub>6</sub> v litem stanju M. Dośpiał, M. Nabiałek . . . . .	823
<b>Metalografska preiskava in korozijska odpornost zvarov feritnega nerjavnega jekla</b> Metallographic investigation and corrosion resistance of welds of ferritic stainless steels M. Torkar, A. Kocijan, R. Celin, J. Burja, B. Podgornik . . . . .	829
<b>The microstructure of metastable austenite in X5CrNi18-10 steel after its strain-induced martensitic transformation</b> Mikrostruktura metastabilnega avstenita po pretvorbi v napetostno inducirani martenziti v jeklu X5CrNi18-10 A. Kurc-Lisiecka, W. Ozgowicz, E. Kalinowska-Ozgowicz, W. Maziarz . . . . .	837
<b>Analysis of twin-roll casting AA8079 alloy 6.35-<math>\mu</math>m foil rolling process</b> Analiza procesa valjanja 6,35 $\mu$ m folije iz zlitine AA8079 ulite med dvema valjema A. Can, H. Arıkan, K. Çınar . . . . .	861
<b>Behaviour of new ods alloys under single and multiple deformation</b> Obnašanje novih ods zlitin pri enojni in večkratni deformaciji B. Mašek, O. Khalaj, Z. Nový, T. Kubina, H. Jirkova, J. Svoboda, C. Štádlr . . . . .	891
<b>Electromagnetic-shielding effectiveness and fracture behavior of laminated (Ni–NiAl<sub>3</sub>) composites</b> Učinkovitost elektromagnetne zaščite in obnašanje pri lomu laminiranega kompozita (Ni–NiAl <sub>3</sub> ) T. Yener, S. C. Yener, S. Zeytin . . . . .	899
<b>Effect of thermomechanical treatment on the intergranular corrosion of Al-Mg-Si-Type alloy bars</b> Vpliv termomehanske predelave na interkristalno korozijo palic iz zlitin Al-Mg-Si P. Sláma, J. Nacházal . . . . .	903
<b>Porous magnesium alloys prepared by powder metallurgy</b> Porozne magnezijeve zlitine, izdelane s pomočjo metalurgije prahov P. Salvetr, P. Novák, D. Vojtěch . . . . .	917
<b>The size effect of heat-transfer surfaces on boiling</b> Vpliv velikosti površin, ki prenašajo toploto na vrenje P. Kracík, M. Balas, M. Lisy, J. Pospíšil . . . . .	939
<b>Effect of gas atmosphere on the non-metallic inclusions in laser-welded trip steel with Al and Si additions</b> Vpliv plinske atmosfere na nekovinske vključke v lasersko varjenem trip jeklu z dodatkom Al in Si A. Grajcar, M. Róžański, M. Kamińska, B. Grzegorzcyk . . . . .	945
<b>Machining parameters influencing in electro chemical machining on AA6061 MMC</b> Parametri strojne obdelave, ki vplivajo na elektrokemijsko strojno obdelavo AA6061 MMC C. J. Thankaraj Mariapushpam, D. Ravindran, M. D. Anand . . . . .	951
<b>Modeling the deep drawing of an AISI 304 stainless-steel rectangular cup using the finite-element method and an experimental validation</b> Modeliranje globokega vleka pravokotne čaše iz AISI 304 nerjavnega jekla z metodo končnih elementov in z eksperimentalnim preverjanjem B. Sener, H. Kurtaran . . . . .	961
<b>Electroslag remelting: A process overview</b> Elektropretaljevanje pod žlindro – pregled procesa B. Arh, B. Podgornik, J. Burja . . . . .	971
<b>Continuous vertical casting of a NiTi alloy</b> Vertikalno kontinuirno litje NiTi zlitine A. Stambolić, I. Anžel, G. Lojen, A. Kocijan, M. Jenko, R. Rudolf . . . . .	981
<b>Hot tensile testing of SAF 2205 duplex stainless steel</b> Vročni natezni preskusi dupleks nerjavnega jekla SAF 2205 F. Tehovnik, B. Žužek, J. Burja . . . . .	989
<b>Impact toughness of WMD after MAG welding with micro-jet cooling</b> Udarna žilavost WMD po MAG varjenju z mikro-jet hlajenjem T. Wegrzyn, J. Piwnik, A. Borek, A. Kurc-Lisiecka . . . . .	1001
<b>Forming-limit diagrams and strain-rate-dependent mechanical properties of AA6019-T4 and AA6061-T4 aluminium sheet materials</b> Mejni diagrami preoblikovanja in odvisnost mehanskih lastnosti od hitrosti preoblikovanja aluminijevih pločevin iz AA6019-T4 in AA6061-T4 O. Çavuşoğlu, A. G. Leacock, H. Gürün . . . . .	1005
<b>Effect of alternative heat-treatment parameters on the aging behavior of short-fiber-reinforced 2124 Al composites</b> Vpliv alternativnih parametrov toplotne obdelave na staranje 2124 Al kompozita, ojačanega s kratkimi vlakni Y. Altunpak, S. Aslan, M. Oğuz Güler, H. Akbulut . . . . .	1011
Materiali in tehnologije / Materials and technology 50 (2016) 6, 1017–1040	1035

## Anorganski materiali – Inorganic materials

<b>Non-traditional non-destructive testing of the alkali-activated slag mortar during the hardening</b> Netradicionalno neporušno preizkušanje z alkalijami aktivirane malte med strjevanjem L. Topolář, P. Rypák, K. Timčáková-Šamárková, L. Pazdera, P. Rovnaník . . . . .	7
<b>Investigation of hole effects on the critical buckling load of laminated composite plates</b> Preiskava vpliva luknje na kritično upogibno obremenitev laminiranih kompozitnih plošč A. Kurşun, E. Topal . . . . .	23
<b>Characterisation of the mechanical and corrosive properties of newly developed glass-steel composites</b> Karakterizacija mehanskih in korozijskih lastnosti novo razvitih kompozitov steklo-jeklo O. Lyubimova, E. Gridasova, A. Gridasov, G. Frieling, M. Klein, F. Walther . . . . .	95
<b>Phase analysis of the slag after submerged-arc welding</b> Analiza faz v žlindri pri obločnem varjenju pod praškom M. Prijanovič Tonkovič, J. Lamut . . . . .	101
<b>Composites based on inorganic matrices for extreme exposure conditions</b> Kompoziti z anorgansko osnovo za izpostavitve ekstremnim razmeram A. Dufka, T. Melichar . . . . .	147
<b>Enhanced stability and electrochemical performance of a BaTiO<sub>3</sub>/PbO<sub>2</sub> electrode via a layer obtained with layer electrodeposition</b> Izboljšana stabilnost in elektrokemijska zmogljivost elektrode BaTiO <sub>3</sub> /PbO <sub>2</sub> , izdelane z elektrodepozicijo plast na plast G. Muthuraman, K. Karunakaran, I. S. Moon . . . . .	211
<b>Deformation behaviour of amorphous Fe-Ni-W/Ni bilayer-confined bulk metallic glasses</b> Obnašanje deformiranega, amorfnega, na dve plasti omejenega kovinskega stekla Fe-Ni-W/Ni H. K. Lau, N. Yip, S. H. Chen, W. Chen, K. C. Chan . . . . .	217
<b>Synergistic effect of organic- and ceramic-based ingredients on the tribological characteristics of brake friction materials</b> Sinergističen vpliv sestavin z organsko in keramično osnovo na tribološke značilnosti materialov za torne zavore R. Ertan . . . . .	223
<b>Chemical synthesis and densification behavior of Ag/ZnO metal-matrix composites</b> Obnašanje Ag/ZnO kompozita s kovinsko osnovo pri kemijski sintezi in zgoščevanju M. Ardestani . . . . .	281
<b>Tensile and compressive tests of textile composites and results analysis</b> Natezni in tlačni preizkusi tekstilnih kompozitov in analiza rezultatov K. Kunc, T. Kroupa, R. Zemčík, J. Krystek . . . . .	295
<b>Printed microstrip line-fed patch antenna on a high-dielectric material for C-band applications</b> Tiskana mikrotrakasta linijsko napajana krpasta antena na visoko dielektričnem materialu za uporabo v C-pasu Md. M. Islam, M. R. I. Faruque, M. F. Mansor, M. T. Islam . . . . .	307
<b>Compressive properties of auxetic structures produced with direct 3D printing</b> Stiskanje struktur materialov z negativnim Poissonovim razmerjem, proizvedenih z neposrednim tridimenzionalnim tiskanjem P. Koudelka, O. Jiroušek, T. Fíla, T. Doktor . . . . .	311
<b>Improvement of selective copper extraction from a heat-treated chalcopyrite concentrate with atmospheric sulphuric-acid leaching</b> Izboljšanje selektivne ekstrakcije bakra iz toplotno obdelanega koncentrata halkopirita z luženjem z žvepleno kislino na zraku E. Uzun, M. Zengin, İ. Atilgan . . . . .	395
<b>Assessment of tubular light guides with respect to building physics</b> Ocena cevastih vodnikov svetlobe glede na gradbeno fiziko F. Vajkay, D. Bečkovský, V. Tichomirov . . . . .	409
<b>Creep behaviour of a short-fibre C/PPS composite</b> Vedenje kratkih vlaken C/PPS kompozitov pri lezenju T. Fíla, P. Koudelka, D. Kytýř, J. Hos, J. Šleichrt . . . . .	413
<b>Vapour-phase condensed composite materials based on copper and carbon</b> Kompoziti na osnovi bakra in ogljika, kondenzirani iz plinske faze V. Bukhanovsky, M. Rudnytsky, M. Grechanyuk, R. Minakova, C. Zhang . . . . .	523
<b>Metal particles size influence on graded structure in composite Al<sub>2</sub>O<sub>3</sub>-Ni</b> Vpliv velikosti kovinskih delcev na gradientno strukturo kompozita Al <sub>2</sub> O <sub>3</sub> -Ni J. Zygmuntowicz, A. Miazga, K. Konopka, W. Kaszuwara . . . . .	537
<b>Fabrication and properties of SiC reinforced copper-matrix-composite contact material</b> Izdelava in lastnosti s SiC utrjenega kompozitnega materiala na osnovi bakra G. F. Celebi Efe, M. İpek, S. Zeytin, C. Bindal . . . . .	585



<b>Impression relaxation and creep behavior of Al/SiC nanocomposite</b> Sprostitve vtisa in obnašanje Al/SiC nanokompozita pri lezenju Y. S. Kakhki, S. Nategh, T. S. Mirdamadi . . . . .	611
<b>Helium atom scattering – a versatile technique in studying nanostructures</b> Sipanje atomov helija – vsestranska tehnika za študij nanostruktur G. Bavdek, D. Cvetko . . . . .	627
<b>Characteristics of dye-sensitized solar cells with carbon nanomaterials</b> Značilnosti na fiksirano barvo občutljivih solarnih celic z ogljikovimi nanomateriali L. A. Dobrzański, A. Mucha, M. Prokopiuk vel Prokopowicz, M. Szindler, A. Drygała, K. Lukaszewicz . . . . .	649
<b>The effect of high-speed grinding technology on the properties of fly ash</b> Vpliv tehnologije hitrega mletja na lastnosti letečega pepela K. Dvořák, I. Hájková . . . . .	683
<b>Growth of K<sub>2</sub>CO<sub>3</sub>-doped KDP crystal from an aqueous solution and an investigation of its physical properties</b> Rast KDP kristalov z dodatkom K <sub>2</sub> CO <sub>3</sub> iz vodne raztopine in preiskava njihovih fizikalnih lastnosti A. Rousta, H. R. Dizaji . . . . .	695
<b>Rheological properties of alumina ceramic slurries for ceramic shell-mould fabrication</b> Reološke lastnosti gošče iz glinice za izdelavo keramičnih kalupov J. Szymańska, P. Wiśniewski, M. Małek, J. Mizera . . . . .	735
<b>Effect of mechanical activation on the synthesis of a magnesium aluminate spinel</b> Vpliv mehanske aktivacije na sintezo magnezij-aluminatnega špinela D. Kirsever, N. K. Karabulut, N. Canikoğlu, H. Ö. Toplan . . . . .	739
<b>Phase and microstructure development of LSCM perovskite materials for SOFC anodes prepared by the carbonate-coprecipitation method</b> Razvoj kristalnih faz in mikrostrukture LSCM perovskitnih materialov za SOFC anode, pripravljenih s karbonatno metodo koprecipitacije K. Zupan, M. Marinšek, T. Skalar . . . . .	743
<b>The structure and morphology of the surface of duplex layers after saturation of the base layer with carbon</b> Struktura in morfologija površine dupleks plasti po nasičenju osnovne plasti z ogljikom W. Skoneczny . . . . .	845
<b>A new wideband negative-refractive-index metamaterial</b> Novi širokopasovni metamaterial z negativnim lomnim količnikom S. S. Islam, M. R. Iqbal Faruque, M. J. Hossain, M. T. Islam . . . . .	873
<b>Non-traditional whiteware based on calcium aluminate cement</b> Netradicionalni porcelan na osnovi kalcij aluminatnega cementa R. Sokolar . . . . .	885
<b>Surface and anticorrosion properties of hydrophobic and hydrophilic TiO<sub>2</sub> coatings on a stainless-steel substrate</b> Površinske in protikorozijske lastnosti hidrofobnih in hidrofilnih TiO <sub>2</sub> prevlek na jekleni podlagi M. Conradi, A. Kocijan . . . . .	967
<b>A high-efficiency automatic de-bubbling system for liquid silicone rubber</b> Visokozmogljiv sistem za odpravljanje mehurčkov v tekoči silikonski gumi C.-C. Kuo, C.-M. Huang . . . . .	995
<b>Organski materiali – Organic materials</b>	
<b>Deformation behaviour of a natural-shaped bone scaffold</b> Obnašanje naravno oblikovanega ogrodja kosti pri deformaciji D. Kytýř, T. Doktor, O. Jiroušek, T. Fíla, P. Koudelka, P. Zlámal . . . . .	301
<b>Investigation of the mechanical properties of a cork/rubber composite</b> Raziskava mehanskih lastnosti kompozita pluta/guma R. Kottner, J. Kocáb, J. Heczko, J. Krystek . . . . .	579
<b>Measurement of bio-impedance on an isolated rat sciatic nerve obtained with specific current stimulating pulses</b> Meritev bioimpedance na izoliranem živcu Ischiadicus pri podgani, vzbujenem s posebnimi tokovnimi stimulacijskimi impulzi J. Rozman, M. C. Žužek, R. Frangež, S. Ribarič . . . . .	797
<b>Polimeri – Polymers</b>	
<b>Effects of an epoxy-resin-fiber substrate for a <math>\Omega</math>-shaped microstrip antenna</b> Vpliv z vlakni ojačane epoksi podlage pri $\Omega$ -obliki mikrotrakaste antene Md. M. Islam, M. R. I. Faruque, M. Tariqul Islam, H. Arshad . . . . .	33
Materiali in tehnologije / Materials and technology 50 (2016) 6, 1017–1040	1037

**Effect of the skin-core morphology on the mechanical properties of injection-moulded parts**

- Vpliv morfologije skorja-jedro na mehanske lastnosti vbrizganih delov  
E. Hnatkova, Z. Dvorak . . . . . 195

**Surface properties of a laser-treated biopolymer**

- Lastnosti površine biopolimera, obdelanega z laserjem  
I. Michaljaničova, P. Slepíčka, S. Rimpelova, P. Sajdl, V. Švorčík . . . . . 331

**Organosoluble xanthone-based polyimides: synthesis, characterization, antioxidant activity and heavy-metal sorption**

- Organsko topni poliamidi na osnovi ksantona: sinteza, karakterizacija, antioksidativna aktivnost in sorpcija težkih kovin  
M. M. Lakouraj, G. Rahpaima, R. Azimi . . . . . 471

**The influence of surface coatings on the tooth tip deflection of polymer gears**

- Vpliv površinskih prevlek na poves vrha zoba polimernih zobnikov  
B. Trobentar, S. Glodež, J. Flašker, B. Zafošnik . . . . . 517

**Investigation of the cutting forces and surface roughness in milling carbon-fiber-reinforced polymer composite material**

- Preiskava sil rezanja in hrapavosti površine pri rezkanju kompozitnega polimernega materiala, ojačanega z ogljikovimi vlakni  
S. Bayraktar, Y. Turgut . . . . . 591

**Chemical cross-linking of chitosan/polyvinyl alcohol electrospun nanofibers**

- Kemijsko zamreženje elektro sprednih nanovlaken iz hitosan/polivinil alkohola  
S. Pouranvari, F. Ebrahimi, G. Javadi, B. Maddah . . . . . 663

**Mechanical properties of polyamide/carbon-fiber-fabric composites**

- Mehanske lastnosti kompozitne tkanine iz poliamid/ogljikovih vlaken  
C.-E. Pelin, G. Pelin, A. Ștefan, E. Andronescu, I. Dincă, A. Ficai, R. Trușcă . . . . . 723

**Cutting-tool performance in the end milling of carbon-fiber-reinforced plastics**

- Zmogljivost rezilnega orodja pri rezkanju plastike, ojačane z ogljikovimi vlakni  
O. Bílek, S. Rusnáková, M. Žaludek . . . . . 819

**Antimicrobial modification of polypropylene with silver nanoparticles immobilized on zinc stearate**

- Protimikrobno spreminjanje polipropilena z nanodelci srebra, imobiliziranih na cinkovem stearatu  
G. Jandikova, P. Holcapkova, M. Hrabalíkova, M. Machovsky, V. Sedlarik . . . . . 869

**Nanomateriali in nanotehnologije – Nanomaterials and nanotechnology****Multi-walled carbon nanotubes effect in polypropylene nanocomposites**

- Vpliv večstenskih ogljikovih nanocevk v nanokompozitih iz polipropilena  
C. E. Ban, A. Stefan, I. Dinca, G. Pelin, A. Ficai, E. Andronescu, O. Oprea, G. Voicu . . . . . 11

**Investigation of the adhesion and wear properties of borided AISI H10 steel**

- Preiskava adhezije in obrabnih lastnosti boriranega jekla AISI H10  
I. Gunes, M. Ozcatay . . . . . 269

**Influence of nano-sized cobalt oxide additions on the structural and electrical properties of nickel-manganite-based NTC thermistors**

- Vpliv dodatka nanodelcev kobaltovega oksida na zgradbo in električne lastnosti ntc termistorjev na osnovi nikljevega manganita  
G. Hardal, B. Y. Price . . . . . 923

**Gradbeni materiali – Materials in civil engineering****Influence of dredged sediment on the shrinkage behavior of self-compacting concrete**

- Vpliv izkopanih sedimentov na krčenje samozgoščevalnega betona  
N. E. Bouhamou, F. Mostefa, A. Mebrouki, K. Bendani, N. Belas . . . . . 127

**Study of the properties and hygrothermal behaviour of alternative insulation materials based on natural fibres**

- Študij lastnosti in higrotermalno obnašanje alternativnih izolacijskih materialov na osnovi naravnih vlaken  
J. Zach, M. Reif, J. Hroudová . . . . . 137

**Acoustic and electromagnetic emission of lightweight concrete with polypropylene fibers**

- Akustična in elektromagnetna emisija lahkega betona s polipropilenskimi vlakni  
R. Štouděk, T. Trčka, M. Matysík, T. Vymazal, I. Plšková . . . . . 547

**Evaluation of the grindability of recycled glass in the production of blended cements**

- Ocena sposobnosti drobljenja recikliranega stekla pri proizvodnji mešanih cementov  
K. Dvořák, D. Dolák, D. Všianský, P. Dobrovolný . . . . . 729

**Artificial aggregate from sintered coal ash**

- Umetni agregat iz sintranega pepela premoga  
V. Cerny, R. Drochytka . . . . . 749

<b>Effect of a combination of fly ash and shrinkage-reducing additives on the properties of alkali-activated slag-based mortars</b> Vpliv kombinacije letečega pepela in dodatka za zmanjšanje krčenja na lastnosti malte iz z alkalijami aktivirane žindre	
V. Bílek, L. Kalina, J. Koplík, M. Mončeková, R. Novotný	813
<b>Evaluation of the degree of degradation using the impact-echo method in civil engineering</b> Ocena stopnje degradacije v gradbeništvu z uporabo metode odmeva zvočnih valov	
D. Štefková, K. Timčaková, L. Topolář, P. Cikrle	879
<b>Valorization of brick wastes in the fabrication of concrete blocks</b> Ocena odpadkov iz opeke pri proizvodnji betonskih zidakov	
Y. Ghernouti, B. Rabehi, T. Bouziani, R. Chaid	911
<b>Durability of alumina silicate concrete based on slag/fly-ash blends against acid and chloride environments</b> Zdržljivost betona na osnovi glinice in silikatov iz mešanice žindra/leteči pepel na kislino in kloridno okolje	
R. Gopalakrishnan, K. Chinnaraju	929
<b>Numerične metode – Numerical methods</b>	
<b>Experimental and numerical study of hot-steel-plate flatness</b> Eksperimentalni in numerični študij ravnosti vročih plošč iz jekla	
J. Hrabovský, M. Pohanka, P. J. Lee, J. H. Kang	17
<b>Application of the Taguchi method to select the optimum cutting parameters for tangential cylindrical grinding of AISI D3 tool steel</b> Uporaba Taguchi metode za izbiro optimalnih parametrov odrezavanja pri tangencialnem cilindričnem brušenju orodnega jekla AISI D3	
C. Ozay, H. Ballikaya, V. Savas	81
<b>Prediction of the elastic moduli of chicken-feather-reinforced PLA and a comparison with experimental results</b> Napovedovanje modulov elastičnosti PLA, ojačanega s piščančjim perjem in primerjava z eksperimentalnimi rezultati	
U. Özmen, B. Okutan Baba	141
<b>Implicit numerical multidimensional heat-conduction algorithm parallelization and acceleration on a graphics card</b> Paralelizacija in pospešitev implicitnega numeričnega večdimenzijskega algoritma prevajanja toplote na grafični kartici	
M. Pohanka, J. Ondroušková	183
<b>Estimation of the number of forward time steps for the sequential Beck approach used for solving inverse heat-conduction problems</b> Ugotavljanje števila vnaprejšnjih časovnih korakov za sekvenčni Beckov približek pri reševanju problemov inverzne toplotne prevodnosti	
J. Komínek, M. Pohanka	207
<b>Optimization of the parameters for the surfactant-added EDM of a Ti–6Al–4V alloy using the GRA-Taguchi method</b> Optimizacija površinsko aktivnih mešanih EDM parametrov na Ti-6Al-4V zlitini z uporabo GRA-Taguchi metode	
M. Kolli, K. Adepu	229
<b>Determination of the cutting-tool performance of high-alloyed white cast iron (Ni-Hard 4) using the Taguchi method</b> Določanje zmogljivosti rezalnih orodij na močno legiranem belem litem železu (Ni-Hard 4) z uporabo Taguchi metode	
D. Kir, H. Öktem, M. Çöl, F. Gül Koç, F. Erzincanlı	239
<b>Experimental verifications and numerical thermal simulations of automobile lamps</b> Eksperimentalna preverjanja in numerične toplotne simulacije avtomobilskih žarometov	
M. Guzej, J. Horský	289
<b>Model of progressive failure for composite materials using the 3D Puck failure criterion</b> Model postopnega popuščenja kompozitnega materiala z uporabo Puckovega tridimenzionalnega kriterija porušitve	
L. Bek, R. Zemčík	319
<b>Mathematical modeling of a cement raw-material blending process using a neural network</b> Matematično modeliranje postopka mešanja sestavin cementa s pomočjo nevronske mreže	
A. Egrisogut Tiryaki, R. Kozan, N. Gokhan Adar	485
<b>Possibilities of determining the air-pore content in cement composites using computed tomography and other methods</b> Možnosti določanja vsebnosti zračnih por v cementnih kompozitih z uporabo računalniške tomografije in drugih metod	
B. Moravcová, P. Pössl, P. Misák, M. Blažek	491
<b>Material and technological modelling of closed-die forging</b> Materialno-tehnološko modeliranje kovanja v zaprtem utopu	
I. Vorel, Š. Jeníček, H. Jirková, B. Mašek	499
<b>Computer tools to determine physical parameters in wooden houses</b> Določanje fizikalnih parametrov z računalniškimi orodji v lesenih hišah	
D. Bečkovský, F. Vajkay, V. Tichomirov	607
Materiali in tehnologije / Materials and technology 50 (2016) 6, 1017–1040	1039

LETNO KAZALO – INDEX

**Modeling of shot-peening effects on the surface properties of a (TiB + TiC)/Ti-6Al-4V composite employing artificial neural networks**

Modeliranje vpliva hladnega površinskega kovanja na lastnosti površine (TiB + TiC)/Ti-6Al-4V kompozita s pomočjo umetnih nevronskih mrež

E. Maleki, A. Zabihollah. . . . . 851

**Editor's Preface – Predgovor urednika**

**Predgovor urednika/Editor's preface**

M. Torkar . . . . . 469

**Predgovor urednika/Editor's preface**

P. J. McGuiness. . . . . 639

**Letno kazalo – Index**

Letnik 50 (2016), 1–6 – Volume 50 (2016), 1–6 . . . . . 995